frontiers | Research Topics

Host cellular responses to viruses

Edited by
Jue Liu, Yongqun Oliver He, Cao Yong chang and Li Yongqing

Published in
Frontiers in Microbiology

ISSN 1664-8714
ISBN 978-2-83251-424-5
DOI 10.3389/978-2-83251-424-5

About Frontiers

Frontiers is more than just an open access publisher of scholarly articles: it is a pioneering approach to the world of academia, radically improving the way scholarly research is managed. The grand vision of Frontiers is a world where all people have an equal opportunity to seek, share and generate knowledge. Frontiers provides immediate and permanent online open access to all its publications, but this alone is not enough to realize our grand goals.

Frontiers journal series

The Frontiers journal series is a multi-tier and interdisciplinary set of open-access, online journals, promising a paradigm shift from the current review, selection and dissemination processes in academic publishing. All Frontiers journals are driven by researchers for researchers; therefore, they constitute a service to the scholarly community. At the same time, the *Frontiers journal series* operates on a revolutionary invention, the tiered publishing system, initially addressing specific communities of scholars, and gradually climbing up to broader public understanding, thus serving the interests of the lay society, too.

Dedication to quality

Each Frontiers article is a landmark of the highest quality, thanks to genuinely collaborative interactions between authors and review editors, who include some of the world's best academicians. Research must be certified by peers before entering a stream of knowledge that may eventually reach the public - and shape society; therefore, Frontiers only applies the most rigorous and unbiased reviews. Frontiers revolutionizes research publishing by freely delivering the most outstanding research, evaluated with no bias from both the academic and social point of view. By applying the most advanced information technologies, Frontiers is catapulting scholarly publishing into a new generation.

What are Frontiers Research Topics?

Frontiers Research Topics are very popular trademarks of the *Frontiers journals series*: they are collections of at least ten articles, all centered on a particular subject. With their unique mix of varied contributions from Original Research to Review Articles, Frontiers Research Topics unify the most influential researchers, the latest key findings and historical advances in a hot research area.

Find out more on how to host your own Frontiers Research Topic or contribute to one as an author by contacting the Frontiers editorial office: frontiersin.org/about/contact

Host cellular responses to viruses

Topic editors

Jue Liu — Yangzhou University, China
Yongqun Oliver He — University of Michigan, United States
Cao Yong chang — Sun Yat-sen University, China
Li Yongqing — Institute of Animal Husbandry and Veterinary Medicine, Beijing Academy of Agriculture and Forestry Sciences, China

Citation

Liu, J., He, Y. O., chang, C. Y., Yongqing, L., eds. (2023). *Host cellular responses to viruses*. Lausanne: Frontiers Media SA. doi: 10.3389/978-2-83251-424-5

Table of contents

frontiers | Frontiers in Microbiology

TYPE Editorial
PUBLISHED 10 January 2023
DOI 10.3389/fmicb.2023.1110197

OPEN ACCESS

EDITED AND REVIEWED BY
Yingli Shang,
Shandong Agricultural University, China

*CORRESPONDENCE
Yongqun He
✉ yongqunh@med.umich.edu
Yongqing Li
✉ chunyudady@sina.com
Yongchang Cao
✉ caoych@mail.sysu.edu.cn
Jue Liu
✉ liujue@263.net

SPECIALTY SECTION
This article was submitted to Virology, a section of the journal Frontiers in Microbiology

RECEIVED 28 November 2022
ACCEPTED 02 January 2023
PUBLISHED 10 January 2023

CITATION
He Y, Li Y, Cao Y and Liu J (2023) Editorial: Host cellular responses to viruses. *Front. Microbiol.* 14:1110197. doi: 10.3389/fmicb.2023.1110197

Editorial: Host cellular responses to viruses

Yongqun He[1]*, Yongqing Li[2]*, Yongchang Cao[3]* and Jue Liu[4]*

[1]Unit for Laboratory Animal Medicine, Department of Microbiology and Immunology, Center of Computational Medicine and Bioinformatics, University of Michigan Medical School, Ann Arbor, MI, United States, [2]Research Center for Infectious Diseases in Livestock and Poultry, Beijing Academy of Agriculture and Forestry Sciences, Beijing, China, [3]State Key Laboratory of Biocontrol, Life Sciences School, Sun Yat-sen University, Guangzhou, China, [4]College of Veterinary Medicine, Yangzhou University, Yangzhou, China

KEYWORDS

virus infection, innate immune response, inflammatory signals, miRNA, host cellular protein networks, pathogenesis

Editorial on the Research Topic
Host cellular responses to viruses

Viruses are intracellular obligate pathogens that rely purely on the host cell for replication. The first step in initiating effective viral infection is to break through the cytomembrane to enter the cell. Next, several adaptor proteins contribute to clathrin-mediated endocytosis of virus entry. After entering the cell, viruses are ultimately dependent on the host cell for their replication *via* altering cellular signal transduction pathways, including IRF3/IRF7, mitogen-activated protein kinases, NF-kappaB, programmed cell death, autophagy, RIG-1-MAVS and cGAS-STING DNA sensing signals, and inflammasome activation signals. Research data documented on the involvement of various cellular proteins or molecules in the replication of viruses have provided essential insights into understanding the viral pathogenesis and have led to the development of antiviral therapeutics. This Research Topic comprises three review articles and 19 research articles from 79 authors, covering many aspects of host cellular responses to DNA and RNA viruses.

The two in-depth reviews by Zhang X.-Z. et al. and Zhou Y. et al. provide readers an up-to-date knowledge of tripartite motif-containing proteins (TRIMs) and Hedgehog (HH) signaling that are targeted by viruses to modulate viral and pathogenesis. Zhang X.-Z. et al. described the regulating functions of TRIMs in host immune signalings and discuss the state-of-the-art research on immune evasion of viruses by targeting TRIMs. Zhou Y. et al. summarized recent advances in functional interaction between HH signaling and viral infections and related diseases. Demonstration of virus-TRIM/HH signaling interactions may provide potential molecular targets for the therapy, or even prevention, of related viral diseases. The third review by Zhang K. et al. reviewed the most recent advances on porcine enteric coronaviruses, including porcine epidemic diarrhea virus, porcine deltacoronavirus, and transmissible gastroenteritis coronavirus, focusing on the molecular mechanisms by which viral components downregulate interferon-modulated innate immune responses, aiming to provide new targets and methods to control and eliminate porcine enteric coronaviruses.

Coxsackievirus B type 3 (CVB3), a member of Enterovirus genus within Picornaviridae, is associated with myocarditis and dilated cardiomyopathy. Qin Y. et al. reported that hsa_circ_0076631 (circ_0076631) significantly enhanced CVB3 replication via modulating viral translation by sponging miR-214-3p, which targeted the CVB3 3D-coding region. Knocking down circ-0076631 resulted in a suppression of CVB3 replication. This study could provide a theoretical basis for clinical treatment of CVB-induced cardiomyopathy.

Bovine herpesvirus 1 (BoHV-1), an alphaherpesvirus, causes infectious rhinotracheitis and pustular vulvovaginitis in cattle. Jiang et al. found that BoIFN-γ pretreatment can significantly inhibit BoHV-1 replication in cultured MDBK cells as evidenced by regulating expression of host protein linked to cellular metabolism and innate immune response, including upregulating ISG transcriptions and expression of IRF1 and GBP5, promoting expression of cellular components participated in complement activation and coagulation cascades as well as antigen presentation and processing, and alleviating metabolism disorder and DNA damage. These findings provide important clues to developing prophylactic measures for prevention and control of BoHV-1 infection.

Severe infection of influenza A virus (IAV) results in overwhelming inflammatory responses, leading to lung injury and high mortality. Liu M. et al. revealed that oral administration of Cangma Huadu (CMHD) granules, a preparation of traditional Chinese medicine, can reduce virus load, inflammatory responses, oxidative stress, and apoptosis in IAV PR8-infected mice. In addition, CMHD granules showed pronounced effects on modulating the diversity and composition of gut microbiota after IAV infection as evidenced by an enhanced abundance of Bacteroides, Bifidobacterium, and Faecalibaculum in PR8-infected mice. This study demonstrated a novel and effective TCM compound, CMHD granules, can be used for the treatment of lethal influenza.

Infection of porcine epidemic diarrhea virus (PEDV) variant has resulted in severe economic losses to the pig industry worldwide. Guo, Yu, et al. found that PEDV infection did not mediate SGs formation in most cultured Vero cells and silencing G3BP1, a stress granules (SGs) marker protein, significantly promoted PEDV replication. Further research showed that PEDV might disrupt SGs formation *via* degrading G3BP1 dependent on activity of viral papain-like proteases. These results illuminated the molecular events participated in the formation of PEDV-induced SGs.

Zhao et al. constructed a novel recombinant bovine herpesvirus type I (BHV-1-ΔgE-G) which expressed rabies virus glycoprotein (RABV G) replaced by its own gE glycoprotein (gE) using CRISPR-Cas9 and homologous recombination technology. Immunization with BHV-1-ΔgE-G can induce a protection against lethal challenge infection in mice. Long-term and protection of RABV-specific neutralizing antibody were detected in mice and cattle. This study demonstrated that the BHV-1 vector-based RABV vaccine can serve as a potential candidate vaccine for cattle.

Infection of Japanese encephalitis virus (JEV) in brain microvascular endothelial cells (BMECs) is considered to be a key step to bring about viral encephalitis. Zhang Y.-G. et al. validated the specific role of activated epidermal growth factor receptor (EGFR) on JEV propagation in human hBMECs. JEV infection induced the phosphorylation of EGFR and its downstream signals. Using specific inhibitors or knocking-out of EGFR showed that EGFR assists JEV virions production by negatively modulating the antiviral interferon response, but does not involve viral attachment or entry. These results revealed the mechanism of how JEV exploits EGFR signaling to promote viral replication, thereby providing a potential target for therapy for infection of JEV.

The transposition of long interspersed element 1 (LINE-1) can result in genetic instability/diseases. Zhang Z. et al. reported that CCHC-type zinc-finger protein ZCCHC3 inhibited LINE-1 retrotransposition via its zinc-finger domain and diminished the LINE-1 RNA level. These results of contribution of ZCCHC3 to LINE-1 replication help avoid the adverse effects of LINE-1 transposition on the host genomic structure and function.

Latorre and Geller identified various members of host cellular protein folding networks involving in respiratory syncytial virus (RSV) replication. The decreased number of chaperones and co-chaperones can facilitate the unmasking of certain chaperone subnetworks essential for critical steps of the RSV life cycle. This study improved our understanding of this host-pathogen interface and revealing new potential targets for therapeutic intervention.

Fiacchini et al. found that the COVID-19 tracheal samples showed a significant alteration of two sets of gene expression related to activation of the proinflammatory response and inhibition of the estrogen response as compared to the non-COVID-19 controls. The altered inflammatory response in the COVID-19 patients could be a possible explanation of the enhancing number of laryngotracheal complications.

Zhou H. et al. observed that the expression of CCN1 was enhanced by PEDV infection and found that porcine epidemic diarrhea virus (PEDV) infection promoted the phosphorylation of CREB and c-Jun in the nucleus through the PKA and p38 pathways, and increased the production of CCN1. Further research showed that the overexpression of CCN1 decreases PEDV replication and promotes p53-dependent apoptosis as well as the knockdown of CCN1 enhanced PEDV proliferation and suppresses p53-dependent apoptosis in Marc-145 cells. This study provides important understanding for the molecular mechanism of PEDV pathogenesis.

Endoplasmic reticulum aminopeptidase 1 (ERAP1) is an important processing enzyme of antigenic peptides which are presented to major histocompatibility complex class I (MHC-I) molecules. Trimming of epitope repertoire dependent on ERAP1 correlates to efficacy of CD8+ T-cell responses in some viral diseases. Liu H. et al. showed that ERAP1 trims HBcAg to generate 9-mers LLDTASALY peptide for binding to HLA-C*04:01 of HepG2.2.15 cells, promoting activation of CD8+ T cells. These findings revealed a previously unknown HBV viral antigen peptides presentation–based immune mechanism that targets a critical step in the MHC-I antigen-processing pathway.

Singapore grouper iridovirus (SGIV), a member within the Iridoviridae family, is a major marine cultured fish causative agent worldwide. Guo, Zhang, et al. determined the expression levels of critical enzymes of glucose metabolism during SGIV infection and demonstrated that glycolysis might be involved in infection of SGIV using specific pharmacological inhibitors and siRNA technology. They also clarified the role of mTOR in glycolysis induced by SGIV. These results provided novel insights into the mechanism in which SGIV infection affected host cell glycolysis and contributed to deep understanding of iridovirus pathogenesis.

Yan et al. investigated the kinetics of neutralizing antibody and T cell response to SARS-CoV-2 in COVID-19 patients and found that most patients had developed and maintained a long term effective neutralizing antibodies and a specific T cell responses to SARS-CoV-2 in at least one and half years after the onset of illness during the study period, even in mild individuals. A positive correlation was seen between SARS-CoV-2-specific neutralizing antibody levels and T-cell responses. This study indicated that effective long-term herd immunity could be achieved through global vaccination.

Lee et al. identified a novel anti-HBV signaling pathway as evidenced by that hepatocyte growth factor (HGF)-induced ACK1 (activated cdc42-associated kinase 1) inhibited HBV gene expression and replication by regulation of Erk1/2-HNF4α signaling cascade. Notably, HGF reduces the HBV replication and cccDNA in HBV-infected cells and ACK1 is involved in anti-HBV activity of HGF. These findings provide a new signaling for anti-HBV activity of HGF during the regeneration of damaged liver tissue by persistent infection of HBV.

Liu P. et al. demonstrated that meclizine showed a significant inhibition against Pseudorabies virus (PRV) *via* interfering with virus entry, cell-to-cell spread, and release in cultured cells. Further animal experiments demonstrated that meclizine decreased the severity of clinical signs and the viral burdens in tissues and delayed the death of mice after PRV challenge. These results lay a foundation for the development of PRV antiviral drugs, thereby providing a new perspective to the study of antiviral mechanism.

Sufficient presence of the hepatitis B virus (HBV) covalently closed circular DNA (cccDNA) is considered to be the failure of antiviral therapies. Qin Y.-P. et al. identified KAT2A as a crucial host factor in HBV transcription and replication by screening a series of succinyltransferases and desuccinylases. KAT2A was shown to affect cccDNA transcriptional activity but not cccDNA production in HBV-infected cells and mouse models. Silencing KAT2A could restrict cccDNA transcription activity by decreasing the level of H3K79succ on cccDNA minichromosomes. These findings demonstrated that KAT2A enhances HBV transcription and replication *via* epigenetic machinery, thereby providing new insight into the therapy of hepatitis B virus infection.

Cyprinid herpesvirus 2 (CyHV-2) has resulted in severe economic loss to the Crucian carp breeding industry. Lu et al. showed that antioxidant-related gene expressions were upregulated in cultured CyHV-2-infected Ryuf-2 cells and found that antioxidants can effectively inhibit the replication of CyHV-2 through reduced reactive oxygen species production.

Chen et al. identified a lnc-LTR5B induced by endogenous retroviral LTR. This lnc-LTR5B participates in regulating translocation of BiP to the cell surface, and the avian leukosis virus subgroup J can exploit such regulatory machinery for completing can be exploited by to complete its life cycle and propagation. This study provides a virus-based lncRNA-modulated mechanism that facilitates to develop new antiviral strategies.

Ma and Niu analyzed the metabolic profiles of hepatocellular carcinoma cell line when infected with fowl adenovirus serotype 4 (FAdV-4), which is the major pathogen of hydropericardium syndrome severely damaging to poultry farming. FAdV-4 was shown to modulate glycolysis, tricarboxylic acid cycle, and metabolism of alanine, aspartate, purines, pyrimidines, glutamate, and sugar moieties in the cultured cells. These findings provide new insights into developing prophylactic measures for prevention and control of FAdV-4 infection.

Selected articles in this Research Topic range from our basic understanding of host cellular responses to virus infections to potential approaches to prevention and therapy for viral diseases. The editors of this topic sincerely thank all authors and reviewers for their contributions.

Author contributions

All authors listed have made a substantial, direct, and intellectual contribution to the work and approved it for publication.

Conflict of interest

The authors declare that the research was conducted in the absence of any commercial or financial relationships that could be construed as a potential conflict of interest.

Publisher's note

frontiers in Microbiology

ORIGINAL RESEARCH
published: 29 November 2021
doi: 10.3389/fmicb.2021.788317

An Endogenous Retroviral LTR-Derived Long Noncoding RNA lnc-LTR5B Interacts With BiP to Modulate ALV-J Replication in Chicken Cells

Shihao Chen[1,2,3†], Ruihan Zhao[1,4†], Ting Wu[1,2], Dedong Wang[1,4], Biao Wang[1,4†], Shiyu Pan[1,2], Xuming Hu[1,2], Zhiming Pan[3] and Hengmi Cui[1,2,5*]*

[1]Institute of Epigenetics and Epigenomics and College of Animal Science and Technology, Yangzhou University, Yangzhou, China, [2]Joint International Research Laboratory of Agricultural & Agri-Product Safety, The Ministry of Education of China, Yangzhou University, Yangzhou, China, [3]Jiangsu Key Laboratory of Zoonosis, Yangzhou University, Yangzhou, China, [4]College of Veterinary Medicine, Yangzhou University, Yangzhou, China, [5]Institute of Comparative Medicine, Yangzhou University, Yangzhou, China

OPEN ACCESS

Edited by:
Li Yongqing,
Beijing Academy of Agriculture and Forestry Sciences, China

Reviewed by:
Xiaojun Wang,
Chinese Academy of Agricultural Sciences, China
Zhao-Hua Zhong,
Harbin Medical University, China
Yulong Gao,
Chinese Academy of Agricultural Sciences, China

***Correspondence:**
Shihao Chen
mrrchen@yzu.edu.cn
Hengmi Cui
hmcui@yzu.edu.cn

†These authors have contributed equally to this work

Specialty section:
This article was submitted to Virology, a section of the journal Frontiers in Microbiology

Received: 02 October 2021
Accepted: 05 November 2021
Published: 29 November 2021

Citation:
Chen S, Zhao R, Wu T, Wang D, Wang B, Pan S, Hu X, Pan Z and Cui H (2021) An Endogenous Retroviral LTR-Derived Long Noncoding RNA lnc-LTR5B Interacts With BiP to Modulate ALV-J Replication in Chicken Cells. Front. Microbiol. 12:788317. doi: 10.3389/fmicb.2021.788317

Infection with the avian leukosis virus subgroup J (ALV-J) impairs host genes and facilitates the establishment of chronic infection and the viral life cycle. However, the involvement of long noncoding RNAs (lncRNAs) in ALV-J infection remains largely unknown. In this study, we identified a novel chicken lncRNA derived from LTR5B of the ERV-L family (namely lnc-LTR5B), which is significantly downregulated in ALV-J infected cells. lnc-LTR5B was localized in the cytoplasm and was relatively high expressed in the chicken lung and liver. Notably, the replication of ALV-J was inhibited by the overexpression of lnc-LTR5B but enhanced when lnc-LTR5B expression was knocked down. We further confirmed that lnc-LTR5B could bind to the binding immunoglobulin protein (BiP), a master regulator of endoplasmic reticulum (ER) function. Mechanistically, lnc-LTR5B serves as a competing endogenous RNA for BiP, restricting its physical availability. Upon ALV-J infection, the reduction of lnc-LTR5B released BiP, which facilitated its translocation to the cell surface. This is crucial for ALV-J entry as well as pro-survival signaling. In conclusion, we identified an endogenous retroviral LTR-activated lnc-LTR5B that is involved in regulating the cell surface translocation of BiP, and such regulatory machinery can be exploited by ALV-J to complete its life cycle and propagate.

Keywords: ALV-J, lncRNA, lnc-LTR5B, BiP, interaction

INTRODUCTION

Avian leukosis virus (ALV), which belongs to the family *Retrovirus*, is an enveloped RNA virus that causes host immunosuppression and various tumors in chicken. ALVs have been classified into seven subgroups, including ALV-A, B, C, D, E, J, and K (Chai and Bates, 2006; Li et al., 2016). ALV-J displays higher transmissibility and pathogenicity than other subgroups, which has been considered as one of the leading causes of morbidity and mortality

in some chicken flocks in China (Li et al., 2019a,b); thus, it presents a great threat to the poultry industry and leads to high economic loss. The lack of understanding of the viral life cycles has hampered the development of specific antiviral drugs or effective vaccines against ALV-J. Therefore, it is important to discover the underlying molecular mechanisms of ALV-J replication and disease progression. Successful ALV-J infection requires host factors at different stages of the viral life cycle. For example, ALV-J infection begins with the viral envelope (Env) protein binding to its specific receptor NHE1 at the surface of host cells, followed by virion internalization (Chai and Bates, 2006; Guan et al., 2018). In addition, ALV-J often has multiple mechanisms to interfere with the host innate immune response. For example, MiR-34b-5p, which is induced by ALV-J infection, targets melanoma differentiation-associated gene 5 (MDA5), which is a major cellular sensor for triggering type I interferon (Li et al., 2017). ALV-J infection blocks the activation of the type I interferon signaling by targeting the transcriptional regulator NF-kB (Lin et al., 2018). Therefore, screening more host factors targeted by ALV-J is beneficial to understand its pathogenic mechanisms and develop effective vaccines.

Long noncoding RNAs (lncRNAs) are transcripts that are longer than 200 nucleotides in length and possess no protein-coding properties. Although they do not code for proteins, lncRNAs are considered to play pivotal roles in diverse biological processes (Carpenter et al., 2013; Durruthy-Durruthy et al., 2016; Olivero et al., 2020). Recently, many lncRNAs have been shown to be associated with host defense responses against viral infections. For example, lncRNA Malat1 suppresses antiviral innate responses by interacting with TDP43 and affecting its cleavage, which is mediated by activated caspase-3 (Liu et al., 2020). The lncRNA NRAV promotes respiratory syncytial virus (RSV) replication by sponging miR-509-3p to release Rab5c and promote RSV vesicle transportation (Li et al., 2020). Our previous research suggested that a chicken lncRNA named lnc-ALVE1-AS1 inhibits ALV-J replication by simulating TLR3 signaling and promoting the transcription of interferon-stimulated genes (Chen et al., 2019). We and others have indicated that numerous lncRNAs were significantly differentially expressed in chicken cells during ALV-J infection (Qiu et al., 2017; Hu et al., 2018; Dai et al., 2019). Among these lncRNAs, some were predicted to be involved in antiviral signaling, but very few have been functionally characterized.

In this study, we identified a chicken endogenous retrovirus LTR-derived lncRNA, lnc-LTR5B, whose expression is downregulated during ALV-J infection. We demonstrated that the overexpressed lnc-LTR5B exhibited an inhibitory effect on ALV-J replication *in vitro*. Our findings suggested that lnc-LTR5B binds to BiP in the cytoplasm, and the reduction of lnc-LTR5B in ALV-J infection is part of establishing the virus cycle by increasing BiP translocation to the plasma membrane and ALV-J entry. Our study provides a plausible, virus-modulating, lncRNA-based disease mechanism that opens avenues for developing new antiviral strategies.

MATERIALS AND METHODS

Cells and Virus

Primary chicken embryo fibroblast cells (CEFs) were prepared from 10-day-old specific pathogen-free chicken embryos, following our approved protocol. The CEFs and DF-1 cells (ATCC and CRL-12203) were maintained in Dulbecco's modified Eagle's medium (GIBCO) supplemented with 10% fetal bovine serum (FBS; GIBCO), penicillin (100 U/ml), and streptomycin (100 μg/ml) at 37°C in a humidified 5% CO_2 incubator.

The ALV-J (JS09GY3 strain) and the monoclonal antibody JE9 against ALV-J Env (gp85) were kindly provided by Prof. Aijian Qin (Yangzhou University, China). The 50% tissue culture infective doses ($TCID_{50}$) of the ALV-J virus were measured in DF-1 cells using the Reed and Muench method. ALV-J RNA was quantified by qPCR using Env gene-specific primers, and the results were normalized to the expression levels of GAPDH.

RNA Extraction and Quantitative Real-Time PCR

Total RNA was extracted from cells or eight kinds of chicken normal tissues using TRIzol reagent (Takara). cDNA was synthesized using a Vazyme cDNA Synthesis Kit with gDNA Eraser Kit (Vazyme, Nanjing, China) according to the manufacturer's protocol. qPCRs were performed with the ChamQ SYBR qPCR Master Mix Kit (Vazyme) on a BioRad CFX Connect Real-time PCR detection system (Bio-Rad). The relative expression levels were normalized with the GAPDH gene by the comparative Ct ($2^{-\Delta\Delta Ct}$) method. The primers sequences for qRT-PCR are listed in **Supplementary Table S1**.

Rapid Amplification of cDNA Ends (5' and 3' Race)

5' RACE and 3' RACE were performed with SMARTer RACE5'/3' Kit (Takara) according to the manufacturer's protocol. Briefly, total RNA from CEF cells was isolated by using TRIzol reagent (Takara) and was reverse-transcribed into the first-strand cDNA using 5' or 3' end primers. Then, the cDNA was used as template for PCR amplification to generate 5' or 3'-end of the clone. 5'- and 3'-specific primer are listed in **Supplementary Table S1**.

Plasmids Construction

To generate pcDNA3.1-lnc-LTR5B, the full-length lnc-LTR5B was PCR-amplified and cloned into a pcDNA3.1 plasmid with the MultiF Seamless Assembly Mix (ABclonal) according to the manufacturer's instructions. The different DNA fragments of lnc-LTR5B promoter were PCR-amplified using the following pairs of primers: FL-F and FL-F for FL region; T1-F and FL-F for T1 region; T2-F and FL-F for T2 region; and FL-F and T3-R for T3 region. Then, these DNA fragments were cloned into the pGL3-basic vector (Promega) to generate the reporter construct. The oligo sequences for the plasmid construct are listed in **Supplementary Table S1**.

Luciferase Reporter Assay

2×10^5 293 T cells were seeded in 24-well plates and cotransfected with a control plasmid pRL-TK (Promega) and indicated plasmids for luciferase activity. After 36 h of incubation, the cells were harvested and luciferase activities were measured using the Dual Luciferase Reporter Assay Kit (Vazyme), according to the manufacturer's instructions. Relative luciferase signals (firefly/Renilla) were normalized against that of the pGL3-basic empty vector.

ASO Transfection

The specific targeting lnc-LTR5B (ASO-1 and ASO-2) or non-targeting control ASO (ASO-NC) were designed and synthesized by RiboBio Company. ASO transfection was performed in 12-well plates with three technical replicates for each sample. Briefly, DF-1 cells were transfected with a final concentration of 50 nM of each ASO until cell density reached ~50% confluence by riboFECT™ CP reagent (RiboBio) according to the manufacturer's instruction. The ASO targeting sites are listed in **Supplementary Table S1**.

Western Blot Analysis

Cells were lysed in a lysis buffer (Cell Signaling Technology) supplemented with the complete protease inhibitor cocktail (Roche) and incubated on ice for 15 min. Protein concentrations were measured by the BCA Protein Assay kit (Beyotime). A total of 25 to 50 μg of protein were separated by SDS-PAGE gel and transferred to a nitrocellulose membrane (Cytiva). The membranes were incubated at 4°C overnight with the appropriate primary antibodies: anti-BiP (HuaBio), anti-Bcl2 (Proteintech), anti-cleaved-caspase-3 (Proteintech), anti-GAPDH (Abcam), and anti-β-actin (Abcam). The images were captured with a FlourChem Q imaging system (ProteinSimple). The relative intensities of the different protein bands were analyzed using Image J program.

Cell Fractionation

The membrane and cytoplasmic cell fractions were extracted using Membrane and Cytosol Protein Extraction Kit (Beyotime), according to the manufacturer's protocol. Briefly, the treated cells were harvested and washed twice with PBS and then incubated with ice-cold Extraction Regent A containing protease inhibitor mixture on ice for 15 min with gentle agitation. The supernatant (cytoplasmic fraction) was obtained by centrifugation at 700 g at 4°C for 10 min. And the sediment was resuspended with 200 μl of ice-cold Extraction Regent B containing the protease inhibitor mixture. Finally, the supernatant was used as the membrane fraction to detect BiP protein expression.

Viral Entry Assay

The viral entry assay was performed as described in a previous publication (Guan et al., 2018) with modifications. The cells were transfected with pcDNA3.1 or pcDNA3.1-lnc-LTR5B as described. After 24 h post-transfection, the cells were washed twice with PBS, followed by incubation with ALV-J (MOI = 5) at 37°C. After 2-h incubation, the cells were washed three times with pre-warmed PBS and then cultured in fresh DMEM supplemented with 2% FBS at 37°C with 5% CO2. The virus entry levels were measured at 12 h post-infection by qRT-PCR for detecting ALV-J RNA.

RNA FISH

Subcellular localization of lnc-LTR5B was assessed in DF-1 cells using Fluorescent *In Situ* Hybridization Kit (RiboBio) as described previously (Chen et al., 2019). The lnc-LTR5B probes labeled with Cy3 fluorescent dye were purchased from RiboBio Company. Briefly, DF-1 cells were fixed with 4% paraformaldehyde in PBS for 10 min and permeabilized with 0.5% Triton X-100 for 10 min. After blocking with pre-hybridization buffer/blocking solution, the cells were incubated with the lnc-LTR5B probes at 37°C overnight. The next day, cells were washed with appropriate saline sodium citrate buffer. The slides were then incubated with anti-BiP antibody at 4°C overnight. After washing three times with chilled PBS, the slides were incubated with Alexa Fluor 488-conjugated secondary antibody. Nuclei were then stained using DAPI (RiboBio) for 10 min and finally analyzed by confocal microscopy (Leica SP8).

RNA Pull Down and Mass Spectrometry

The DNA fragments of full-length lnc-LTR5B and its antisense were amplified with primers containing a T7 promoter sequences (listed in **Supplementary Table S1**). The PCR products were transcribed to RNA *in vitro* using the TranscriptAid T7 High Yield Transcription Kit (Thermo Fisher Scientific). Then, the biotinylated RNAs were produced using the Pierce RNA 3′ Desthiobiotinylation Kit (Thermo Scientific) and purified with phenol/chloroform/isoamyl alcohol, followed by ethanol precipitation. Next, 50 pmol of biotin-labeled RNA was mixed with Pierce nucleic-acid compatible streptavidin magnetic beads in Protein-RNA Binding Buffer (Thermo Scientific) followed by incubation with DF-1 cell lysates for 1 h with gentle agitation. After washing, the RNA-protein mixtures were extracted and further subjected to 12% SDS-PAGE for silver staining or western blotting. The selected bands were cut and subjected to mass spectrometry analyses.

RNA Immunoprecipitation Assay

For RIP assay, 2×10^7 DF-1 cells were washed twice with PBS and lysed in RIP lysis buffer (25 mM Tris–HCl pH 7.4, 150 mM KCl, 5 mM EDTA, 0.5 mM DTT, and 0.5% NP-40) supplemented with protease inhibitor cocktail and an RNase inhibitor, for 30 min on ice. The lysates were then incubated with prewashed Protein A/G magnetic beads and coated with 5 μg BiP (HuaBio) or normal Rabbit IgG (Abcam), with overnight shaking at 4°C. The next day, the beads were washed three times with ice-cold NT2 buffer (50 mM Tris–HCl (pH 7.4), 150 mM NaCl, 1 mM MgCl2, and 0.05% NP-40) with protease inhibitor cocktail and an RNase inhibitor, to obtain the RNA-Protein complex. RNA was then isolated using TRIzol and detected by qRT-PCR.

Immunofluorescence and Confocal Microscopy

DF-1 cells were grown on glass coverslips; after 24 h, cells were washed with PBS three times. To visualize intracellular proteins, cells were fixed with 4% paraformaldehyde in PBS for 10 min at room temperature (RT) and permeabilized with 0.25% Triton X-100 in PBS for 10 min on ice. After blocking with 5% BSA and 2% donkey serum in PBS for 30 min, the slides were then subjected to incubation with primary antibodies. To visualize cell surface proteins, cells were immediately fixed in 4% paraformaldehyde in PBS (4°C, 15 min), followed by blocking with 5% BSA and 2% donkey serum in PBS (4°C, 30 min). All primary antibodies diluted in PBS were incubated overnight at 4°C. The primary antibodies used were as follows: mouse anti-Env (1:300) and rabbit anti-BiP (1:200, HuaBio). The secondary antibodies used in this study were Alexa Fluor 488 donkey anti-rabbit antibody (1:1000; Invitrogen) and Alexa Fluor 594 donkey anti-mouse antibody (1,1,000; Invitrogen). The slides were washed three times with PBS, and nuclei were stained using DAPI (Sigma-Aldrich). Imaging was obtained using a Leica SP8 Confocal system with 63x oil objective and analyzed by the LAS X software version 3.0.2.16120.

Statistical Analysis

The data are represented as mean ± standard deviation (SD) of three independent experiments for each group and statistically analyzed by GraphPad Prism version 7.0 (GraphPad software). Statistical significance was assessed by Student's t test or one-way ANOVA as shown in each figure legend. Differences with p values less than 0.05 were considered as statistically significant.

RESULTS

Identification of a Host lncRNA, lnc-LTR5B, Which Is Downregulated in ALV-J-Infected Cells

To identify the host lncRNAs involved in ALV-J replication, we used RNA-seq to perform transcriptional analysis of CEF that were infected with ALV-J (JS09GY3 strain) or were mock-infected. The analysis data were presented in our previous work (Hu et al., 2018). Based on the idea that host lncRNAs targeted by viruses may participate in cellular antiviral responses, we focused on these downregulated lncRNAs during ALV-J infection. One of these lncRNAs, lnc-LTR5B (NCBI accession number: MG066622.1), was robustly downregulated in CEFs following ALV-J infection. RepeatMasker analysis showed that the MG066622.1 transcript has higher similarity with LTR5B elements, suggesting that lnc-LTR5B is an ERV-associated lncRNA. Considering that LTR contains a cis-regulatory region, the potential function of lnc-LTR5B in ALV-J infection requires urgent investigation.

We first examined lnc-LTR5B expression during ALV-J infection using reverse transcription quantitative PCR (qRT-PCR) and confirmed its downregulation upon ALV-J infection of primary CEFs (**Figure 1A**). Subsequently, we examined the expression of lnc-LTR5B in DF-1 cells infected with ALV-J. qRT-PCR and semi-quantitative RT-PCR showed that lnc-LTR5B was downregulated during ALV-J infection (**Figures 1B,C**). To identify the full-length sequence of lnc-LTR5B, we performed 5' and 3' rapid amplification of cDNA ends (RACE; **Figure 1D**) and the sequencing result show that the full-length transcript was 590 nucleotides (**Supplementary Table S2**). Subsequently, its protein-coding potential was assessed using the Coding Potential Calculator (CPC) program. The data showed that the CPC score for lnc-LTR5B was −0.980, which was similar to that of the validated lncRNA XIST (−0.945), suggesting that lnc-LTR5B lacks coding potential (**Supplementary Figure S1**). We further measured the relative abundance of lnc-LTR5B in several chicken tissues. Our results suggest that lnc-LTR5B is detectable in the brain, heart, liver, lung, spleen, kidney, intestines, and bursa. In addition, lnc-LTR5B was highly expressed in the lung and liver tissues, with a relatively low expression level in the brain tissues (**Figure 1E**).

Characterization of lnc-LTR5B

BLAST analysis of the chicken genome from the UCSC Genome Browser[1] database showed that lnc-LTR5B is located on chicken chromosome 17 and has two exons and is flanked by the upstream and downstream protein-coding genes TUBB4B and ENTPD2L (**Figure 2A**). Interestingly, the first exon of lnc-LTR5B was shown to be derived from an LTR5B element, which belongs to the ERV-L LTR family. Next, a dual luciferase assay was performed to verify whether lnc-LTR5B is an LTR-activated lncRNA. We inserted the full-length (from −2000 to +198) lnc-LTR5B promoter and truncated promoter fragments into a luciferase reporter vector. The luciferase activity of the T2 promoter region (from −341 to +198) was higher than that of the other promoter fragments (**Figure 2B**). The results indicate that lnc-LTR5B is an ERV LTR-derived lncRNA and is a member of the ERV-L lncRNA family. Next, we analyzed the subcellular localization of lnc-LTR5B by performing RNA fluorescence *in situ* hybridization (FISH). The results indicated that lnc-LTR5B is localized in both cytoplasm and nucleus, with distinct perinuclear aggregation (**Figure 2C**). Altogether, we identified that lnc-LTR5B is a novel LTR-derived lncRNA and its expression is suppressed in chicken cells infected with ALV-J.

lnc-LTR5B Inhibits ALV-J Replication

To investigate the role of lnc-LTR5B in ALV-J replication, we transfected DF-1 cells with either negative control vector pcDNA3.1 or the lnc-LTR5B expression vector and infected them with ALV-J at 12 h post-transfection. At 48 hpi, the cells were harvested for immunoblotting and qRT-PCR analysis. With increasing levels of lnc-LTR5B (**Figure 3A**), ALV-J RNA levels and Env protein expression decreased in a dose-dependent manner (**Figures 3B,C**). Next, the impact of lnc-LTR5B silencing on viral replication was assessed. Two different sets (ASO-1

[1]http://genome.ucsc.edu/

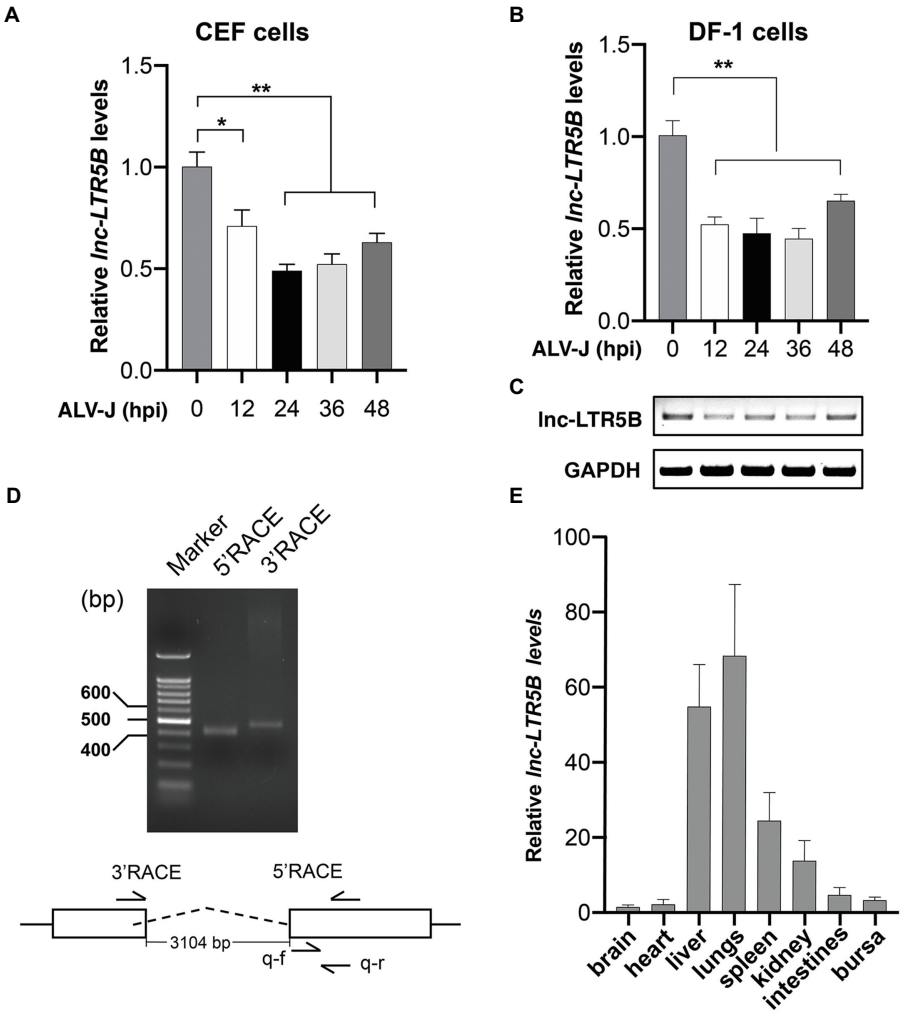

FIGURE 1 | ALV-J infection downregulates lnc-LTR5B expression. **(A,B)** CEF cells **(A)** and DF-1 **(B)** cells were infected with ALV-J (Multiplicity of infection, MOI = 0.5) for the indicated time intervals. The relative levels of lnc-LTR5B were measured by qRT-PCR. **(C)** RT-PCR analysis of the expression of lnc-LTR5B in DF-1 cells treated as described in **(B)**. **(D)** Agarose gel analysis of 5' and 3' RACE PCR products for lnc-LTR5B. DNA ladders (400 bp, 500 bp, and 600 bp) are shown (left lane). **(E)** qRT-PCR analysis of the expression of lnc-LTR5B in multiple tissues in chicken. GAPDH mRNA served as an internal control to normalize the level of lnc-LTR5B. Data are presented as the mean ± SD, $n = 3$; $^{*}p < 0.05$, $^{**}p < 0.01$ (one-way ANOVA).

and ASO-2) of antisense oligonucleotides (ASO) targeting lnc-LTR5B or ASO-NC as a control were used. The results of qRT-PCR showed that DF-1 cells transfected with ASO-1 achieved the highest silencing efficiency (**Figure 3D**). Consistent with this, the levels of ALV-J RNA and protein Env expression were both significantly increased in the DF-1 cells transfected with ASO-1 compared to those in the ASO-2 and ASO-NC groups at 36 hpi (**Figures 3E,F**). In addition, our data showed that overexpression of lnc-LTR5B did not have a significant effect on the activation of IFN signaling and its downstream gene, MX1 (**Supplementary Figure S2A**). Furthermore, the expression of lnc-LTR5B was not affected by poly(I:C)-induced IFN signaling (**Supplementary Figure S2B**). Together, these data suggest that lnc-LTR5B-mediated inhibition of ALV-J replication might not involve the activation of the innate immune response.

Identification of BiP as a Binding Protein of lnc-LTR5B

Because lncRNAs can exert their functions through RNA-protein interactions to modulate target genes, we attempted to identify the proteins that bind lnc-LTR5B to explore the mechanism by which lnc-LTR5B restricts ALV-J replication. Therefore, we used RNA pull-down assays followed by silver staining and mass spectrometry (MS) to identify the protein partners of lnc-LTR5B (**Figure 4A**). MS analysis of the differentially displayed bands associated with lnc-LTR5B revealed that BiP is a potential protein that binds to lnc-LTR5B (**Figure 4B**). Subsequently, significant pulldown of BiP by the biotin-labeled sense lnc-LTR5B compared with the antisense sequence was confirmed by western blotting (**Figure 4C**). Next, the interactions between lnc-LTR5B and BiP were verified using RNA immunoprecipitation (RIP) assays (**Figure 4D**). Moreover, RNA FISH and immunofluorescence

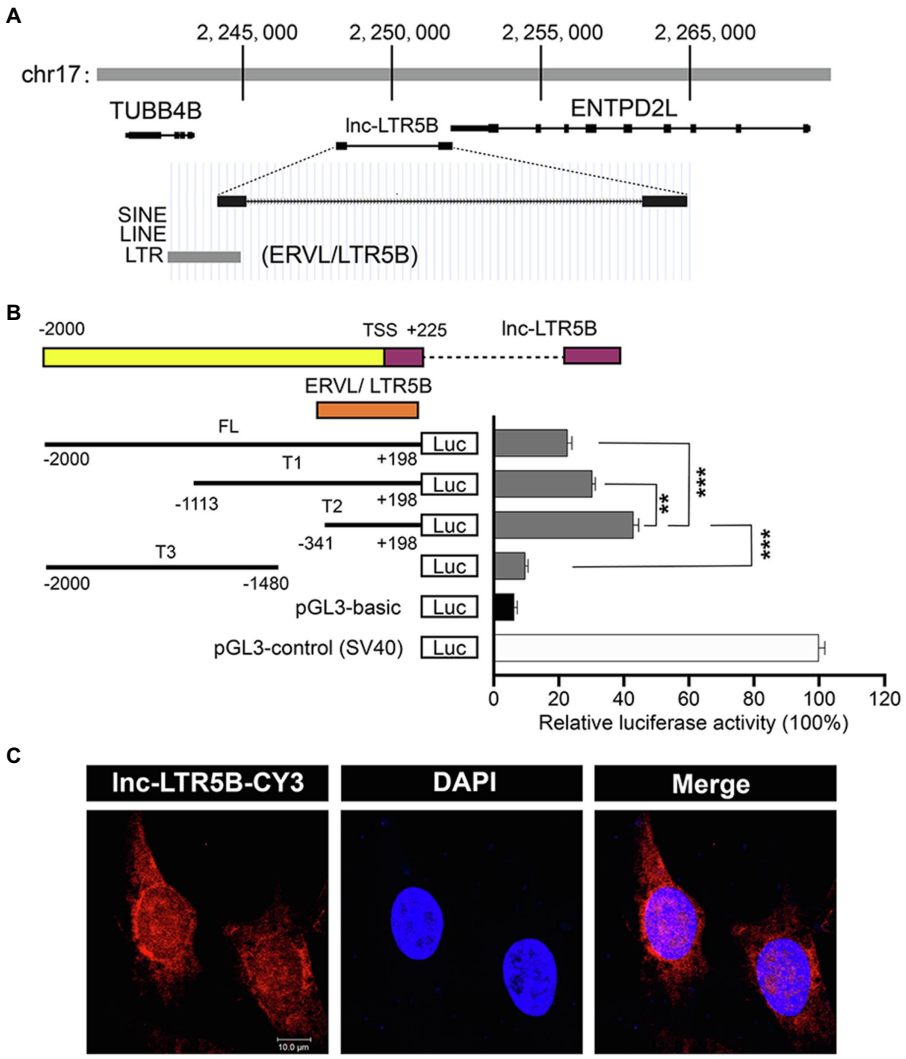

FIGURE 2 | Characterization of the lnc-LTR5B. **(A)** Schematic map of lnc-LTR5B. lnc-LTR5B is located on chromosome 17 and is flanked by the coding genes TUBB4B and ENTPD2L. **(B)** Dual-luciferase assays of lnc-LTR5B promoter activity in HEK293T cells transfected with the indicated plasmids. Schematic illustration of truncation constructs of lnc-LTR5B promoter region (−2000 to +198 relative to TSS). Data are presented as the mean ± SD, $n = 3$; $^{**}p < 0.01$, $^{***}p < 0.001$ (two-tailed unpaired Student's t test). **(C)** Confocal RNA FISH images showing the distribution of lnc-LTR5B in DF-1 cells. The lnc-LTR5B probes labeled with CY3 (red), and nuclei are stained with 4', 6-diamidino-2-phenylindole (DAPI; blue), Scale bars, 10 μm.

assays demonstrated the colocalization of lnc-LTR5B and BiP in the cytoplasm of DF-1 cells (**Figure 4E**).

ALV-J Infection Induces the Translocation of BiP to the DF-1 Cell Surface

Because the lnc-LTR5B interacting protein BiP was reported as an entry receptor for ALV-J, it must be located on the plasma membrane of DF-1 cells. However, the expression levels of cell surface BiP are generally considered to be low under normal physiological conditions. The translocation of BiP to the cell surface can be observed under conditions of cellular stress, including viral infection (Gonzalez-Gronow et al., 2021). To examine whether ALV-J infection induces the translocation of BiP to the DF-1 cell surface, we performed immunocytochemical staining to analyze the distribution patterns of BiP in both permeabilized and non-permeabilized cells (**Figure 5**). We observed colocalization of intracellular BiP and ALV-J Env, implying that BiP plays an important role in ALV-J infection through its direct interaction with the ALV-J protein. In addition, we found that BiP colocalized on the cell surface with ALV-J Env, and the colocalization was stronger at 24 hpi compared to that at 4 hpi, suggesting that ALV-J infection induces BiP translocation to the cell surface during ALV-J infection.

lnc-LTR5B Inhibits ALV-J by Decreasing Surface Expression of Bip and Promoting Apoptosis of Infected Cells

Next, we sought to find an association between lnc-LTR5B and BiP. Therefore, we quantified the expression of the BiP

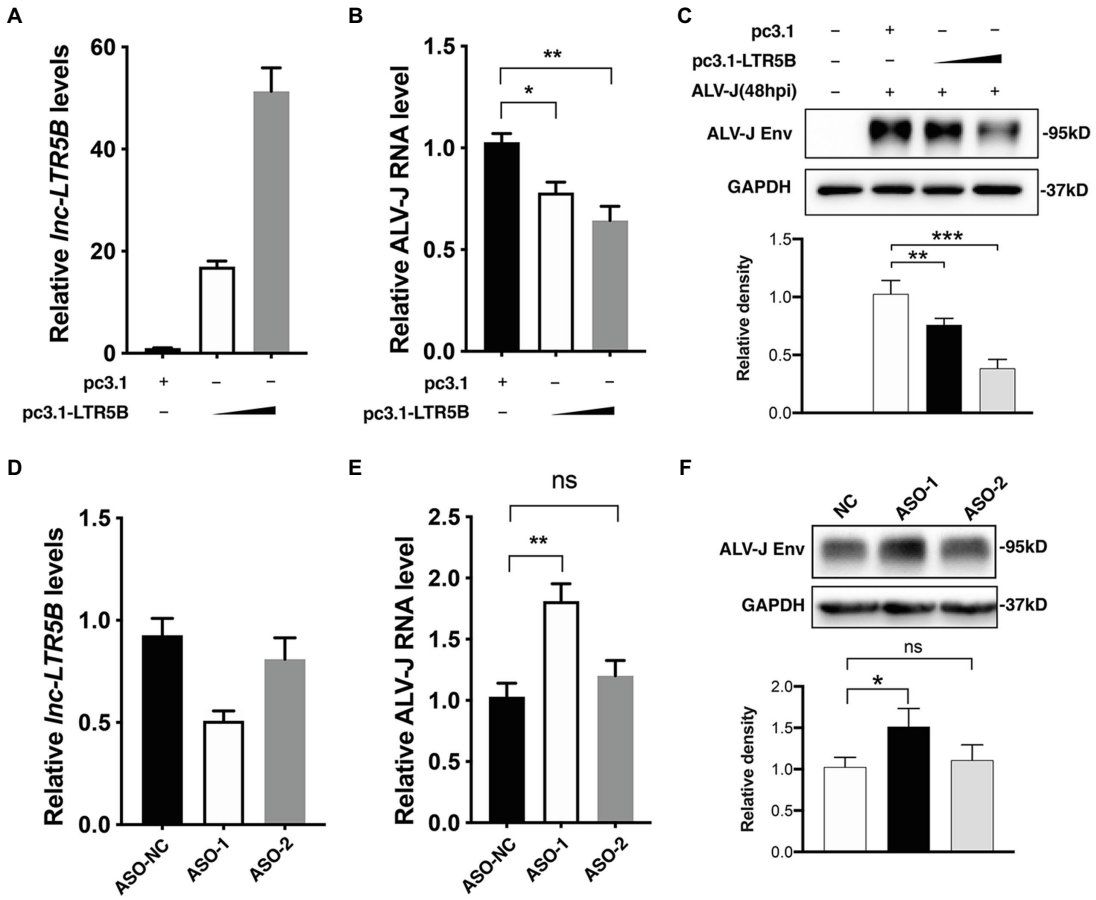

FIGURE 3 | lnc-LTR5B restricts ALV-J replication in DF-1 cells. **(A-C)** Overexpression of lnc-LTR5B suppressed ALV-J production. DF-1 cells were transfected with increasing amounts of pcDNA3.1-lnc-LTR5B or control pcDNA3.1 for 12 h, followed by infection with ALV-J (MOI = 0.5). Forty-eight hours post-infection, cells were harvested, and the level of lnc-LTR5B **(A)** and viral RNA **(B)** was measured by qRT-PCR. **(C)** ALV-J Env was measured by western blotting (top), and the density of each band was analyzed using Image J software. (bottom). **(D-F)** Knockdown of lnc-LTR5B in DF-1 cells promoted ALV-J production. DF-1 cells were transfected with either negative control ASO (ASO-NC) or ASO against lnc-LTR5B (50 nM) for 36 h. **(D)** The levels of lnc-LTR5B were quantified by qRT-PCR to examine the silencing efficiency. The cells transfected with ASO were then infected with ALV-J (MOI = 0.5) for 36 h. **(E)** The viral RNA was determined by qRT-PCR. **(F)** ALV-J Env was measured by western blotting (top), and the density of each band was quantified by ImageJ software. (bottom). Expression data were normalized to those of the negative vector or ASO-NC group. Data are presented as the mean ± SD, $n = 3$; *$p < 0.05$, **$p < 0.01$, ***$p < 0.001$, ns, not significant (one-way ANOVA).

protein in DF-1 cells during ALV-J infection. The results of western blotting revealed that the expression of BiP was unchanged during the ALV-J infection within 12 h, followed by a slight increase at 24 hpi (**Figure 6A**). However, the expression of lnc-LTR5B began to decrease at 12 hpi, the time point at which we first detected the expression of lnc-LTR5B (**Figure 1B**). Meanwhile, the overexpression of lnc-LTR5B did not affect the protein expression of BiP (**Figure 6B**). These data suggest that lnc-LTR5B is not directly involved in the regulation of BiP expression.

Because lnc-LTR5B binds BiP in the cytoplasm, we deduced that lnc-LTR5B can affect the BiP action that may be involved in BiP translocation to the cell surface. Western blot analysis of membrane fractions was performed to assess the effect of lnc-LTR5B overexpression on the surface expression of BiP upon ALV-J infection. As presented in **Figure 6C**, the expression of BiP on the membrane was attenuated in DF-1 cells overexpressing lnc-LTR5B compared to that in the corresponding control. Following this observation, we examined ALV-J binding and entry in lnc-LTR5B overexpressed DF-1 cells. As expected, we found that the overexpression of lnc-LTR5B markedly reduced the entry of ALV-J (**Figure 6D**). In addition, cell surface BiP has been reported to promote cell survival, which is considered an important target for cancer treatment (Araujo et al., 2018; Samanta et al., 2021). We speculate that the reduction of cell surface BIP caused by lnc-LTR5B leads to increased apoptosis. To test this, we assessed the effect of lnc-LTR5B overexpression on cell apoptosis signaling following ALV-J infection. The data showed that lnc-LTR5B overexpression inhibited the expression of the anti-apoptotic protein Bcl-2 and increased caspase-3 activation (**Figure 6E**), suggesting that lnc-LTR5B is involved in the activation of apoptotic signaling pathways in ALV-J-infected cells.

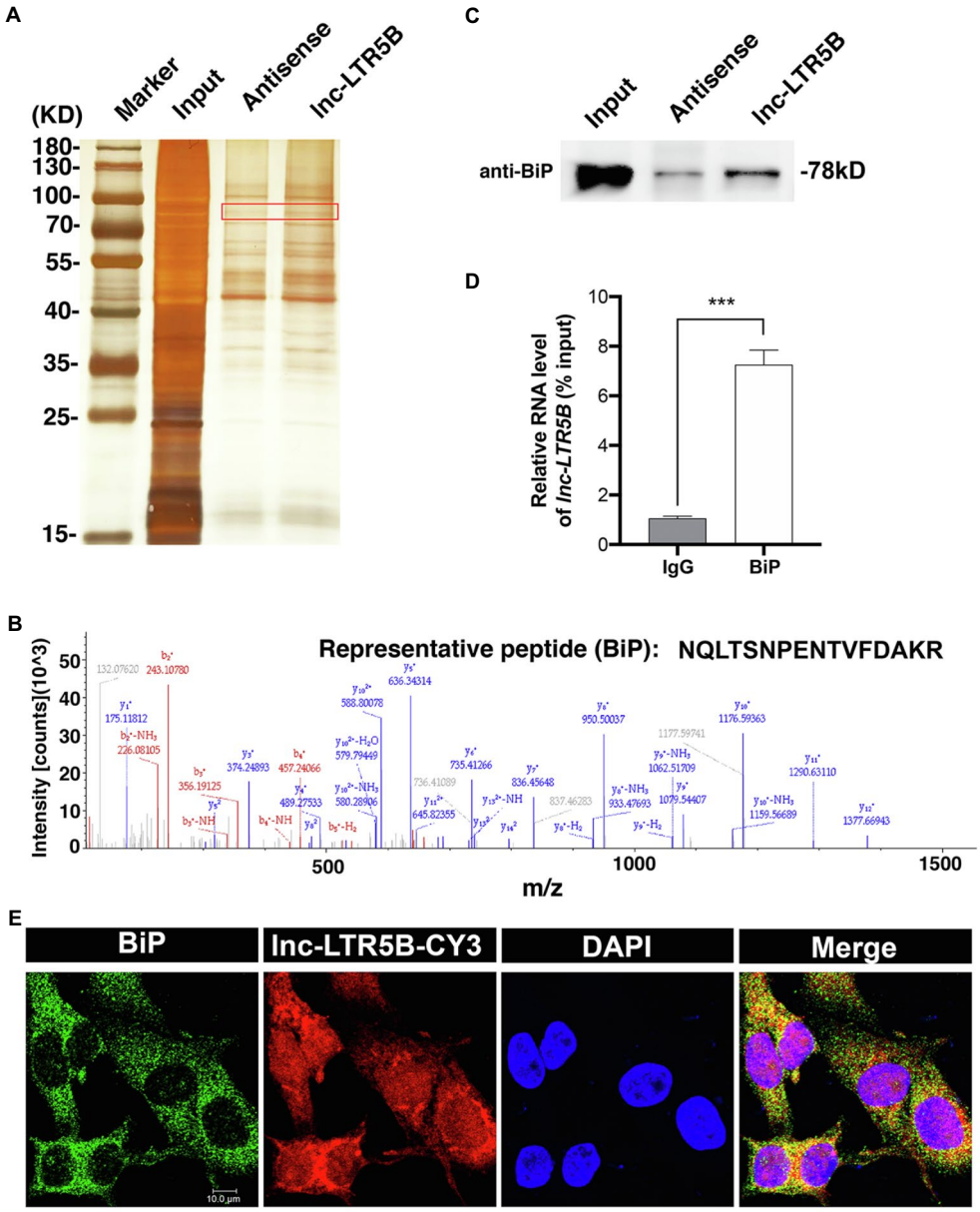

FIGURE 4 | Identification of BiP as a binding protein of lnc-LTR5B. **(A)** Silver staining of biotinylated lnc-LTR5B-associated proteins. The lnc-LTR5B-specific bands (highlighted bands) were excised and analyzed by mass spectrometry. **(B)** Mass spectrometry of highlighted band digests identifies the fragment ions from the representative peptide of BiP protein. **(C)** Western blot analysis of BiP from RNA pulldown assay using biotinylated lnc-LTR5B or antisense RNA. **(D)** RNA immunoprecipitation (RIP)-qPCR analysis of lnc-LTR5B immunoprecipitated by BiP antibody from DF-1 cells. Data are presented as the mean ± SD, $n = 3$; ***$p < 0.001$ (two-tailed unpaired Student's t test). **(E)** RNA FISH detecting endogenous lnc-LTR5B (red) combined with immunofluorescence staining of BiP (green) in DF-1 cells. DAPI staining is shown in blue. Scale bars, 10 μm.

DISCUSSION

Many studies have highlighted the functional role of lncRNAs in several infectious diseases. Viruses can utilize lncRNAs to regulate the signaling pathways involved in innate immunity (Wang et al., 2020), cell metabolism (Khatun et al., 2020), and cell stress (Chattopadhyay et al., 2021), to survive and replicate in host cells. Like other viruses, it is conceivable that some lncRNAs for virus replication that are regulated by ALV-J infection exist, which has not been documented.

In the present study, lnc-LTR5B was discovered as a novel chicken lncRNA, which was markedly downregulated in ALV-J-infected cells. We demonstrated that overexpressed lnc-LTR5B exhibited an inhibitory effect on ALV-J replication *in vitro*. Notably, we identified that lnc-LTR5B is a long terminal repeat (LTR)-derived lncRNA, whose promoter and first exon are mostly

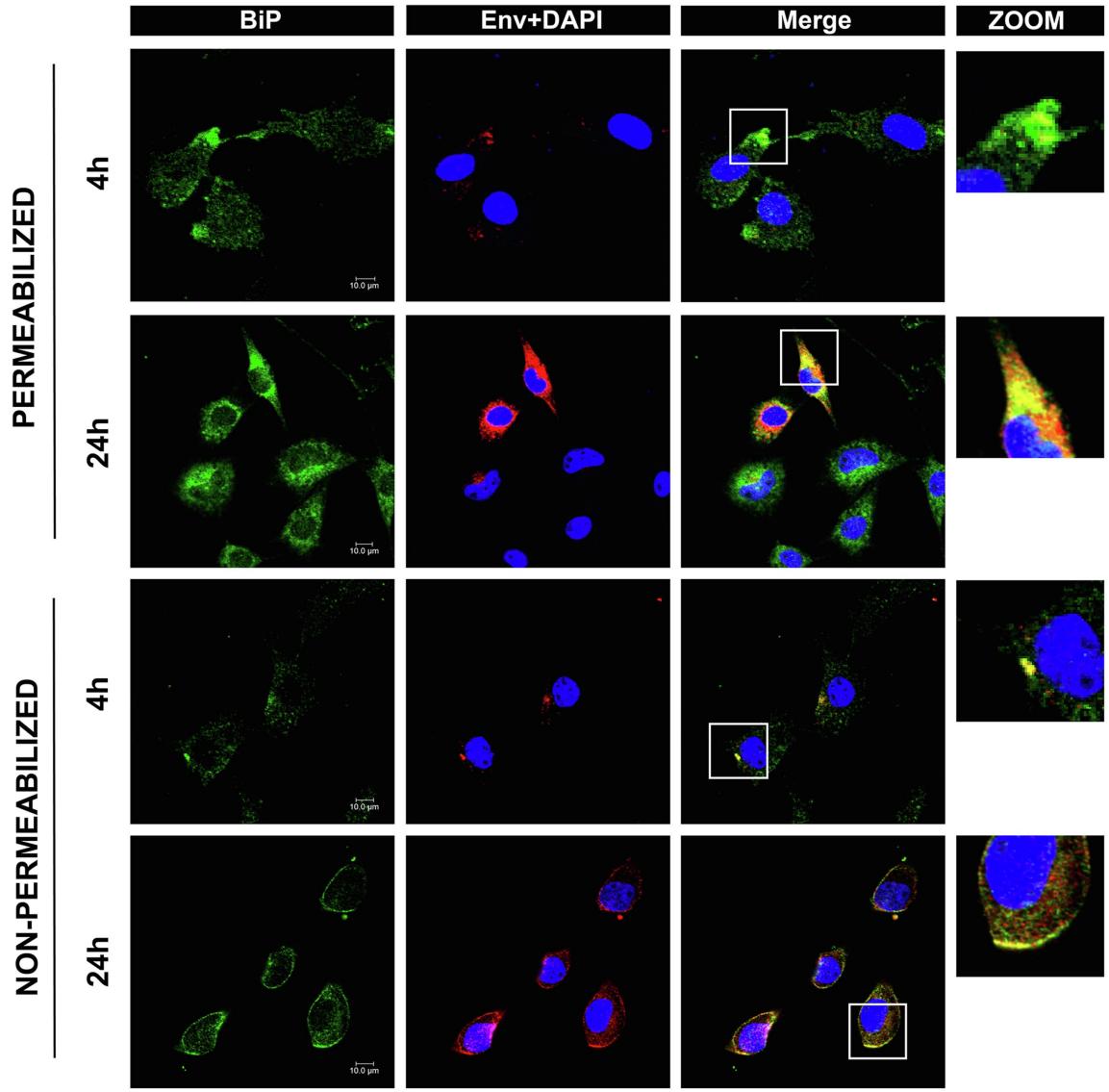

FIGURE 5 | Confocal immunofluorescence shows BiP interactions with ALV-J Env protein. DF-1 cells grown on glass coverslips were infected with ALV-J at an MOI of 5 for the indicated time. The cells were fixed, permeabilized, or non-permeabilized, followed by immunofluorescence labeling of BiP (green) and ALV-J Env (red). DAPI (blue) indicates nuclear staining. Yellow indicates colocalization (scale bars, 10 μm).

present within an LTR5B element of ERV-L LTR family (**Figures 2A,B**). Research has shown that solitary LTRs are frequently "exonized" into novel lncRNAs (Kapusta et al., 2013). For example, lncRNA TROJAN was shown to promote breast cancer progression, and its sequence highly overlaps that of a long terminal repeat, LTR70 (Jin et al., 2019). The lncRNA PRLH1 is derived from the human LTR element LTR12C and regulates hepatocellular carcinoma progression (Deng et al., 2019). Solitary LTRs probably contain regulatory elements that are likely promoter, enhancer, and transcriptional binding sites, which act in cis to activate the transcription of downstream genes (Rebollo et al., 2012). Therefore, we speculated that transcriptional factors might participate in the regulation of lnc-LTR5B expression. This will be interesting to explore in future studies.

lncRNAs exert their regulatory functions through distinct mechanisms that are closely related to their cellular localization. For example, nuclear lncRNAs tend to control the chromosome architecture or the epigenetic state of genes, whereas cytoplasmic lncRNAs may function as competing endogenous RNAs by serving as sponges that bind miRNAs or proteins (Kim et al., 2016). To dissect the antiviral action of lnc-LTR5B against ALV-J, we first examined its cellular distribution and found that it was mainly expressed in the cytoplasm, suggesting that lnc-LTR5B may function at the post-transcriptional level. We then screened for proteins that may interact with lnc-LTR5B. The RNA pulldown and RNA immunoprecipitation (RIP) assay showed that lnc-LTR5B directly binds to BiP (**Figures 4B,D**). BiP, also known as

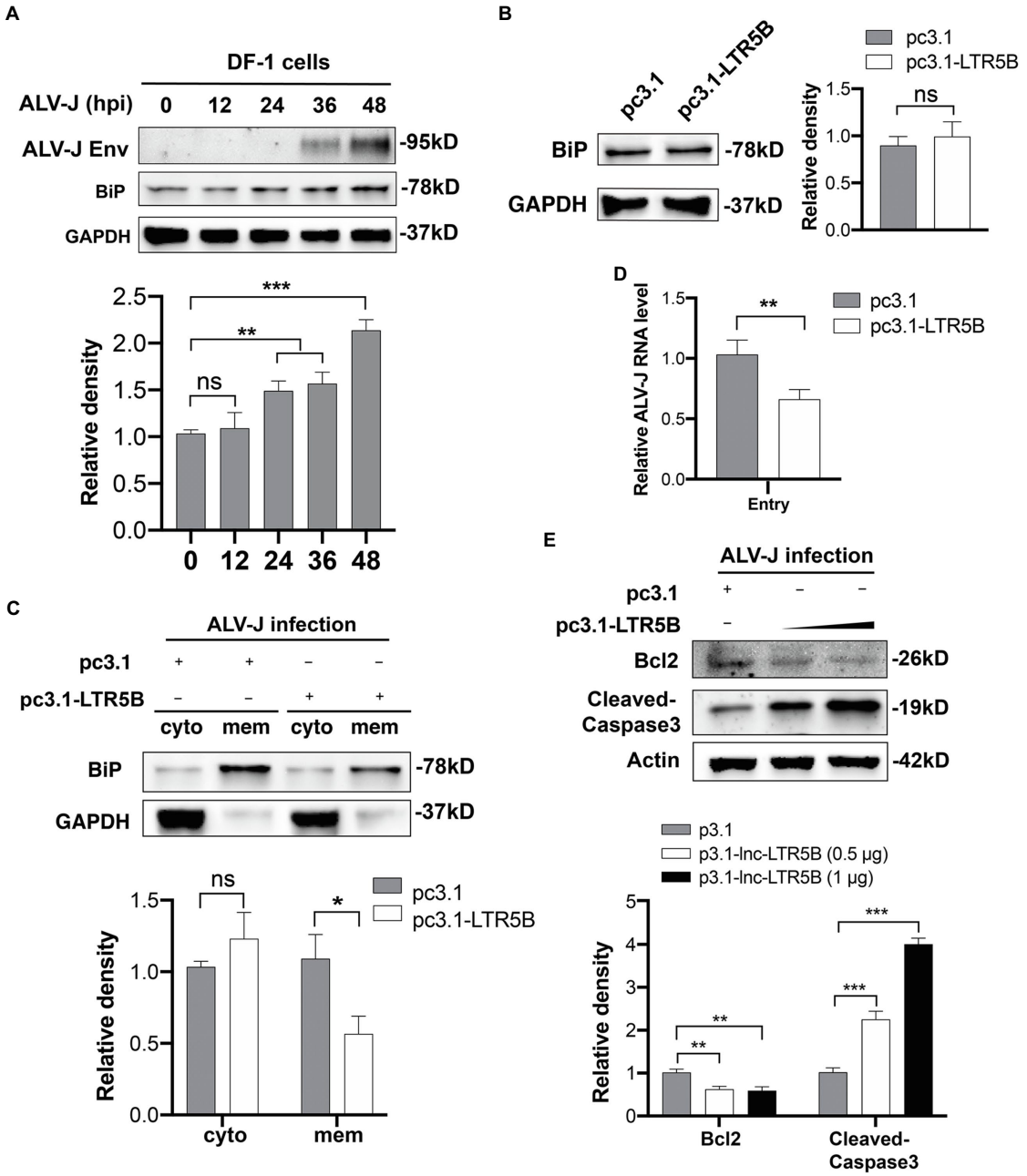

FIGURE 6 | lnc-LTR5B inhibits ALV-J by decreasing surface expression of BiP and promoting apoptosis of infected cells. **(A)** Western blot analysis of BiP expression in DF-1 cells infected with ALV-J for the indicated time. **(B)** Western blot analysis of BiP expression in DF-1 cells transfected with either pcDNA3.1-lnc-LTR5B or control vector. **(C)** Western blot analysis of cell surface distribution of BiP in DF-1 cells transfected with either pcDNA3.1-lnc-LTR5B or control for 24 h, followed by infection with ALV-J at MOI 5 for another 24 h. GAPDH served as markers for the plasma membrane and cytosol fractions. **(D)** DF-1 cells were transfected with pcDNA3.1-lnc-LTR5B or control vector for 24 h, followed by infection with ALV-J at MOI 20 on ice. At 1 h post-infection, the cells were cultured at 37°C for another 1 h. Then, the endocytosed-virus levels were determined by qRT-PCR for ALV-J genomic RNA. **(E)** Western blot analysis of Bcl2 and cleaved-caspase3 in DF-1 cells transfected with increasing amounts of pcDNA3.1-lnc-LTR5B or control pcDNA3.1, followed by infection with ALV-J at MOI 0.5 for 48 h. The relative intensities of the different protein bands were analyzed and quantified by ImageJ software (**A,C,E**, lower panel; **B**, right panel). Data are presented as mean ± SD, $n = 3$; $^{*}p < 0.05$, $^{**}p < 0.01$, $^{***}p < 0.001$, ns, not significant. Statistical analysis was carried out by one-way ANOVA **(A)** or two-tailed unpaired Student's *t*-test **(B,C,E)**.

GRP78, is encoded by the HSPA5 gene and belongs to the heat shock protein 70 (HSP70) family. As a typical chaperone in the endoplasmic reticulum (ER), BiP plays an essential role in controlling the unfolded protein response, which aims to restore ER homeostasis and promote cell survival (Wang et al., 2017).

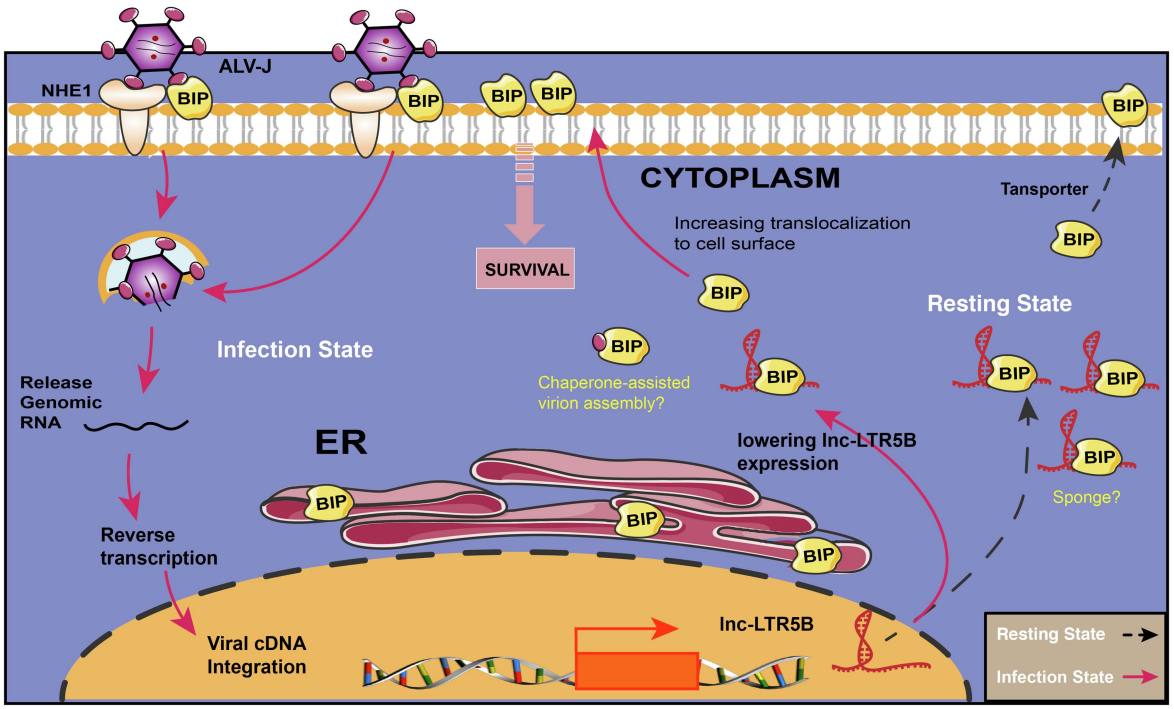

FIGURE 7 | Schematic diagram showing the proposed mechanism for the effects of lnc-LTR5B on regulating ALV-J infection *via* BiP. In resetting cells, lnc-LTR5B localizes in the cytoplasm where it is abundant and binds free BiP to control cell homeostasis. Upon ALV-J infection, lnc-LTR5B expression is reduced, which favors the dissociation of BiP from its binding state, allowing its translocation to the cell surface, which is crucial for ALV-J entry as well as pro-survival signaling.

Under ER stress conditions, BiP can be expressed at the cell surface, acting as a receptor for several signaling pathways, including anti-apoptotic and proliferative signals (Ni et al., 2011). Accumulating evidence has indicated that the translocation of BiP to the cell surface is associated with several pathological conditions, such as autoimmune diseases, cancers, and viral infections (Ni et al., 2011; Chu et al., 2018; Lenin et al., 2019). Viruses, such as SARS-CoV-2 (Carlos et al., 2021), were able to utilize cell surface BiP as an attachment factor mediating virus entry and pathogenesis. BiP has recently been described as a receptor for ALV-J entry into cells (Wang et al., 2016). Our data indicate that ALV-J causes BiP translocation to the cell surface, where the ALV-J envelope glycoprotein recognizes BiP, and mediates virus entry into host cells. Importantly, some BiP actions depend on its interaction with other proteins. For example, BiP surface translocation is required for different cotransporters, such as DNAJC3 (Vig et al., 2019), Par-4 (Cohen et al., 2013), and MTJ-1 (Misra et al., 2005), in a context-dependent manner. Recent studies have indicated that lncRNAs can directly interact with the molecular chaperone HSP90, regulating signaling or protein stability by altering chaperone function (Guo et al., 2018; Cui et al., 2020). Our data indicated that lnc-LTR5B binds to BiP in the cytoplasm. We investigated the potential influence of this interaction on BiP translocation to the cell surface. As expected, our data show that overexpression of lnc-LTR5B decreased BiP expression on cell surface induced by ALV-J infection in DF-1 cells (**Figure 6C**). Accumulating evidence has indicated that cell surface BiP is also implicated in pro-survival signals; an antibody that blocked cell surface BiP was used as an anti-tumor therapeutic (Shu et al., 2020). Consistent with this, we found lnc-LTR5B overexpression inhibited the expression of the anti-apoptotic protein Bcl-2 and increased caspase-3 activation, suggesting the activation of apoptotic signaling pathways. In addition, the cytoplasmic colocalization of BiP and ALV-J Env was observed in this study, and the impact of lnc-LTR5B on this interaction requires further investigation.

In summary, our study highlights the importance of lnc-LTR5B that modulates BiP cell surface translocation during ALV-J infection. In resetting cells, lnc-LTR5B expression is abundant and binds free BiP to control cell homeostasis; However, upon ALV-J infection, the expression of lnc-LTR5B is decreased, which releases BiP and allows its translocation to the cell surface; this is crucial for ALV-J entry and pro-survival signaling (**Figure 7**). We posit that the surface translocation of BiP is a critical process for cell survival in response to ALV-J infection (mild ER stress), while the presence of BiP at the cell surface might be exploited by ALV-J to complete its life cycle and propagate. Conversely, the overexpression of lnc-LTR5B sponges BiP, leading to cell apoptosis due to the interruption of the translocation process and prolonged ER stress. This study expands our knowledge of the LTR-derived lncRNAs in virus-host interactions and reveals novel cellular targets that have the potential to control ALV-J replication.

DATA AVAILABILITY STATEMENT

The original contributions presented in the study are included in the article/**Supplementary Material**, further inquiries can be directed to the corresponding authors.

ETHICS STATEMENT

The animal study was reviewed and approved by the Committee on the Ethics of Animal Experiments of Yangzhou University, Jiangsu Province, China.

AUTHOR CONTRIBUTIONS

SC and HC designed the experiment. SC, RZ, TW, DW, SP, and BW performed experiments. SC, RZ, DW, XH, and ZP analyzed the data. SC and RZ wrote and edited the manuscript. HC supervised the research project. All authors reviewed and approved the final manuscript.

FUNDING

This research was funded by the grant from the National Nature Science Foundation of China (32002271 and 91540117), the China Postdoctoral Science Foundation (2019M651986), and the Open Project Program of Jiangsu Key Laboratory of Zoonosis (R1911).

SUPPLEMENTARY MATERIAL

The Supplementary Material for this article can be found online at: https://www.frontiersin.org/articles/10.3389/fmicb.2021.788317/full#supplementary-material

REFERENCES

Araujo, N., Hebbar, N., and Rangnekar, V. M. (2018). GRP78 is a targetable receptor on cancer and stromal cells. *EBioMedicine* 33, 2–3. doi: 10.1016/j.ebiom.2018.06.030

Carlos, A. J., Ha, D. P., Yeh, D. W., Van Krieken, R., Tseng, C. C., Zhang, P., et al. (2021). The chaperone GRP78 is a host auxiliary factor for SARS-CoV-2 and GRP78 depleting antibody blocks viral entry and infection. *J. Biol. Chem.* 296:100759. doi: 10.1016/j.jbc.2021.100759

Carpenter, S., Aiello, D., Atianand, M. K., Ricci, E. P., Gandhi, P., Hall, L. L., et al. (2013). A long noncoding RNA mediates both activation and repression of immune response genes. *Science* 341, 789–792. doi: 10.1126/science.1240925

Chai, N., and Bates, P. (2006). Na+/H+ exchanger type 1 is a receptor for pathogenic subgroup J avian leukosis virus. *Proc. Natl. Acad. Sci. U. S. A.* 103, 5531–5536. doi: 10.1073/pnas.0509785103

Chattopadhyay, P., Srinivasa Vasudevan, J., and Pandey, R. (2021). Noncoding RNAs: modulators and modulatable players during infection-induced stress response. *Brief. Funct. Genomics* 20, 28–41. doi: 10.1093/bfgp/elaa026

Chen, S., Hu, X., Cui, I. H., Wu, S., Dou, C., Liu, Y., et al. (2019). An endogenous retroviral element exerts an antiviral innate immune function via the derived lncRNA lnc-ALVE1-AS1. *Antivir. Res.* 170:104571. doi: 10.1016/j.antiviral.2019.104571

Chu, H., Chan, C. M., Zhang, X., Wang, Y., Yuan, S., Zhou, J., et al. (2018). Middle East respiratory syndrome coronavirus and bat coronavirus HKU9 both can utilize GRP78 for attachment onto host cells. *J. Biol. Chem.* 293, 11709–11726. doi: 10.1074/jbc.RA118.001897

Cohen, M., Ribaux, P., Epiney, M., and Irion, O. (2013). Role of prostate apoptosis response 4 in translocation of GRP78 from the endoplasmic reticulum to the cell surface of trophoblastic cells. *PLoS One* 8:e80231. doi: 10.1371/journal.pone.0080231

Cui, R., Liu, C., Lin, P., Xie, H., Wang, W., Zhao, J., et al. (2020). LncRNA AC245100.4 binds HSP90 to promote the proliferation of prostate cancer. *Epigenomics* 12, 1257–1271. doi: 10.2217/epi-2020-0270

Dai, M., Feng, M., Xie, T., and Zhang, X. (2019). Long non-coding RNA and MicroRNA profiling provides comprehensive insight into non-coding RNA involved host immune responses in ALV-J-infected chicken primary macrophage. *Dev. Comp. Immunol.* 100:103414. doi: 10.1016/j.dci.2019.103414

Deng, B., Xu, W., Wang, Z., Liu, C., Lin, P., Li, B., et al. (2019). An LTR retrotransposon-derived lncRNA interacts with RNF169 to promote homologous recombination. *EMBO Rep.* 20:e47650. doi: 10.15252/embr.201847650

Durruthy-Durruthy, J., Sebastiano, V., Wossidlo, M., Cepeda, D., Cui, J., Grow, E. J., et al. (2016). The primate-specific noncoding RNA HPAT5 regulates pluripotency during human preimplantation development and nuclear reprogramming. *Nat. Genet.* 48, 44–52. doi: 10.1038/ng.3449

Gonzalez-Gronow, M., Gopal, U., Austin, R. C., and Pizzo, S. V. (2021). Glucose-regulated protein (GRP78) is an important cell surface receptor for viral invasion, cancers, and neurological disorders. *IUBMB Life* 73, 843–854. doi: 10.1002/iub.2502

Guan, X., Zhang, Y., Yu, M., Ren, C., Gao, Y., Yun, B., et al. (2018). Residues 28 to 39 of the extracellular loop 1 of chicken Na(+)/H(+) exchanger type I mediate cell binding and entry of subgroup J Avian Leukosis virus. *J. Virol.* 92:e01627-17. doi: 10.1128/JVI.01627-17

Guo, H., Zhao, L., Shi, B., Bao, J., Zheng, D., Zhou, B., et al. (2018). GALNT5 uaRNA promotes gastric cancer progression through its interaction with HSP90. *Oncogene* 37, 4505–4517. doi: 10.1038/s41388-018-0266-4

Hu, X., Chen, S., Jia, C., Xue, S., Dou, C., Dai, Z., et al. (2018). Gene expression profile and long non-coding RNA analysis, using RNA-Seq, in chicken embryonic fibroblast cells infected by avian leukosis virus. *J. Arch. Virol.* 163, 639–647. doi: 10.1007/s00705-017-3659-8

Jin, X., Xu, X. E., Jiang, Y. Z., Liu, Y. R., Sun, W., Guo, Y. J., et al. (2019). The endogenous retrovirus-derived long noncoding RNA TROJAN promotes triple-negative breast cancer progression via ZMYND8 degradation. *Sci. Adv.* 5:eaat9820. doi: 10.1126/sciadv.aat9820

Kapusta, A., Kronenberg, Z., Lynch, V. J., Zhuo, X., Ramsay, L., Bourque, G., et al. (2013). Transposable elements are major contributors to the origin, diversification, and regulation of vertebrate long noncoding RNAs. *PLoS Genet.* 9:e1003470. doi: 10.1371/journal.pgen.1003470

Khatun, M., Sur, S., Steele, R., Ray, R., and Ray, R. B. (2020). Inhibition of long noncoding RNA Linc-Pint by hepatitis C virus in infected hepatocytes enhances lipogenesis. *Hepatology* 74, 41–54. doi: 10.1002/hep.31656

Kim, J., Abdelmohsen, K., Yang, X., De, S., Grammatikakis, I., Noh, J. H., et al. (2016). LncRNA OIP5-AS1/cyrano sponges RNA-binding protein HuR. *Nucleic Acids Res.* 44, 2378–2392. doi: 10.1093/nar/gkw017

Lenin, R., Nagy, P. G., Jha, K. A., and Gangaraju, R. (2019). GRP78 translocation to the cell surface and O-GlcNAcylation of VE-cadherin contribute to ER stress-mediated endothelial permeability. *Sci. Rep.* 9:10783. doi: 10.1038/s41598-019-47246-w

Li, J., Li, M., Wang, X., Sun, M., Ma, C., Liang, W., et al. (2020). Long noncoding RNA NRAV promotes respiratory syncytial virus replication by targeting the MicroRNA miR-509-3p/Rab5c axis to regulate vesicle transportation. *J. Virol.* 94:e00113-20. doi: 10.1128/JVI.00113-20

Li, X., Lin, W., Chang, S., Zhao, P., Zhang, X., Liu, Y., et al. (2016). Isolation, identification and evolution analysis of a novel subgroup of avian leukosis virus isolated from a local Chinese yellow broiler in South China. *Arch. Virol.* 161, 2717–2725. doi: 10.1007/s00705-016-2965-x

Li, Z., Luo, Q., Xu, H., Zheng, M., Abdalla, B. A., Feng, M., et al. (2017). MiR-34b-5p suppresses melanoma differentiation-associated gene 5 (MDA5)

signaling pathway to promote avian leukosis virus subgroup J (ALV-J)-infected cells proliferaction and ALV-J replication. *Front. Cell. Infect. Microbiol.* 7:17. doi: 10.3389/fcimb.2017.00017

Li, H., Wang, P., Lin, L., Shi, M., Gu, Z., Huang, T., et al. (2019a). The emergence of the infection of subgroup J avian leucosis virus escalated the tumour incidence in commercial yellow chickens in southern China in recent years. *Transbound. Emerg. Dis.* 66, 312–316. doi: 10.1111/tbed.13023

Li, T., Xie, J., Liang, G., Ren, D., Sun, S., Lv, L., et al. (2019b). Co-infection of vvMDV with multiple subgroups of avian leukosis viruses in indigenous chicken flocks in China. *BMC Vet. Res.* 15:288. doi: 10.1186/s12917-019-2041-3

Lin, W., Xu, Z., Yan, Y., Zhang, H., Li, H., Chen, W., et al. (2018). Avian leukosis virus subgroup J Attenuates type I interferon production through blocking IkappaB phosphorylation. *Front. Microbiol.* 9:1089. doi: 10.3389/fmicb.2018.01089

Liu, W., Wang, Z., Liu, L., Yang, Z., Liu, S., Ma, Z., et al. (2020). LncRNA Malat1 inhibition of TDP43 cleavage suppresses IRF3-initiated antiviral innate immunity. *Proc. Natl. Acad. Sci. U. S. A.* 117, 23695–23706. doi: 10.1073/pnas.2003932117

Misra, U. K., Gonzalez-Gronow, M., Gawdi, G., and Pizzo, S. V. (2005). The role of MTJ-1 in cell surface translocation of GRP78, a receptor for alpha 2-macroglobulin-dependent signaling. *J. Immunol.* 174, 2092–2097. doi: 10.4049/jimmunol.174.4.2092

Ni, M., Zhang, Y., and Lee, A. S. (2011). Beyond the endoplasmic reticulum: atypical GRP78 in cell viability, signalling and therapeutic targeting. *Biochem. J.* 434, 181–188. doi: 10.1042/BJ20101569

Olivero, C. E., Martinez-Terroba, E., Zimmer, J., Liao, C., Tesfaye, E., Hooshdaran, N., et al. (2020). p53 activates the long noncoding RNA Pvt1b to inhibit Myc and suppress tumorigenesis. *Mol. Cell* 77, 761.e8–761.e774. doi: 10.1016/j.molcel.2019.12.014

Qiu, L., Li, Z., Chang, G., Bi, Y., Liu, X., Xu, L., et al. (2017). Discovery of novel long non-coding RNAs induced by subgroup J avian leukosis virus infection in chicken. *Dev. Comp. Immunol.* 76, 292–302. doi: 10.1016/j.dci.2017.06.015

Rebollo, R., Romanish, M. T., and Mager, D. L. (2012). Transposable elements: an abundant and natural source of regulatory sequences for host genes. *Annu. Rev. Genet.* 46, 21–42. doi: 10.1146/annurev-genet-110711-155621

Samanta, S., Yang, S., Debnath, B., Xue, D., Kuang, Y., Ramkumar, K., et al. (2021). The Hydroxyquinoline analogue YUM70 inhibits GRP78 to induce ER stress-mediated apoptosis in pancreatic cancer. *Cancer Res.* 81, 1883–1895. doi: 10.1158/0008-5472.CAN-20-1540

Shu, W., Guo, Z., Li, L., Xiong, Z., Wang, Z., Yang, Y., et al. (2020). Regulation of molecular chaperone GRP78 by hepatitis B virus: control of viral replication and cell survival. *Mol. Cell. Biol.* 40:e00475-19. doi: 10.1128/MCB.00475-19

Vig, S., Buitinga, M., Rondas, D., Crevecoeur, I., van Zandvoort, M., Waelkens, E., et al. (2019). Cytokine-induced translocation of GRP78 to the plasma membrane triggers a pro-apoptotic feedback loop in pancreatic beta cells. *Cell Death Dis.* 10:309. doi: 10.1038/s41419-019-1518-0

Wang, J., Lee, J., Liem, D., and Ping, P. (2017). HSPA5 gene encoding Hsp70 chaperone BiP in the endoplasmic reticulum. *Gene* 618, 14–23. doi: 10.1016/j.gene.2017.03.005

Wang, L., Mei, M., Qin, A., Ye, J., Qian, K., and Shao, H. (2016). Membrane-associated GRP78 helps subgroup J avian leucosis virus enter cells. *Vet. Res.* 47:92. doi: 10.1186/s13567-016-0373-6

Wang, Y., Wang, P., Zhang, Y., Xu, J., Li, Z., Li, Z., et al. (2020). Decreased expression of the host long-noncoding RNA-GM facilitates viral escape by inhibiting the kinase activity TBK1 via S-glutathionylation. *Immunity* 53, 1168.e7–1181.e7. doi: 10.1016/j.immuni.2020.11.010

Conflict of Interest: The authors declare that the research was conducted in the absence of any commercial or financial relationships that could be construed as a potential conflict of interest.

Publisher's Note: All claims expressed in this article are solely those of the authors and do not necessarily represent those of their affiliated organizations, or those of the publisher, the editors and the reviewers. Any product that may be evaluated in this article, or claim that may be made by its manufacturer, is not guaranteed or endorsed by the publisher.

frontiers in Microbiology

REVIEW
published: 01 December 2021
doi: 10.3389/fmicb.2021.794882

Regulation of Tripartite Motif-Containing Proteins on Immune Response and Viral Evasion

Xiu-Zhong Zhang[1], Fu-Huang Li[2] and Xiao-Jia Wang[1]**

[1]Key Laboratory of Animal Epidemiology of the Ministry of Agriculture, College of Veterinary Medicine, China Agricultural University, Beijing, China, [2]Beijing General Station of Animal Husbandry Service (South Section), Beijing, China

Tripartite motif-containing proteins (TRIMs), exhibiting ubiquitin E3 ligase activity, are involved in regulation of not only autophagy and apoptosis but also pyrotosis and antiviral immune responses of host cells. TRIMs play important roles in modulating signaling pathways of antiviral immune responses *via* type I interferon, NF-κB, Janus kinase/signal transducer and activator of transcription (JAK/STAT), and Nrf2. However, viruses are able to antagonize TRIM activity or evenly utilize TRIMs for viral replication. This communication presents the current understanding of TRIMs exploited by viruses to evade host immune response.

Keywords: TRIM proteins, type I interferon, NF-kappa B, immune evasion, signaling pathways, immune response

OPEN ACCESS

Edited by:
Jue Liu,
Yangzhou University, China

Reviewed by:
Junji Xing,
Houston Methodist Research Institute, United States
Yang Linwei,
Sun Yat-sen University, China

****Correspondence:***
Fu-Huang Li
lfh5118@126.com
Xiao-Jia Wang
wangxj@cau.edu.cn

Specialty section:
This article was submitted to Virology, a section of the journal Frontiers in Microbiology

Received: *14 October 2021*
Accepted: *08 November 2021*
Published: *01 December 2021*

Citation:
Zhang X-Z, Li F-H and Wang X-J (2021) Regulation of Tripartite Motif-Containing Proteins on Immune Response and Viral Evasion. Front. Microbiol. 12:794882. doi: 10.3389/fmicb.2021.794882

INTRODUCTION

Tripartite motif-containing proteins (TRIMs), an expanding family of proteins characterized by their N-terminal domains, containing a tripartite motif, are widely present in mammals (Marin, 2012). They are also known as RBCC proteins from the presence of an RBCC motif, consisting of a RING domain, one or two B-boxes, and a coiled-coil region (**Figure 1**; Reddy and Etkin, 1991; Meroni and Diez-Roux, 2005). In contrast to the conserved N-terminal domains, the additional C-terminal domains are variable and can be used to classify TRIMs into 11 subfamilies (Ozato et al., 2008).

Presenting in most TRIMs, the RING domain is comprised of a zinc finger motif (Borden, 2000). This motif confers E3-ligase activity and is able to catalyze the conjugation of ubiquitin and ubiquitin-like proteins (ISG15 or SUMO), leading to the degradation of targeted proteins (Meroni and Diez-Roux, 2005; Ozato et al., 2008; Marin, 2012). Following the RING domain, the B-box domains are also zinc finger motifs. However, their functions are still largely unclear (Nisole et al., 2005; Meroni, 2012). It seems that they are involved in viral recognition, self-association, or interactions with other proteins (Nisole et al., 2005; Meroni, 2012). The coiled-coil domain (CCD) is the third domain of the RBCC motif. This domain has the ability to assemble with other coiled-coil structures, mediating homomeric self-association and heteromeric assemblies (Nisole et al., 2005). So far, 10 different types of C-terminal domain have been described, one or more of which can be present (Ozato et al., 2008). Specific C-terminal domains confer different functions by recruiting unique functional partners (Nisole et al., 2005; Khan et al., 2019).

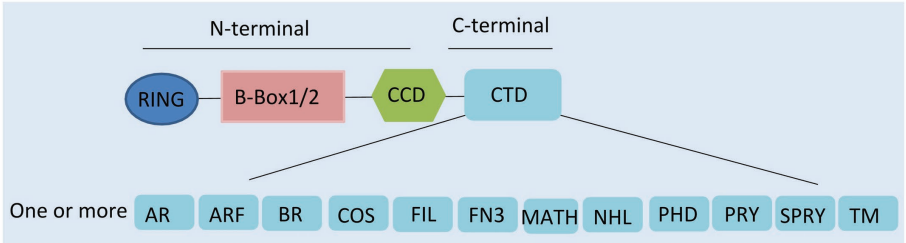

FIGURE 1 | Domain structure of tripartite motif-containing protein (TRIM) family proteins. TRIM contains a RING domain, a B-box 1 and/or B-box 2 domain, a coiled-coil domain (CCD), and distinct C-terminal domains. AR, acid-rich region; ARF, ADP ribosylation-like factor; BR, bromodomain; COS, C-terminal subgroup one signature; FIL, filamin-type immunoglobulin; FN3, fibronectin type 3; MATH, meprin and tumor-necrosis receptor-associated factor homology; NHL, NHL repeats; PHD, plant homeodomain; PRY, SPRY-associated domain; SPRY, SPla, and the ryanodine receptor domain; and TM, transmembrane.

TRIMs have been characterized in detail as members of E3-ubiquitin ligase group according to their interactions with E2-ubiquitin ligase (Rajsbaum et al., 2014a). Briefly, TRIMs transfer ubiquitin to the target protein by facilitating interaction with E2 enzymes *via* their RING domain. It has been shown that TRIMs can catalyze synthesis of K48-, K63-, or unanchored K63-linked poly-ubiquitin chains. Proteins that with K48-linked poly-ubiquitin are usually targeted for degradation by the proteasome. However, proteins with K63-linked polyubiquitin are involved in activation of antiviral signaling pathways. In addition, unanchored K63-linked poly-ubiquitin chains have also been proposed to activate kinases involved in signaling pathways in a proteasomal degradation-independent manner.

Tripartite motif-containing proteins are involved in various biological functions, including apoptosis, pyroptosis, antiviral activity, and viral evasion (Hatakeyama, 2017; Chen et al., 2018b; Koepke et al., 2021). TRIMs are involved in innate immune responses to restrict the replication of various viruses, while viruses have evolved strategies to antagonize TRIMs (Nisole et al., 2005; Rajsbaum et al., 2014a; Koepke et al., 2021). In addition, viruses are able to employ TRIMs to enhance their replication (Xing et al., 2017; Li et al., 2018; Zheng et al., 2019a).

In this review, we describe the functions of TRIMs in immune signaling pathways and discuss the latest research on viral evasion of immune system by antagonizing or utilizing TRIMs.

TRIM REGULATION OF INNATE IMMUNE RESPONSE

In response to viral infection, eukaryotes have evolved many strategies to restrict viral replication. As the first line of defense, the innate immune response is initiated when pattern recognition receptors (PRRs) recognize pathogen-associated molecular patterns (PAMPs; Medzhitov, 2007). There are a number of types of PRRs, including Toll-like receptors (TLRs), NOD-like receptors (NLRs), C-type lectin receptors (CLRs), and RIG-I-like receptors (RLRs; Kagan and Barton, 2014). PRRs use various adaptor proteins to activate downstream signaling pathways, and this leads to the production of interferons (IFNs) and inflammatory factors as well as interferon-stimulated genes (ISGs); those factors are important in the defense against incoming pathogens (Rajsbaum et al., 2014a).

Some review articles demonstrated that TRIMs act as important positive and negative modulators of PRR signaling pathways (Ozato et al., 2008; Rajsbaum et al., 2014a). In this section, we detail the role of TRIMs in regulating several main pathways, including TLR, RLR, STING, and Janus kinase/signal transducer and activator of transcription (JAK/STAT) signaling.

Toll-Like Receptor

Human TLR1, TLR2, TLR4, TLR5, and TLR6 are associated with the plasma membrane, while TLR3, TLR7, TLR8, and TLR9 are located in the endosome (Jimenez-Dalmaroni et al., 2016; Odendall and Kagan, 2017). Although TLR4 is mainly located in the plasma membrane, it can also be internalized in the endosome (van Tol et al., 2017). TLRs were first identified as receptors of bacterial PAMPs and also have recently been found to respond to viral infection (Bottermann and James, 2018; van Gent et al., 2018). TLR3 senses both double-stranded RNA (dsRNA) and single-stranded RNA (ssRNA) of viruses, TLR7 and TLR8 can recognize viral single-stranded RNA, and TLR9 recognizes CpG motifs (Thompson et al., 2011; Tatematsu et al., 2013; Jimenez-Dalmaroni et al., 2016). All TLRs except TLR3 signal through the adaptor molecule MyD88 by recruiting the kinases IRAK1/4 and E3 ubiquitin ligase TRAF6, and this results in the activation of the NF-κB and AP-1 signaling pathways (Villano et al., 2014; Jimenez-Dalmaroni et al., 2016). TLR3 and TLR4 can interact with adaptor TRIF, resulting in the activation of IRF, NF-κB, and AP-1 signaling pathways *via* TRAF3 and TBK1/IKKε (Gay et al., 2014).

Tripartite motif-containing proteins are able to modulate the TLR signaling pathways (Shen et al., 2012; Hu et al., 2014; Sundquist and Pornillos, 2018; Ganser-Pornillos and Pornillos, 2019). It has been proposed that TRIM5α is implicated in NF-κB signaling pathways and promotes the synthesis of unanchored K63-linked polyubiquitin chains, which can in turn activate the TAK1 (Sundquist and Pornillos, 2018; Ganser-Pornillos and Pornillos, 2019). TRIM56 has been shown to interact with TRIF in TLR3-mediated IFN/ISG production (Shen et al., 2012). TRIM38 negatively regulates TLR signaling

by targeting TRAF6, TRIF, and NAP1 for degradation, leading to the suppression of TAB2/3, TBK1/IKKε, and IRF3/7 (Zhao et al., 2012; Hu et al., 2014, 2015). TRIM8 negatively affects TLR3/4-mediated response by catalyzing the polyubiquitination of TRIF, resulting in disruption of the TRIF–TBK1 interaction (Ye et al., 2017).

RIG-I-Like Receptor

RIG-I-like receptors are essential sensors in the process of viral infection, responding to dsRNA or ssRNA containing 5'-triphophates (Runge et al., 2014). RIG-I and melanoma differentiation-associated protein (MDA5) induce antiviral pathways and contain a central DEAD (Asp-Glu-Ala-Asp) box, a C-terminal domain (CTD), and two N-terminal caspase-activated recruitment domains (CARDs; Chan and Gack, 2015). RIG-I encoded by *Ddx58* binds small dsRNA, while MDA5 encoded by *Ifih1* recognizes long ssRNA (Chiang et al., 2018b; van Gent et al., 2018). Binding viral RNA to RIG-I or MDA5 induces the activation of RLR pathways. Then the CARDs are exposed, which leads to the recruitment of RIG-I or MDA5 to their common adaptor mitochondrial antiviral signaling protein (MAVS; Yoneyama et al., 2004; Jiang et al., 2012). MAVS can activate NF-κB and IRF3/7 pathways, finally *via* recruiting IKK-related kinases IKKα/β/γ complex and IKKε, respectively (Takeuchi and Akira, 2010).

Some TRIMs act as key regulators of RLR signaling (Tan et al., 2017; Chen et al., 2019; Sun et al., 2020). As a positive regulator of RLR signaling, TRIM35 directly catalyzes K63-linked polyubiquitination of TRAF3. This promotes the formation of a signaling complex TRAF3-MAVS-TBK1, facilitating the activation of IRF3/7 (Sun et al., 2020). TRIM14 provides a docking platform for the assembly of MAVS complex, consisting of Werner helicase interacting protein 1 (WHIP) and protein phosphatase PPP6C (Tan et al., 2017). TRIM14 is also reported to recruit adaptor protein IKKγ/NEMO to MAVS, taking part in RIG-1-mediated IRF3 and NF-κB signaling (Zhou et al., 2014). TRIM65, identified as an E3 ligase of MDA5, catalyzes K63-linked polyubiquitination of MDA5 at the RNA helicase domain K743, promoting IRF3/7 signaling to restrict encephalomyocarditis virus (EMCV; Lang et al., 2017). EcTRIM44L, identified from the orange spotted grouper fish, negatively regulates MAVS-mediated IFN response rather than IRF3-mediated (Zheng et al., 2019b).

STING

STING is at the outer mitochondrial membrane and ER, and most cytosolic DNA sensors activate it. Various cytosolic DNA sensors have been identified in recent years, including cyclic GMP-AMP synthase (cGAS), DDX41, and DHDX36 (Ishikawa et al., 2009). It has been reported that they can detect various DNA viruses, including adenoviruses (AdV), human cytomegalovirus (HCMV), and HSV-1, as well as retroviruses such as vesicular stomatitis virus (VSV), human immunodeficiency virus (HIV), and Dengue virus (DENV; Paijo et al., 2016; Reinert et al., 2016; Sun et al., 2017; Tan et al., 2018). Upon DNA binding, STING signaling is activated. It has been shown that STING interacts with TBK1, which phosphorylates IRF3/7, resulting in type I IFN induction (Vance, 2016).

Several TRIMs have been demonstrated to modulate STING-mediated signaling *via* regulatory modifications (Tsuchida et al., 2010; Zhang et al., 2012; Wang et al., 2014; Seo et al., 2018). Mammalian TRIM32 may target STING for K63-linked ubiquitination to promote dimerization and enhance type I IFN production (Zhang et al., 2012). The function of TRIM 56 in the induction of antiviral response is controversial. An initial report described TRIM56 interacting with STING by inducing K63-linked polyubiquitination of STING upon cytosolic DNA stimulation, but a later study failed to detect any ubiquitination signal of STING in the presence of TRIM56. A very recent study showed that TRIM56 directly targets cGAS, rather than STING or its downstream signaling, against HSV-1 infection but not against influenza A virus (IAV) infection (Tsuchida et al., 2010; Wang et al., 2014; Seo et al., 2018), similar to the SUMOylation of RIG-I and MDA5, TRIM38 SUMOylates cGAS, and STING, which inhibits the ligation of K48-linked ubiquitin and proteasomal degradation (Hu et al., 2016).

Janus Kinase/Signal Transducer and Activator of Transcription

Janus kinase/signal transducer and activator of transcription signaling induces multiple molecular immune responses and is essential in cytokine and growth factor signaling (Ghoreschi et al., 2009). Four different JAKs have been identified, including JAK1, JAK2, JAK3, and TyK2 (Tyrosine kinase 2), and seven members of STAT, including STAT1, STAT2, STAT3, STAT4, STAT5a, STAT5b, and STAT6 (Meyts and Casanova, 2021). JAK/STAT is initially activated by binding of cytokines, such as IFNα/β, IFNγ, and IL-6. IFNα/β employs TYK2 and JAK1 to phosphorylate STAT1 and STAT2, IFNγ recruits JAK1 and JAK2 to phosphorylate STAT1, and IL-6 leads to one or both JAK-mediated phosphorylations of STAT3 (Majoros et al., 2017; Banji et al., 2021). These activated STAT dimers are then transported to the nucleus and promote the transcription of interferon stimulated genes (ISGs; Raftery and Stevenson, 2017). Negative regulators, protein tyrosine phosphatase, non-receptor type 6 (PTPN6), suppressor of cytokine signaling (SOCS-1) and protein inhibitor of activated STAT (PIAS-1), suppress the JAK/STAT pathway (Cokic et al., 2012; Tikhe and Dimopoulos, 2021).

Reports have indicated that the JAK/STAT pathway can be regulated by some TRIMs (Rajsbaum et al., 2014b; Teng et al., 2020; van Tol et al., 2020). TRIM6 was found to modulate IFNα/β-induced JAK/STAT signaling for antiviral response *via* cooperation with E2-ubiquitin conjugase UbE2K and promotion of the synthesis of unanchored K48-linked polyubiquitin chains, which activated IKKε for subsequent STAT1 phosphorylation (Rajsbaum et al., 2014b). Another study identified VAMP8, a regulator of IFNα/β-induced JAK/STAT signaling, and mediator of the phosphorylation of STAT1 in West Nile virus infection. Its expression and function are dependent on TRIM6 activity (van Tol et al., 2020). TRIM59 interacts with STAT1 by recruiting much more PIAS1 to suppress

the activation of STAT1, and it also suppresses IL-1β-induced activation of the JAK2/STAT3 pathway (Su et al., 2020; Teng et al., 2020). TRIM8 enhances IL-6-dependent activation of STAT3 by degradation of PIAS3, which is the protein inhibitor of activated STAT3 (Okumura et al., 2010).

VIRAL ANTAGONIZATION OF TRIMs

Researches have shown that TRIMs play a critical role in restricting viral replication *via* regulating the innate immune signaling (Masroori et al., 2016; Choudhury et al., 2020). Viruses, however, have developed various strategies to antagonize the antiviral function of TRIM proteins, including improving their proteasomal degradation, affecting their relocation, and ubiquitination (Schilling et al., 2017; Chen et al., 2018a; Koepke et al., 2021). For example, IAV is able to antagonize TRIM25 for its replication (Gack et al., 2009). In this section, we discussed the mechanism of viral evasion by antagonization of TRIMs, including TRIM6, TRIM19, TRIM23, and TRIM25, as depicted in **Figure 2**.

TRIM6

TRIM6 restricts viral replication *via* enhancing type I IFN production. It interacts with IKKε and catalyzes the synthesis of unanchored K48-linked polyubiquitin chains, which in turn activates IKKε for subsequent STAT1 phosphorylation, resulting in increasing of IRF3-mediated type I IFN production (Rajsbaum et al., 2014b). This pathway can be evaded by the matrix structural protein (M) of Nipah virus (NiV). The NiV-M protein interacts with TRIM6 and promotes TRIM6 degradation, so the synthesis of unanchored K48-linked polyubiquitin chains and production of type I IFNs are inhibited (Bharaj et al., 2016). It has been reported that the Ebola virus VP35 protein hijacks TRIM6 to promote its ubiquitination and polymerase activity, which results in the reduction of type I IFNs and increase of virus replication (Bharaj et al., 2017).

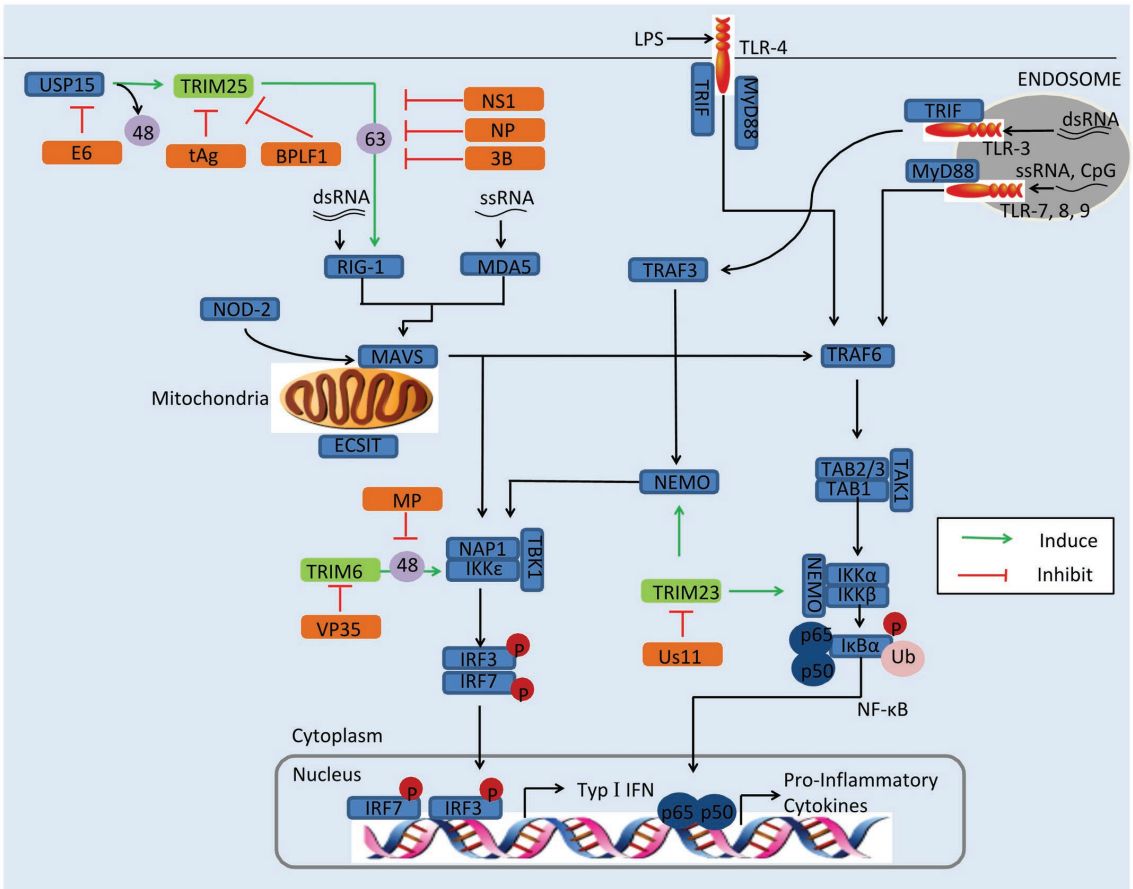

FIGURE 2 | Viral evasion of immunity *via* antagonization of TRIMs. Some TRIMs (green) positively regulate innate immune response. Viral proteins (orange) antagonize these TRIMs to reduce the production of type I IFNs and inflammatory factors. BPLF1, the deconjugases of HSV; E6, the oncoprotein of HPV16; MP, the matrix structural protein of NiV; NS1, the nonstructural protein 1 of IAV; NSs, the nonstructural protein NSs of SFTSV; NP, the nucleocapsid protein of SARS-CoV, MERS-CoV, or SARS-CoV-2; tAg, the small t antigen of JCV; Us11, the Us11 protein of HSV-1; VP35, the VP35 protein of EBOV; 3B, the 3B protein of FMDV; 48, K48-linked polyubiquitination; and 63, K63-linked polyubiquitination.

TRIM19/PML

TRIM19/PML, also named leukemia (PML) protein, localizes both in the nucleoplasm and in the nuclear bodies (NBs). The function of TRIM19 in viral restriction has been fairly thoroughly investigated, for both DNA viruses and RNA viruses, such as vesicular stomatitis virus (VSV), HSV, IAV, varicella-zoster virus (VZV), HIV, HCMV, and rabies virus (Blondel et al., 2010; Reichelt et al., 2011; Dutrieux et al., 2015; Masroori et al., 2016). The mechanisms of restriction are various and include the silencing of viral genomes, entrapment of newly synthesized nucleocapsids (Ns), indirect interference with reverse transcription, and regulating of type I IFN induction.

On the other hand, some viruses have developed strategies to suppress PML. The HCMV immediate-early protein IE1, for instance, directly binds to the CCD of TRIM19 through its globular core, and it prevents the SUMOylation of TRIM19 and disrupts the nuclear bodies (Scherer et al., 2014). Binding of IE1 to TRIM19 abrogates the *de novo* SUMOylation of PML at specific lysine residues, but this does not affect global protein SUMOylation (Schilling et al., 2017). TRIM19 represses the replication of EV71 by inhibiting autophagy and increasing response to IFNs (Chen et al., 2018a). In EV71-infected Hela cells, the expression of TRIM19 is reduced and the reduction is caused by viral protease $3C^{pro}$ rather than proteasome pathway (Chen et al., 2018a). The degradation of NB-associated PML has also been identified in HSV-1-infected cells. The HSV-1 immediate-early protein ICP0 directly binds to PML and Sp100, inducing proteasome-dependent degradation (Chelbi-Alix and de The, 1999; Boutell et al., 2003). The ORF75c protein encoded by murine gammaherpesvirus 68 (MHV68) contains ubiquitin E3 ligase activity and mediates direct ubiquitination of PML, resulting in its degradation by the proteasome (Sewatanon and Ling, 2013). Arenaviruses use a different strategy to incapacitate TRIM19: The Z protein of arenaviruses colocalizes with PML *via* the RING domain and induces its relocation from NBs to the cytoplasm (Kentsis et al., 2001) This results in PML and the Z protein binding directly to the translation initiation factor eIF4E and inhibiting translation (Kentsis et al., 2001).

TRIM19 plays an important role against various viral infections, and the restriction of TRIM19 to viruses depends on the antiviral mechanisms induced by IFNs (Nisole et al., 2005; Chen et al., 2018a). Viruses have developed strategies to antagonize TRIM19, but the NB disruption induced by TRIM19 degradation to overcome a cellular antiviral defense remains controversial (Kentsis et al., 2001; Lopez et al., 2002). In PML overexpression cells, ICP0 colocalized with PML in ND10 early in infection, but the two proteins did not overlap or were juxtaposed in orderly structures and PML overexpression had no significant effect on HSV-1 replication (Lopez et al., 2002). It is possible that other virus mechanisms may block PML-mediated repression, and further studies are needed.

TRIM23

It has been demonstrated that TRIM23 is involved in the induction of autophagy to decrease viral replication (Sparrer et al., 2017). Upon viral infection, the GTP hydrolysis activity of TRIM23 is activated by the autoubiquitination of ARF with unconventional K27-linked polyubiquitin. This facilitates TBK1 dimerization, which proceeds to phosphorylate p62 and ultimately induces autophagic degradation of viral components (Sparrer et al., 2017).

HSV-1 has developed strategy to enhance its replication by antagonizing TRIM23. In HSV-1-infected cells, on the other hand, expression of the HSV-1 Us11 protein promotes HSV-1 growth, while expression of TRIM23 restricts HSV-1 replication in the absence of US11 (Liu et al., 2019). The Us11 protein binds the ARF domain in TRIM23 and disrupts the TRIM23-TBK1 complex, causing decrease of autophagy-mediated restriction of HSV-1 infection (Liu et al., 2019).

TRIM25

TRIM25 restricts the replication of viruses, such as MERS-CoV, NDV, IAV, SinV, SARS-CoV-2, porcine reproductive and respiratory syndrome virus (PRRSV), and Sendai virus (SeV; Zeng et al., 2010; Sanchez et al., 2016; Hu et al., 2017; Zhao et al., 2019; Choudhury et al., 2020). TRIM25 catalyzes K63-linked polyubiquitination on the N-terminal CARD at K172 of RIG-I *via* its B30.2 domain chains, and this facilitates its recruitment to MAVS and thus induces downstream IFNs induction (Sanchez et al., 2016). However, K48-linked ubiquitination of TRIM25 negatively regulates RIG-I activation, though this can be reversed by the deubiquitinating enzyme USP15 (Pauli et al., 2014). Recently, it was found that TRIM25 enhances the antiviral activity of zinc finger antiviral protein (ZAP) with both ubiquitin ligase activity and multimerization (Li et al., 2017; Zheng et al., 2017). In addition, TRIM25 ubiquitinates DDX3X (a critical component of TBK1) at K55, and TRIM25 and DDX3X cooperatively enhance type I IFN induction following RIG-I activation (Soulat et al., 2008; Atkinson et al., 2021).

TRIM25 plays an important role in a broad range of antiviral activity; however, viruses have evolved a diverse collection of strategies to antagonize TRIM25 activity. The nonstructural protein 1 (NS1) of IAV, for instance, targets the TRIM25 coiled-coil domain directly, thus inhibiting TRIM25 dimerization and preventing the activation of RIG-I with K63-polyubiquitin (Gack et al., 2009). The interaction between NS1 and TRIM25 has been shown to be species-specific, in that human TRIM25 binds to all species-adapted IAV strains, while chicken TRIM25 interacts with NS1 only from avian strains, and murine TRIM25 does not bind with any NS1 interacts (Rajsbaum et al., 2012). However, a recent study of the crystal structures of TRIM25-NS1 complexes showed that the formation of unanchored K63-linked polyubiquitin chains is unchanged by NS1 binding. And the binding of NS1 interferes with the correct positioning of the PRYSPRY domain of TRIM25, which is required for substrate ubiquitination (Koliopoulos et al., 2018). Moreover, the N-terminal domain of NS1 encoded by IBV is responsible for interaction with TRIM25, and this interaction blocks the Lys63-linked ubiquitination of RIG-I (Jiang et al., 2016). Recently, it was found that NS1 disrupts the TRIM25:DDX3X interaction, abrogating both TRIM25-mediated ubiquitination

of DDX3X and cooperative activation of the IFNB1 promoter (Atkinson et al., 2021).

Like IAV/IBV, the coronaviruses, including SARS-CoV, MERS-CoV, and SARS-CoV-2, are able to suppress TRIM25 activity *via* the viral N protein. The N protein of SARS-CoV has been demonstrated to interact with the C-terminal SPRY domain of TRIM25, interfering with subsequent ubiquitination of the RIG-I CARD domains and negative regulating type I IFNs (Hu et al., 2017). This strategy of RIG-I-induced IFN-β reduction is also seen in SARS-CoV-2 and MERS-CoV (Hu et al., 2017; Oh and Shin, 2021). In addition to modulating type I IFNs, the N protein of MERS-CoV also suppresses type III expression, and this offers a plausible mechanism for coronavirus evasion of the host immune response (Chang et al., 2020). Interestingly, although not a coronavirus, PRRSV exhibits a similar loss of RIG-I-induced IFN-β when its N protein associates with TRIM25 (Zhao et al., 2019). In foot-and-mouth disease virus (FMDV), it is 3B protein that suppresses type I IFN production and host antiviral response by blocking the interaction between RIG-I and TRIM25, which prevents the TRIM25-mediated, K63-linked ubiquitination of RIG-I (Zhang et al., 2020b).

Severe fever with thrombocytopenia syndrome virus (SFTSV), a highly pathogenic member of the *Bunyavirales*, has developed a different mechanism to inhibit TRIM25. The nonstructural protein NSs of SFTSV interacts with and redistributes RIG-I, TRIM25, and TBK1 into NSs-induced cytoplasmic structures, which circumvents IFN responses (Santiago et al., 2014). Another report demonstrated that NSs specifically trap TRIM25 into viral inclusion bodies and inhibits TRIM25-mediated RIG-ILys-63-linked ubiquitination/activation, contributing to suppression of RLR-mediated antiviral signaling at its initial stage (Min et al., 2020).

The DENV and human papillomavirus Type 16 (HPV16) suppress TRIM25 activity by USP15 to attenuate RIG-I signaling. PR-2B, an epidemic strain of dengue virus, encodes subgenomic flavivirus RNA, which binds to host TRIM25 and prevents USP15-mediated deubiquitination (Manokaran et al., 2015). The E6 oncoprotein of HPV16 interacts with TRIM25 and USP15, promoting K48-linked ubiquitination of TRIM25 and suppressing TRIM25-mediated K63-linked ubiquitination of RIG-I to evade the host antiviral response (Chiang et al., 2018a).

The small t antigen (tAg) of JC polyomavirus (JCV) interacts with TRIM25, preventing it from binding with RNA and inhibiting the K63-linked ubiquitination of RIG-I (Chiang et al., 2021). This antagonism strategy is also conserved in tAg presented polyomavirus BK virus (BKV; Chiang et al., 2021). Herpesviruses use a different strategy to antagonize TRIM25 activity. BPLF1 of herpesvirus promotes the dimerization and autoubiquitination of TRIM25, which inactivates the RIG-I signalosome (Gupta et al., 2018).

VIRAL UTILIZATION OF TRIMs

Some of TRIMs exhibit negatively regulatory effect in the innate immune. Thus, apart from antagonizing TRIMs, some viruses directly utilize TRIMs or induce their gene expression to promote viral replication. In this section, we discuss viruses employ TRIMs to enhance their replication, including TRIM21, TRIM26, TRIM27, TRIM29, and TRIM30a, as depicted in **Figure 3**.

TRIM21

TRIM21, also named Ro52, seems to follow two strategies; some studies indicate that TRIM21 restricts viral replication and positively regulates antiviral pathways, while other reports show that TRIM21 negatively regulates innate immune response to promote viral production (Higgs et al., 2008; Yang et al., 2009; McEwan et al., 2013; Zhang et al., 2013; Manocha et al., 2014). On the one hand, TRIM21 has exhibited antiviral activity. TRIM21 catalyzes the formation of Lys63 (K63)-linked ubiquitin chains and activates the NF-κB, AP-1, and IRF signaling pathways (McEwan et al., 2013). However, in porcine epidemic diarrhea virus (PEDV) infection, TRIM21 exhibits a different strategy; TRIM21 was found to interact and colocalize with the N protein, inducing the degradation of the N protein in a proteasome-dependent manner (Wang et al., 2021).

On the other hand, TRIM21 is also able to facilitate viral evasion of the innate immune response. TRIM21 interacts with IRF3 *via* its C-terminal SPRY domain post-pathogen recognition, resulting in the polyubiquitination and proteasomal degradation of IRF3 (Higgs et al., 2008). The SPRY-PRY domain of TRIM21 targets the DEADc domain of DDX41 at Lys9 and Lys115, inducing the Lys48 (K48)-linked ubiquitination and degradation of DDX41 and thereby inhibiting the innate immune response to intracellular dsDNA (Zhang et al., 2013). Evidence shows that Japanese encephalitis virus (JEV) evades the innate immune response by inducing transcriptional expression of TRIM21 (Manocha et al., 2014). In JEV-infected human microglial cells, TRIM21 overexpression inhibited phosphorylation of IRF3 and activation of IFN-β, while TRIM21 silencing contributed to the type I IFN responses (Manocha et al., 2014).

Other mechanisms involved in antiviral evasion have been reported recently. HPV E7 was found to recruit TRIM21 to ubiquitinate and degrade the IFI16 inflammasome, leading to the inhibition of cell pyroptosis and production of inflammatory factors including IL-18 and IL-1β (Song et al., 2020). SFTSV NSs binds to the carboxylterminal SPRY subdomain of TRIM21, promoting p62 stability and oligomerization and causing activation of the Nrf2 antioxidant signal pathway (Choi et al., 2020). The activation of the p62-Keap1-Nrf2 antioxidant response provides an optimal environment for SFTSV replication (Choi et al., 2020).

TRIM23

At least two studies have revealed that TRIM23 is an important factor in virus replication (Laurent-Rolle et al., 2014). TRIM23 interacts with and polyubiquitinates yellow fever virus (YFV) NS5 to promote its binding to STAT2 and trigger IFN-I signaling inhibition, thus overcoming the antiviral action of IFN-I (Laurent-Rolle et al., 2014). MnTrim23 identified from *Macrobrachium nipponense* negatively regulates the Relish transcription factor-mediated expression of antimicrobial peptides (AMPs), promoting WSSV replication (Zhang et al., 2020a). It has been also shown that knockdown of MnTrim23 inhibits WSSV replication and VP28 expression.

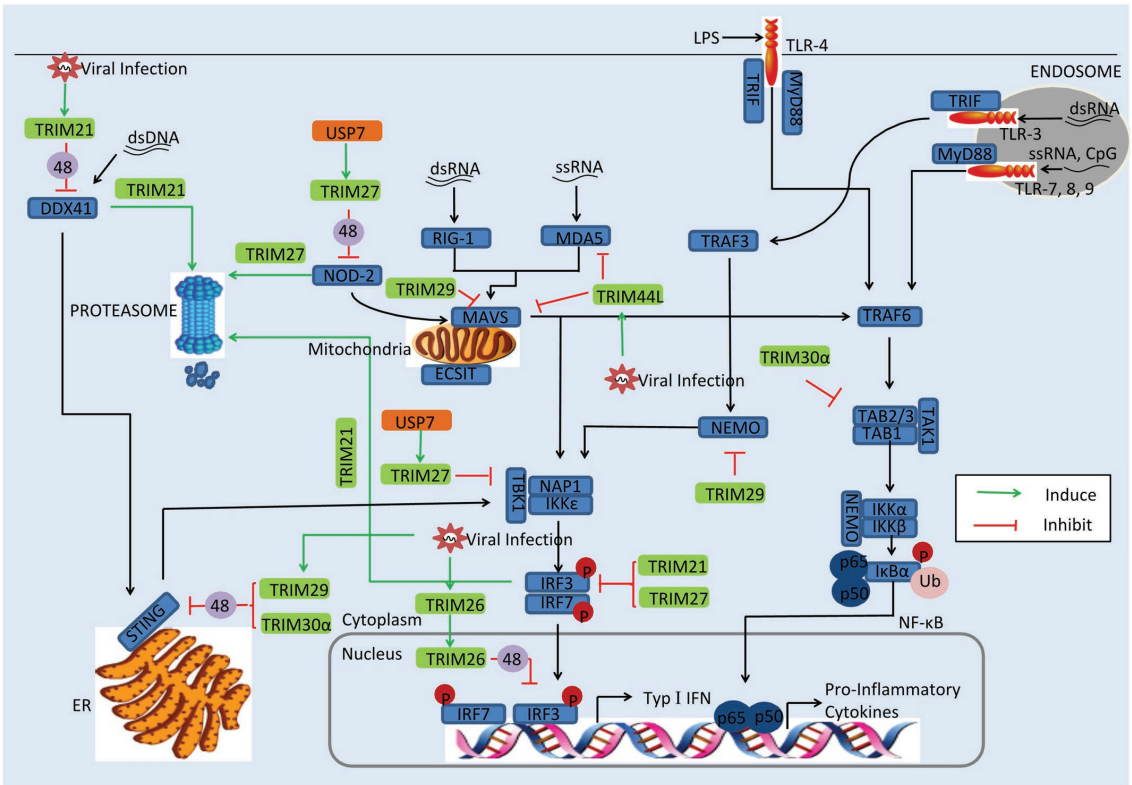

FIGURE 3 | Viral evasion of immune response *via* induction of TRIMs. Some TRIMs (green) negatively regulate innate immune response. Viral proteins (orange) can utilize these TRIMs to reduce the production of type I IFNs and inflammatory factors. USP7, the ubiquitin-specific peptidase 7 of SeV; 48, K48-linked polyubiquitination; and 63, K63-linked polyubiquitination.

TRIM26

Identified as a negative regulator of IFN-β, TRIM26 binds to IRF3 and promotes its K48-linked polyubiquitination and degradation in the nucleus. More important, viral infection promotes TRIM26 nuclear translocation, which in turn increases IRF3 degradation (Wang et al., 2015a). The suppression of IFN-β-involved IRF3 has also been observed in HSV-2, VSV, and PRRSV infection (Huang et al., 2020). It is worth noting that a different report showed that TRIM26 positively regulates type I IFNs, upon RNA viral infection; TRIM26 undergoes autoubiquitination and subsequently associates with NEMO, to promote TBK1–NEMO interaction and the activation of IRF3 and NF-kB (Ran et al., 2016). Some of the discrepancies among these results might be attributed to the different experimental systems (Ran et al., 2016).

TRIM27

Report mentioned that TRIM27 positive regulates RIG-I signaling, leading to increased production of IFN-β in response to viral infection (Blaine et al., 2015; Conwell et al., 2015). However, other studies have proven that TRIM27 is a negative modulator of immune response. It has been suggested that TRIM27 negatively regulates NOD2-induced NF-κB signaling *via* the K48-linked ubiquitination and subsequent proteasomal degradation of NOD2, which can recognize viral RNA and DNA (Moreira and Zamboni, 2012; Kapoor et al., 2014). In SeV infection there seems to be another mechanism at work; the ubiquitin-specific peptidase 7 (USP7) interacts with and stabilizes TRIM27, promoting the degradation of TBK1 and suppressing the activation of IFN-β (Cai et al., 2018). As in SeV infection, TRIM27 inhibits type I IFN response to HCV infection by inhibiting the IRF3 and NF-κB pathways (Zheng et al., 2019a).

TRIM29

TRIM29 acts as a negative regulator of proinflammatory cytokines in macrophages and directly binds NEMO, inducing its ubiquitination and proteolytic degradation, which in turn inhibits the NF-κB pathway (Xing et al., 2016). TRIM29 expression is especially induced by DNA virus and cytosolic DNA in macrophages and dendritic cells and targets STING for K48 ubiquitination and degradation, negatively regulating immune response in infection by DNA viruses like HSV-1 and Epstein-Barr virus (Xing et al., 2017; Li et al., 2018). Recently, a different regulatory function of TRIM29 was reported in the context of RNA virus infection in human mDCs; TRIM29 was found to interact with MAVS and subsequently induce K11-linked ubiquitination and degradation, causing decrease of type I IFN (Xing et al., 2018). In addition, TRIM29 ubiquitinates and degrades TAB2, suppressing IFN-γ production

in NK cells (Dou et al., 2019). Indeed, deficiency of TRIM29 resulted in an enhanced IFN-γ production and consequently protected mice from murine CMV infection (Dou et al., 2019).

TRIM30α

TRIM30α enhances the degradation of STING *via* K48-linked ubiquitination at Lys275 in a proteasome-dependent pathway and suppresses innate immune response to DNA viruses (Wang et al., 2015b). TRIM30α also negatively regulates TRAF6-induced NF-κB activation involved in TLR by degrading TAB2 and TAB3 (Shi et al., 2008). Although TRIM30a is well known in mouse, it is phylogenetically related to human TRIMs 5, 6, 22, and 34, which provide the possibility that TRIMs serve as immune regulator in mouse in a similar manner with that in humans (Song et al., 2005).

CONCLUSION AND FUTURE PERSPECTIVES

Here we have collected recent studies on the regulatory effects of TRIMs in several main signaling pathways, and we have discussed the latest research on immune evasion of viruses by antagonizing TRIM activity or utilizing TRIMs. There seems to be no direct correlation between the immune regulation and any particular subfamily of TRIMs. Thus, TRIM6 and TRIM25, belonging to the C-IV group, positive regulate PRR signaling pathways, while TRIM21 and TRIM26, also members of the C-IV group, act as negative regulators of antiviral immune response (Manocha et al., 2014; Rajsbaum et al., 2014b; Ran et al., 2016; Sanchez et al., 2016).

Over the past decade, multiple studies have explored the function of TRIMs in the innate immunity. It is clear that TRIMs play critical roles in regulating immune response to restrict viral infection, especially in NF-κB and IRF signaling. However, TRIMs whose mechanisms are not limited to innate immune regulation. Recently, previously uncharacterized phenomenon has been detected, for example, TRIM25 presentation of RNA-binding activity, TRIM23 induction of autophagy, TRIM21 participation in cell pyroptosis, and TRIM21 activation of the Nrf2 antioxidant signal pathway (Choudhury et al., 2017; Sparrer et al., 2017; Choi et al., 2020; Song et al., 2020). The functions of TRIMs in the innate immunity remain to be further defined, but the functions of TRIMs likely go far beyond immune regulation.

The viral evasions are mainly involved in the regulatory function of TRIMs in immune response. TRIMs, including TRIM25, TRIM6, TRIM14, and TRIM30α (Wang et al., 2015b; Sanchez et al., 2016), act as positive or negative modulator in the innate immune. Nevertheless, reports have shown that some TRIMs are able to regulate immune pathways both positively and negatively, such as TRIM21, TRIM27, and TRIM32 (Higgs et al., 2008; Yang et al., 2009; Conwell et al., 2015). A comprehensive understanding of the regulation of TRIMs on immune response can support further research on antiviral innate immunity pathway dependencies during the process of viral infection. Of highly topical interest, the SARS-CoV, MERS-CoV, and SARS-CoV-2, belonging to the *Coronaviridae* family, have caused devastating pandemic disease in humans. There is evidence to show that the coronaviral nucleocapsid (N) protein suppresses TRIM25 activity to defend against human immune response (Hu et al., 2017; Chang et al., 2020; Oh and Shin, 2021). On the other hand, the N protein can be degraded by TRIM21 (Wang et al., 2021). It is therefore of urgent interest to clarify the dynamic interaction of the N protein with TRIMs, which can provide new clues to understand coronavirus pathogenesis.

The current understanding of the role of TRIMs in immune regulation is broad and well supported, but the knowledge of the mechanisms by which TRIMs participate in viral immune evasion is weakness. This review would be a fruitful line for future investigations. Demonstration of virus-TRIM interactions may reveal new molecular targets for the treatment, or even prevention, of viral infectious diseases.

AUTHOR CONTRIBUTIONS

X-ZZ wrote the manuscript. F-HL and X-JW improved the manuscript. All authors contributed to the article and approved the submitted version.

FUNDING

This work was supported by the National Natural Science Foundation of China (31772739 and 32172821) and a CAU-Grant for the Prevention and Control of Immunosuppressive Disease in Animals of the China Agricultural University.

ACKNOWLEDGMENTS

We appreciate HCR Wang at the University of Tennessee for his critical review of this report.

REFERENCES

Atkinson, S. C., Heaton, S. M., Audsley, M. D., Kleifeld, O., and Borg, N. A. (2021). TRIM25 and DEAD-Box RNA Helicase DDX3X Cooperate to Regulate RIG-I-Mediated Antiviral Immunity. *Int. J. Mol. Sci.* 22:9094. doi: 10.3390/ijms22169094

Banji, D., Alqahtani, S. S., Banji, O. J. F., Machanchery, S., and Shoaib, A. (2021). Calming the inflammatory storm in severe COVID-19 infections: role of biologics—a narrative review. *Saudi Pharm. J.* 29, 213–222. doi: 10.1016/j.jsps.2021.01.005

Bharaj, P., Atkins, C., Luthra, P., Giraldo, M. I., Dawes, B. E., Miorin, L., et al. (2017). The host E3-ubiquitin ligase TRIM6 ubiquitinates the ebola virus VP35 protein and promotes virus replication. *J. Virol.* 91, e00833–e00917. doi: 10.1128/JVI.00833-17

Bharaj, P., Wang, Y. E., Dawes, B. E., Yun, T. E., Park, A., Yen, B., et al. (2016). The matrix protein of Nipah virus targets the E3-ubiquitin ligase TRIM6 to inhibit the IKKepsilon kinase-mediated type-I IFN antiviral response. *PLoS Pathog.* 12:e1005880. doi: 10.1371/journal.ppat.1005880

Blaine, A. H., Miranzo-Navarro, D., Campbell, L. K., Aldridge, J. R., Webster, R. G., and Magor, K. E. (2015). Duck TRIM27-L enhances MAVS signaling and

is absent in chickens and turkeys. *Mol. Immunol.* 67, 607–615. doi: 10.1016/j.molimm.2015.07.011

Blondel, D., Kheddache, S., Lahaye, X., Dianoux, L., and Chelbi-Alix, M. K. (2010). Resistance to rabies virus infection conferred by the PMLIV isoform. *J. Virol.* 84, 10719–10726. doi: 10.1128/JVI.01286-10

Borden, K. L. (2000). RING domains: master builders of molecular scaffolds? *J. Mol. Biol.* 295, 1103–1112. doi: 10.1006/jmbi.1999.3429

Bottermann, M., and James, L. C. (2018). Intracellular antiviral immunity. *Adv. Virus Res.* 100, 309–354. doi: 10.1016/bs.aivir.2018.01.002

Boutell, C., Orr, A., and Everett, R. D. (2003). PML residue lysine 160 is required for the degradation of PML induced by herpes simplex virus type 1 regulatory protein ICP0. *J. Virol.* 77, 8686–8694. doi: 10.1128/JVI.77.16.8686-8694.2003

Cai, J., Chen, H. Y., Peng, S. J., Meng, J. L., Wang, Y., Zhou, Y., et al. (2018). USP7-TRIM27 axis negatively modulates antiviral type I IFN signaling. *FASEB J.* 32, 5238–5249. doi: 10.1096/fj.201700473RR

Chan, Y. K., and Gack, M. U. (2015). RIG-I-like receptor regulation in virus infection and immunity. *Curr. Opin. Virol.* 12, 7–14. doi: 10.1016/j.coviro.2015.01.004

Chang, C. Y., Liu, H. M., Chang, M. F., and Chang, S. C. (2020). Middle east respiratory syndrome coronavirus nucleocapsid protein suppresses type I and type III interferon induction by targeting RIG-I signaling. *J. Virol.* 94, e00099–e00020. doi: 10.1128/JVI.00099-20

Chelbi-Alix, M. K., and de The, H. (1999). Herpes virus induced proteasome-dependent degradation of the nuclear bodies-associated PML and Sp100 proteins. *Oncogene* 18, 935–941. doi: 10.1038/sj.onc.1202366

Chen, D., Feng, C., Tian, X., Zheng, N., and Wu, Z. (2018a). Promyelocytic leukemia restricts enterovirus 71 replication by inhibiting autophagy. *Front. Immunol.* 9:1268. doi: 10.3389/fimmu.2018.01268

Chen, Y., Cao, S., Sun, Y., and Li, C. (2018b). Gene expression profiling of the TRIM protein family reveals potential biomarkers for indicating tuberculosis status. *Microb. Pathog.* 114, 385–392. doi: 10.1016/j.micpath.2017.12.008

Chen, B., Huo, S., Liu, W., Wang, F., Lu, Y., Xu, Z., et al. (2019). Fish-specific finTRIM FTR36 triggers IFN pathway and mediates inhibition of viral replication. *Fish Shellfish Immunol.* 84, 876–884. doi: 10.1016/j.fsi.2018.10.051

Chiang, C., Dvorkin, S., Chiang, J. J., Potter, R. B., and Gack, M. U. (2021). The small t antigen of JC virus antagonizes RIG-I-mediated innate immunity by inhibiting TRIM25's RNA binding ability. *mBio* 12, e00620–e00621. doi: 10.1128/mBio.00620-21

Chiang, C., Pauli, E. K., Biryukov, J., Feister, K. F., Meng, M., White, E. A., et al. (2018a). The human papillomavirus E6 oncoprotein targets USP15 and TRIM25 to suppress RIG-I-mediated innate immune signaling. *J. Virol.* 92, e01737–e01717. doi: 10.1128/JVI.01737-17

Chiang, J. J., Sparrer, K. M. J., van Gent, M., Lassig, C., Huang, T., Osterrieder, N., et al. (2018b). Viral unmasking of cellular 5S rRNA pseudogene transcripts induces RIG-I-mediated immunity. *Nat. Immunol.* 19, 53–62. doi: 10.1038/s41590-017-0005-y

Choi, Y., Jiang, Z., Shin, W. J., and Jung, J. U. (2020). Severe fever with thrombocytopenia syndrome virus NSs interacts with TRIM21 to activate the p62-Keap1-Nrf2 pathway. *J. Virol.* 94, e01684–e01619. doi: 10.1128/JVI.01684-19

Choudhury, N. R., Heikel, G., and Michlewski, G. (2020). TRIM25 and its emerging RNA-binding roles in antiviral defense. *Wiley Interdiscip. Rev. RNA* 11:e1588. doi: 10.1002/wrna.1588

Choudhury, N. R., Heikel, G., Trubitsyna, M., Kubik, P., Nowak, J. S., Webb, S., et al. (2017). RNA-binding activity of TRIM25 is mediated by its PRY/SPRY domain and is required for ubiquitination. *BMC Biol.* 15:105. doi: 10.1186/s12915-017-0444-9

Cokic, V. P., Bhattacharya, B., Beleslin-Cokic, B. B., Noguchi, C. T., Puri, R. K., and Schechter, A. N. (2012). JAK-STAT and AKT pathway-coupled genes in erythroid progenitor cells through ontogeny. *J. Transl. Med.* 10:116. doi: 10.1186/1479-5876-10-116

Conwell, S. E., White, A. E., Harper, J. W., and Knipe, D. M. (2015). Identification of TRIM27 as a novel degradation target of herpes simplex virus 1 ICP0. *J. Virol.* 89, 220–229. doi: 10.1128/JVI.02635-14

Dou, Y., Xing, J., Kong, G., Wang, G., Lou, X., Xiao, X., et al. (2019). Identification of the E3 ligase TRIM29 as a critical checkpoint regulator of NK cell functions. *J. Immunol.* 203, 873–880. doi: 10.4049/jimmunol.1900171

Dutrieux, J., Maarifi, G., Portilho, D. M., Arhel, N. J., Chelbi-Alix, M. K., and Nisole, S. (2015). PML/TRIM19-dependent inhibition of retroviral reverse-transcription by Daxx. *PLoS Pathog.* 11:e1005280. doi: 10.1371/journal.ppat.1005280

Gack, M. U., Albrecht, R. A., Urano, T., Inn, K. S., Huang, I. C., Carnero, E., et al. (2009). Influenza A virus NS1 targets the ubiquitin ligase TRIM25 to evade recognition by the host viral RNA sensor RIG-I. *Cell Host Microbe* 5, 439–449. doi: 10.1016/j.chom.2009.04.006

Ganser-Pornillos, B. K., and Pornillos, O. (2019). Restriction of HIV-1 and other retroviruses by TRIM5. *Nat. Rev. Microbiol.* 17, 546–556. doi: 10.1038/s41579-019-0225-2

Gay, N. J., Symmons, M. F., Gangloff, M., and Bryant, C. E. (2014). Assembly and localization of toll-like receptor signalling complexes. *Nat. Rev. Immunol.* 14, 546–558. doi: 10.1038/nri3713

Ghoreschi, K., Laurence, A., and O'Shea, J. J. (2009). Janus kinases in immune cell signaling. *Immunol. Rev.* 228, 273–287. doi: 10.1111/j.1600-065X.2008.00754.x

Gupta, S., Yla-Anttila, P., Callegari, S., Tsai, M. H., Delecluse, H. J., and Masucci, M. G. (2018). Herpesvirus deconjugases inhibit the IFN response by promoting TRIM25 autoubiquitination and functional inactivation of the RIG-I signalosome. *PLoS Pathog.* 14:e1006852. doi: 10.1371/journal.ppat.1006852

Hatakeyama, S. (2017). TRIM family proteins: roles in autophagy, immunity, and carcinogenesis. *Trends Biochem. Sci.* 42, 297–311. doi: 10.1016/j.tibs.2017.01.002

Higgs, R., Gabhann, J. N., Larbi, N. B., Breen, E. P., Fitzgerald, K. A., and Jefferies, C. A. (2008). The E3 ubiquitin ligase Ro52 negatively regulates IFN-beta production post-pathogen recognition by polyubiquitin-mediated degradation of IRF3. *J. Immunol.* 181, 1780–1786. doi: 10.4049/jimmunol.181.3.1780

Hu, Y., Li, W., Gao, T., Cui, Y., Jin, Y., Li, P., et al. (2017). The severe acute respiratory syndrome coronavirus nucleocapsid inhibits type I interferon production by interfering with TRIM25-mediated RIG-I ubiquitination. *J. Virol.* 91, e02143–e02116. doi: 10.1128/JVI.02143-16

Hu, M. M., Xie, X. Q., Yang, Q., Liao, C. Y., Ye, W., Lin, H., et al. (2015). TRIM38 negatively regulates TLR3/4-mediated innate immune and inflammatory responses by two sequential and distinct mechanisms. *J. Immunol.* 195, 4415–4425. doi: 10.4049/jimmunol.1500859

Hu, M. M., Yang, Q., Xie, X. Q., Liao, C. Y., Lin, H., Liu, T. T., et al. (2016). Sumoylation promotes the stability of the DNA sensor cGAS and the adaptor STING to regulate the kinetics of response to DNA virus. *Immunity* 45, 555–569. doi: 10.1016/j.immuni.2016.08.014

Hu, M. M., Yang, Q., Zhang, J., Liu, S. M., Zhang, Y., Lin, H., et al. (2014). TRIM38 inhibits TNFalpha- and IL-1beta-triggered NF-kappaB activation by mediating lysosome-dependent degradation of TAB2/3. *Proc. Natl. Acad. Sci. U. S. A.* 111, 1509–1514. doi: 10.1073/pnas.1318227111

Huang, H., Sharma, M., Zhang, Y., Li, C., Liu, K., Wei, J., et al. (2020). Expression profile of porcine TRIM26 and its inhibitory effect on interferon-beta production and antiviral response. *Genes* 11:1226. doi: 10.3390/genes11101226

Ishikawa, H., Ma, Z., and Barber, G. N. (2009). STING regulates intracellular DNA-mediated, type I interferon-dependent innate immunity. *Nature* 461, 788–792. doi: 10.1038/nature08476

Jiang, X., Kinch, L. N., Brautigam, C. A., Chen, X., Du, F., Grishin, N. V., et al. (2012). Ubiquitin-induced oligomerization of the RNA sensors RIG-I and MDA5 activates antiviral innate immune response. *Immunity* 36, 959–973. doi: 10.1016/j.immuni.2012.03.022

Jiang, J., Li, J., Fan, W., Zheng, W., Yu, M., Chen, C., et al. (2016). Robust Lys63-linked ubiquitination of RIG-I promotes cytokine eruption in early influenza B virus infection. *J. Virol.* 90, 6263–6275. doi: 10.1128/JVI.00549-16

Jimenez-Dalmaroni, M. J., Gerswhin, M. E., and Adamopoulos, I. E. (2016). The critical role of toll-like receptors--from microbial recognition to autoimmunity: a comprehensive review. *Autoimmun. Rev.* 15, 1–8. doi: 10.1016/j.autrev.2015.08.009

Kagan, J. C., and Barton, G. M. (2014). Emerging principles governing signal transduction by pattern-recognition receptors. *Cold Spring Harb. Perspect. Biol.* 7:a016253. doi: 10.1101/cshperspect.a016253

Kapoor, A., Forman, M., and Arav-Boger, R. (2014). Activation of nucleotide oligomerization domain 2 (NOD2) by human cytomegalovirus initiates innate immune responses and restricts virus replication. *PLoS One* 9:e92704. doi: 10.1371/journal.pone.0092704

Kentsis, A., Dwyer, E. C., Perez, J. M., Sharma, M., Chen, A., Pan, Z. Q., et al. (2001). The RING domains of the promyelocytic leukemia protein PML and the arenaviral protein Z repress translation by directly inhibiting translation initiation factor eIF4E. *J. Mol. Biol.* 312, 609–623. doi: 10.1006/jmbi.2001.5003

Khan, R., Khan, A., Ali, A., and Idrees, M. (2019). The interplay between viruses and TRIM family proteins. *Rev. Med. Virol.* 29:e2028. doi: 10.1002/rmv.2028

Koepke, L., Gack, M. U., and Sparrer, K. M. (2021). The antiviral activities of TRIM proteins. *Curr. Opin. Microbiol.* 59, 50–57. doi: 10.1016/j.mib.2020.07.005

Koliopoulos, M. G., Lethier, M., van der Veen, A. G., Haubrich, K., Hennig, J., Kowalinski, E., et al. (2018). Molecular mechanism of influenza A NS1-mediated TRIM25 recognition and inhibition. *Nat. Commun.* 9:1820. doi: 10.1038/s41467-018-04214-8

Lang, X., Tang, T., Jin, T., Ding, C., Zhou, R., and Jiang, W. (2017). TRIM65-catalized ubiquitination is essential for MDA5-mediated antiviral innate immunity. *J. Exp. Med.* 214, 459–473. doi: 10.1084/jem.20160592

Laurent-Rolle, M., Morrison, J., Rajsbaum, R., Macleod, J. M. L., Pisanelli, G., Pham, A., et al. (2014). The interferon signaling antagonist function of yellow fever virus NS5 protein is activated by type I interferon. *Cell Host Microbe* 16, 314–327. doi: 10.1016/j.chom.2014.07.015

Li, M. M., Lau, Z., Cheung, P., Aguilar, E. G., Schneider, W. M., Bozzacco, L., et al. (2017). TRIM25 enhances the antiviral action of zinc-finger antiviral protein (ZAP). *PLoS Pathog.* 13:e1006145. doi: 10.1371/journal.ppat.1006145

Li, Q., Lin, L., Tong, Y., Liu, Y., Mou, J., Wang, X., et al. (2018). TRIM29 negatively controls antiviral immune response through targeting STING for degradation. *Cell Discov.* 4:13. doi: 10.1038/s41421-018-0010-9

Liu, X., Matrenec, R., Gack, M. U., and He, B. (2019). Disassembly of the TRIM23-TBK1 complex by the Us11 protein of herpes simplex virus 1 impairs autophagy. *J. Virol.* 93, e00497–e00419. doi: 10.1128/JVI.00497-19

Lopez, P., Jacob, R. J., and Roizman, B. (2002). Overexpression of promyelocytic leukemia protein precludes the dispersal of ND10 structures and has no effect on accumulation of infectious herpes simplex virus 1 or its proteins. *J. Virol.* 76, 9355–9367. doi: 10.1128/JVI.76.18.9355-9367.2002

Majoros, A., Platanitis, E., Kernbauer-Holzl, E., Rosebrock, F., Muller, M., and Decker, T. (2017). Canonical and non-canonical aspects of JAK-STAT signaling: lessons from interferons for cytokine responses. *Front. Immunol.* 8:29. doi: 10.3389/fimmu.2017.00029

Manocha, G. D., Mishra, R., Sharma, N., Kumawat, K. L., Basu, A., and Singh, S. K. (2014). Regulatory role of TRIM21 in the type-I interferon pathway in Japanese encephalitis virus-infected human microglial cells. *J. Neuroinflammation* 11:24. doi: 10.1186/1742-2094-11-24

Manokaran, G., Finol, E., Wang, C., Gunaratne, J., Bahl, J., Ong, E. Z., et al. (2015). Dengue subgenomic RNA binds TRIM25 to inhibit interferon expression for epidemiological fitness. *Science* 350, 217–221. doi: 10.1126/science.aab3369

Marin, I. (2012). Origin and diversification of TRIM ubiquitin ligases. *PLoS One* 7:e50030. doi: 10.1371/journal.pone.0050030

Masroori, N., Merindol, N., and Berthoux, L. (2016). The interferon-induced antiviral protein PML (TRIM19) promotes the restriction and transcriptional silencing of lentiviruses in a context-specific, isoform-specific fashion. *Retrovirology* 13:19. doi: 10.1186/s12977-016-0253-1

McEwan, W. A., Tam, J. C., Watkinson, R. E., Bidgood, S. R., Mallery, D. L., and James, L. C. (2013). Intracellular antibody-bound pathogens stimulate immune signaling via the Fc receptor TRIM21. *Nat. Immunol.* 14, 327–336. doi: 10.1038/ni.2548

Medzhitov, R. (2007). Recognition of microorganisms and activation of the immune response. *Nature* 449, 819–826. doi: 10.1038/nature06246

Meroni, G. (2012). Genomics and evolution of the TRIM gene family. *Adv. Exp. Med. Biol.* 770, 1–9. doi: 10.1007/978-1-4614-5398-7_1

Meroni, G., and Diez-Roux, G. (2005). TRIM/RBCC, a novel class of 'single protein RING finger' E3 ubiquitin ligases. *Bioessays* 27, 1147–1157. doi: 10.1002/bies.20304

Meyts, I., and Casanova, J. L. (2021). Viral infections in humans and mice with genetic deficiencies of the type I IFN response pathway. *Eur. J. Immunol.* 51, 1039–1061. doi: 10.1002/eji.202048793

Min, Y. Q., Ning, Y. J., Wang, H., and Deng, F. (2020). A RIG-I-like receptor directs antiviral responses to a bunyavirus and is antagonized by virus-induced blockade of TRIM25-mediated ubiquitination. *J. Biol. Chem.* 295, 9691–9711. doi: 10.1074/jbc.RA120.013973

Moreira, L. O., and Zamboni, D. S. (2012). NOD1 and NOD2 signaling in infection and inflammation. *Front. Immunol.* 3:328. doi: 10.3389/fimmu.2012.00328

Nisole, S., Stoye, J. P., and Saib, A. (2005). TRIM family proteins: retroviral restriction and antiviral defence. *Nat. Rev. Microbiol.* 3, 799–808. doi: 10.1038/nrmicro1248

Odendall, C., and Kagan, J. C. (2017). Activation and pathogenic manipulation of the sensors of the innate immune system. *Microbes Infect.* 19, 229–237. doi: 10.1016/j.micinf.2017.01.003

Oh, S. J., and Shin, O. S. (2021). SARS-CoV-2 nucleocapsid protein targets RIG-I-like receptor pathways to inhibit the induction of interferon response. *Cells* 10:530. doi: 10.3390/cells10030530

Okumura, F., Matsunaga, Y., Katayama, Y., Nakayama, K. I., and Hatakeyama, S. (2010). TRIM8 modulates STAT3 activity through negative regulation of PIAS3. *J. Cell Sci.* 123, 2238–2245. doi: 10.1242/jcs.068981

Ozato, K., Shin, D. M., Chang, T. H., and Morse, H. C. (2008). TRIM family proteins and their emerging roles in innate immunity. *Nat. Rev. Immunol.* 8, 849–860. doi: 10.1038/nri2413

Paijo, J., Doring, M., Spanier, J., Grabski, E., Nooruzzaman, M., Schmidt, T., et al. (2016). cGAS senses human cytomegalovirus and induces type I interferon responses in human monocyte-derived cells. *PLoS Pathog.* 12:e1005546. doi: 10.1371/journal.ppat.1005546

Pauli, E. K., Chan, Y. K., Davis, M. E., Gableske, S., Wang, M. K., Feister, K. F., et al. (2014). The ubiquitin-specific protease USP15 promotes RIG-I-mediated antiviral signaling by deubiquitylating TRIM25. *Sci. Signal.* 7:ra3. doi: 10.1126/scisignal.2004577

Raftery, N., and Stevenson, N. J. (2017). Advances in anti-viral immune defence: revealing the importance of the IFN JAK/STAT pathway. *Cell. Mol. Life Sci.* 74, 2525–2535. doi: 10.1007/s00018-017-2520-2

Rajsbaum, R., Albrecht, R. A., Wang, M. K., Maharaj, N. P., Versteeg, G. A., Nistal-Villan, E., et al. (2012). Species-specific inhibition of RIG-I ubiquitination and IFN induction by the influenza A virus NS1 protein. *PLoS Pathog.* 8:e1003059. doi: 10.1371/journal.ppat.1003059

Rajsbaum, R., Garcia-Sastre, A., and Versteeg, G. A. (2014a). TRIMmunity: the roles of the TRIM E3-ubiquitin ligase family in innate antiviral immunity. *J. Mol. Biol.* 426, 1265–1284. doi: 10.1016/j.jmb.2013.12.005

Rajsbaum, R., Versteeg, G. A., Schmid, S., Maestre, A. M., Belicha-Villanueva, A., Martinez-Romero, C., et al. (2014b). Unanchored K48-linked polyubiquitin synthesized by the E3-ubiquitin ligase TRIM6 stimulates the interferon-IKKepsilon kinase-mediated antiviral response. *Immunity* 40, 880–895. doi: 10.1016/j.immuni.2014.04.018

Ran, Y., Zhang, J., Liu, L. L., Pan, Z. Y., Nie, Y., Zhang, H. Y., et al. (2016). Autoubiquitination of TRIM26 links TBK1 to NEMO in RLR-mediated innate antiviral immune response. *J. Mol. Cell Biol.* 8, 31–43. doi: 10.1093/jmcb/mjv068

Reddy, B. A., and Etkin, L. D. (1991). A unique bipartite cysteine-histidine motif defines a subfamily of potential zinc-finger proteins. *Nucleic Acids Res.* 19:6330. doi: 10.1093/nar/19.22.6330

Reichelt, M., Wang, L., Sommer, M., Perrino, J., Nour, A. M., Sen, N., et al. (2011). Entrapment of viral capsids in nuclear PML cages is an intrinsic antiviral host defense against varicella-zoster virus. *PLoS Pathog.* 7:e1001266. doi: 10.1371/journal.ppat.1001266

Reinert, L. S., Lopusna, K., Winther, H., Sun, C., Thomsen, M. K., Nandakumar, R., et al. (2016). Sensing of HSV-1 by the cGAS-STING pathway in microglia orchestrates antiviral defence in the CNS. *Nat. Commun.* 7:13348. doi: 10.1038/ncomms13348

Runge, S., Sparrer, K. M., Lassig, C., Hembach, K., Baum, A., Garcia-Sastre, A., et al. (2014). In vivo ligands of MDA5 and RIG-I in measles virus-infected cells. *PLoS Pathog.* 10:e1004081. doi: 10.1371/journal.ppat.1004081

Sanchez, J. G., Chiang, J. J., Sparrer, K. M. J., Alam, S. L., Chi, M., Roganowicz, M. D., et al. (2016). Mechanism of TRIM25 catalytic activation in the antiviral RIG-I pathway. *Cell Rep.* 16, 1315–1325. doi: 10.1016/j.celrep.2016.06.070

Santiago, F. W., Covaleda, L. M., Sanchez-Aparicio, M. T., Silvas, J. A., Diaz-Vizarreta, A. C., Patel, J. R., et al. (2014). Hijacking of RIG-I signaling proteins into virus-induced cytoplasmic structures correlates with the inhibition of type I interferon responses. *J. Virol.* 88, 4572–4585. doi: 10.1128/JVI.03021-13

Scherer, M., Klingl, S., Sevvana, M., Otto, V., Schilling, E. M., Stump, J. D., et al. (2014). Crystal structure of cytomegalovirus IE1 protein reveals targeting of TRIM family member PML via coiled-coil interactions. *PLoS Pathog.* 10:e1004512. doi: 10.1371/journal.ppat.1004512

Schilling, E. M., Scherer, M., Reuter, N., Schweininger, J., Muller, Y. A., and Stamminger, T. (2017). The human cytomegalovirus IE1 protein antagonizes PML nuclear body-mediated intrinsic immunity via the inhibition of PML de novo SUMOylation. *J. Virol.* 91, e02049–e02016. doi: 10.1128/JVI.02049-16

Seo, G. J., Kim, C., Shin, W. J., Sklan, E. H., Eoh, H., and Jung, J. U. (2018). TRIM56-mediated monoubiquitination of cGAS for cytosolic DNA sensing. *Nat. Commun.* 9:613. doi: 10.1038/s41467-018-02936-3

Sewatanon, J., and Ling, P. D. (2013). Murine gammaherpesvirus 68 ORF75c contains ubiquitin E3 ligase activity and requires PML SUMOylation but not other known cellular PML regulators, CK2 and E6AP, to mediate PML degradation. *Virology* 440, 140–149. doi: 10.1016/j.virol.2013.02.014

Shen, Y., Li, N. L., Wang, J., Liu, B., Lester, S., and Li, K. (2012). TRIM56 is an essential component of the TLR3 antiviral signaling pathway. *J. Biol. Chem.* 287, 36404–36413. doi: 10.1074/jbc.M112.397075

Shi, M., Deng, W., Bi, E., Mao, K., Ji, Y., Lin, G., et al. (2008). TRIM30 alpha negatively regulates TLR-mediated NF-kappa B activation by targeting TAB2 and TAB3 for degradation. *Nat. Immunol.* 9, 369–377. doi: 10.1038/ni1577

Song, B., Gold, B., O'Huigin, C., Javanbakht, H., Li, X., Stremlau, M., et al. (2005). The B30.2(SPRY) domain of the retroviral restriction factor TRIM5alpha exhibits lineage-specific length and sequence variation in primates. *J. Virol.* 79, 6111–6121. doi: 10.1128/JVI.79.10.6111-6121.2005

Song, Y., Wu, X., Xu, Y., Zhu, J., Li, J., Zou, Z., et al. (2020). HPV E7 inhibits cell pyroptosis by promoting TRIM21-mediated degradation and ubiquitination of the IFI16 inflammasome. *Int. J. Biol. Sci.* 16, 2924–2937. doi: 10.7150/ijbs.50074

Soulat, D., Burckstummer, T., Westermayer, S., Goncalves, A., Bauch, A., Stefanovic, A, et al. (2008). The DEAD-box helicase DDX3X is a critical component of the TANK-binding kinase 1-dependent innate immune response. *EMBO J.* 27, 2135–2146. doi: 10.1038/emboj.2008.126

Sparrer, K. M. J., Gableske, S., Zurenski, M. A., Parker, Z. M., Full, F., Baumgart, G. J., et al. (2017). TRIM23 mediates virus-induced autophagy via activation of TBK1. *Nat. Microbiol.* 2, 1543–1557. doi: 10.1038/s41564-017-0017-2

Su, X., Zhang, Q., Yue, J., Wang, Y., Zhang, Y., and Yang, R. (2020). TRIM59 suppresses NO production by promoting the binding of PIAS1 and STAT1 in macrophages. *Int. Immunopharmacol.* 89:107030. doi: 10.1016/j.intimp.2020.107030

Sun, N., Jiang, L., Ye, M., Wang, Y., Wang, G., Wan, X., et al. (2020). TRIM35 mediates protection against influenza infection by activating TRAF3 and degrading viral PB2. *Protein Cell* 11, 894–914. doi: 10.1007/s13238-020-00734-6

Sun, B., Sundstrom, K. B., Chew, J. J., Bist, P., Gan, E. S., Tan, H. C., et al. (2017). Dengue virus activates cGAS through the release of mitochondrial DNA. *Sci. Rep.* 7:3594. doi: 10.1038/s41598-017-03932-1

Sundquist, W. I., and Pornillos, O. (2018). Retrovirus restriction by TRIM5alpha: RINGside at a cage fight. *Cell Host Microbe* 24, 751–753. doi: 10.1016/j.chom.2018.11.013

Takeuchi, O., and Akira, S. (2010). Pattern recognition receptors and inflammation. *Cell* 140, 805–820. doi: 10.1016/j.cell.2010.01.022

Tan, P., He, L., Cui, J., Qian, C., Cao, X., Lin, M., et al. (2017). Assembly of the WHIP-TRIM14-PPP6C mitochondrial complex promotes RIG-I-mediated antiviral signaling. *Mol. Cell* 68:e295. doi: 10.1016/j.molcel.2017.09.035

Tan, X., Sun, L., Chen, J., and Chen, Z. J. (2018). Detection of microbial infections through innate immune sensing of nucleic acids. *Annu. Rev. Microbiol.* 72, 447–478. doi: 10.1146/annurev-micro-102215-095605

Tatematsu, M., Nishikawa, F., Seya, T., and Matsumoto, M. (2013). Toll-like receptor 3 recognizes incomplete stem structures in single-stranded viral RNA. *Nat. Commun.* 4:1833. doi: 10.1038/ncomms2857

Teng, Y., Ni, G., Zhang, W., Hua, J., Sun, L., Zheng, M., et al. (2020). TRIM59 attenuates IL-1beta-driven cartilage matrix degradation in osteoarthritis via direct suppression of NF-kappaB and JAK2/STAT3 signaling pathway. *Biochem. Biophys. Res. Commun.* 529, 28–34. doi: 10.1016/j.bbrc.2020.05.130

Thompson, M. R., Kaminski, J. J., Kurt-Jones, E. A., and Fitzgerald, K. A. (2011). Pattern recognition receptors and the innate immune response to viral infection. *Viruses* 3, 920–940. doi: 10.3390/v3060920

Tikhe, C. V., and Dimopoulos, G. (2021). Mosquito antiviral immune pathways. *Dev. Comp. Immunol.* 116:103964. doi: 10.1016/j.dci.2020.103964

Tsuchida, T., Zou, J., Saitoh, T., Kumar, H., Abe, T., Matsuura, Y., et al. (2010). The ubiquitin ligase TRIM56 regulates innate immune responses to intracellular double-stranded DNA. *Immunity* 33, 765–776. doi: 10.1016/j.immuni.2010.10.013

van Gent, M., Sparrer, K. M. J., and Gack, M. U. (2018). TRIM proteins and their roles in antiviral host defenses. *Annu. Rev. Virol.* 5, 385–405. doi: 10.1146/annurev-virology-092917-043323

van Tol, S., Atkins, C., Bharaj, P., Johnson, K. N., Hage, A., Freiberg, A. N., et al. (2020). VAMP8 contributes to the TRIM6-mediated type I interferon antiviral response during west nile virus infection. *J. Virol.* 94, e01454–e01419. doi: 10.1128/JVI.01454-19

van Tol, S., Hage, A., Giraldo, M. I., Bharaj, P., and Rajsbaum, R. (2017). The TRIMendous role of TRIMs in virus-host interactions. *Vaccines* 5:23. doi: 10.3390/vaccines5030023

Vance, R. E. (2016). Cytosolic DNA sensing: the field narrows. *Immunity* 45, 227–228. doi: 10.1016/j.immuni.2016.08.006

Villano, J. S., Rong, F., and Cooper, T. K. (2014). Bacterial infections in Myd88-deficient mice. *Comp. Med.* 64, 110–114.

Wang, H., Chen, X., Kong, N., Jiao, Y., Sun, D., Dong, S., et al. (2021). TRIM21 inhibits porcine epidemic diarrhea virus proliferation by proteasomal degradation of the nucleocapsid protein. *Arch. Virol.* 166, 1903–1911. doi: 10.1007/s00705-021-05080-4

Wang, P., Zhao, W., Zhao, K., Zhang, L., and Gao, C. (2015a). TRIM26 negatively regulates interferon-beta production and antiviral response through polyubiquitination and degradation of nuclear IRF3. *PLoS Pathog.* 11:e1004726. doi: 10.1371/journal.ppat.1004726

Wang, Y., Lian, Q., Yang, B., Yan, S., Zhou, H., He, L., et al. (2015b). TRIM30alpha is a negative-feedback regulator of the intracellular DNA and DNA virus-triggered response by targeting STING. *PLoS Pathog.* 11:e1005012. doi: 10.1371/journal.ppat.1005012

Wang, Q., Liu, X., Cui, Y., Tang, Y., Chen, W., Li, S., et al. (2014). The E3 ubiquitin ligase AMFR and INSIG1 bridge the activation of TBK1 kinase by modifying the adaptor STING. *Immunity* 41, 919–933. doi: 10.1016/j.immuni.2014.11.011

Xing, J., Weng, L., Yuan, B., Wang, Z., Jia, L., Jin, R., et al. (2016). Identification of a role for TRIM29 in the control of innate immunity in the respiratory tract. *Nat. Immunol.* 17, 1373–1380. doi: 10.1038/ni.3580

Xing, J., Zhang, A., Minze, L. J., Li, X. C., and Zhang, Z. (2018). TRIM29 negatively regulates the type I IFN production in response to RNA virus. *J. Immunol.* 201, 183–192. doi: 10.4049/jimmunol.1701569

Xing, J., Zhang, A., Zhang, H., Wang, J., Li, X. C., Zeng, M. S., et al. (2017). TRIM29 promotes DNA virus infections by inhibiting innate immune response. *Nat. Commun.* 8:945. doi: 10.1038/s41467-017-00101-w

Yang, K., Shi, H. X., Liu, X. Y., Shan, Y. F., Wei, B., Chen, S., et al. (2009). TRIM21 is essential to sustain IFN regulatory factor 3 activation during antiviral response. *J. Immunol.* 182, 3782–3792. doi: 10.4049/jimmunol.0803126

Ye, W., Hu, M. M., Lei, C. Q., Zhou, Q., Lin, H., Sun, M. S., et al. (2017). TRIM8 negatively regulates TLR3/4-mediated innate immune response by blocking TRIF-TBK1 interaction. *J. Immunol.* 199, 1856–1864. doi: 10.4049/jimmunol.1601647

Yoneyama, M., Kikuchi, M., Natsukawa, T., Shinobu, N., Imaizumi, T., Miyagishi, M., et al. (2004). The RNA helicase RIG-I has an essential function in double-stranded RNA-induced innate antiviral responses. *Nat. Immunol.* 5, 730–737. doi: 10.1038/ni1087

Zeng, W., Sun, L., Jiang, X., Chen, X., Hou, F., Adhikari, A., et al. (2010). Reconstitution of the RIG-I pathway reveals a signaling role of unanchored polyubiquitin chains in innate immunity. *Cell* 141, 315–330. doi: 10.1016/j.cell.2010.03.029

Zhang, Z., Bao, M., Lu, N., Weng, L., Yuan, B., and Liu, Y. J. (2013). The E3 ubiquitin ligase TRIM21 negatively regulates the innate immune response to intracellular double-stranded DNA. *Nat. Immunol.* 14, 172–178. doi: 10.1038/ni.2492

Zhang, R., Dai, X., Cao, X., Zhang, C., Wang, K., Huang, X., et al. (2020a). Trim23 promotes WSSV replication though negative regulation of antimicrobial peptides expression in *Macrobrachium nipponense*. *Mol. Immunol.* 124, 172–179. doi: 10.1016/j.molimm.2020.06.007

Zhang, J., Hu, M. M., Wang, Y. Y., and Shu, H. B. (2012). TRIM32 protein modulates type I interferon induction and cellular antiviral response by targeting MITA/STING protein for K63-linked ubiquitination. *J. Biol. Chem.* 287, 28646–28655. doi: 10.1074/jbc.M112.362608

Zhang, X., Zhu, Z., Wang, C., Yang, F., Cao, W., Li, P., et al. (2020b). Foot-and-mouth disease virus 3B protein interacts with pattern recognition receptor

RIG-I to block RIG-I-mediated immune signaling and inhibit host antiviral response. *J. Immunol.* 205, 2207–2221. doi: 10.4049/jimmunol.1901333

Zhao, K., Li, L. W., Jiang, Y. F., Gao, F., Zhang, Y. J., Zhao, W. Y., et al. (2019). Nucleocapsid protein of porcine reproductive and respiratory syndrome virus antagonizes the antiviral activity of TRIM25 by interfering with TRIM25-mediated RIG-I ubiquitination. *Vet. Microbiol.* 233, 140–146. doi: 10.1016/j.vetmic.2019.05.003

Zhao, W., Wang, L., Zhang, M., Wang, P., Yuan, C., Qi, J., et al. (2012). Tripartite motif-containing protein 38 negatively regulates TLR3/4- and RIG-I-mediated IFN-beta production and antiviral response by targeting NAP1. *J. Immunol.* 188, 5311–5318. doi: 10.4049/jimmunol.1103506

Zheng, X., Wang, X., Tu, F., Wang, Q., Fan, Z., and Gao, G. (2017). TRIM25 is required for the antiviral activity of zinc finger antiviral protein. *J. Virol.* 91, e00088–e00017. doi: 10.1128/JVI.00088-17

Zheng, F., Xu, N., and Zhang, Y. (2019a). TRIM27 promotes hepatitis C virus replication by suppressing type I interferon response. *Inflammation* 42, 1317–1325. doi: 10.1007/s10753-019-00992-5

Zheng, J., Zhang, Y., Zhi, L., Lv, S., Xiao, L., Huang, X., et al. (2019b). The novel gene TRIM44L from orange-spotted grouper negatively regulates the interferon response. *Fish Shellfish Immunol.* 92, 746–755. doi: 10.1016/j.fsi.2019.06.062

Zhou, Z., Jia, X., Xue, Q., Dou, Z., Ma, Y., Zhao, Z., et al. (2014). TRIM14 is a mitochondrial adaptor that facilitates retinoic acid-inducible gene-I-like receptor-mediated innate immune response. *Proc. Natl. Acad. Sci. U. S. A.* 111, E245–E254. doi: 10.1073/pnas.1316941111

Conflict of Interest: The authors declare that the research was conducted in the absence of any commercial or financial relationships that could be construed as a potential conflict of interest.

Publisher's Note: All claims expressed in this article are solely those of the authors and do not necessarily represent those of their affiliated organizations, or those of the publisher, the editors and the reviewers. Any product that may be evaluated in this article, or claim that may be made by its manufacturer, is not guaranteed or endorsed by the publisher.

frontiers in Microbiology

ORIGINAL RESEARCH
published: 22 December 2021
doi: 10.3389/fmicb.2021.795593

Meclizine Inhibits Pseudorabies Virus Replication by Interfering With Virus Entry and Release

Panrao Liu[1], Danhe Hu[1], Lili Yuan[1], Zhengmin Lian[1], Xiaohui Yao[1], Zhenbang Zhu[1], Norbert Nowotny[2], Yi Shi[3,4] and Xiangdong Li[1,5]**

[1]Jiangsu Co-innovation Center for Prevention and Control of Important Animal Infectious Diseases and Zoonoses, College of Veterinary Medicine, Yangzhou University, Yangzhou, China, [2]Viral Zoonoses, Emerging and Vector-Borne Infections Group, Institute of Virology, University of Veterinary Medicine Vienna, Vienna, Austria, [3]CAS Key Laboratory of Pathogenic Microbiology and Immunology, Institute of Microbiology, Chinese Academy of Sciences, Beijing, China, [4]Savaid Medical School, University of Chinese Academy of Sciences, Beijing, China, [5]Joint International Research Laboratory of Agriculture and Agri-Product Safety, The Ministry of Education of China, Yangzhou University, Yangzhou, China

OPEN ACCESS

Edited by:
Li Yongqing,
Beijing Academy of Agriculture and Forestry Sciences, China

Reviewed by:
Yan-Dong Tang,
Harbin Veterinary Research Institute, Chinese Academy of Agricultural Sciences (CAAS), China
Muhammad Abid,
Pirbright Institute, United Kingdom

***Correspondence:**
Xiangdong Li
007352@yzu.edu.cn
Yi Shi
shiyi@im.ac.cn

Specialty section:
This article was submitted to Virology, a section of the journal Frontiers in Microbiology

Received: *15 October 2021*
Accepted: *30 November 2021*
Published: *22 December 2021*

Citation:
Liu P, Hu D, Yuan L, Lian Z, Yao X, Zhu Z, Nowotny N, Shi Y and Li X (2021) Meclizine Inhibits Pseudorabies Virus Replication by Interfering With Virus Entry and Release. Front. Microbiol. 12:795593. doi: 10.3389/fmicb.2021.795593

Pseudorabies virus (PRV) is a pathogen that causes substantial economic losses to the swine industry. With the emergence and widespread of PRV variants since 2011 in China, current commercial vaccines cannot provide complete protection against PRV infection. Therefore, antiviral drugs may work as an alternative way to control and prevent PRV. In this study, the inhibitory effects and underlying molecular mechanisms of meclizine against PRV were studied. Meclizine displayed a significant inhibitory effect against PRV when it was added before, simultaneously with, or after virus infection. The inhibitory effect of meclizine occurred during viral entry and cell-to-cell spreading but not at viral attachment into PK-15 cells. Meclizine also inhibited viral particle release at the late stage of infection. The antiviral effect of meclizine was tested in mice, and the results showed that meclizine reduced the severity of clinical symptoms and the viral loads in tissues, and delayed the death, after PRV challenge. The above results indicated that meclizine had an inhibitory effect on PRV. Our findings will contribute to the development of potential therapeutic drugs against PRV infection.

Keywords: pseudorabies virus, meclizine, antiviral activity, virus entry, virus release

INTRODUCTION

Pseudorabies (PR) is an acute highly contagious disease caused by pseudorabies virus (PRV). It was first described in Hungary in 1902 (Lee and Wilson, 1979). PRV, an enveloped and double-stranded linear DNA virus, is a member of the *Herpesviridae* family (Sun et al., 2016). It was also called Aujeszky's disease virus (ADV), which causes fever, itching (except pigs), and encephalomyelitis in many livestock and wild animals (Müller et al., 2011; Tan et al., 2021). PRV can infect pigs of different ages. The clinical signs of infected pigs were fever, diarrhea, vomiting, nervous system disorders, with high mortality for newborn piglets, nonsignificant symptoms for adult pigs, abortion, stillbirth and respiratory symptoms for sows, and reproductive disorder for boars (Tan et al., 2021). Recently, it has been reported that PRV infects and causes human endophthalmitis or

encephalitis, which highlights the potential threat of this pathogen to public health (Wong et al., 2019; Yang et al., 2019; Liu et al., 2020).

In China, PRV were firstly identified in cats in 1947, then were reported in swine and other animals. At present, both inactivated and attenuated live vaccines are widely used to prevent and control PR (Freuling et al., 2017; Delva et al., 2020). However, PRV variants emerged and spread in China since 2011, leading to huge economic losses (An et al., 2013; Wu et al., 2013; Tong et al., 2015). Compared to classical virulent PRV, PRV variants were more pathogenic on pigs and commercial vaccines failed to provide complete protection against the variants (Luo et al., 2014; Hu et al., 2021).

Besides developing new vaccines using current PRV circulating strains, researchers have also been working to identify inhibitors or drugs against PRV infection. Some diaminopurine-based acyclic nucleoside phosphonate analogues exhibited effective anti-PRV activity (Zouharova et al., 2016). Resveratrol, a polyphenolic stilbenoid, was identified to show efficient anti-PRV activities *in vitro* and *in vivo* (Zhao et al., 2017, 2018). The inhibitory effect of resveratrol occurred during viral multiplication by inhibiting IκB kinase activity but not at viral entry into porcine kidney cells (PK-15; Zhao et al., 2017). Further studies showed that resveratrol treatment effectively relieved pathological symptoms, reduced PRV-induced inflammation, and increased the growth performance of PRV-infected piglets (Zhao et al., 2018). Fang et al. (2020) demonstrated that hydroquinone inhibited PRV replication during viral attachment and internalization into PK-15 cells by activating the phosphorylation of AKT. In addition, platycodon grandiflorus polysaccharides were confirmed to inhibit PRV replication *via* downregulating PRV-induced autophagy (Xing et al., 2021).

Meclizine is a first-generation piperazine class of H1-antihistamine, which are usually used for vertigo, nausea and vomiting (Cohen and Dejong, 1972). Meclizine can also treat the same symptoms caused by viral infection, pregnancy, or radiation therapy. Meclizine has some anticholinergic activity as H1-antihistamines, and it is also reported to regulate constitutive androstane receptor (Huang et al., 2004). Recently, meclizine has been identified as an inhibitor of mitochondrial respiration or mitochondrial oxidative phosphorylation (Gohil et al., 2010, 2013). Gohil et al. revealed that meclizine inhibited mitochondrial respiration by inhibiting phosphoethanolamine cytidylyltransferase (PCYT2) activity. HSV-1 replication was significantly reduced after treatment with meclizine in Hela cells and in mice experiment (Arii et al., 2020).

In this study, we investigated whether meclizine could inhibit PRV replication *in vitro* and *in vivo*. Our findings showed that meclizine displayed antiviral activity against PRV infection in PK-15 cells, while the antiviral effect was not significant in mice. The mechanisms of meclizine still need to be further clarified. The study laid a foundation for the development of potential therapeutic drugs against PRV infection.

MATERIALS AND METHODS

Ethics Statement

All the animal experiments were approved by the Jiangsu Administrative Committee for Laboratory Animals (Permission Number: SYXKSU-2017-0044) and complied with the Guidelines of Laboratory Animal Welfare and Ethics of Jiangsu Administrative Committee and Laboratory Animal Welfare and Ethics Committee of Yangzhou University for Laboratory Animals.

Cells and Virus

PK-15 cells were obtained from the American Type Culture Collection (ATCC) and cultured in Dulbecco's modified Eagle medium (DMEM, CORNING, United States) containing 10% fetal bovine serum (FBS, Thermo Fisher Scientific, Waltham, United States) and 1% penicillin/streptomycin at 37°C with 5% CO_2. PRV variant strain JS21 with abbreviation of PRV-W and PRV Bartha K61 strain (GenBank accession no. JF797217; with abbreviation of PRV-V) were preserved in our laboratory. PRV titers were determined as the median tissue culture infective doses ($TCID_{50}$) on PK-15 cells.

Cell Viability Assay

The viability of PK-15 cells after meclizine treatment was determined using the Enhanced Cell Counting Kit-8 (CCK-8; Beyotime, Shanghai, China) to detect the relative cytotoxicity of agents according to the manufacturer's instructions. Briefly, PK-15 cells were seeded in 96-well plates (1×10^4 cells/well) and then exposed to different concentrations of meclizine or DMSO. Plates were incubated for 24 h at 37°C with 5% CO_2. After incubation, added 10 μl CCK-8 solution (containing WST-8, which can be reduced by some dehydrogenase in mitochondria to form orange formazan) to each well and continue incubated for 3 h. The absorbance was measured at 450 nm.

Virus Infection

PK-15 cells were seeded into 6-well plates (1×10^6/well) overnight at 37°C with 5% CO_2. When the cells reached approximately 70–80% confluence, they were infected with PRV at a multiplicity of infection (MOI) of 1 and incubated at 37°C with 5% CO_2 for 1 h. Then the supernatant was removed by washing with phosphate-buffered saline (PBS) for three times and incubated in DMEM supplemented with 2% FBS.

Meclizine Treatment

PK-15 cells were seeded into 6-well plates (1×10^6/well) overnight at 37°C with 5% CO_2. When the cells reached 70–80% confluence, they were infected with PRV (PRV-W and PRV-V) at MOI of 1 and cells were treated with meclizine at different concentrations (50, 100, 150, and 200 μM) or DMSO (used as negative control). Twenty-four hours later, the supernatant and cell samples were harvested for further detection.

Western Blot Analysis

PK-15 cells seeded in 6-well plates were washed with cold PBS and harvested with lysis buffer (containing 50 mM Tris (pH 7.4), 150 mM NaCl, 1% Triton X-100, 1% sodium deoxycholate, 0.1% SDS, etc.; Beyotime, Shanghai, China) on ice. After centrifugation, the supernatant was denatured and subjected to SDS-PAGE and transferred to polyvinylidene difluoride (PVDF) membranes (Millipore, MA, United States). The membranes were blocked in TBST with 5% nonfat dry milk for 1 h at room temperature and then incubated with antibodies of anti-PRV glycoprotein B (gB) mAb (1:1,000, preserved in our laboratory) and anti-glyceraldehyde-3-phosphate dehydrogenase (GAPDH; 1:1,000, Cell Signaling Technology, MA, United States) overnight at 4°C. After washing, the membranes were incubated with HRP-conjugated secondary antibodies for 1 h at room temperature (Jackson ImmunoResearch, PA, United States). The signals were visualized using an enhanced chemiluminescence reagent kit (NCM Biotech, Suzhou, China) through Tanon 5200 system (Tanon, Shanghai, China).

Immunofluorescence Assay

The cells were washed with PBS and fixed with 4% paraformaldehyde for 10 min and permeabilized with 0.5% Triton X-100 at room temperature. After blocking with 3% bovine serum albumin (BSA) in TBST for 30 min, the cells were incubated with anti-PRV gB protein mAb (1:1,000) for 1 h, followed by incubation with FITC-conjugated anti-mouse IgG secondary antibody (1:500, Cell Signaling Technology, MA, United States) for 45 min at 37°C. The cell nuclei were stained with DAPI (Beyotime, Shanghai, China) for 10 min at room temperature. Finally, the cells were visualized with a LSM 880 Zeiss confocal fluorescence microscope (Oberkochen, Germany).

DNA Extraction and Quantitative PCR

Total DNAs from cells or tissues were extracted using a DNA Extraction Kit according to the manufacturer's instructions (Omega, GA, United States). Viral loads were tested and assayed by real-time PCR. Briefly, serial 10-fold dilutions of the PRV-gD standard plasmid were used to construct a standard curve for each experiment. The CT value of the sample is substituted into the standard curve to calculate the corresponding copy number of viral genome DNA. Primers and probes are as follows: PRV-F: GTGGGCGTG TGCGTCTACA, PRV-R: GACCGGGCTGCGCT TTTA, the probe: FAM-CGAAGGGGTATCGCCTCCT-BHQ1. The PCR Mix (TaKaRa, Dalian, China) was used following the manufacturer's recommendations. The Quantitative PCR (qPCR) was performed on an ABI QuantStudioTM 3 (Applied Biosystems, CA, United States). The qPCR reaction was performed under the following conditions: 95°C for 1 min, followed by 40 cycles at 95°C for 5 s and 60°C for 1 min.

Viral Attachment, Entry, Replication, and Cell-to-Cell Spreading Assays

In the viral attachment assay, PK-15 cells were pre-cooled at 4°C for 30 min and then challenged with PRV strains (MOI = 5) with or without meclizine (150 μM) for 3 h at 4°C. After washing with PBS for three times, the cells were harvested for qPCR to test and analyze the copy numbers of PRV DNA.

In the viral entry assay, PK-15 cells were infected with PRV strains (MOI =5) for 3 h at 4°C. After washing, the cells were incubated at 37°C and meclizine was added at scheduled time points. Meclizine (150 μM) was added at 0, 0.5, 1, 1.5, 2, and 4 h (the time when the cells were transferred to 37°C was set as 0 h). After incubation for 6 h, the cells were washed for three times and harvested for qPCR to quantify viral DNA.

In the viral release assay, PK-15 cells were infected with PRV strains (MOI = 0.1/0.01) at 37°C for 24 h. After washing with PBS for three times, the medium was replaced with DMEM of 2% FBS and meclizine (150 μM) for another 4 h in 5% CO_2 at 37°C. Then the supernatants were harvested to quantify the viral DNA using qPCR.

In the cell-to-cell spreading assay, PK-15 cells were infected with PRV strains (MOI = 1) and treated with meclizine (150 μM) in 5% CO_2 at 37°C. After washing with PBS for three times, PK-15 cells were collected for immunofluorescence assay (IFA) at 0, 6, 9, 12, 18, and 24 h post-infection.

Animal Experiments

Twenty 5-week-old female BALB/c mice were randomly divided into five groups: control group, the administration group (Mec100), PRV-infected group (PRV), PRV-infected and administration groups (meclizine at doses of 50 mg/kg and 100 mg/kg respectively, PRV + Mec50, PRV + Mec100). Mice in different groups were fed separately. The infected mice were intraperitoneally injected with PRV-W at a dose of $10^{2.5}$ $TCID_{50}$. The administration group was injected with meclizine at doses of 100 mg/kg. The control group was injected with the same amount of DMEM. The other two groups were challenged with PRV in the same way and dose. At 8 h after PRV infection, the mice were administered intraperitonially with meclizine at doses of 50 mg/kg or 100 mg/kg respectively, which was repeated every 12 h until the end of the study. Meanwhile, 0.9% NaCl solution was injected into the first three groups. After inoculation, the daily behavior, mental status, and survival of mice were monitored every day for 7 days. Mice were humanely euthanized and brain, lung, and liver samples were subjected for gross pathology examination. DNA extraction and the viral load in tissues were quantified by qPCR.

Statistical Analysis

GraphPad Prism 7.0 (GraphPad Software, CA, United States) was used for the statistical analyses. The data was analyzed with student's t test and one-way test among groups and expressed as the mean ± standard deviation. The values of p of <0.05 was considered as statistically significant. Significance in all figures is indicated as follows: *, $p < 0.05$; **, $p < 0.01$; ***, $p < 0.001$.

RESULTS

Meclizine Inhibited PRV Infection in PK-15 Cells

To evaluate the antiviral activity of meclizine against PRV infection, we first investigated its cytotoxicity on PK-15 cells. The viability of PK-15 cells after different concentration of meclizine treatment for 24 h was determined. Compared with DMSO control, no significant cytotoxicity was observed when the drug concentration did not exceed 200 μM (**Figure 1A**). To further examine the antiviral effect of meclizine on different PRV strains, PK-15 cells were treated with meclizine of 50, 100, 150, and 200 μM and infected with PRV-W and PRV-V at a MOI of 1, respectively. At 24 h post infection (h.p.i.), virus titration, immunoblotting, qPCR, and IFA assays were performed. As shown by **Figure 1B**, virus titers in PK-15 cells significantly decreased by meclizine (≥100 μM) compared with the DMSO control. The results of immunoblotting showed that the expression levels of PRV-gB protein were markedly reduced by meclizine (**Figure 1C**). The inhibitory effect was more significant when meclizine was used in higher concentration. Besides, a notable decrease of copy numbers of PRV was also observed in meclizine-treated groups by using qPCR (**Figure 1D**). Consistently, the fluorescence intensity of cells treated with meclizine was significantly weaker than that in the DMSO groups (**Figure 2**). These results indicated that

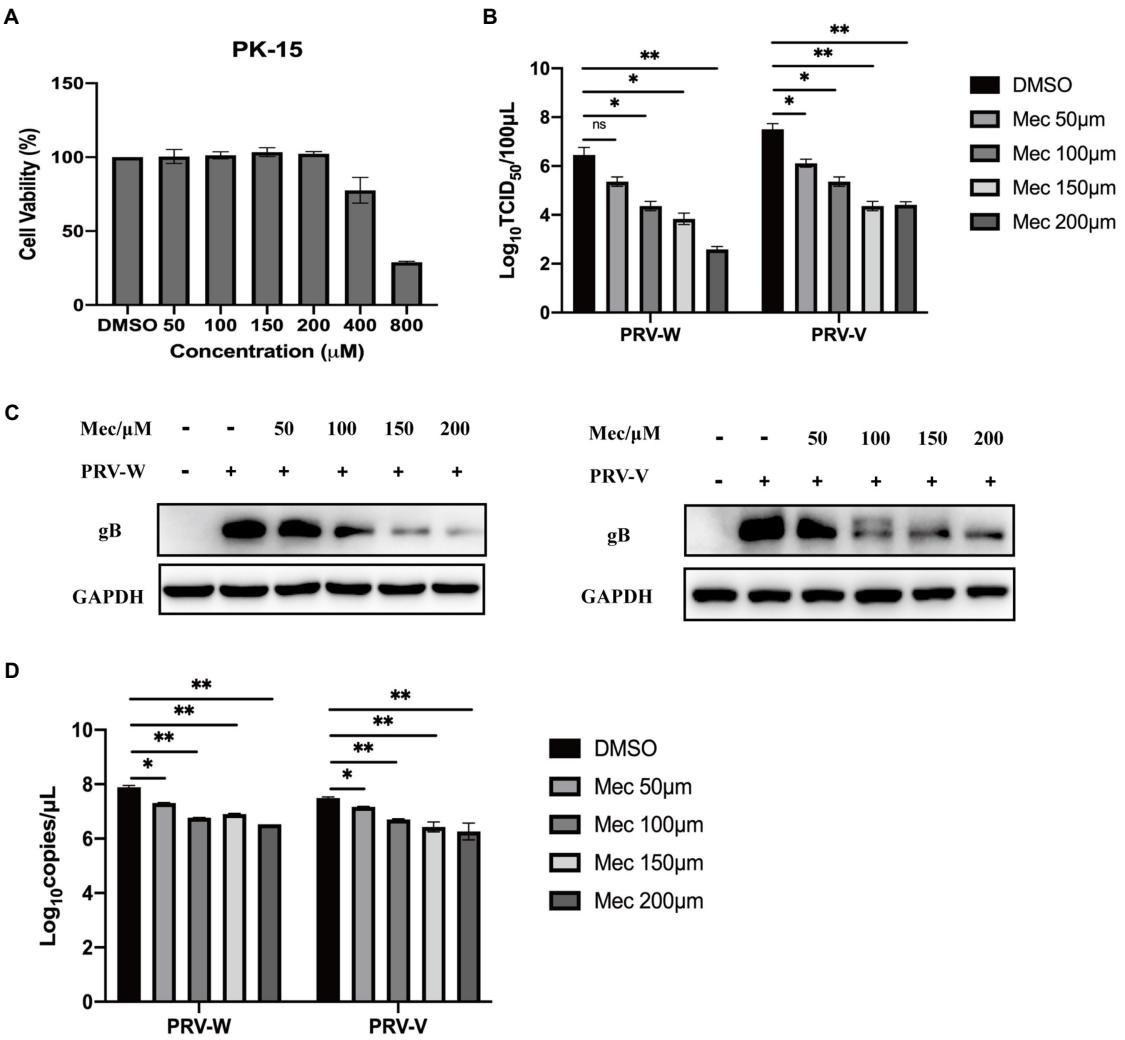

FIGURE 1 | Meclizine inhibited PRV infection and replication in PK-15 cells. **(A)** Potential cytotoxicity of meclizine against PK-15 cells was detected with the Enhanced Cell Counting Kit-8. PK-15 cells were seeded in 96-well plates and then exposed to different concentrations of meclizine or DMSO. After 24 h of incubation, 10 μl CCK-8 solution was added for another 3 h. The absorbance was measured at 450 nm. **(B–D)** PK-15 cells were infected with PRV variant strain (PRV-W) and Bartha K61 strain (PRV-V) at MOI of 1 in the presence of different concentrations of meclizine, DMSO (control) for 24 h at 37°C with 5% CO_2. The supernatant and cell samples were harvested. Supernatants were subjected to virus titration. The expression levels of gB protein were analyzed by immunoblotting **(C)**. The copy numbers of PRV-W and PRV-V DNA were quantified by real-time PCR **(D)**. Data were presented as means±SD from three independent experiments. *, $p < 0.05$; **, $p < 0.01$; ***, $p < 0.001$.

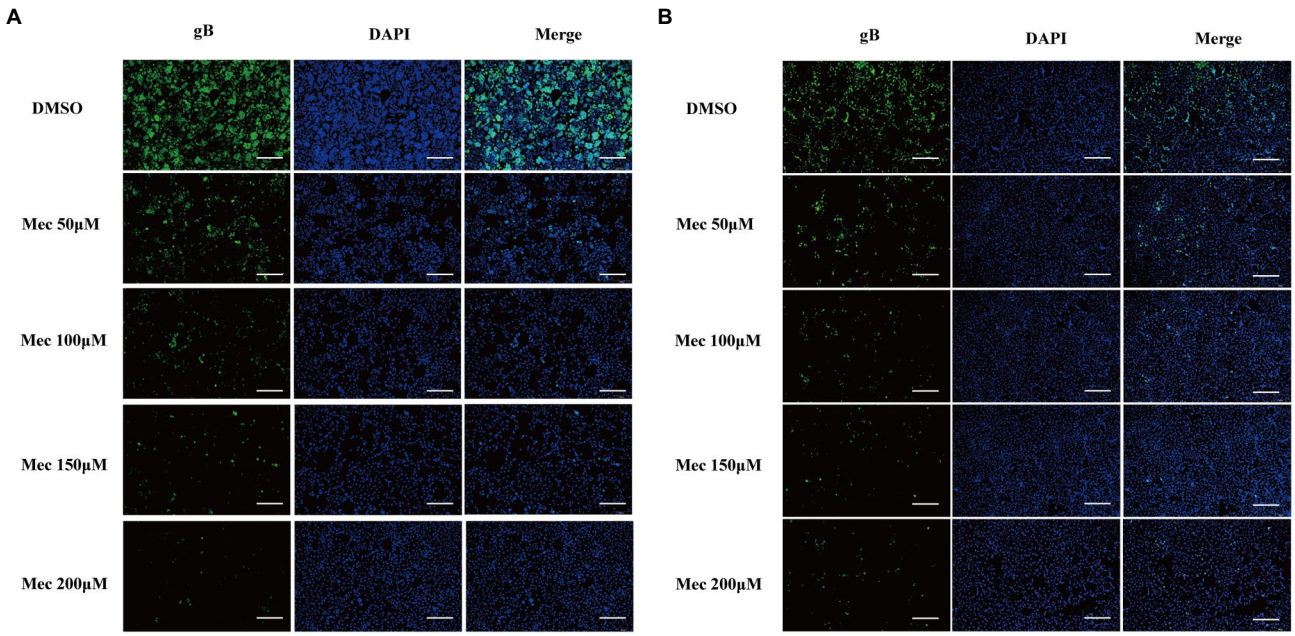

FIGURE 2 | Meclizine decreased the expression levels of PRV gB protein detected by IFA. PK-15 cells were infected with PRV-W **(A)** and PRV-V **(B)** at MOI of 1 in the presence of different concentrations of meclizine or DMSO (control groups) for 24 h at 37°C with 5% CO_2. Cells were detected by IFA. Scale bars = 200 μm. Typical figures were presented from three independent experiments.

treatment with meclizine effectively inhibited PRV infection in PK-15 cells.

Meclizine Inhibited PRV Infection During the Different Stages of Infection

To investigate the stages that meclizine affects PRV infection *in vitro*, meclizine treatment was performed either before, simultaneously with, or after PRV infection, respectively (**Figure 3A**). PK-15 cells were treated with meclizine of 150 μM and infected with different PRV strains at a MOI of 1. At 24 h.p.i., cells were harvested for qPCR and Western blot analysis. Compared with DMSO control, the production of viral DNA was significantly decreased with meclizine at three different approaches (**Figure 3B**). Consistent with qPCR results, the expression of gB was significantly reduced with treatment of meclizine on protein level (**Figures 3C–F**). In addition, the inhibitory effect was the most significantly in meclizine treatment before PRV infection. These results showed that meclizine inhibited PRV infection during the different stages of infection, particularly in the early stage.

Meclizine Inhibited PRV Infection by Interfering With Virus Entry, Release, and Cell-to-Cell Spreading

Replication cycle of PRV includes four stages: adsorption, entry, replication, and release. To explore the mechanism of meclizine against PRV infection, viral attachment assay, entry assay, release assay, and cell-to-cell spreading assay were performed. For the viral attachment assay, PK-15 cells were infected with PRV with or without meclizine. After washing, the cells were harvested for qPCR to quantify the copy number of viral DNA. The results showed that the copy numbers of PRV DNA in meclizine-treated cells were not significantly different from those in the control cells (**Figure 4A**).

For the viral entry assay, PRV-infected cells were incubated at 37°C and meclizine was added at scheduled time points. Finally, intracellular viral DNA was quantified using qPCR. The results showed that the copy numbers of PRV DNA were remarkable decreased after adding meclizine (**Figures 4B,C**). Interestingly, the inhibition effect was better when meclizine was added at the earlier stage of incubation at 37°C.

For the viral release assay, the medium was replaced with DMEM containing 2% FBS and meclizine (150 μM) at 24 h after PRV infection. Four hours later, the supernatants were harvested to quantify the viral DNA using qPCR. Compared to control cells, the copy numbers of PRV DNA in meclizine-treated cells were significantly lower (**Figures 4D,E**).

As shown in **Figure 4F**, the fluorescence intensity in the DMSO groups increased over time after PRV-W infection. However, the amount of fluorescence in the cells treated with meclizine was much late and significantly less than that in DMSO groups (**Figure 4G**). Expectedly, meclizine also showed a similar effect during PRV-V infection, the results were showed in **Supplementary Figure S1**. The results indicated that meclizine inhibited cell-to-cell spreading step during PRV replication.

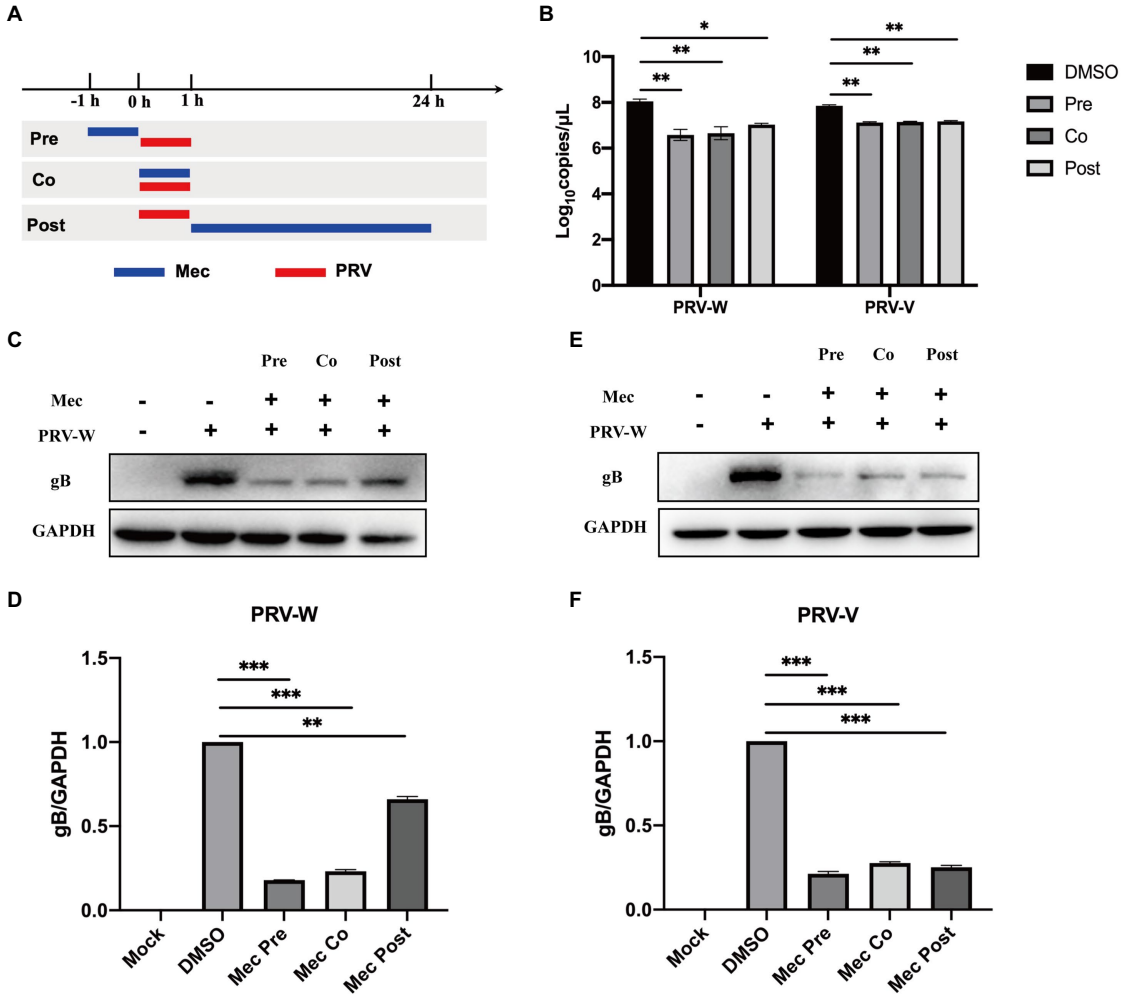

FIGURE 3 | Meclizine inhibited PRV infection during the different stages of infection. **(A)** Schematic diagram of meclizine administration. PK-15 cells were infected with different PRV strains (PRV-W and PRV-V) at MOI of 1 for 1 h, and cells were treated with 150 μM meclizine at different time points. Meclizine treatment was performed either before (pre), simultaneously with (co), or after PRV infection (post), respectively. At 24 h, cell samples were harvested. **(B)** The copy numbers of PRV DNA were quantified by qPCR. **(C–F)** The expression levels of gB protein and GAPDH were analyzed by immunoblotting. The analysis of WB band gray value was visualized by Image J software. Data were presented as means±SD from three independent experiments. *, $p < 0.05$; **, $p < 0.01$; ***, $p < 0.001$.

Taken together, these data indicated that meclizine negatively affected the entry, release, and cell-to-cell spreading stages of viral life cycle to inhibit PRV infection.

Meclizine Inhibition on PRV Infection *in vivo*

After PRV-W challenge, the daily behavior, mental status, and survival of mice were monitored and recorded. Mice that were not administered with meclizine showed clinical symptoms, including loss of appetite, lethargy, and scratching. On the 3rd day after viral challenge, the mice in the PRV group began to die and the mortality rate was 75% on the 4th day (**Figures 5A,B**). While the mice in PRV + Mec groups were found dead from the 4th day. At the end of the experiment, there was one mouse survived in both PRV group and PRV + Mec group. All mice in control group and administration group survived within 7 days (**Figure 5B**). Brain, lung, and liver samples of mice were collected and subjected to gross pathology evaluation. Pathological examination results showed that lungs and brains of mice in PRV group had hemorrhage and congestion, which were more severe than that in PRV + Mec groups. There was more serious edema in livers of mice in PRV group than in other groups (**Figure 5C**). No significant lesions were observed in the tissues from Mec100 group and control group.

In addition, viral load in tissues were quantified to further explore the effect of meclizine on PRV replication *in vivo*. The results of qPCR showed that the viral loads in mice brain were higher than that in the lungs and livers (**Figure 6**). PRV loads in the brains of mice from PRV + Mec groups were lower than those from PRV group (**Figure 6A**). There

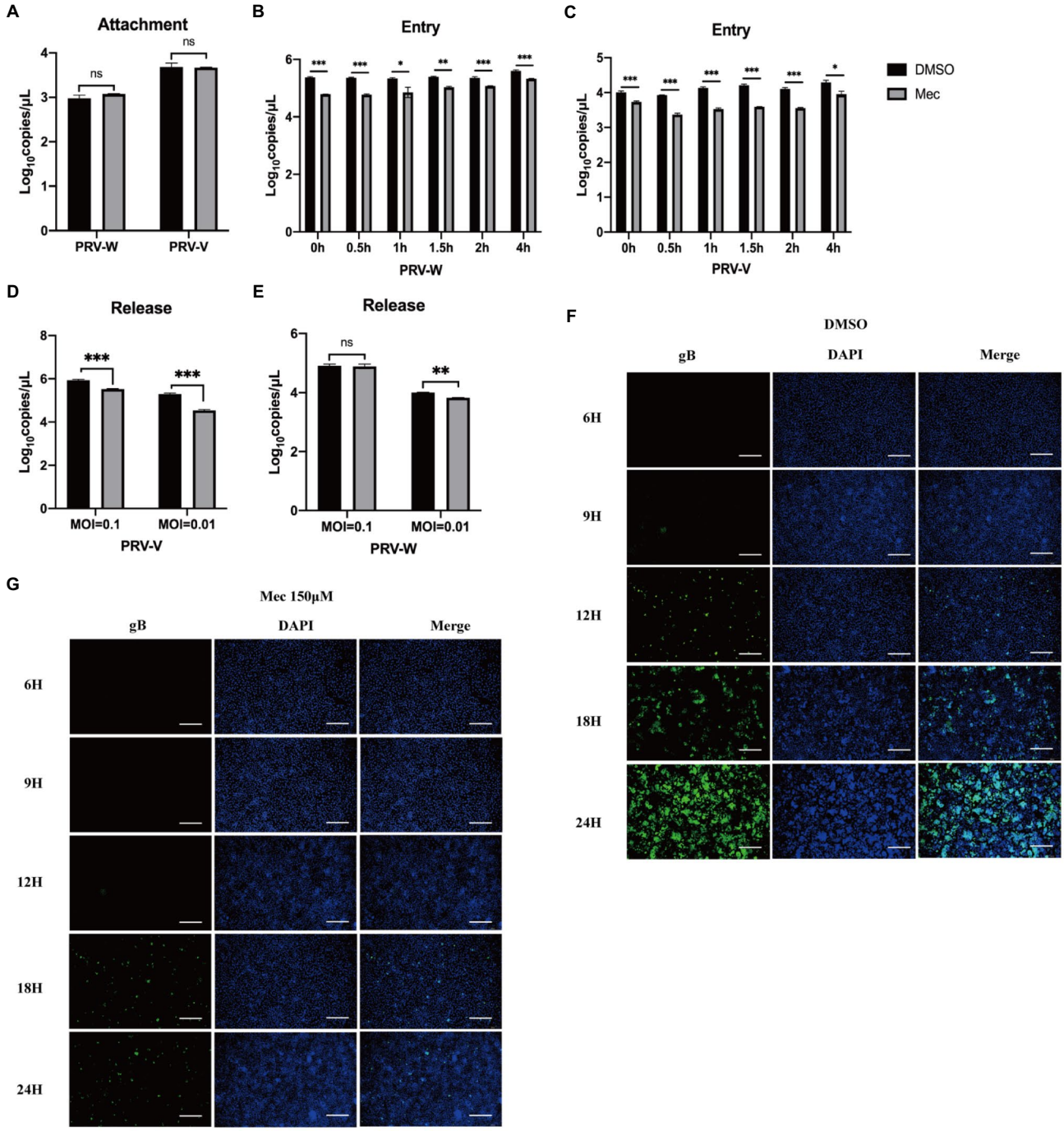

FIGURE 4 | Meclizine inhibited PRV infection by interfering with the entry, release and cell-to-cell spreading but not attachment into PK-15 cells. PK-15 cells were seeded in 6-well plates and cultured overnight. When the cells reached approximately 70–80% confluence before carrying out antiviral assays. **(A)** Virus attachment assay. **(B,C)** Virus entry assay. **(D,E)** Virus release assay. **(F,G)** The cell-to-cell spreading assay of meclizine about PRV-W. The results of PRV-V were showed in **Supplementary Figure S1**. Scale bars = 200 μm. Data were presented as means±SD from three independent experiments. *, $p < 0.05$; **, $p < 0.01$; ***, $p < 0.001$.

was no significant difference among PRV group and PRV + Mec groups in the lungs and livers of mice (**Figures 6B,C**). The above results suggested that meclizine treatment could decrease the severity of clinical symptoms, delay death, and reduce viral loads in tissues after viral challenge. However, the inhibit effect of meclizine in mice were not as good as those *in vitro*, and the mechanism was unknown.

A

Groups	Drugs	Mice	Mortality
Control	/	4	0/4
Mec 100	100mg/kg	4	0/4
PRV	/	4	3/4
PRV+Mec 50	50mg/kg	4	3/4
PRV+Mec 100	100mg/kg	4	3/4

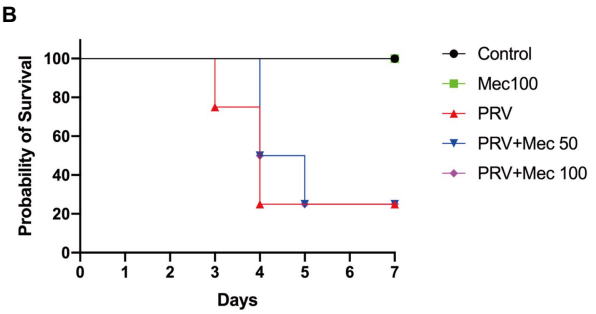

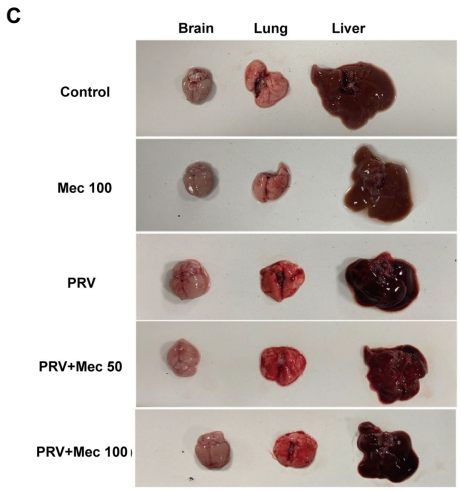

FIGURE 5 | Meclizine inhibits PRV infection in mice. **(A)** Schematic diagram of mice experiment and mortality of mice in different groups. **(B)** Survival profile of mice after PRV challenge in different groups. **(C)** Brain, lung, and liver samples of mice were collected for pathological examination. Typical figures were presented from three independent experiments.

DISCUSSION

Since the emergence and widespread of PRV variants, commercial vaccines could not prevent completely PRV infection in pigs, which led to huge economic losses to the Chinese pig industry. Besides developing new PRV vaccines, research on antiviral drugs with inhibitory effects on PRV is an alternative solution for disease control. In this study, we for the first time verified that meclizine had potent inhibitory effect on PRV variant strain and Bartha K61 strain both *in vitro* and *in vivo*.

Our results indicated that meclizine reduced PRV replication at multiple stages of virus life cycle by impairing the production of viral particles and protein synthesis (**Figure 3**). Antiviral assay of meclizine administration with three different methods showed that meclizine treatment no matter before or simultaneously with PRV infection displayed more effective antiviral activity against PRV replication than treatment after PRV infection. Antiviral drugs were reported to destroy virus replication by targeting different stages of life cycle of infectious viruses, such as the attachment, entry, and release of viral particles (Yasin et al., 2004; Kausar et al., 2021; Tompa et al., 2021). As for meclizine, our results suggested it could interfere with viral entry, release and cell-to-cell spreading stages of the viral life cycle (**Figure 4**), which was similar to the effect of it inhibiting HSV-1 replication (Arii et al., 2020).

Viruses interact and regulate with cell membrane in several stages of replication, which need to pass through cell membrane to entry for infection and exit for release virus particles (Lorizate and Kräusslich, 2011). Lipids are the structural basis of cell biofilm, which mainly include glycerophospholipids, sphingolipids, and sterols. Glycerol phospholipids in cell biofilms and viral envelope play a variety of roles in membrane related virological events (Ketter and Randall, 2019). Phosphatidylethanolamine (PE) is a kind of glycerophospholipids, which is involved in the composition of biofilm (Hishikawa et al., 2014). Meclizine is also an inhibitor of metabolic enzyme PCYT2, in addition to being an antihistamine. PCYT2 is a key enzyme for the biosynthesis of PE from ethanolamine and diacylglycerol (Pavlovic and Bakovic, 2013; Vance and Tasseva, 2013). In our study, PRV replication was significantly decreased after treatment with meclizine. The possible mechanism could be attributed to PE biosynthesis pathway was disrupted by meclizine and reduced the production of cell biofilms, which were adverse to virus entry, protein biosynthesis, and virus egress. The antiviral mechanism of meclizine needs further investigation.

The antiviral activity of meclizine was also tested in mice. Compared with PRV group, the severity of clinical symptoms was decreased, and death of mice in the PRV + Mec groups was delayed (**Figure 5**). Decreased viral loads were observed

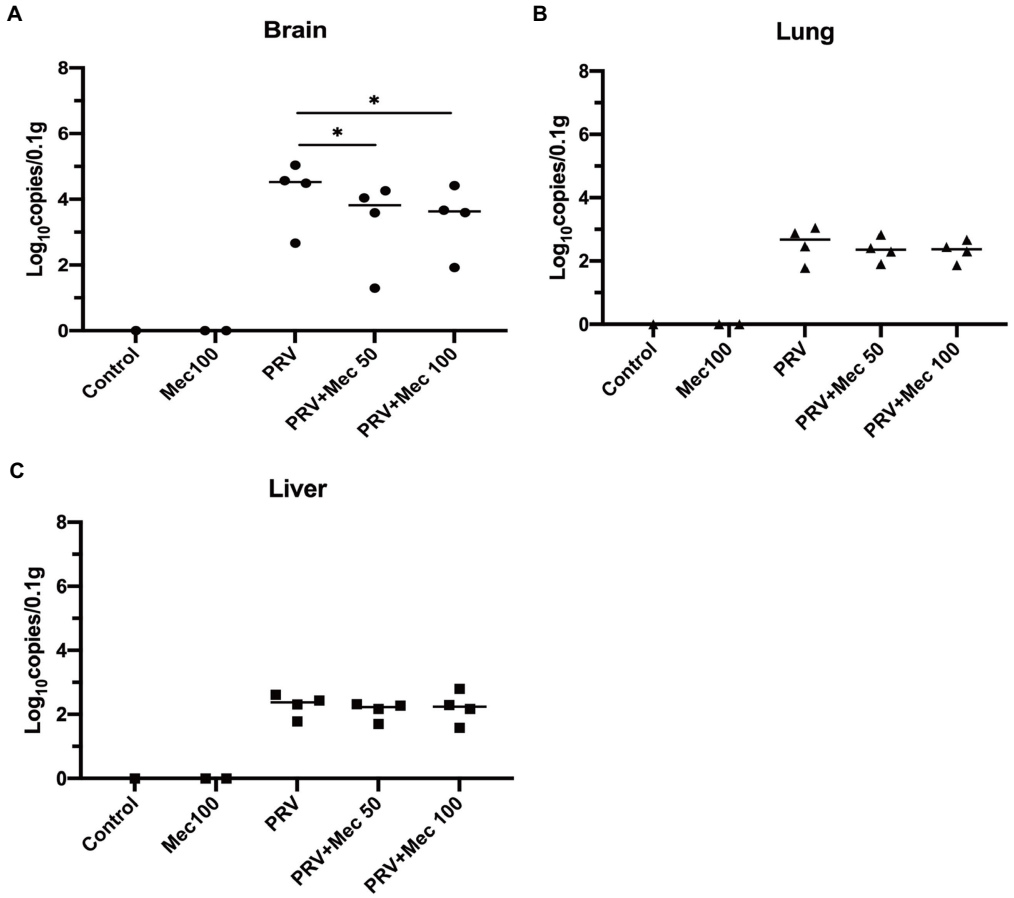

FIGURE 6 | Meclizine treatment decreased the viral loads in tissues after viral challenge. 0.1 g of brain **(A)**, lung **(B)**, and liver **(C)** samples were taken for DNA extraction. The viral loads in tissues were analyzed by qPCR. *, $p < 0.05$; Data were presented as means ± SD from three independent experiments.

in tissues of mice in PRV + Mec groups compared with those in PRV group (**Figure 6**). The viral loads in the brain were higher than that in the lungs and livers, which was consistent with the previous research (Huang et al., 2020). In our study, meclizine only delayed the death of mice but not reduce the mortality. It suggested that the inhibitory mechanism of meclizine on PRV was complex, and its effect in mice may be inconsistent with those *in vitro*. In addition to pharmacological activity, the function of meclizine in mice was also related to their absorption, distribution, metabolism, excretion and so on. When drugs act on cells, they can exert their effect directly. When the drug is used in animals, it needs to enter the blood circulation through the barrier membrane (vascular wall and mucosa, etc.) from the site of administration, then be distributed in various organs or cells, and be absorbed by the body to play roles. Meanwhile, with the prolongation of time, the drug will undergo varying degrees of structural changes and gradually be metabolized by the body, which led to its pharmacological effects weakened or completely lost. In our experiment, although mice were administered with meclizine every 12 h, the time to maintain effective working concentration of meclizine was still unclear. It was possible that medicine had a short time to maintain its antiviral activity in mice and did not display the expected protective effect on them. The detailed mechanism was unknown.

To sum up, our findings revealed that meclizine not only has antiviral activity, but also showed inhibitory effects on PRV replication *in vitro*, when it was administered either before, simultaneously with, or after PRV infection, respectively. Meclizine also decreased viral replication in brains *in vivo*. Therefore, meclizine has the potential for the development of preventive and therapeutic strategies for PRV infection.

DATA AVAILABILITY STATEMENT

The original contributions presented in the study are included in the article/**Supplementary Material**; further inquiries can be directed to the corresponding authors.

ETHICS STATEMENT

The animal study was reviewed and approved by the Laboratory Animal Welfare and Ethics Committee of Yangzhou University.

AUTHOR CONTRIBUTIONS

PL, YS, and XL conceived and designed the experiments. PL and DH performed the experiments, analyzed the data, and drafted the manuscript. LY, ZL, XY, and ZZ contributed reagents, materials, and analysis tools. PL, NN, YS, and XL thoroughly revised the manuscript. All authors contributed to the article and approved the submitted version.

FUNDING

This work was funded by the National Natural Science Foundation of China (nos. 32102637 and 32172823), Yangzhou University Interdisciplinary Research Foundation for Veterinary Medicine Discipline of Targeted Support (to YS), and the Project of the Priority Academic Program Development of Jiangsu Higher Education Institutions (PAPD).

SUPPLEMENTARY MATERIAL

The Supplementary Material for this article can be found online at: https://www.frontiersin.org/articles/10.3389/fmicb.2021.795593/full#supplementary-material

Supplementary Figure S1 | Meclizine inhibited cell-to-cell spreading step during PRV-V replication. Scale bars = 200 μm. Typical figures were presented from three independent experiments.

REFERENCES

An, T. Q., Peng, J. M., Tian, Z. J., Zhao, H. Y., Li, N., Liu, Y. M., et al. (2013). Pseudorabies virus variant in Bartha-K61-vaccinated pigs, China, 2012. *Emerg. Infect. Dis.* 19, 1749–1755. doi: 10.3201/eid1911.130177

Arii, J., Fukui, A., Shimanaka, Y., Kono, N., Arai, H., Maruzuru, Y., et al. (2020). Role of Phosphatidylethanolamine biosynthesis in herpes simplex virus 1-infected cells in progeny virus morphogenesis in the cytoplasm and in viral pathogenicity in vivo. *J. Virol.* 94, e01572–e015720. doi: 10.1128/jvi.01572-20

Cohen, B., and Dejong, J. M. (1972). Meclizine and placebo in treating vertigo of vestibular origin. Relative efficacy in a double-blind study. *JAMA Neurol.* 27, 129–135. doi: 10.1001/archneur.1972.00490140033006

Delva, J. L., Nauwynck, H. J., Mettenleiter, T. C., and Favoreel, H. W. (2020). The attenuated Pseudorabies virus vaccine strain Bartha K61: a brief review on the knowledge gathered during 60 years of research. *Pathogens* 9:897. doi: 10.3390/pathogens9110897

Fang, L., Gao, Y., Lan, M., Jiang, P., Bai, J., Li, Y., et al. (2020). Hydroquinone inhibits PRV infection in neurons *in vitro* and *in vivo*. *Vet. Microbiol.* 250:108864. doi: 10.1016/j.vetmic.2020.108864

Freuling, C. M., Müller, T. F., and Mettenleiter, T. C. (2017). Vaccines against pseudorabies virus (PrV). *Vet. Microbiol.* 206, 3–9. doi: 10.1016/j.vetmic.2016.11.019

Gohil, V. M., Sheth, S. A., Nilsson, R., Wojtovich, A. P., Lee, J. H., Perocchi, F., et al. (2010). Nutrient-sensitized screening for drugs that shift energy metabolism from mitochondrial respiration to glycolysis. *Nat. Biotechnol.* 28, 249–255. doi: 10.1038/nbt.1606

Gohil, V. M., Zhu, L., Baker, C. D., Cracan, V., Yaseen, A., Jain, M., et al. (2013). Meclizine inhibits mitochondrial respiration through direct targeting of cytosolic phosphoethanolamine metabolism. *J. Biol. Chem.* 288, 35387–35395. doi: 10.1074/jbc.M113.489237

Hishikawa, D., Hashidate, T., Shimizu, T., and Shindou, H. (2014). Diversity and function of membrane glycerophospholipids generated by the remodeling pathway in mammalian cells. *J. Lipid Res.* 55, 799–807. doi: 10.1194/jlr.R046094

Hu, R., Wang, L., Liu, Q., Hua, L., Huang, X., Zhang, Y., et al. (2021). Whole-genome sequence analysis of Pseudorabies virus clinical isolates from pigs in China between 2012 and 2017 in China. *Viruses* 13:1322. doi: 10.3390/v13071322

Huang, J., Qi, Y., Wang, A., Huang, C., Liu, X., Yang, X., et al. (2020). Porcine β-defensin 2 inhibits proliferation of pseudorabies virus in vitro and in transgenic mice. *Virol. J.* 17:18. doi: 10.1186/s12985-020-1288-4

Huang, W., Zhang, J., Wei, P., Schrader, W. T., and Moore, D. D. (2004). Meclizine is an agonist ligand for mouse constitutive androstane receptor (CAR) and an inverse agonist for human CAR. *Mol. Endocrinol.* 18, 2402–2408. doi: 10.1210/me.2004-0046

Kausar, S., Said Khan, F., Rehman, I. M. U., Akram, M., Riaz, M., Rasool, G., et al. (2021). A review: mechanism of action of antiviral drugs. *Int. J. Immunopathol. Pharmacol.* 35:20587384211002621. doi: 10.1177/20587384211002621

Ketter, E., and Randall, G. (2019). Virus impact on lipids and membranes. *Annu. Rev. Virol.* 6, 319–340. doi: 10.1146/annurev-virology-092818-015748

Lee, J. Y., and Wilson, M. R. (1979). A review of pseudorabies (Aujeszky's disease) in pigs. *Can. Vet. J.* 20, 65–69

Liu, Q., Wang, X., Xie, C., Ding, S., Yang, H., Guo, S., Li, J., Qin, L., Ban, F., Wang, D., Wang, C., Feng, L., Ma, H., Wu, B., Zhang, L., Dong, C., Xing, L., Zhang, J., Chen, H., Yan, R., Wang, X., and Li, W. (2020). A novel human acute encephalitis caused by pseudorabies virus variant strain. *Clin. Infect. Dis.* doi: 10.1093/cid/ciaa987 [Epub ahead of print].

Lorizate, M., and Kräusslich, H. G. (2011). Role of lipids in virus replication. *Cold Spring Harb. Perspect. Biol.* 3:a004820. doi: 10.1101/cshperspect.a004820

Luo, Y., Li, N., Cong, X., Wang, C. H., Du, M., Li, L., et al. (2014). Pathogenicity and genomic characterization of a pseudorabies virus variant isolated from Bartha-K61-vaccinated swine population in China. *Vet. Microbiol.* 174, 107–115. doi: 10.1016/j.vetmic.2014.09.003

Müller, T., Hahn, E. C., Tottewitz, F., Kramer, M., Klupp, B. G., Mettenleiter, T. C., et al. (2011). Pseudorabies virus in wild swine: a global perspective. *Arch. Virol.* 156, 1691–1705. doi: 10.1007/s00705-011-1080-2

Pavlovic, Z., and Bakovic, M. (2013). Regulation of Phosphatidylethanolamine Homeostasis—The Critical Role of CTP:Phosphoethanolamine Cytidylyltransferase (Pcyt2). *Int. J. Mol. Sci.* 14, 2529–2550. doi: 10.3390/ijms14022529

Sun, Y., Luo, Y., Wang, C. H., Yuan, J., Li, N., Song, K., et al. (2016). Control of swine pseudorabies in China: opportunities and limitations. *Vet. Microbiol.* 183, 119–124. doi: 10.1016/j.vetmic.2015.12.008

Tan, L., Yao, J., Yang, Y., Luo, W., Yuan, X., Yang, L., et al. (2021). Current status and challenge of Pseudorabies virus infection in China. *Virol. Sin.* 36, 588–607. doi: 10.1007/s12250-020-00340-0

Tompa, D. R., Immanuel, A., Srikanth, S., and Kadhirvel, S. (2021). Trends and strategies to combat viral infections: A review on FDA approved antiviral drugs. *Int. J. Biol. Macromol.* 172, 524–541. doi: 10.1016/j.ijbiomac.2021.01.076

Tong, W., Liu, F., Zheng, H., Liang, C., Zhou, Y. J., Jiang, Y. F., et al. (2015). Emergence of a Pseudorabies virus variant with increased virulence to piglets. *Vet. Microbiol.* 181, 236–240. doi: 10.1016/j.vetmic.2015.09.021

Vance, J. E., and Tasseva, G. (2013). Formation and function of phosphatidylserine and phosphatidylethanolamine in mammalian cells. *Biochim. Biophys. Acta* 1831, 543–554. doi: 10.1016/j.bbalip.2012.08.016

Wong, G., Lu, J., Zhang, W., and Gao, G. F. (2019). Pseudorabies virus: a neglected zoonotic pathogen in humans? *Emerg. Microbes Infect.* 8, 150–154. doi: 10.1080/22221751.2018.1563459

Wu, R., Bai, C., Sun, J., Chang, S., and Zhang, X. (2013). Emergence of virulent pseudorabies virus infection in northern China. *J. Vet. Sci.* 14, 363–365. doi: 10.4142/jvs.2013.14.3.363

Xing, Y., Wang, L., Xu, G., Guo, S., Zhang, M., Cheng, G., et al. (2021). Platycodon grandiflorus polysaccharides inhibit Pseudorabies virus replication via downregulating virus-induced autophagy. *Res. Vet. Sci.* 140, 18–25. doi: 10.1016/j.rvsc.2021.08.004

Yang, X., Guan, H., Li, C., Li, Y., Wang, S., Zhao, X., et al. (2019). Characteristics of human encephalitis caused by pseudorabies virus: A case series study. *Int. J. Infect. Dis.* 87, 92–99. doi: 10.1016/j.ijid.2019.08.007

Yasin, B., Wang, W., Pang, M., Cheshenko, N., Hong, T., Waring, A. J., et al. (2004). Theta defensins protect cells from infection by herpes simplex virus by inhibiting viral adhesion and entry. *J. Virol.* 78, 5147–5156. doi: 10.1128/jvi.78.10.5147-5156.2004

Zhao, X., Cui, Q., Fu, Q., Song, X., Jia, R., Yang, Y., et al. (2017). Antiviral properties of resveratrol against pseudorabies virus are associated with the inhibition of IκB kinase activation. *Sci. Rep.* 7:8782. doi: 10.1038/s41598-017-09365-0

Zhao, X., Tong, W., Song, X., Jia, R., Li, L., Zou, Y., et al. (2018). Antiviral effect of resveratrol in piglets infected with virulent Pseudorabies virus. *Viruses* 10:457. doi: 10.3390/v10090457

Zouharova, D., Lipenska, I., Fojtikova, M., Kulich, P., Neca, J., Slany, M., et al. (2016). Antiviral activities of 2,6-diaminopurine-based acyclic nucleoside phosphonates against herpesviruses: In vitro study results with pseudorabies virus (PrV, SuHV-1). *Vet. Microbiol.* 184, 84–93. doi: 10.1016/j.vetmic.2016.01.010

Conflict of Interest: The authors declare that the research was conducted in the absence of any commercial or financial relationships that could be construed as a potential conflict of interest.

Publisher's Note: All claims expressed in this article are solely those of the authors and do not necessarily represent those of their affiliated organizations, or those of the publisher, the editors and the reviewers. Any product that may be evaluated in this article, or claim that may be made by its manufacturer, is not guaranteed or endorsed by the publisher.

frontiers in Microbiology

ORIGINAL RESEARCH
published: 23 December 2021
doi: 10.3389/fmicb.2021.800935

Hepatocyte Growth Factor-Dependent Antiviral Activity of Activated cdc42-Associated Kinase 1 Against Hepatitis B Virus

Hye Won Lee[1], Yongwook Choi[1], Ah Ram Lee[2], Cheol-Hee Yoon[1], Kyun-Hwan Kim[2], Byeong-Sun Choi[1] and Yong Kwang Park[1]**

[1] Division of Chronic Viral Diseases, Center for Emerging Virus Research, National Institute of Infectious Disease, National Institute of Health, Cheongju, South Korea, [2] Department of Precision Medicine, School of Medicine, Sungkyunkwan University, Suwon, South Korea

Activated cdc42-associated kinase 1 (ACK1) is a well-known non-receptor tyrosine kinase that regulates cell proliferation and growth through activation of cellular signaling pathways, including mitogen-activated protein kinase (MAPK). However, the anti-HBV activity of ACK1 has not been elucidated. This study aimed to investigate the role of ACK1 in the HBV life cycle and the mechanism underlying the anti-HBV activity of ACK1. To examine the antiviral activity of ACK1, we established HepG2-ACK1 cells stably overexpressing ACK1. The HBV life cycle, including HBeAg/HBsAg secretion, HBV DNA/transcription, and enhancer activity, was analyzed in HepG2 and HepG2-ACK1 cells with HBV replication-competent HBV 1.2mer (HBV 1.2). Finally, the anti-HBV activity of ACK1 was examined in an HBV infection system. ACK1 suppressed HBV gene expression and transcription in HepG2 and HepG2-ACK1 cells. Furthermore, ACK1 inhibited HBV replication by decreasing viral enhancer activity. ACK1 exhibited its anti-HBV activity via activation of Erk1/2, which consequently downregulated the expression of HNF4α binding to HBV enhancers. Furthermore, hepatocyte growth factor (HGF) induced ACK1 expression at an early stage. Finally, ACK1 mediated the antiviral effect of HGF in the HBV infection system. These results indicated that ACK1 induced by HGF inhibited HBV replication at the transcriptional level by activating the MAPK-HNF signaling pathway. Our findings suggest that ACK1 is a potentially novel upstream molecule of MAPK-mediated anti-HBV activity.

Keywords: activated cdc42-associated kinase 1, hepatitis B virus, HBV enhancer, hepatocyte nuclear factor, hepatocyte growth factor

OPEN ACCESS

Edited by:
Li Yongqing,
Institute of Animal Husbandry and Veterinary Medicine, Beijing Academy of Agriculture and Forestry Sciences, China

Reviewed by:
Lin Deng,
Kobe University, Japan
Masahiko Ito,
Hamamatsu University School of Medicine, Japan

****Correspondence:***
Byeong-Sun Choi
byeongsun@korea.kr
Yong Kwang Park
yk1029@korea.kr

Specialty section:
This article was submitted to Virology, a section of the journal Frontiers in Microbiology

Received: *24 October 2021*
Accepted: *06 December 2021*
Published: *23 December 2021*

Citation:
Lee HW, Choi Y, Lee AR, Yoon C-H, Kim K-H, Choi B-S and Park YK (2021) Hepatocyte Growth Factor-Dependent Antiviral Activity of Activated cdc42-Associated Kinase 1 Against Hepatitis B Virus. Front. Microbiol. 12:800935. doi: 10.3389/fmicb.2021.800935

INTRODUCTION

Activated cdc42-associated kinase 1 (ACK1), encoded by tyrosine kinase non-receptor 2, is a ubiquitously expressed non-receptor tyrosine kinase and well-known adaptor of activated receptor tyrosine kinases (RTKs) (Galisteo et al., 2006; Mahajan and Mahajan, 2015). ACK1 is phosphorylated by Src family kinase (SFK) (Chan et al., 2011), and phosphorylation of ACK1 promotes cancer progression and growth via activation of tyrosine kinase signaling (Mahajan and Mahajan, 2015). In prostate cancer, activated ACK1 promotes tumor growth via androgen receptor (AR) tyrosine phosphorylation, facilitating androgen-independent transactivation of

AR (Mahajan et al., 2007) and degradation of tumor suppressor WW domain containing oxidoreductase (Wwox) (Mahajan et al., 2005). ACK1 activation by RTK HER2 induces phosphorylation of the histone demethylase KDM3A and recruits the estrogen receptor (ER) to form a complex with KDM3A. This promotes the homeobox A1 (HOAX1) transcription associated with breast cancer progression in the absence of estrogen (Mahajan et al., 2014). ACK1 overexpression enhances invasive and metastatic properties of hepatocellular carcinoma (HCC) via AKT-activated epithelial-mesenchymal transition (EMT) (Lei et al., 2015). In addition to tumorigenesis, ACK1 contains the clathrin interaction domain and is involved in clathrin-mediated endocytosis. Variations in ACK1 expression regulate endocytosis of the transferrin receptor (Teo et al., 2001). ACK1 interacts with epidermal growth factor receptor (EGFR) to regulate its degradation, thereby inhibiting EGFR signaling (Shen et al., 2007; Grovdal et al., 2008). Collectively, these studies suggest that ACK1 plays an important role in kinase-mediated cellular processes. It is therefore important to address the precise function of ACK1 in viral infection.

Hepatitis B virus (HBV) has a partially double-stranded DNA genome of 3.2 kb. Persistent HBV infection is a major cause of chronic hepatitis B (CHB), cirrhosis, and HCC, increasing the risk for developing HCC in over 200 million infected individuals worldwide (Trepo et al., 2014; Seeger and Mason, 2015). HBV proteins, particularly HBx and large HBV surface proteins (LHBs), disrupt various cellular signaling cascades, leading to chronic liver disease (Seeger and Mason, 2015). Interestingly, signaling cascades regulated by ACK1, namely SFK, EGFR, AR, ER, and Akt signaling, are associated with HBV replication and pathogenesis. HBx and LHBs are implicated in liver carcinogenesis via activation of Src and Akt signaling, respectively (Klein and Schneider, 1997; Liu et al., 2011), and the activation of SFK by HBx stimulates HBV replication (Klein et al., 1999). Furthermore, AR signaling promotes HCC and increases HBV replication *in vitro* and *in vivo* by binding to the androgen response elements of the HBV enhancer I (Wang et al., 2009; Wu et al., 2010; Tian et al., 2012). In contrast, ER signaling attenuates viral enhancer activity by interacting with and disrupting the binding of hepatocyte nuclear factor 4α (HNF4α) to the enhancer I region, thus suppressing HBV gene transcription (Wang et al., 2012). EGFR is also a co-factor that facilitates the internalization of HBV via the NTCP-EGFR complex (Iwamoto et al., 2019). HBx is a substrate of Akt kinase and augments the oncogenic function of HBx through phosphorylation (Khattar et al., 2012). Together, these studies indicate ACK1 may potentially affect HBV replication. Thus, this study aimed to investigate the role of ACK1 in the HBV life cycle and examine the molecular mechanism underlying the anti-HBV activity of ACK1.

MATERIALS AND METHODS

Cell Culture and Transfection

Human hepatoma (HepG2) cells were purchased from the Korean Cell Line Bank (KCLB), and HepG2-NTCP and HepAD38 cells were cultured as described previously (Park et al., 2016, 2020). HepG2 cells stably expressing ACK1 (HepG2-ACK1), were established via puromycin (1 μg/mL) selection. All cell lines were maintained in Dulbecco's modified Eagle's medium supplemented with 10% fetal bovine serum (Gibco, Grand Island, NY, United States) at 37°C in a 5% CO_2 humidified incubator. HepG2-ACK1 and HepAD38 cells were cultured in medium supplemented with puromycin and tetracycline, respectively. Plasmids and small interfering RNA (siRNA) were transfected at 40–50% confluence in 6- or 12-well plates with Lipofectamine 2000 (Invitrogen, Carlsbad, CA, United States) and RNAiMAX (Invitrogen) according to the manufacturer's protocols.

Plasmids and Reagents

The HBV 1.2mer, encoding 1.2 copies of the HBV genome (3·8 kb, genotype D), EnhI·II, EnhI·ΔEnhII, and EnhII/Cp, used in previous studies (Park et al., 2016, 2020), were used. ACK1 and ACK1·ΔSK were cloned into pIRES-FLAG (Creative Biogene, NY, United States) at the *Afl*II and *Xba*I sites, respectively. PD98059 (Cell Signaling Technology, Danvers, MA, United States), AIM-100 (Sigma, St. Louis, MO, United States), and hepatocyte growth factor (HGF) (R&D Systems, Minneapolis, MN, United States) were purchased. Control siRNA (Cat. No. sc-37007, Santa Cruz biotechnology, Dallas, TX, United States) and ACK1 siRNA (SMARTpool, Dharmacon) were also used in this study.

HBeAg and HBsAg Levels

To assess the secretion of HBeAg and HBsAg, the culture supernatants were harvested at 3-day after HBV 1.2 transfection into HepG2 and HepG2-ACK1 cells. HBeAg and HBsAg levels were determined using a hepatitis B e/s antigen kit (Wantai Bio-Pharm, Beijing, China) according to the manufacturer's protocol. Supernatants were diluted in phosphate-buffered saline to prevent signal saturation, and the absorbance was measured at 450 nm using a spectrophotometer (Epoch, BioTek, United States).

Hepatitis B Virus Enhancer Activity

HepG2 and HepG2-ACK1 cells were cultured to 40–50% confluence in 12-well plates, following which the plasmids of enhancer mutants (**Figure 3A**) were transfected. After 48 h, luciferase activity was determined using the Luciferase Assay System (Promega, Madison, WI, United States). To normalize the transfection efficiency, β-Galactosidase activity was measured using a β-galactosidase enzyme assay system (Promega).

Southern Blotting

HBV replication was evaluated as previously described (Park et al., 2016, 2020). Briefly, HepG2 and HepG2-ACK1 cells were grown to 40–50% confluence in 6-well plates and co-transfected with HBV 1.2 and/or ACK1. At 72 h after transfection, cell pellets were lysed in HEPES buffer containing 1% NP-40 and subsequently treated with DNase I (Sigma) and mung bean nuclease (Takara, Shiga, Japan) at 37°C for 30 min. Core particles were precipitated with 26% polyethylene glycol 8000 solution (1.2 M NaCl, 60 mM EDTA, 30% sucrose, and 26% polyethylene glycol). To degradate the core particle and

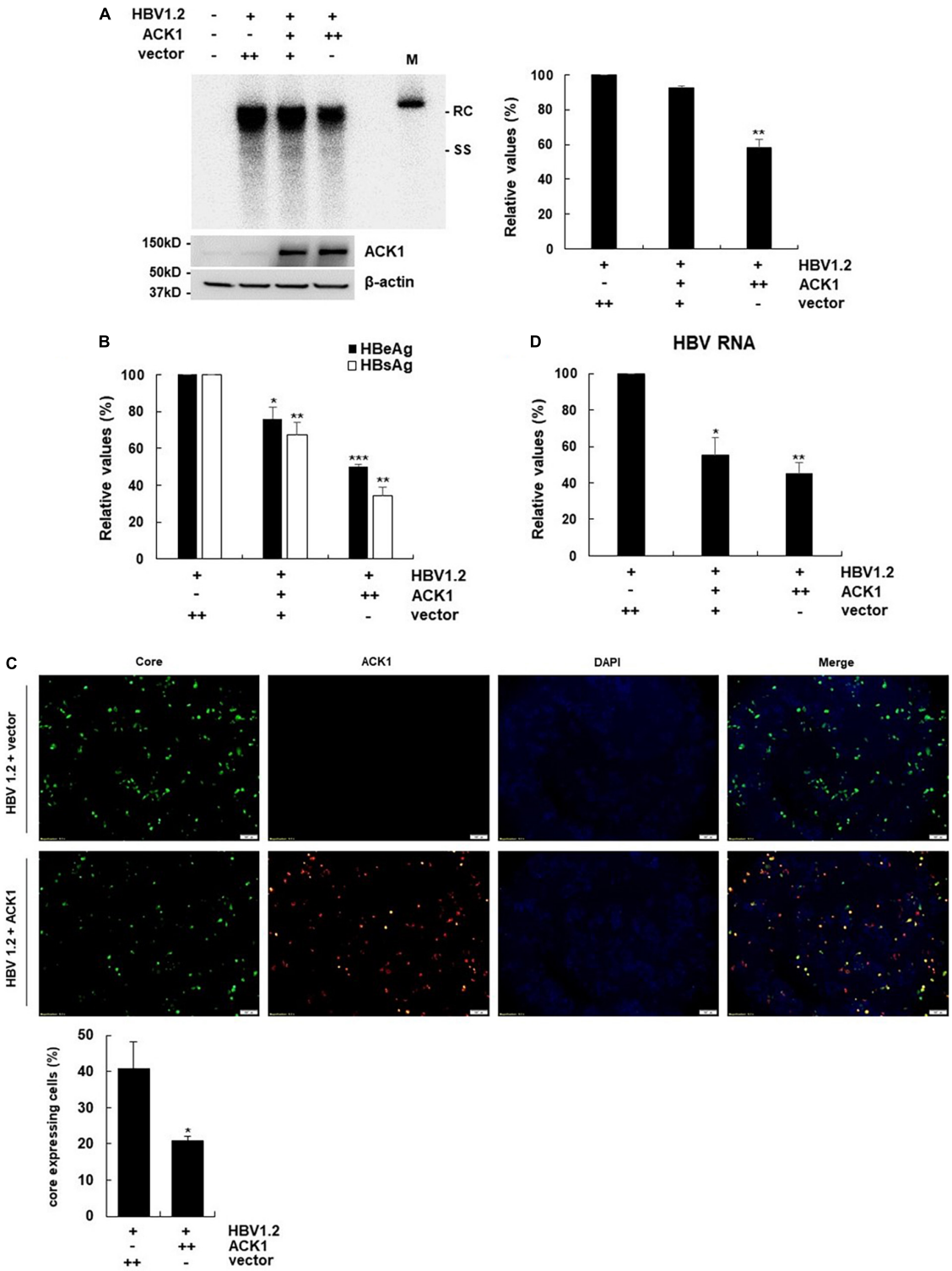

FIGURE 1 | Overexpression of ACK1 inhibits HBV replication. The constructs of HBV 1.2, with or without ACK1, were transfected into HepG2 cells grown in a 6-well plate and cells were harvested after 3-day. Cell lysates were subjected to viral DNA and RNA analysis. Culture supernatants were assessed to determine HBeAg and HBsAg levels. **(A)** Effect of ACK1 on HBV replication. HBV DNA was detected by southern blotting. +, 1 μg; ++, 2 μg; rc, relaxed circular HBV DNA; ss, single-stranded HBV DNA; M, size marker (3.2kb). $^{**}p < 0.01$. **(B)** Effect of ACK1 on the secretion of HBeAg and HBsAg. +, 1 μg; ++, 2 μg. $^{*}p < 0.05$; $^{**}p < 0.01$; $^{***}p < 0.001$. **(C)** Effect of ACK1 on core protein expression. HBV core and ACK1 detected by immunofluorescence. Scale bar indicates 100 μm. core, green; ACK1, red. $^{*}p < 0.05$. **(D)** Effect of ACK1 on HBV RNA. HBV RNA was analyzed using real-time PCR. +, 1 μg; ++, 2 μg. $^{*}p < 0.05$; $^{**}p < 0.01$.

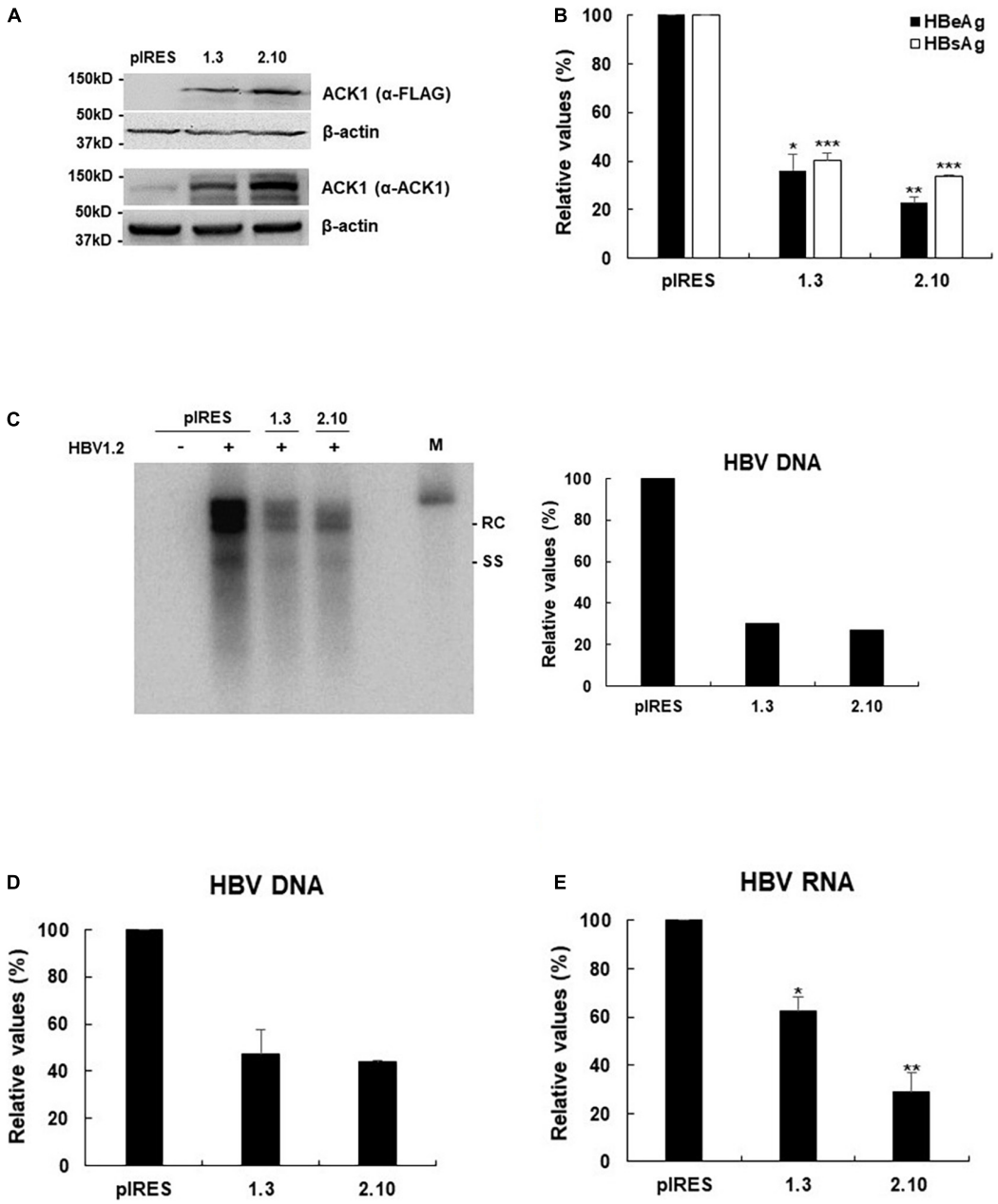

FIGURE 2 | Stable expression of ACK1 strongly inhibits HBV replication. One microgram of HBV 1.2 was transfected into HepG2-ACK1 cells grown in a 6-well plate, and cells were harvested after 3-day. Cell lysates were subjected to viral DNA and RNA analysis. Culture supernatants were assessed to determine HBeAg and HBsAg levels. **(A)** Establishment of HepG2-ACK1 cells. **(B)** Secretion of HBeAg and HBsAg in HepG2-ACK1 cells. $^{*}p < 0.05$; $^{**}p < 0.01$; $^{***}p < 0.001$. **(C)** HBV replication in HepG2-ACK1 cells. HBV DNA was detected by southern blotting. +, 1 μg; ++, 2 μg; rc, relaxed circular HBV DNA; ss, single-stranded HBV DNA; M, size marker (3.2kb). **(D)** HBV replication in HepG2-ACK1 cells. HBV rcDNA was analyzed using real-time PCR. Values represent the mean ± SD determined from two independent experiments (each performed in triplicates). **(E)** HBV RNA levels in HepG2-ACK1 cells. HBV RNA was analyzed using real-time PCR. $^{*}p < 0.05$; $^{**}p < 0.01$.

polymerase, proteinase K (20 mg/mL, Roche, Basel, Switzerland) and 0.5% SDS solution (25 mM Tris pH 7.5, 10 mM EDTA, 100 mM NaCl, and 0.5% SDS) were added, and the mixture was incubated at 37°C for 2.5 h. Finally, HBV DNA was purified with a mixture of phenol/chloroform/isoamyl alcohol (25:24:1; Sigma) and precipitated with ethanol. Purified HBV DNA was separated on a 0.8% agarose gel and transferred onto a Hybond-N + nylon membrane (GE Healthcare). HBV DNA was detected with highly pure randomly primed probes labeled with [α-^{32}P] dCTP (PerkinElmer, Waltham, MA, United States) and quantified using a Phosphorimager (Fujifilm, Tokyo, Japan).

Western Blotting

To analyze the indicated proteins, HepG2 and HepG2-ACK1 cells were cultured to 40–50% confluence in 6-well plates, after which transfection was performed. The cells were harvested 2 or 3-day after transfection with the indicated plasmids. Thereafter, cells were harvested using the M-PER Mammalian Protein Extraction Reagent (Thermo Fisher Scientific, Waltham, MA, United States) containing protease inhibitor cocktail and phosphatase inhibitor (Thermo Fisher Scientific). Cell lysates in Laemmli sample buffer (Bio-Rad, Hercules, CA, United States) were subjected to SDS-PAGE in 4–20% Mini-Protein TGX Precast Protein gels (Bio-Rad) and electro-transferred to Trans-Blot Turbo Mini PVDF Transfer packs (Bio-Rad). Proteins were detected using primary anti-ACK1 (Cat. No. sc-28336; Santa Cruz Biotechnology), anti-FLAG (Cat. No. A5316, Sigma), anti-Erk1/2 (Cat. No.9102; Cell Signaling Technology), anti-phospho-Erk1/2 (Cat. No.9101; Cell Signaling Technology), anti-JNK (Cat. No.9252, Cell Signaling Technology), anti-phospho-JNK (Cat. No.9251, Cell Signaling Technology), anti-p38 (Cat. No.9212, Cell Signaling Technology), anti-phospho-p38 (Cat. No.9211, Cell Signaling Technology), anti-C/EBPα (Cat. No. sc-365318; Santa Cruz Biotechnology), anti-HNF1α (Cat. No. sc-393668; Santa Cruz Biotechnology), anti-HNF4α (Cat. No. sc-374229; Santa Cruz Biotechnology), anti-HNF3β (Cat. No. sc-374376; Santa Cruz Biotechnology), and anti-β-actin (Cat. No. A5316; Sigma) antibodies.

Immunofluorescence Staining

HepG2 cells were seeded on 6-well plates and transfected with HBV 1.2 and/or ACK1. Three days after transfection, cells were fixed in 4% paraformaldehyde and permeabilized with 0.2% Triton X-100. Following blocking with 3% bovine serum albumin, the cells were treated with primary antibodies against HBV core (Cat. No. B0586, Dako) and ACK1 (Cat. No. sc-28336; Santa Cruz Biotechnology) proteins at 4°C overnight. The nuclei were stained with ProLong Gold antifade reagent (Cat. No. 8961S, Cell signaling).

Reverse-Transcription Polymerase Chain Reaction and Real-Time Polymerase Chain Reaction

To analyze the mRNA level of HNF1α, C/EBP1α, HNF3β, HNF4α, and HBV RNA, total RNA was extracted using the RNeasy Plus mini kit (Qiagen, Hilden, Germany) and reverse-transcribed to cDNA using the SuperScript III First-strand synthesis kit for reverse-transcription polymerase chain reaction (RT-PCR) (Invitrogen) according to the manufacturer's instructions. RT-PCR was performed using indicated primers with the following conditions: denaturation at 95°C for 5 min, followed by 25∼30 cycles of 95°C for 30 s, 55∼60°C for 30 s, and 72°C for 1 min, with final extension at 72°C for 5 min. For the HBV rcDNA and cccDNA, total genomic and viral DNAs were extracted using the QIAamp DNA mini kit (Qiagen). To purify the cccDNA, 500 ng of extracted DNA was treated with plasmid safe DNase I (PSD, Epicentre Technologies, United States) and inactivated by incubation for 30 min at 70°C. To assess HBV RNA, rcDNA, and cccDNA levels, real-time PCR was performed using Power SYBR green PCR master mix (Applied Biosystems, Foster City, CA, United States) with primers for HBV RNA, rcDNA (nt 256 to 421) and cccDNA (nt 1824 to 2068) (**Supplementary Table 1**) and amplified using the QuantStudio 3.0 (Applied Biosystems). Relative gene expression levels were normalized against those of *GAPDH*.

Hepatitis B Virus Infection

To isolate HBV particles, HepAD38 cells were maintained for 60-day. Culture media was changed every 3∼4-day with fresh DMEM/F-12 (1:1) medium. The supernatant was harvested from day 15 until day 60 and concentrated 50–fold using the PEG Virus Precipitation Kit (BioVision, United States). HepG2-NTCP cells (1×10^6 cells) were seeded onto 6-well plates coated with collagen I (Gibco) and infected with 2000 HBV genome equivalents per cell (Geq/cell) in DMEM supplemented with 4% PEG 8000 (Sigma) and 2.5% dimethyl sulfoxide (DMSO, Sigma) for 16–20 h. Thereafter, cells were washed thrice with DMEM, maintained in DMEM containing 2% DMSO, and harvested 7-day post-infection (dpi).

Statistical Analysis

All data were obtained from at least two or three independent experiments and values represent the mean ± SD. Indicated figures show representative data, and statistical significance was determined by comparison with the control group. The p value was analyzed by paired t-test using GraphPad Prism 5 software.

RESULTS

Ectopic Activated cdc42-Associated Kinase 1 Expression Inhibits Hepatitis B Virus Replication

To address whether ACK1 regulates HBV replication, a plasmid expressing ACK1 was constructed and transfected into HepG2 cells with HBV replication-competent HBV 1.2mer (HBV 1.2). Ectopic ACK1 expression inhibited HBV replication and viral antigen (HBeAg/HBsAg) secretion. ACK1 expression was confirmed with western blotting (**Figures 1A,B**). The effect of ACK1 on core protein expression was analyzed by immunofluorescence staining. In cells co-transfected with HBV 1.2 and ACK1, the expression of core proteins was decreased (**Figure 1C**). This indicated that ACK1 suppressed core protein expression. To determine the inhibitory effect of ACK1 on HBV replication and gene expression, we investigated HBV RNA level. As shown in **Figure 1D**, ACK1 reduced HBV transcription in a dose-dependent manner. These results indicated that ACK1 overexpression suppress HBV transcription. Previous studies reported that cellular expression of ACK1 is retained at low level (Yokoyama and Miller, 2003; Mahajan et al., 2005). Thus, to validate the anti-HBV activity of ACK1, we established HepG2-ACK1 cells constitutively expressing ACK1. Two HepG2-ACK1 clones (1.3 and 2.10) showing different expression levels of ACK1 were selected for further analysis (**Figure 2A**). In HepG2-ACK1

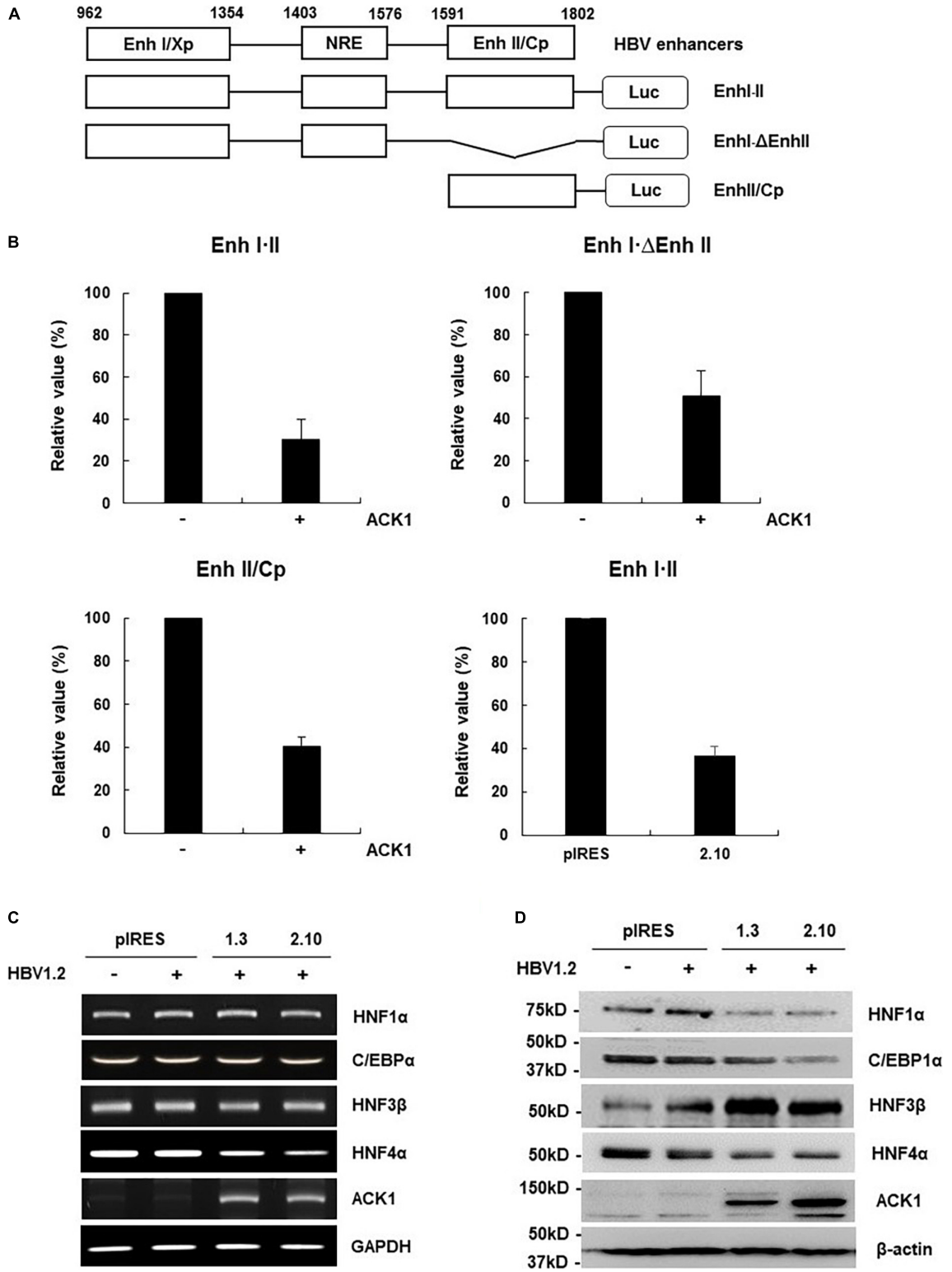

FIGURE 3 | ACK1 decreases viral enhancer activity by HNF4α regulation. **(A)** Schematic diagram of the reporter plasmids containing HBV enhancers of various lengths. **(B)** Relative luciferase activity of HBV enhancer. HepG2 and HepG2-ACK1 cells were grown in a 12-well plate and transfected with each enhancer construct with or without ACK1. At 48 h post-transfection, cell lysates were assessed to determine luciferase activity. Values represent the mean ± SD determined from two or three independent experiments (each performed in duplicate). +, 1 μg. **(C)** mRNA level of C/EBPα and HNFs in HepG2-ACK1 cells. Each mRNA was analyzed by RT-PCR using the indicated primers (**Supplementary Table 1**). +, 1 μg. **(D)** Expression of C/EBPα and HNFs in HepG2-ACK1 cells. The proteins were detected by western blotting using the indicated antibodies. +, 1 μg.

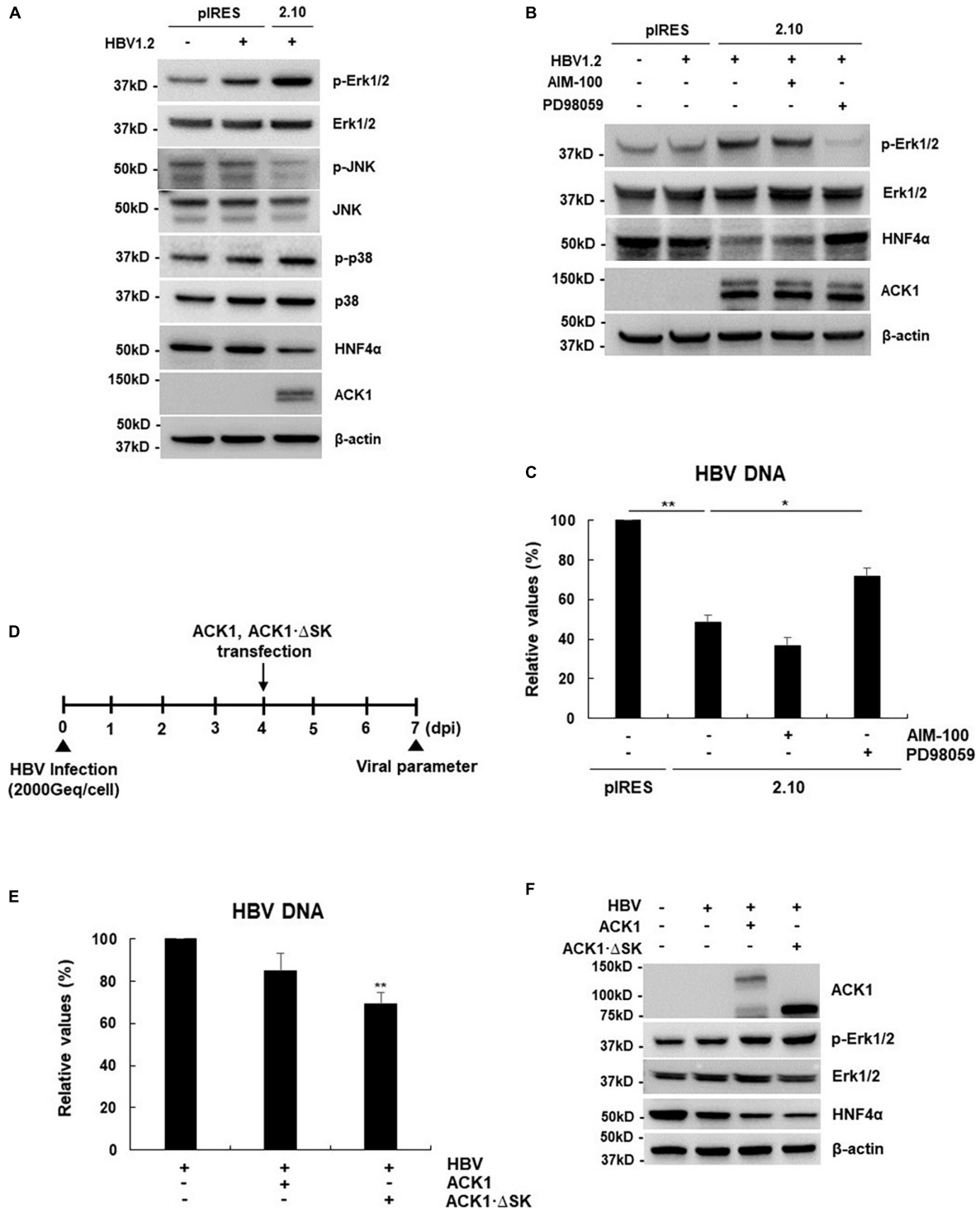

FIGURE 4 | ACK1 activates the Erk1/2-HNF4α signaling pathway in a kinase-independent manner. **(A)** Effect of ACK1 expression on MAPK-HNF4α signaling pathway. One microgram of HBV 1.2 was transfected into HepG2-ACK1 cells grown in a 6-well plate, and cells were harvested after 3-day. Cell lysates were subjected to western blotting analysis. The proteins were detected by western blotting using the indicated antibodies. **(B,C)** One microgram of HBV 1.2 was transfected into HepG2-ACK1 cells grown in a 6-well plate, and cells were harvested after 3-day. HepG2-ACK1 cells were treated with AIM-100 (10 μM) and PD98059 (20 μM) for 16 h before harvest. **(B)** Effect of kinase inhibitors on HNF4α expression. **(C)** Effect of kinase inhibitors on HBV replication. HBV DNA was analyzed using real-time PCR. $^{*}p < 0.05$; $^{**}p < 0.01$. **(D)** Experimental procedure for panels **(E,F)**. Geq/cell, genome equivalents per cell. **(E)** Effects of ACK1 and ACK1·ΔSK on HBV replication in HBV-infected HepG2-NTCP cells. HBV DNA was analyzed using real-time PCR. HBV 1.2, 1 μg; ACK1 and ACK1·ΔSK, 2 μg. $^{**}p < 0.01$. **(F)** Effect of ACK1 expression on MAPK-HNF4α signaling pathway in HBV-infected HepG2-NTCP cells. HBV 1.2, 1 μg; ACK1 and ACK1·ΔSK, 2 μg.

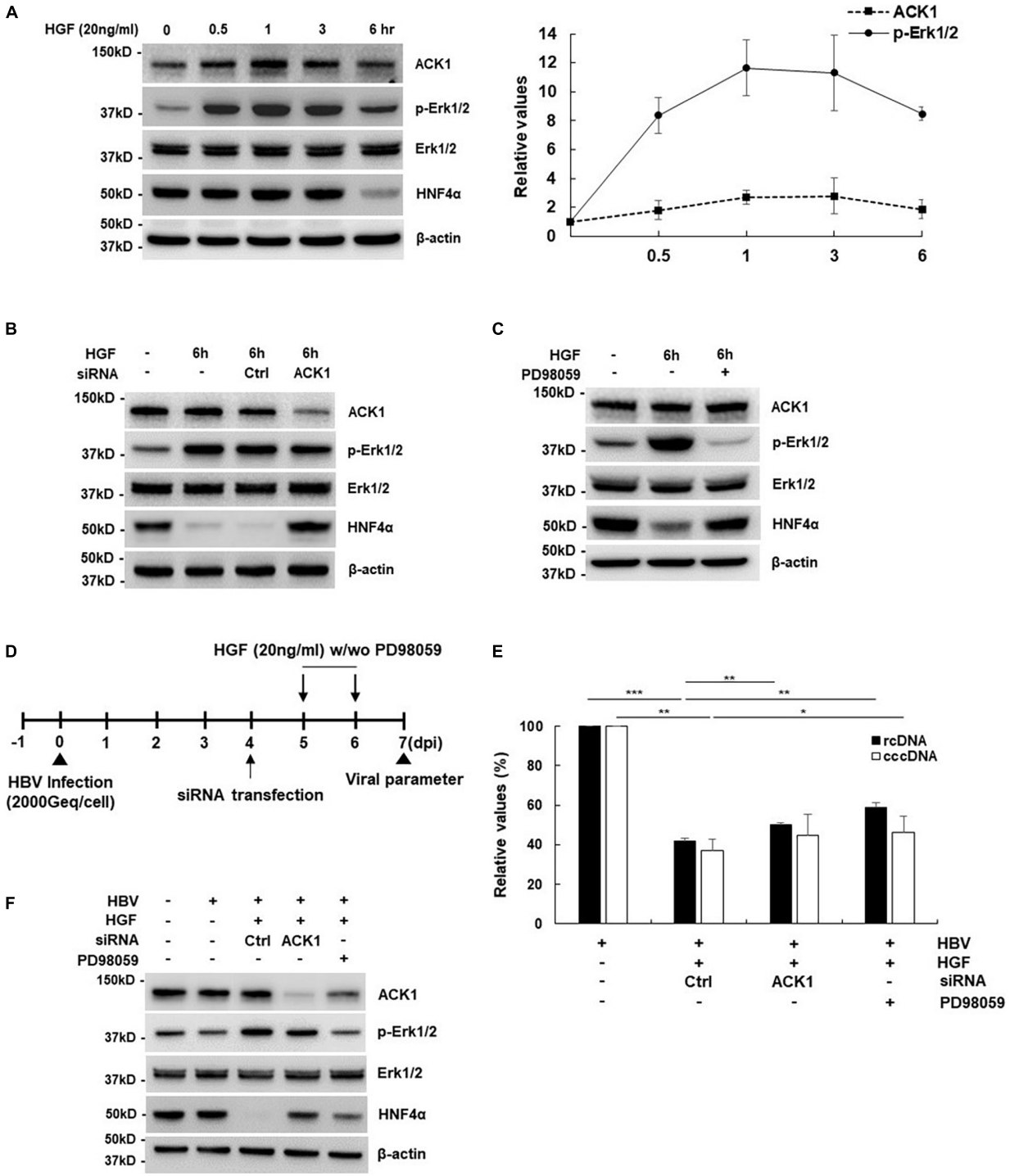

FIGURE 5 | ACK1 is involved in HGF-mediated inhibitory effect of HBV. **(A)** Effect of HGF treatment on the ACK1-Erk1/2- HNF4α signaling cascade. HepG2 cells were treated with HGF (20 ng/mL) for indicated times before harvest. Values represent the mean ± SD calculated from at least three independent experiments. **(B)** Effect of siRNA on the ACK1-Erk1/2- HNF4α signaling cascade. siRNAs of control (Ctrl) and ACK1 (20 nM) were transfected into HepG2 cells. HepG2 cells were treated with HFG (20 ng/mL) for 6 h before harvest. **(C)** Effect of PD98059 treatment on the ACK1-Erk1/2- HNF4α signaling cascade. HepG2 cells were seeded in a 6-well plate and treated with HGF and/or PD98059 (20 μM) for 6 h before harvest. **(D)** Experimental procedure for panels **(E,F)**. Geq/cell, genome equivalents per cell. **(E)** Effect of HGF on rcDNA and cccDNA level in an HBV infection system. HGF (20 ng/mL) with/without PD98059 (20 μM) used for treatment for the indicated times. HBV rcDNA and cccDNA were analyzed using real-time PCR. $^{*}p < 0.05$; $^{**}p < 0.01$; $^{***}p < 0.001$. **(F)** Effect of HGF on the ACK1-Erk1/2-HNF4α signaling cascade in an HBV infection system. HGF (20 ng/mL) with/without PD98059 (20 μM) was used for treatment for the indicated times.

cells, HBeAg/HBsAg levels and HBV replication were markedly inhibited as compared to those in cells ectopically expressing ACK1 (**Figures 2B–D**). Consistently, the expression levels of HBV RNA, core, and surface protein were attenuated by ACK1 (**Figure 2E** and **Supplementary Figure 1**). These results indicate that ACK1 exerts anti-HBV activity at the transcriptional level. Furthermore, ACK1 expression was increased in HBV-expressing cells (**Supplementary Figure 2A**), and knockdown of ACK1 by siRNA enhanced HBV DNA (**Supplementary Figures 2B,C**). Taken together, our data demonstrate that ACK1 is a novel antiviral molecule against HBV.

Activated cdc42-Associated Kinase 1 Suppresses Viral Enhancer Activity by Downregulating Hepatocyte Nuclear Factor 4α

HBV transcription is reportedly regulated by the viral enhancers, enhancer I (Enh I) and enhancer II overlapping with the core promoter (Enh II/Cp) (Yuh and Ting, 1990; Su and Yee, 1992; Moolla et al., 2002; Doitsh and Shaul, 2004). Since ACK1 inhibits HBV transcription, we first investigated whether ACK1 affects viral enhancer activity. Enh I·II and its deletion mutants were constructed to determine which enhancer region is affected by ACK1 (**Figure 3A**). The activities of all enhancer constructs were decreased by ACK1 (**Figure 3B**), indicating that ACK1 suppresses the activity of both Enh I and Enh II/Cp. HBV enhancers possess specific DNA binding sequences for several transcription factors. Our group and others have reported that HBV enhancers are regulated by HNF1α, HNF4α, and CCAAT/enhancer binding protein 1α (C/EBP1α) and HNF3β (Lopez-Cabrera et al., 1990; Garcia et al., 1993; Tang and Mclachlan, 2001, 2002; Banks et al., 2002; Zheng et al., 2004; Park et al., 2016; Kim et al., 2018). Hence, to elucidate the mechanism underlying the suppression of HBV enhancer activity by ACK1, we first examined the expression of these transcription factors. Notably, ACK1 dysregulated the protein levels of HNF1α, C/EBP1α, HNF3β, and HNF4α. Among them, only HNF4α expression was regulated at the transcriptional level (**Figures 3C,D**). HNF4α is the most potent regulator of HBV transcription (Tang and Mclachlan, 2001; Park et al., 2016; Kim et al., 2018). Therefore, our data suggest that ACK1 inhibits HBV replication by suppressing viral enhancer activity via HNF4α downregulation.

Activated cdc42-Associated Kinase 1 Downregulates Hepatocyte Nuclear Factor 4α by Activating Erk1/2 in a Kinase-Independent Manner

Since HNF4α expression is regulated by the mitogen-activated protein kinase (MAPK) cascade (Hösel et al., 2009; Zhao et al., 2012; Park et al., 2016; Kim et al., 2018), we examined whether ACK1 regulates MAPK signaling. Although MAPK phosphorylation was dysregulated, phosphorylation of Erk1/2 was most strongly increased (**Figure 4A**), indicating that activation of Erk1/2 by ACK1 correlated with HNF4α downregulation. To confirm ACK1-Erk1/2 signaling-mediated HNF4α expression, HepG2-ACK1 cells were treated with ACK1 and Erk1/2 inhibitors. Treatment with PD98059, an inhibitor of Erk1/2 phosphorylation, reverted HNF4α expression to baseline levels (**Figure 4B**), indicating that ACK1 attenuates HNF4α expression via Erk1/2 activation. Intriguingly, AIM-100, a specific inhibitor of ACK1 phosphorylation, did not affect the levels of phosphorylated Erk1/2 and HNF4α (**Figure 4B** and **Supplementary Figure 3**). Consistent with HNF4α expression, HBV replication was only rescued by PD98509 treatment (**Figure 4C**). These results suggest that the kinase activity of ACK1 is not responsible for the regulation of Erk1/2 phosphorylation, HNF4α expression, and HBV DNA. To validate whether ACK1 regulates HBV DNA irrespective of its kinase activity, an ACK1 mutant (ACK1·ΔSK) lacking the kinase domain was constructed (**Supplementary Figure 4A**). ACK1·ΔSK overexpression was a more potent inhibitor of HBeAg/HBsAg secretion and HBV DNA than ACK1 (**Supplementary Figures 4B,C**). Finally, the anti-HBV activity of ACK1·ΔSK was confirmed using an HBV infection system (**Figure 4D**). Ectopic ACK1·ΔSK expression also significantly inhibited HBV DNA, consistent with that of ACK1 (**Figure 4E**). Both ACK1 and ACK1·ΔSK commonly regulated the activation of Erk1/2 and inhibition of HNF4α expression in HBV-infected HepG2-NTCP cells (**Figure 4F**). Together, our data revealed that ACK1 suppresses HBV replication by decreasing viral enhancer activity via activation of the Erk1/2-HNF4α signaling pathway without kinase activity.

Hepatocyte Growth Factor Is the Upstream Stimulator of the Activated cdc42-Associated Kinase 1-Erk1/2-HNFs Signaling Pathway

ACK1 is activated by growth factors and extracellular stimuli such as EGF, platelet-derived growth factor (PDGF), and integrin (Galisteo et al., 2006). Since ACK1 exhibited anti-HBV activity in hepatocytes, we investigated whether ACK1 expression is stimulated by the hepatocyte-enriched growth factor, HGF. As shown in **Figure 5A**, ACK1 expression level following treatment with HGF rapidly increased (0.5 h) and peaked (2.6–fold increase) after 1–3 h in HepG2 cells. At later time points (6 h), ACK1 expression decreased. Similar to ACK1 expression, Erk1/2 phosphorylation peaked (11.6–fold increase) at 1 h and subsequently declined. Conversely, HNF4α expression was downregulated at 6 h (**Figure 5A**, left panel) and was salvaged by siRNA of ACK1 and PD98059 treatment (**Figures 5B,C**) after HGF stimulation. These results suggest that HGF-induced ACK1 rapidly activated Erk1/2 phosphorylation and consequently decreased HNF4α expression. Finally, we determined whether HGF is involved in the ACK1-mediated HBV inhibition in an HBV infection system by infecting HepG2-NTCP cells with HBV (**Figure 5D**). Notably, HGF suppressed rcDNA and cccDNA levels, which were significantly recovered by inhibition of the ACK1-Erk1/2 signaling cascade (**Figure 5E**). Moreover, HGF induced Erk1/2 activation and HNF4α suppression, which were reversed by siRNA of ACK1 and PD98059 treatment (**Figure 5F**).

Collectively, these results indicate that HGF play a role as an upstream regulator of the ACK1-Erk1/2-HNF4α signaling cascade, exerting HBV inhibitory effect.

DISCUSSION

ACK1 plays important roles as an adaptor kinase in cellular signaling pathways, including carcinogenesis, receptor trafficking, and epigenetic modulation (Teo et al., 2001; Mahajan and Mahajan, 2015). However, the antiviral activity of ACK1 has not been investigated thus far. Although one study reported that single nucleotide polymorphism rs2278034 in ACK1 affects the outcomes of IFN-α therapy in chronic hepatitis C patients (Fujimoto et al., 2011), the precise mechanism underlying the antiviral activity of ACK1 had not been elucidated. This study provides novel insight into the anti-HBV activity of ACK1. Our results show that ACK1 inhibits HBV replication by downregulating HNF4α, thus suppressing viral enhancer activity (**Figure 3**). Intriguingly, the antiviral activity of ACK1 was independent of its kinase activity. The ACK1·ΔSK construct was expressed at high levels and was a more potent inhibitor of HBV replication than ACK1 in HepG2 cells (**Supplementary Figure 4**). Moreover, ACK1·ΔSK strongly activated Erk1/2 phosphorylation and decreased HNF4α expression (**Figure 4F**) in HBV-infected HepG2-NTCP cells. Furthermore, knockdown of endogenous ACK1 enhanced HBV DNA level (**Supplementary Figure 2D**). These data indicated that ACK1 is a cellular inhibitor of HBV infection.

Various cytokines are involved in Erk1/2-HNF4α signaling-mediated inhibition of HBV transcription in hepatocytes. Interleukin (IL)-6 and TGF-1β attenuate HBV replication by suppressing HNF4α via Erk1/2 phosphorylation (Hösel et al., 2009; Hong et al., 2012). Furthermore, p22-FLIP, hepatocystin, and IL-32 induced by TNF-α and IFN-γ control HBV transcription by downregulating HNF4α via Erk1/2 activation in HepG2 and primary human hepatocytes (Shin et al., 2014; Park et al., 2016; Kim et al., 2018). Moreover, this study shows that HGF-induced ACK1 suppressed HBV DNA by downregulating HNF4α expression via Erk1/2 activation in HBV-infected cells (**Figure 5**). These findings indicated that HNF4α is responsible for the cytokine-mediated inhibition of HBV transcription. HNF4α is regulated by a transcription factor complex comprising HNF6β, HNF1α, and C/EBPα in the promoter region (Hatzis and Tallanidis, 2001; Hatzis et al., 2006). ACK1 suppressed HNF1α and C/EBPα expression (**Figures 3C,D**), suggesting that ACK1 may be implicated in the transcription factor complex-mediated suppression of HNF4α as well as Erk1/2 activation.

HGF is a mesenchymal cell-derived protein with mitogenic function during liver regeneration and the development of primary hepatocytes (Tsukada et al., 2001). However, the antiviral effect of HGF has not been investigated. Here, we first identified the inhibitory effect of HGF against HBV infection. HGF simultaneously induced ACK1 expression and phosphorylated Erk1/2, thereby decreasing HNF4α levels (**Figures 5A,F**). Moreover, Erk1/2 inhibition by siRNA of ACK1 and PD98059 rescued HNF4α expression (**Figures 5B,C,F**). These findings reveal that HGF is an upstream molecule in the ACK1-dependent anti-HBV signaling pathway. Although siRNA of ACK1 and PD98059 treatment significantly recovered HBV rcDNA levels, HGF strongly downregulated cccDNA levels (**Figure 5E**). This result suggests that HGF primarily suppresses cccDNA rather than the ACK1-Erk1/2-HNF4α signaling cascade. The cccDNA conformation depends on rcDNA level during new HBV infections and capsid recycling, and the conversion of rcDNA to cccDNA is regulated by host DNA repair systems, such as topoisomerase and tyrosyl-DNA-phosphodiesterase (Nassal, 2015). Therefore, HGF may reduce cccDNA levels by affecting the host DNA repair system or blocking capsid recycling via an unknown mechanism. These hypotheses suggest a novel antiviral activity of HGF against HBV infection. We are currently investigating the molecular mechanism of HGF-mediated cccDNA reduction. Interestingly, we previously reported that HBV inhibits HGF maturation via epigenetic regulation of urokinase-type plasminogen activator (uPA) by HBx during liver regeneration (Park et al., 2013). uPA is a serine protease that cleaves and activates pro-HGF (Naldini et al., 1992; Mars et al., 1993). HBx suppresses uPA expression by hypermethylation of the uPA promoter, consequently inhibiting HGF maturation (Park et al., 2013), which is a protective mechanism against the antiviral activity of HGF. This phenomenon may be considered a novel mechanism for persistent HBV infection.

In conclusion, this study elucidates the role of ACK1 in HGF-mediated suppression of HBV. Our results show that ACK1 is induced by HGF in HepG2 cells and that it inhibits HBV transcription and replication. Notably, HGF decreased HBV DNA and cccDNA levels in an HBV infection system, and ACK1 was implicated in the inhibitory effect of HGF on HBV infection. Furthermore, this study demonstrates that ACK1 attenuates HBV enhancer activity by downregulating HNF4α, leading to the suppression of viral transcription and replication. Finally, the antiviral signaling cascade of HGF was confirmed in an HBV infection system. Our findings suggest a novel signaling pathway for anti-HBV activity through which HGF suppresses HBV replication during the regeneration of liver tissue damaged by persistent HBV infection.

DATA AVAILABILITY STATEMENT

The original contributions presented in the study are included in the article/**Supplementary Material**, further inquiries can be directed to the corresponding authors.

AUTHOR CONTRIBUTIONS

HL performed the experiment and wrote the draft of the manuscript. YC and AL performed the experiment. C-HY suggested the conception of study. K-HK revised the manuscript critically for important intellectual content. B-SC was a project administrator and revised the manuscript. YP designed, performed the experiment, wrote and revised the manuscript. All authors contributed to the article and approved the submitted version.

FUNDING

This work was supported by the intramural fund (Grant No. 2019-NI-065) from Korea National Institutes of Health.

SUPPLEMENTARY MATERIAL

The Supplementary Material for this article can be found online at: https://www.frontiersin.org/articles/10.3389/fmicb.2021.800935/full#supplementary-material

REFERENCES

Banks, K. E., Anderson, A. L., Tang, H., Hughes, D. E., Costa, R. H., and McLachlan, A. (2002). Hepatocyte nuclear factor 3b inhibits hepatitis B virus replication in vivo. *J. Virol.* 76, 12974–12980. doi: 10.1128/jvi.76.24.12974-12980.2002

Chan, W., Sit, S. T., and Manser, E. (2011). The Cdc42–associated kinase ACK1 is not autoinhibited but requires Src for activation. *Biochem. J.* 435, 355–364. doi: 10.1042/BJ20102156

Doitsh, G., and Shaul, Y. (2004). Enhancer I predominance in hepatitis B virus gene expression. *Mol. Cell Biol.* 24, 1799–1808. doi: 10.1128/MCB.24.4.1799-1808.2004

Fujimoto, Y., Ochi, H., Maekawa, T., Abe, H., Hayes, C. N., Kumada, H., et al. (2011). A single nucleotide polymorphism in activated cdc42 associated tyrosine kinase 1 influences the interferon therapy in hepatitis C patients. *J. Hepatol.* 54, 629–639. doi: 10.1016/j.jhep.2010.07.021

Galisteo, M. L., Yang, Y., Urena, J., and Schlessinger, J. (2006). Activation of the nonreceptor protein tyrosine kinase Ack1 by multiple extracellular stimuli. *Proc. Natl. Acad. Sci. U. S. A.* 103, 9796–9801. doi: 10.1073/pnas.0603714103

Garcia, A. D., Ostapchuk, P., and Hearing, P. (1993). Functional interaction of nuclear factors EF–C, HNF–4, and RXRa with hepatitis B virus enhancer I. *J. Virol.* 67, 3940–3950. doi: 10.1128/JVI.67.7.3940-3950.1993

Grovdal, L. M., Johannessen, L. E., Rodland, M. S., Madshus, I. H., and Stang, E. (2008). Dysregulation of Ack1 inhibits down–regulation of the EGF receptor. *Exp. Cell Res.* 314, 1292–1300. doi: 10.1016/j.yexcr.2007.12.017

Hatzis, P., Kyrmizi, I., and Tallanidis, I. (2006). Mitogen–activated protein kinase–mediated disruption of enhancer–promoter communication inhibits hepatocyte nuclear factor 4α expression. *Mol. Cell Biol.* 26, 7017–7029. doi: 10.1128/MCB.00297-06

Hatzis, P., and Tallanidis, I. (2001). Regulatory mechanisms controlling human hepatocyte nuclear factor 4α gene expression. *Mol. Cell Biol.* 21, 7320–7330. doi: 10.1128/mcb.21.21.7320-7330.2001

Hong, M. H., Chou, Y. C., Wu, Y. C., Tsai, K. N., Hu, C., Jeng, K. S., et al. (2012). Transforming growth factor–β1 suppresses hepatitis B virus replication by the reduction of hepatocyte nuclear factor–4α expression. *PLoS One* 7:e30360. doi: 10.1371/journal.pone.0030360

Hösel, M., Quasdorff, M., Wiegmann, K., Webb, D., Zedler, U., Broxtermann, M., et al. (2009). Not interferon, but interleukin–6 controls early gene expression in hepatitis B virus infection. *Hepatology* 50, 1773–1782. doi: 10.1002/hep.23226

Iwamoto, M., Saso, W., Sugiyama, R., Ishii, K., Ohki, M., Nagamori, S., et al. (2019). Epidermal growth factor receptor is a host–entry cofactor triggering hepatitis B virus internalization. *Proc. Natl. Acad. Sci. U. S. A.* 116, 8487–8492. doi: 10.1073/pnas.1811064116

Khattar, E., Mukherji, A., and Kumar, V. (2012). Akt augments the oncogenic potential of the HBx protein of hepatitis B virus by phosphorylation. *FEBS J.* 279, 1220–1230. doi: 10.1111/j.1742-4658.2012.08514.x

Kim, D. H., Park, E. S., Lee, A. R., Park, S., Park, Y. K., Ahn, S. H., et al. (2018). Intracellular interleukin–32γ mediates antiviral activity of cytokines against hepatitis B virus. *Nat. Commun.* 9:3284 . doi: 10.1038/s41467-018-05782-5

Klein, N. P., Bouchard, M. J., Wang, L. H., Kong, C., and Schneider, R. J. (1999). Src kinase involved in hepatitis B virus replication. *EMBO J.* 18, 5019–5027. doi: 10.1093/emboj/18.18.5019

Klein, N. P., and Schneider, R. J. (1997). Activation of Src family kinases by hepatitis B virus HBx protein and coupled signaling Ras. *Mol. Cell Biol.* 17, 6427–6436. doi: 10.1128/MCB.17.11.6427

Lei, X., Li, Y. F., Chen, G. D., Ou, D. P., Qiu, X. X., Zuo, C. H., et al. (2015). Ack1 overexpression promotes metastasis and indicates poor prognosis of hepatocellular carcinoma. *Oncotarget* 6, 40622–40641. doi: 10.18632/oncotarget.5872

Liu, H., Xu, J., Zhou, L., Yun, X., Chen, L., Wang, S., et al. (2011). Hepatitis B virus large surface antigen promotes liver carcinogenesis by activating the Src/PI3K/Akt pathway. *Cancer Res.* 71, 7547–7557. doi: 10.1158/0008-5472.CAN-11-2260

Lopez-Cabrera, M., Letovsky, J., Hu, K. Q., and Siddiqui, A. (1990). Multiple liver–specific factors bind to the hepatitis B virus core/pregenomic promoter, transactivation and repression by CCAAT/enhancer binding protein. *Proc. Natl. Acad. Sci. U. S. A.* 87, 5069–5073. doi: 10.1073/pnas.87.13.5069

Mahajan, K., Lawrence, H. R., Lawrence, N., and Mahajan, N. P. (2014). ACK1 tyrosine kinase interacts with histone demethylase KDM3A to regulate the mammary tumor oncogene HOXA1. *J. Biol. Chem.* 289, 28179–28191. doi: 10.1074/jbc.M114.584425

Mahajan, K., and Mahajan, N. P. (2015). ACK1/TNK2 tyrosine kinase: molecular signaling and evolving role in cancers. *Oncogene* 34, 4162–4167. doi: 10.1038/onc.2014.350

Mahajan, N. P., Liu, Y., Majumder, S., Warren, M. R., Parker, C. E., Mohler, J. L., et al. (2007). Activated Cdc42–associated kinase Ack1 promotes prostate cancer progression via androgen receptor tyrosine phosphorylation. *Proc. Natl. Acad. Sci. U. S. A.* 104, 8438–8443. doi: 10.1073/pnas.0700420104

Mahajan, N. P., Whang, Y. E., Mohler, J. L., and Earp, H. S. (2005). Activated tyrosine kinase Ack1 promotes prostate tumorigenesis: role of ACk1 in polyubiquitination of tumor suppressor Wwox. *Cancer Res.* 65, 10514–10523. doi: 10.1158/0008-5472.CAN-05-1127

Mars, W. M., Zarnegar, R., and Michalopoulos, G. K. (1993). Activation of hepatocyte growth factor by the plasminogen activators uPA and tPA. *Am. J. Pathol.* 143, 949–958.

Moolla, N., Kew, M., and Arbuthnot, P. (2002). Regulatory element of hepatitis B virus transcription. *J. Viral Hepat.* 9, 323–331. doi: 10.1046/j.1365-2893.2002.00381.x

Naldini, L., Tamagnone, L., Vigna, E., Sachs, M., Hartmann, G., Birchmeier, W., et al. (1992). Extracellular proteolytic cleavage by urokinase is required for activation of hepatocyte growth factor/scatter factor. *EMBO J.* 11, 4825–4833. doi: 10.1002/j.1460-2075.1992.tb05588.x

Nassal, M. (2015). HBV cccDNA, viral persistence reservoir and key obstacle for a cure of chronic hepatitis B. *Gut* 64, 1972–1984. doi: 10.1136/gutjnl-2015-309809

Park, E. S., Park, Y. K., Shin, C. Y., Park, S. H., Ahn, S. H., Kim, D. H., et al. (2013). Hepatitis B virus inhibits liver regeneration via epigenetic regulation of urokinase–type plasminogen activator. *Hepatology* 58, 762–776. doi: 10.1002/hep.26379

Park, Y. K., Lee, S. Y., Lee, A. R., Kim, K. C., Kim, K., Kim, K. H., et al. (2020). Antiviral activity of interferon–stimulated gene 20, as a putative repressor binding to hepatitis B virus enhancer II and core promoter. *J. Gasrtroenterol. Hepatol.* 35, 1426–1436. doi: 10.1111/jgh.14986

Park, Y. K., Park, E. S., Kim, D. H., Ahn, S. H., Park, S. H., Lee, A. R., et al. (2016). Cleaved c–FLIP mediates the antiviral effect of TNF–α against hepatitis B virus by dysregulating hepatocyte nuclear factors. *J. Hepatol.* 64, 268–277. doi: 10.1016/j.jhep.2015.09.012

Seeger, C., and Mason, W. S. (2015). Molecular biology of hepatitis B virus infection. *Virology* 479, 672–686.

Shen, F., Lin, Q., Gu, Y., Childress, C., and Yang, W. (2007). Activated cdc42–associated kinase 1 is a component of EGF receptor signaling complex and regulates EGF receptor degradation. *Mol. Biol. Cell* 18, 732–742. doi: 10.1091/mbc.e06-02-0142

Shin, G. C., Ahn, S. H., Choi, H. S., Kim, J., Park, E. S., Kim, D. H., et al. (2014). Hepatocystin contributes to interferon–mediated antiviral response to hepatitis B virus by regulating hepatocyte nuclear factor 4α. *Biochim. Biophys. Acta* 1842, 1648–1657. doi: 10.1016/j.bbadis.2014.04.016

Su, H., and Yee, J. K. (1992). Regulation of hepatitis B virus gene expression by its two enhancers. *Proc. Natl. Acad. Sci. U. S. A.* 89, 2708–2712.

Tang, H., and Mclachlan, A. (2001). Transcriptional regulation of hepatitis B virus by nuclear hormone receptors is a critical determinant of viral tropism. *Proc. Natl. Acad. Sci. U. S. A.* 98, 1841–1846. doi: 10.1073/pnas.041479698

Tang, H., and Mclachlan, A. (2002). Mechanisms of inhibition of nuclear hormone receptor–dependent hepatitis B virus replication by hepatocyte nuclear factor 3β. *J. Virol.* 76, 8572–8581. doi: 10.1128/jvi.76.17.8572-8581.2002

Teo, M., Tan, L., Lim, L., and Manser, E. (2001). The tyrosine kinase ACK1 associated with clathrin–coated vesicles through a binding motif share by arrestin and other adaptors. *J. Biol. Chem.* 276, 18392–18398. doi: 10.1074/jbc.M008795200

Tian, Y., Kuo, C. F., Chen, W. L., and Ou, J. J. (2012). Enhancement of hepatitis B virus replication by androgen and its receptor in mice. *J. Virol.* 86, 1904–1910. doi: 10.1128/JVI.06707-11

Trepo, C., Chan, H. L. Y., and Lok, A. (2014). Hepatitis B virus infection. *Lancet* 384, 2053–2063.

Tsukada, Y., Miyazawa, K., and Kitamura, N. (2001). High intensity Erk signal mediates hepatocyte growth factor induced proliferation inhibition of the human hepatocellular carcinoma cell line HepG2. *J. Biol. Chem.* 276, 40968–40976. doi: 10.1074/jbc.M010890200

Wang, S. H., Yeh, S. H., Lin, W. H., Wang, H. Y., Chen, D. S., and Chen, P. J. (2009). Identification of androgen response elements in the enhancer I of hepatitis B virus: a mechanism for sex disparity in chronic hepatitis B. *Hepatology* 50, 1392–1402. doi: 10.1002/hep.23163

Wang, S. H., Yeh, S. H., Lin, W. H., Yeh, K. H., Yuan, Q., Xia, N. S., et al. (2012). Estrogen receptor α represses transcription of HBV genes via interaction with hepatocyte nuclear factor 4α. *Gastroenterology* 142, 989–998. doi: 10.1053/j.gastro.2011.12.045

Wu, M. H., Ma, W. L., Hsu, C. L., Chen, Y. L., Ou, J. H. J., Ryan, C. K., et al. (2010). Androgen receptor promotes hepatitis B virus–induced hepatocarcinogenesis through modulation of hepatitis B virus RNA transcription. *Sci. Transl. Med.* 2:32r35. doi: 10.1126/scitranslmed.3001143

Yokoyama, N., and Miller, W. T. (2003). Biochemical properties of cdc42–associated tyrosine kinase ACK1. *J. Biol. Chem.* 278, 47713–47723.

Yuh, C. H., and Ting, L. P. (1990). The genome of hepatitis B virus contains a second enhancer, cooperation of two elements within this enhancer is required for its function. *J. Virol.* 64, 4281–4287. doi: 10.1128/JVI.64.9.4281-4287.1990

Zhao, Z., Hong, W., Zeng, Z., Wu, Y., Hu, K., Tian, X., et al. (2012). Mucroporin–M1 inhibits hepatitis B virus replication by activating mitogen–activated protein kinase (MAPK) pathway and down–regulating HNF4a in vitro and in vivo. *J. Biol. Chem.* 287, 30181–30190. doi: 10.1074/jbc.M112.370312

Zheng, Y., Li, J., and Ou, J. H. (2004). Regulation of hepatitis B virus core promoter by transcription factors HNF1 and HNF4 and the viral X protein. *J. Virol.* 78, 6908–6914. doi: 10.1128/JVI.78.13.6908-6914.2004

Conflict of Interest: The authors declare that the research was conducted in the absence of any commercial or financial relationships that could be construed as a potential conflict of interest.

Publisher's Note: All claims expressed in this article are solely those of the authors and do not necessarily represent those of their affiliated organizations, or those of the publisher, the editors and the reviewers. Any product that may be evaluated in this article, or claim that may be made by its manufacturer, is not guaranteed or endorsed by the publisher.

frontiers in Microbiology

ORIGINAL RESEARCH
published: 17 January 2022
doi: 10.3389/fmicb.2021.784745

Metabolomic Profiling Reveals New Insight of Fowl Adenovirus Serotype 4 Infection

*Haiying Ma and Yujuan Niu**

The Biomedical Sciences Institute of Qingdao University (Qingdao Branch of SJTU Bio-X Institutes), Qingdao University, Qingdao, China

Highly pathogenic fowl adenovirus serotype 4 (FAdV-4) is the causative agent of hydropericardium syndrome (HPS), which is characterized by pericardial effusion and hepatitis, and is one of the foremost causes of economic losses to the poultry industry over the last 30 years. However, the metabolic changes in cells in response to FAdV-4 infection remain unclear. In order to understand the metabolic interactions between the host cell and virus, we utilized ultra-high-performance liquid chromatography/quadrupole time-of-flight tandem mass spectrometry to analyze the metabolic profiles with hepatocellular carcinoma cell line (LMH) infected with FAdV-4. The results showed that FAdV-4 could restore metabolic networks in LMH cells and tricarboxylic acid cycle, glycolysis, and metabolism of purines, pyrimidines, alanine, aspartate, glutamate, and amino sugar and nucleotide sugar moieties. Moreover, FAdV-4 production was significantly reduced in LMH cells cultured in glucose or glutamine-deficient medium. These observations highlighted the importance of host cell metabolism in virus replication. Therefore, similarities and disparities in FAdV-4-regulation of the metabolism of host cells could help improve targeted drug and reduce infection.

Keywords: metabolomics, FAdV-4, LMH cells, UHPLC-QTOF-MS, glycolysis, glutamine metabolism

OPEN ACCESS

Edited by:
Cao Yong chang,
Sun Yat-sen University, China

Reviewed by:
Md. Golzar Hossain,
Bangladesh Agricultural University, Bangladesh
Feifei Yin,
Hainan Medical University, China

***Correspondence:**
Yujuan Niu
yujuanniu@163.com

Specialty section:
This article was submitted to Virology, a section of the journal Frontiers in Microbiology

Received: *28 September 2021*
Accepted: *20 December 2021*
Published: *17 January 2022*

Citation:
Ma H and Niu Y (2022) Metabolomic Profiling Reveals New Insight of Fowl Adenovirus Serotype 4 Infection. Front. Microbiol. 12:784745. doi: 10.3389/fmicb.2021.784745

INTRODUCTION

Fowl adenovirus serotype 4 (FAdV-4) is a highly pathogenic hepatotropic virus and the etiological agent of hydropericardium syndrome (HPS), which is an infectious disease of broiler chickens characterized by pericardial effusion and acute hemorrhagic hepatitis, resulting in high mortality rates (Schachner et al., 2014; Steer et al., 2015; Zhao et al., 2015; Niu et al., 2018a,b; Wang and Zhao, 2019). Although the diagnostic criteria for HPS are relatively well established, the intrinsic mechanisms underlying FAdV-4 infection of host cells remain unclear.

To elucidate the molecular mechanisms underlying the pathogenesis of FAdV-4 infection, high throughput techniques can be used to reveal global changes in the expression profiles of gene and proteins associated with metabolism and disease progression. Metabolomics is a powerful tool to analyze changes to molecular metabolites caused by viral infection in order to clarify

the interactions between host cells and viruses (Lu et al., 2012). Mounting evidence indicates that similarities and disparities in virus-induced regulation of host cell metabolism could help to improve the efficacy of targeted drug therapies and reduce the incidence of infection (Cui et al., 2013; Sun et al., 2013; Ni et al., 2014). However, relatively few studies have investigated changes to host cell metabolomics in response to FAdV-4 infection. The liver, which is one of the main organs involved in metabolism (Han et al., 2016; Sato et al., 2017; Cappel et al., 2019; Zhou et al., 2020), is the target of FAdV-4 infection. Therefore, metabolomics might be useful to elucidate the pathogenic mechanisms underlying FAdV-4 infection of hepatic cells.

However, there are too many different kinds of cells in the liver to simply clarify the metabolomic changes of hepatocytes, so we chose the hepatocellular carcinoma cell line (LMH) which are often employed as an *in vitro* model to study the replication and pathogenesis of FAdV-4 (Niu et al., 2019; Zhao et al., 2020). In our study, ultra-high-performance liquid chromatography/quadrupole time-of-flight tandem mass spectrometry (UHPLC-QTOF-MS) was used to assess regulation of the metabolic network of LMH cells infected with FAdV-4 in order to control the onset and progression of HPS.

MATERIALS AND METHODS

Cell Culture, Virus and Antibodies

Chicken LMH (ATCC® CRL-2117™) were obtained from the American Type Culture Collection (Manassas, VA, United States) and cultured as described in a previous study (Niu et al., 2018a). The FAdV-4 strain (SDDM-4/15) used in the study was prepared as described previously (Niu et al., 2016). Self-prepared rabbit polyclonal antibodies against the FAdV-4 hexon protein were used for indirect immunofluorescence (Niu et al., 2018a).

Virus Growth Curve

LMH cells at 80% confluence were seeded in the six-well culture plates and infected with FAdV-4 at a multiplicity of infection (MOI) of 1, while mock-infected cells were treated with an equal volume of Dulbecco's modified Eagle's medium (DMEM). After 2 h, the inoculum was aspirated and the cells were washed twice with phosphate-buffered saline (PBS). Subsequently, the cells were collected at 12, 24, 36, and 48 h post-infection (hpi). A virus growth curve was constructed based on the data acquired by quantitative real-time polymerase chain reaction (qRT-PCR).

Sample Preparation

At 24 h before FAdV-4 infection, ~8.0 × 10^6 LMH cells were seeded in 100-mm culture plates and cultured to 80–90% confluence. Twelve plates were prepared, six of which were infected with FAdV-4 at an MOI of 1, while the others were used as the mock group. All cells (about 1.2 × 10^7) were harvested at 24 hpi. Briefly, after the medium was discarded, the cells were washed twice with cold PBS followed by cold 0.9% sodium chloride solution, then quenched with 1 mL of methanol:acetonitrile: water (2:2:1, v/v), and stored at −80°C until metabolomics analysis.

Metabolite Extraction and Derivatization

After thawing, the cell suspensions were sonicated in an ice bath for 30 min and cooled at −20°C for 10 min before centrifugation at 14,000 × *g* for 20 min at 4°C. Then, the

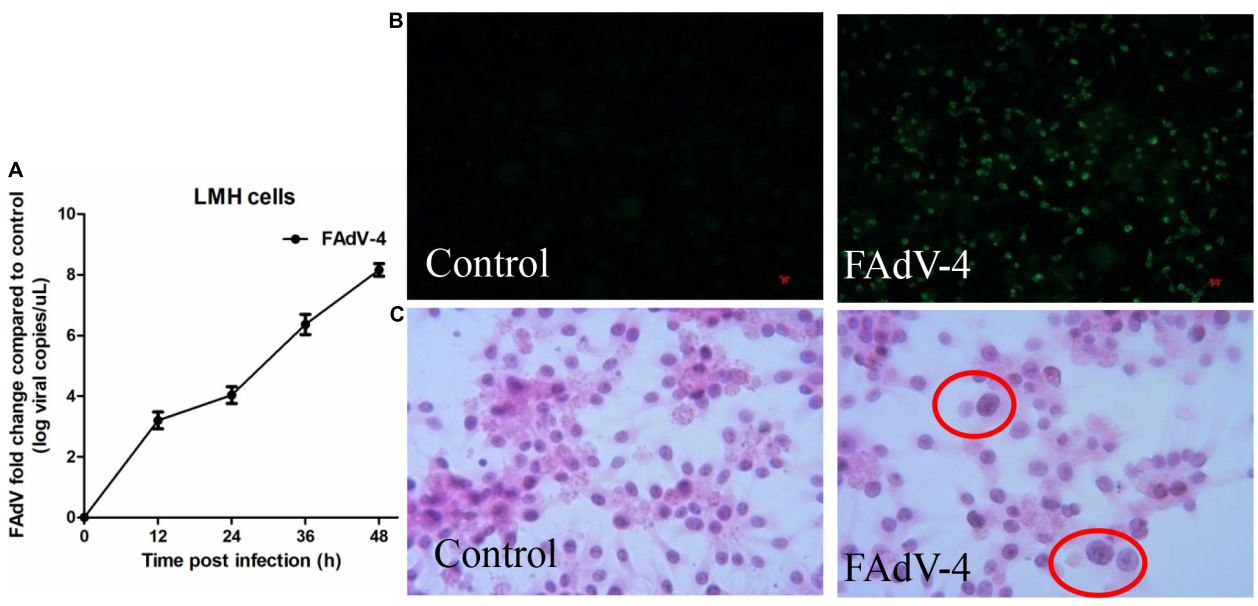

FIGURE 1 | Characteristics of FAdV-4 infected LMH cells. **(A)** The replication characteristics of the virus in LMH cells were determined by qRT-PCR. 50% of the cells were infected with FAdV-4 at 24 hpi by indirect immunofluorescence **(B)**, and viral inclusion bodies were observed in LMH cells (hematoxylin and eosin staining; × 400) **(C)**.

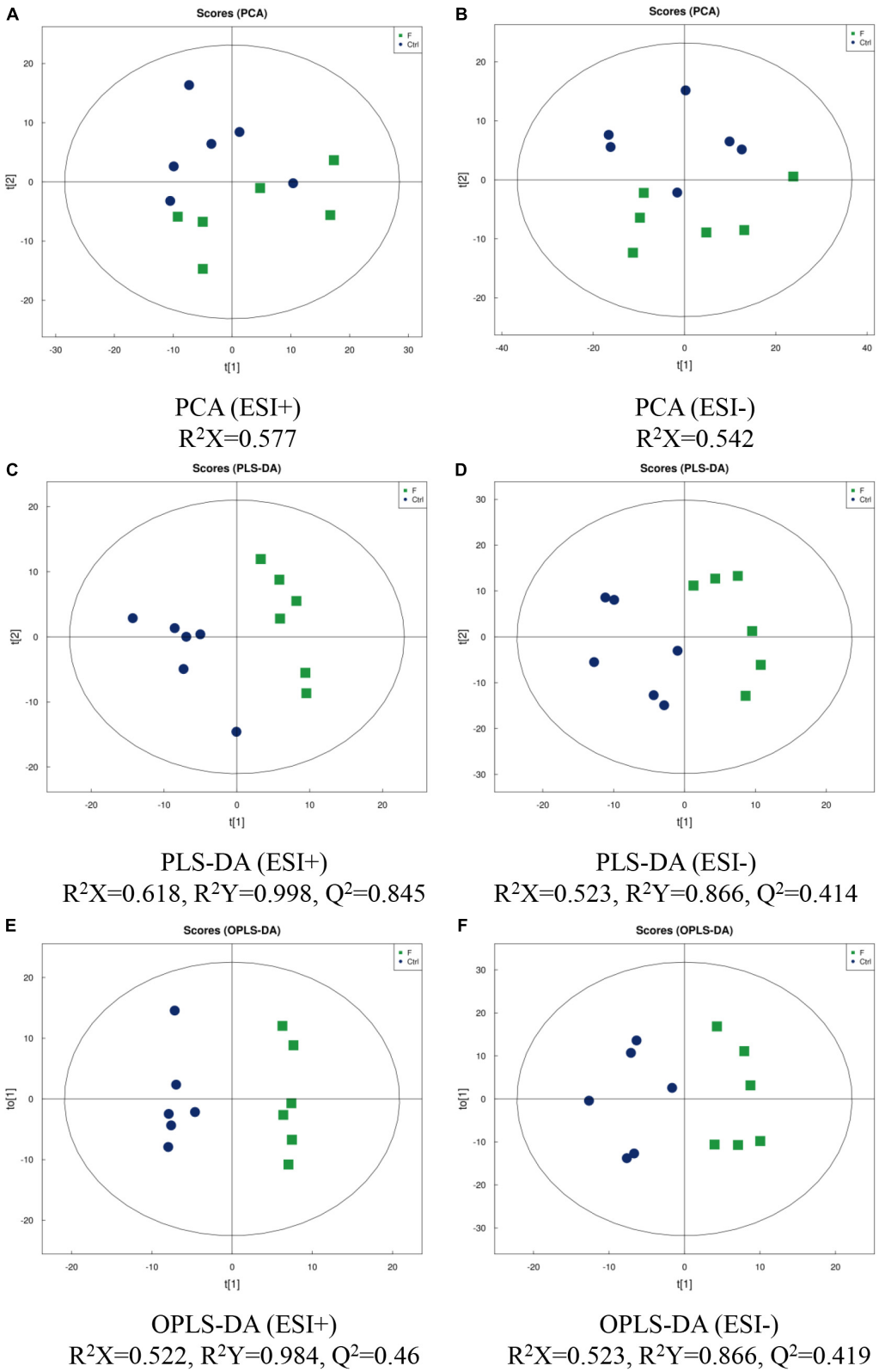

FIGURE 2 | Score plots of PCA, PLS-DA and OPLS-DA of LMH cells infected with FAdV-4. PCA [**(A)** positive ion mode-ESI + ; **(B)** negative ion mode-ESI-], PLS-DA [**(C)** positive ion mode-ESI + ; **(D)** negative ion mode-ESI-], and OPLS-DA [**(E)** positive ion mode-ESI + ; **(F)** negative ion mode-ESI-] models were constructed using LC-MS/MS metabolomics data. Results indicate the separation of control and FAdV-4 group. The ellipses represent 95% confidence intervals of all samples.

supernatant was evaporated under a stream of nitrogen gas in a vacuum concentrator. Prior to LC-MS/MS analysis, 100 μL of acetonitrile:water solution (1:1, v/v) was added to each tube for resolution and the tubes were swirled and centrifuged at 14,000 × *g* at 4°C for 15 min.

LC-MS/MS Analysis

The samples were assayed using an Agilent 1290 Infinity UHPLC system (Agilent Technologies, Inc., Santa Clara, CA, United States) and a Triple TOF 6600 mass spectrometer (AB SCIEX, Concord, ON, Canada). Electrospray ionization (ESI) in positive and negative ion modes was used to detect the samples with the following parameters: atomization auxiliary heating gas 1, 60 Psi; auxiliary heating gas 2, 60 Psi; curtain gas, 30 Psi; ion source temperature, 600°C; spray voltage, ± 5,500 V (positive and negative modes); first-grade mass charge ratio detection range, 60–1,000 Da; second grade ion mass charge ratio detection range, 25–1,000 Da; first grade mass spectrum scanning accumulation time, 0.20 s/spectra; and second grade mass spectrum scanning accumulation time, 0.05 s/spectra. The secondary mass spectrum was obtained in data-dependent acquisition mode with a dynamic exclusion of isotopic ion range of 4 Da with scanning and collecting of 10 debris at a time.

Data Preprocessing and Statistical Analysis

The raw MS data (wiff.scan files) were converted to MzXML files using ProteoWizard MSConvert software before importing into freely available XCMS software. For peak picking, the following parameters were used: centWave m/z, 25 ppm; peakwidth, c (10, 60); and prefilter, c (10, 100). For peak grouping, the following parameters were used: bw, 5; mzwid, 0.025; and minfrac, 0.5. CAMERA (Collection of Algorithms of MEtabolite pRofile Annotation) was used for annotation of isotopes and adducts. In the extracted ion features, only variables with more than 50% of non-zero measurement values in at least one group were retained. Compound identification of metabolites was performed by comparing the accuracies of the m/z values (<25 ppm) and MS/MS spectra with an in-house database established with available authentic standards.

After sum-normalization, the processed data were subjected to multivariate data analysis with the R package "ropls," including

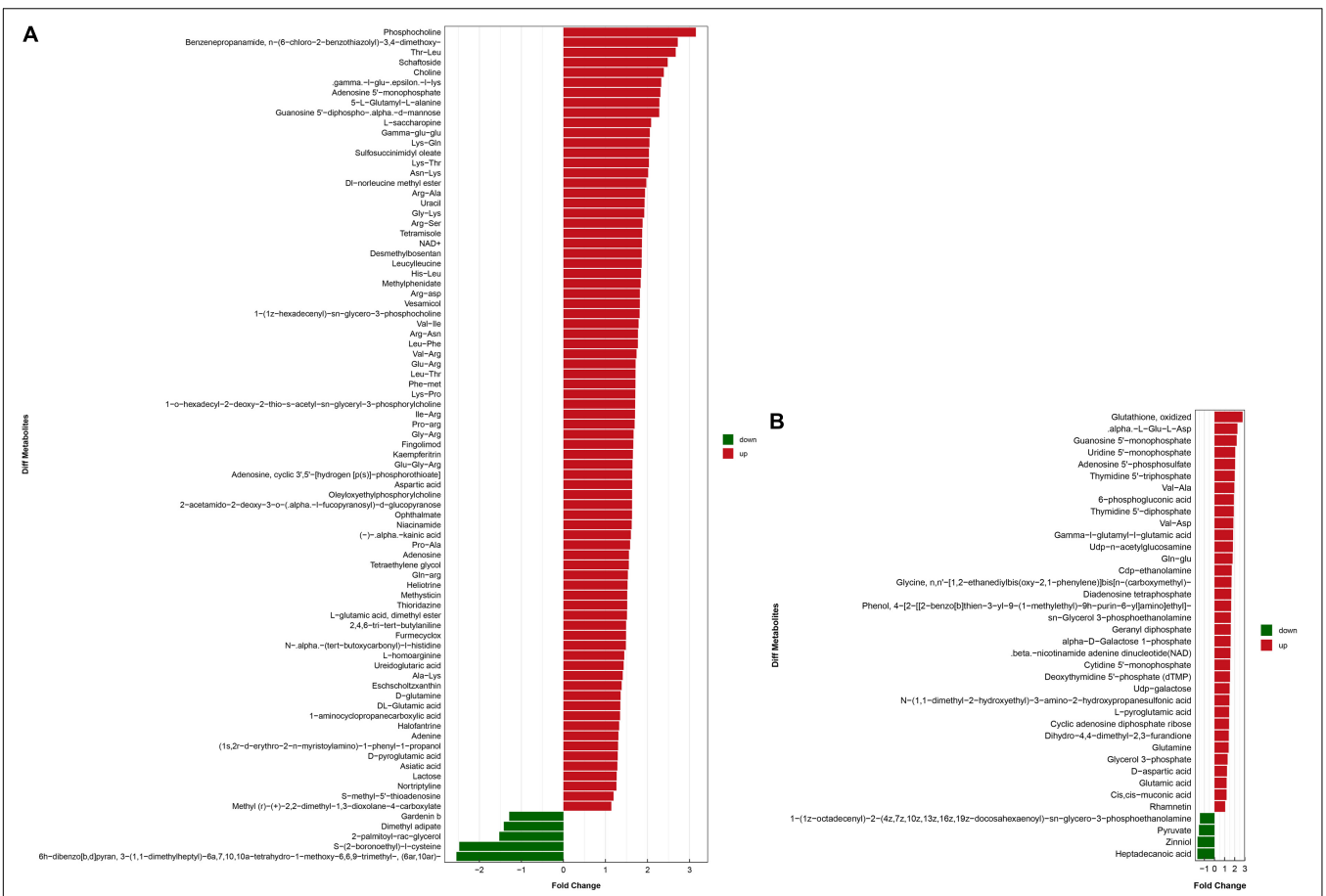

FIGURE 3 | Analysis of the multiple of the difference of metabolite expression in positive ion mode **(A)** and negative ion mode **(B)**. The X-axis indicates the differential expression multiple, red indicates that the differential expression multiple is greater than 1, and green indicates that the differential expression multiple is less than 1. The Y-axis indicates the significant difference metabolites.

TABLE 1 | Differential metabolites in FAdV-4-infected LMH cells compared to controls in positive ion mode.

Name	VIP	*P*-value	FC (F vs. Ctrl)	KEGG ID
Gly-Arg	2.19	7.79E-07	1.67	
Phe-met	1.02	7.80E-07	1.71	
Pro-arg	1.69	3.49E-05	1.69	
Asn-Lys	1.44	4.11E-05	2.02	
Methylphenidate	1.19	6.48E-05	1.84	C07196
Thr-Leu	1.07	6.63E-05	2.67	
Leucylleucine	1.34	7.61E-05	1.86	C11332
2,4,6-tri-tert-butylaniline	3.71	8.32E-05	1.49	
His-Leu	1.01	9.90E-05	1.85	C05010
Arg-asp	1.13	1.48E-04	1.82	
Pro-Ala	1.03	1.73E-04	1.59	
Leu-Thr	1.17	2.20E-04	1.71	
Leu-Phe	1.94	2.79E-04	1.77	
Arg-Ser	2.01	3.30E-04	1.88	
.gamma.-l-glu-.epsilon.-l-lys	1.45	3.78E-04	2.33	C21730
Lys-Pro	1.36	3.93E-04	1.71	
Glu-Arg	1.68	4.69E-04	1.72	
Ureidoglutaric acid	1.95	4.90E-04	1.43	
Choline	1.33	5.09E-04	2.39	C00114
Adenosine 5′-monophosphate	10.4	5.81E-04	2.31	C00020
Desmethylbosentan	1.54	6.12E-04	1.86	
1-(1z-hexadecenyl)-sn-glycero-3-phosphocholine	1.65	8.45E-04	1.81	
Val-Ile	1.21	9.01E-04	1.79	
Val-Arg	1.46	9.37E-04	1.74	
1-o-hexadecyl-2-deoxy-2-thio-s-acetyl-sn-glyceryl-3-phosphorylcholine	13.5	9.84E-04	1.71	
Nortriptyline	1.03	1.01E-03	1.26	C07274
NAD^+	2.20	1.02E-03	1.87	C00003
Sulfosuccinimidyl oleate	7.85	1.08E-03	2.03	
Fingolimod	1.34	1.42E-03	1.66	
Eschscholtzxanthin	1.13	1.49E-03	1.38	C08593
Gly-Lys	1.08	1.56E-03	1.92	
Gamma-glu-glu	7.01	1.65E-03	2.06	
Niacinamide	3.88	1.67E-03	1.62	C00153
Benzenepropanamide, n-(6-chloro-2-benzothiazolyl)-3,4-dimethoxy-	2.48	1.74E-03	2.72	
Phosphocholine	8.26	1.75E-03	3.15	C00588
Heliotrine	1.09	1.86E-03	1.53	C10324
Arg-Ala	3.86	1.99E-03	1.94	
Aspartic acid	1.59	2.93E-03	1.64	C00049
Methysticin	6.17	3.10E-03	1.52	C09952
L-saccharopine	1.18	3.40E-03	2.09	C00449
L-glutamic acid, dimethyl ester	1.50	3.44E-03	1.51	
Adenosine, cyclic 3′,5′-[hydrogen [p(s)]-phosphorothioate]	1.31	3.68E-03	1.64	
Ala-Lys	1.85	4.18E-03	1.41	
D-glutamine	4.64	4.22E-03	1.36	C00064
Oleyloxyethylphosphorylcholine	1.62	4.32E-03	1.63	
Schaftoside	5.81	4.46E-03	2.48	C10181
5-L-Glutamyl-L-alanine	1.63	4.60E-03	2.28	C03740
Lactose	4.92	4.71E-03	1.27	C00243
Glu-Gly-Arg	2.90	4.74E-03	1.64	
Lys-Gln	1.73	5.05E-03	2.05	
S-(2-boronoethyl)-l-cysteine	1.64	5.59E-03	0.40	
Guanosine 5′-diphospho-.alpha.-d-mannose	1.91	5.69E-03	2.28	C00096
L-homoarginine	1.34	6.45E-03	1.45	C01924

(Continued)

TABLE 1 | (Continued)

Name	VIP	*P*-value	FC (F vs. Ctrl)	KEGG ID
Asiatic acid	1.50	6.67E-03	1.28	C08617
Uracil	1.18	7.46E-03	1.93	C00106
1-aminocyclopropanecarboxylic acid	1.21	7.53E-03	1.35	C01234
Dl-norleucine methyl ester	1.05	8.40E-03	1.97	
(-)-.alpha.-kainic acid	1.76	9.11E-03	1.61	C12819
(1s,2r-d-erythro-2-n-myristoylamino)-1-phenyl-1-propanol	1.14	9.42E-03	1.30	
DL-Glutamic acid	3.29	1.05E-02	1.35	C00025
Tetramisole	1.65	1.08E-02	1.87	
Gardenin b	1.84	1.26E-02	0.78	C15109
Furmecyclox	1.70	1.29E-02	1.49	C18912
2-palmitoyl-rac-glycerol	1.35	1.32E-02	0.66	
2-acetamido-2-deoxy-3-o-(.alpha.-l-fucopyranosyl)-d-glucopyranose	1.39	1.35E-02	1.63	
D-pyroglutamic acid	2.70	1.38E-02	1.29	C02237
Tetraethylene glycol	1.15	1.43E-02	1.56	
6h-dibenzo[b,d]pyran, 3-(1,1-dimethylheptyl)-6a,7,10,10a-tetrahydro-1-methoxy-6,6,9- trimethyl-, (6ar,10ar)-	1.15	1.49E-02	0.39	
Thioridazine	1.61	1.52E-02	1.52	
Ile-Arg	1.83	1.53E-02	1.70	
Vesamicol	1.09	1.83E-02	1.82	
Adenosine	4.76	2.09E-02	1.56	C00212
Lys-Thr	1.05	2.14E-02	2.03	
Adenine	2.54	2.58E-02	1.31	C00147
Halofantrine	1.87	2.71E-02	1.33	C07634
Ophthalmate	2.10	3.06E-02	1.63	C21016
S-methyl-5′-thioadenosine	3.63	3.42E-02	1.19	C00170
N-.alpha.-(tert-butoxycarbonyl)-l-histidine	3.48	4.22E-02	1.49	
Gln-arg	1.05	4.37E-02	1.53	
Kaempferitrin	1.04	4.45E-02	1.65	C16981
Methyl (r)-(+)-2,2-dimethyl-1,3-dioxolane-4-carboxylate	1.33	4.46E-02	1.14	
Arg-Asn	1.01	4.47E-02	1.77	
Dimethyl adipate	1.74	4.74E-02	0.71	C14570

Name is the name of the metabolite.
FC (fold changes) is the difference multiple.
KEGG ID is the KEGG number of the metabolite.
E-a represents 10^a in P-value.

pareto-scaled principal component analysis (PCA), partial least squares discrimination analysis (PLS-DA), and orthogonal partial least-squares discriminant analysis (OPLS-DA). Sevenfold cross-validation and response permutation testing was used to evaluate the robustness of the model. The variable importance in the projection (VIP) value of each variable in the PLS-DA and OPLS-DA models was calculated to indicate potential contribution to the classification. The quality of the models is described by the R^2X or R^2Y and Q^2 values. The Student's *t*-test was applied to determine the significance of differences between two groups of independent samples. VIP > 1 and a probability (p) value < 0.05 were used to screen for significant changes in metabolites. Pearson's correlation analysis was performed to identify potential correlations between two variables.

Inhibitory Effects of Related Metabolic Pathways on FAdV-4 Replication

To investigate the impact of host cell metabolism of glucose and glutamine on FAdV-4 replication, LMH cells were cultured in DMEM without glucose or glutamine. As drug treatment samples, FAdV-4-infected LMH cells were treated with 10 or 40 μM 2-deoxy-D-glucose (2dGlc) (a commonly used inhibitor of glycolysis), 1 or 10 μM CB-839, or dimethyl sulfoxide (DMSO) for 48 h. Cells in the DMSO group were infected with FAdV-4 and cultured in DMEM supplemented with glucose and glutamine. Cells were lysed for western blot analysis.

RESULTS

Characteristics of FAdV-4 Infected LMH Cells

FAdV-4 is known to cause cytopathologic effects in LMH cells. Firstly, the replication characteristics of the virus in LMH cells were determined by qRT-PCR. As shown in **Figure 1A**, virus titers in LMH cells reached 10^4 at 24 hpi. Indirect immunofluorescence showed that about 50% of the cells were infected with FAdV-4 at 24 hpi (**Figure 1B**), and hematoxylin and eosin staining confirmed the formation of

viral inclusion bodies (**Figure 1C**). Combined with previous research results (Niu et al., 2018a), FAdV-4 could cause significant apoptosis, autophagy, and a severe inflammatory response in LMH cells at 24 hpi. Therefore, mock and FAdV-4-infected LMH cells were prepared at 24 hpi for early metabolomics analysis.

Analysis of Metabolomics Based on LC-MS/MS

The metabolomic profiles of LMH cells infected with FAdV-4 were characterized using LC-MS/MS techniques, and PCA, PLS-DA, and OPS-DA were applied to the data. Analysis of data quality, including total ion chromatogram, PCA, Pearson's correlation, Hotelling's t^2 statistic, multivariate control chart, and relative standard deviation, indicated that the quality of data was acceptable for the following metabolomics analysis. PCA score plots revealed clear separation between the control and FAdV-4-infected groups, under both positive and negative modes (**Figures 2A,B**). The LC-MS/MS data were further subjected to PLS-DA and OPLS-DA. The quality of the PLS-DA and OPLS-DA models was evaluated based on the parameters R^2Y and Q^2, which are measures of fitness and prediction ability,

TABLE 2 | Differential metabolites in FAdV-4-infected LMH cells compared to controls in negative ion mode.

Name	VIP	*P*-value	FC (F vs. Ctrl)	KEGG ID
Val-Ala	1.03	1.01E-04	1.96	
Adenosine 5′-phosphosulfate	5.84	5.41E-04	2.04	C00224
Guanosine 5′-monophosphate	2.03	1.20E-03	2.20	C00144
Deoxythymidine 5′-phosphate (dTMP)	1.14	1.47E-03	1.54	C00364
.beta.-nicotinamide adenine dinucleotide (NAD)	1.04	1.52E-03	1.58	C00003
Gamma-l-glutamyl-l-glutamic acid	3.53	2.69E-03	1.84	C05282
.alpha.-L-Glu-L-Asp	2.92	2.78E-03	2.27	
Uridine 5′-monophosphate	7.41	3.03E-03	2.05	C00105
Cdp-ethanolamine	1.63	4.19E-03	1.71	C00570
Cyclic adenosine diphosphate ribose	2.07	4.53E-03	1.44	C13050
Thymidine 5′-triphosphate	1.78	5.38E-03	2.00	C00459
Val-Asp	1.29	6.41E-03	1.87	
Heptadecanoic acid	1.47	6.91E-03	0.59	
Glutamine	4.79	1.00E-02	1.40	C00064
Diadenosine tetraphosphate	1.02	1.02E-02	1.66	
Geranyl diphosphate	1.67	1.05E-02	1.61	C05847
6-phosphogluconic acid	1.03	1.07E-02	1.91	C00345
Udp-n-acetylglucosamine	12.1	1.14E-02	1.82	C00043
Dihydro-4,4-dimethyl-2,3-furandione	2.30	1.54E-02	1.41	C01125
Gln-glu	2.31	2.18E-02	1.80	
Thymidine 5′-diphosphate	2.13	2.23E-02	1.91	C00363
Pyruvate	1.37	2.30E-02	0.65	C00022
alpha-D-Galactose 1-phosphate	3.09	2.46E-02	1.59	C00103
N-(1,1-dimethyl-2-hydroxyethyl)-3-amino-2-hydroxypropanesulfonic acid	1.18	2.66E-02	1.48	
1-(1z-octadecenyl)-2-(4z,7z,10z,13z,16z,19z-docosahexaenoyl)-sn-glycero-3-phosphoethanolamine	2.21	2.85E-02	0.69	
Cis, *cis*-muconic acid	9.05	2.90E-02	1.20	C02480
Zinniol	2.73	2.99E-02	0.60	C10840
Glycine, n,n′-[1,2-ethanediylbis(oxy-2,1-phenylene)]bis[n-(carboxymethyl)-	2.60	3.23E-02	1.68	
sn-Glycerol 3-phosphoethanolamine	3.80	3.44E-02	1.62	
D-aspartic acid	3.19	3.51E-02	1.23	C00402
Phenol,4-[2-[[2-benzo[b]thien-3-yl-9-(1-methylethyl)-9h-purin-6-yl]amino]ethyl]-	1.25	3.58E-02	1.65	
Glycerol 3-phosphate	1.35	3.74E-02	1.30	C00093
Udp-galactose	2.14	3.81E-02	1.50	C00052
Cytidine 5′-monophosphate	1.25	3.92E-02	1.55	C00055
Rhamnetin	2.63	4.18E-02	1.05	C10176
L-pyroglutamic acid	3.53	4.48E-02	1.45	C01879
Glutathione, oxidized	9.09	4.76E-02	2.78	C00127
Glutamic acid	4.00	4.99E-02	1.20	C00025

Name is the name of the metabolite.
FC (fold changes) is the difference multiple.
KEGG ID is the KEGG number of the metabolite.
E-a represents 10^a in P-value.

respectively. Generally, Q^2 is greater than 0.5, indicating that the model is stable and reliable, where $0.3 < Q2 \leq 0.5$ indicates that the model is stable and $Q2 < 0.3$ indicates low reliability of the model. PLS-DA and OPLA-DA score plots revealed excellent separation of the control and FAdV-4-infected groups (**Figures 2C–F**).

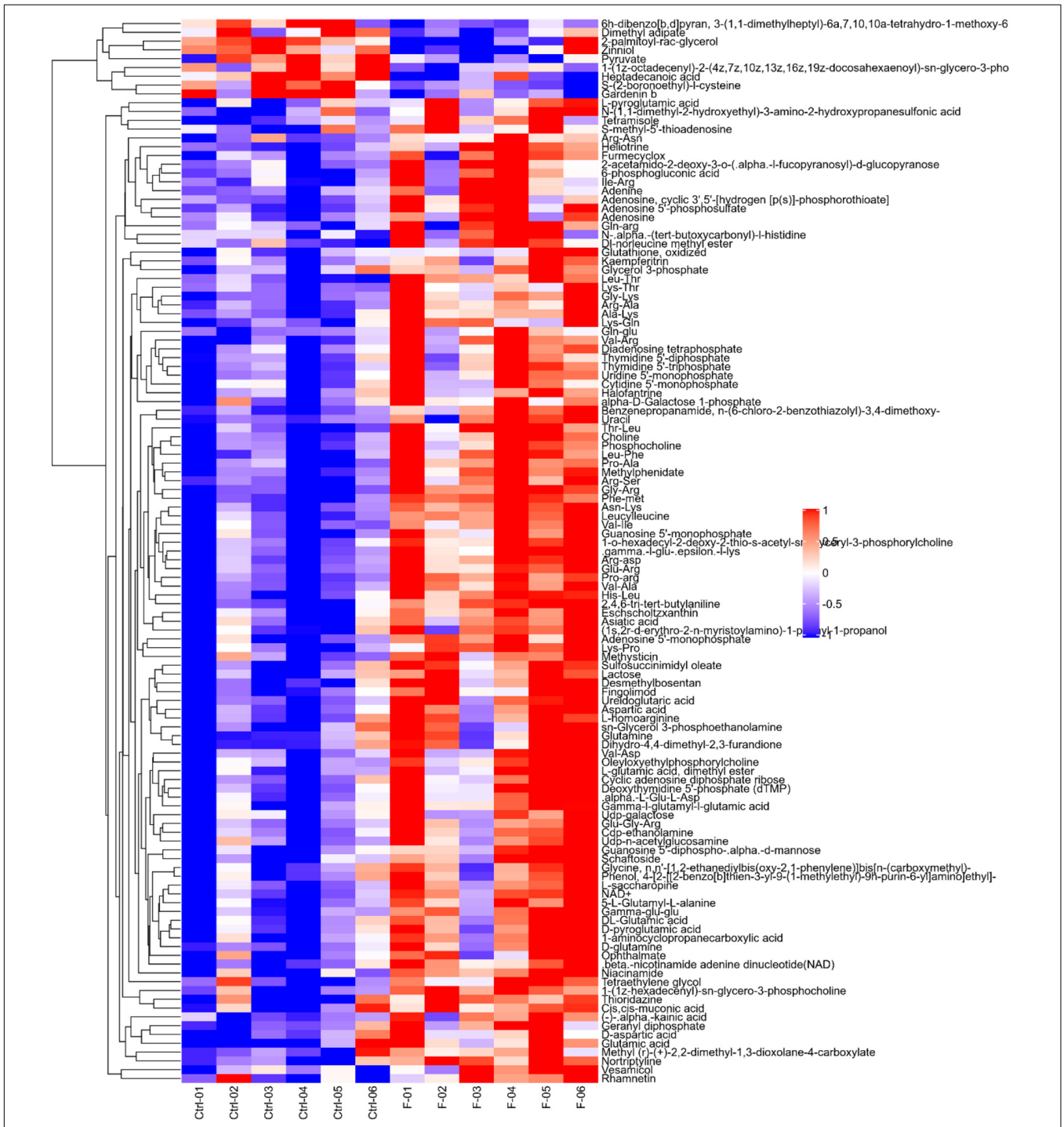

FIGURE 4 | Heatmap of differentially expressed metabolites in LMH cells infected with FAdV-4. Each row in the figure represents a differential metabolite (the ordinate is the metabolite with significant differential expression), and each column represents a group of samples (the abscissa is the sample information). Red represents significant up regulation, blue represents significant down regulation, color depth indicates the degree of up regulation and down regulation, and metabolites with similar expression patterns gather in the same cluster on the left.

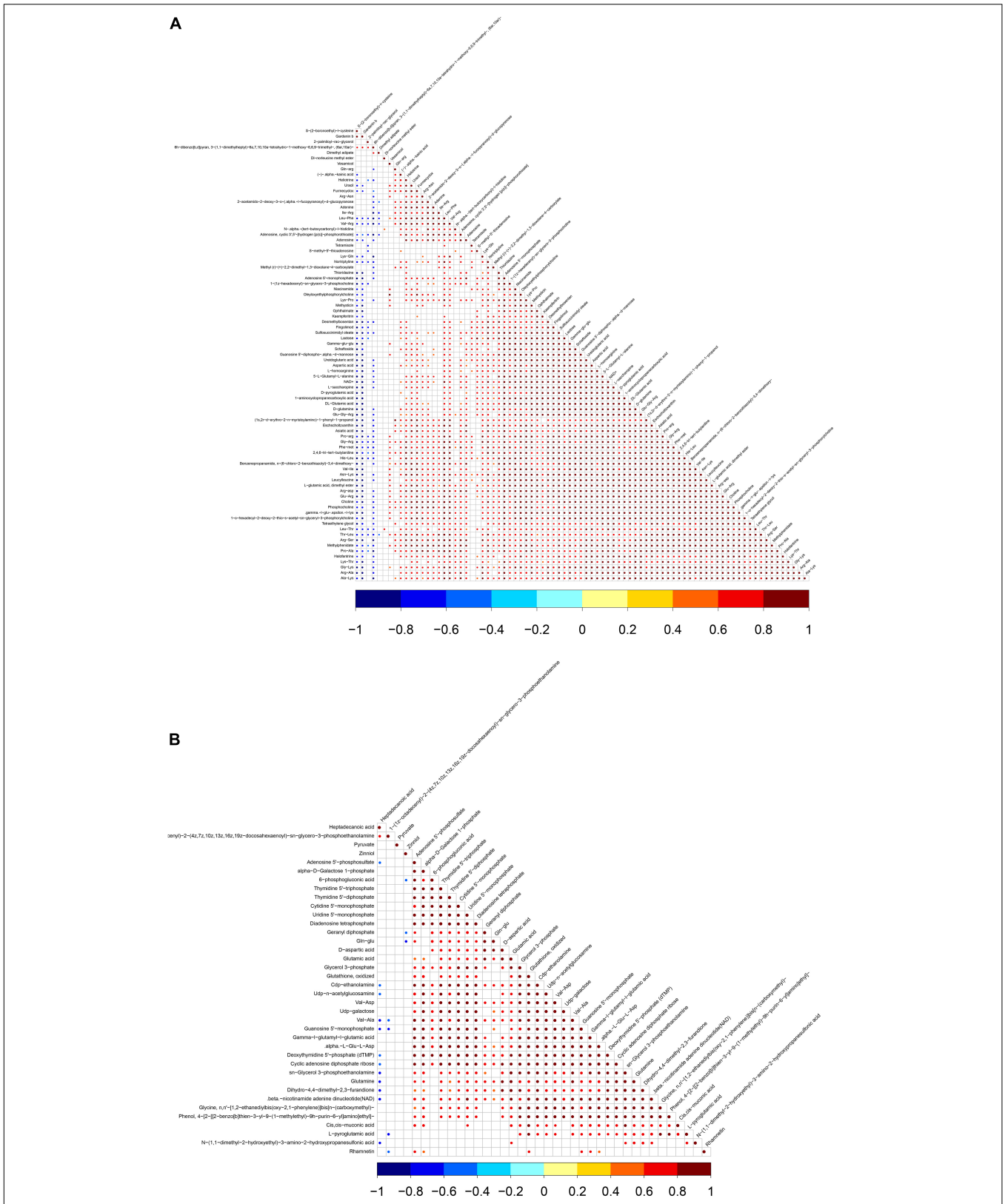

FIGURE 5 | Pearson's of differentially expressed metabolites in positive ion mode **(A)** and negative ion mode **(B)**. Red indicates positive correlation, blue indicates negative correlation, and white indicates no significant correlation. The color depth is related to the absolute value of correlation coefficient. The higher the degree of positive correlation or negative correlation, the darker the color. The size of the point is related to the significance of the correlation, the more significant.

Differential Metabolites

OPLS-DA based on a VIP > 1 in and $P < 0.05$ (Student's *t*-test) revealed significant differences in metabolite screening criteria. The metabolites and associated fold changes in response to FAdV-4 infection of LMH cells are shown in **Figure 3** and **Tables 1**, **2**. The differential metabolites, which included 49 amino acids and related derivatives, of LMH cells caused by FAdV-4 infection, included 78 that were increased and five that were decreased in positive ion mode, while 34 were increased and four were decreased in negative ion mode.

Changes to Metabolic Pathways

Differential metabolites were further analyzed to explore the effects of FAdV-4 infection on the metabolic pathways of LMH cells. The relationships among the differential metabolites were investigated using heatmap analysis (**Figure 4**) and Pearson's correlation (**Figure 5**). The results indicated that metabolites in the same or related metabolic pathways were closely connected. When the significance level of metabolite enrichment in each pathway was analyzed and calculated with the Fisher's exact test, 60 pathways were potentially changed in LMH cells infected with FAdV-4 (**Table 3**). The top 20 metabolic pathways with the highest significance were selected based on *P* values and presented in the form of a histogram (**Figure 6**). The top 20 metabolic pathways mainly involved pyrimidine metabolism, purine metabolism, amino acid metabolism, carbohydrate metabolism, glutathione metabolism, and cofactor and vitamin metabolism, in addition to some signal transduction pathways. Next, some metabolites with significant differences were further screened to establish connections among the related metabolic pathways (**Figure 7**). The results showed that the tricarboxylic acid (TCA) cycle, purine metabolism, pyrimidine metabolism, alanine, aspartate, and glutamate metabolism, amino sugar and nucleotide sugar metabolism, and glycolysis were significantly up-regulated and closely connected.

Glucose and Glutamine Metabolism on FAdV-4 Replication

As shown in **Figure 8**, treatment of LMH cells with either glutamine withdrawal or 1 or 10 μM CB-839 significantly reduced FAdV-4 replication and lowered viral yields relative to DMSO treatment in the presence of 4 mM glutamine. Moreover, the inhibitory effect of CB-839 on FAdV-4 was dose-dependent. FAdV-4 production was significantly reduced in LMH cells cultured in glucose-deficient medium. Treatment of FAdV-4-infected cells with 20 or 40 μM 2dGlc also effectively impaired the production of infectious particles.

DISCUSSION

Viruses, as obligate intracellular parasites, are completely dependent on host cell metabolism for replication, production, and release (Harries et al., 2010; Thaker et al., 2019b). In order to fulfill these requirements, viruses have evolved different mechanisms to reprogram and exploit the host

TABLE 3 | Differential metabolites in FAdV-4-infected LMH cells compared to controls in negative ion mode.

Metabolic pathway	*P*-value
Pyrimidine metabolism	0.00
Neuroactive ligand-receptor interaction	0.00
Zeatin biosynthesis	0.00
Purine metabolism	0.00
Alanine, aspartate and glutamate metabolism	0.00
FoxO signaling pathway	0.00
ABC transporters	0.00
Taste transduction	0.00
Renin secretion	0.00
AMPK signaling pathway	0.00
cGMP-PKG signaling pathway	0.00
D-Glutamine and D-glutamate metabolism	0.00
Cysteine and methionine metabolism	0.00
Oxidative phosphorylation	0.00
Lysosome	0.00
Glutathione metabolism	0.00
Taurine and hypotaurine metabolism	0.00
Protein digestion and absorption	0.00
Arginine biosynthesis	0.00
Glycerophospholipid metabolism	0.00
Aminoacyl-tRNA biosynthesis	0.00
Metabolic pathways	0.00
Biosynthesis of amino acids	0.00
Nicotinate and nicotinamide metabolism	0.00
Olfactory transduction	0.00
Longevity regulating pathway	0.00
Glutamatergic synapse	0.00
GABAergic synapse	0.00
Pantothenate and CoA biosynthesis	0.00
Longevity regulating pathway—worm	0.01
beta-Alanine metabolism	0.01
Calcium signaling pathway	0.01
Photosynthesis	0.01
Insulin secretion	0.01
Synaptic vesicle cycle	0.01
Monobactam biosynthesis	0.01
Regulation of lipolysis in adipocytes	0.01
Platelet activation	0.01
Bacterial secretion system	0.01
HIF-1 signaling pathway	0.01
Galactose metabolism	0.02
Proximal tubule bicarbonate reclamation	0.02
Histidine metabolism	0.02
Glycine, serine and threonine metabolism	0.02
Nitrogen metabolism	0.02
Biosynthesis of various secondary metabolites—part 3	0.02
Two-component system	0.02
Aldosterone synthesis and secretion	0.03
Carbon fixation in photosynthetic organisms	0.03
Thermogenesis	0.03
cAMP signaling pathway	0.03
Glyoxylate and dicarboxylate metabolism	0.03
Amino sugar and nucleotide sugar metabolism	0.03
Glucagon signaling pathway	0.03
Carbon metabolism	0.04
Ferroptosis	0.04
mTOR signaling pathway	0.04
PI3K-Akt signaling pathway	0.04
Thiamine metabolism	0.05
Glycolysis/Gluconeogenesis	0.05

0.00 means that P-value is less than 0.01.

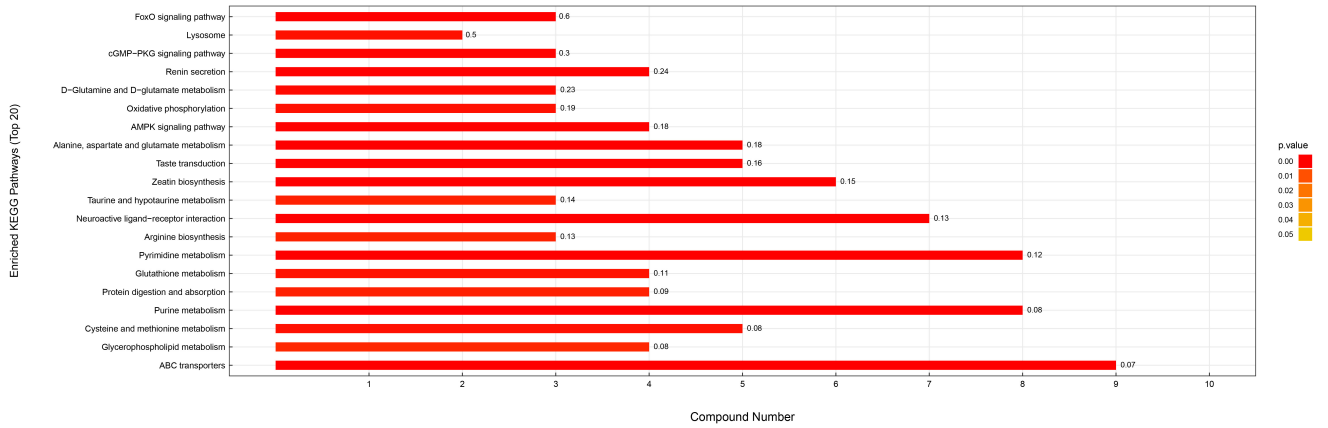

FIGURE 6 | KEGG enrichment pathway map. The vertical axis represents each KEGG metabolic pathway, and the horizontal axis represents the number of differentially expressed metabolites in each KEGG metabolic pathway. Color represents the *P* value of enrichment analysis. The darker the color is, the smaller the *P* value is, and the more significant the enrichment degree is. The number on the column represents the proportion of different metabolites in the detected metabolites.

metabolism (Mesquita and Estaquier, 2018). Therefore, understanding changes to the metabolism of virus-infected host cells would be useful to develop targeted therapies. In recent years, metabolomics analysis has been conducted of various viruses, such as Zika virus (Thaker et al., 2019a), Newcastle disease virus (Liu et al., 2019), and classical swine fever virus (Gou et al., 2017). This study is the first to employ metabolomics to analyze changes in metabolites and metabolic pathways in FAdV-4-infected LMH cells, which revealed insights into the mechanisms of the pathogenesis and host cell interactions of FAdV-4.

The results of this study provide useful information on alterations to metabolites and associated pathways in LMH cells infected with FAdV-4 (**Figures 3**, **4**, **6**). Several pathways involved in energy metabolism were found to be perturbed during FAdV-4 infection, including the TCA, purine metabolism, pyrimidine metabolism, glycolysis, and the metabolism of some amino acids. In a sense, changes to these metabolic pathways could reflect the contributions of host cells to virus proliferation.

Glucose oxidation is a major source of carbon and energy in cellular bioprocesses. During glycolysis, glucose is metabolized to pyruvate (Tohyama et al., 2016). In the presence of oxygen or under oxygen-limiting conditions, pyruvate is catabolized in the TCA to generate large amounts of adenosine triphosphate (ATP) or lactate. Increased amounts of glycolytic intermediates provide the precursors required for synthesis of nucleotides, amino acids, and lipids, as well as cellular redox homeostasis (Vander Heiden et al., 2009; DeBerardinis and Chandel, 2016). Metabolomics analysis revealed that FAdV-4 significantly affected glycolysis and, subsequently, the intermediates of purine metabolism. However, FAdV-4 infection did not induce significant changes to the intermediates of the TCA cycle for ATP production, with the exception of citrate. In a previous study, FAdV-4 infection induced swelling of the mitochondria of hepatocytes and the disappearance of cristae. Oxidative phosphorylation and ATP synthesis occur in the mitochondria (Zorova et al., 2018). However, FAdV-4 infection impairs oxidative phosphorylation, at least to a certain extent, which can result in mitochondrial injury. On the other hand, pyruvate carboxylation will replenish the metabolites involved in the TCA cycle, while redirecting other TCA intermediates to pyrimidine biosynthesis (Vastag et al., 2011). In this study, pyrimidine biosynthesis was increased (**Figures 6**, **7**). The metabolism of purines and pyrimidines can be summarized as nucleic acid metabolism. Increase metabolism of purines and pyrimidines provides materials for virus replication. In general, glycolysis is a key metabolic pathway. Previous studies have shown that glucose metabolism can affect virus replication (Yu et al., 2011; Thai et al., 2014; Kong et al., 2015). The results showed that in glucose-deficient medium, FAdV-4 production was reduced in LMH cells. Later studies showed that treatment of FAdV-4-infected cells with 2dGlc, a commonly used inhibitor of glycolysis, also effectively impaired the production of infectious particles (**Figure 8**), likely due to reduced glycosylation of viral glycoproteins. Although it is clear that glucose metabolism is important for FAdV-4 infection, the exact mechanisms responsible for virus-induced activation of glycolysis are still not fully understood. Since glucose uptake is important for bioenergy requirements and cell biomass, increased glycolysis may be used by viruses as a source of biomass replication. Increasing glucose uptake may also be required for other metabolic pathways, such as the pentose phosphate and nucleic acid pathways. In fact, virus-induced changes to glucose metabolism seem to play a key role in successful infection, thus it is important to understand the precise molecular mechanisms that drive this reprogramming.

Apart from glucose, glutamine, which is classified as a non-essential amino acid, plays a crucial role in cell proliferation. Virus infection of cells will enhance bioenergetics and macromolecular synthesis, which may include glutamine uptake and utilization. Glutamine serves as a carbon source to support the biosynthesis of lipids, amino acids, and nucleotides (Lunt and Vander Heiden, 2011; DeBerardinis and Chandel, 2016).

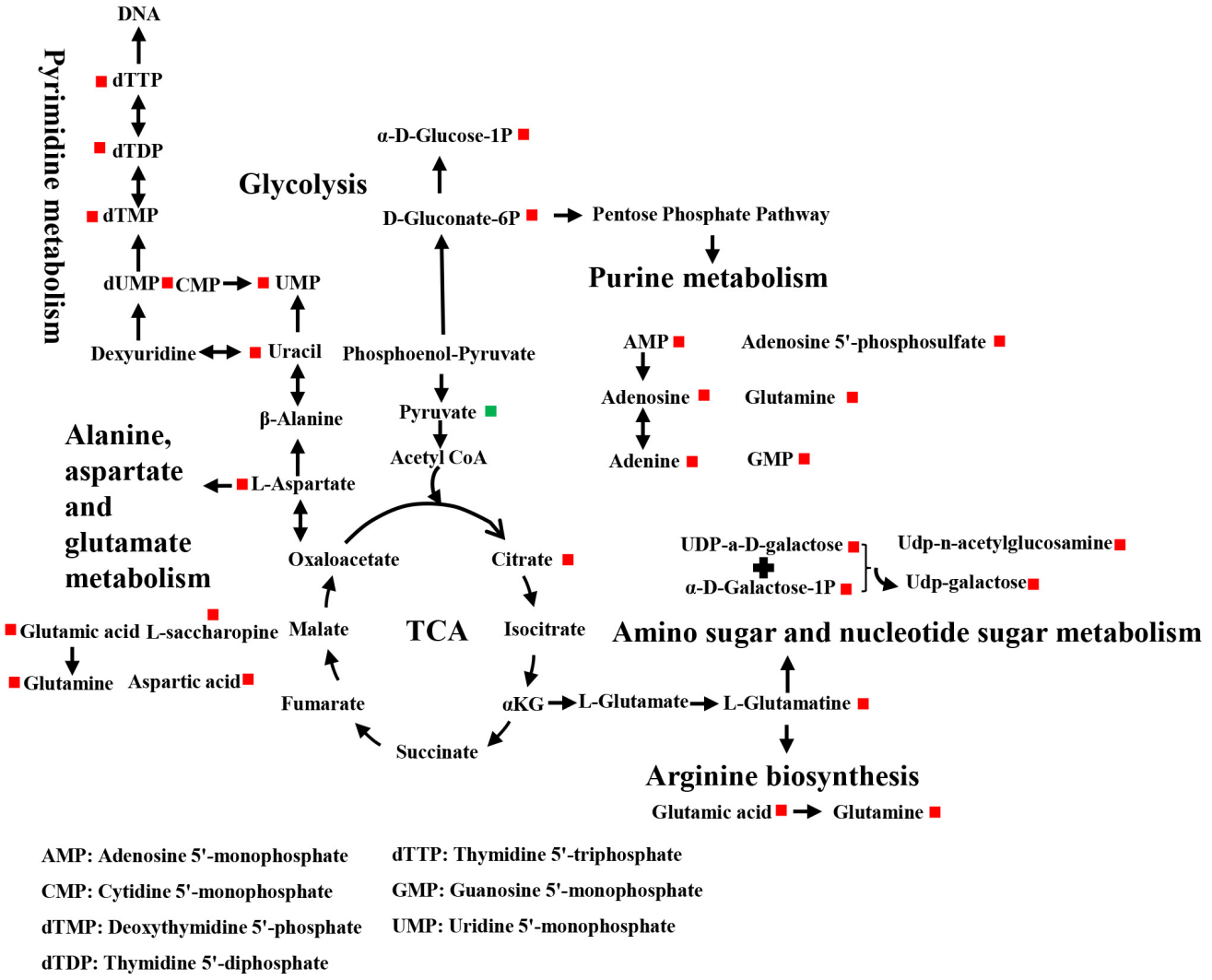

FIGURE 7 | Schematic representation of altered metabolic pathways in LMH cells infected with FAdV-4.

Therefore, glutamine availability is essential for the replication of several viruses. In this study, glutamine metabolism was notably increased in response to FAdV-4 infection (**Figures 6**, **7**). Moreover, FAdV-4 replication was found to be glutamine-dependent as cultivation in glutamine-free medium completely abolished the production of infectious viral particles. Treatment of LMH cells with 1.0 or 10 μM CB-839 significantly decreased replication of FAdV-4 as compared with DMSO treatment (**Figure 8**). This observation highlights the importance of glutamine in virus replication, although future studies are needed to further clarify the underlying molecular mechanisms.

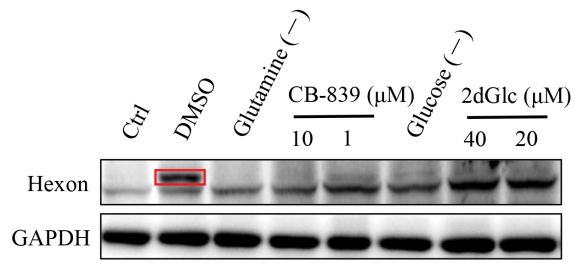

FIGURE 8 | Western blot analysis hexon expression in LMH cells by affecting glucose and glutamine metabolism. The destination strip is marked in the red box, and the below bands are non-specific.

FAdV-4 infection caused changes to a variety of metabolic pathways, among which the metabolism of purines and pyrimidines is particularly important. It is a known that virus infection affects nucleotide metabolism of the host cells in order to meet the nucleic acid needs of the virus (Munger et al., 2006; Vastag et al., 2011; Thai et al., 2014). In this study, the concentrations of the intermediates of the purine and pyrimidine biosynthesis pathways had increased (**Figure 7**).

In summary, these metabolomics data provide evidence that FAdV-4 restored the metabolic networks in LMH cells. Various metabolic pathways, including glycolysis and the metabolism of glutamine, amino acids, purines, and pyrimidines, were altered. Hence, virus infection modified the metabolism of the host cell to provide energy and materials for replication. The identification of these changes will provide considerable important information for further understanding of FAdV-4 replication, pathogenesis, and drug sensitivity.

DATA AVAILABILITY STATEMENT

The original contributions presented in the study are included in the article/supplementary material, further inquiries can be directed to the corresponding author/s.

AUTHOR CONTRIBUTIONS

YN contributed to design of the study and revised the manuscript. HM drafted the manuscript. Both authors contributed to the article and approved the submitted version.

FUNDING

This study was funded by National Natural Science Foundation of China (31902232).

ACKNOWLEDGMENTS

We would like to thank Shanghai APT Biotech Co., Ltd., for assistance with the LC-MS/MS metabolomics experiments.

REFERENCES

Cappel, D. A., Deja, S., Duarte, J. A. G., Kucejova, B., Inigo, M., Fletcher, J. A., et al. (2019). Pyruvate-carboxylase-mediated anaplerosis promotes antioxidant capacity by sustaining TCA cycle and redox metabolism in liver. *Cell Metab.* 29, 1291.e8–1305.e8. doi: 10.1016/j.cmet.2019.03.014

Cui, L., Lee, Y. H., Kumar, Y., Xu, F. G., Lu, K., Ooi, E. E., et al. (2013). Serum metabolome and lipidome changes in adult patients with primary dengue infection. *PLoS Negl. Trop. Dis.* 7:e2373. doi: 10.1371/journal.pntd.0002373

DeBerardinis, R. J., and Chandel, N. S. (2016). Fundamentals of cancer metabolism. *Sci. Adv.* 2:e1600200. doi: 10.1126/sciadv.1600200

Gou, H., Zhao, M., Yuan, J., Xu, H., Ding, H., and Chen, J. (2017). Metabolic profiles in cell lines infected with classical swine fever virus. *Front. Microbiol.* 8:691.

Han, H. S., Kang, G., Kim, J. S., Choi, B. H., and Koo, S. H. (2016). Regulation of glucose metabolism from a liver-centric perspective. *Exp. Mol. Med.* 48:e218. doi: 10.1038/emm.2015.122

Harries, P. A., Schoelz, J. E., and Nelson, R. S. (2010). Intracellular transport of viruses and their components: utilizing the cytoskeleton and membrane highways. *Mol. Plant Microbe Interact.* 23, 1381–1393. doi: 10.1094/MPMI-05-10-0121

Kong, K., Kumar, M., Taruishi, M., and Javier, R. T. (2015). Adenovirus E4-ORF1 dysregulates epidermal growth factor and insulin/insulin-like growth factor receptors to mediate constitutive myc expression. *J. Virol.* 89, 10774–10785. doi: 10.1128/JVI.01463-15

Liu, P., Yin, Y., Gong, Y., Qiu, X., Sun, Y., Tan, L., et al. (2019). In vitro and in vivo metabolomic profiling after infection with virulent newcastle disease virus. *Viruses* 11:962. doi: 10.3390/v11100962

Lu, K., Knutson, C. G., Wishnok, J. S., Fox, J. G., and Tannenbaum, S. R. (2012). Serum metabolomics in a *Helicobacter* hepaticus mouse model of inflammatory bowel disease reveal important changes in the microbiome, serum peptides, and intermediary metabolism. *J. Proteome Res.* 11, 4916–4926. doi: 10.1021/pr300429x

Lunt, S. Y., and Vander Heiden, M. G. (2011). Aerobic glycolysis: meeting the metabolic requirements of cell proliferation. *Annu. Rev. Cell Dev. Biol.* 27, 441–464. doi: 10.1146/annurev-cellbio-092910-154237

Mesquita, I., and Estaquier, J. (2018). Viral manipulation of the host metabolic network. *Exp. Suppl.* 109, 377–401. doi: 10.1007/978-3-319-74932-7_10

Munger, J., Bajad, S. U., Coller, H. A., Shenk, T., and Rabinowitz, J. D. (2006). Dynamics of the cellular metabolome during human cytomegalovirus infection. *PLoS Pathog.* 2:e132. doi: 10.1371/journal.ppat.0020132

Ni, Y., Xie, G. X., and Jia, W. (2014). Metabonomics of human colorectal cancer: new approaches for early diagnosis and biomarker discovery. *J. Proteome Res.* 13, 3857–3870. doi: 10.1021/pr500443c

Niu, Y., Sun, Q., Shi, Y., Ding, Y., Li, Z., Sun, Y., et al. (2019). Immunosuppressive potential of fowl adenovirus serotype 4. *Poult. Sci.* 98, 3514–3522. doi: 10.3382/ps/pez179

Niu, Y., Sun, Q., Zhang, G., Liu, X., Shang, Y., Xiao, Y., et al. (2018a). Fowl adenovirus serotype 4-induced apoptosis, autophagy, and a severe inflammatory response in liver. *Vet. Microbiol.* 223, 34–41. doi: 10.1016/j.vetmic.2018.07.014

Niu, Y., Sun, Q., Zhang, G., Sun, W., Liu, X., Xiao, Y., et al. (2018b). Epidemiological investigation of outbreaks of fowl adenovirus infections in commercial chickens in China. *Transbound. Emerg. Dis.* 65, e121–e126. doi: 10.1111/tbed.12691

Niu, Y., Sun, W., Zhang, G., Qu, Y., and Liu, S. (2016). Hydropericardium syndrome outbreak caused by fowl adenovirus serotype 4 in china in 2015. *J. Gen. Virol.* 97:2684. doi: 10.1099/jgv.0.000567

Sato, S., Solanas, G., Peixoto, F. O., Bee, L., Symeonidi, A., Schmidt, M. S., et al. (2017). Circadian reprogramming in the liver identifies metabolic pathways of aging. *Cell* 170, 664–677. doi: 10.1016/j.cell.2017.07.042

Schachner, A., Marek, A., Jaskulska, B., Bilic, I., and Hess, M. (2014). Recombinant FAdV-4 fiber-2 protein protects chickens against hepatitis–hydropericardium syndrome (HHS). *Vaccine* 32, 1086–1092. doi: 10.1016/j.vaccine.2013.12.056

Steer, P. A., Sandy, J. R., O'Rourke, D., Scott, P. C., Browning, G. F., and Noormohammadi, A. H. (2015). Chronological analysis of gross and histological lesions induced by field strains of fowl adenovirus serotypes 1, 8b and 11 in one-day-old chickens. *Avian Pathol.* 44, 106–113. doi: 10.1080/03079457.2015.1007919

Sun, H., Zhang, A. H., Yan, G. L., Piao, C. Y., Li, W. Y., Sun, C., et al. (2013). Metabolomic analysis of key regulatory metabolites in hepatitis C virus-infected tree shrews. *Mol. Cell. Proteomics* 12, 710–719. doi: 10.1074/mcp.M112.019141

Thai, M., Graham, N. A., Braas, D., Nehil, M., Komisopoulou, E., Kurdistani, S. K., et al. (2014). Adenovirus e4orf1-induced myc activation promotes host cell anabolic glucose metabolism and virus replication. *Cell Metab.* 19, 694–701. doi: 10.1016/j.cmet.2014.03.009

Thaker, S. K., Ch'ng, J., and Christofk, H. R. (2019b). Viral hijacking of cellular metabolism. *BMC Biol.* 17:59. doi: 10.1186/s12915-019-0678-9

Thaker, S. K., Chapa, T., Garcia, G. Jr., Gong, D., Schmid, E. W., Arumugaswami, V., et al. (2019a). Differential metabolic reprogramming by Zika virus promotes cell death in human versus mosquito cells. *Cell Metab.* 29, 1206.e1204–1216.e1204. doi: 10.1016/j.cmet.2019.01.024

Tohyama, S., Fujita, J., Hishiki, T., Matsuura, T., Hattori, F., Ohno, R., et al. (2016). Glutamine oxidation is indispensable for survival of human pluripotent stem cells. *Cell Metab.* 23, 663–674. doi: 10.1016/j.cmet.2016.03.001

Vander Heiden, M. G., Cantley, L. C., and Thompson, C. B. (2009). Understanding the warburg effect: the metabolic requirements of cell proliferation. *Science* 324, 1029–1033. doi: 10.1126/science.1160809

Vastag, L., Koyuncu, E., Grady, S. L., Shenk, T. E., and Rabinowitz, J. D. (2011). Divergent effects of human cytomegalovirus and herpes simplex virus-1 on cellular metabolism. *PLoS Pathog.* 7:e1002124. doi: 10.1371/journal.ppat.1002124

Wang, Z., and Zhao, J. (2019). Pathogenesis of hypervirulent fowl adenovirus serotype 4: the contributions of viral and host factors. *Viruses* 11:741. doi: 10.3390/v11080741

Yu, Y., Maguire, T. G., and Alwine, J. C. (2011). Human cytomegalovirus activates glucose transporter 4 expression to increase glucose uptake during infection. *J. Virol.* 85, 1573–1580. doi: 10.1128/JVI.01967-10

Zhao, J., Zhong, Q., Zhao, Y., Hu, Y. X., and Zhang, G. Z. (2015). Pathogenicity and complete genome characterization of fowl adenoviruses isolated from chickens associated with inclusion body hepatitis and hydropericardium syndrome in China. *PLoS One* 10:e0133073. doi: 10.1371/journal.pone.0133073

Zhao, M., Duan, X., Wang, Y., Gao, L., Cao, H., Li, X., et al. (2020). A novel role for PX, a structural protein of fowl adenovirus serotype 4 (FAdV4), as an apoptosis-inducer in leghorn male hepatocellular cell. *Viruses* 12:228. doi: 10.3390/v12020228

Zhou, M., Deng, Y., Liu, M., Liao, L., Dai, X., Guo, C., et al. (2020). The pharmacological activity of berberine, a review for liver protection. *Eur. J. Pharmacol.* 890:173655. doi: 10.1016/j.ejphar.2020.173655

Zorova, L. D., Popkov, V. A., Plotnikov, E. Y., Silachev, D. N., Pevzner, I. B., Jankauskas, S. S., et al. (2018). Mitochondrial membrane potential. *Anal Biochem.* 552, 50–59. doi: 10.1016/j.ab.2017.07.009

Conflict of Interest: The authors declare that the research was conducted in the absence of any commercial or financial relationships that could be construed as a potential conflict of interest.

Publisher's Note: All claims expressed in this article are solely those of the authors and do not necessarily represent those of their affiliated organizations, or those of the publisher, the editors and the reviewers. Any product that may be evaluated in this article, or claim that may be made by its manufacturer, is not guaranteed or endorsed by the publisher.

frontiers in Microbiology

ORIGINAL RESEARCH
published: 24 January 2022
doi: 10.3389/fmicb.2021.795388

KAT2A Promotes Hepatitis B Virus Transcription and Replication Through Epigenetic Regulation of cccDNA Minichromosome

*Yi-Ping Qin[1†], Hai-Bo Yu[1†], Si-Yu Yuan[1†], Zhen Yang[1], Fang Ren[1], Qing Wang[1], Fan Li[2], Ji-Hua Ren[1], Sheng-Tao Cheng[1], Yu-Jiao Zhou[1], Xin He[1], Hong-Zhong Zhou[1], Yuan Zhang[1], Ming Tan[1], Min-Li Yang[1], Da-Peng Zhang[1], Xu Wen[1], Mei-Ling Dong[1], Hui Zhang[1], Jing Liu[1], Zhi-Hong Li[1], Yao Chen[3], Ai-Long Huang[1], Wei-Xian Chen[4] and Juan Chen[1]**

[1] The Key Laboratory of Molecular Biology of Infectious Diseases Designated by the Chinese Ministry of Education, Chongqing Medical University, Chongqing, China, [2] Department of Endocrine and Breast Surgery, The First Affiliated Hospital of Chongqing Medical University, Chongqing, China, [3] Department of Medical Examination Centre, The Second Affiliated Hospital of Chongqing Medical University, Chongqing, China, [4] Department of Clinical Laboratory, The Second Affiliated Hospital of Chongqing Medical University, Chongqing, China

OPEN ACCESS

Edited by:
Yongqun Oliver He,
University of Michigan, United States

Reviewed by:
Guochun Jiang,
University of North Carolina at Chapel Hill, United States
Keiji Ueda,
Osaka University, Japan

***Correspondence:**
Juan Chen
chenjuan2014@cqmu.edu.cn

[†] These authors have contributed equally to this work and share first authorship

Specialty section:
This article was submitted to Virology, a section of the journal Frontiers in Microbiology

Received: 15 October 2021
Accepted: 13 December 2021
Published: 24 January 2022

Citation:
Qin Y-P, Yu H-B, Yuan S-Y, Yang Z, Ren F, Wang Q, Li F, Ren J-H, Cheng S-T, Zhou Y-J, He X, Zhou H-Z, Zhang Y, Tan M, Yang M-L, Zhang D-P, Wen X, Dong M-L, Zhang H, Liu J, Li Z-H, Chen Y, Huang A-L, Chen W-X and Chen J (2022) KAT2A Promotes Hepatitis B Virus Transcription and Replication Through Epigenetic Regulation of cccDNA Minichromosome. Front. Microbiol. 12:795388. doi: 10.3389/fmicb.2021.795388

Hepatitis B virus (HBV) infection remains a major health problem worldwide. Sufficient maintenance of the HBV covalently closed circular DNA (cccDNA), which serves as a template for HBV transcription, is responsible for the failure of antiviral therapies. While accumulating evidence suggests that cccDNA transcription is regulated by epigenetic machinery, particularly the acetylation and methylation of cccDNA-bound histone 3 (H3) and histone 4 (H4), the potential contributions of histone succinylation and related host factors remain obscured. Here, by screening a series of succinyltransferases and desuccinylases, we identified KAT2A as an important host factor of HBV transcription and replication. By using HBV-infected cells and mouse models with HBV infection, KAT2A was found to affect the transcriptional activity of cccDNA but did not affect cccDNA production. Mechanism studies showed that KAT2A is mainly located in the nucleus and could bind to cccDNA through interaction with HBV core protein (HBc). Moreover, we confirmed histone H3K79 succinylation (H3K79succ) as a histone modification on cccDNA minichromosome by using the cccDNA ChIP-Seq approach. Importantly, KAT2A silencing specifically reduced the level of cccDNA-bound succinylated H3K79. In conclusion, KAT2A promotes HBV transcription and replication through epigenetic machinery, and our findings may provide new insight into the treatment of HBV infection.

Keywords: lysine acetyltransferase 2A (KAT2A), hepatitis B virus (HBV), covalently closed circular DNA (cccDNA), histone modification, succinylation

Abbreviations: KAT2A, Lysine acetyltransferase 2A; HBV, Hepatitis B virus; cccDNA, covalently closed circular DNA; rcDNA, relaxed-circular partially double-stranded DNA; pcRNA, precore RNA; pgRNA, pregenomic RNA; Pol, viral polymerase; HBeAg, Hepatitis B e antigen; HBsAg, Hepatitis B surface antigen; HBc, HBV core protein; HBx, HBV x protein; nucleocapsids, core protein particles; PHH, Primary human hepatocytes; PTM, posttranslational modification; ac, acetylation; Ksucc, Lysine succinylation; H3K79succ, Succinylation of histone H3K79; ChIP, Chromatin immunoprecipitation; Co-IP, Co-immunoprecipitation; H3, Histone 3; H4, Histone 4; GAPDH, Glyceraldehyde-3-phosphate dehydrogenase; MYH6, Myosin heavy chain 6.

INTRODUCTION

Hepatitis B virus (HBV) infection remains a major global public health issue despite the availability of an effective vaccine and antiviral drugs that prevent HBV infection and arrest disease progression. Recent global hepatitis report estimates indicate 257 million people living with chronic HBV infection (Schweitzer et al., 2015; Salerno et al., 2020, p. 2). Moreover, among individuals with chronic hepatitis B (CHB) who are untreated, 15–40% develop cirrhosis and hepatocellular carcinoma (HCC) (Tang et al., 2018). HBV is a small hepatotropic virus with a 3.2-kb relaxed-circular partially double-stranded DNA (rcDNA) genome (Caballero et al., 2018). Upon entry into a hepatocyte, rcDNA in the HBV virion is delivered into the nucleus and converted into covalently closed circular DNA (cccDNA), which then serves as a transcription template for all viral transcripts, including the 3.5-kb precore RNA (pcRNA) and pregenomic RNA (pgRNA), the 2.4-kb and 2.1-kb surface mRNAs, and a 0.7-kb X mRNA (Block et al., 2007). pgRNA is a template for viral reverse transcription and translation into viral polymerase (Pol) and HBV core protein (HBc) (Jones and Hu, 2013). HBV replication begins with packaging of the pgRNA and Pol protein into core protein particles (nucleocapsids), then transforming pgRNA within the nucleocapsid into HBV core DNA (including ssDNA, dsDNA, and rcDNA). Eventually, mature rcDNA-containing nucleocapsids can re-deliver rcDNA to the nucleus to replenish the cccDNA pool or be secreted via interaction with envelope proteins as progeny virions. Therefore, HBV cccDNA is the key intermediate in the viral life cycle, which is responsible for the persistence of the infection during the natural course of chronic infection and prolonged antiviral treatment (Hong et al., 2017). Targeting cccDNA represents the key approach to cure HBV infection.

HBV cccDNA accumulates in the nucleus of infected cells as a stable episome and organises into a minichromosomes with histone 3 (H3) and histone 4 (H4) proteins and non-histone proteins, such as HBc, HBV x protein (HBx) and host transcription factors (Bock et al., 1994, 2001; Belloni et al., 2009). Accumulating evidence suggests that epigenetic modifications on cccDNA minichromosomes, such as histone modifications, play vital roles in the regulation of cccDNA transcriptional activity (Hong et al., 2017). Previous studies have suggested that the acetylation (ac) status of H3 and H4 on the HBV minichromosome is associated with cccDNA transcriptional activity, and that histone acetyltransferases CBP/p300 and deacetylase HDAC1 are involved in the regulation of HBV transcription (Pollicino et al., 2006; Belloni et al., 2009). A recent study reported that protein arginine methyltransferase 5 (PRMT5) could restrict HBV replication through epigenetic repression of cccDNA transcription and interference with encapsidation of pgRNA (Zhang et al., 2017, p. 5). Moreover, SIRT3 is a host factor epigenetically restricts HBV cccDNA transcription by acting cooperatively with histone methyltransferase (Ren et al., 2018, p. 3). Lysine succinylation (Ksucc), defined as the transfer of a succinyl group to a lysine residue of a protein, is a newly identified protein posttranslational modification (PTM) (Sreedhar et al., 2020). It has been found that histone succinylation has important roles in nucleosome and chromatin dynamics (Jing et al., 2018, 2020). At present, there are few reports about the regulation of histone succinylation on cccDNA minichromosomes (Yuan et al., 2020, p. 5; Yu et al., 2021, p. 7).

Here, by screening a series of succinyltransferases and desuccinylases, we demonstrate KAT2A, as an important host factor for HBV replication, catalyses the succinylation of H3K79 (H3K79succ) on cccDNA through its succinyltransferase activity to promote cccDNA transcription.

MATERIALS AND METHODS

Cell Culture

HepG2 cells were obtained from American Type Culture Collection (ATCC) and the stabled cell line HepG2-NTCP (Na^+/taurocholate co-transporting polypeptide) was constructed in our lab reference to previous study (Sun et al., 2017); Huh-7 cells were obtained from Health Science Research Resource Bank (HSRRB). HepAD38 cells were kindly provided by Prof. Ningshao Xia (The Xiamen University, Fujian, China). Primary human hepatocytes (PHHs) were acquired from ScienCell Research Laboratories; HepG2 and Huh-7 cells were maintained in Dulbecco's modified Eagle medium (DMEM) (D6429, Sigma-Aldrich, United States) with 10% fetal bovine serum (FBS) (10270, Corning, New York, United States), 100 U/mL penicillin, and 100 μg/mL streptomycin (SV30010, HyClone, United States). HepG2-NTCP and HepAD38 cells were cultured in DMEM with 10% FBS and 400 μg/mL of G418 (345810, Merck Millipore, Germany). PHHs were maintained in hepatocyte medium (5201, ScienCell, United States). All cells were maintained in a humidified incubator at 37°C with 5% CO_2.

Plasmids, Antibodies, and Drugs

pCMV6-XL5-KAT2A was purchased from OriGene (SC125929). Lentivirus expressing KAT2A was purchased from Shanghai Genechem Company Limited (lentivector CMV-MCS-EF1-ZsGreen1-T2A-puromycin). Short hairpin RNA targeting KAT2A (shKAT2A-1 and shKAT2A-2) or non-targeting shRNA (shCont) were purchased from Shanghai Genechem Company Limited (lentivector hU6-MCS-ubiquitin-EGFP-IRES-puromycin). pCH9/3091 was presented by prof. Lin Lan (The Third Military Medical University, China). pCH9/3091 containing a 1.1-unit length HBV genome-wide (1818-3182(0)-1988 of HBV) (Genotype D, GenBank accession No. V01460) driven by the CMV promoter for HBV pgRNA transcription. Flag-HBc was constructed by in-frame insertion of full-length HBc into pcDNA3.1 that contains a Flag tag at the C-terminus. pcDNA3.1-HBc was constructed by in-frame insertion of full-length HBc into pcDNA3.1. pCH9/3091-ΔHBc, with a stop codon mutation in the HBc gene (codon 69) based on pCH9/3091. 3 × Flag-HBx was constructed by in-frame insertion of full-length HBx into p3 × Flag-CMV-7.1. The monomeric linearised HBV DNA was amplified

from pCH9/3091 and purified by gel extraction kit (D2111, Magen, China). The primers used are listed in **Supplementary Table 1**. The siRNA and plasmid were transfected into cells by using Lipofectamine^{TM} 3000 Transfection Reagent (L3000015, Thermo Fisher Scientific, United States). prcccDNA (the precursor plasmid of recombinant covalently closed circular DNA of HBV) and pCMV-Cre (encoding Cre recombinase) were obtained from Prof. Qiang Deng (Fudan University, Shanghai, China).

Mouse anti-p300 monoclonal antibody (NB100-616) and rabbit anti-HBsAg polyclonal antibody (NB100-62652) were obtained from Novus (United States). Rabbit anti-KAT2A monoclonal antibody (#3305S), rabbit anti-H3K14ac monoclonal antibody (#7627S), rabbit anti-CPT1A monoclonal antibody (#97361), rabbit anti-Flag monoclonal antibody (#14793), rabbit anti-SIRT5 monoclonal antibody (#8779), mouse anti-Histone H3 monoclonal antibody (#3638) and rabbit anti-GAPDH monoclonal antibody (#2118) were obtained from Cell Signaling Technology (United States). Rabbit anti-SIRT7 polyclonal antibody (S5947) was from Sigma-Aldrich (United States). Rabbit anti-HBV core antigen (HBcAg) polyclonal antibody (B0586) was obtained from Dako (United States). Mouse anti-HBcAg monoclonal antibody (sc-23945), mouse anti-GAPDH monoclonal antibody (sc-47724) and rabbit anti-β-actin monoclonal antibody (sc-47778) were obtained from Santa Cruz Biotechnology (United States). Rabbit anti-H3ac polyclonal antibody (06-599), rabbit anti-H3K9ac polyclonal antibody (06-942), normal rabbit IgG (NI01) and normal mouse IgG (12–371) were obtained from Merck Millipore (Germany). Rabbit anti-succinyllysine polyclonal antibody (PTM-401), rabbit anti-H3K122succ polyclonal antibody (PTM-413) and rabbit anti-H3K79succ polyclonal antibody (PTM-412) were obtained from PTM-Bio (China).

KAT2A inhibitor γ-butyrolactone (MB-3) (HY-129039) was obtained from MedChemExpress (United States).

Virus Particles Production and Cell Infection

HBV particles were collected from the culture supernatant of HepAD38 cells. HBV wild type virus (HBV WT virus) were produced from Huh-7 cells transiently transfected with HBV expressing plasmid pCH9/3091 (containing a 1.1-unit length HBV genome driven by the CMV promoter). HBV HBc protein-deficient virus (HBV-ΔHBc virus) were collected from the supernatant of Huh-7 cells co-transfected with pCH9/3091-ΔHBc and vector expressing of HBc. Briefly, supernatants of cells were collected and mixed with polyethylene glycol (PEG)8000 at final concentration of 5%. Following gently rotated overnight at 4°C, the mixture was concentrated at 4,000 rpm for 30 min at 4°C to collect HBV particles. Centrifugal sediment was re-dissolved in serum-free opti-MEM at 1% volume of the original supernatant samples. For infection, cells were inoculated in plates. Then, the cells were infected with 1,000 vge/cell HBV particles diluted in culture medium supplemented with 2% dimethyl sulphoxide (DMSO) and 4% PEG8000. After 24 h post-infection, the cells were washed by phosphate buffer saline (PBS) three times.

Real-Time Reverse-Transcription PCR

Total cellular RNA was extracted using TRNzol Universal reagent (DP424, TIANGEN, China) followed by DNase treatment. cDNA was synthesised from 1 μg extracted total RNA using an IScript^{TM} cDNA Synthesis kit (KR116-02, TIANGEN, China). Relative quantification of target genes was determined by Fast Start Universal SYBR Green Master with β-actin mRNA as an internal control. The expression of target genes was calculated by the $2^{-\Delta\Delta Ct}$ method. The primers used are listed in **Supplementary Table 1**.

Hirt Extraction of Hepatitis B Virus Covalently Closed Circular DNA and Analysis

Briefly, cells were lysed in 500 μL SDS lysis buffer (50 mM Tris-HCl, pH8.0, 10 mM EDTA, 150 mM NaCl, 1% SDS) at 37°C for 20 min. Then the cell lysate was mixed with 125 μL of 2.5 M KCl and rested overnight at 4°C. After centrifugation at 12,000 g for 20 min, the supernatant was collected (containing the cccDNA). Following purified by phenol/chloroform (1:1), the DNA was precipitated with ethanol and finally dissolved in TE buffer (10 mM Tris-HCl, pH7.5, 1 mM EDTA).

For liver samples, 10–20 mg liver tissues were lysed in lysis buffer (20 mM Tris-HCl, pH8.0, 5 mM EDTA, 400 mM NaCl, 1% SDS) by tissue homogenising apparatus. The cell lysate was incubated with 100 μg/mL protease K at 37°C overnight. Following purified by phenol/chloroform (1:1), DNA was precipitated with ethanol and finally dissolved in TE buffer.

Extracted DNA was digested by exonuclease V (M0345S, New England Biolabs, United States) for 30 min at 37°C. Taqman probe PCR was carried out to quantify the cccDNA level with specific primers. The primers and probe used are listed in **Supplementary Table 1**.

Hepatitis B Virus Core DNA Extraction and Quantification

Cells were lysed in 500 μL lysis buffer (10 mM Tris-HCl pH8.0, 1 mM EDTA, 1% NP-40, 2% sucrose) and incubated for 15 min at 37°C. The nuclei were removed by centrifugation at 16,000 g for 5 min. 10 μL of cytoplasmic cell lysate was put aside and β-actin was detected by western blot. The free nuclei acids in remaining cell lysates were digested with 40 IU/mL DNase I and 10 mM $MgCl_2$ for 4 h at 37°C. After precipitation with 5% PEG8000, the HBV core capsids were incubated with proteinase K overnight at 45°C to release HBV DNA. Following purified by phenol/chloroform (1:1), the HBV DNA was precipitated with ethanol and finally dissolved in TE buffer.

For liver samples, 10–20 mg liver tissues were homogenised in 500 μL lysis buffer (10 mM Tris-HCl pH 8.0, 1 mM EDTA, 1% NP-40, 2% sucrose) by tissue homogenising apparatus and incubated for 15 min at 37°C. The subsequent steps are same as the above described. Extracted HBV DNA was subjected to absolute quantification PCR by using Fast Start Universal SYBR Green Master Mix. The primers used are listed in **Supplementary Table 1**.

A

The reported succinyltransferases and desuccinylases

Name	Property	Effect on gene transcription
p300	succinyltransferase	activation
KAT2A	succinyltransferase	activation
CPT1A	succinyltransferase	activation
SIRT5	desuccinylase	represstion
SIRT7	desuccinylase	represstion

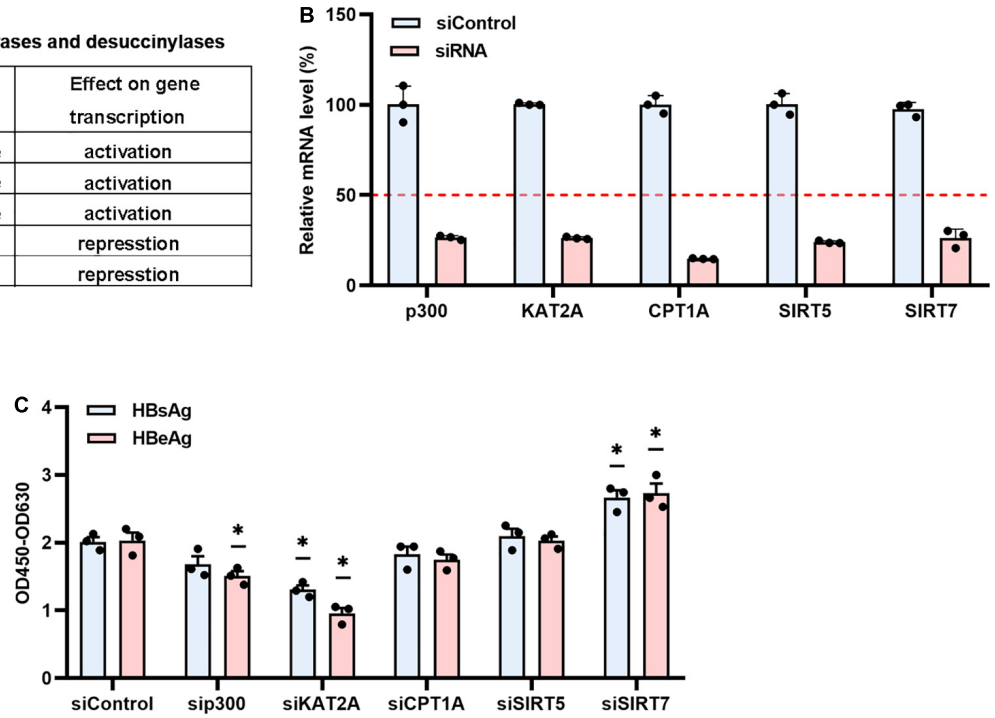

FIGURE 1 | Identification of KAT2A as a host factor promoting cccDNA transcription. **(A)** The reported succinyltransferases and desuccinylases were summarised in the table. **(B)** After 4 days of siRNA treatment, total RNA was extracted by TRNzol Universal reagent. The silencing efficiency of related genes in Huh-7 cells was analysed by real-time PCR with specific primers. β-actin was used as the internal control. **(C)** The indicated siRNA (50 pmol) and monomeric linearised HBV DNA (1 μg) were co-transfected into huh-7 cells by using Lipofectamine™ 3000 Transfection Reagent. The supernatant was collected and HBeAg and HBsAg levels were detected by ELISA. *$P < 0.05$.

Southern Blotting

The DIG-High Prime DNA Labelling and Detection Starter Kit (11585614910, Roche, Germany) was used in the experiments. The HBV core DNA and Hirt-extracted DNA samples were subjected to 1% agarose gel electrophoresis and transferred onto a nylon membrane. The nylon membrane was cross-linked by exposure to UV light in a Stratalinker UV crosslinker and hybridised with a digoxigenin-labelled HBV full-length genomic DNA probe overnight at 42°C. The membrane was incubated in blocking solution for 30 min and antibody solution for another 30 min at 37°C. The signal was detected by exposing on an X-ray film. The mitochondrial gene Cox1 was hybridised as the loading control for HBV cccDNA.

For HBV DNA probe, full-length HBV DNA was amplified by PCR using pCH9/3091 plasmid as template. Electrophoresis of the PCR products was identified, and finally PCR product was purified by gel extraction kit (D2111-02, Magen, China) and PCR product purification kit (11732676001, Roche, Germany). Full-length HBV DNA was labelled with digoxigenin-11-dUTP with a kit supplied by Roche (11585614910). Labelling was carried out by following the manufacturers' instructions.

Northern Blotting

The DIG Northern Starter Kit (12039672910, Roche, Germany) was used in the experiments. Briefly, total cellular RNA was extracted and electrophoresed on 1.4% formaldehyde-agarose gel. The RNA was then transferred onto a nylon membrane and fixed by UV cross-linking. The nylon membrane was hybridised with a digoxigenin-labelled specific RNA probe (corresponding to nucleotides 126–1,225 of the HBV genome) overnight at 68°C. The membrane was incubated in blocking solution for 30 min and antibody solution for 30 min at 37°C. The signal was detected by exposing on an X-ray film.

For HBV RNA probe, three 500 bp HBV DNA fragments (corresponding to nucleotides 126–1,225 of the HBV genome) were amplified by PCR using pCH9/3091 plasmid as template. Electrophoresis of the PCR products was identified, and finally PCR product was purified by gel extraction kit (D2111-02, Magen, China) and PCR product purification kit (11732676001, Roche, Germany). Three 500 bp HBV DNA fragments (corresponding to nucleotides 126–1,225 of the HBV genome) were labelled with digoxigenin-11-UTP with a kit supplied by Roche (12039672910). Labelling was carried out by following the manufacturers' instructions.

Chromatin Immunoprecipitation

The chromatin immunoprecipitation (ChIP) assays were performed using Magna ChIP™ A/G Chromatin Immunoprecipitation Kit (17-10086, Merck Millipore, Germany) and with minor modifications (Belloni et al., 2012). Cells were

scraped with cold PBS (containing protease inhibitor) and centrifuged at 1,000 g at 4°C for 5 min to pellet the cells. The cell pellets were resuspended in 500 μL ChIP Cell Lysis Buffer and the lysate was centrifuged to pellet the nuclei. The nuclei were fixed in 1% formaldehyde at 4°C for 30 min and neutralised by glycine. Isolated cross-linked nuclei were washed and resuspended in 500 μL Nuclear Lysis Buffer. Nuclear extract was sheared to ∼200–1,000 base pairs in length by sonication. After centrifugation, 50 μL of the supernatant was diluted 1:10 in dilution buffer and 5 μL of the sample was put aside as input, and the rest was then subjected to immunoprecipitation using the indicated antibodies and 20 μL protein A/G magnetic beads (17-10086, Merck Millipore, Germany) at 4°C with rotation for 14–16 h. Immunoprecipitation with normal IgG antibody was conducted in the experiment to exclude non-specific binding. The next day, bead-antibody/chromatin complex was washed by Low Salt Wash Buffer, High Salt Wash Buffer, LiCl Wash Buffer, TE Buffer, successively, and eluted in ChIP Elution Buffer containing Proteinase K at 62°C for 2 h with shaking. The immunoprecipitated chromatin was purified using Spin Columns according to the product manual (17-10086, Merck Millipore, Germany), and Taq-man probe qPCR with a specific cccDNA primer and probe was used to measure the level of cccDNA. Host genes glyceraldehyde-3-phosphate dehydrogenase (*GAPDH*) and cardiac gene myosin heavy chain 6 (*MYH6*) were used as control genes. The promoter regions of *GAPDH* and *MYH6* were targeted in the ChIP-PCR. The primers and probe used are listed in **Supplementary Table 1**.

For liver tissues, 25 mg liver tissues were finely minced by using the razor blade on ice and homogenised in tissue lysis buffer and the lysate was centrifuged to pellet the nuclei. The subsequent steps were the same as described above.

Covalently Closed Circular DNA Chromatin Immunoprecipitation-Seq Assay

cccDNA ChIP-Seq assay was performed according to the method described previously with minor modifications (Tropberger et al., 2015). Briefly, HBV-infected PHHs were resuspended in cold nuclei isolation buffer (PBS with 0.1% Triton X-100, 0.1% NP-40, 1 mM DTT, 10 mM sodium butyrate, 1 × protease inhibitor) for 15 min on ice with gentle mixing every 5 min. After centrifugation at 1,000 g at 4°C for 5 min, the nuclei were pelleted and fixed in 1% formaldehyde for 30 min at 4°C. Cross-linked nuclei were washed and resuspended in Mnase digestion buffer (50 mM Tris-HCl pH7.5, 4 mM $MgCl_2$, 1 mM $CaCl_2$, 10% glycerol, 10 mM sodium butyrate, 1 × protease inhibitor). The nuclei were cut into mainly single nucleosome-sized pieces by digesting with 50 U/mL Mnase (New England Biolabs, United States) at 37°C for 10 min and ultrasonic crushing on ice. The sample was centrifugated at 6,500 g for 5 min and the supernatant was applied to 5–30% sucrose (sucrose, 50 mM Tris-HCl pH7.5, 50 mM NaCl, 5 mM EDTA pH8.0, 0.01% NP-40, 10 mM sodium butyrate, 1 × protease inhibitor) gradient centrifuge at 40,000 rpm at 4°C for 4 h. Mononucleosome containing fractions were pooled and subjected to ChIP assay. The immuno-enriched DNA sample was then used for sequencing.

Co-immunoprecipitation and Western Blotting

The cells were lysed in IP lysis buffer (20 mM Tris (pH7.5), 150 mM NaCl, 1% Triton X-100, 20 mM sodium pyrophosphate, 20 mM β-glycerophosphate, 2 mM EDTA, 1 mM Na_3VO_4, 1 mM PMSF) containing 1 × protease inhibitors cocktail (04693159001, Roche, Germany) on ice for 20 min. After centrifugation, 500 μg of total protein was pre-cleared with protein A/G magnetic beads (88803, Thermo Fisher Scientific, United States) 1 h at 4°C. Then the protein complexes were immunoprecipitated with the indicated antibodies overnight at 4°C, followed by incubating with 20 μL protein A/G magnetic beads for another 2 h at room temperature. The protein complexes bound to the beads were washed three times with IP lysis buffer and eluted with loading buffer, followed by resolving on denaturing SDS/PAGE for Western blotting analysis. In general, the protein samples were separated by SDS-PAGE gel and transferred onto a PVDF membrane. Following being blocked in 5% non-fat milk, the membrane was incubated with primary antibody overnight at 4°C. The next day the membrane was incubated with a secondary antibody and the signal was visualised by ECL western blot reagents.

Hepatitis B Virus Infection Mouse Model Involving Hepatitis B Virus Recombinant Covalently Closed Circular DNA Construction

All experiments using mice were carried out in the Laboratory Animal Centre of Chongqing Medical University. The animal study was reviewed and approved by Chongqing Medical University Institutional Animal Experimental Ethics Committee. Wild-type (wt) male mice (C57BL/6), aged 6–7 weeks, from the Laboratory Animal Centre of Chongqing Medical University were anaesthetised with ketamine and xylazine. For hydrodynamic injection, 4 μg prcccDNA and 4 μg pCMV-Cre plasmids were injected through tail veins (diluted to 8% of the mouse body weight with PBS) within 5–8 s (n = 20) (Yang et al., 2002, 2010; Huang et al., 2006). After 1 week, serum HBV DNA copies were determined by absolute quantification PCR. Next, mice were assigned to two groups randomly: negative group (1×10^8 lentivirus-packaged control shRNA was injected into mice via the tail vein, n = 5). positive group (1×10^8 lentivirus-packaged KAT2A shRNA was injected into mice via the tail vein, n = 5). Blood samples were collected via the orbital sinus every 2 days. At 8 days after treatment, the mice were euthanised by slow-fill CO_2, and liver tissues were collected and immediately frozen in liquid nitrogen and stored at −80°C for further study.

Immunofluorescence Staining

Cells grown on a coverslip were fixed in 4% paraformaldehyde for 15 min and then permeabilised in 0.5% Triton X-100 for 30 min. After blocking in PBS containing 2% bovine serum albumin (BSA) for 1 h, cells were incubated with the indicated antibodies overnight at 4°C. The cells were washed by PBS three times and incubated with secondary antibodies conjugated with Alexa Fluor 594 (goat anti-mouse, 1:1,000) and Alexa Fluor 488 (goat anti-rabbit, 1:400) for 2 h at room temperature. Then the cells were then incubated with 4′,6-diamidino-2-phenylindole (DAPI) for nuclear counterstaining, and images were captured by using a confocal laser scanning microscope (LEICA DMi8, Germany).

Immunohistochemistry

Formalin-fixed and paraffin-embedded liver tissue from the mouse model were serially sectioned. Deparaffinisation was performed in xylene and dehydration in a gradient ethanol solution. Then, antigen retrieval was performed in a sodium citrate buffer (10 mmol/L, pH 6.0) using the microwaved heating method. The specimens were incubated with primary antibody overnight at 4℃. Then, the specimens were treated with a secondary antibody for 1 h at room temperature. Immunoreactivity was detected by using diaminobenzidine (DAB) staining. Counterstaining nuclei were performed using haematoxylin.

Cell Counting Kit-8 Cell Viability Assay

The cells were mixed with CCK-8 (HY-K0301, MedChemExpress, United States) solutions and maintained for 2 h at 37°C. The amount of formazan generated by cellular mitochondrial dehydrogenase activity was measured at 450 nm by using Synergy H1 (BioTek Instruments, Inc.). The difference in cell viability was detected by comparing the absorbance of each well.

Enzyme-Linked Immunosorbent Assay

The levels of HBsAg and HBeAg in the culture medium were assessed by using a direct double-antibody sandwich enzyme-linked immunosorbent assay (ELISA) according to the manufacturer's protocol (KHB, Shanghai, China).

Alanine Aminotransferase/Aspartate Aminotransferase Assay

The levels of alanine aminotransferase (ALT)/aspartate aminotransferase (AST) in liver tissue were detected by colorimetric microplate assay according to the manufacturer's protocol (C009-2-1/C010-2-1, Nanjing Jiancheng Bioengineering Institute, China).

Statistical Analysis

Statistics were performed with the non-parametric Mann-Whitney *U*-test. A value of $P < 0.05$ was considered significant. All statistical analyses were performed by using SPSS 19.0 software. Results are expressed as the average of three independent experiments. Data are shown as mean value ± standard error.

RESULTS

Identification of Lysine Acetyltransferase 2A as a Host Factor Promoting Covalently Closed Circular DNA Transcription

Multiple pieces of evidence have revealed the critical role of histone modification in regulating the transcription of cccDNA, particularly the acetylation and methylation of cccDNA-bound histone 3 (H3) and histone 4 (H4) (Zhang et al., 2017, p. 5; Ren et al., 2018, p. 3). To investigate whether histone succinylation plays a potential role in the HBV life cycle, we used the RNA interference method to screen a series of the reported histone succinyltransferases and desuccinylases, including p300, KAT2A, CPT1A, SIRT5, and SIRT7 (**Figure 1A**), which are known to catalyse histone succinylation or desuccinylation to result in transcription activation or repression (Zhang et al., 2011; Li et al., 2016; Wang et al., 2017; Kurmi et al., 2018; Ou et al., 2020). The data showed that the histone succinyltransferases and desuccinylases (including p300, KAT2A, CPT1A, SIRT5, and SIRT7) were efficiently knocked down (**Figure 1B** and **Supplementary Figure 1A**). Then the monomeric linear full-length HBV DNA genomes was transfected into Huh-7 cells (**Supplementary Figure 1B**), in which the cccDNA minichromosome could be formed and the level of the antigen in the supernatant was proven to serve as a surrogate marker for cccDNA transcription (Belloni et al., 2009). Our results suggested that KAT2A knockdown led to significant downregulation of both hepatitis B e antigen (HBeAg) and hepatitis B surface antigen (HBsAg) in the supernatant (**Figure 1C**). Therefore, we focused on KAT2A for further study.

Lysine Acetyltransferase 2A Knockdown Suppresses Covalently Closed Circular DNA Transcription in an Hepatitis B Virus Infection Cell Model

To confirm whether KAT2A is involved in HBV transcription and replication, the HepG2-NTCP cell model was used in our experiments. HepG2-NTCP cells were transduced with two individual lentiviruses expressing shRNA targeting KAT2A before HBV infection. Lentivirus-mediated shRNA effectively knocked down KAT2A and had no obvious cytotoxicity (**Figure 2A** and **Supplementary Figure 2A**). Knockdown of KAT2A distinctly reduced HBV 3.5-kb RNA and total HBV RNAs as evidenced by Northern blotting and real-time PCR (**Figure 2B**). Next, we investigated whether KAT2A could regulate the level of cccDNA, which is the only transcription template for all HBV RNAs in HepG2-NTCP cell model. Then, cccDNA was extracted and detected. Knockdown of KAT2A had no obvious effect on the level of cccDNA (**Figure 2C** and **Supplementary Figure 2B**), but could markedly silence

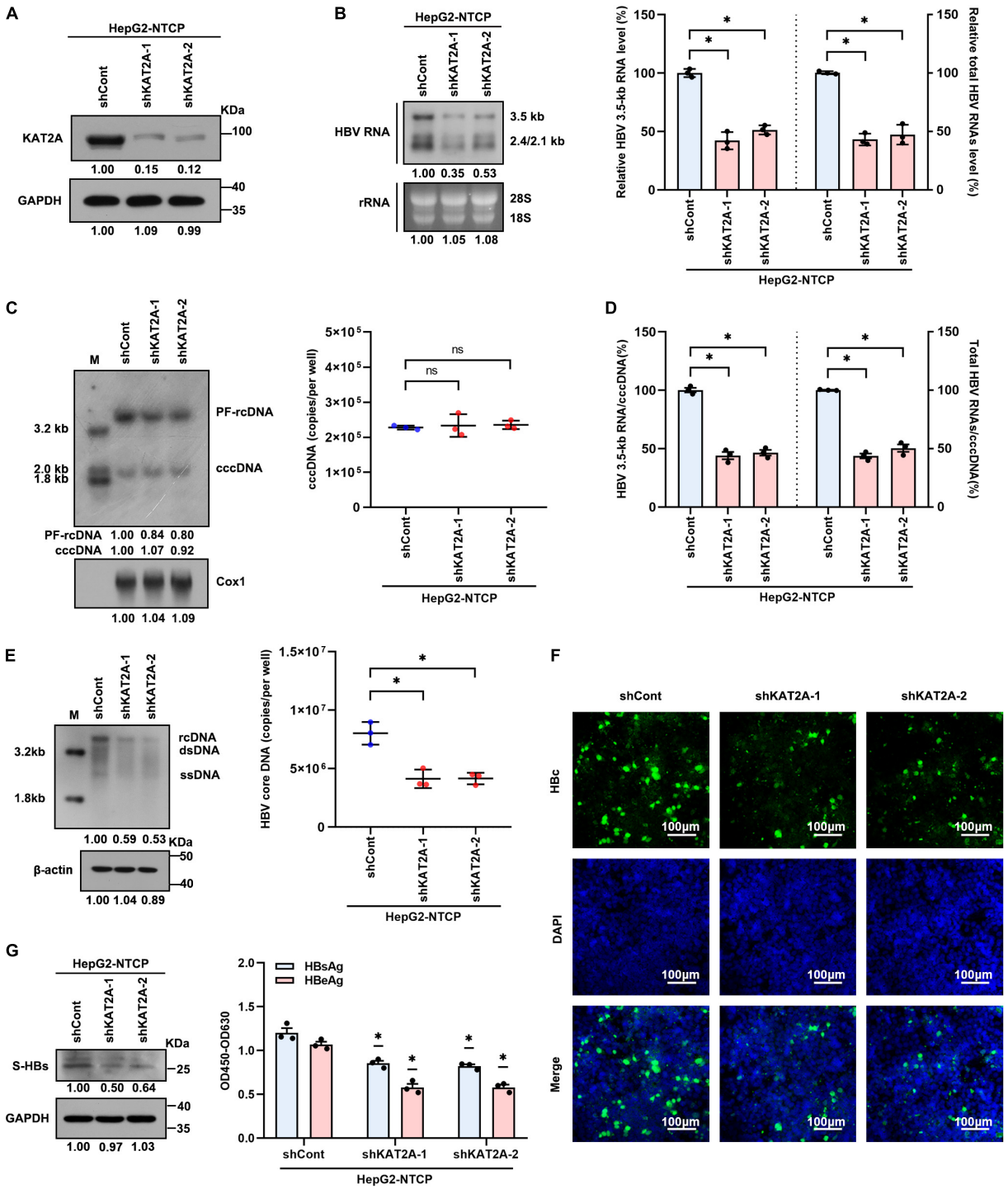

FIGURE 2 | KAT2A knockdown suppresses cccDNA transcription in the HBV infection cell model. HepG2-NTCP cells were infected HBV particles at 1-day post shRNA transduction. At 4 days after infection. **(A)** The expression of KAT2A was detected by western blot. **(B)** Northern blotting and real-time PCR were used to analyse the effect of KAT2A knockdown on HBV RNAs. **(C)** HBV cccDNA was extracted by a modified Hirt DNA extraction protocol and then Southern blotting and Taq-man probe qPCR were used to detect the HBV cccDNA level. The mitochondrial gene Cox1 was hybridised as the loading control for HBV cccDNA. **(D)** The level of HBV 3.5-kb RNA, total HBV RNAs, and cccDNA were used to calculate the ratio of HBV 3.5-kb RNA to cccDNA and total HBV RNAs to cccDNA. **(E)** HBV core DNA was quantified by Southern blotting and absolute quantification PCR. The level of β-actin was used as a loading control for HBV core DNA. **(F)** HBV core protein (HBc) was produced by HBV infected HepG2-NTCP cells. Intracellular HBc was visualised by immunofluorescence staining. The scale bar is 100 μm. **(G)** Western blot was used to detect the level of HBsAg in cells (left). Cell culture supernatant was collected for HBsAg and HBeAg analysis via ELISA (right). Cox1, cyclooxygenase 1; rRNA, ribosomal RNA. *$P < 0.05$.

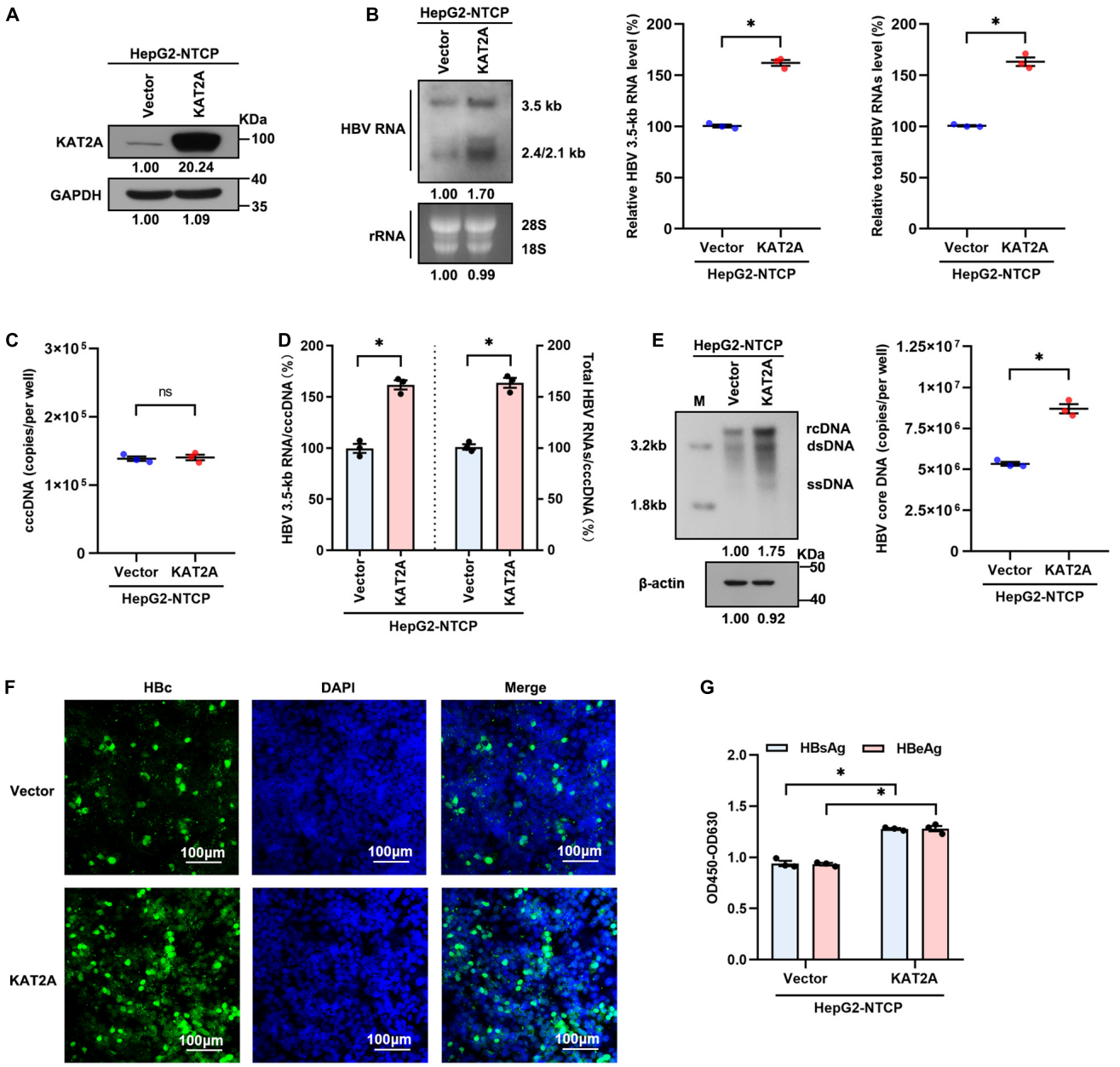

FIGURE 3 | KAT2A overexpression promotes HBV transcription in the HBV infection cell model. HepG2-NTCP cells were infected HBV particles at 1-day post lentivirus expressing KAT2A plasmids transduction. At 4 days after infection. **(A)** The expression of KAT2A was detected by western blot. **(B)** The effect of KAT2A overexpression on HBV RNAs was analysed by Northern blotting and real-time PCR. **(C)** Taq-man probe qPCR was used to detect the HBV cccDNA level. **(D)** The level of HBV 3.5-kb RNA, total HBV RNAs, and cccDNA were used to calculate the ratio of HBV 3.5-kb RNA to cccDNA and total HBV RNAs to cccDNA. **(E)** HBV core DNA was quantified by Southern blotting and absolute quantification PCR. The level of β-actin was used as a loading control for HBV core DNA. **(F)** HBc was produced by HBV-infected HepG2-NTCP cells. Intracellular HBc was visualised by immunofluorescence staining. The scale bar is 100 μm. **(G)** Cell culture supernatant was collected for HBsAg and HBeAg analysis via ELISA. *$P < 0.05$.

cccDNA transcriptional activity, which was determined by the ratios of HBV 3.5-kb RNA to cccDNA or total HBV RNAs to cccDNA (**Figure 2D**). We also detected other HBV replicative intermediates including virus core DNA and proteins that are directly from cccDNA in HBV-infected HepG2-NTCP cells. Consistently, silencing KAT2A markedly reduced the level of HBV core DNA in the cytoplasm (**Figure 2E**), HBV core protein (HBc) in cytoplasm and nucleus (**Figure 2F**), surface antigen protein (S-HBs) in the intracellular space (**Figure 2G**, left), and HBeAg and HBsAg in the supernatant (**Figure 2G**, right). The results confirmed the role of KAT2A knockdown in the suppression of the cccDNA transcription and HBV replication.

Lysine Acetyltransferase 2A Overexpression Promotes Hepatitis B Virus Transcription in Hepatitis B Virus Infection Cell Model

We next transduced HepG2-NTCP cells with lentivirus expressing KAT2A before HBV infection to further determine the effect of KAT2A on HBV transcription and replication. Concordantly, overexpression of KAT2A significantly increased HBV RNA levels, as verified by Northern blotting and real-time PCR (**Figures 3A,B**). Overexpression of KAT2A also promoted cccDNA transcription without affecting the level of cccDNA (**Figures 3C,D**). Moreover, the levels of HBV core DNA in the cytoplasm (**Figure 3E**), HBc protein in the intracellular space (**Figure 3F**), and viral antigens in the supernatant (**Figure 3G**) were markedly increased after KAT2A overexpression. Together, these data suggest that KAT2A is a host factor that could promote HBV cccDNA transcription.

Lysine Acetyltransferase 2A Bound to Covalently Closed Circular DNA and Regulated H3K79 Succinylation on the Covalently Closed Circular DNA Minichromosome

The obtained data encouraged us to investigate how KAT2A regulates cccDNA transcription. Considering that cccDNA transcription is a nuclear event, we first observed the subcellular localisation of KAT2A. Consistent with previous studies, KAT2A is a nuclear protein (**Figure 4A**). Following ChIP analysis, we found that KAT2A was recruited onto the cccDNA minichromosome after HBV infection (**Figure 4B**). As previously reported, KAT2A has acetyltransferase and succinyltransferase activity. KAT2A facilitates H3K9 and H3K14 acetylation, which are associated with transcription regulation (Benhamed et al., 2006; Hu et al., 2015; Fournier et al., 2016). It was also reported that H3K79succ could be catalysed by KAT2A and activate gene expression (Wang et al., 2017). Previous studies have shown that acetyl-CoA has a lower binding affinity to KAT2A than succinyl-CoA, and succinyl-CoA markedly reduces KAT2A-mediated acetylation (Wang et al., 2017). To further explore the role of the acetyltransferase function of KAT2A in cccDNA transcriptional regulation, HepG2-NTCP cells were treated with γ-butyrolactone (MB-3). MB-3 has been discovered as a small, cell-permeable KAT2A inhibitor with an IC_{50} of 100 μM, which can specifically reduce the acetylation of histone H3 catalysed by KAT2A (Mai et al., 2006). MB-3 at concentrations higher than 500 μM exhibited cell toxicity in HepG2-NTCP cells (CC50 > 800 μM) (**Supplementary Figure 3A**). H3K9 acetylation levels were reduced by MB-3 treatment and H3K79 succinylation levels were not affected at 12 and 24 h (**Supplementary Figure 3B**). We found that MB-3 treatment did not affect the level of HBV RNA (**Supplementary Figure 3C**). Then, a ChIP experiment was carried out after silencing KAT2A, and it was found that H3ac, H3K9ac, and H3K14ac modification on cccDNA histones was not affected compared with the control group (**Figure 4C** and **Supplementary Figure 3D**). Therefore, we preliminarily ruled out the role of the acetyltransferase function of KAT2A in cccDNA transcriptional regulation. Then, we asked whether the cccDNA minichromosome could undergo histone succinylation and be regulated by KAT2A. ChIP assays found that knockdown of KAT2A significantly reduced pan-succ (**Figure 4D**) and H3K79succ (**Figure 4E**) on the cccDNA minichromosome, and no effect was observed on H3K122succ (**Figure 4E**). The host genes GAPDH and MYH6 were chosen as the controls in the ChIP assay. Furthermore, we used HBV-infected primary human hepatocytes (PHHs) to prepare chromatin for the cccDNA ChIP-Seq assay as described previously (Tropberger et al., 2015). By mapping sequencing reads to the HBV genome, we confirmed H3K79succ as a histone modification on the cccDNA minichromosome (**Figure 4F**). Our results suggest that KAT2A binds to cccDNA and regulates H3K79 succinylation on the cccDNA minichromosome.

Lysine Acetyltransferase 2A Binds to the Covalently Closed Circular DNA Minichromosome Through Interaction With HBc

Since the HBV HBc and HBV x protein (HBx) participate in the structural organisation of the cccDNA minichromosome (Bock et al., 2001; Belloni et al., 2009; Nassal, 2015), this may be the reason that KAT2A binds to the cccDNA minichromosome. Therefore, we further clarified whether there is an interaction between KAT2A and HBc or HBx protein. The Co-IP results showed that ectopically expressed KAT2A interacted with HBc (**Figure 5A**). However, no interaction between KAT2A and HBx was observed (**Supplementary Figure 4A**). In addition, HBc was mainly located in the nucleus and partially colocalised with KAT2A in HBV infected HepG2-NTCP cells (**Figure 4A**). To further explore the functional role of HBc in the binding of KAT2A to the cccDNA minichromosome, HBV wild type virus (HBV WT virus) and HBV HBc-deficient virus (HBV-ΔHBc virus) were collected from the supernatant of Huh-7 cells transfected with HBV wild type plasmids (HBV WT) or co-transfected with HBV-ΔHBc and a plasmid expressing HBc (**Supplementary Figure 4B**). After overexpression or silencing of KAT2A, the transcriptional activity of cccDNA could not be regulated in the group infected with HBV-ΔHBc virus (**Figures 5B,C** and **Supplementary Figures 4C,D**). Moreover, we found that the binding of KAT2A to the cccDNA minichromosomes was reduced in the HBV-ΔHBc group compared with the HBV WT group (**Figure 5D**). These results suggest that KAT2A may be targeted to HBV cccDNA minichromosome through its interaction with HBc.

Antiviral Activity of Lysine Acetyltransferase 2A Knockdown *in vivo*

To investigate whether KAT2A silencing could inhibit HBV transcription *in vivo*. A mouse model of HBV infection involving the generation of HBV recombinant cccDNA (rcccDNA) using site-specific DNA recombination techniques was used (Qi et al., 2014; **Supplementary Figure 5A**). The workflow of the mouse model was shown (**Figure 6A**), wild-type (wt) male mice

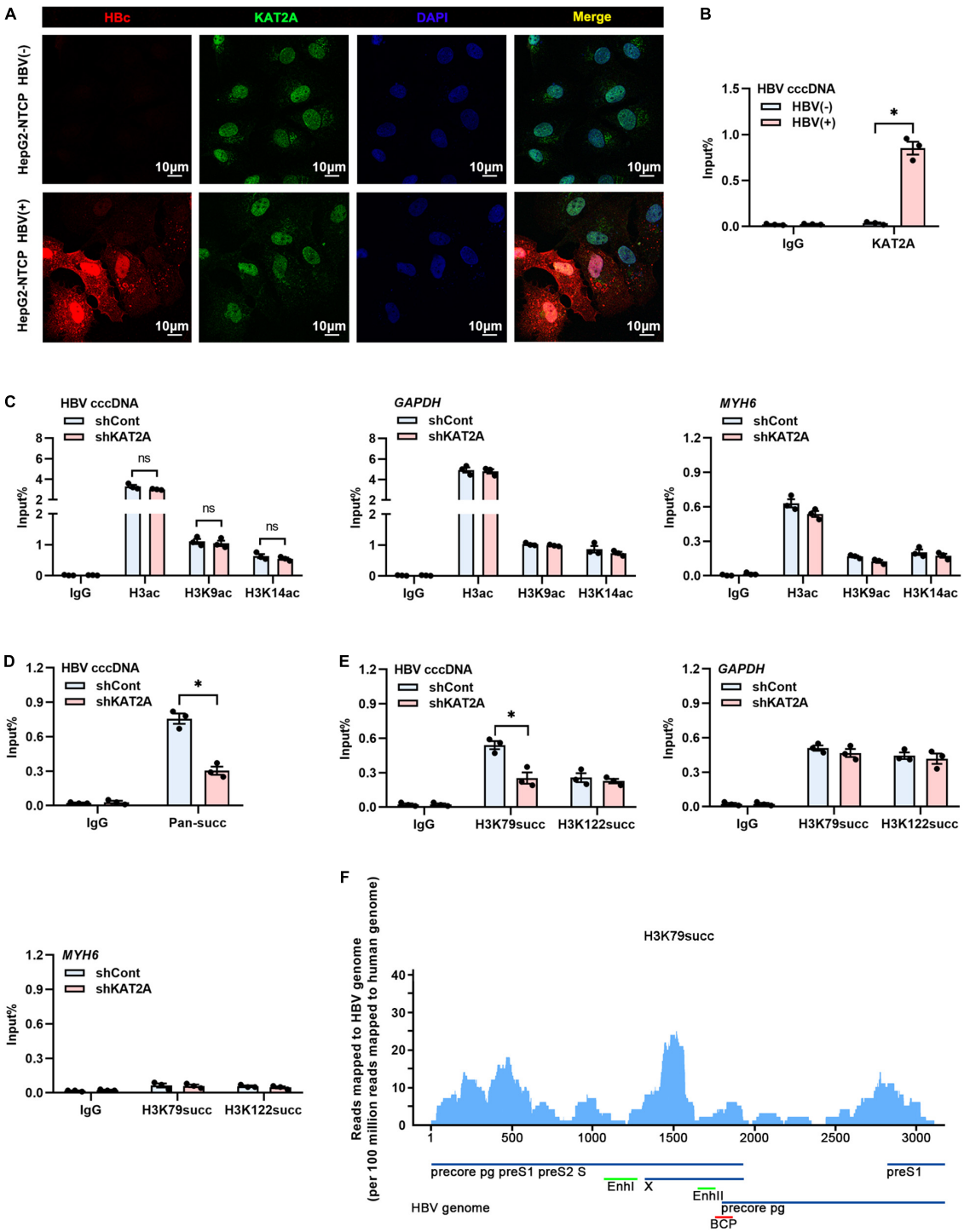

FIGURE 4 | KAT2A bound to cccDNA and regulated H3K79 succinylation on the cccDNA minichromosome. **(A)** HepG2-NTCP cells were infected with HBV particles for 4 days, HBV core protein and endogenous KAT2A were observed by immunofluorescence assay using the specific antibodies. The scale bar is 10 μm. **(B)** Cross-linked chromatin from the HBV-infected and non-infected HepG2-NTCP nucleus was immunoprecipitated with a specific antibody or the control IgG. Taq-man probe qPCR was used to detect the HBV cccDNA level. ChIP results are expressed as% of input. **(C–E)** HepG2-NTCP cells were infected with HBV particles at 1-day post shKAT2A transduction. On 4 days post-infection. **(C)** The levels of H3ac, H3K9ac, and H3K14ac associated with cccDNA, GAPDH, or MYH6 promoter were analysed by ChIP assay with anti-H3ac, anti-H3K9ac, anti-H3K14ac, and the corresponding IgG, respectively. **(D)** ChIP assay was performed with anti-Pan-succ antibody. **(E)** The levels of H3K79succ and H3K122succ associated with cccDNA, GAPDH, or MYH6 promoter were analysed by ChIP assay with anti-H3K79succ, anti-H3K122succ, and the corresponding IgG, respectively. **(F)** ChIP-Seq analysis of the H3K79succ modification on the cccDNA minichromosome. The HBV-specific reads were quantified and normalised by the reads mapped to the human genome. *$P < 0.05$.

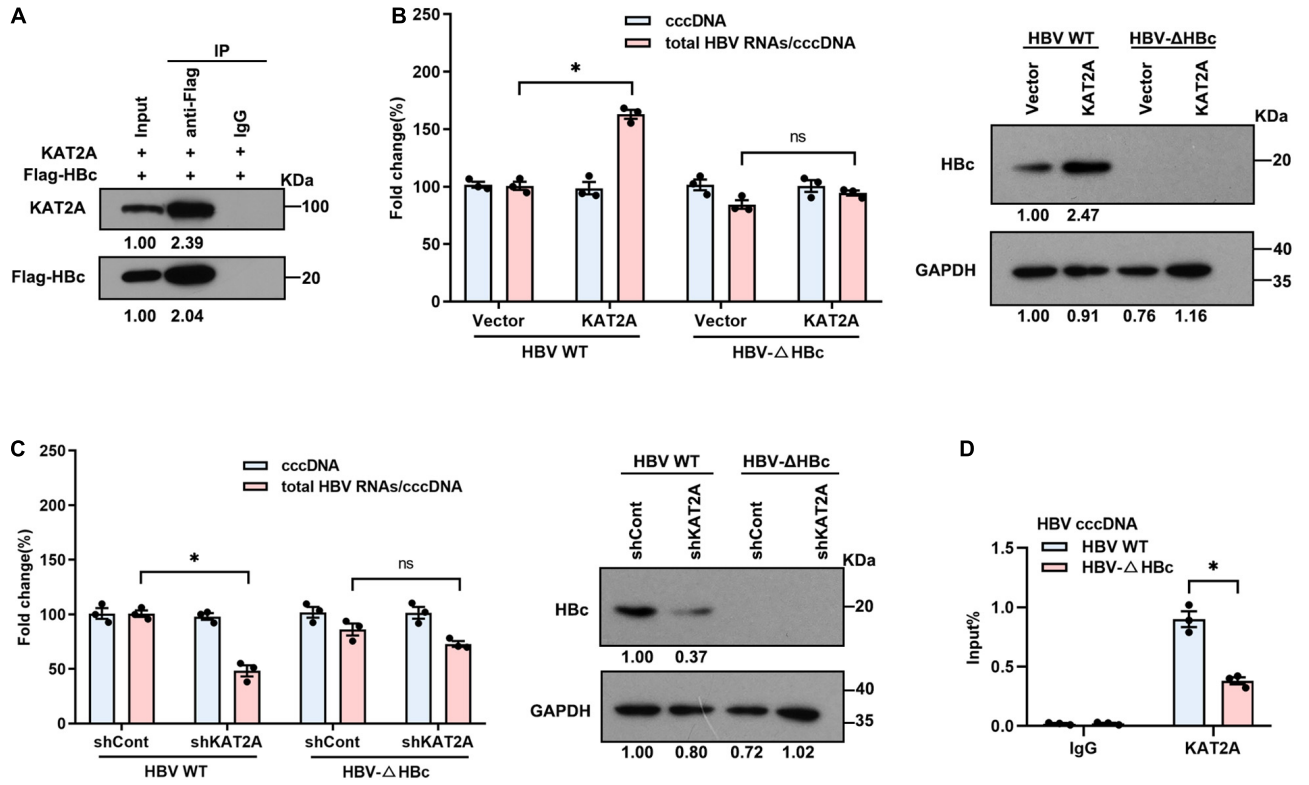

FIGURE 5 | KAT2A binds to the cccDNA minichromosome through interaction with HBc. **(A)** HepG2-NTCP cells were co-transfected with plasmids encoding KAT2A and Flag-HBc for 3 days, the cells were subjected to Co-IP assay with the indicated antibody. The expression of the indicated proteins was analysed by western blot. **(B,C)** HepG2-NTCP cells were transduced with lentivirus expressing KAT2A or shKAT2A for 24 h, then infected with HBV wild type virus (HBV WT virus) and HBc-deficient virus (HBV-ΔHBc virus) for 4 days. Total HBV RNAs and cccDNA were extracted and quantified by real-time PCR and Taq-man probe qPCR for calculating the ratio of total HBV RNAs to cccDNA. The HBc proteins were detected by immunoblotting analysis. **(D)** HepG2-NTCP cells in 100 mm dishes were infected by HBV WT virus and HBV-ΔHBc virus. The cells were used for ChIP assays with the anti-KAT2A antibody. *$P < 0.05$.

(C57BL/6) were hydrodynamically injected with prcccDNA and pCMV-Cre, which resulted in the accumulation of nuclear cccDNA that was epigenetically organised as a minichromosome. Then the wt C57BL/6 mice were hydrodynamically injected with 1×10^8 lentivirus-packaged control/KAT2A shRNA for 8 days. Body weight was monitored every 2 days, all animals were sacrificed to collect liver tissue on day 8, liver weight was measured. There were no significant differences in body weight or liver weight in shKAT2A-treated mice compared to the control group (**Supplementary Figures 5B,C**). The expression of KAT2A, the level of ALT/AST were detected in liver tissues. The data showed that lentivirus-mediated shRNA could effectively knock down KAT2A and had no significant hepatotoxicity (**Supplementary Figures 5D,E**). Serum viral markers were detected during treatment, and our results showed that silencing KAT2A decreased the serum HBV DNA levels (**Figure 6B**), as well as HBsAg (**Figure 6C**). We further evaluate the effect of silencing KAT2A on intrahepatic HBV RNAs, cccDNA, HBV DNA, and HBc protein. It turned out that silencing KAT2A reduced HBV 3.5-kb RNA and total HBV RNAs (**Figure 6D**) without affecting the level of HBV cccDNA (**Figure 6E**). Consistently, silencing KAT2A reduced HBV DNA levels (**Figure 6F**). Immunohistochemical analysis showed that that the expression of HBc was inhibited by KAT2A silencing (**Figure 6G**). Interestingly, the cccDNA-ChIP assay was carried out in liver tissue and found that silencing KAT2A did not affect levels of H3K9ac and H3K14ac modification on the cccDNA minichromosome (**Figures 6H,I**), but decreased the level of H3K79succ (**Figure 6J**). Taken together, these results demonstrated that silencing KAT2A could restrict HBV transcription and replication *in vivo*, and our study may provide new insight into the treatment of HBV infection.

DISCUSSION

Sufficient maintenance of the HBV covalently closed circular DNA (cccDNA), which serves as a template for HBV transcription, is responsible for the failure of antiviral therapies. Identification of the molecular mechanisms regulating cccDNA transcriptional activity may reveal new potential therapeutic targets for anti-HBV drugs. Multiple pieces of evidence have revealed the critical role of histone modification in regulating the transcription of cccDNA (Zhang et al., 2017, p. 5; Ren et al., 2018, p. 3). For example, histone acetylation and methylation have been well characterised (Belloni et al., 2012;

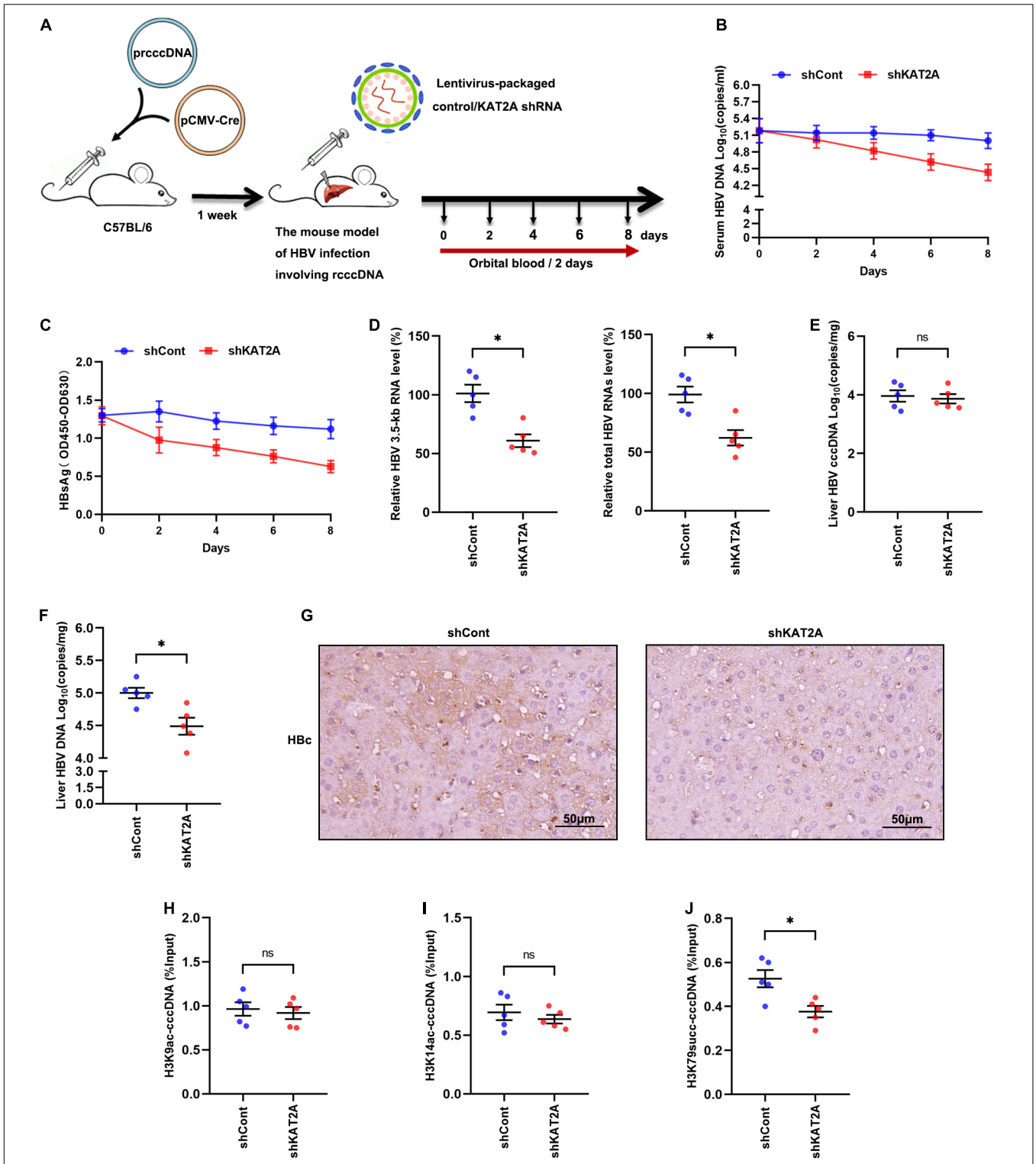

FIGURE 6 | Antiviral activity of KAT2A knockdown *in vivo*. **(A)** Schematic depiction of experiments in C57BL/6 mice. **(B)** Serum HBV DNA was detected by absolute quantification PCR. **(C)** Serum HBsAg was measured via ELISA. **(D)** HBV 3.5-kb RNA and total HBV RNAs in liver tissue were measured by real-time PCR. **(E)** HBV cccDNA in liver tissue was detected by Taq-man probe qPCR. **(F)** The level of HBV DNA in liver tissue was detected by absolute quantification PCR. **(G)** HBc in liver tissues was analysed by IHC. The scale bar is 50 μm. **(H,I)** The levels of H3K9ac, H3K14ac associated with cccDNA were analysed by ChIP assay. **(J)** The level of H3K79succ associated with cccDNA was analysed by ChIP assay. *$P < 0.05$.

Palumbo et al., 2015; Rivière et al., 2015; Yuan et al., 2019). Succinylation is a recently discovered PTM. It has been reported that succinylation, acetylation, and monomethylation of lysine residues change the charge state from + 1 to −1, and from + 1 to 0, and do not change the charge state at all, respectively. Therefore, succinylation may lead to more substantial changes in the structure and function of proteins than acetylation and methylation (Wang et al., 2017). Moreover, succinylation is also a frequently occurring histone modification that is central to the regulation of chromatin-based processes (Zhang et al., 2011; Weinert et al., 2013). However, at present, there are few reports on the regulation of cccDNA minichromosomes by histone succinylation (Yuan et al., 2020, p. 5; Yu et al., 2021, p. 7). Our previous study had identified that SIRT7 inhibited HBV transcription and replication by catalysing cccDNA-bound histone H3K122 desuccinylation (Yu et al., 2021), indicating that histone succinylation may play a crucial role in cccDNA transcription.

Previous studies demonstrated that KAT2A histone succinyltransferase coupled with the α-ketoglutarate dehydrogenase (α-KGDH) complex regulated H3K79 succinylation and gene expression (Wang et al., 2017) and KAT2A could be recruited to the HBV cccDNA minichromosome, thus contributing to HBV replication (Belloni et al., 2009). Recently, a paper by Yuan et al. came to a similar conclusion: KAT2A-mediated succinylation of histone H3K79 contributed to the epigenetic regulation of cccDNA minichromosomes, thus was beneficial to HBV replication (Yuan et al., 2020, p. 5). They also concluded that IFN-α effectively depressed histone H3K79 succinylation in the HBV cccDNA minichromosome. However, the mechanism by which KAT2A is recruited to the HBV cccDNA minichromosome remains elusive. In our study, we proved that KAT2A could bind to cccDNA through interaction with HBc where it catalysed H3K79 succinylation. Moreover, we confirmed histone H3K79 succinylation as a histone modification on the cccDNA minichromosome by using the cccDNA ChIP-Seq approach. Since the effect of KAT2A on HBV replication has not been validated *in vivo*, our data demonstrated that KAT2A modulated histone H3K79 succinylation on cccDNA minichromosome to enhance HBV transcription and replication *in vivo*.

HBV cccDNA exists in the nucleus as the template for HBV RNA transcription. One previous study showed that the α-KGDH complex interacted with KAT2A in the nucleus (Wang et al., 2017). In our study, we validated the subcellular localisation of KAT2A in HepG2-NTCP cells. And similarly, we found that KAT2A was a nuclear protein which might be related to cccDNA minichromosomes. The viral proteins HBc and HBx have been shown to be associated with the cccDNA minichromosome and thus were candidates to mediate the preferential binding of KAT2A to cccDNA (Lucifora et al., 2014; Zhang et al., 2017, p. 5). Therefore, we further found that ectopically expressed KAT2A co-precipitated with HBc rather than HBx. More importantly, compared with HBV-WT virus infected cells, the recruitment of KAT2A to cccDNA was markedly reduced in HBV-ΔHBc virus infected cells (**Figure 5D**). Together, these results suggest that HBc plays a functional role in the regulation of KAT2A on cccDNA transcription.

In conclusion, the present study revealed that KAT2A could bind to cccDNA through interaction with HBc where it catalysed H3K79 succinylation, thus facilitated HBV transcription and replication. These findings broaden our knowledge regarding the physiological functions of KAT2A and the roles of histone succinylation in epigenetic regulation of HBV cccDNA. In addition, our results may reveal new potential therapeutic targets for anti-HBV drugs and hence assist in the design of strategies aimed at silencing and eventually depleting the cccDNA reservoir.

DATA AVAILABILITY STATEMENT

The datasets presented in this study can be found in online repositories. The names of the repository/repositories and accession number(s) can be found below: https://www.ncbi.nlm.nih.gov/geo/query/acc.cgi?acc=GSE188634.

ETHICS STATEMENT

The animal study was reviewed and approved by the Chongqing Medical University Institutional Animal Experimental Ethics Committee, Chongqing Medical University, Chongqing, China.

AUTHOR CONTRIBUTIONS

JC designed the study. Y-PQ, H-BY, S-YY, and ZY performed the experiments. FL, J-HR, S-TC, and FR acquired the data. YZ, MT, Y-JZ, M-LD, HZ, XW, and A-LH analysed the data. Y-PQ and H-BY wrote the manuscript. All authors contributed to manuscript revision, read, and approved the submitted version.

FUNDING

This work was supported by the National Natural Science Foundation of China (Grant Nos. 81861168035, 81922011, and 81871656 to JC), the National Science and Technology Major Project (Grant No. 2017ZX10202203 to A-LH), the Creative Research Group of CQ University (Grant No. CXQT19016 to JC), the Chongqing Natural Science Foundation (Grant No. cstc2018jcyjAX0114 to JC), the National Natural Science Foundation of China (Grant No. 31971084 to YC), and the Chongqing Talents Project (Grant No. cstc2021ycjh-bgzxm0121 to FL).

SUPPLEMENTARY MATERIAL

The Supplementary Material for this article can be found online at: https://www.frontiersin.org/articles/10.3389/fmicb.2021.795388/full#supplementary-material

REFERENCES

Belloni, L., Allweiss, L., Guerrieri, F., Pediconi, N., Volz, T., Pollicino, T., et al. (2012). IFN-α inhibits HBV transcription and replication in cell culture and in humanized mice by targeting the epigenetic regulation of the nuclear cccDNA minichromosome. *J. Clin. Invest.* 122, 529–537. doi: 10.1172/JCI 58847

Belloni, L., Pollicino, T., De Nicola, F., Guerrieri, F., Raffa, G., Fanciulli, M., et al. (2009). Nuclear HBx binds the HBV minichromosome and modifies the epigenetic regulation of cccDNA function. *Proc. Natl. Acad. Sci. U.S.A.* 106, 19975–19979. doi: 10.1073/pnas.0908365106

Block, T. M., Guo, H., and Guo, J.-T. (2007). Molecular virology of hepatitis B virus for clinicians. *Clin. Liver Dis.* 11, 685–706,vii. doi: 10.1016/j.cld.2007.08.002

Bock, C. T., Schranz, P., Schröder, C. H., and Zentgraf, H. (1994). Hepatitis B virus genome is organized into nucleosomes in the nucleus of the infected cell. *Virus Genes* 8, 215–229. doi: 10.1007/bf01703079

Bock, C. T., Schwinn, S., Locarnini, S., Fyfe, J., Manns, M. P., Trautwein, C., et al. (2001). Structural organization of the hepatitis B virus minichromosome. *J. Mol. Biol.* 307, 183–196. doi: 10.1006/jmbi.2000.4481

Caballero, A., Tabernero, D., Buti, M., and Rodriguez-Frias, F. (2018). Hepatitis B virus: the challenge of an ancient virus with multiple faces and a remarkable replication strategy. *Antiviral Res.* 158, 34–44.

Fournier, M., Orpinell, M., Grauffel, C., Scheer, E., Garnier, J.-M., Ye, T., et al. (2016). KAT2A/KAT2B-targeted acetylome reveals a role for PLK4 acetylation in preventing centrosome amplification. *Nat. Commun.* 7:13227. doi: 10.1038/ncomms13227

Hong, X., Kim, E. S., and Guo, H. (2017). Epigenetic regulation of hepatitis B virus covalently closed circular DNA: implications for epigenetic therapy against chronic hepatitis B. *Hepatology* 66, 2066–2077. doi: 10.1002/hep.29479

Hu, Z., Song, N., Zheng, M., Liu, X., Liu, Z., Xing, J., et al. (2015). Histone acetyltransferase GCN5 is essential for heat stress-responsive gene activation and thermotolerance in *Arabidopsis*. *Plant J.* 84, 1178–1191. doi: 10.1111/tpj.13076

Huang, L.-R., Wu, H.-L., Chen, P.-J., and Chen, D.-S. (2006). An immunocompetent mouse model for the tolerance of human chronic hepatitis B virus infection. *Proc. Natl. Acad. Sci. U.S.A.* 103, 17862–17867. doi: 10.1073/pnas.0608578103

Jing, Y., Ding, D., Tian, G., Kwan, K. C. J., Liu, Z., Ishibashi, T., et al. (2020). Semisynthesis of site-specifically succinylated histone reveals that succinylation regulates nucleosome unwrapping rate and DNA accessibility. *Nucleic Acids Res.* 48, 9538–9549. doi: 10.1093/nar/gkaa663

Jing, Y., Liu, Z., Tian, G., Bao, X., Ishibashi, T., and Li, X. D. (2018). Site-specific installation of succinyl lysine analog into histones reveals the effect of H2BK34 succinylation on nucleosome dynamics. *Cell Chem. Biol.* 25, 166–174.e7. doi: 10.1016/j.chembiol.2017.11.005

Jones, S. A., and Hu, J. (2013). Hepatitis B virus reverse transcriptase: diverse functions as classical and emerging targets for antiviral intervention. *Emerg. Microbes Infect.* 2:e56. doi: 10.1038/emi.2013.56

Kurmi, K., Hitosugi, S., Wiese, E. K., Boakye-Agyeman, F., Gonsalves, W. I., Lou, Z., et al. (2018). Carnitine palmitoyltransferase 1A has a lysine succinyltransferase activity. *Cell Rep.* 22, 1365–1373. doi: 10.1016/j.celrep.2018.01.030

Li, L., Shi, L., Yang, S., Yan, R., Zhang, D., Yang, J., et al. (2016). SIRT7 is a histone desuccinylase that functionally links to chromatin compaction and genome stability. *Nat. Commun.* 7:12235. doi: 10.1038/ncomms12235

Lucifora, J., Xia, Y., Reisinger, F., Zhang, K., Stadler, D., Cheng, X., et al. (2014). Specific and nonhepatotoxic degradation of nuclear hepatitis B virus cccDNA. *Science* 343, 1221–1228. doi: 10.1126/science.1243462

Benhamed, M., Bertrand, C., Servet, C., and Zhou, D. X. (2006). Arabidopsis GCN5, HD1, and TAF1/HAF2 interact to regulate histone acetylation required for light-responsive gene expression. *Plant Cell* 18, 2893–2903. doi: 10.1105/tpc.106.043489

Mai, A., Rotili, D., Tarantino, D., Ornaghi, P., Tosi, F., Vicidomini, C., et al. (2006). Small-molecule inhibitors of histone acetyltransferase activity: identification and biological properties. *J. Med. Chem.* 49, 6897–6907. doi: 10.1021/jm060601m

Nassal, M. (2015). HBV cccDNA: viral persistence reservoir and key obstacle for a cure of chronic hepatitis B. *Gut* 64, 1972–1984. doi: 10.1136/gutjnl-2015-309809

Ou, T., Yang, W., Li, W., Lu, Y., Dong, Z., Zhu, H., et al. (2020). SIRT5 deficiency enhances the proliferative and therapeutic capacities of adipose-derived mesenchymal stem cells via metabolic switching. *Clin. Transl. Med.* 10:e172. doi: 10.1002/ctm2.172

Palumbo, G. A., Scisciani, C., Pediconi, N., Lupacchini, L., Alfalate, D., Guerrieri, F., et al. (2015). IL6 inhibits HBV Transcription by targeting the epigenetic control of the nuclear cccDNA minichromosome. *PLoS One* 10:e0142599. doi: 10.1371/journal.pone.0142599

Pollicino, T., Belloni, L., Raffa, G., Pediconi, N., Squadrito, G., Raimondo, G., et al. (2006). Hepatitis B virus replication is regulated by the acetylation status of hepatitis B virus cccDNA-bound H3 and H4 histones. *Gastroenterology* 130, 823–837. doi: 10.1053/j.gastro.2006.01.001

Ren, J.-H., Hu, J.-L., Cheng, S.-T., Yu, H.-B., Wong, V. K. W., Law, B. Y. K., et al. (2018). SIRT3 restricts hepatitis B virus transcription and replication through epigenetic regulation of covalently closed circular DNA involving suppressor of variegation 3-9 homolog 1 and SET domain containing 1A histone methyltransferases. *Hepatology* 68, 1260–1276. doi: 10.1002/hep.29912

Rivière, L., Gerossier, L., Ducroux, A., Dion, S., Deng, Q., Michel, M.-L., et al. (2015). HBx relieves chromatin-mediated transcriptional repression of hepatitis B viral cccDNA involving SETDB1 histone methyltransferase. *J. Hepatol.* 63, 1093–1102. doi: 10.1016/j.jhep.2015.06.023

Salerno, D., Chiodo, L., Alfano, V., Floriot, O., Cottone, G., Paturel, A., et al. (2020). Hepatitis B protein HBx binds the DLEU2 lncRNA to sustain cccDNA and host cancer-related gene transcription. *Gut* 69, 2016–2024. doi: 10.1136/gutjnl-2019-319637

Schweitzer, A., Horn, J., Mikolajczyk, R. T., Krause, G., and Ott, J. J. (2015). Estimations of worldwide prevalence of chronic hepatitis B virus infection: a systematic review of data published between 1965 and 2013. *Lancet* 386, 1546–1555. doi: 10.1016/S0140-6736(15)61412-X

Sreedhar, A., Wiese, E. K., and Hitosugi, T. (2020). Enzymatic and metabolic regulation of lysine succinylation. *Genes Dis.* 7, 166–171. doi: 10.1016/j.gendis.2019.09.011

Sun, Y., Qi, Y., Peng, B., and Li, W. (2017). NTCP-reconstituted in vitro HBV infection system. *Methods Mol. Biol.* 1540, 1–14. doi: 10.1007/978-1-4939-6700-1_1

Tang, L. S. Y., Covert, E., Wilson, E., and Kottilil, S. (2018). Chronic hepatitis b infection: a review. *JAMA* 319, 1802–1813. doi: 10.1001/jama.2018.3795

Tropberger, P., Mercier, A., Robinson, M., Zhong, W., Ganem, D. E., and Holdorf, M. (2015). Mapping of histone modifications in episomal HBV cccDNA uncovers an unusual chromatin organization amenable to epigenetic manipulation. *Proc. Natl. Acad. Sci. U.S.A.* 112, E5715–E5724. doi: 10.1073/pnas.1518090112

Wang, Y., Guo, Y. R., Liu, K., Yin, Z., Liu, R., Xia, Y., et al. (2017). KAT2A coupled with the α-KGDH complex acts as a histone H3 succinyltransferase. *Nature* 552, 273–277. doi: 10.1038/nature25003

Weinert, B. T., Schölz, C., Wagner, S. A., Iesmantavicius, V., Su, D., Daniel, J. A., et al. (2013). Lysine succinylation is a frequently occurring modification in prokaryotes and eukaryotes and extensively overlaps with acetylation. *Cell Rep.* 4, 842–851. doi: 10.1016/j.celrep.2013.07.024

Yang, P. L., Althage, A., Chung, J., and Chisari, F. V. (2002). Hydrodynamic injection of viral DNA: a mouse model of acute hepatitis B virus infection. *Proc. Natl. Acad. Sci. U.S.A.* 99, 13825–13830. doi: 10.1073/pnas.202398599

Yang, P. L., Althage, A., Chung, J., Maier, H., Wieland, S., Isogawa, M., et al. (2010). Immune effectors required for hepatitis B virus clearance. *Proc Natl Acad Sci U S A* 107, 798–802. doi: 10.1073/pnas.0913498107

Yu, H.-B., Cheng, S.-T., Ren, F., Chen, Y., Shi, X.-F., Wong, V. K. W., et al. (2021). SIRT7 restricts HBV transcription and replication through catalyzing desuccinylation of histone H3 associated with cccDNA minichromosome. *Clin. Sci. (Lond.)* 135, 1505–1522. doi: 10.1042/CS20210392

Yuan, Y., Yuan, H., Yang, G., Yun, H., Zhao, M., Liu, Z., et al. (2020). IFN-α confers epigenetic regulation of HBV cccDNA minichromosome by modulating GCN5-mediated succinylation of histone H3K79 to clear HBV cccDNA. *Clin. Epigenet.* 12:135. doi: 10.1186/s13148-020-00928-z

Yuan, Y., Zhao, K., Yao, Y., Liu, C., Chen, Y., Li, J., et al. (2019). HDAC11 restricts HBV replication through epigenetic repression of cccDNA transcription. *Antiviral Res.* 172:104619. doi: 10.1016/j.antiviral.2019.104619

Qi, Z., Li, G., Hu, H., Yang, C., Zhang, X., Leng, Q., et al. (2014). Recombinant covalently closed circular hepatitis B virus DNA induces prolonged viral

persistence in immunocompetent mice. *J. Virol.* 88, 8045–8056. doi: 10.1128/JVI.01024-14

Zhang, W., Chen, J., Wu, M., Zhang, X., Zhang, M., Yue, L., et al. (2017). PRMT5 restricts hepatitis B virus replication through epigenetic repression of covalently closed circular DNA transcription and interference with pregenomic RNA encapsidation. *Hepatology* 66, 398–415. doi: 10.1002/hep.29133

Zhang, Z., Tan, M., Xie, Z., Dai, L., Chen, Y., and Zhao, Y. (2011). Identification of lysine succinylation as a new post-translational modification. *Nat. Chem. Biol.* 7, 58–63. doi: 10.1038/nchembio.495

Conflict of Interest: The authors declare that the research was conducted in the absence of any commercial or financial relationships that could be construed as a potential conflict of interest.

Publisher's Note: All claims expressed in this article are solely those of the authors and do not necessarily represent those of their affiliated organizations, or those of the publisher, the editors and the reviewers. Any product that may be evaluated in this article, or claim that may be made by its manufacturer, is not guaranteed or endorsed by the publisher.

frontiers in Microbiology

ORIGINAL RESEARCH
published: 28 January 2022
doi: 10.3389/fmicb.2021.792655

Induction of Reactive Oxygen Species Is Necessary for Efficient Onset of Cyprinid Herpesvirus 2 Replication: Implications for Novel Antiviral Strategy With Antioxidants

Cuiyu Lu[1†], Ruizhe Tang[1†], Meizhen Su[2], Jixing Zou[3] and Liqun Lu[1]*

[1] National Pathogen Collection Center for Aquatic Animals, Shanghai Ocean University, Shanghai, China, [2] Key Laboratory of Agriculture Ministry for Freshwater Aquatic Genetic Resources, Shanghai Ocean University, Shanghai, China, [3] Guangdong Laboratory for Lingnan Modern Agriculture, South China Agricultural University, Guangzhou, China

OPEN ACCESS

Edited by:
Yongqun Oliver He,
University of Michigan, United States

Reviewed by:
Sonam Popli,
University of Toledo, United States
Md. Golzar Hossain,
Bangladesh Agricultural University, Bangladesh

***Correspondence:**
Liqun Lu
lqlv@shou.edu.cn

† These authors have contributed equally to this work and share first authorship

Specialty section:
This article was submitted to Virology, a section of the journal Frontiers in Microbiology

Received: 10 October 2021
Accepted: 02 December 2021
Published: 28 January 2022

Citation:
Lu C, Tang R, Su M, Zou J and Lu L (2022) Induction of Reactive Oxygen Species Is Necessary for Efficient Onset of Cyprinid Herpesvirus 2 Replication: Implications for Novel Antiviral Strategy With Antioxidants. Front. Microbiol. 12:792655. doi: 10.3389/fmicb.2021.792655

Cyprinid herpesvirus 2 (CyHV-2) has caused great economic loss to the crucian carp breeding industry. Upon viral stimulation, eukaryotic cells generally activate the expression of anti-oxidative genes to maintain the intracellular oxidative balance and resist viral infection. Here, intracellular reactive oxygen species (ROS) levels in CyHV-2-infected cells were monitored to show that CyHV-2 induced the increase of intracellular ROS during early infection, and intracellular excessive accumulation of ROS was ameliorated during late infection, which was accompanied by activated expression of genes related to Nrf2 signaling pathway. In order to explore the interaction between CyHV-2 infection and ROS production, RyuF-2 cells were treated with either antioxidant epigallocatechin-3-gallate (EGCG) or berberine hydrochloride (BBH) and then infected with CyHV-2. Both BBH and EGCG could effectively inhibit the amplification of CyHV-2 while inhibiting the accumulation of intracellular ROS. Consistent with this, the oxidant stress-related genes were up-regulated by CyHV-2 infection and down-regulated in cells treated with either BBH or EGCG, through which the production of intracellular ROS was modulated. These results collectively demonstrated that early ROS accumulation favored the replication of CyHV-2, while antioxidants (BBH and EGCG) could inhibit the amplification of CyHV-2 by inhibiting ROS induction.

Keywords: Keap1-Nrf2 pathway, BBH, EGCG, CyHV-2, ROS

INTRODUCTION

Cyprinid herpesvirus 2 (CyHV-2), belonging to the genus *Cyprinivirus* and the family *Alloherpesviridae*, was first isolated and characterized from juvenile goldfish (*Carassius auratus auratus*) in Japan (Jung and Miyazaki, 1995). Recently, CyHV-2 has emerged as a virulent pathogen for cultured crucian carp (*Carassius auratus gibelio*) with high mortality and significant economic loss in cultured crucian carp and allogynogenetic gibel carp (Wang et al., 2012; Xu et al., 2013). CyHV-2 is an enveloped DNA virus with a 290.3-kb linear double-stranded DNA genome that

encodes approximately 150 genes (Davison et al., 2013). Goldfish are regarded as the natural host for CyHV-2, and the symptoms are generally represented by pale gills and swollen spleens and kidneys. CyHV-2 causes high mortality among juvenile goldfish at water temperatures between 15 and 25°C (Jeffery et al., 2007). Typical symptoms for crucian carp include lethargy and lack of appetite, bleeding and pale gills, pink ascites in the abdominal cavity, and enlarged spleen and kidneys, and death can occur within 1 to 2 days following the onset of clinical signs (Xu et al., 2014). Notably, the symptoms of CyHV-2 infection in crucian carp are significantly more severe than those in goldfish. Currently, neither vaccine nor medicine is available for the control of disease caused by CyHV-2 infection.

Virus generally stimulates the host's immune system response during the infection process and destroys the homeostasis of the cell. The balance of pro-oxidation/anti-oxidation in the internal environment is very important for maintaining the integrity of cellular structure and function. An excess of bad radical species, including reactive oxygen species (ROS) and reactive nitrogen species (RNS), is often associated with important diseases such as cancer and neurodegeneration (Liguori et al., 2018). Under normal physiological conditions, excessive free radicals will be cleared by the endogenous antioxidant defense through either enzymatic or non-enzymatic pathways. The primary antioxidant enzymes are superoxide dismutase (SOD), catalase (CAT), and glutathione peroxidase (GPx), while the major non-enzymatic antioxidants include bilirubin, α-tocopherol, β-carotene, albumin, and uric acid (Liguori et al., 2018). However, virus infection generally results in a transient ROS induction followed by a continuous and weak antioxidant defense in infected tissues to facilitate viral infection (Kumar et al., 2009; Souza et al., 2011). ROS suppresses the type-I interferon response by oxidizing cysteine 147 on murine stimulator of interferon genes (STING), indicating that ROS orchestrates anti-viral immune responses and can be exploited by viruses to evade cellular defenses (Tao et al., 2020). ROS is usually induced to a higher level immediately following viral attachment and manipulated by the virus to alternate cellular antiviral response; some viruses might modulate the ROS to a normal level after the onset of viral replication for avoiding its adverse effect on viral replication (Baruchel and Wainberg, 1992). ROS is also involved in tissue damage through regulating host inflammatory and immune responses (Akaike, 2001), and virus-induced oxidative stress serves as a common and important pathogenic mechanism for diseases caused by viral infection (Jackson et al., 2010).

Berberine (BBR), the most abundant isoquinoline alkaloid with a concentration range of 4.5–8% in different medical plant species, has been used to treat various inflammatory disorders and related diseases (Wang et al., 2019). Interestingly, low concentrations of berberine (5–20 μM) inhibited increased oxidative stress in 3T3-L1 cells by suppressing ROS production *via* increased GPx gene expression and GPx activity (Dong et al., 2015), while a higher concentration of berberine (40–160 μmol/l) dose-dependently induced ROS generation, G(2)/M phase arrest, and apoptosis in U266 cells (Hu et al., 2013). Furthermore, BBR has a great potential to reduce the effects of oxidative stress *in vivo* through markedly reducing Nox2-dependent cytoplasmic and mitochondrial ROS production (Sun et al., 2017).

Epigallocate-chin-3-gallate (EGCG) from green tea extract is a natural antioxidant that confers strong resistance against oxidation and free radicals (Lotito and Fraga, 1998; Yao et al., 2008) and is also regarded as a multifunctional molecule with anti-cancer (Yang and Wang, 2010) and immunity-enhancing properties (Sheikhzadeh et al., 2011). Favorable effects of EGCG have been largely attributed to its scavenging effects on free radicals, inhibition of ROS-generating mechanisms, and upregulation of major antioxidant enzymes including CAT, superoxide dismutase 1 (SOD1), superoxide dismutase 2 (SOD2), and GPx (Potenza et al., 2020).

The understanding of the interplay between virus-induced oxidative stress and anti-oxidative host response has shed light on the application of antioxidants as potential antiviral supplements for better management of some human viral diseases (Lee, 2018). For example, the upregulation of intracellular ROS during the early phase of retroviral infection plays an important role in viral establishment in the host cell, and the treatment of apocynin, an inhibitor of NADPH oxidase, could decrease viral titer in the mouse brain and increase the lifespan of infected mice (Kim and Wong, 2013). Recently, we reported that BBR could systematically impede CyHV-2 replication and protect crucian carp from CyHV-2 challenge in a dose-dependent manner (Su et al., 2021). However, it is not clear whether BBR-mediated modulation of ROS signaling involves the anti-CyHV-2 activity of BBR. In the present study, we monitored the ROS level and progeny virus production of susceptible cells during the infection course of CyHV-2 in the presence of either BBR or EGCG and provided evidence to show that antioxidants could serve as potential therapeutic agents against cyprinid herpesvirus 2 infection.

MATERIALS AND METHODS

Materials and Reagents

Berberine hydrochloride (BBH) and EGCG standards were purchased from Shanghai Macklin Biochemical Co., Ltd. (Shanghai, China). Dimethyl sulfoxide (DMSO) was purchased from Sigma (Shanghai, China). DCFDA/H2DCFDA cellular ROS assay kit was purchased from Abcam (Shanghai, China). M199 medium, FBS serum, penicillin/streptomycin, second antibodies, Pierce BCA Protein Assay Kit, and TRIzol reagent were purchased from Thermo Fisher Scientific (Shanghai, China). PrimeSTAR® Max DNA Polymerase, PrimeScript™ II 1st Strand cDNA Synthesis Kit, TaKaRa MiniBEST Viral RNA/DNA Extraction Kit Ver.5.0, and One-Step SYBR RT-PCR kit were purchased from Takara Bio (Beijing, China). All other reagents were purchased from Sangon Biotech (Shanghai, China). CyHV-2 strain ST-J1 (NCBI: NC_019495) and RyuF-2 cell line were provided by Dr. Motohiko Sano, University of Marine Science and Technology, Tokyo.

Cell Culture

Our cell lines are from the generous sharing of Dr. Motohiko Sano from Tokyo Ocean University. Cryopreserved samples of RyuF-2 cell stock at −150°C were thawed in a 37°C water bath before cell passage and virus propagation. Frozen cells were quickly thawed in a water bath, and the cryopreserved liquid was removed by centrifugation at 850 rpm for 3 min. M199 medium was used to resuspend RyuF-2 cells and supplemented with 10% heat-inactivated FBS and penicillin/streptomycin (50 U/ml/50 mg/ml). The suspension cells are adjusted to a density of 5 by the culture medium and then seeded on a 75-cm^2 culture flask/cm^2 coated with collagen. The cultured flask was placed in a humidified incubator at 27°C for culture. Before subculturing, the cells were grown to 80% confluence.

Virus Infection and Amplification

The virus was saved in normal M199 medium with 2% FBS (2% medium). After CyHV-2 was taken out from −150°C, the titer was quantified by gradient dilution counting. The 2% medium dilution was used to adjust the virus concentration until the multiplicity of infection (MOI) = 1. To infect the RyuF-2 cells with CyHV-2, the supernatant of the cells was removed, and viral inoculum was added immediately for an incubation time of 2 h. After that, the inoculum was replaced with 2% medium. Infected cells were cultured until CPE was developed in 80% of the cells. The remaining cells were scraped off with a spatula, the suspension was collected, and the cells and cell debris were removed by centrifugation at 12,000 *g* at 4°C for 20 min. The supernatant was filtered with a 0.22-μm filter to collect the virus. The harvested virus was equally divided and placed at −80°C for subsequent experiments. Before the experiment, the gradient dilution method was used to detect the virus titer again, and the virus concentration was adjusted according to the experimental cell density so that MOI = 1. CyHV-2 virus with a known titer was used to infect RyuF-2, which has a density of about 80%. After incubating for 2 h, the virus solution was removed, and the time point was counted as the start of infection 0 h post-infection (p.i.). The cultures were maintained for up to 96 h and were used between 0 and 96 h in culture.

Antioxidant Drug Treatment

Berberine hydrochloride and EGCG were separately dissolved in DMSO to prepare a 1-mg/ml preservation solution. RyuF-2 cells were used for experiments when their cell density was close to 80%. To adjust the concentration of BBH storage solution to 15, 20, and 25 μg/ml, 2% M199 medium was used. EGCG storage solution was diluted to 10, 20, and 30 μg/ml in the same way. The pretreatment was performed on RyuF-2 cells with different concentrations of drugs for 30 min. The drug treatment group kept the drug concentration unchanged and continued to incubate. In the virus infection group, the supernatant was removed and replaced with a virus solution, keeping the drug concentration unchanged. After incubating for 2 h, the virus solution was removed and 2% M199 medium was added with the same drug concentration. The cultures were maintained for up to 72 h and were used between 0 and 72 h in culture.

Measurement of Intracellular Reactive Oxygen Species

The intracellular ROS levels were estimated using a DCFDA/H2DCFDA cellular ROS assay kit according to a classic method (Heo et al., 2018). Briefly, the RyuF-2 cells were seeded into 96-well microtiter plates at 2.5×10^4 cells/well and were allowed to attach for 24 h at 27°C, and 100 μl of 1 × PBS buffer was added. The cells were then washed with 1 × PBS buffer. The 1 × PBS buffer was removed, and the cells were stained by adding 50 μl of the diluted DCFDA solution. Then, the cells were incubated for 45 min at 37°C in the dark. The fluorescence intensity was measured using a fluorescence microtiter ELISA plate reader at excitation and emission wavelengths of 485 and 535 nm, respectively. For cells infected with CyHV-2, cells were collected at 6, 12, 24, 36, 48, 60, 72, and 96 h after infection, and the intracellular ROS levels were quantified using the DCFDA/H2DCFDA cell ROS detection kit. For CyHV-2-infected cells in the presence of 15, 20, and 25 μg/ml BBR or 10, 20, and 30 μg/ml EGCG, the cells were harvested at 24 and 48 h p.i., and the intracellular ROS levels were quantitated using a DCFDA/H2DCFDA cellular ROS assay kit.

Nucleic Acid Extraction and Quantitative Real-Time Reverse Transcription Polymerase Chain Reaction Analysis

The supernatant of infected cells was obtained at different time points after infection for total DNA extraction. Viral DNA was extracted from the supernatant according to the instructions of the Viral Genomic DNA Extraction Kit (Qiagen). The total RNA of the RyuF-2 sample was extracted with 1 ml TRIzol reagent and purified using phenol/chloroform and ethanol precipitation. The NanoDrop Technologies instrument is used to quantify RNA. Each group of samples used 5 μg of RNA as the sample to generate cDNA for real-time quantitative qPCR, which was achieved by the corresponding reverse transcription reaction of PrimeScript RT Master Mix reagent. TB Green Premix Ex Taq II (2x) was used to amplify 1 μl of the resulting cDNA. According to the gene sequence obtained by the analysis of the transcriptome results in the laboratory, Primer Premier 5.1 (**Table 1**) was used to design a specific primer set for each open reading frame (ORF). The reaction contained 12.5 μl TB Green Premix Ex Taq II (2x) (Takara, Japan), 0.4 μM forward/reverse primers, and 200 ng cDNA. The thermal cycle program included the following: 95°C for 30 s, then 95°C for 5 s and 59°C for 30 min for 39 cycles. The qPCR reaction was repeated three times. In order to construct a standard curve, the DNA extracted from RyuF-2 cells was used for continuous decimal dilution. Primers from β-actin were successfully used in qPCR, using cDNA prepared from infected and uninfected cells as a template. A one-way analysis of variance (ANOVA) was used to calculate statistical significance. Origin 9.0 was used for data analysis and graphing. Values were considered as significant (*) if they had a *p*-value of 0.01 to 0.05, very significant (**) if they had a *p*-value of 0.001 to 0.01, and extremely significant (***) if they had a *p*-value of 0.0001 to 0.001.

TABLE 1 | Verification primers for oxidative stress-related genes.

Gene name	Nucleotide sequence (5′–3′)	Amplification efficiency (%)	r^2	Amplicon size (bp)
β-actin	F:CACTGTGCCCATCTACGAG	97.6	0.990	224
	R:CCATCTCCTGCTCGAAGTC			
Nrf2	F:TGCCGGAGTCGTTGGATATG	105.5	0.999	364
	R:TGCAGATCCATGGGGTTCAC			
Keap1	F:ACGCACGCATTTATGTGCTC	103	0.996	105
	R:TCATGTTGGTGACCTCGCTC			
CAT	F:AGAATTTGACCGTTGAAGAGG	101.7	0.986	253
	R:GGAAGTTGCCGTTGGAGAT			
GSS	F:AGAGGCTCTTTGTAGATGGC	106.6	0.981	261
	R:GCGAGATGGGTACTGATGTC			
SOD	F:CAGGGCACTACAGGTCTC	98.1	0.980	128
	R:ACATTCTCCCAGTTCACAA			
ORF121	F:GGACATCAAATCGGCAGCTC	101.4	0.9938	193
	R:CTCCTCCATGGTCACATCGG			

Western Blot

Cell samples were collected to extract total protein by boiling with 2X SDS-PAGE protein loading buffer. Thermo Scientific Pierce BCA protein detection kit was used to quantify protein concentration. The protein (20 g) was separated on 10–12% SDS-PAGE and then transferred to PVDF membrane. The membrane was blocked in 1% TBS-T buffer containing 5% skim milk for 1 h at room temperature and then incubated overnight with homemade anti-ORF121 polyclonal antibody (Yu et al., 2019) (1:200 dilution). After washing the membrane with TBS-T three times, horseradish peroxidase-conjugated secondary antibody (diluted 1:1,000) was added and incubated for 2 h at room temperature and then washed with TBS-T three times for 15 min. A chemiluminescence imaging system (Bio-Rad, China) was used to detect the signal with the ECL + western blot kit.

RESULTS

Cyprinid Herpesvirus 2 Induced the Expression of Genes in Keap1-Nrf2 Pathway and Modulated Cellular Reactive Oxygen Species Accumulation During Infection

In a recent study to probe host response to viral infection, we identified the differential expression genes in crucian carp cells underlying CyHV-2 infection by transcriptomics analysis (Fei et al., 2020). Primary data analysis of genes involved in the Keap1-Nrf2 pathway indicated that the TPM (transcripts per kilobase million) values of Nrf2, CAT, and SOD2 genes in CyHV-2-infected cells at 48 h post-infection were dramatically higher than those in the negative control (NC), and the values of Keap 1 and GSS were also shown to be slightly higher than those of the control (**Figure 1**). In order to verify the effect of CyHV-2 infection on the expression of related genes in the Keap1-Nrf2 pathway, we used quantitative real-time RT-PCR analysis to compare the transcriptional expression levels of Keap1, Nrf2, CAT, GSS, and SOD2 in normal cells and CyHV-2-infected cells (**Figure 2**). At 24, 48, and 72 h after infection with CyHV-2, RyuF-2 cells were collected for total RNA extraction. All qRT-PCR assays were performed in triplicate, with β-actin used as an endogenous control. As shown in **Figure 2**, CyHV-2 significantly up-regulates all tested genes to higher levels compared to the corresponding low steady-state levels in the control cells. Specifically, the highest induction rate was recorded for Nrf2 and GSS genes at 48 h p.i. (**Figures 2B,E**). In general, 48 h p.i. seemed to be a time point for all the genes to be upregulated to a peak level.

The Keap1-Nrf2 pathway regulates both mitochondrial and cytosolic ROS production (Kovac et al., 2015); thus, the above data predicted that CyHV-2 infection might interfere with ROS synthesis and activate host oxidative stress response. To clarify whether CyHV-2 infection disturbed the host cellular redox balance, we monitored the ROS level following CyHV-2 infection using DCFDA/H2DCFDA cellular ROS assay. Following CyHV-2 infection at a MOI = 1, the ROS level in RyuF-2 cells was dramatically induced to a higher level with maximum ROS accumulation at 24 h p.i. and then gradually reversed to a constant and lower level (**Figure 3A**). Successful replication of CyHV-2 in RyuF-2 cells was reflected by the titration of progeny virus from the virus supernatant after infection by quantitating the genome copy number using a real-time polymerase chain reaction (PCR) analysis. As shown in **Figure 3B**, the produced CyHV-2 in supernatant significantly rose to a higher level of more than 10^7 genome copy number/ml since 24 h p.i. and then gradually increased until late infection of 96 h p.i. The experiments indicated that higher ROS accumulation was only induced at early phase of CyHV-2 infection, and the high level of ROS was reversed during late infection.

The Effects of Antioxidants on the Keap1-Nrf2 Pathway During Cyprinid Herpesvirus 2 Infection

Epigallocatechin-3-gallate, the most abundant polyphenolic substance in green tea, typically plays a critical role in free radical scavenging owing to its antioxidant nature and subsequently

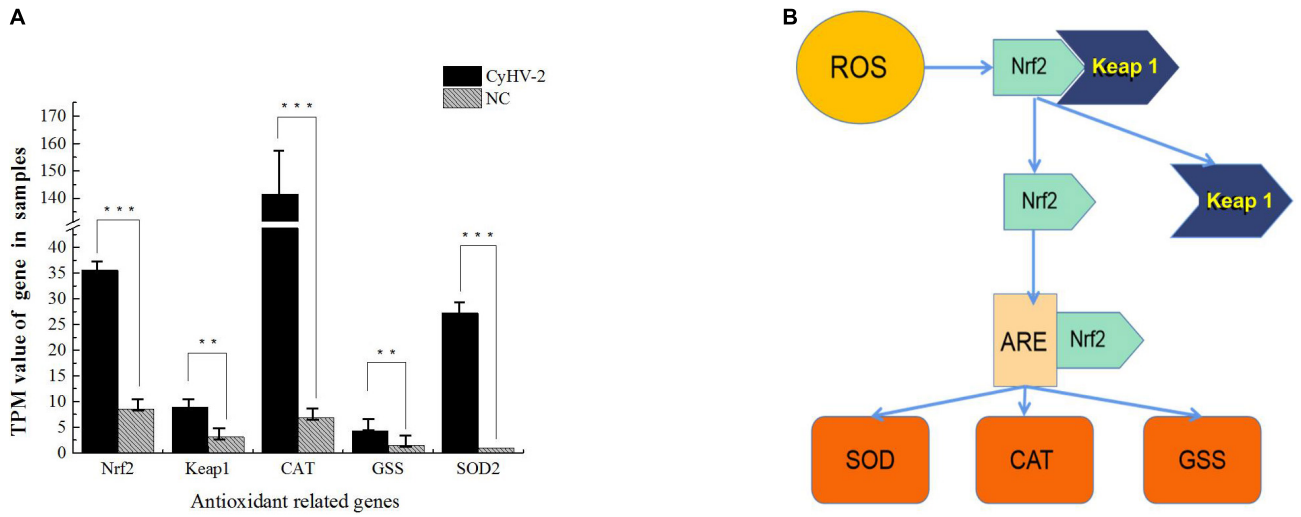

FIGURE 1 | Key molecules of Nrf2 signaling pathway are induced by cyprinid herpesvirus 2 (CyHV-2) in RNA-seq analysis. TPM is transcripts per kilobase million, the transcripts per kilobase of exon model per million mapped reads. TPM is a method of gene expression standardization, which visualizes differential expression analysis. The transcriptome related to CyHV-2 infection was analyzed in the laboratory using the Mega Cloud platform. The differences in the expression of antioxidant-related genes were analyzed and compared between the groups. The result is shown in **(A)**, the difference of TPM values in the Nrf2 signaling pathway identified in transcriptome analysis. According to the known reaction mode of Nrf2-ARE antioxidant element combined with the analysis result, **(B)** is inferred. **(B)** Flow chart of proposed Nrf2 signaling pathway induced by CyHV-2.

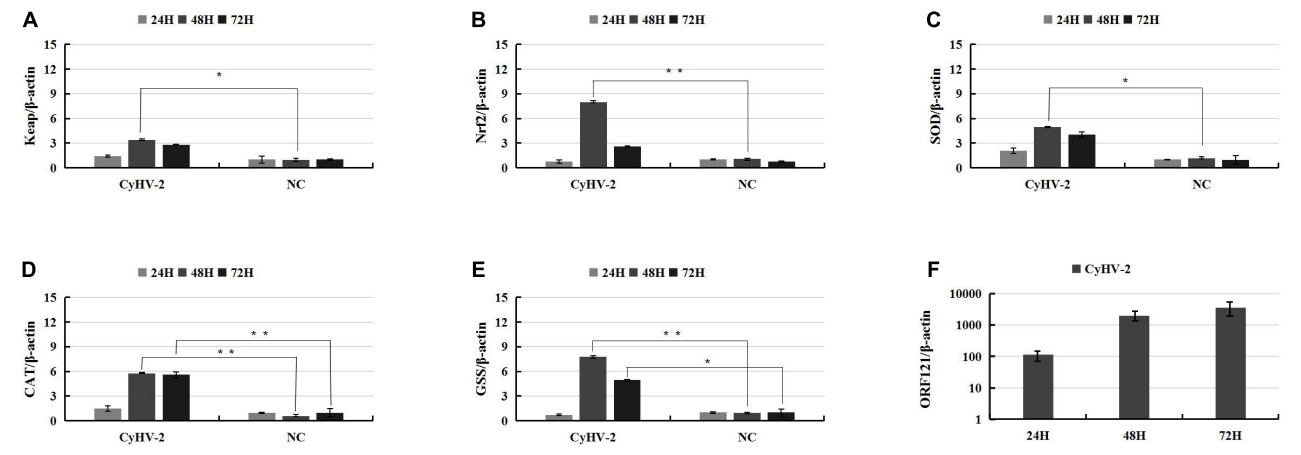

FIGURE 2 | CyHV-2 induces expression of key genes of Nrf2 signaling pathway in RyuF-2 cells. Quantitative real-time RT-PCR analysis was performed to compare the transcriptional expression levels of Keap1 **(A)**, Nrf2 **(B)**, SOD2 **(C)**, CAT **(D)**, GSS **(E)** and viral ORF121 **(F)** in infected cells. The mRNA level was normalized against housekeeping gene β-actin. Mock infected cells served as negative control. Similar results were obtained from three independent experiments. Data were represented as Means SD. $^{*}P < 0.05$, $^{**}P < 0.01$.

exerts a large number of medical activities in cancer control, viral diseases, bacterial diseases, neurodegenerative diseases, etc. (Xu et al., 2017). Thus, we were interested to test the effect of EGCG on the CyHV-2-mediated upregulation of Keap1-Nrf2 pathway. For this purpose, RyuF-2 cells were infected with CyHV-2 at a MOI = 1 in the presence of 10 μg/ml EGCG. At 24, 48, and 72 h post-infection, the infected cells were harvested for total RNA extraction and subjected to gene expression assay by quantitative real-time RT-PCR analysis. MOCK-infected cells treated with 10 μg/ml EGCG served as negative control, and CyHV-2-infected cells without EGCG treatment served as positive control. As shown in **Figure 4**, the treatment of MOCK-infected cells with EGCG could result in an increased expression of Keap1, Nrf2, GSS, and CAT gene; in comparison to CyHV-2-infected cell controls, the treatment of CyHV-2-infected cells with EGCG could result in a significant increase of Nrf2 at 48 h p.i., Keap 1 at 72 h p.i., GSS at all three time points, and CAT at 72 h p.i. Thus, EGCG could enhance the expression of key genes in the Keap1-Nrf2 pathway except for SOD gene, which was independent of CyHV-2 infection.

Affecting various signaling pathways, berberine has been shown to decrease the activity of xanthine oxidase, COX2,

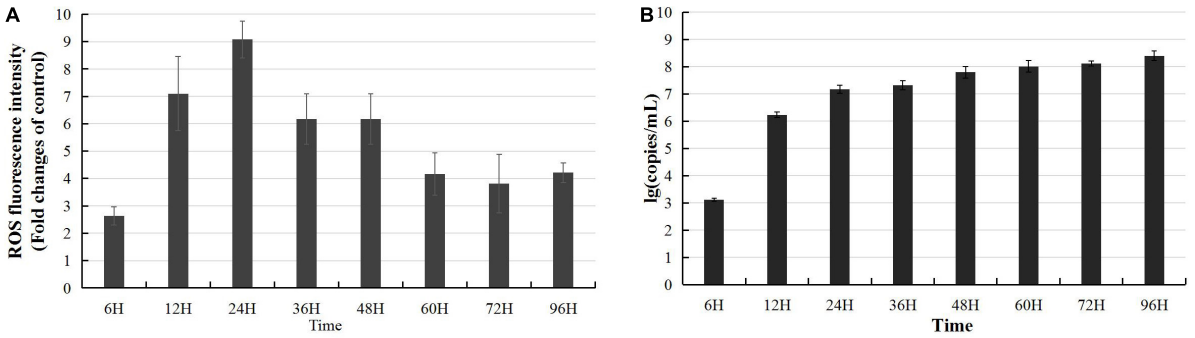

FIGURE 3 | Modulation of reactive oxygen species (ROS) accumulation during CyHV-2 infection in RyuF-2 cells. CyHV-2 with MOI = 1 was used to infect RyuF-2. Cell samples and supernatant after infection were obtained at 6, 12, 24, 36, 48, 60, 72, and 92 h after infection. The DCFDA/H2DCFDA cellular ROS assay kit is used to detect changes in the accumulation of intracellular ROS after virus infection. The control group cells were used as the normalization standard to reduce the differences between groups. The results are shown in **(A)**. After infection, the supernatant was used to obtain total DNA for detection of virus amplification. The early gene ORF121 was used as a representative gene for detection of CyHV-2 replication, as shown in **(B)**. The RT-PCR results were processed using the absolute quantification standard program, and the data were expressed as the mean SD.

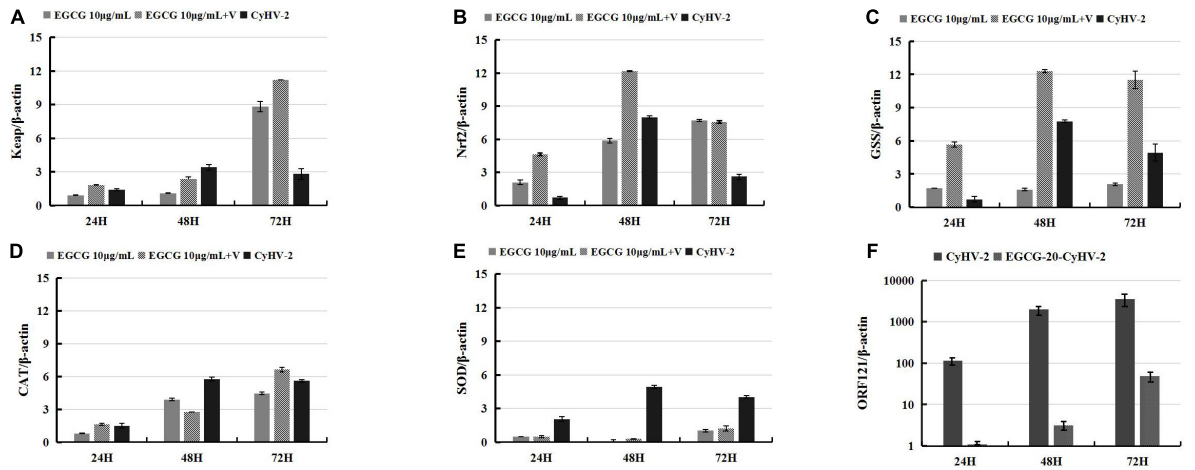

FIGURE 4 | Epigallocate-chin-3-gallate (EGCG) enhanced the CyHV-2-induced expression of genes of Nrf2 signaling pathway in RyuF-2 cells. Quantitative real-time RT-PCR analysis was performed to compare the transcriptional expression levels of Keap1 **(A)**, Nrf2 **(B)**, GSS **(C)**, CAT **(D)**, SOD2 **(E)** and viral ORF121 **(F)** in infected cells. The mRNA level was normalized against housekeeping gene β-actin. MOCK-infected cells treated with 10 μg/ml EGCG and CyhV-2-infected cells without EGCG treatment served as controls. Similar results were obtained from three independent experiments. Data were represented as means SD.

and superoxide dismutase and subsequently reduce ROS levels (Kaboli et al., 2014). As an alternative antioxidant, BBR was subjected for analysis on its effect on the CyHV-2-mediated upregulation of the Keap1-Nrf2 pathway. For this purpose, RyuF-2 cells were infected with CyHV-2 at a MOI = 1 in the presence of 20 μg/ml BBH. At 24, 48, and 72 h post-infection, the infected cells were harvested for total RNA extraction and subjected to gene expression assay by quantitative real-time RT-PCR analysis. MOCK-infected cells treated with 20 μg/ml BBH served as negative control, and CyHV-2 infected cells without BBH treatment served as positive control. As shown in **Figure 5**, in contrast to MOCK-infected cells treated with BBH, CyHV-2 infection resulted in an increased expression of all tested genes; compared with CyHV-2-infected control cells, the treatment of CyHV-2-infected cells with BBH could result in a significant increase of Nrf2, Keap 1, and GSS at 48 h p.i. The gene expression level was not affected at 48 h p.i. for CAT and at 72 h p.i. for SOD. The results even suggested that these two genes might be downregulated at other time points (**Figures 5D,E**). Overall, the above experiments suggested that antioxidants, such as EGCG and BBH, could efficiently activate the Keap1-Nrf2 pathway that was induced to a higher level by CyHV-2 challenge in RyuF-2 cells.

The Effects of Antioxidants on Cyprinid Herpesvirus 2-Modulated Reactive Oxygen Species and Viral Replication in RyuF-2 Cells

The above experiments indicated that CyHV-2 modulated ROS level in infected cells and could induce dramatic ROS accumulation during early infection. We are interested to know

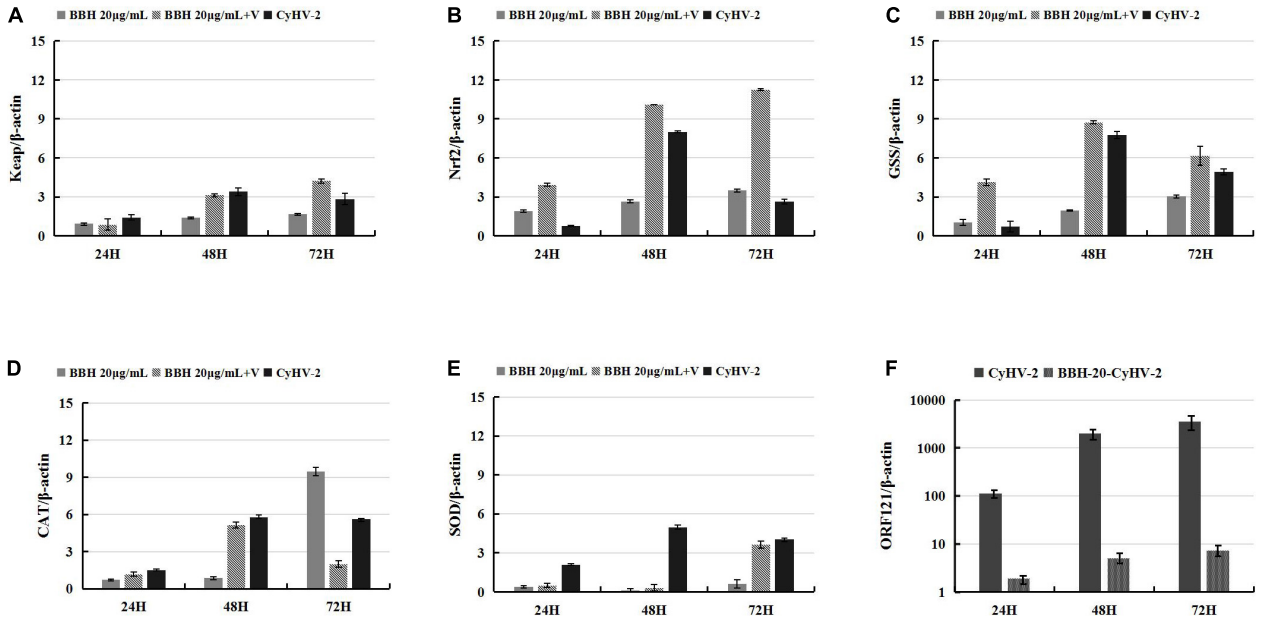

FIGURE 5 | Berberine hydrochloride (BBH) enhanced the CyHV-2-induced expression of genes of Nrf2 signaling pathway in RyuF-2 cells. Quantitative real-time RT-PCR analysis was performed to compare the transcriptional expression levels of Keap1 **(A)**, Nrf2 **(B)**, GSS **(C)**, CAT **(D)**, SOD2 **(E)** and viral ORF121 **(F)** in infected cells. The mRNA level was normalized against housekeeping gene β-actin. MOCK-infected cells treated with 20 μg/ml BBH and CyhV-2-infected cells without BBH treatment served as controls. Similar results were obtained from three independent experiments. Data were represented as means SD.

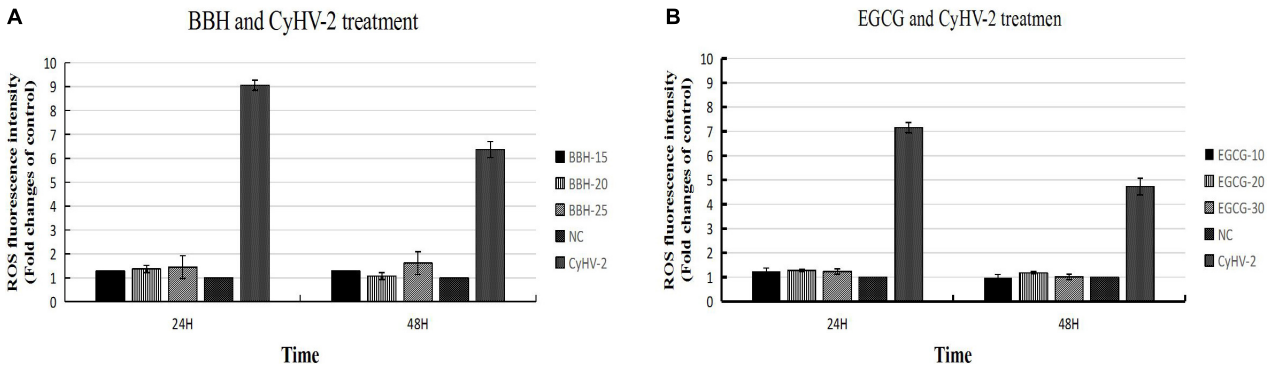

FIGURE 6 | BBH and EGCG antagonized the ROS induction mediated by CyHV-2 infection in RyuF-2 cells. RyuF-2 cells were treated with 15, 20, and 25 μg/ml BBH **(A)** or 10, 20, and 30 μg/ml EGCG **(B)** and infected with CyHV-2 at a MOI = 1. At 24 and 48 h p.i., cells were harvested for ROS detection as reflected by the strength of fluorescence signal. MOCK-infected cells served as the negative control and CyhV-2-infected cells without BBH or EGCG treatment served as positive control. Similar results were obtained from three independent experiments. Data were represented as means SD.

what will happen if the ROS accumulation is inhibited by antioxidants such as BBR and EGCG during CyHV-2 infection. RyuF-2 cells were treated with various doses of BBH (0, 15, 20, and 25 μg/ml BBH) or EGCG (0, 10, 20, and 30 μg/ml EGCG) and subjected to CyHV-2 infection at a MOI = 1. At 24 and 48 h post-infection, the cells were harvested for DCFDA/H2DCFDA cellular ROS assay, in which the ROS level was reflected by the fluorescence strength detected from the cellular extract. The NC group referred to normal cells without antioxidant treatment and viral infection. Cells infected with CyHV-2 and treated with 0 μg/ml antioxidant served as positive control (CyHV-2 group). As shown in **Figure 6**, both BBH and EGCG effectively counteracted the accumulation of ROS induced by CyHV-2 infection at 24 and 48 h post-infection. In contrast to the dramatic increase of ROS level at indicated time points post-infection, treatment with BBH (**Figure 6A**) or EGCG (**Figure 6B**) resulted in low ROS accumulation in CyHV-2-infected cells, which was close to the level of the NC group.

The above experiments indicated that ROS accumulation was efficiently inhibited by BBH or EGCG during CyHV-2 infection. Then, it will be interesting to know the effect of these antioxidants on CyHV-2 replication. For this purpose, we determined the progeny virus in the supernatants of infected cells by quantifying the viral genome copy number through real-time

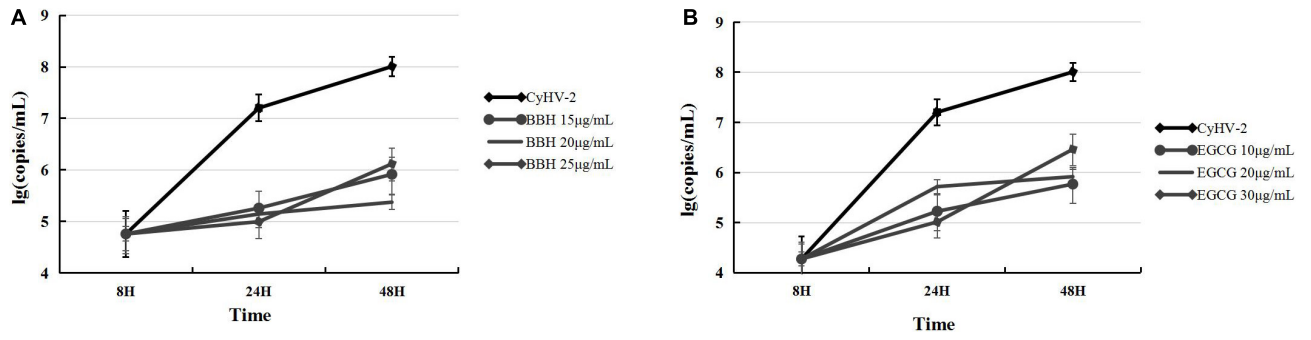

FIGURE 7 | BBH and EGCG inhibited the production of progeny virus in RyuF-2 cells infected with CyHV-2. RyuF-2 cells were treated with 15, 20, and 25 μg/ml BBH **(A)** or 10, 20, and 30 μg/ml EGCG **(B)** and infected with CyHV-2 at a MOI = 1. At 8, 24, and 48 h p.i., supernatants of infected cells were harvested for viral genome copy quantification by real-time polymerase chain reaction (PCR) analysis. CyhV-2-infected cells without BBH or EGCG treatment served as positive control. Similar results were obtained from three independent experiments. Data were represented as means SD.

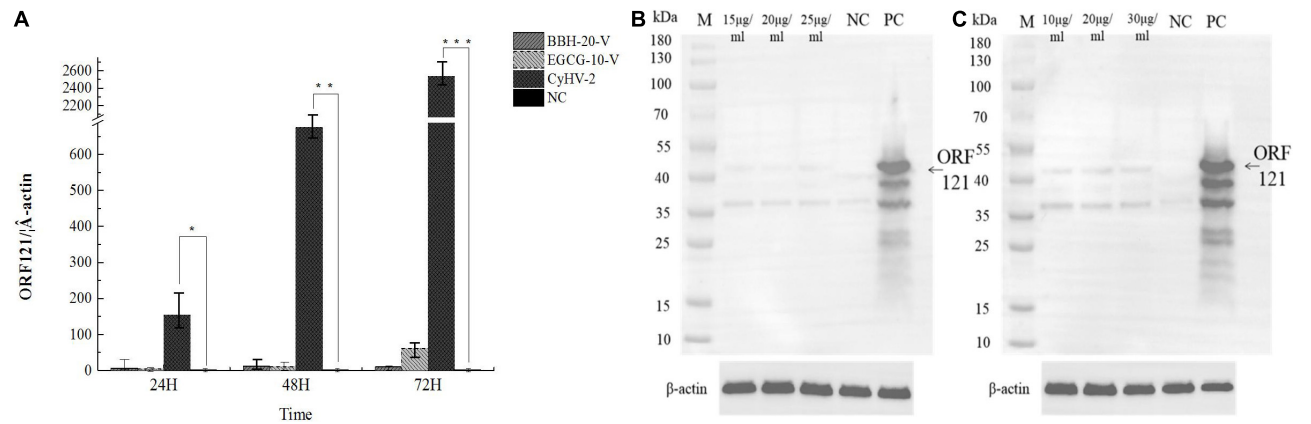

FIGURE 8 | Inhibition of viral gene transcription and viral protein synthesis by either BBH or EGCG. RyuF-2 cells were treated with 15, 20, and 25 μg/ml BBH or 10, 20, and 30 μg/ml EGCG and infected with CyHV-2 at a MOI = 1. At 24, 48, and 72 h p.i., infected cells treated with 20 μg/ml BBH or 10 μg/ml EGCG were harvested for viral gene expression analysis with the ORF121 as target by real-time RT-PCR analysis **(A)**. At 72 h p.i., infected cells treated with 15, 20, and 25 μg/ml BBH **(B)** or 10, 20, and 30 μg/ml EGCG **(C)** were harvested for protein expression analysis by western blot, which targeted ORF121 with a home-made anti-ORF121 polyclonal antibody. Real-time RT-PCR results were obtained from three independent experiments, and data were presented as means SD. $^{*}P < 0.05$; $^{**}P < 0.01$. MOCK-infected cells served as the negative control and CyhV-2-infected cells without BBH or EGCG treatment served as the positive control. Housekeeping protein β-actin served as the internal control in the western blot analysis.

PCR analysis. The antiviral activity of antioxidants *in vitro* was evaluated according to the reduced level of progeny virus produced from CyHV-2-infected RyuF-2 cells in the presence of different concentrations of EGCG or BBH. The supernatants of infected RyuF-2 cells, in the presence of BBH at 0, 15, 20, and 25 μg/ml or EGCG at 0, 10, 20, and 30 μg/ml, were collected at 8, 24, and 48 h post-infection for total viral genome extraction and quantification. As shown in **Figure 7**, both BBH and EGCG dose-dependently suppressed the production of progeny virus from infected cells, and the overall efficiency of these two antioxidants was similar at 48 h post-infection. At 8 h post-infection, the treatment of EGCG (**Figure 7B**) displayed a lower level of CyHV-2 (**Figure 7A**) in supernatants than that of BBH, suggesting a more robust effect of EGCG in antagonizing viral replication at this time point.

To confirm the antiviral effects of BBH and EGCG, we continued to investigate the transcriptional and translational expression levels of ORF121, an immediately early gene encoded by CyHV-2 (Tang et al., 2020). The infected RyuF-2 cells in the presence of 20 μg/ml BBH or 10 μg/ml EGCG were harvested at 24, 48, and 72 h post-infection, and total protein samples were extracted from the infected cells for ORF121 detection by western blot analysis; total RNA samples were extracted from the infected cells for ORF121 mRNA detection by real-time RT-PCR analysis. As shown in **Figure 8A**, the RyuF-2 cells infected with CyHV-2 resulted in robust transcriptional expression of ORF121, which lasted until 72 h post-infection; treatment with either BBH or EGCG significantly suppressed the transcriptional expression of ORF121 throughout the infection course. As shown in **Figures 8B,C**, in contrast to the strong signal of ORF121 protein from CyHV-2-infected RyuF-2 cells in the immunoblot analysis, the treatment of BBH or EGCG at indicated concentrations demonstrated a dramatic decrease of protein signal, which

indicated that either BBH or EGCG was effective in inhibiting viral protein synthesis.

Thus, the above experiments suggested that BBH and EGCG could significantly block CyHV-2-induced ROS accumulation, inhibit viral gene transcription and protein synthesis, and reduce the production of progeny virus.

DISCUSSION

A virus needs to keep oxidative stress at a level optimal for viral reproduction, which is usually higher than normal; viral infection thus generally induces oxidative stress in infected cells, which must be in tight control in order to minimize the potentially detrimental effects of ROS on the overall health of the infected host cell (Lee, 2018). Although infection-initiated oxidative stress plays a key role in the activation of innate immunity to fight off pathogenic microbes, a number of viruses were shown to induce oxidative stress on purpose to facilitate their replication inside the cell, which at least included influenza virus, respiratory syncytial virus (RSV), human metapneumovirus (hMPV), dengue virus (DENV), rotavirus, herpes simplex virus, Zika virus, and HIV (McCord et al., 2020). CyHV-2 infection in crucian carp remains a challenge for the aquaculture section worldwide, and the lack of vaccine or medicine in the field urgently required the development of a novel antiviral strategy (Su et al., 2021). Nrf2 and its principal negative regulator Keap1 play a central role in the maintenance of intracellular redox homeostasis and regulation of inflammation. The purpose of this study is to evaluate the effects of antioxidants (BBH and EGCG) on CyHV-2 infection in crucian carp cells, which is based on the knowledge that CyHV-2 regulates the Keap1-Nrf2 pathway (**Figures 1**, **2**) and modulates ROS accumulation in infected cells (**Figure 3**).

The Nrf2-dependent antioxidative pathway is regarded as an adaptive cellular response to oxidative and electrophilic stress and a responsive host defense system if caused by a viral infection. In a study to apply Nrf2 agonists as anti-rotaviral drugs, initial induction of Nrf2 concurred with a virus-induced early burst of oxidative stress, and rotavirus infection was determined to be sensitive to antioxidant treatments (Patra et al., 2020). NrF2 belongs to the CNC family and is mainly involved in the elimination of cell endogenous ROS. In a normal cell environment, Nrf2 and Keap1 combine through the Neh2 structure of Nrf2 to promote ubiquitination of Nrf2 and degrade it through the proteasome pathway. It has been found that Nrf2 can regulate hundreds of different genes involved in the maintenance of cell homeostasis, including heme oxygenase-1, NADPH quinone reductase, superoxide dismutase, and other antioxidant enzymes related to ROS elimination (**Figure 1B**). Our data indicated that BBH and EGCG could efficiently activate the Nrf2-dependent antioxidative pathway in normal RyuF-2 cells (**Figures 4**, **5**), as well as CyHV-2-infected cells (**Figures 4**, **5**); the induction of ROS accumulation during early viral infection (**Figure 3**) could be abolished through treatment of BBH or EGCG (**Figure 6**). Thus, CyHV-2-mediated induction could be modulated by antioxidants, which was consistent with reports from other viruses (McCord et al., 2020). As expected, either BBH or EGCG efficiently blocks viral gene transcription (**Figure 8A**), viral protein synthesis (**Figure 8B**), and progeny virus production (**Figure 7**). Thus, our study is the first to successfully apply antioxidants to counter fish herpes virus infection *in vitro*.

It is generally believed that virus has evolved to gain the ability to manipulate the Nrf2 pathway and control the ROS level to its favor. However, it is still not understood how the early ROS accumulation was produced for CyHV-2, neither is the mechanism involved in maintaining low ROS level during late infection known. Based on our data, the treatment of antioxidants seemed to upregulate the cytoprotective and detoxifying genes of the Keap1-Nrf2 pathway (**Figures 4**, **5**), which is also targeted and regulated by CyHV-2 (**Figures 1**, **2**). Antioxidants like EGCG and BBH should be beneficial not only for disruption of the ROS-dependent steps of the viral life cycle but also for the direct amelioration of the stressed conditions of the infected host cells. Our data thus supported the idea that Nrf2 modulators might be able to serve as a promising supplement for viral diseases by therapeutic modulation of virus-induced oxidative stress (Lee, 2018). Although the transcriptional regulation of the host Keap1-Nrf2 pathway by CyHV-2 merits further investigation, complex regulatory mechanisms were believed to occur in oxidative stress-related pathogenesis, such as the reduction of mitochondrial damage, regulation of calcium ions in the cell, programmed cell death, and autophagy (Liu et al., 2021).

CONCLUSION

Cyprinid herpesvirus 2 activated the Keap1-Nrf2 pathway and modulated ROS accumulation in host cells, especially during early infection. Antioxidants such as BBH and EGCG further enhanced the expression of genes involved in the Keap1-Nrf2 pathway and abolished the ROS-induction effect of CyHV-2 in infected cells. In the presence of antioxidants, viral gene expression and protein synthesis were dramatically inhibited resulting in decreased replication efficacy of CyHV-2. The current study should shed light on developing antioxidants as environmentally friendly reagents toward fighting the disease caused by CyHV-2 infection in aquaculture.

DATA AVAILABILITY STATEMENT

The original contributions presented in the study are included in the article/supplementary material of referenced article (Fei et al., 2020), further inquiries can be directed to the corresponding author. The previously analysed transcriptome data can be found in online repositories. The names of the repository/repositories and accession number(s) can be found below: NCBI BioProject, PRJNA596297, and PRJNA596598.

AUTHOR CONTRIBUTIONS

LL, RT, and CL conceptualized the study. RT and CL made contributions in the methodology and wrote the original draft. RT, CL, MS, and JZ performed the investigation. LL reviewed

and edited the manuscript, supervised the study, administrated the project, and acquired funding. All authors contributed to the article and approved the submitted version.

FUNDING

This work was funded by the Technology Innovation Action Program of Shanghai, China (no. 17391902100) and the China Agriculture Research System of MOF and MARA (no. CARS-45-19).

ACKNOWLEDGMENTS

We acknowledge the technical support from the Experimental Center of College of Fishery and Life Science, Shanghai Ocean University.

REFERENCES

Akaike, T. (2001). Role of free radicals in viral pathogenesis and mutation. *Rev. Med. Virol.* 11, 87–101. doi: 10.1002/rmv.303

Baruchel, S., and Wainberg, M. A. (1992). The role of oxidative stress in disease progression in individuals infected by the human immunodeficiency virus. *J. Leukoc. Biol.* 52, 111–114. doi: 10.1002/jlb.52.1.111

Davison, A. J., Kurobe, T., Gatherer, D., Cunningham, C., Korf, I., Fukuda, H., et al. (2013). Comparative genomics of carp herpesviruses. *J. Virol.* 87, 2908–2922. doi: 10.1128/JVI.03206-12

Dong, S.-F., Yasui, N., Negishi, H., Kishimoto, A., Sun, J.-N., and Ikeda, K. (2015). Increased oxidative stress in cultured 3T3-L1 cells was attenuated by berberine treatment. *Nat. Product Commun.* 10:1934578X1501000626. doi: 10.1177/1934578X1501000626

Fei, Y., Han, M., Chu, X., Feng, Z., Yu, L., Luo, Y., et al. (2020). Transcriptomic and proteomic analyses reveal new insights into the regulation of immune pathways during cyprinid herpesvirus 2 infection in vitro. *Fish Shellf. Immunol.* 106, 167–180. doi: 10.1016/j.fsi.2020.07.044

Heo, J.-R., Lee, G.-A., Kim, G.-S., Hwang, K.-A., and Choi, K.-C. (2018). Phytochemical-induced reactive oxygen species and endoplasmic reticulum stress-mediated apoptosis and differentiation in malignant melanoma cells. *Phytomedicine* 39, 100–110. doi: 10.1016/j.phymed.2017.12.006

Hu, H.-y., Li, K.-p., Wang, X.-j., Liu, Y., Lu, Z.-g., Dong, R.-h., et al. (2013). Set9, NF-κB, and microRNA-21 mediate berberine-induced apoptosis of human multiple myeloma cells. *Acta Pharmacol. Sin.* 34, 157–166. doi: 10.1038/aps.2012.161

Jackson, A. C., Kammouni, W., Zherebitskaya, E., and Fernyhough, P. (2010). Role of oxidative stress in rabies virus infection of adult mouse dorsal root ganglion neurons. *J. Virol.* 84, 4697–4705. doi: 10.1128/JVI.02654-09

Jeffery, K., Bateman, K., Bayley, A., Feist, S., Hulland, J., Longshaw, C., et al. (2007). Isolation of a cyprinid herpesvirus 2 from goldfish, *Carassius auratus* (L.), in the UK. *J. Fish Dis.* 30, 649–656. doi: 10.1111/j.1365-2761.2007.00847.x

Jung, S., and Miyazaki, T. (1995). Herpesviral haematopoietic necrosis of goldfish, *Carassius auratus* (L.). *J. Fish Dis.* 18, 211–220. doi: 10.1111/j.1365-2761.1995.tb00296.x

Kaboli, P. J., Rahmat, A., Ismail, P., and Ling, K.-H. (2014). Targets and mechanisms of berberine, a natural drug with potential to treat cancer with special focus on breast cancer. *Eur. J. Pharmacol.* 740, 584–595. doi: 10.1016/j.ejphar.2014.06.025

Kim, S. J., and Wong, P. K. (2013). ROS upregulation during the early phase of retroviral infection plays an important role in viral establishment in the host cell. *J. Gen. Virol.* 94(Pt 10):2309. doi: 10.1099/vir.0.055228-0

Kovac, S., Angelova, P. R., Holmström, K. M., Zhang, Y., Dinkova-Kostova, A. T., and Abramov, A. Y. (2015). Nrf2 regulates ROS production by mitochondria and NADPH oxidase. *Biochim. Biophys. Acta Gen. Sub.* 1850, 794–801. doi: 10.1016/j.bbagen.2014.11.021

Kumar, S., Misra, U. K., Kalita, J., Khanna, V. K., and Khan, M. Y. (2009). Imbalance in oxidant/antioxidant system in different brain regions of rat after the infection of Japanese encephalitis virus. *Neurochem. Int.* 55, 648–654. doi: 10.1016/j.neuint.2009.06.008

Lee, C. (2018). Therapeutic modulation of virus-induced oxidative stress via the Nrf2-dependent antioxidative pathway. *Oxidat. Med. Cell. Long.* 2018:6208067. doi: 10.1155/2018/6208067

Liguori, I., Russo, G., Curcio, F., Bulli, G., Aran, L., Della-Morte, D., et al. (2018). Oxidative stress, aging, and diseases. *Clin. Interven. Aging* 13:757. doi: 10.2147/CIA.S158513

Liu, Y., Yang, X., Liu, Y., Jiang, T., Ren, S., Chen, J., et al. (2021). NRF2 signalling pathway: new insights and progress in the field of wound healing. *J. Cell. Mol. Med.* 25, 5857–5868. doi: 10.1111/jcmm.16597

Lotito, S. B., and Fraga, C. G. (1998). (+)-Catechin prevents human plasma oxidation. *Free Radic. Biol. Med.* 24, 435–441. doi: 10.1016/S0891-5849(97)00276-1

McCord, J. M., Hybertson, B. M., Cota-Gomez, A., Geraci, K. P., and Gao, B. (2020). Nrf2 activator PB125® as a potential therapeutic agent against COVID-19. *Antioxidants* 9:518. doi: 10.3390/antiox9060518

Patra, U., Mukhopadhyay, U., Mukherjee, A., Sarkar, R., and Chawla-Sarkar, M. (2020). Progressive rotavirus infection downregulates Redox-Sensitive transcription factor Nrf2 and Nrf2-Driven transcription units. *Oxidat. Med. Cell. Long.* 2020:7289120. doi: 10.1155/2020/7289120

Potenza, M. A., Iacobazzi, D., Sgarra, L., and Montagnani, M. (2020). The intrinsic virtues of EGCG, an extremely good cell guardian, on prevention and treatment of diabesity complications. *Molecules* 25:3061. doi: 10.3390/molecules25133061

Sheikhzadeh, N., Nofouzi, K., Delazar, A., and Oushani, A. K. (2011). Immunomodulatory effects of decaffeinated green tea (*Camellia sinensis*) on the immune system of rainbow trout (*Oncorhynchus mykiss*). *Fish Shellf. Immunol.* 31, 1268–1269. doi: 10.1016/j.fsi.2011.09.010

Souza, F. N., Monteiro, A. M., dos Santos, P. R., Sanchez, E. M. R., Blagitz, M. G., Latorre, A. O., et al. (2011). Antioxidant status and biomarkers of oxidative stress in bovine leukemia virus-infected dairy cows. *Vet. Immunol. Immunopathol.* 143, 162–166. doi: 10.1016/j.vetimm.2011.05.028

Su, M., Tang, R., Wang, H., and Lu, L. (2021). Suppression effect of plant-derived berberine on cyprinid herpesvirus 2 proliferation and its pharmacokinetics in Crucian carp (*Carassius auratus* gibelio). *Antiv. Res.* 186:105000. doi: 10.1016/j.antiviral.2020.105000

Sun, Y., Yuan, X., Zhang, F., Han, Y., Chang, X., Xu, X., et al. (2017). Berberine ameliorates fatty acid-induced oxidative stress in human hepatoma cells. *Sci. Rep.* 7, 1–11. doi: 10.1038/s41598-017-11860-3

Tang, R., Lu, L., Wang, B., Yu, J., and Wang, H. (2020). Identification of the immediate-early genes of cyprinid herpesvirus 2. *Viruses* 12:994. doi: 10.3390/v12090994

Tao, L., Lemoff, A., Wang, G., Zarek, C., Lowe, A., Yan, N., et al. (2020). Reactive oxygen species oxidize STING and suppress interferon production. *ELife* 9:e57837. doi: 10.7554/eLife.57837.sa2

Wang, J., Wang, L., Lou, G.-H., Zeng, H.-R., Hu, J., Huang, Q.-W., et al. (2019). Coptidis Rhizoma: a comprehensive review of its traditional uses, botany, phytochemistry, pharmacology and toxicology. *Pharmaceut. Biol.* 57, 193–225. doi: 10.1080/13880209.2019.1577466

Wang, L., He, J., Liang, L., Zheng, X., Jia, P., Shi, X., et al. (2012). Mass mortality caused by Cyprinid Herpesvirus 2 (CyHV-2) in Prussian carp (*Carassius gibelio*) in China. *Bull. Eur. Assoc. Fish Pathol.* 32, 164–173.

Xu, J., Xu, Z., and Zheng, W. (2017). A review of the antiviral role of green tea catechins. *Molecules* 22:1337. doi: 10.3390/molecules22081337

Xu, J., Zeng, L., Zhang, H., Zhou, Y., Ma, J., and Fan, Y. (2013). Cyprinid herpesvirus 2 infection emerged in cultured gibel carp, *Carassius auratus*

gibelio in China. *Vet. Microbiol.* 166, 138–144. doi: 10.1016/j.vetmic.2013.05.025

Xu, L., Podok, P., Xie, J., and Lu, L. (2014). Comparative analysis of differential gene expression in kidney tissues of moribund and surviving crucian carp (*Carassius auratus* gibelio) in response to cyprinid herpesvirus 2 infection. *Arch. Virol.* 159, 1961–1974. doi: 10.1007/s00705-014-2011-9

Yang, C. S., and Wang, X. (2010). Green tea and cancer prevention. *Nutr. Cancer* 62, 931–937. doi: 10.1080/01635581.2010.509536

Yao, K., Yin, Y.-L., Chu, W., Liu, Z., Deng, D., Li, T., et al. (2008). Dietary arginine supplementation increases mTOR signaling activity in skeletal muscle of neonatal pigs. *J. Nutr.* 138, 867–872. doi: 10.1093/jn/138.5.867

Yu, L., Lu, L., and Wang, H. (2019). Preparation and characterization of polyclonal antibody against Cyprinid herpesvirus 2 ORF121. *J. Fisher. China* 43, 1463–1471.

Conflict of Interest: The authors declare that the research was conducted in the absence of any commercial or financial relationships that could be construed as a potential conflict of interest.

Publisher's Note: All claims expressed in this article are solely those of the authors and do not necessarily represent those of their affiliated organizations, or those of the publisher, the editors and the reviewers. Any product that may be evaluated in this article, or claim that may be made by its manufacturer, is not guaranteed or endorsed by the publisher.

frontiers in Microbiology

REVIEW
published: 14 February 2022
doi: 10.3389/fmicb.2022.845137

Modulation of Innate Antiviral Immune Response by Porcine Enteric Coronavirus

Kunli Zhang[1,2], Sen Lin[3], Jianhao Li[1], Shoulong Deng[4], Jianfeng Zhang[2,5] and Sutian Wang[1]**

[1]State Key Laboratory of Livestock and Poultry Breeding, Guangdong Key Laboratory of Animal Breeding and Nutrition, Institute of Animal Science, Guangdong Academy of Agricultural Sciences, Guangzhou, China, [2]Institute of Animal Health, Guangdong Academy of Agricultural Sciences, Key Laboratory of Livestock Disease Prevention of Guangdong Province, Scientific Observation and Experiment Station of Veterinary Drugs and Diagnostic Techniques of Guangdong Province, Ministry of Agriculture and Rural Affairs, Guangzhou, China, [3]Sericultural & Agri-Food Research Institute, Guangdong Academy of Agricultural Sciences, Guangzhou, China, [4]Institute of Laboratory Animal Sciences, Chinese Academy of Medical Sciences and Comparative Medicine Center, Peking Union Medical College, Beijing, China, [5]Maoming Branch, Guangdong Laboratory for Lingnan Modern Agriculture, Guangdong, China

OPEN ACCESS

Edited by:
Cao Yong Chang,
Sun Yat-sen University, China

Reviewed by:
Zheng Chen,
Jiangxi Agricultural University, China
Puxian Fang,
Huazhong Agricultural University, China

***Correspondence:**
Sutian Wang
wstlyt@126.com
Jianfeng Zhang
zhang-jianfeng@139.com

Specialty section:
This article was submitted to Virology, a section of the journal Frontiers in Microbiology

Received: *29 December 2021*
Accepted: *13 January 2022*
Published: *14 February 2022*

Citation:
Zhang K, Lin S, Li J, Deng S, Zhang J and Wang S (2022) Modulation of Innate Antiviral Immune Response by Porcine Enteric Coronavirus. Front. Microbiol. 13:845137. doi: 10.3389/fmicb.2022.845137

Host's innate immunity is the front-line defense against viral infections, but some viruses have evolved multiple strategies for evasion of antiviral innate immunity. The porcine enteric coronaviruses (PECs) consist of porcine epidemic diarrhea virus (PEDV), porcine deltacoronavirus (PDCoV), transmissible gastroenteritis coronavirus (TGEV), and swine acute diarrhea syndrome-coronavirus (SADS-CoV), which cause lethal diarrhea in neonatal pigs and threaten the swine industry worldwide. PECs interact with host cells to inhibit and evade innate antiviral immune responses like other coronaviruses. Moreover, the immune escape of porcine enteric coronaviruses is the key pathogenic mechanism causing infection. Here, we review the most recent advances in the interactions between viral and host's factors, focusing on the mechanisms by which viral components antagonize interferon (IFN)-mediated innate antiviral immune responses, trying to shed light on new targets and strategies effective for controlling and eliminating porcine enteric coronaviruses.

Keywords: porcine enteric coronaviruses, innate immunity response, immune evasion, PEDV, PDCoV, TGEV, SADS-CoV

INTRODUCTION

As the largest positive-sense RNA viruses that exist widely in nature, coronaviruses have genetic diversity and host diversity. Specific coronavirus populations have been found in humans, mice, bats, pigs, chickens, cows, cats, dogs, and many other animals, some of which are zoonotic and pose serious threats to human health and livestock safety. Due to the mild clinical manifestations after infection, coronaviruses have long been ignored by people. However, the outbreak of Severe Acute Respiratory Syndromes (SARS) in 2003 caused a total of 8,000 cases of infection worldwide, including 774 deaths, with a mortality rate of about 10% (Drosten et al., 2003). Even worse, the worldwide spread of the Severe Acute Respiratory Syndrome Coronavirus 2 (SARS-CoV-2) since 2019 caused hundreds of millions of infections and millions of deaths. Its high infectivity and transmission speed

and the lack of specific medicines and vaccines caused a worldwide panic. In the past few decades, with the continuous development of the breeding mode, various coronavirus, including porcine epidemic diarrhea virus (PEDV) and infectious chicken bronchial virus, have been world-widely prevalent and pose great challenges to the health and safety of the breeding industry. Some animals have been proved to carry coronaviruses that can spread from one species to another. A most recent research has revealed a surprising result showing that porcine deltacoronavirus (PDCoV) strains exist in plasma samples of three Haitian children with acute undifferentiated febrile illness (Lednicky et al., 2021). Therefore, systematic analysis of animal coronavirus, especially porcine enteric coronavirus (PEC), appeared to be extremely necessary.

Interferons (IFNs) are key components of the host's antiviral innate immunity. IFNs are consisted of type I IFNs, type II IFNs, and type III IFNs. Type I IFN is a non-glycosylated protein composed of 165–300 amino acids. Almost all cells can produce type I IFNs when pattern recognition receptors (PRRs) recognize the microbial pathogen-associated molecular patterns (PAMPs). IFN-I binds to type IFN-I receptor (IFNAR) to induce a powerful antiviral defense program involving hundreds of interferon-stimulated genes (ISGs) by activating the JAK–STAT pathway. Furthermore, ISGs are capable of interfering with every step of viral replication (Schoggins and Rice, 2011). Like IFN-I, type III IFNs bind to the type III IFN receptor (IFNLR) and share the same pathway to induce a similar antiviral transcriptional program (Kotenko et al., 2019). It is now well-recognized that the IFN-λ-based antiviral system plays a major role in the antiviral protection of epithelial barriers. Due to the different expression of receptors, IFN-I signaling leads to a more rapid induction and decline of ISG expression. In contrast, IFN-III signaling induces the expression of ISGs in a more sustained way (Lazear et al., 2019). IFNs establish the cellular state of viral resistance and activate the adaptive immune responses to viruses. However, some viruses have evolved quite complicated mechanisms to escape immune recognition and antagonize the effects of IFNs and ISGs. The mechanisms by which different components of these viruses antagonize immune responses are also different. In the present review, the characteristics of PEC biology are elucidated, the mechanisms by which viruses antagonize immune responses are illustrated, and finally, the potential targets and strategies effective for controlling and eliminating porcine enteric coronaviruses are discussed.

OVERVIEW OF PORCINE ENTERIC CORONAVIRUSES

In 2019, the International Committee on Taxonomy of Viruses divided the Coronaviridae into Letovirinae and Orthocoronavirinae, containing five genuses: Alphacoronavirus, Betacoronavirus, Gammacoronavirus, Deltacoronavirus, and Alphaletovires. To date, there are six known swine coronaviruses, including four alphacoronavirus, one betacoronavirus, and one deltacoronavirus. Transmissible gastroenteritis coronavirus (TGEV), porcine respiratory coronavirus (PRCV), PEDV, and swine acute diarrhea syndrome-coronavirus (SADS-CoV) belong to the alphacoronavirus. Porcine hemagglutinating encephalomyelitis virus (PHEV) belongs to the betacoronavirus, and PDCoV belongs to the deltacoronavirus. Furthermore, the evolutionary genetic analysis suggested that PEDV and SADS-CoV were thought to originate from the bat CoVs and PDCoV from a sparrow CoV (Zhou et al., 2018; Wang et al., 2019), which suggested coronaviruses could spread from species to species. PEDV, PDCoV, and TGEV SADS-CoV can cause gastrointestinal infections and similar characteristics (**Table 1**). These porcine enteric coronaviruses mainly affect the digestive tract of piglets, and the clinical symptoms include weight loss, lethargy, vomiting, anorexia, watery diarrhea, and even death. The pathological features were necrosis and shedding of intestinal cells and intestinal villi injury (Jung et al., 2014; Pan et al., 2017; Suzuki et al., 2018; Xia et al., 2018). PEDV was first reported in the United Kingdom in the 1970s but was not found in the United States until 2013 (Wood, 1977; Stevenson et al., 2013). In the short time that followed, PEDV spread worldwide, with high morbidity and mortality rates, and caused huge economic losses to the global pig industry (Jung et al., 2015). The incubation period of the virus is generally 5–8 days. In addition, PEDV can infect pigs of all ages, but the severity and mortality of infected pigs are inversely proportional to pigs. The morbidity and mortality of suckling piglets within 7 days were up to 100% (Li et al., 2020). So far, PEDV has only been found to infect pigs and has no impact on public health.

TABLE 1 | Characteristics of porcine enteric coronaviruses.

Viruses (Genera)	Year of emergence	Mortality in neonatal piglets	Pathogenicity for other species	Clinical symptoms
PEDV (Alphacoronavirus)	1970s	Almost 100%	No report	Vomiting, watery diarrhea, dehydration, and weight loss
PDCoV (Deltacoronavirus)	2009	50%–100%	Humans, Calves, chickens, and turkeys	Vomiting, watery diarrhea, dehydration, and weight loss
TGEV (Alphacoronavirus)	1946	Up to 100%	No report	Vomiting, watery diarrhea, dehydration, weight loss, and abortion
SADS-CoV (Alphacoronavirus)	2016	More than 90 in pigs ≤ 5 days of age	No report	Acute diarrhea, acute vomiting, and acute death

Since 2012, PDCoV has been detected in several countries, including China, the United States, Japan, and Canada (Woo et al., 2012; Wang et al., 2014b; Ajayi et al., 2018). PDCoV can cause diarrhea of piglets in different degrees and PDCoV disease, and the incidence and mortality of PDCOV disease in suckling piglets are about 50%–100%. The ability to spread across species is the most obvious feature of coronavirus. Researchers believed that PDCoV could only infect chickens and calves but not humans for a long time. Furthermore, the virus does not cause serious health problems in these animals (Jung et al., 2017; Liang et al., 2019; Boley et al., 2020). However, a research team has identified porcine deltacoronavirus strains in plasma samples of three Haitian children with acute undifferentiated febrile illness (Lednicky et al., 2021). This discovery makes us aware that these porcine coronaviruses may cause threats to public health.

Transmissible gastroenteritis coronavirus was first reported in the United States in 1946 and then broke out worldwide (Doyle and Hutchings, 1946; Kim et al., 2000). TGEV infection mainly causes infectious gastroenteritis, which leads to vomiting, watery diarrhea, and even death in piglets (Garwes, 1988). TGEV infection is fatal to piglets born less than 1 week, since the mortality rate can reach high up to 100%. Although the mortality rate of infected pigs over 2 weeks old is low, their growth and development are slow, which can cause economic losses to the pig breeding industry (Saif, 1999; Penzes et al., 2001). Significantly, TGEV is a highly contagious disease with a short incubation period (usually 1–3 days) and can quickly affect the entire pig population (Liu and Wang, 2021). Pigs are the only host of TGEV, and no human infection has been reported to date. SADS-CoV was first reported in the southeast of China in 2016, which is the sixth porcine coronavirus identified so far. The SADS-CoV infection leads to acute diarrhea, acute vomiting, and even acute death in piglets, and the mortality rate of virus infection in piglets within 5 days of age is more than 90% (Zhou et al., 2018). Tests on 35 people who had close contact with infected pigs found no evidence of human infection, suggesting the virus may not be capable of transmitting to humans.

THE GENOME STRUCTURE AND FUNCTION OF PORCINE ENTERIC CORONAVIRUSES

The PEDV genome is about 28 kb in length and consists of 3′, 5′ untranslated regions (UTR) and seven open reading frames (ORFs). The ORF sequence is ORF1a, ORF1b, spike protein (S), ORF3, envelope protein (E), membrane protein (M), and nucleoprotein (N; Kocherhans et al., 2001). ORF1 occupies two-thirds of the length of the genome at the end of the 5′ UTR and encodes two proteins (pp1a and pp1ab), which can be hydrolyzed by papain-like protease and serine type 3C-like protease to non-structural proteins (NSP) 1α, NSP1β, and NSP3-16. And then, these NSPs participate in virus replication, transcription, translation, and viral protein processing (Kadoi et al., 2002; Huang et al., 2013). The S protein of PEDV consists of S1 (1-789aa) and S2 (790-1383aa) subunits. The S1 helps PEDV bind to host receptors, and S2 induces membrane fusion and PEDV invasion (Liu et al., 2015). In addition, PEDV S protein also induces neutralizing antibodies in the host body (Song and Park, 2012). PEDV ORF3 sits between the S and E genes and encodes ORF3 protein, which plays an essential role in virulence (Park et al., 2011). The E gene of PEDV is only 231 nt in length and encodes E protein, which is essential for virus assembly and budding (Brian and Baric, 2005). The M gene of PEDV is 681 nt in length and can encode M protein (226aa), which is a transmembrane protein on the viral envelope (Narayanan et al., 2000). It has been reported that M protein is involved in virion assembly, budding, and host innate immune induction (Utiger et al., 1995). The PEDV N protein is a highly conserved protein that consists of 441aa and is involved in the survival of the virus (Wang et al., 2020c).

The TGEV genome is about 28.5 kb in length, consisting of 3′, 5′ UTR, and seven open reading frames. The gene sequence arrangement is 5′-UTR-ORF1a-ORF1b-S-ORF3a-ORF3b-E-M-N-NS7-3′-UTR (**Figure 1**). TGEV ORF1a and ORF1b encode pp1a and pp1b, respectively, which can be hydrolyzed by papain-like protease and 3C-like protease to NSP1-16 (Van Reeth et al., 2002; Wang et al., 2018). Moreover, ORF3a/b and NS7 encode accessory proteins which are also involved in virus infection and virulence (Park et al., 2008). The TGEV S gene is about 4,344 bp and encodes S protein (1447aa), which has multiple functions, including inducing neutralizing antibodies, influencing host cell affinity, and determining virus activity (Gack et al., 2007). E protein of TGEV is a kind of membrane-associated small structural protein. A study has reported that 64-AYKNF-68 residues are the core sequences for binding E monoclonal antibodies (Yachdav et al., 2014). The M protein of TGEV consists of 263aa, is a kind of glycosylated protein that plays an important role in virus assembly. TGEV M protein is involved in inducing interferons (Sawicki et al., 2005). The N protein of TGEV is a conserved phosphorylated protein that binds to the genome to form an RNA complex. Because of its conserved nature, N is often used as an antigen for PEDV detection.

The SADS-CoV genome is approximately 27.2 kb in length and consists of 3′, 5′-UTR, and nine open reading frames, which are ORF1a, ORF1b, S, NS3a, E, M, N, NS7a, and NS7b in sequence (Pan et al., 2017; Xu et al., 2019a). SADS-CoV ORF1a encodes pp1a, which can be hydrolyzed to NSP 1–11. Moreover, ORF1b encodes pp1b, which can be hydrolyzed to NSP 12–16. NS3a, NS7a, and NS7b encode accessory proteins that affect viruses' virulence (Xu et al., 2019a). The membrane protein interacts with the nucleoprotein of SADS-CoV during viral assembly and enhances viral transcription and assembly efficiency. The spike of SADS-CoV (1130aa) determines viral host range and tissue tropism. Notably, SADS-CoV S is highly homologous (95%) to bat α-coronavirus HKU2, which suggests that it may have the potential to spread across species (Yu et al., 2020).

The length of the PDCoV genome is approximately 25.4 kb, which is the smallest known coronavirus. PDCoV genome consists of 3′, 5′ UTR, and eight open reading frames, which

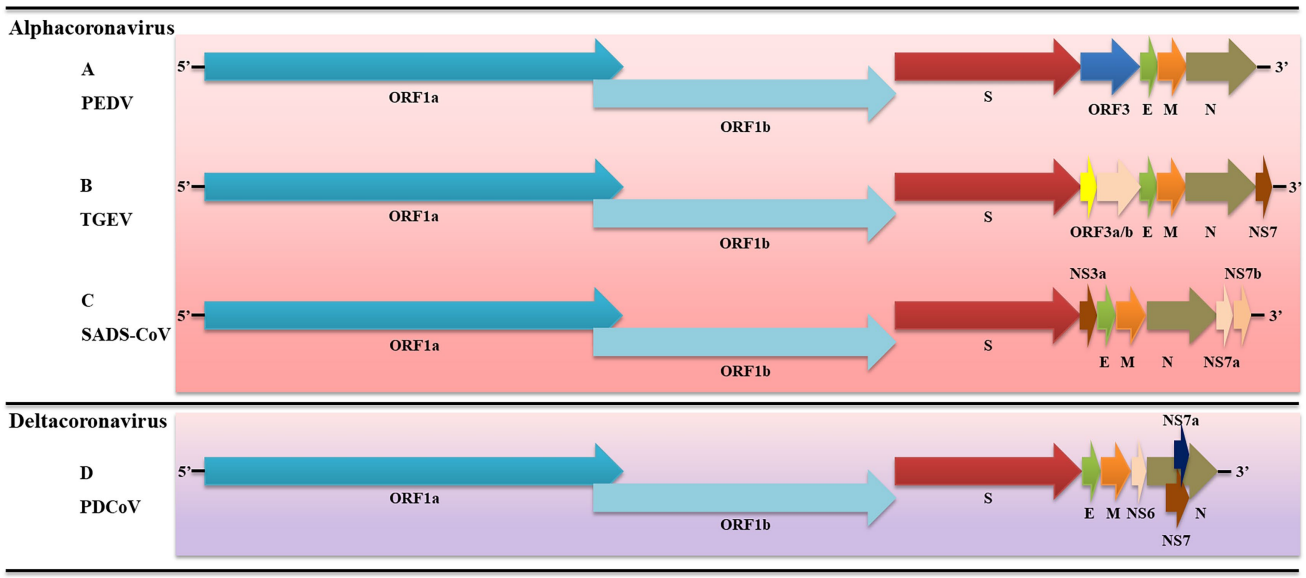

FIGURE 1 | Schematic diagram of porcine enteric coronaviruses (PECs). **(A)** Genome structure of PDEV; **(B)** Genome structure of transmissible gastroenteritis coronavirus (TGEV); **(C)** Genome structure of swine acute diarrhea syndrome-coronavirus (SADS-CoV); **(D)** Genome structure of porcine deltacoronavirus (PDCoV). S, spike; E, envelope; M, membrane; N, nucleoprotein; and Ns, accessory genes.

are ORF1a, ORF1b, S, E, M, NS6, N, NS7a, and NS7 in order (Woo et al., 2010; Chen et al., 2015; Fang et al., 2017; **Figure 1**). PDCoV ORF1a and ORF1ab encode 1a polyprotein (3627aa) and 1ab polyprotein (6268aa), which can be hydrolyzed to NSP 2–16. It is widely accepted that PDCoV did not encode non-structural protein 1 (nsp1). These NSPs are associated with virus transcription, replication, and host immune response (Zhang, 2016). In addition, there are two ORFs between the M gene and N gene and within the N gene, which encode NS6, NS7a, and NS7. When PDCoV infects host cells, they are located in the endoplasmic reticulum (ER) and mitochondria, respectively (Fang et al., 2016; Choi and Lee, 2019). The structural analysis of PDCoV S protein showed that it was composed of S1 and S2 subunits. The N-terminal domain of PDCoV S1 recognizes carbohydrates as potential receptors, and the C-terminal domain of PDCoV S1 binds to receptors on the surface of mammalian cells (Shang et al., 2018). PDCoV N protein is located in the cytoplasm and nucleus of the host cell and participates in viral RNA synthesis by interacting with ribosomal subunits or nucleoproteins (Lee and Lee, 2015). In addition, PDCoV N protein is also involved in influencing the immune response of host cells (Likai et al., 2019).

INNATE RECOGNITION OF PORCINE ENTERIC CORONAVIRUS

Innate immunity is the first line of the host to defense against virus infection. The host cells recognize the invading pathogens through the interactions between PAMPs and host PRRs and induce the production of pro-inflammatory cytokines and interferons to elicit antiviral responses (Akira et al., 2006). When coronaviruses invade cells, PRRs, such as retinoic acid-inducible gene I (RIG-I)-like receptors (RLR) and Toll-like receptors (TLRs), are essential for the innate recognition of viral RNAs and are involved in the restriction of viral replication and dissemination. RLR, a family of cytoplasmic RNA helicases, including RIG-I, melanoma differentiation-associated gene 5 (MDA5), and Laboratory of Genetics and Physiology 2 (LGP2; Liu and Cao, 2016). Activation of RIG-I and MDA5 by double-stranded RNA (dsRNA) from coronaviruses leads to recruitment of the caspase recruitment domain (CARD)-containing adaptor protein mitochondrial antiviral signaling (MAVS) protein to activate TANK-binding kinase 1 (TBK1)/inhibitor-kb kinase ε (IKKε) kinases (Seth et al., 2005). Activated TBK1 and IKKε induce type I and type III IFNs production through phosphorylating interferon regulatory factors (IRFs; Meylan et al., 2006).

Other RNA sensors, TLR3, TLR7, and TLR8, located in the endosomal membrane, also recognize viral nucleotides, among which TLR3 recognizes dsRNA, TLR7 and TLR8 recognize ssRNA. The expression of TLR7 was significantly upregulated in PEDV-infected IPEC-J2 cells (Wang et al., 2020a). Cao et al. (2015) reported that PEDV infection induces nuclear factor-κB (NF-κB) activation through the TLR2, TLR3, and TLR9 pathways in porcine intestinal epithelial cells. PDCoV infection also significantly upregulates the mRNA transcription level of TLR3 and IFN-α *in vivo* (Xu et al., 2019b). In addition, TLR7 recognizes SARS-CoV, MERS-CoV, and MHV and induces IFN-a production in plasmacytoid dendritic cells (Cervantes-Barragan et al., 2007; Scheuplein et al., 2015). The receptors that sit on the surface of certain cells, especially TLR4, recognize MHV, SARS-CoV, SARS-CoV-2, and respiratory syncytial virus (Kurt-Jones et al., 2000; Khanolkar et al., 2009; Choudhury and Mukherjee, 2020). It has been reported that TLR4 also

participates in PEDV infection-related pathogenesis (Huan et al., 2017). Once TLRs recognize the PAMPs of the virus, the factors NF-κB signaling will be activated to stimulate the production of pro-inflammatory cytokines and type I IFNs.

ESCAPE FROM INNATE IMMUNITY BY PORCINE ENTERIC CORONAVIRUSES STRUCTURAL PROTEINS

The structural proteins of porcine enteric coronaviruses consist of spike protein, envelope protein, membrane protein, and nucleocapsid protein. These proteins are essential components of viral structure and play important roles in fighting against the host's immune responses (**Figure 2**). It is generally believed that the S protein of coronaviruses mainly plays a key role in the invasion of host cells and the induction of neutralizing antibodies (Song and Park, 2012; Li, 2015; Guan et al., 2020). However, a study has found that compared with other structural proteins and NSPs of PEDV, S protein has the strongest ability to induce apoptosis. Similarly, the S protein of TGEV can also strongly induce Vero-E6 cells apoptosis (Chen et al., 2018). Studies have suggested that some viruses actively induce apoptosis to promote the release of virus progeny and spread to neighboring cells for further invasion (Favreau et al., 2012; Lan et al., 2013). Thus, S protein probably helps these porcine enteric coronaviruses evade the host immune response by regulating apoptosis, although the exact mechanism is unclear. Moreover, another recent research has found that PEDV S protein directly interacts with epidermal growth factor receptor (EGFR) and activates EGFR downstream signal transduction, inhibiting IFN and exacerbating viral infection (Yang et al., 2018). Still, more evidence is needed to explore whether porcine enteric coronaviruses S protein is directly involved in viral immune escape or S protein mediates NSPs to realize virus immune escape.

The nucleocapsid protein is the most abundant protein of the known porcine enteric coronavirus components. It performs various functions, including viral genome transcription, translation, viral replication, and virus assembly (McBride et al., 2014). The PEDV N protein suppresses NF-κB nuclear translocation and further antagonizes Type II interferon production (Shan et al., 2018). Furthermore, the PEDV N protein targets TBK1 by direct interaction to inhibit IRF3 activation, further antagonizing type I interferon production. PDCoV N protein inhibits the activation of porcine IFN-β promoter by competing with dsRNA for porcine RIG-I binding (Chen et al., 2019). Moreover, the N-terminal region (1-246aa) of PDCoV N protein is the key part of interacting with porcine RIG-I (Likai et al., 2019). In addition, the N protein of PDCoV and SADS-CoV mediates K63-linked ubiquitination

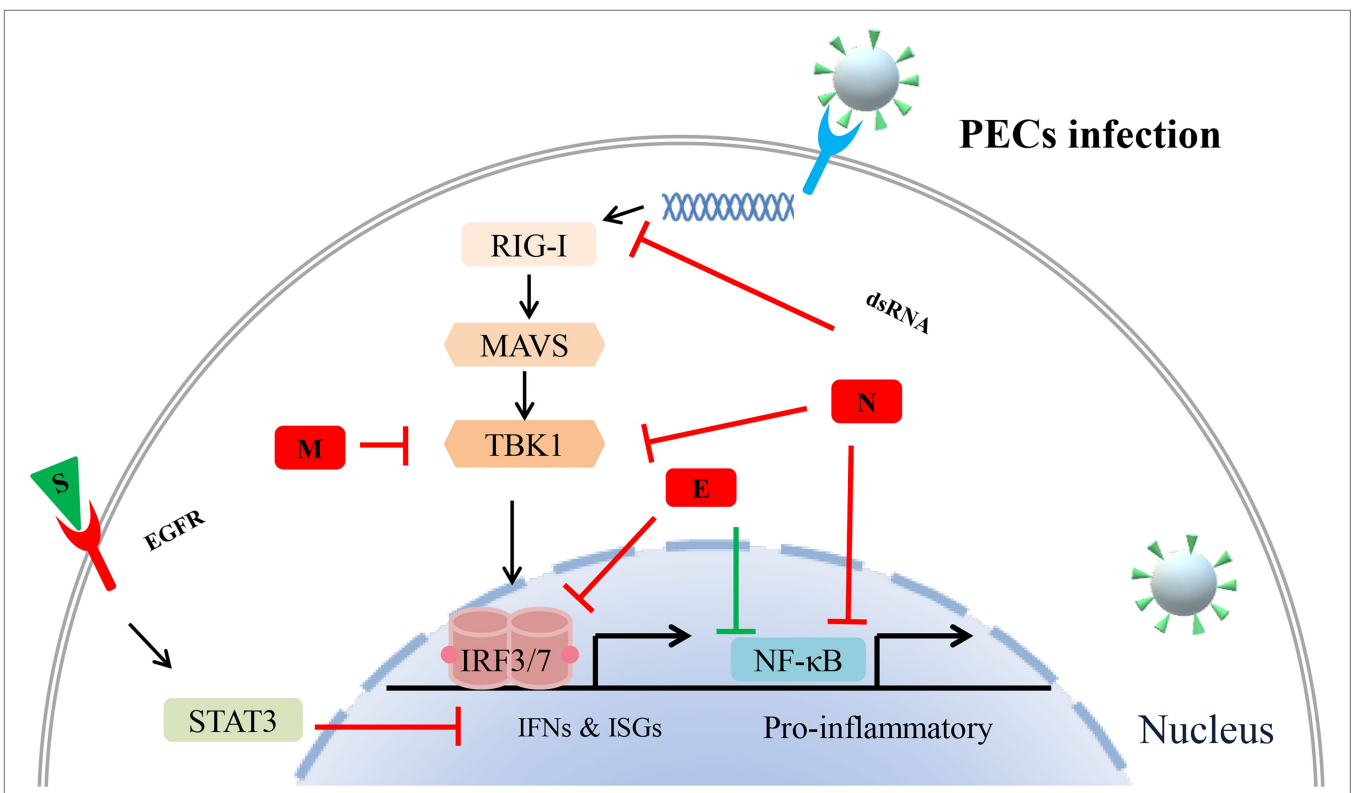

FIGURE 2 | Potential mechanisms of porcine enteric coronavirus (PEC) structural proteins antagonize innate antiviral immune response. Different structural proteins of different porcine enteric coronaviruses used different strategies to antagonize the host's immune responses. During PEC infection, interferons (IFNs) and pro-inflammatory are activated to fight against invading virus. It is noteworthy that STAT, retinoic acid-inducible gene I (RIG-I), and nuclear factor-κB (NF-κB) signalings are involved in this structural proteins-induced immune evasion. ⊤ stands for negative regulation, ⊤ stands for positive regulation.

of porcine RIG-I, thereby, inhibit the host IFN-β production (Likai et al., 2019; Liu et al., 2021). The expression of the TGEV N gene promotes the accumulation of p53 and p21 and suppresses the expression of cyclin B1, cdc2, and cdk2. Meanwhile, TGEV N protein induces Bax mitochondria translocation and results in the activation of caspase-3, leading to apoptosis (Eleouet et al., 2000; Ding et al., 2014). In contrast, another study found that TGEV N protein, located in mitochondria, may contribute to mitophagy and suppress oxidative stress and apoptosis (Zhu et al., 2016). These different results may be due to their use of different cell lines for infection. These studies also suggested that the N proteins of different porcine enteric coronaviruses used different strategies to antagonize the host's immune responses.

The member protein of porcine coronaviruses is a kind of transmembrane glycoprotein, which plays an important role in virion assembly, budding, and host immune regulation (Nguyen and Hogue, 1997; Riffault et al., 1997). Though the PEDV M protein affects cell cycle and interleukin 8 expressions, it does not induce ER stress and activation of NF-κB (Xu et al., 2015). Moreover, the PEDV M protein can form a complex with heat shock protein 70, affecting the host's innate immune response and virus replication (Park et al., 2021). A recent study has identified 218 host cell proteins directly interacting with PDEV M protein. Moreover, these proteins were mainly associated with multiple biological processes such as immune response, apoptosis, and cell cycle (Wang et al., 2020b). In addition, some researches have reported that M proteins of TGEV and PDCoV help virus replication, which may be related to its regulation of IFN expression (Riffault et al., 1997; Gu et al., 2019; Li et al., 2019). So far, there are few studies on M proteins of porcine enteric coronavirus. M protein mediating porcine enteric coronavirus antagonism against host innate immune responses remains to be further studied.

The envelope protein is the smallest structural protein in porcine enteric coronavirus, involved in virus-host interactions. When the viruses invade the host cell, the E proteins are mainly located in the ER and play an essential role in virion assembly and budding (Xu et al., 2013a; Mora-Diaz et al., 2019). Based on its specific location in the cell, a study has found that PEDV E protein-induced ER stress and NF-κB activation upregulate the expression of IL-8 and Bcl-2. On the other hand, PEDV E protein directly interacts with IRF3 to inhibit its nuclear translocation, which further antagonizes interferon-β production (Zheng et al., 2021). The results of protein structure analysis suggest that porcine enteric coronavirus E protein may be involved in inducing humoral and cellular immunity during viral infection (Escors et al., 2001).

RESEARCH PROGRESS ON ACCESSORY PROTEINS OF PORCINE ENTERIC CORONAVIRUSES ANTAGONIZING ANTIVIRAL INNATE IMMUNE RESPONSES

The porcine coronavirus accessory proteins are unique kinds of protein with special functions. Different numbers of accessory proteins are scattered in different porcine coronavirus genomes. Although they are unnecessary for virus proliferation, they play key roles in regulating innate immunity and viral pathogenicity (Fang et al., 2018; Wu et al., 2020b). PEDV has only one accessory protein, the ORF3. A study showed that ORF3 could suppress IFN-β and IRF3 promoter activities, but a detailed analysis of the certain mechanism is lacking (Zhang et al., 2016). Several studies have reported that PDEV ORF3 can interact with the host's immune cells. PDEV ORF3 antagonizes the host's antiviral innate immunity mainly by regulating NF-κB signaling pathway activity. PEDV ORF3 inhibits phosphorylation of IκBα and nuclear factor p65 and interfering p65 nuclear translocation, which in turn reduces the production of pro-inflammatory cytokines such as IL-6 and IL-8 (Wu et al., 2020b). Interestingly, ORF3 directly interacts with the IκB kinase β and upregulates the IκB kinase β-meditated NF-κB promoter activity. However, PEDV ORF3 suppresses the IκB kinase β-meditated IFN-β production (Kaewborisuth et al., 2020). Moreover, PEDV ORF3 induces ER stress *via* the PERK-eIF2α signaling pathway by upregulating the expression of GRP78, and then inducing autophagy, which benefits viral replication and affects the production of various inflammatory cytokines (Guo et al., 2017; Zou et al., 2019). In addition, conflicting studies have shown that proteins can inhibit or promote apoptosis, which is involved in viral replication and immune escape (Favreau et al., 2012; Si et al., 2020). Cells infected with Ns7-deletion mutant TGEV (TGEV-Δ7) showed an increased cytopathic effect by activation of caspase signaling. Further research found that the C-terminus of accessory protein 7 bound to protein phosphatase 1 catalytic subunit and regulated dephosphorylation of eukaryotic translation initiation factor 2 to counteract the host's cell defenses (Cruz et al., 2011). Moreover, innate immunity genes such as IL-15, C–C motif chemokine 2/4/5, C–X–C motif chemokine 9/11, tumor necrosis factor, and IFN-β were upregulated during TGEV-Δ7 infection. *In vitro* and *in vivo* results suggested that the absence of TGEV accessory protein 7 increased innate immunity responses and acute tissue damage, which proved its antagonistic function from the opposite angle (Cruz et al., 2013). PDCoV accessory protein NS6 cannot prevent RIG-I, MDA5, and their downstream molecules from activating the IFN-β promoter. However, PDCoV NS6 can directly interact with the carboxyl terminus domain of RIG-I and the helicase and carboxyl terminus domains of MDA5 to inhibit dsRNA binding RIG-I/MDA5 and thus antagonize IFN-β production (Fang et al., 2018). PDCoV NS7a can also function as an IFN antagonist. Unlike NS6a, the NS7a inhibits RIG-I, MDA5, and their downstream molecules to activate the IFN-β promoter. Furthermore, NS7a can compete with TRAF3 and IRF3 for binding to IKK, thereby, reducing RLR-mediated IFN-β production. Moreover, the kinase and the scaffold dimerization domains of IKKε are key regions that can directly bond to NS7a (Fang et al., 2020). From those researches, the mechanisms by which different accessory proteins of porcine enteric coronaviruses suppress host antiviral innate immunity are different.

MECHANISM OF NON-STRUCTURAL PROTEINS OF PORCINE ENTERIC CORONAVIRUSES ANTAGONIZING INNATE IMMUNE RESPONSE

Non-structural proteins are the earliest expression proteins essential for the virus replication process. They usually act as viruses evade, circumvent, or subvert the host innate immune system roles. During the process of porcine enteric coronavirus infection, NSP1, NSP3, NSP5, NSP15, and NSP16 have been observed to play additional roles in host immune-modulatory functions. Of 16 PEDV NSPs, NSP1, NSP3, NSP7, NSP14, NSP15, and NSP16 were found to inhibit the IFN-β and IRF3 promoter activities (Zhang et al., 2016). In addition, these porcine coronaviruses NSPs are also involved in downregulating the NF-κB activity (Zhang et al., 2017). In 2018, NSP1, NSP3, NSP5, NSP8, NSP14, NSP15, and NSP16 of PEDV were found to suppress type III IFN activities (Zhang et al., 2018). Here, we review the detailed mechanism of these non-structural proteins that antagonize interferon production.

Non-structural protein 1 is only characterized in alphacoronaviruses (α-CoVs) and betacoronaviruses (β-CoVs; Woo et al., 2010). Under the catalysis of the proteasome, the NSP1 of PEDV interrupted the enhanceosome assembly of IRF3 and CREB-binding protein (CBP) by degrading CBP to antagonize IFN-I production (Zhang et al., 2016). The CBP is the key molecular for the activated IRF3 to induce the transcription of IFN-I genes. After IRF3 phosphorylation and dimerization into the nucleus, IRF3 interacts with CBP to form the IRF3-CBP complex. And then, the complex binds to the positive regulatory domain (PRD) I–IV regions of the IFN-β promoter to assemble the enhanceosome with NF-κB and other factors to turn on the transcription of IFN-I genes (Honda and Taniguchi, 2006; Dragan et al., 2007; Panne et al., 2007). Another target gene for NSP1 to inhibit innate immunity is IRF1. IRF1 is the key adaptor protein for type III IFNs production. PEDV NSP1 blocked the nuclear translocation of IRF1 and reduced the number of peroxisomes to suppress IRF1-induced type III IFNs (Zhang et al., 2018). PEDV inhibited both NF-κB and pro-inflammatory cytokines production in porcine epithelial cells. Zhang et al. (2017) found that NSP1 was the most effective NF-κB antagonist among all proteins of PEDV. Moreover, NSP1 suppressed the phosphorylation and degradation of IκBα and blocked the p65 activation (Zhang et al., 2017). It is worth pointing out that the conserved residues of NSP1 were crucial to suppress IRF1-mediated IFN-λ and NF-κB mediated IFN-I and pro-inflammatory cytokines (Zhang et al., 2017, 2018). In addition, Shen et al. (2020) found that seven representative α-CoVs: SADS-CoV, PEDV, HCoV-229E, human NL63 CoV (HCoV-NL63), FIPV, TGEV, and PRCV NSP1s could significantly inhibit the phosphorylation of STAT1-S727 and interfere with the effect of IFN-I. The multiple functions of NSP1 to inhibit innate immune responses through different mechanisms suggest that it is one of the key molecules of porcine coronaviruses to escape innate immunity. Drugs targeting NSP1 conserved sites are likely to prevent and control these viruses.

NSP3 is the largest protein encoded by the porcine coronavirus genome and contains two domains of papain-like protease (PLP1 and PLP2). PLP2 has deubiquitinase (DUB) activity that recognizes and processes K-48 and K-63 linked polyubiquitin chains. Ubiquitin modification is a key mechanism to regulate the activity and stability of the antiviral innate immune. In recent years, several viral DUBs have been found to antagonize IFN-I production by deubiquitination of key host factors, such as the lead protease (Lbpro) of the foot-and-mouth disease virus (FMDV) and the NSP2 of Porcine Reproductive and Respiratory syndrome virus (PRRSV; Sun et al., 2010; Wang et al., 2011). Moreover, the DUB activity is conserved in all members of the arterivirus family. Both arteri- and nairovirus DUBs inhibit RIG-I mediated innate immune signaling (van Kasteren et al., 2012). The PLP2 of HCoV-NL63 and PLPs of SARS-CoV also antagonize IFN induction through disruption of STING dimer and deubiquitination of RIG-I (Chen et al., 2007; Clementz et al., 2010; Sun et al., 2012a). Accordingly, PEDV PLP2 strongly inhibits RIG-I- and STING-activated IFN expression by deubiquitination and co-immunoprecipitating with RIG-I and STING (Xing et al., 2013).

CoVs NSP5 and NSP3 genes encode 3C-like protease (3CLpro) and papain-like proteinase, respectively. These two proteinases can degrade the polyprotein into various non-structural proteins, which further facilitate virus replication. It has been found that many viruses' 3C protease (3Cpro) antagonizes innate immune signaling pathways dependent on its protease activity. For example, encephalomyocarditis virus (EMCV) 3C protease cleaved TANK and disrupted the TANK-TBK1-IKKε-IRF3 complex, inhibiting IRF3 phosphorylation and IFN-I production (Huang et al., 2017). Coxsackievirus B 3C protease cleaves MAVS and TRIF to attenuate IFN-I and apoptotic signaling (Mukherjee et al., 2011). Enterovirus 71 3C protein induces TRIF cleavage to inhibit TLR-mediated antiviral responses (Lei et al., 2011). Similar to the Hepatitis A virus and FMDV 3Cpro, PEDV and PDCoV 3C-like proteases cleave NEMO to impair induction of IFN-β (Wang et al., 2012, 2014a, 2016). The cleave site of NEMO has been identified at Gln231 both in PEDV and PDCoV, suggesting NEMO may be a common target for coronaviruses (Wang et al., 2016; Zhu et al., 2017a). However, it cannot exclude the possibility that other non-active site residues of their NSP5 are also involved. Soon afterward, other target molecules of PDCoV NSP5 inhibit IFN-I signaling was revealed. Like NS5 protein of dengue virus (DENV), Zika virus (ZIKV) and the hepatitis C virus (HCV), PDCoV NSP5 target the JAK–STAT pathway to antagonize IFN-I signaling (Lin et al., 2006; Ashour et al., 2009; Grant et al., 2016). In PDCoV-infected cells, NSP5 cleaved STAT2 at glutamine 685 (Q685) and Q758As to impair ISGs induction (Zhu et al., 2017b). As NSP5 is involved in the cleavage of the viral polyprotein, the inhibitors target its 3C-like protease domain that can suppress porcine enteric coronavirus infection, such as quercetin, GC376 (Zhou et al., 2019; Ye et al., 2020).

NSP15 is identified as a component of the coronavirus replication complex, which has endoribonuclease (EndoU) activity. The role of EndoU was revealed, which showed that EndoU mediates the evasion of viral double-stranded RNA recognition by host

sensors in macrophages. In previous studies, SARS-CoV NSP15 was identified as an inhibitor of MAVS-mediated apoptotic responses (Lei et al., 2009). MHV and HCoV-229E NSP15 efficiently prevent simultaneous activation of host cells dsRNA sensors, such as MDA5, OAS, and PKR (Kindler et al., 2017). A study has reported that the EndoU activity of PEDV NSP15 is not required for virus replication. Still, PEDV NSP15 is important for suppressing the type I and type III IFN response in epithelial cells and macrophages. NSP15 facilitates virus replication, shedding, and pathogenesis *in vivo* (Deng et al., 2019). With the study forward, the mechanism of PEDV NSP15 inhibits the host's IFN response was found. PEDV NSP15 can directly degrade the mRNA of TBK1 and IRF3 dependent on its EndoU activity to suppress the production of IFN and ISGs, antagonizing the host innate response to facilitate its replication (Wu et al., 2020a). PDCoV NSP15 is also an IFN antagonist. However, PDCoV NSP15 disrupts the phosphorylation and nuclear translocation of the NF-κB p65 subunit but does not antagonize the activation of transcription factor IRF3. Moreover, PDCoV NSP15 inhibits IFN-β production independent of EndoU activity (Liu et al., 2019).

NSP16 is one of the RNA modification enzymes involved in forming cap structures in PEDV (Chen et al., 2011). Compared with NSP14, which is another methyltransferase in PEDV, NSP16 is a more efficient regulator in the antagonist of innate immunity. Mechanistically, NSP16 downregulates the activities of RIG-I and MDA5 mediated IFN-β and ISRE dependent on the KDKE tetrad. Moreover, NSP10 enhanced the inhibitory effect of NSP16 on IFN-β (Shi et al., 2019). However, whether NSP16 of PDCoV and SADS-CoV antagonizes interferon production is still unknown.

These studies suggest that the NSPs of porcine enteric coronaviruses antagonize the host's innate immune responses by regulating IFN signaling pathways (**Figure 3**). Therefore, further

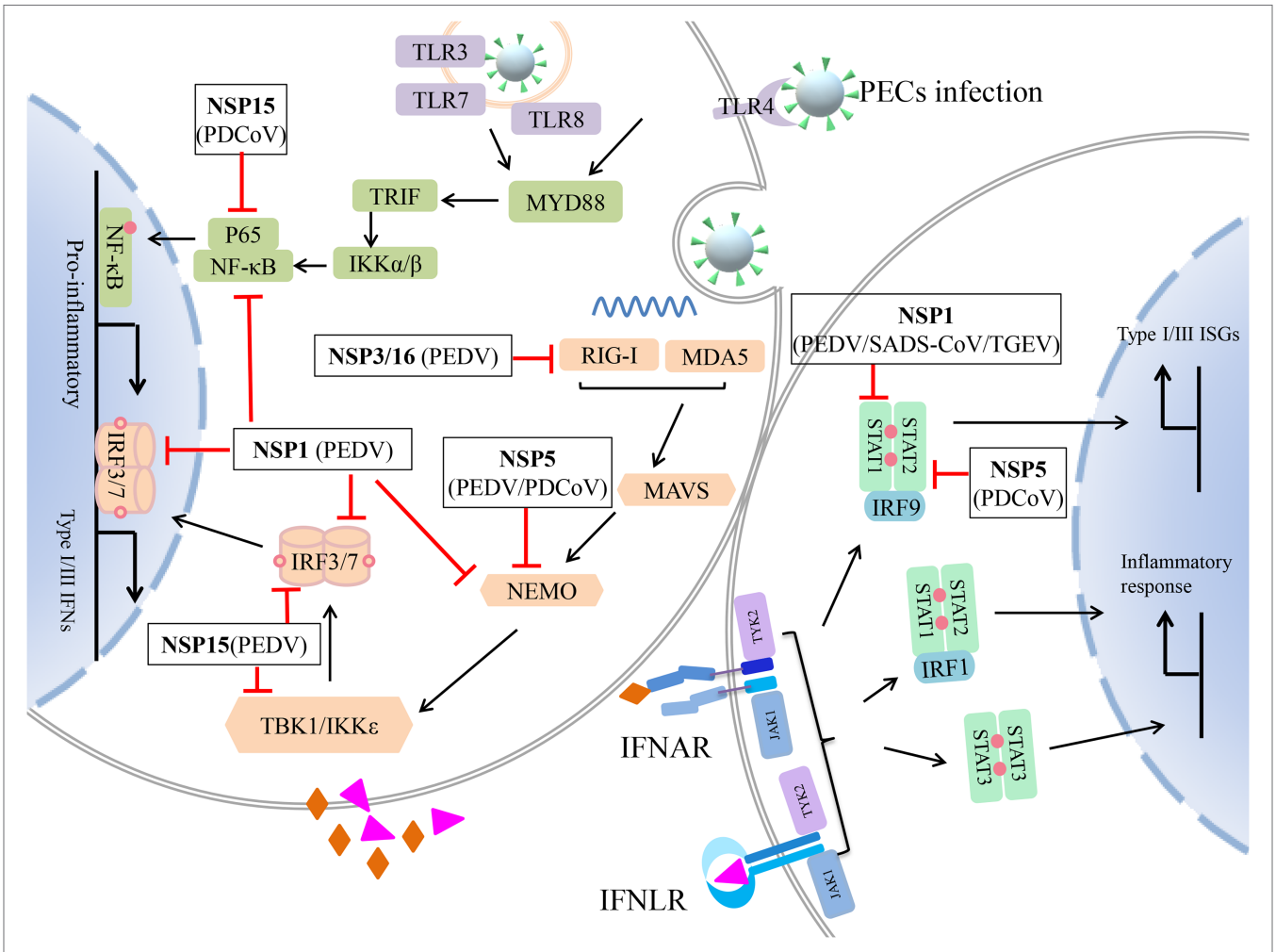

FIGURE 3 | Non-structural protein (NSP) of porcine enteric coronavirus (PEC) antagonizes innate immune response. Retinoic acid-inducible gene I (RIG-I), melanoma differentiation-associated gene 5 (MDA5), and Toll-like receptors (TLRs) recognize the invading virus and induce pro-inflammatory cytokines, type I/III interferons (IFNs) by nuclear factor-κB (NF-κB) and (RIG-I)-like receptors (RLRs) signaling pathway, respectively. Extracellular Type I and III IFNs recognized by IFN-I receptor (IFNAR) and type III IFN receptor (IFNLR) to phosphorylate JAK1 and TYK2. And then, STAT1/2 is recruited and phosphorylated to form three STAT complexes. STAT1 and STAT2 form heterodimers and recruit IRF9 or IRF1. These complexes enter the nucleus and induce type I and III ISGs, inflammatory cytokines production. NSPs of PEC antagonize various steps of this antiviral response. ⊤ stands for negative regulation; ◆ stands for type I IFN; and ▲ stands for type III IFN.

study of the biological functions of NSPs will help us elucidate the pathogenesis of coronaviruses and possibly provide new targets for developing antiviral vaccines and drugs.

CONCLUSION AND PERSPECTIVES

The host's innate immune response protects itself from most pathogenic microorganisms, but some viruses have evolved strategies to antagonize innate immune responses. Coronaviruses are the largest positive-sense RNA viruses that exist widely in nature and are highly genetically variable. This review summarizes how porcine enteric coronaviruses evade the host's innate immune responses. First, since IFN is the most important regulator of the antiviral innate immunity, these viruses typically inhibit IFN production by various means, including inhibition of RIG-I/TLR signaling and inhibiting dsRNA bind to RIG-I/MDA5 or directly downregulates IFN promoter activity. Second, porcine enteric coronaviruses also attenuate inflammatory response by targeting the NF-κB signaling pathway. In addition, some porcine enteric coronaviruses can regulate apoptosis and evade ISGs to promote virus replication.

Also, some cellular physiological processes, such as autophagy, endoplasmic reticulum stress, programmed cell death, are probably involved in the evasion of the innate immune response of these viruses (Lin et al., 2020; Sun et al., 2021; Wei et al., 2021). Some viruses use autophagy to evade the host immune response and hide in the autophagosome to accumulate RNA and proteins (Sun et al., 2012b; Liu et al., 2016). A recent study has reported that PEDV infection induced autophagy, which promotes virus replication. Moreover, NSP6 and ORF3 of the virus are two of the important inducers of autophagy. Further study showed that PI3K/Akt/mTOR pathway is the key signal of PEDV NSP6-induced autophagy (Lin et al., 2020). During porcine coronavirus infection, some of the viral proteins are located in the endoplasmic reticulum of host cells. E protein, N protein, and ORF3 of PEDV can all induce ER stress *via* PERK and IRE1 signaling and then upregulate inflammatory factors (Xu et al., 2013a,b; Sun et al., 2021). In addition, PEDV-induced ER stress facilitates autophagy (Zou et al., 2019). Furthermore, TGEV infection in porcine intestinal epithelial cells can induce IL-1β release and pyroptosis, dependent on the expression and assembly of the NOD-like receptor protein 3. The above evidence highlights the importance of investigating virus-host interactions to elucidate viral immune evasion. Some viruses would like to alter the intracellular environment to ensure their survival. Exploring these programs will help us further understand how porcine enteric coronaviruses evade innate immune responses and also provide us with new ideas for developing antiviral vaccines and drugs.

AUTHOR CONTRIBUTIONS

KZ, SL, SD, JL, JZ, and SW conceived and wrote the manuscript. KZ and SW prepared the figure. All authors approved the final version of this review and agreed to be accountable for the content of the work.

FUNDING

The authors thank the following funding sources: Independent Research and Development Projects of Maoming Laboratory (2021ZZ003), the Special Fund for Scientific Innovation Strategy-Construction of High-Level Academy of Agriculture Science (R2021PY–QF006, R2019YJ–YB2005, R2019YJ–YB2004, and R2019YJ–YB3002), and the Science and Technology Planning Project of Guangzhou (202103000096).

REFERENCES

Ajayi, T., Dara, R., Misener, M., Pasma, T., Moser, L., and Poljak, Z. (2018). Herd-level prevalence and incidence of porcine epidemic diarrhoea virus (PEDV) and porcine deltacoronavirus (PDCoV) in swine herds in Ontario, Canada. *Transbound. Emerg. Dis.* 65, 1197–1207. doi: 10.1111/tbed.12858

Akira, S., Uematsu, S., and Takeuchi, O. (2006). Pathogen recognition and innate immunity. *Cell* 124, 783–801. doi: 10.1016/j.cell.2006.02.015

Ashour, J., Laurent-Rolle, M., Shi, P. Y., and Garcia-Sastre, A. (2009). NS5 of dengue virus mediates STAT2 binding and degradation. *J. Virol.* 83, 5408–5418. doi: 10.1128/JVI.02188-08

Boley, P. A., Alhamo, M. A., Lossie, G., Yadav, K. K., Vasquez-Lee, M., Saif, L. J., et al. (2020). Porcine deltacoronavirus infection and transmission in poultry, United States(1). *Emerg. Infect. Dis.* 26, 255–265. doi: 10.3201/eid2602.190346

Brian, D. A., and Baric, R. S. (2005). Coronavirus genome structure and replication. *Curr. Top. Microbiol. Immunol.* 287, 1–30. doi: 10.1007/3-540-26765-4_1

Cao, L., Ge, X., Gao, Y., Ren, Y., Ren, X., and Li, G. (2015). Porcine epidemic diarrhea virus infection induces NF-kappaB activation through the TLR2, TLR3 and TLR9 pathways in porcine intestinal epithelial cells. *J. Gen. Virol.* 96, 1757–1767. doi: 10.1099/vir.0.000133

Cervantes-Barragan, L., Zust, R., Weber, F., Spiegel, M., Lang, K. S., Akira, S., et al. (2007). Control of coronavirus infection through plasmacytoid dendritic-cell-derived type I interferon. *Blood* 109, 1131–1137. doi: 10.1182/blood-2006-05-023770

Chen, J., Fang, P., Wang, M., Peng, Q., Ren, J., Wang, D., et al. (2019). Porcine deltacoronavirus nucleocapsid protein antagonizes IFN-beta production by impairing dsRNA and PACT binding to RIG-I. *Virus Genes* 55, 520–531. doi: 10.1007/s11262-019-01673-z

Chen, Y., Su, C., Ke, M., Jin, X., Xu, L., Zhang, Z., et al. (2011). Biochemical and structural insights into the mechanisms of SARS coronavirus RNA ribose 2'-O-methylation by nsp16/nsp10 protein complex. *PLoS Pathog.* 7:e1002294. doi: 10.1371/journal.ppat.1002294

Chen, Z., Wang, Y., Ratia, K., Mesecar, A. D., Wilkinson, K. D., and Baker, S. C. (2007). Proteolytic processing and deubiquitinating activity of papain-like proteases of human coronavirus NL63. *J. Virol.* 81, 6007–6018. doi: 10.1128/JVI.02747-06

Chen, Y., Zhang, Z., Li, J., Gao, Y., Zhou, L., Ge, X., et al. (2018). Porcine epidemic diarrhea virus S1 protein is the critical inducer of apoptosis. *Virol. J.* 15:170. doi: 10.1186/s12985-018-1078-4

Chen, F., Zhu, Y., Wu, M., Ku, X., Yao, L., and He, Q. (2015). Full-length genome characterization of chinese porcine deltacoronavirus strain CH/SXD1/2015. *Genome Announc.* 3, e01284–e01315. doi: 10.1128/genomeA.01284-15

Choi, S., and Lee, C. (2019). Functional characterization and proteomic analysis of porcine deltacoronavirus accessory protein NS7. *J. Microbiol. Biotechnol.* 29, 1817–1829. doi: 10.4014/jmb.1908.08013

Choudhury, A., and Mukherjee, S. (2020). In silico studies on the comparative characterization of the interactions of SARS-CoV-2 spike glycoprotein with ACE-2 receptor homologs and human TLRs. *J. Med. Virol.* 92, 2105–2113. doi: 10.1002/jmv.25987

Clementz, M. A., Chen, Z., Banach, B. S., Wang, Y., Sun, L., Ratia, K., et al. (2010). Deubiquitinating and interferon antagonism activities of coronavirus papain-like proteases. *J. Virol.* 84, 4619–4629. doi: 10.1128/JVI.02406-09

Cruz, J. L., Becares, M., Sola, I., Oliveros, J. C., Enjuanes, L., and Zuniga, S. (2013). Alphacoronavirus protein 7 modulates host innate immune response. *J. Virol.* 87, 9754–9767. doi: 10.1128/JVI.01032-13

Cruz, J. L., Sola, I., Becares, M., Alberca, B., Plana, J., Enjuanes, L., et al. (2011). Coronavirus gene 7 counteracts host defenses and modulates virus virulence. *PLoS Pathog.* 7:e1002090. doi: 10.1371/journal.ppat.1002090

Deng, X., van Geelen, A., Buckley, A. C., O'Brien, A., Pillatzki, A., Lager, K. M., et al. (2019). Coronavirus endoribonuclease activity in porcine epidemic diarrhea virus suppresses type I and type III interferon responses. *J. Virol.* 93, e02000–e02018. doi: 10.1128/JVI.02000-18

Ding, L., Huang, Y., Du, Q., Dong, F., Zhao, X., Zhang, W., et al. (2014). TGEV nucleocapsid protein induces cell cycle arrest and apoptosis through activation of p53 signaling. *Biochem. Biophys. Res. Commun.* 445, 497–503. doi: 10.1016/j.bbrc.2014.02.039

Doyle, L. P., and Hutchings, L. M. (1946). A transmissible gastroenteritis in pigs. *J. Am. Vet. Med. Assoc.* 108, 257–259.

Dragan, A. I., Hargreaves, V. V., Makeyeva, E. N., and Privalov, P. L. (2007). Mechanisms of activation of interferon regulator factor 3: the role of C-terminal domain phosphorylation in IRF-3 dimerization and DNA binding. *Nucleic Acids Res.* 35, 3525–3534. doi: 10.1093/nar/gkm142

Drosten, C., Gunther, S., Preiser, W., van der Werf, S., Brodt, H. R., Becker, S., et al. (2003). Identification of a novel coronavirus in patients with severe acute respiratory syndrome. *N. Engl. J. Med.* 348, 1967–1976. doi: 10.1056/NEJMoa030747

Eleouet, J. F., Slee, E. A., Saurini, F., Castagne, N., Poncet, D., Garrido, C., et al. (2000). The viral nucleocapsid protein of transmissible gastroenteritis coronavirus (TGEV) is cleaved by caspase-6 and -7 during TGEV-induced apoptosis. *J. Virol.* 74, 3975–3983. doi: 10.1128/JVI.74.9.3975-3983.2000

Escors, D., Ortego, J., Laude, H., and Enjuanes, L. (2001). The membrane M protein carboxy terminus binds to transmissible gastroenteritis coronavirus core and contributes to core stability. *J. Virol.* 75, 1312–1324. doi: 10.1128/JVI.75.3.1312-1324.2001

Fang, P., Fang, L., Hong, Y., Liu, X., Dong, N., Ma, P., et al. (2017). Discovery of a novel accessory protein NS7a encoded by porcine deltacoronavirus. *J. Gen. Virol.* 98, 173–178. doi: 10.1099/jgv.0.000690

Fang, P., Fang, L., Liu, X., Hong, Y., Wang, Y., Dong, N., et al. (2016). Identification and subcellular localization of porcine deltacoronavirus accessory protein NS6. *Virology* 499, 170–177. doi: 10.1016/j.virol.2016.09.015

Fang, P., Fang, L., Ren, J., Hong, Y., Liu, X., Zhao, Y., et al. (2018). Porcine deltacoronavirus accessory protein NS6 antagonizes interferon beta production by interfering with the binding of RIG-I/MDA5 to double-stranded RNA. *J. Virol.* 92, e00712–e00718. doi: 10.1128/JVI.00712-18

Fang, P., Fang, L., Xia, S., Ren, J., Zhang, J., Bai, D., et al. (2020). Porcine deltacoronavirus accessory protein NS7a antagonizes IFN-beta production by competing with TRAF3 and IRF3 for binding to IKKepsilon. *Front. Cell. Infect. Microbiol.* 10:257. doi: 10.3389/fcimb.2020.00257

Favreau, D. J., Meessen-Pinard, M., Desforges, M., and Talbot, P. J. (2012). Human coronavirus-induced neuronal programmed cell death is cyclophilin d dependent and potentially caspase dispensable. *J. Virol.* 86, 81–93. doi: 10.1128/JVI.06062-11

Gack, M. U., Shin, Y. C., Joo, C. H., Urano, T., Liang, C., Sun, L., et al. (2007). TRIM25 RING-finger E3 ubiquitin ligase is essential for RIG-I-mediated antiviral activity. *Nature* 446, 916–920. doi: 10.1038/nature05732

Garwes, D. J. (1988). Transmissible gastroenteritis. *Vet. Rec.* 122, 462–463. doi: 10.1136/vr.122.19.462

Grant, A., Ponia, S. S., Tripathi, S., Balasubramaniam, V., Miorin, L., Sourisseau, M., et al. (2016). Zika virus targets human STAT2 to inhibit type I interferon signaling. *Cell Host Microbe* 19, 882–890. doi: 10.1016/j.chom.2016.05.009

Gu, W. Y., Li, Y., Liu, B. J., Wang, J., Yuan, G. F., Chen, S. J., et al. (2019). Short hairpin RNAs targeting M and N genes reduce replication of porcine deltacoronavirus in ST cells. *Virus Genes* 55, 795–801. doi: 10.1007/s11262-019-01701-y

Guan, H., Wang, Y., Perculija, V., Saeed, A., Liu, Y., Li, J., et al. (2020). Cryo-electron microscopy structure of the swine acute diarrhea syndrome coronavirus spike glycoprotein provides insights into evolution of unique coronavirus spike proteins. *J. Virol.* 94, e01301–e01320. doi: 10.1128/JVI.01301-20

Guo, X., Zhang, M., Zhang, X., Tan, X., Guo, H., Zeng, W., et al. (2017). Porcine epidemic diarrhea virus induces autophagy to benefit its replication. *Viruses* 9:53. doi: 10.3390/v9030053

Honda, K., and Taniguchi, T. (2006). IRFs: master regulators of signalling by toll-like receptors and cytosolic pattern-recognition receptors. *Nat. Rev. Immunol.* 6, 644–658. doi: 10.1038/nri1900

Huan, C. C., Wang, H. X., Sheng, X. X., Wang, R., Wang, X., and Mao, X. (2017). Glycyrrhizin inhibits porcine epidemic diarrhea virus infection and attenuates the proinflammatory responses by inhibition of high mobility group box-1 protein. *Arch. Virol.* 162, 1467–1476. doi: 10.1007/s00705-017-3259-7

Huang, Y. W., Dickerman, A. W., Pineyro, P., Li, L., Fang, L., Kiehne, R., et al. (2013). Origin, evolution, and genotyping of emergent porcine epidemic diarrhea virus strains in the United States. *mBio* 4, e00737–e00713. doi: 10.1128/mBio.00737-13

Huang, L., Xiong, T., Yu, H., Zhang, Q., Zhang, K., Li, C., et al. (2017). Encephalomyocarditis virus 3C protease attenuates type I interferon production through disrupting the TANK-TBK1-IKKepsilon-IRF3 complex. *Biochem. J.* 474, 2051–2065. doi: 10.1042/BCJ20161037

Jung, K., Annamalai, T., Lu, Z., and Saif, L. J. (2015). Comparative pathogenesis of US porcine epidemic diarrhea virus (PEDV) strain PC21A in conventional 9-day-old nursing piglets vs. 26-day-old weaned pigs. *Vet. Microbiol.* 178, 31–40. doi: 10.1016/j.vetmic.2015.04.022

Jung, K., Hu, H., and Saif, L. J. (2017). Calves are susceptible to infection with the newly emerged porcine deltacoronavirus, but not with the swine enteric alphacoronavirus, porcine epidemic diarrhea virus. *Arch. Virol.* 162, 2357–2362. doi: 10.1007/s00705-017-3351-z

Jung, K., Wang, Q., Scheuer, K. A., Lu, Z., Zhang, Y., and Saif, L. J. (2014). Pathology of US porcine epidemic diarrhea virus strain PC21A in gnotobiotic pigs. *Emerg. Infect. Dis.* 20, 662–665. doi: 10.3201/eid2004.131685

Kadoi, K., Sugioka, H., Satoh, T., and Kadoi, B. K. (2002). The propagation of a porcine epidemic diarrhea virus in swine cell lines. *New Microbiol.* 25, 285–290.

Kaewborisuth, C., Koonpaew, S., Srisutthisamphan, K., Viriyakitkosol, R., Jaru-Ampornpan, P., and Jongkaewwattana, A. (2020). PEDV ORF3 independently regulates IkappaB kinase beta-mediated NF-kappaB and IFN-beta promoter activities. *Pathogens* 9:376. doi: 10.3390/pathogens9050376

Khanolkar, A., Hartwig, S. M., Haag, B. A., Meyerholz, D. K., Harty, J. T., and Varga, S. M. (2009). Toll-like receptor 4 deficiency increases disease and mortality after mouse hepatitis virus type 1 infection of susceptible C3H mice. *J. Virol.* 83, 8946–8956. doi: 10.1128/JVI.01857-08

Kim, L., Chang, K. O., Sestak, K., Parwani, A., and Saif, L. J. (2000). Development of a reverse transcription-nested polymerase chain reaction assay for differential diagnosis of transmissible gastroenteritis virus and porcine respiratory coronavirus from feces and nasal swabs of infected pigs. *J. Vet. Diagn. Invest.* 12, 385–388. doi: 10.1177/104063870001200418

Kindler, E., Gil-Cruz, C., Spanier, J., Li, Y., Wilhelm, J., Rabouw, H. H., et al. (2017). Early endonuclease-mediated evasion of RNA sensing ensures efficient coronavirus replication. *PLoS Pathog.* 13:e1006195. doi: 10.1371/journal.ppat.1006195

Kocherhans, R., Bridgen, A., Ackermann, M., and Tobler, K. (2001). Completion of the porcine epidemic diarrhoea coronavirus (PEDV) genome sequence. *Virus Genes* 23, 137–144. doi: 10.1023/A:1011831902219

Kotenko, S. V., Rivera, A., Parker, D., and Durbin, J. E. (2019). Type III IFNs: beyond antiviral protection. *Semin. Immunol.* 43:101303. doi: 10.1016/j.smim.2019.101303

Kurt-Jones, E. A., Popova, L., Kwinn, L., Haynes, L. M., Jones, L. P., Tripp, R. A., et al. (2000). Pattern recognition receptors TLR4 and CD14 mediate response to respiratory syncytial virus. *Nat. Immunol.* 1, 398–401. doi: 10.1038/80833

Lan, Y., Zhao, K., Wang, G., Dong, B., Zhao, J., Tang, B., et al. (2013). Porcine hemagglutinating encephalomyelitis virus induces apoptosis in a porcine kidney cell line via caspase-dependent pathways. *Virus Res.* 176, 292–297. doi: 10.1016/j.virusres.2013.05.019

Lazear, H. M., Schoggins, J. W., and Diamond, M. S. (2019). Shared and distinct functions of type I and type III interferons. *Immunity* 50, 907–923. doi: 10.1016/j.immuni.2019.03.025

Lednicky, J. A., Tagliamonte, M. S., White, S. K., Elbadry, M. A., Alam, M. M., Stephenson, C. J., et al. (2021). Independent infections of porcine

deltacoronavirus among Haitian children. *Nature* 600, 133–137. doi: 10.1038/s41586-021-04111-z

Lee, S., and Lee, C. (2015). Functional characterization and proteomic analysis of the nucleocapsid protein of porcine deltacoronavirus. *Virus Res.* 208, 136–145. doi: 10.1016/j.virusres.2015.06.013

Lei, Y., Moore, C. B., Liesman, R. M., O'Connor, B. P., Bergstralh, D. T., Chen, Z. J., et al. (2009). MAVS-mediated apoptosis and its inhibition by viral proteins. *PLoS One* 4:e5466. doi: 10.1371/journal.pone.0005466

Lei, X., Sun, Z., Liu, X., Jin, Q., He, B., and Wang, J. (2011). Cleavage of the adaptor protein TRIF by enterovirus 71 3C inhibits antiviral responses mediated by toll-like receptor 3. *J. Virol.* 85, 8811–8818. doi: 10.1128/JVI.00447-11

Li, F. (2015). Receptor recognition mechanisms of coronaviruses: a decade of structural studies. *J. Virol.* 89, 1954–1964. doi: 10.1128/JVI.02615-14

Li, K., Li, H., Bi, Z., Song, D., Zhang, F., Lei, D., et al. (2019). Significant inhibition of re-emerged and emerging swine enteric coronavirus in vitro using the multiple shRNA expression vector. *Antivir. Res.* 166, 11–18. doi: 10.1016/j.antiviral.2019.03.010

Li, Z., Ma, Z., Li, Y., Gao, S., and Xiao, S. (2020). Porcine epidemic diarrhea virus: molecular mechanisms of attenuation and vaccines. *Microb. Pathog.* 149:104553. doi: 10.1016/j.micpath.2020.104553

Liang, Q., Zhang, H., Li, B., Ding, Q., Wang, Y., Gao, W., et al. (2019). Susceptibility of chickens to porcine deltacoronavirus infection. *Viruses* 11:573. doi: 10.3390/v11060573

Likai, J., Shasha, L., Wenxian, Z., Jingjiao, M., Jianhe, S., Hengan, W., et al. (2019). Porcine deltacoronavirus nucleocapsid protein suppressed IFN-beta production by interfering porcine RIG-I dsRNA-binding and K63-linked polyubiquitination. *Front. Immunol.* 10:1024. doi: 10.3389/fimmu.2019.01024

Lin, W., Kim, S. S., Yeung, E., Kamegaya, Y., Blackard, J. T., Kim, K. A., et al. (2006). Hepatitis C virus core protein blocks interferon signaling by interaction with the STAT1 SH2 domain. *J. Virol.* 80, 9226–9235. doi: 10.1128/JVI.00459-06

Lin, H., Li, B., Liu, M., Zhou, H., He, K., and Fan, H. (2020). Nonstructural protein 6 of porcine epidemic diarrhea virus induces autophagy to promote viral replication via the PI3K/Akt/mTOR axis. *Vet. Microbiol.* 244:108684. doi: 10.1016/j.vetmic.2020.108684

Liu, J., and Cao, X. (2016). Cellular and molecular regulation of innate inflammatory responses. *Cell. Mol. Immunol.* 13, 711–721. doi: 10.1038/cmi.2016.58

Liu, X., Fang, P., Fang, L., Hong, Y., Zhu, X., Wang, D., et al. (2019). Porcine deltacoronavirus nsp15 antagonizes interferon-beta production independently of its endoribonuclease activity. *Mol. Immunol.* 114, 100–107. doi: 10.1016/j.molimm.2019.07.003

Liu, Y., Liang, Q. Z., Lu, W., Yang, Y. L., Chen, R., Huang, Y. W., et al. (2021). A comparative analysis of coronavirus nucleocapsid (N) proteins reveals the SADS-CoV N protein antagonizes IFN-beta production by inducing ubiquitination of RIG-I. *Front. Immunol.* 12:688758. doi: 10.3389/fimmu.2021.688758

Liu, C., Tang, J., Ma, Y., Liang, X., Yang, Y., Peng, G., et al. (2015). Receptor usage and cell entry of porcine epidemic diarrhea coronavirus. *J. Virol.* 89, 6121–6125. doi: 10.1128/JVI.00430-15

Liu, Q., and Wang, H. Y. (2021). Porcine enteric coronaviruses: an updated overview of the pathogenesis, prevalence, and diagnosis. *Vet. Res. Commun.* 45, 75–86. doi: 10.1007/s11259-021-09808-0

Liu, G., Zhong, M., Guo, C., Komatsu, M., Xu, J., Wang, Y., et al. (2016). Autophagy is involved in regulating influenza A virus RNA and protein synthesis associated with both modulation of Hsp90 induction and mTOR/p70S6K signaling pathway. *Int. J. Biochem. Cell Biol.* 72, 100–108. doi: 10.1016/j.biocel.2016.01.012

McBride, R., van Zyl, M., and Fielding, B. C. (2014). The coronavirus nucleocapsid is a multifunctional protein. *Viruses* 6, 2991–3018. doi: 10.3390/v6082991

Meylan, E., Tschopp, J., and Karin, M. (2006). Intracellular pattern recognition receptors in the host response. *Nature* 442, 39–44. doi: 10.1038/nature04946

Mora-Diaz, J. C., Pineyro, P. E., Houston, E., Zimmerman, J., and Gimenez-Lirola, L. G. (2019). Porcine hemagglutinating encephalomyelitis virus: a review. *Front. Vet. Sci.* 6:53. doi: 10.3389/fvets.2019.00053

Mukherjee, A., Morosky, S. A., Delorme-Axford, E., Dybdahl-Sissoko, N., Oberste, M. S., Wang, T., et al. (2011). The coxsackievirus B 3C protease cleaves MAVS and TRIF to attenuate host type I interferon and apoptotic signaling. *PLoS Pathog.* 7:e1001311. doi: 10.1371/journal.ppat.1001311

Narayanan, K., Maeda, A., Maeda, J., and Makino, S. (2000). Characterization of the coronavirus M protein and nucleocapsid interaction in infected cells. *J. Virol.* 74, 8127–8134. doi: 10.1128/JVI.74.17.8127-8134.2000

Nguyen, V. P., and Hogue, B. G. (1997). Protein interactions during coronavirus assembly. *J. Virol.* 71, 9278–9284. doi: 10.1128/jvi.71.12.9278-9284.1997

Pan, Y., Tian, X., Qin, P., Wang, B., Zhao, P., Yang, Y. L., et al. (2017). Discovery of a novel swine enteric alphacoronavirus (SeACoV) in southern China. *Vet. Microbiol.* 211, 15–21. doi: 10.1016/j.vetmic.2017.09.020

Panne, D., Maniatis, T., and Harrison, S. C. (2007). An atomic model of the interferon-beta enhanceosome. *Cell* 129, 1111–1123. doi: 10.1016/j.cell.2007.05.019

Park, J. E., Cruz, D. J., and Shin, H. J. (2011). Receptor-bound porcine epidemic diarrhea virus spike protein cleaved by trypsin induces membrane fusion. *Arch. Virol.* 156, 1749–1756. doi: 10.1007/s00705-011-1044-6

Park, S. J., Moon, H. J., Luo, Y., Kim, H. K., Kim, E. M., Yang, J. S., et al. (2008). Cloning and further sequence analysis of the ORF3 gene of wild- and attenuated-type porcine epidemic diarrhea viruses. *Virus Genes* 36, 95–104. doi: 10.1007/s11262-007-0164-2

Park, J. Y., Ryu, J., Park, J. E., Hong, E. J., and Shin, H. J. (2021). Heat shock protein 70 could enhance porcine epidemic diarrhoea virus replication by interacting with membrane proteins. *Vet. Res.* 52:138. doi: 10.1186/s13567-021-01006-9

Penzes, Z., Gonzalez, J. M., Calvo, E., Izeta, A., Smerdou, C., Mendez, A., et al. (2001). Complete genome sequence of transmissible gastroenteritis coronavirus PUR46-MAD clone and evolution of the purdue virus cluster. *Virus Genes* 23, 105–118. doi: 10.1023/A:1011147832586

Riffault, S., Carrat, C., Besnardeau, L., La Bonnardiere, C., and Charley, B. (1997). In vivo induction of interferon-alpha in pig by non-infectious coronavirus: tissue localization and in situ phenotypic characterization of interferon-alpha-producing cells. *J. Gen. Virol.* 78, 2483–2487. doi: 10.1099/0022-1317-78-10-2483

Saif, L. J. (1999). Comparative pathogenesis of enteric viral infections of swine. *Adv. Exp. Med. Biol.* 473, 47–59. doi: 10.1007/978-1-4615-4143-1_4

Sawicki, S. G., Sawicki, D. L., Younker, D., Meyer, Y., Thiel, V., Stokes, H., et al. (2005). Functional and genetic analysis of coronavirus replicase-transcriptase proteins. *PLoS Pathog.* 1:e39. doi: 10.1371/journal.ppat.0010039

Scheuplein, V. A., Seifried, J., Malczyk, A. H., Miller, L., Hocker, L., Vergara-Alert, J., et al. (2015). High secretion of interferons by human plasmacytoid dendritic cells upon recognition of middle east respiratory syndrome coronavirus. *J. Virol.* 89, 3859–3869. doi: 10.1128/JVI.03607-14

Schoggins, J. W., and Rice, C. M. (2011). Interferon-stimulated genes and their antiviral effector functions. *Curr. Opin. Virol.* 1, 519–525. doi: 10.1016/j.coviro.2011.10.008

Seth, R. B., Sun, L., Ea, C. K., and Chen, Z. J. (2005). Identification and characterization of MAVS, a mitochondrial antiviral signaling protein that activates NF-kappaB and IRF 3. *Cell* 122, 669–682. doi: 10.1016/j.cell.2005.08.012

Shan, Y., Liu, Z. Q., Li, G. W., Chen, C., Luo, H., Liu, Y. J., et al. (2018). Nucleocapsid protein from porcine epidemic diarrhea virus isolates can antagonize interferon-lambda production by blocking the nuclear factor-kappaB nuclear translocation. *J. Zhejiang Univ. Sci. B* 19, 570–580. doi: 10.1631/jzus.B1700283

Shang, J., Zheng, Y., Yang, Y., Liu, C., Geng, Q., Tai, W., et al. (2018). Cryo-electron microscopy structure of porcine deltacoronavirus spike protein in the prefusion state. *J. Virol.* 92, e01556–e01617. doi: 10.1128/JVI.01556-17

Shen, Z., Yang, Y., Yang, S., Zhang, G., Xiao, S., Fu, Z. F., et al. (2020). Structural and biological basis of alphacoronavirus nsp1 associated with host proliferation and immune evasion. *Viruses* 12:812. doi: 10.3390/v12080812

Shi, P., Su, Y., Li, R., Liang, Z., Dong, S., and Huang, J. (2019). PEDV nsp16 negatively regulates innate immunity to promote viral proliferation. *Virus Res.* 265, 57–66. doi: 10.1016/j.virusres.2019.03.005

Si, F., Hu, X., Wang, C., Chen, B., Wang, R., Dong, S., et al. (2020). Porcine epidemic diarrhea virus (PEDV) ORF3 enhances viral proliferation by inhibiting apoptosis of infected cells. *Viruses* 12:214. doi: 10.3390/v12020214

Song, D., and Park, B. (2012). Porcine epidemic diarrhoea virus: a comprehensive review of molecular epidemiology, diagnosis, and vaccines. *Virus Genes* 44, 167–175. doi: 10.1007/s11262-012-0713-1

Stevenson, G. W., Hoang, H., Schwartz, K. J., Burrough, E. R., Sun, D., Madson, D., et al. (2013). Emergence of porcine epidemic diarrhea virus

in the United States: clinical signs, lesions, and viral genomic sequences. *J. Vet. Diagn. Investig.* 25, 649–654. doi: 10.1177/1040638713501675

Sun, Z., Chen, Z., Lawson, S. R., and Fang, Y. (2010). The cysteine protease domain of porcine reproductive and respiratory syndrome virus nonstructural protein 2 possesses deubiquitinating and interferon antagonism functions. *J. Virol.* 84, 7832–7846. doi: 10.1128/JVI.00217-10

Sun, M. X., Huang, L., Wang, R., Yu, Y. L., Li, C., Li, P. P., et al. (2012b). Porcine reproductive and respiratory syndrome virus induces autophagy to promote virus replication. *Autophagy* 8, 1434–1447. doi: 10.4161/auto.21159

Sun, P., Jin, J., Wang, L., Wang, J., Zhou, H., Zhang, Q., et al. (2021). Porcine epidemic diarrhea virus infections induce autophagy in vero cells via ROS-dependent endoplasmic reticulum stress through PERK and IRE1 pathways. *Vet. Microbiol.* 253:108959. doi: 10.1016/j.vetmic.2020.108959

Sun, L., Xing, Y., Chen, X., Zheng, Y., Yang, Y., Nichols, D. B., et al. (2012a). Coronavirus papain-like proteases negatively regulate antiviral innate immune response through disruption of STING-mediated signaling. *PLoS One* 7:e30802. doi: 10.1371/journal.pone.0030802

Suzuki, T., Shibahara, T., Imai, N., Yamamoto, T., and Ohashi, S. (2018). Genetic characterization and pathogenicity of Japanese porcine deltacoronavirus. *Infect. Genet. Evol.* 61, 176–182. doi: 10.1016/j.meegid.2018.03.030

Utiger, A., Tobler, K., Bridgen, A., Suter, M., Singh, M., and Ackermann, M. (1995). Identification of proteins specified by porcine epidemic diarrhoea virus. *Adv. Exp. Med. Biol.* 380, 287–290. doi: 10.1007/978-1-4615-1899-0_46

van Kasteren, P. B., Beugeling, C., Ninaber, D. K., Frias-Staheli, N., van Boheemen, S., Garcia-Sastre, A., et al. (2012). Arterivirus and nairovirus ovarian tumor domain-containing deubiquitinases target activated RIG-I to control innate immune signaling. *J. Virol.* 86, 773–785. doi: 10.1128/JVI.06277-11

Van Reeth, K., Van Gucht, S., and Pensaert, M. (2002). In vivo studies on cytokine involvement during acute viral respiratory disease of swine: troublesome but rewarding. *Vet. Immunol. Immunopathol.* 87, 161–168. doi: 10.1016/S0165-2427(02)00047-8

Wang, L., Byrum, B., and Zhang, Y. (2014b). Detection and genetic characterization of deltacoronavirus in pigs, Ohio, USA, 2014. *Emerg. Infect. Dis.* 20, 1227–1230. doi: 10.3201/eid2007.140296

Wang, D., Fang, L., Li, P., Sun, L., Fan, J., Zhang, Q., et al. (2011). The leader proteinase of foot-and-mouth disease virus negatively regulates the type I interferon pathway by acting as a viral deubiquitinase. *J. Virol.* 85, 3758–3766. doi: 10.1128/JVI.02589-10

Wang, D., Fang, L., Li, K., Zhong, H., Fan, J., Ouyang, C., et al. (2012). Foot-and-mouth disease virus 3C protease cleaves NEMO to impair innate immune signaling. *J. Virol.* 86, 9311–9322. doi: 10.1128/JVI.00722-12

Wang, D., Fang, L., Shi, Y., Zhang, H., Gao, L., Peng, G., et al. (2016). Porcine epidemic diarrhea virus 3C-like protease regulates its interferon antagonism by cleaving NEMO. *J. Virol.* 90, 2090–2101. doi: 10.1128/JVI.02514-15

Wang, D., Fang, L., Wei, D., Zhang, H., Luo, R., Chen, H., et al. (2014a). Hepatitis A virus 3C protease cleaves NEMO to impair induction of beta interferon. *J. Virol.* 88, 10252–10258. doi: 10.1128/JVI.00869-14

Wang, L., Qiao, X., Zhang, S., Qin, Y., Guo, T., Hao, Z., et al. (2018). Porcine transmissible gastroenteritis virus nonstructural protein 2 contributes to inflammation via NF-kappaB activation. *Virulence* 9, 1685–1698. doi: 10.1080/21505594.2018.1536632

Wang, Q., Vlasova, A. N., Kenney, S. P., and Saif, L. J. (2019). Emerging and re-emerging coronaviruses in pigs. *Curr. Opin. Virol.* 34, 39–49. doi: 10.1016/j.coviro.2018.12.001

Wang, F., Wang, S. Q., Wang, H. F., Wu, Z. C., Bao, W. B., and Wu, S. L. (2020a). Effects of porcine epidemic diarrhea virus infection on toll-like receptor expression and cytokine levels in porcine intestinal epithelial cells. *Pol. J. Vet. Sci.* 23, 119–126. doi: 10.24425/pjvs.2020.132755

Wang, X. W., Wang, M., Zhan, J., Liu, Q. Y., Fang, L. L., Zhao, C. Y., et al. (2020c). Pathogenicity and immunogenicity of a new strain of porcine epidemic diarrhea virus containing a novel deletion in the N gene. *Vet. Microbiol.* 240:108511. doi: 10.1016/j.vetmic.2019.108511

Wang, R., Yu, R., Chen, B., Si, F., Wang, J., Xie, C., et al. (2020b). Identification of host cell proteins that interact with the M protein of porcine epidemic diarrhea virus. *Vet. Microbiol.* 246:108729. doi: 10.1016/j.vetmic.2020.108729

Wei, G., Luo, S., Wu, W., Hu, J., and Zhou, R. (2021). Activation of interleukin-1beta release and pyroptosis by transmissible gastroenteritis virus is dependent on the NOD-like receptor protein 3 inflammasome in porcine intestinal epithelial cell line. *Viral Immunol.* 34, 401–409. doi: 10.1089/vim.2020.0227

Woo, P. C., Huang, Y., Lau, S. K., and Yuen, K. Y. (2010). Coronavirus genomics and bioinformatics analysis. *Viruses* 2, 1804–1820. doi: 10.3390/v2081803

Woo, P. C., Lau, S. K., Lam, C. S., Lau, C. C., Tsang, A. K., Lau, J. H., et al. (2012). Discovery of seven novel mammalian and avian coronaviruses in the genus deltacoronavirus supports bat coronaviruses as the gene source of alphacoronavirus and betacoronavirus and avian coronaviruses as the gene source of gammacoronavirus and deltacoronavirus. *J. Virol.* 86, 3995–4008. doi: 10.1128/JVI.06540-11

Wood, E. N. (1977). An apparently new syndrome of porcine epidemic diarrhoea. *Vet. Rec.* 100, 243–244. doi: 10.1136/vr.100.12.243

Wu, Z., Cheng, L., Xu, J., Li, P., Li, X., Zou, D., et al. (2020b). The accessory protein ORF3 of porcine epidemic diarrhea virus inhibits cellular interleukin-6 and interleukin-8 productions by blocking the nuclear factor-kappaB p65 activation. *Vet. Microbiol.* 251:108892. doi: 10.1016/j.vetmic.2020.108892

Wu, Y., Zhang, H., Shi, Z., Chen, J., Li, M., Shi, H., et al. (2020a). Porcine epidemic diarrhea virus nsp15 antagonizes interferon signaling by RNA degradation of TBK1 and IRF3. *Viruses* 12:599. doi: 10.3390/v12060599

Xia, L., Yang, Y., Wang, J., Jing, Y., and Yang, Q. (2018). Impact of TGEV infection on the pig small intestine. *Virol. J.* 15:102. doi: 10.1186/s12985-018-1012-9

Xing, Y., Chen, J., Tu, J., Zhang, B., Chen, X., Shi, H., et al. (2013). The papain-like protease of porcine epidemic diarrhea virus negatively regulates type I interferon pathway by acting as a viral deubiquitinase. *J. Gen. Virol.* 94, 1554–1567. doi: 10.1099/vir.0.051169-0

Xu, Z., Zhang, Y., Gong, L., Huang, L., Lin, Y., Qin, J., et al. (2019a). Isolation and characterization of a highly pathogenic strain of porcine enteric alphacoronavirus causing watery diarrhoea and high mortality in newborn piglets. *Transbound. Emerg. Dis.* 66, 119–130. doi: 10.1111/tbed.12992

Xu, X. G., Zhang, H. L., Zhang, Q., Dong, J., Huang, Y., and Tong, D. W. (2015). Porcine epidemic diarrhea virus M protein blocks cell cycle progression at S-phase and its subcellular localization in the porcine intestinal epithelial cells. *Acta Virol.* 59, 265–275. doi: 10.4149/av_2015_03_265

Xu, X., Zhang, H., Zhang, Q., Dong, J., Liang, Y., Huang, Y., et al. (2013a). Porcine epidemic diarrhea virus E protein causes endoplasmic reticulum stress and up-regulates interleukin-8 expression. *Virol. J.* 10:26. doi: 10.1186/1743-422X-10-26

Xu, X., Zhang, H., Zhang, Q., Huang, Y., Dong, J., Liang, Y., et al. (2013b). Porcine epidemic diarrhea virus N protein prolongs S-phase cell cycle, induces endoplasmic reticulum stress, and up-regulates interleukin-8 expression. *Vet. Microbiol.* 164, 212–221. doi: 10.1016/j.vetmic.2013.01.034

Xu, Z., Zhong, H., Huang, S., Zhou, Q., Du, Y., Chen, L., et al. (2019b). Porcine deltacoronavirus induces TLR3, IL-12, IFN-alpha, IFN-beta and PKR mRNA expression in infected peyer's patches in vivo. *Vet. Microbiol.* 228, 226–233. doi: 10.1016/j.vetmic.2018.12.012

Yachdav, G., Kloppmann, E., Kajan, L., Hecht, M., Goldberg, T., Hamp, T., et al. (2014). PredictProtein--an open resource for online prediction of protein structural and functional features. *Nucleic Acids Res.* 42, W337–W343. doi: 10.1093/nar/gku366

Yang, L., Xu, J., Guo, L., Guo, T., Zhang, L., Feng, L., et al. (2018). Porcine epidemic diarrhea virus-induced epidermal growth factor receptor activation impairs the antiviral activity of type I interferon. *J. Virol.* 92, e02095–e02117. doi: 10.1128/JVI.02095-17

Ye, G., Wang, X., Tong, X., Shi, Y., Fu, Z. F., and Peng, G. (2020). Structural basis for inhibiting porcine epidemic diarrhea virus replication with the 3C-like protease inhibitor GC376. *Viruses* 12:240. doi: 10.3390/v12020240

Yu, J., Qiao, S., Guo, R., and Wang, X. (2020). Cryo-EM structures of HKU2 and SADS-CoV spike glycoproteins provide insights into coronavirus evolution. *Nat. Commun.* 11:3070. doi: 10.1038/s41467-020-16876-4

Zhang, J. (2016). Porcine deltacoronavirus: overview of infection dynamics, diagnostic methods, prevalence and genetic evolution. *Virus Res.* 226, 71–84. doi: 10.1016/j.virusres.2016.05.028

Zhang, Q., Ke, H., Blikslager, A., Fujita, T., and Yoo, D. (2018). Type III interferon restriction by porcine epidemic diarrhea virus and the role of viral protein nsp1 in IRF1 signaling. *J. Virol.* 92, e01677–e01717. doi: 10.1128/JVI.01677-17

Zhang, Q., Ma, J., and Yoo, D. (2017). Inhibition of NF-kappaB activity by the porcine epidemic diarrhea virus nonstructural protein 1 for innate immune evasion. *Virology* 510, 111–126. doi: 10.1016/j.virol.2017.07.009

Zhang, Q., Shi, K., and Yoo, D. (2016). Suppression of type I interferon production by porcine epidemic diarrhea virus and degradation of CREB-binding protein by nsp1. *Virology* 489, 252–268. doi: 10.1016/j.virol.2015.12.010

Zheng, L., Wang, X., Guo, D., Cao, J., Cheng, L., Li, X., et al. (2021). Porcine epidemic diarrhea virus E protein suppresses RIG-I signaling-mediated interferon-beta production. *Vet. Microbiol.* 254:108994. doi: 10.1016/j.vetmic.2021.108994

Zhou, P., Fan, H., Lan, T., Yang, X. L., Shi, W. F., Zhang, W., et al. (2018). Fatal swine acute diarrhoea syndrome caused by an HKU2-related coronavirus of bat origin. *Nature* 556, 255–258. doi: 10.1038/s41586-018-0010-9

Zhou, J., Fang, L., Yang, Z., Xu, S., Lv, M., Sun, Z., et al. (2019). Identification of novel proteolytically inactive mutations in coronavirus 3C-like protease using a combined approach. *FASEB J.* 33, 14575–14587. doi: 10.1096/fj.201901624RR

Zhu, X., Fang, L., Wang, D., Yang, Y., Chen, J., Ye, X., et al. (2017a). Porcine deltacoronavirus nsp5 inhibits interferon-beta production through the cleavage of NEMO. *Virology* 502, 33–38. doi: 10.1016/j.virol.2016.12.005

Zhu, L., Mou, C., Yang, X., Lin, J., and Yang, Q. (2016). Mitophagy in TGEV infection counteracts oxidative stress and apoptosis. *Oncotarget* 7, 27122–27141. doi: 10.18632/oncotarget.8345

Zhu, X., Wang, D., Zhou, J., Pan, T., Chen, J., Yang, Y., et al. (2017b). Porcine deltacoronavirus nsp5 antagonizes type I interferon signaling by cleaving STAT2. *J. Virol.* 91, e00003–e00017. doi: 10.1128/JVI.00003-17

Zou, D., Xu, J., Duan, X., Xu, X., Li, P., Cheng, L., et al. (2019). Porcine epidemic diarrhea virus ORF3 protein causes endoplasmic reticulum stress to facilitate autophagy. *Vet. Microbiol.* 235, 209–219. doi: 10.1016/j.vetmic.2019.07.005

Conflict of Interest: The authors declare that the research was conducted in the absence of any commercial or financial relationships that could be construed as a potential conflict of interest.

Publisher's Note: All claims expressed in this article are solely those of the authors and do not necessarily represent those of their affiliated organizations, or those of the publisher, the editors and the reviewers. Any product that may be evaluated in this article, or claim that may be made by its manufacturer, is not guaranteed or endorsed by the publisher.

frontiers in Microbiology

ORIGINAL RESEARCH
published: 03 March 2022
doi: 10.3389/fmicb.2021.803031

Neutralizing Antibodies and Cellular Immune Responses Against SARS-CoV-2 Sustained One and a Half Years After Natural Infection

Li-na Yan[1], Pan-pan Liu[1], Xu-gui Li[2], Shi-jing Zhou[2], Hao Li[3], Zhi-yin Wang[4], Feng Shen[5], Bi-chao Lu[6], Yu Long[6], Xiao Xiao[1], Zhen-dong Wang[7], Dan Li[1], Hui-ju Han[1], Hao Yu[8], Shu-han Zhou[6], Wen-liang Lv[6]* and Xue-jie Yu[1]**

[1] State Key Laboratory of Virology, School of Public Health, Wuhan University, Wuhan, China, [2] The Department of Clinical Laboratory Medicine, Hubei 672 Orthopaedics Hospital, Wuhan, China, [3] The First School of Clinical Medicine, Hubei University of Chinese Medicine, Wuhan, China, [4] Department of Clinical Laboratory Medicine, Hubei University of Chinese Medicine Huangjiahu Hospital, Wuhan, China, [5] College of Acupuncture and Orthopedics, Hubei University of Chinese Medicine, Wuhan, China, [6] Clinical College, Hubei University of Chinese Medicine, Wuhan, China, [7] School of Public Health, Xi'an Medical University, Xi'an, China, [8] Department of Neuroscience, Cell Biology, and Anatomy, University of Texas Medical Branch, Galveston, TX, United States*

OPEN ACCESS

Edited by:
Cao Yong Chang, Sun Yat-sen University, China

Reviewed by:
Irene Ramos, Icahn School of Medicine at Mount Sinai, United States
James Tristan Gordy, Johns Hopkins University, United States

***Correspondence:**
Shu-han Zhou
shuhan_zhou@hbtcm.edu.cn
Wen-liang Lv
wenliang_lv@hbtcm.edu.cn
Xue-jie Yu
yuxuejie@whu.edu.cn

Specialty section:
This article was submitted to Virology, a section of the journal Frontiers in Microbiology

Received: *27 October 2021*
Accepted: *20 December 2021*
Published: *03 March 2022*

Citation:
Yan L-n, Liu P-p, Li X-g, Zhou S-j, Li H, Wang Z-y, Shen F, Lu B-c, Long Y, Xiao X, Wang Z-d, Li D, Han H-j, Yu H, Zhou S-h, Lv W-l and Yu X-j (2022) Neutralizing Antibodies and Cellular Immune Responses Against SARS-CoV-2 Sustained One and a Half Years After Natural Infection. Front. Microbiol. 12:803031. doi: 10.3389/fmicb.2021.803031

Background: COVID-19 has caused more than 2.6 billion infections and several million deaths since its outbreak 2 years ago. We know very little about the long-term cellular immune responses and the kinetics of neutralizing antibodies (NAbs) to SARS-CoV-2 because it has emerged only recently in the human population.

Methods: We collected blood samples from individuals who were from the first wave of the COVID-19 epidemic in Wuhan between December 30, 2019, and February 24, 2020. We analyzed NAbs to SARS-CoV-2 using pseudoviruses and IgG antibodies to SARS-CoV-2 spike (S) and nucleocapsid (N) protein using enzyme-linked immunosorbent assay in patients' sera and determined SARS-CoV-2-specific T-cell responses of patients with ELISpot assays.

Results: We found that 91.9% (57/62) and 88.9% (40/45) of COVID-19 patients had NAbs against SARS-CoV-2 in a year (10–11 months) and one and a half years (17–18 months), respectively, after the onset of illness, indicating that NAbs against SARS-CoV-2 waned slowly and possibly persisted over a long period time. Over 80% of patients had IgG antibodies to SARS-CoV-2 S and N protein one and a half years after illness onset. Most patients also had robust memory T-cell responses against SARS-CoV-2 one and a half years after the illness. Among the patients, 95.6% (43/45) had an IFN-γ-secreting T-cell response and 93.8% (15/16) had an IL-2-secreting T-cell response. The T-cell responses to SARS-CoV-2 were positively correlated with antibodies (including neutralizing antibodies and IgG antibodies to S and N protein) in COVID-19 patients. Eighty percent (4/5) of neutralizing antibody-negative patients also had SARS-CoV-2-specific T-cell response. After long-term infection, protective immunity was independent of disease severity, sex, and age.

Conclusions: We concluded that SARS-CoV-2 infection elicited a robust and persistent neutralizing antibody and memory T-cell response in COVID-19 patients, indicating that these sustained immune responses, among most SARS-CoV-2-infected people, may play a crucial role in protection against reinfection.

Keywords: neutralizing antibody, T-cell response, antigen-specific, SARS-CoV-2, COVID-19

INTRODUCTION

Coronavirus disease 2019 (COVID-19), caused by a newly discovered beta coronavirus, severe acute respiratory syndrome coronavirus 2 (SARS-CoV-2), has become a global pandemic with no end in sight. As of December 12, 2021, 267.9 million cases of COVID-19 had been confirmed worldwide and 5.2 million cases had died (World Health Organization [WHO], 2021). The protective immune responses triggered by viral infection consist of two main components, humoral and cell-mediated immune responses. Neutralizing antibodies (NAbs) can neutralize the viral pathogen and are considered crucial for protection against viral infections. Specific T-cell immune responses are usually directed against virus-infected cells, accelerate viral clearance, and restrict viral spread *in vivo* (Feng et al., 2021). Studies have indicated a protective role of NAbs and antigen-specific memory T-cell responses in COVID-19 patients (Addetia et al., 2020; Huang et al., 2020). SARS-CoV-2 convalescent patients usually generate robust immune responses in the early stages of convalescence (Choe et al., 2020; Robbiani et al., 2020; Rydyznski Moderbacher et al., 2020; Wang Y. et al., 2020; Cassaniti et al., 2021). Previous studies reported that SARS-CoV-2-specific T-cell responses occurred in virtually all patients (Grifoni et al., 2020; Feng et al., 2021; Sandberg et al., 2021). However, the long-term role of NAbs and cellular immunity against SARS-CoV-2 is unknown due to the recent outbreak of COVID-19, which may contribute to protection against reinfection.

In this study, blood samples were obtained from COVID-19 patients with mild and severe illness from 1 to 18 months after disease onset to evaluate neutralizing antibodies, antigen-specific antibodies, and T-cell responses to SARS-CoV-2.

MATERIALS AND METHODS

Blood Samples

The study was conducted with the approval of the Ethics Committee of Wuhan University (2020YF0051). Informed consent was obtained from all participants. A total of 170 participants were recruited in this study. Inclusion criteria were as follows: (1) no history of COVID-19 vaccination; and (2) no individuals living with human immunodeficiency virus (HIV). All COVID-19 cases were diagnosed according to the guidelines for the diagnosis and treatment of new coronavirus pneumonia issued by the Chinese government, and were confirmed to be infected with SARS-CoV-2 by RT-PCR test of nasopharyngeal swabs. A total of 150 hospitalized patients who were the first wave of COVID-19 in Wuhan between December 30, 2019, and February 24, 2020 were recruited (**Figure 1**). The 1- to 2.5-month sera were obtained from inpatients, and the 10- to 11-month sera and the 17- to 18-month sera were obtained from volunteers who had been hospitalized and recovered from COVID-19. We divided the observation period into 1–2.5 months (n = 43), 10–11 months (n = 62), and 17–18 months (n = 45). The samples collected at different time points came from different patients. A total of 20 healthy control subjects who were neither infected with SARS-CoV-2 nor vaccinated against COVID-19 were recruited. All sera were aliquoted and stored at −80°C.

Generation of the Human Angiotensin-Converting Enzyme 2 (ACE2) Overexpression Cell Lines (Vero-E6$_{ACE2}$ Cells)

The lentiviral expression vectors were used to transfect Vero-E6 cells to stably express human ACE2. The retroviral plasmid for human ACE2 expression (pCDH-CMV-hACE-EF1-RFP) was purchased from Tsingke Biological Technology (Nanjing, China). HEK293T cells were transfected with the retroviral vector pCDH-CMV-hACE-EF1-RFP and the packaging plasmids pMD2.G and psPAX2 at a ratio of 2:1:1 with Lipofectamine 3000 (Invitrogen, Carlsbad, CA, United States). After 48 h of incubation, the supernatant was harvested and the lentiviruses in the supernatant were purified with polyethylene glycol (PEG) 8000 (Solarbio, Beijing, China). Confluence monolayers (80–90%) of Vero-E6 cells were infected with purified lentiviruses with polybrene (2 μg/ml). Stable Vero-E6$_{ACE2}$ cells were selected by puromycin resistance.

Production of SARS-CoV2 S Pseudovirus

To construct an HIV-1 pseudovirus carrying the spike (S) protein of SARS-CoV-2, the full length of the S gene with a C-terminal 19-amino-acid deletion from the Wuhan-Hu-1 strain (GenBank: MN908947) was codon-optimized and synthesized (Sino Biology Inc., Shanghai, China). The S gene was cloned into the eukaryotic expression plasmid pCMV to generate the plasmid pCMV-3Flag-SARS-CoV-2-S19del. The HIV-1 NL4-3 ΔEnv Vpr luciferase reporter vector (pNL4.3-R-E-luc) was kindly provided by Professor Cheguo Cai (Wuhan University, Wuhan, China). HEK293T cells were co-transfected with pNL4.3-R-E-luc and pCMV-3Flag-SARS-CoV-2-S19del using Lipofectamine 3000 to package the pseudovirus. The Supernatant containing pseudovirus was collected at 72 h post-transfection. To construct the vesicular stomatitis virus (VSV) pseudovirus as control, plasmid pMD2.G was co-transfected with plasmid pNL4.3-R-E-luc.

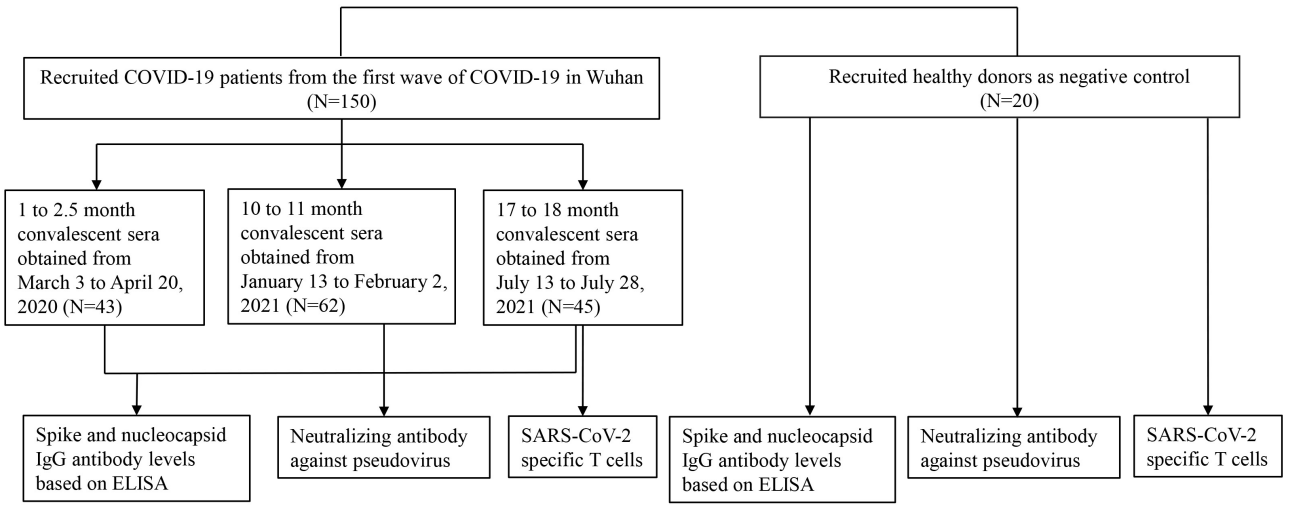

FIGURE 1 | Enrollment of COVID-19 patients and healthy persons. A total of 150 COVID-19 patients including inpatients and convalescent patients were enrolled in this study and patients' sera were obtained from 1 to 18 months after the onset of illness in three periods (1–2.5, 10–11, and 17–18 months). A total of 20 healthy persons were recruited as the negative control.

Pseudovirus titers were determined on Vero-E6$_{ACE2}$ cells by measuring relative luminescence units (RLU). Briefly, Vero-E6$_{ACE2}$ cells (2×10^4 cells/well) were seeded into 96-well culture plates and infected with 50 μl of pseudovirus with polybrene (2 μg/ml). After incubation for 24 h, the supernatant containing pseudovirus was removed and replaced with fresh Dulbecco's modified Eagle's medium containing 2% fetal bovine serum (Gibco, Rockville, MD, United States). After 72 h post-infection, RLU was detected using the Bio-Lite Luciferase Assay kit (Vazyme, Nanjing, China). The luminescence was read using a Tecan Spark multifunction microplate reader (Tecan, Austria).

Confirm the Expression of SARS-CoV-2 Pseudovirus by Western Blot

To confirm the expression of SARS-CoV-2 pseudovirus, HEK293T cells were cotransfected with pNL4.3-R-E-luc and pCMV-3Flag-SARS-CoV2-S19del using Lipofectamine 3000, and the virus-containing supernatant and cell lysates were collected separately. To construct the VSV pseudovirus as control, plasmid pMD2.G was cotransfected with pNL4.3-R-E-luc. Twelve milliliters of SARS-CoV-2 or VSV pseudoviruses was concentrated with PEG 8000 and resuspended with 20 μl of 5 × sodium dodecyl sulfate-polyacrylamide gel electrophoresis (SDS-PAGE) loading buffer. Cell lysates were denatured in a 5 × SDS-PAGE loading buffer. Proteins were electrophoresed on a 10% SDS-PAGE and transferred onto a polyvinylidene difluoride membrane for 2.5 h at 200 mA at 4°C. Immunoblots were probed with primary antibodies (SARS-CoV-2 convalescent patient serum, anti-Flag, and anti-β-actin antibodies, Proteintech, Wuhan, China) and secondary antibodies conjugated with horseradish peroxidase. Protein bands were detected using Western Lightning Plus ECL (PerkinElmer, Boston, MA, United States).

Neutralization Assay Based on the Pseudovirus

Vero-E6$_{ACE2}$ cells (2×10^4 cells/well) were seeded in 96-well plates. For the pseudovirus neutralization assay, heat-inactivated serum samples were diluted in twofold increments with Dulbecco's modified Eagle's medium containing 2% fetal bovine serum. SARS-CoV2-S pseudoviruses (50 μl, approximately 5×10^4 RLU) were co-incubated with 50 μl of diluted sera of COVID-19 patients for 1 h at 37°C and then the sera-pseudoviruses mixture was added to 96-well Vero-E6$_{ACE2}$ cells. Sera of healthy donors were used as negative serum controls. VSV pseudovirus was a negative virus control to prove the specificity of the neutralization assay-based pseudovirus. Fresh medium was added to each well 24 h post-infection and RLU was measured 72 h post-infection. The percentage of neutralization was calculated as (RLUvirus − RLUvirus + serum)/(RLUvirus − RLUmock) × 100. The 50% neutralization (ND_{50}) was expressed as the reciprocal dilution of serum, which resulted in a 50% reduction in RLU compared to the positive virus control. In this study, neutralizing antibody titers were calculated as ND_{50}. The ND_{50} titer of ≥1:8 indicated positivity. All serum samples were tested at least in duplicate.

Enzyme-Linked Immunosorbent Assay

We detected the SARS-CoV-2 IgG antibody to S and nucleocapsid (N) in 1- to 2.5-month sera, 10- to 11-month sera, and 17- to 18-month sera using ELISA. The IgG levels in sera were tested using the commercially available SARS-CoV-2 human S antibody Titer Assay Kit and SARS-CoV-2 human N antibody Titer Assay Kit (Nanjing Miaodi Biotechnology Co., Ltd., Nanjing, China) (Liu et al., 2021). A total of 100 μl of diluted serum sample (1:50 for S and 1:100 for N) was added to each well coated with purified SARS-CoV-2 S or N protein. Following

30 min of incubation at 37°C, each well was washed and was incubated with horseradish peroxidase-labeled anti-human IgG. Tetramethylbenzidine and H_2O_2 substrate were used to develop color. After color development stopped, the optical density (OD) values were measured at 450 nm (OD_{450}) with a microplate reader. Positive control and negative control were performed as the same procedure. Based on the manufacturer's instructions, samples with OD_{450} greater than the cutoff value were considered positive.

SARS-CoV-2 Peptides for the T-Cell Enzyme-Linked Immunospot Assay (ELISpot)

For the T-cell ELISpot assay, the SARS-CoV-2 S peptide pools (Sino Biological, Beijing, China) containing S1 and S2 peptide pools were used, which mainly consisted of 15-mer sequences with 11-amino-acid overlap. The S1 peptide pool consists of 169 peptides (amino acids 1–686) and the S2 peptide pool consists of 144 peptides (amino acids 687–1,273), with a purity of >95% as determined by SEC-HPLC analysis.

ELISpot Assay

To investigate SARS-CoV-2-specific T-cell responses in convalescent patients, we used the human IFN-γ and IL-2 ELISpot Kits (Dakewe Biotech, Shenzhen, China). Fresh peripheral blood mononuclear cells (PBMCs) were isolated from the blood of convalescent COVID-19 patients 17–18 months after disease onset. PBMCs from healthy individuals who had not been vaccinated against COVID-19 served as controls. As a standard, 5×10^5 PBMCs per well were stimulated with the S1 and S2 mixture peptides at a concentration of 1 μg/ml of each peptide for 24 h. An equimolar amount of dimethyl sulfoxide (DMSO) and phytohemagglutinin (PHA, Dakewe, 2.5 μg/ml) were used as negative and positive controls, respectively. Spots were counted using an ELISpot reader (Mabtech, Stockholm, Sweden). The threshold for a positive reaction was set at three times above the mean value of the spots of the negative controls.

Statistical Analysis

Categorical variables were described as percentages, and compared using the Chi-squared test. Continuous variables were described using geometric mean antibody titers (GMT), median, and interquartile range (IQR). The Mann–Whitney *U* test was used to compare differences between groups. Spearman rank correlation test was used to evaluate the correlation between the levels of different antibodies and the correlation between antibody levels and T-cell responses. The generalized linear model (GLM) was applied to evaluate the association between immune response (including antibodies and T-cell responses) and potential factors (i.e., disease severity, sex, and age). All analyses were performed using SPSS 22.0 software (SPSS Inc., Chicago, IL, United States). Graphs were generated using GraphPad Prism 8.3.0. $p < 0.05$ was considered statistically significant. $^*p < 0.05$, $^{**}p < 0.01$, $^{***}p < 0.001$.

RESULTS

Characteristics of the Patients

In this study, we recruited 150 COVID-19 patients and 20 healthy donors (**Figure 1**). Among the 150 COVID-19 patients who participated in this study, 43 sera were obtained in 1–2.5 months, 62 sera were obtained in 10–11 months, and 45 sera were obtained in 17–18 months after the onset of illness. Patients were grouped according to the severity of the disease. Patients with fever, fatigue, runny nose, cough, myalgia, and mild pneumonia on imaging examination were included in the mild group; patients with dyspnea, hypoxemia, acute respiratory distress syndrome, septic shocks, and multifunctional organ failure requiring intensive care were included in the severe group. General information about patients enrolled in neutralizing antibody tests is listed in **Table 1**, including sex, age, and the severity of COVID-19. The median age of the patients was 55 years (IQR, 47–63 years) and 68 (45.6%) were female. Among them, 81 (54.4%) were younger than 60 and 36 (39.7%) were over 60 years old. Eighty-four (56.4%) patients had mild clinical manifestations and 65 (43.6%) were in severe condition.

Neutralization Assay With SARS-CoV-2 and Vesicular Stomatitis Virus Pseudoviruses

Western blot showed that anti-Flag antibody detected a 190-kDa band in the cell lysates of SARS-CoV-2 S plasmid pCMV-3Flag-SARS-CoV-2-S19del transfected cells, but not in the plasmid pMD2.G transfected cells (**Figure 2A**), indicating that SARS-CoV-2 S protein was expressed in the S plasmid transfected cells. SARS-CoV-2 pseudoviruses were purified from cell culture supernatant using PEG 8000. Western blot showed that a COVID-19 patient serum reacted with a 190-kDa band in the purified SARS-CoV-2 pseudovirus, but not in the VSV pseudovirus (**Figure 2B**), indicating that SARS-CoV-2 pseudovirus S protein was correctly expressed in the cell culture supernatant.

Determination of neutralization antibody titers in sera depended on measuring the inhibition rate of RLU from pseudovirus in cells, which corresponded to the inhibition of virus entry into Vero-E6$_{ACE2}$ cells. Dose-dependent inhibition of SARS-CoV-2 pseudovirus was observed in seropositive serum samples; in contrast, the sera of healthy donors showed no significant changes in the RLU at any dilution (**Figure 2C**). As expected, sera of both COVID-19 patients and healthy donors had no inhibition against VSV pseudovirus (**Figure 2D**). These results demonstrated that COVID-19 positive sera specifically neutralized the SARS-CoV-2 pseudovirus and the SARS-CoV-2 pseudovirus can substitute live SARS-CoV-2 to test neutralizing antibodies.

Neutralizing Antibody Kinetic Change

We measured neutralizing antibodies in serum samples from confirmed COVID-19 cases at early and late time points after onset of illness. We found that 97.7% (42/43) of COVID-19 patients developed neutralizing antibodies with a median of 1:237

TABLE 1 | General information about cases enrolled in the neutralizing antibody test.

Characteristic	Total (*N* = 170)	COVID-19 patients			Healthy persons (*N* = 20)
		1–2.5 months (*N* = 43)	10–11 months (*N* = 62)	17–18 moths (*N* = 45)	
Admission/discharge		**Inpatients**	**Convalescents**	**Convalescents**	**NA**
Sex, *n* (%)					
Male	75 (44.1)	22 (51.2)	21 (29.4)	25 (55.6)	7 (35.0)
Female	95 (55.9)	21 (48.8)	41 (70.6)	20 (44.5)	13 (65.0)
Age, years, median (IQR)	53 (42.5, 63)	59.5 (36.5, 70)	55.0 (30, 86)	55.4 (33, 85)	38 (27, 42)
Age (year)					
<60, *n* (%)	110 (64.7)	22 (51.2)	42 (67.7)	28 (62.2)	18 (90.0)
≥60, *n* (%)	60 (35.3)	21 (48.8)	20 (32.3)	17 (37.8)	2 (10.0)
Severity of COVID-19, *n* (%)					
Mild	85 (56.7)	15 (34.9)	34 (54.8)	36 (80.0)	NA
Severe	65 (43.3)	28 (65.1)	28 (45.2)	9 (20.0)	
The median time between symptom onset to blood sampling (min, max)		50 (21,76) days	10–11 months	17–18 months	NA

IQR, interquartile range; NA, not available.

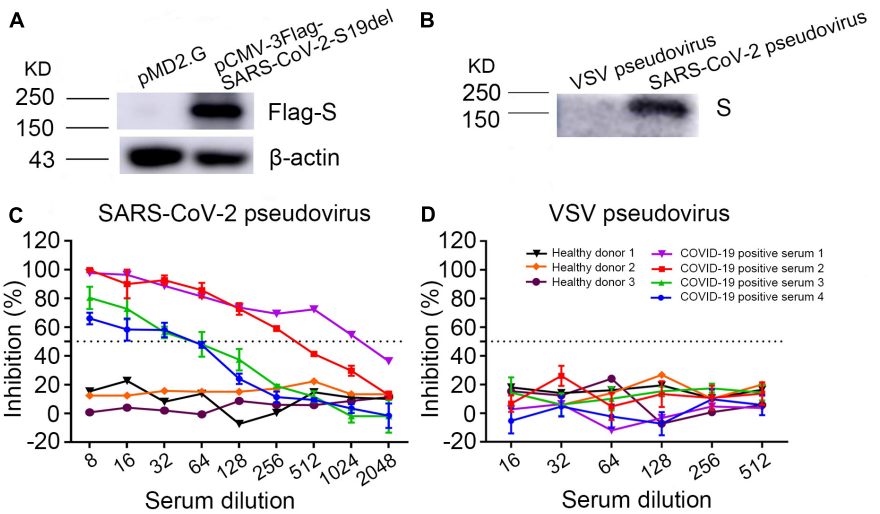

FIGURE 2 | Validation of the SARS-CoV-2 pseudovirus neutralizing assay. **(A)** Detection of SARS-CoV-2 spike protein expression in plasmid pCMV-3Flag-SARS-CoV-2-S19del transfected cell lysates by Western blot using anti-Flag antibody. Plasmid pMD2.G was used as the negative control. **(B)** Detection of SARS-CoV-2 spike protein expression in PEG 8000 concentrated pseudoviruses from cell culture supernatant with a serum of COVID-19 convalescent patient. VSV pseudovirus was used as the negative control. **(C,D)** Inhibition of SARS-CoV-2 pseudovirus or VSV pseudovirus using COVID-19 patients' and healthy persons' sera.

(IQR, 1:149–1:508) in 1- to 2.5-month sera, of which 69.0% (29/42) had a titer ≥1:128, and 21.4% (9/42) had a titer ≥1:512 (**Figures 3A,B**). Our data showed that most convalescent patients had detectable NAbs 10–11 months after illness onset and the seropositive rate remained at 91.9% (57/62) with the median of 1:99 (IQR, 1:47–1:212). However, 37.3% (19/51) of convalescent patients showed low levels of serum neutralizing antibodies between 1:8 and 1:64. Only a small proportion (5.9%) of patients had a serum neutralizing antibody titer ≥1:512. To explore how long neutralizing antibodies exist in convalescent patients, we tested neutralizing antibodies in the sera of these patients 17–18 months after illness onset. Surprisingly, we found that 88.9% (40/45) of patients had detectable NAbs 17–18 months after illness onset with a median of 1:80.0 (IQR, 1:40–1:164.5). Among them, 28.9% (13/45) showed low levels of serum neutralizing antibodies with NAbs between 1:8 and 1:64. No patient had a serum neutralizing antibody titer ≥1:512. The neutralizing antibody titers decreased from the early time point to the late time point after illness onset (1–2.5 months vs. 10–11 months, $p < 0.001$; 1–2.5 months vs. 17–18 months, $p < 0.001$). Besides,

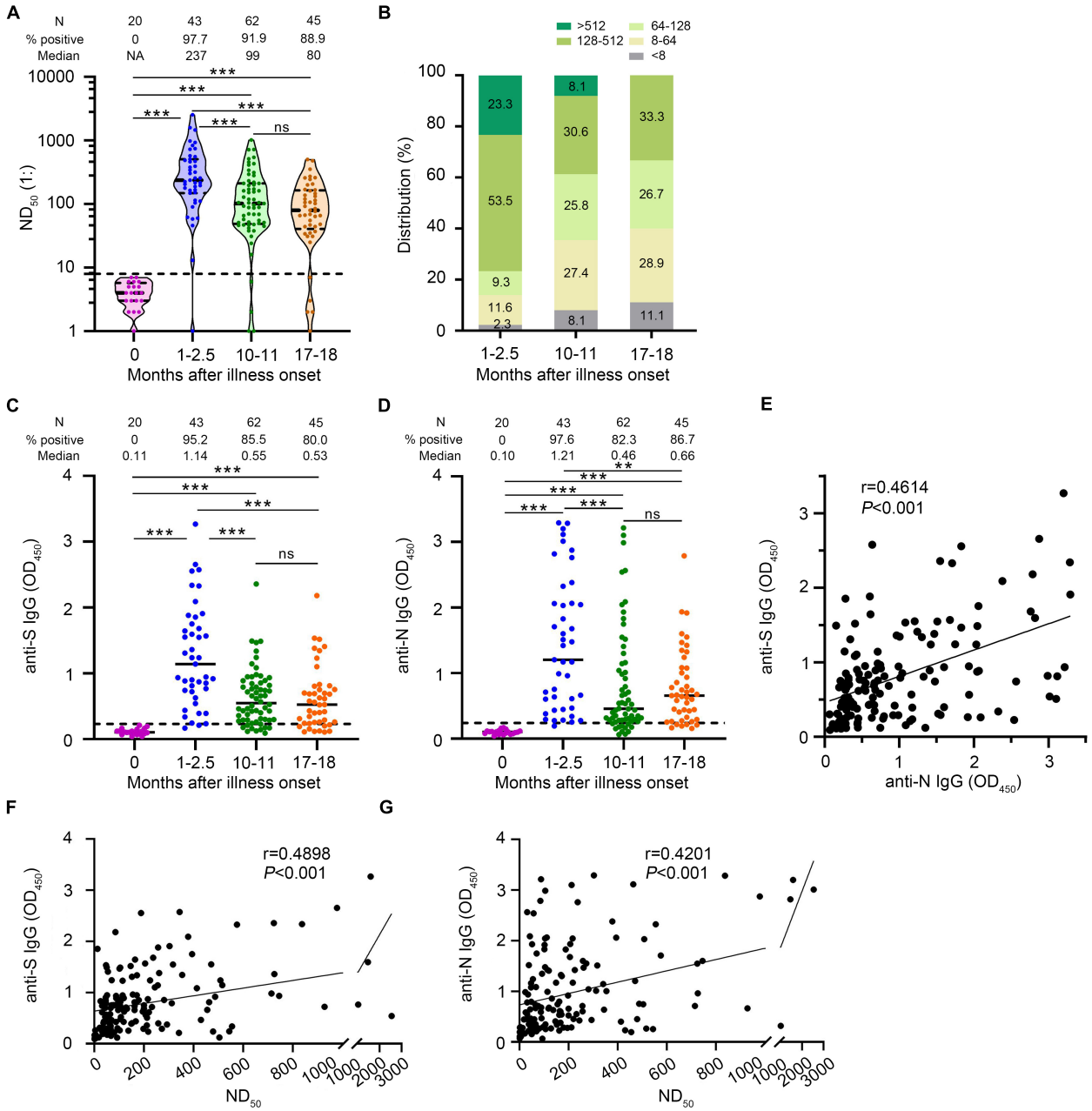

FIGURE 3 | Changes in antibody levels against SARS-CoV-2 after illness onset. **(A)** Neutralizing antibody titers (ND_{50}) of COVID-19 patients' serum sample. **(B)** Distribution of the neutralizing antibody titer in serum samples from COVID-19 patients. **(C)** SARS-CoV-2 spike (S) IgG antibody levels. **(D)** SARS-CoV-2 nucleocapsid (N) IgG antibody levels. **(E)** Correlation of anti-S IgG levels and anti-N IgG levels ($N = 150$). **(F)** Correlation of ND_{50} and anti-S IgG levels ($N = 150$). **(G)** Correlation of ND_{50} and anti-N IgG levels ($N = 150$). Statistical significance of antibody levels was determined using the Mann–Whitney *U*-test. A two-sided Spearman rank correlation test was used to evaluate the correlation of the levels of different antibodies. Healthy persons were indicated as 0 month after illness onset. Each dot represents an individual patient. Bars represent the median and interquartile range (IQR). The dotted line represents the threshold for positive in this assay. All serum samples were tested at least in duplicate. N, number; NA, not available; ns, not significant; $^{**}p < 0.01$, $^{***}p < 0.001$.

we observed a slight decline of the NAbs between the 10- to 11-month and the 17- to 18-month groups though the difference was not significant ($p = 0.195$) (**Figures 3A,B**).

Serum samples at different time points after illness onset showed differences in the distribution of NAbs (**Figure 3B**). The proportion of sera with a titer <1:64 increased from 1–2.5 months to 10–11 months (14.0–35.5%, $p = 0.014$) and remained stable from 10–11 to 17–18 months (35.4–40.0%, $p = 0.006$). The proportion with a titer >1:128 decreased from 1–2.5 to 10–11 months (76.7–38.7%, $p < 0.001$) and remained stable

from 10–11 to 17–18 months (38.7–33.3%, $p = 0.568$). These data indicated that the neutralizing antibody declined from 1–2.5 to 10–11 months after illness onset, and remained relatively stable after that, even up to 17–18 months.

Changes of SARS-CoV-2 Anti-S and Anti-N IgG

The IgG antibody positive rates to SARS-CoV-2 S protein were 95.2% (40/42), 85.5% (53/62), and 80.0% (36/45) with a medium OD (IQR) of 1.14 (0.72–1.75), 0.55 (0.29–0.86), and 0.53 (0.25–0.78) at the 1- to 2.5-month sera, 10- to 11-month sera, and 17- to 18-month sera, respectively. The IgG antibody positive rates to SARS-CoV-2 N protein were 97.6% (41/42), 82.3% (51/62), and 86.7% (39/45) with a medium OD (IQR) of 1.21 (0.47–2.07), 0.46 (0.28–1.15), and 0.66 (0.31–1.08) at the 1- to 2.5-month sera, 10- to 11-month sera, and 17- to 18-month sera, respectively. A progressive decline in IgG antibody to S protein (anti-S IgG) and IgG antibody to N protein (anti-N IgG) was observed from the 1st to the 18th month after illness onset (**Figures 3C,D**). We found that the anti-S IgG levels were strongly correlated with the anti-N IgG levels (Spearman rank correlation coefficients = 0.461, $p < 0.001$) (**Figure 3E**). The anti-S IgG and anti-N IgG levels were positively correlated with neutralizing antibody titers against SARS-CoV-2 in convalescent sera, respectively (**Figures 3F,G**).

Comparison of Antibody Levels in Different Groups of Patients

We used multivariate GLM to estimate the association between neutralizing antibodies and potential factors (i.e., age, gender, and disease severity). It has been widely reported that the severity of the disease is a factor affecting the neutralizing antibody response (Choe et al., 2020; Lei et al., 2021; Yamayoshi et al., 2021). We explored whether the disease severity affected neutralizing antibody titer after a prolonged infection. Multivariate GLM analysis showed that the NAbs in the severe group were significantly higher than that in the mild group in the 1- to 2.5-month sera ($\beta = -0.933$, $p = 0.004$) (**Figure 4A**). We found that 35.7% (10/28) of severe patients developed high levels (>1:512) of neutralizing antibodies; in contrast, no mild patient maintained high titers in the 1- to 2.5-month sera (**Figure 4B**). Unexpectedly, 10–11 and 17–18 months after illness onset, the difference of the NAbs between the severe group and the mild group was not significantly different (severe group 105.9 vs. mild group 73.7 in 10–11 months, $p = 0.946$; severe group 95.4 vs. mild group 66.0 in 17–18 months, $p = 0.636$) (**Figure 4A**). There was no difference in the distribution of NAbs between the severe group and mild group of patients 10–11 or 17–18 months after COVID-19 onset (**Figure 4B**). Consistent with the trend of neutralizing antibodies, we found that anti-S IgG in the severe group was significantly higher than that in the mild group in the 1- to 2.5-month sera. The difference of anti-S IgG and anti-N IgG between the severe and mild group was not significant between the 10- to 11-month and 17- to 18-month sera (**Figures 5A,D**).

Multivariate GLM analysis showed that the NAb titers were not related to gender and age (**Supplementary Table 1** and **Figures 4C,D**) and that anti-S IgG and anti-N IgG levels were not related to gender and age either (**Supplementary Table 2** and **Figures 5B,C,E,F**).

SARS-CoV-2-Specific T-Cell Memory Persisted at Least 17–18 Months After Illness Onset

To determine whether SARS-CoV-2-specific T-cell immunity was generated and sustained in COVID-19 convalescent patients, we utilized ELISpot assay to measure the number of IFN-γ- and IL-2-secreting T cells, respectively (**Figure 6A**). PBMCs were obtained from 45 convalescent patients sampled 17–18 months after illness onset together with 12 unexposed and unvaccinated healthy individuals and then stimulated with SARS-CoV-2 spike S1 and S2 mixture peptides. Representative ELISpots from COVID-19 convalescent patients against SARS-CoV-2 antigens were presented, with PHA as positive and DMSO as negative control (**Figure 6B**). IFN-γ- as well as IL-2-secreting cell numbers were significantly higher in convalescent patients than in healthy persons. We found that 95.6% (43/45) of COVID-19 patients developed robust SARS-CoV-2-specific IFN-γ-secreting T-cell responses [median: 161 spot-forming cells (SFCs)/5 × 10^5 PBMCs, IQR: 74, 351 SFCs/5 × 10^5 PBMCs] and 93.8% (15/16) developed SARS-CoV-2-specific IL-2-secreting T-cell responses (median: 234 SFCs/5 × 10^5 PBMCs, IQR: 167, 380 SFCs/5 × 10^5 PBMCs) (**Figures 6C,D**). Patients with higher SARS-CoV-2-specific IFN-γ secreting T-cell numbers also had higher IL-2 secreting T-cell numbers (Spearman correlation coefficient = 0.515, $p = 0.041$) (**Figure 6E**). In addition, using multivariate GLM analysis, we found that there was no significant difference in the IFN-γ-secreting T-cell immune response against SARS-CoV-2 between the severe and mild groups (**Supplementary Table 4** and **Figure 6F**), between the male and female groups (**Supplementary Table 4** and **Figure 6G**), and between the younger (<60 years old) and older groups (≥60 years old) (**Supplementary Table 4** and **Figure 6H**). These results demonstrated that SARS-CoV-2-specific T-cell responses persisted at least 17–18 months after illness onset.

The SARS-CoV-2-Specific T-Cell Response Correlated With Neutralizing Antibody Level 17–18 Months After Infection

We found that IFN-γ-secreting T-cell numbers against SARS-CoV-2 strongly correlated with the titers of neutralizing antibody, and the Spearman rank correlation coefficient was 0.430 ($p = 0.003$) (**Figure 7A**). A similar correlation was observed between the IL-2-secreting T-cell numbers against SARS-CoV-2 and the titers of neutralizing antibody ($r = 0.509$, $p = 0.044$) (**Figure 7B**). We also found that SARS-CoV-2-specific IFN-γ-secreting T-cell responses were positively correlated with the anti-S and anti-N IgG levels, respectively (**Figures 7C,E**). Limited by the small sample size, we did not find that IL-2-secreting T-cell response was associated with the anti-S or anti-N IgG levels, respectively (**Figures 7D,F**). It is worth noting that five convalescent patients had no detectable neutralizing antibody

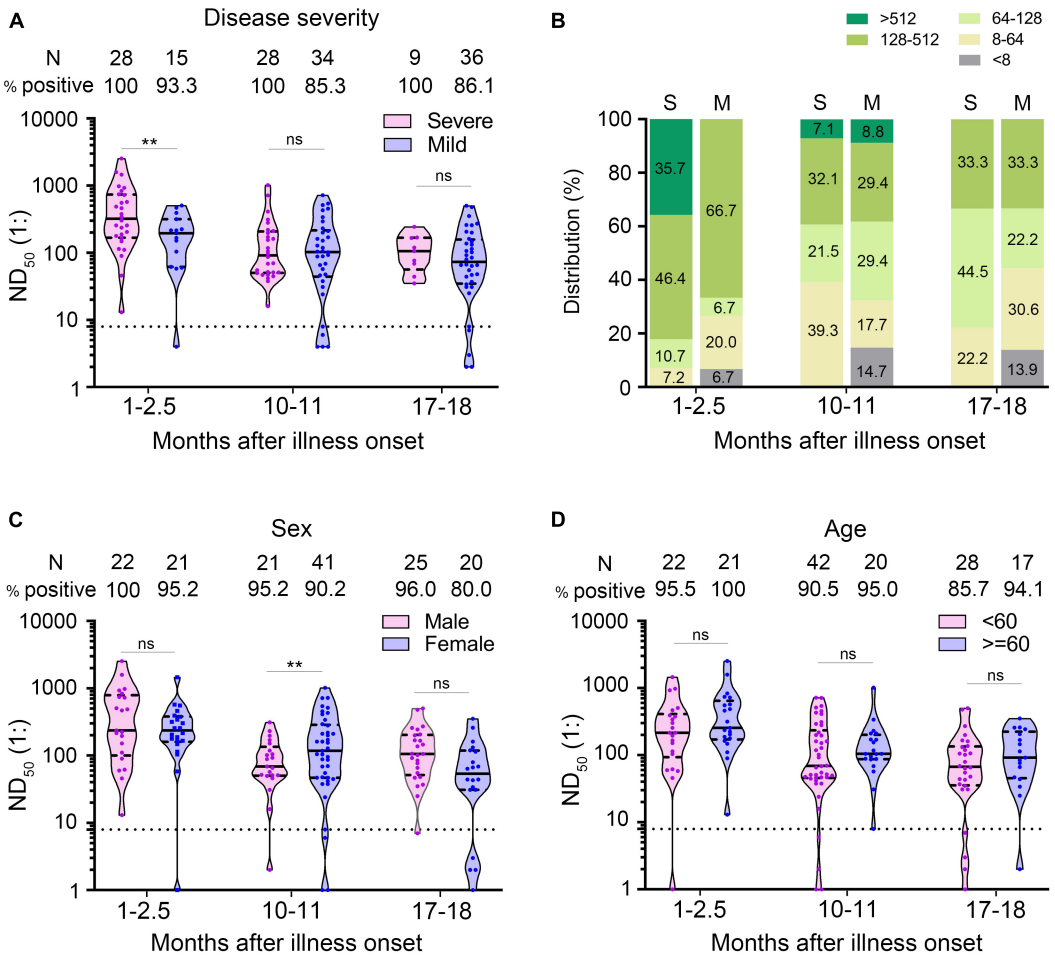

FIGURE 4 | Comparison of neutralizing antibodies in different groups of patients. **(A)** ND_{50} of COVID-19 patients at different times after illness onset according to the severity of the disease. **(B)** Distribution of ND_{50} in sera of COVID-19 patients according to the severity of the disease. **(C,D)** The ND_{50} of COVID-19 patients according to sex **(C)** and age **(D)**. Bars represent the median and interquartile range (IQR). The dotted line represents the threshold for positive in this assay. All serum samples were tested at least in duplicate. Multivariate generalized linear models were used to compare the difference between ND_{50} and potential factors (i.e., disease severity, sex and age). $^{**}p < 0.01$. ns, not significant; S, severe; M, mild; N, number.

response after 17- to 18-month infection, but four of them had a positive IFN-γ-secreting T-cell response.

DISCUSSION

The devastating COVID-19 outbreak is the biggest global health challenge in decades. Neutralizing antibodies and antigen-specific memory T cells had been implicated as critical for the control and elimination of viral infections. Previous studies have shown that neutralizing antibodies were significantly correlated with protection against SARS-CoV-2 infection in animal models (Deng et al., 2020; Hassan et al., 2020; Kim Y. I. et al., 2021; Selvaraj et al., 2021) and humans (Addetia et al., 2020; Huang et al., 2020; Legros et al., 2021). The presence of SARS-CoV-2-specific T-cell immunity was highly associated with protection from clinical disease after re-exposure in mice (Zhuang et al., 2021). Understanding the kinetics of neutralizing antibodies and cellular immunity to SARS-CoV-2 is critical for the prevention of reinfection.

Previous studies have reported that SARS-CoV-2 induced neutralization antibodies in the early time point of COVID-19 and neutralization antibodies declined with a prolonged recovery time from the disease (Choe et al., 2020; Ni et al., 2020; Wajnberg et al., 2020; Wang Y. et al., 2020; Zhou et al., 2020; Crawford et al., 2021). Several studies reported that antibodies against SARS-CoV-2 were detectable in most COVID-19 patients in a study period of up to 12 months (Choe et al., 2020; Dan et al., 2021; Feng et al., 2021; Peng et al., 2021; Wang H. et al., 2021; Zhang et al., 2021). The limitation of these studies is the short study period due to the recent emergence of SARS-CoV-2. We have no knowledge about the duration of neutralization antibodies in COVID-19 patients' blood. Therefore, we carried out possibly the longest study period for SARS-CoV-2 neutralization antibody by recruiting patients from the first wave of COVID-19 in Wuhan City. We used HIV-1-based pseudovirus to evaluate the

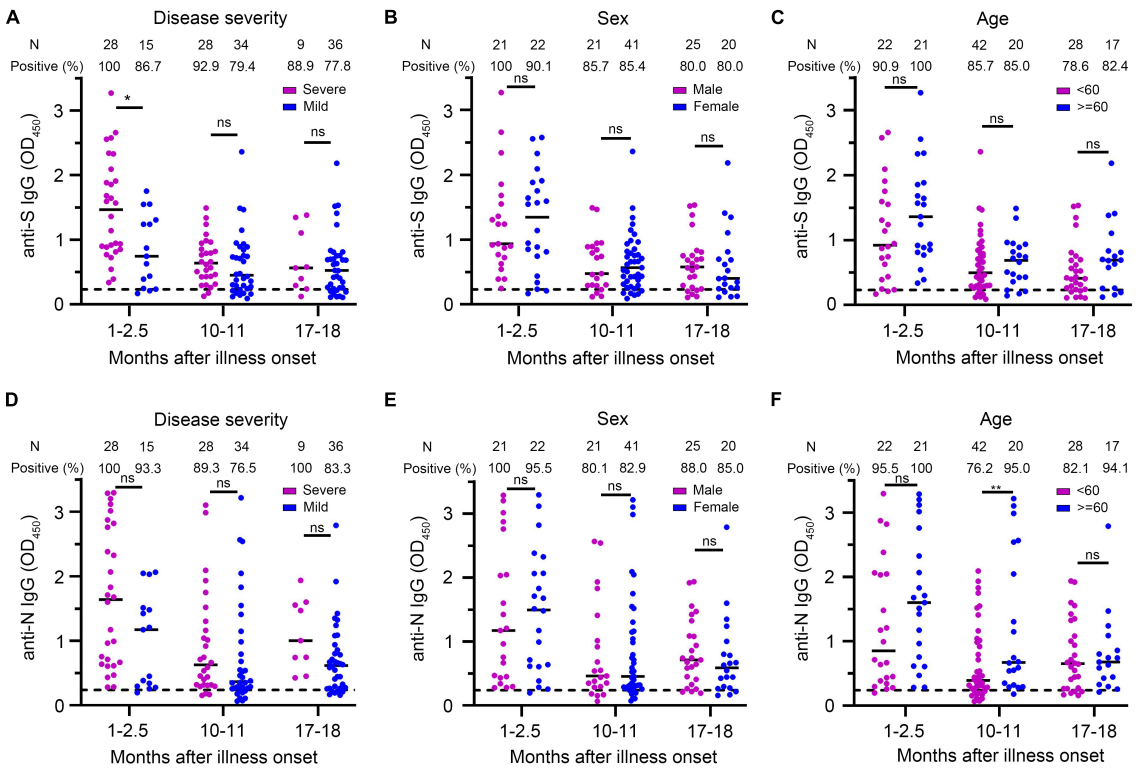

FIGURE 5 | Comparison of anti-S IgG and anti-N IgG levels in different groups of patients. **(A–C)** Anti-S IgG levels of COVID-19 patients at different times after illness onset according to the severity of the disease **(A)**, sex **(B)**, and age **(C)**. **(D–F)** Anti-N IgG levels of COVID-19 patients at different times after illness onset according to the severity of the disease **(D)**, sex **(E)**, and age **(F)**. Bars represent the medium. Dotted lines represent the threshold for positive in these assays. Multivariate generalized linear models were used to compare the difference between antibody levels and potential factors (i.e., disease severity, sex, and age). $^{*}p < 0.05$; $^{**}p < 0.01$; ns, not significant; N, number.

neutralizing antibody for SARS-CoV-2. Previous studies have shown that neutralizing antibody titers against SARS-CoV-2 pseudovirus correlated quite well with the results obtained using the live SARS-CoV-2 (Schmidt et al., 2020; Wang Y. et al., 2020; Sholukh et al., 2021; Wang H. et al., 2021; Yu et al., 2021). Due to not needing a biosafety laboratory and specificity of the SARS-CoV-2 pseudovirus, it has been widely used to detect neutralizing antibodies against SARS-CoV-2 since the COVID-19 outbreak (Robbiani et al., 2020; Tan et al., 2020; Wang Y. et al., 2020; Lei et al., 2021; Wang H. et al., 2021; Wang et al., 2021a,b; Yu et al., 2021).

We found that nearly all COVID-19 patients (97.7%) developed NAbs in the early time point within 2.5 months after illness onset and a majority of patients (88.9%) maintained NAbs for at least one and a half years. The neutralizing antibody titer waned slowly as the patient's recovery time was extended. However, NAbs declined more rapidly within a year and significantly slowed afterward. It is possible that neutralizing antibodies induced by SARS-CoV-2 may persist for several years, which is supported by high positive rates of neutralizing antibodies against SARS-CoV-1 and MERS-CoV nearly 3 years after infection (Liu et al., 2006; Cao et al., 2007; Payne et al., 2016; Kim Y. S. et al., 2021). We found that anti-S IgG and anti-N IgG levels were strongly correlated with neutralizing antibody titers, indicating that IgG levels tested using ELISA could predict neutralizing antibody levels to some extent.

Several studies demonstrated that neutralizing antibody response was dependent on the severity of disease (Bošnjak et al., 2020; Choe et al., 2020). Consistent with previous studies at the early time of SARS-CoV-2 infection (Bošnjak et al., 2020; Choe et al., 2020; Long et al., 2020; Wang P. et al., 2020), we found that patients with severe infection tend to have a higher neutralizing antibody response than patients with mild infection. There is evidence that a high neutralizing antibody with severe SARS-CoV-2 infection was correlated with a higher viral load (To et al., 2020; Wang Y. et al., 2020). Surprisingly, the difference of the neutralizing antibody titers between the severe group and the mild group was not significant in 1 year to one and a half years after disease onset. It seems possible that neutralizing antibodies wane more dramatically in more severe patients than in mild patients, and this difference equalized after a long period of infection (Crawford et al., 2021). The same pattern was found in SARS-CoV-1. Cao et al. found that there were no significant differences in the specific antibodies against SARS-CoV-1 according to disease severity 30 months and even 36 months after infection (Cao et al., 2007).

The natural infection of COVID-19 elicits a massive T-cell immune response within a year (Grifoni et al., 2020;

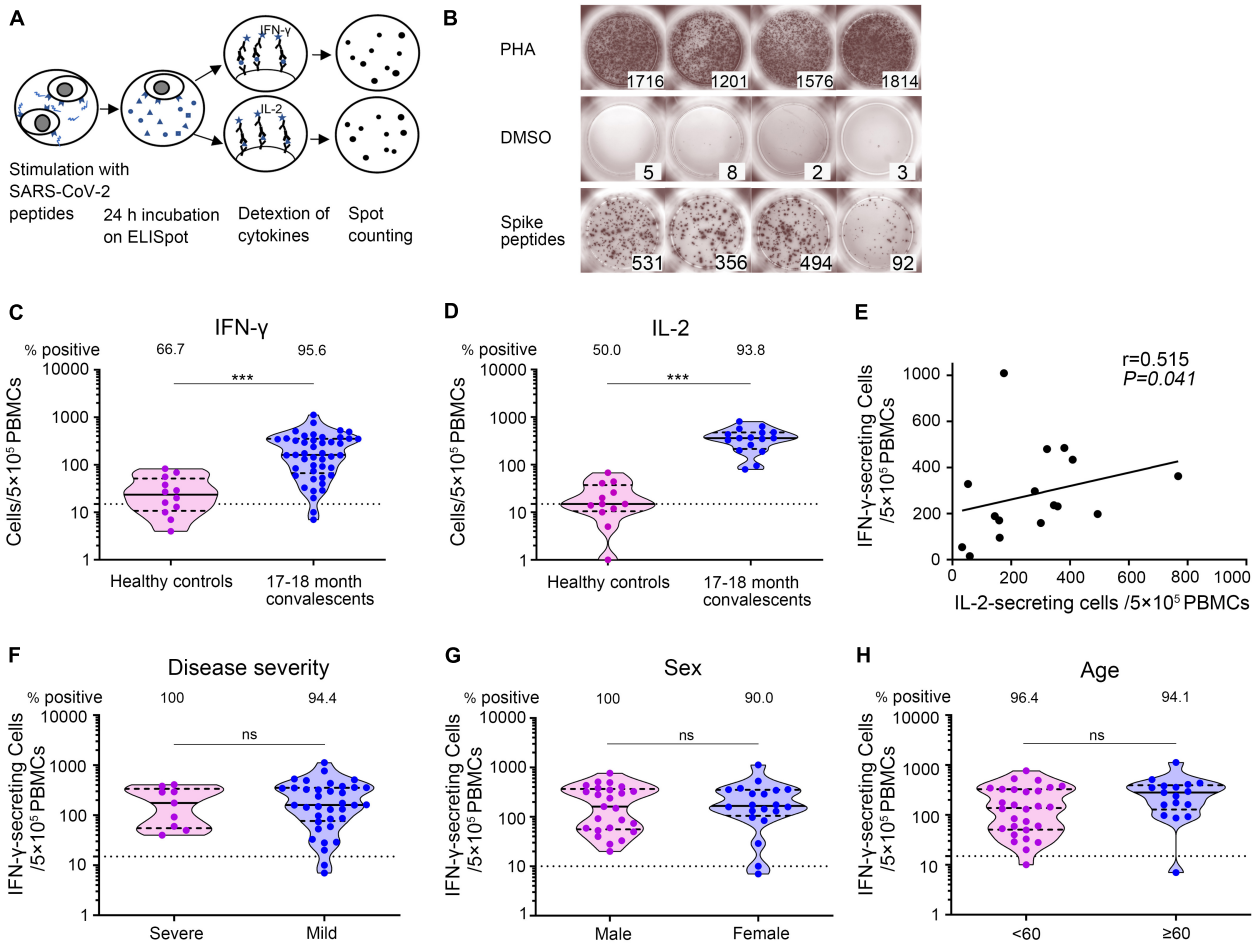

FIGURE 6 | SARS-CoV-2-specific T-cell responses 17–18 months after COVID-19 onset. **(A)** Schematic of memory T-cell ELISpot assay. **(B)** Representative ELISpots from COVID-19 convalescent patients 17–18 months after illness onset with SARS-CoV-2 spike S1 and S2 mixture peptides as the specific stimulus, DMSO as the negative control, and PHA as the positive control. The numbers in the lower right corner represented the spots counting. **(C,D)** The total number of SARS-CoV-2-specific IFN-γ- secreting T cells and IL-2 secreting T cells per 5×10^5 PBMCs. Each dot represents an individual patient. Bars represent the median and interquartile range (IQR). Statistical significance was determined using the Mann–Whitney *U*-test, and represented as $^{***}p < 0.001$. **(E)** Correlation of SARS-CoV-2-specific IFN-γ-secreting T cells and IL-2-secreting T cells 17–18 months after illness onset ($N = 16$). A two-sided Spearman rank correlation test was used to evaluate the correlation of the two cytokines. **(F–H)** IFN-γ-secreting T cells of COVID-19 patients according to disease severity **(F)**, sex **(G)**, and age **(H)**. Multivariate generalized linear models were used to compare the difference between IFN-γ spots and potential factors (i.e., disease severity, sex, and age). The dotted horizontal line represents the threshold for positive in this assay. $^{***}p < 0.001$. PBMCs, peripheral blood mononuclear cells; DMSO, dimethyl sulfoxide; PHA, phytohemagglutinin.

Ni et al., 2020; Zhou et al., 2020; Zhang et al., 2021). We found that a large majority of COVID-19 patients (more than 90%) developed SARS-CoV-2 S peptide-specific T-cell response in one and a half years post-infection, although T-cell responses vary greatly from person to person. From SARS, we learned that virus-specific memory T-cell response was detectable from 6 to 17 years after primary infection, suggesting a long-lasting immune memory (Tang et al., 2011; Ng et al., 2016; Le Bert et al., 2020). Our study provides evidence that COVID-19 infection could provide a lasting T-cell memory response.

Consistent with a previous study, a positive correlation was observed between SARS-CoV-2-specific T-cell responses and neutralizing antibody titers (Cassaniti et al., 2021), which suggested a correlation between cellular immunity and humoral responses. SARS-CoV-2 S specific T-cell responses were also found in 80% (4/5) of neutralizing antibody-negative COVID-19 patients, albeit at lower levels than in seropositive individuals. According to our data, the virus-specific T-cell response might be useful in cases of asymptomatic infection in the absence of a detectable antibody response against SARS-CoV-2.

Our data provide evidence that durable memory T-cell response was not significantly different between mild and severe patients one and a half years after SARS-CoV-2 infection. This suggested that the majority of mild and severe patients are likely to develop a long-lasting humoral and cellular immunity toward SARS-CoV-2, regardless of disease severity.

We found no significant differences in neutralizing antibody levels and T-cell responses between male and female individuals

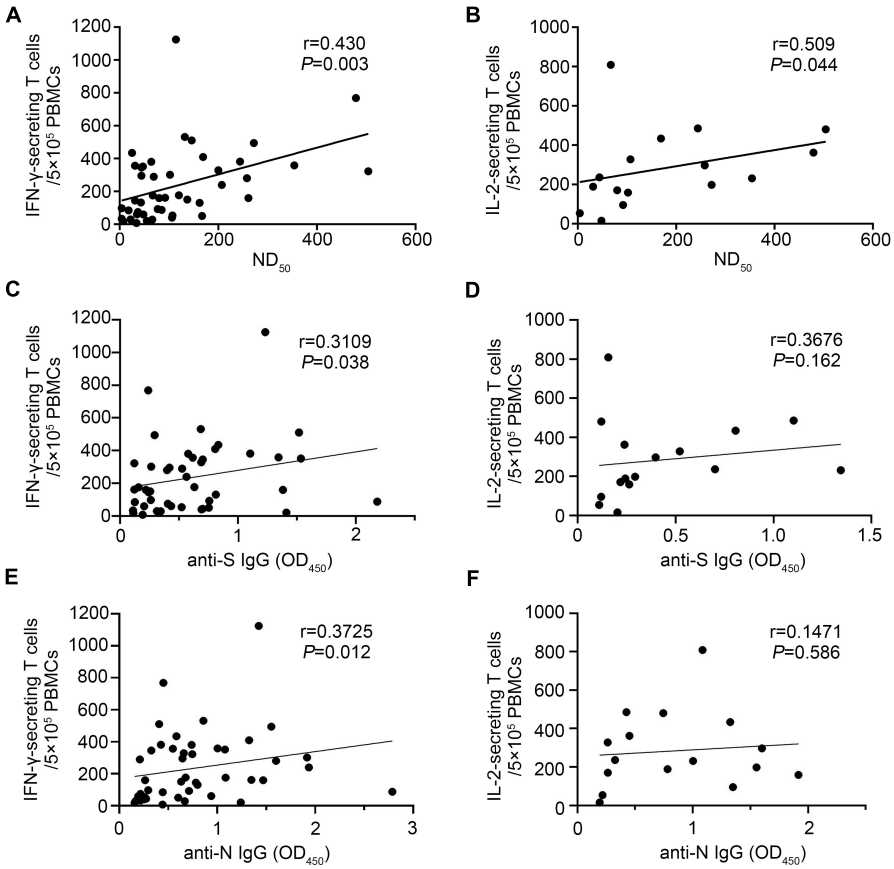

FIGURE 7 | The SARS-CoV-2-specific T-cell response correlated with antibody levels 17–18 months after infection. IFN-γ- and IL-2-secreting T-cell responses and antibody (ND50, anti-S IgG, and anti-N IgG) levels were performed in COVID-19 convalescent patients 17–18 months after illness onset. **(A)** Correlation of ND_{50} and SARS-CoV-2-specific IFN-γ-secreting T cells (*N* = 45). **(B)** Correlation of ND_{50} and SARS-CoV-2-specific IL-2-secreting T cells (*N* = 16). **(C)** Correlation of anti-S IgG levels and SARS-CoV-2-specific IFN-γ-secreting T cells (*N* = 45). **(D)** Correlation of anti-S IgG levels and SARS-CoV-2-specific IL-2-secreting T cells (*N* = 16). **(E)** Correlation of anti-N IgG levels and SARS-CoV-2-specific IFN-γ-secreting T cells (*N* = 45). **(F)** Correlation of anti-N IgG levels and SARS-CoV-2-specific IL-2-secreting T cells (*N* = 16). A two-sided Spearman rank correlation test was used to evaluate the correlation between SARS-CoV-2-specific T-cell responses and antibody levels.

over time. Some studies reported that neutralizing antibody levels were higher in men than in women during the acute stage (Robbiani et al., 2020), which might be correlated with more severe symptoms and higher case fatality seen in men (Takahashi et al., 2020). Adjusting for disease severity and sex, we found that there was no significant difference in immunity level between those in the ≥60-year group and younger group. Neutralizing antibodies and virus-specific T-cell response could be detected in COVID-19 patients over 80 years old 17–18 months after disease onset. Thus, age was not considered to be a compromiser to antibody immune responses and SARS-CoV-2-specific T-cell responses (Lau et al., 2021). The effects of gender and age on the modulation of protective immunity needed to be explored in further studies.

Our study might be limited by the sample size and did not include asymptomatic patients. Due to limited information about the patients' comorbidities in this study, we did not investigate the impact of diverse comorbidities on neutralizing antibody levels and T-cell response.

We concluded that SARS-CoV-2 infection induced robust and persistent neutralizing antibody response and SARS-CoV-2-specific T-cell responses at least one and a half years post-symptom onset in both mild and severe COVID-19 patients. Our findings may have crucial implications for COVID-19 epidemic control and long-term herd immunity.

DATA AVAILABILITY STATEMENT

The original contributions presented in the study are included in the article/**Supplementary Material**, further inquiries can be directed to the corresponding authors.

ETHICS STATEMENT

The studies involving human participants were reviewed and approved by Wuhan University. The patients/participants

provided their written informed consent to participate in this study.

AUTHOR CONTRIBUTIONS

X-JY: project conception. X-JY and L-NY: experimental design. L-NY, XX, P-PL, W-LL, S-HZ, X-GL, S-JZ, HL, Z-YW, FS, B-CL, YL, DL, and H-JH: sample collection. L-NY: experimental work and writing of original draft. L-NY and Z-DW: data analysis. X-JY, L-NY, and HY: revising and editing. All authors reviewed and approved the final the manuscript.

FUNDING

This work was supported by the National Natural Science Funds of China (No. 81971939), the National Key Research and Development Program of China (No. 2020YFC0845300), and the Research and Development Program of Hubei Province (Nos. B2020093 and ZY2021F015).

ACKNOWLEDGMENTS

We are grateful to Cheguo Cai (Wuhan University, Wuhan, China) for providing the pNL4.3-R-E-luc plasmid.

SUPPLEMENTARY MATERIAL

The Supplementary Material for this article can be found online at: https://www.frontiersin.org/articles/10.3389/fmicb.2021.803031/full#supplementary-material

REFERENCES

Addetia, A., Crawford, K. H. D., Dingens, A., Zhu, H., Roychoudhury, P., Huang, M. L., et al. (2020). Neutralizing antibodies correlate with protection from SARS-CoV-2 in humans during a fishery vessel outbreak with a high attack rate. *J. Clin. Microbiol.* 58:e02107-20. doi: 10.1128/JCM.02107-20

Bošnjak, B., Stein, S. C., Willenzon, S., Cordes, A. K., Puppe, W., Bernhardt, G., et al. (2020). Low serum neutralizing anti-SARS-CoV-2 S antibody levels in mildly affected COVID-19 convalescent patients revealed by two different detection methods. *Cell. Mol. Immunol.* 18, 936–944. doi: 10.1038/s41423-020-00573-9

Cao, W. C., Liu, W., Zhang, P. H., Zhang, F., and Richardus, J. H. (2007). Disappearance of antibodies to SARS-associated coronavirus after recovery. *N. Engl. J. Med.* 357, 1162–1163. doi: 10.1056/NEJMc070348

Cassaniti, I., Percivalle, E., Bergami, F., Piralla, A., Comolli, G., Bruno, R., et al. (2021). SARS-CoV-2 specific T-cell immunity in COVID-19 convalescent patients and unexposed controls measured by ex vivo ELISpot assay. *Clin. Microbiol. Infect.* 27, 1029–1034. doi: 10.1016/j.cmi.2021.03.010

Choe, P. G., Kang, C. K., Suh, H. J., Jung, J., Kang, E., Lee, S. Y., et al. (2020). Antibody responses to SARS-CoV-2 at 8 weeks postinfection in asymptomatic patients. *Emerg. Infect. Dis.* 26, 2484–2487. doi: 10.3201/eid2610.202211

Crawford, K. H. D., Dingens, A. S., Eguia, R., Wolf, C. R., Wilcox, N., Logue, J. K., et al. (2021). Dynamics of neutralizing antibody titers in the months after severe acute respiratory Syndrome Coronavirus 2 infection. *J. Infect. Dis.* 223, 197–205. doi: 10.1093/infdis/jiaa618

Dan, J. M., Mateus, J., Kato, Y., Hastie, K. M., Yu, E. D., Faliti, C. E., et al. (2021). Immunological memory to SARS-CoV-2 assessed for up to 8 months after infection. *Science* 371:eabf4063. doi: 10.1126/science.abf4063

Deng, W., Bao, L., Liu, J., Xiao, C., Liu, J., Xue, J., et al. (2020). Primary exposure to SARS-CoV-2 protects against reinfection in rhesus macaques. *Science* 369, 818–823. doi: 10.1126/science.abc5343

Feng, C., Shi, J., Fan, Q., Wang, Y., Huang, H., Chen, F., et al. (2021). Protective humoral and cellular immune responses to SARS-CoV-2 persist up to 1 year after recovery. *Nat. Commun.* 12:4984. doi: 10.1038/s41467-021-25312-0

Grifoni, A., Weiskopf, D., Ramirez, S. I., Mateus, J., Dan, J. M., Moderbacher, C. R., et al. (2020). Targets of T cell responses to SARS-CoV-2 Coronavirus in humans with COVID-19 disease and unexposed individuals. *Cell* 181, 1489–1501.e15. doi: 10.1016/j.cell.2020.05.015

Hassan, A. O., Case, J. B., Winkler, E. S., Thackray, L. B., Kafai, N. M., Bailey, A. L., et al. (2020). A SARS-CoV-2 infection model in mice demonstrates protection by neutralizing antibodies. *Cell* 182, 744–753.e4. doi: 10.1016/j.cell.2020.06.011

Huang, A. T., Garcia-Carreras, B., Hitchings, M. D. T., Yang, B., Katzelnick, L. C., Rattigan, S. M., et al. (2020). A systematic review of antibody mediated immunity to coronaviruses: kinetics, correlates of protection, and association with severity. *Nat. Commun.* 11:4704. doi: 10.1038/s41467-020-18450-4

Kim, Y. I., Kim, S. M., Park, S. J., Kim, E. H., Yu, K. M., Chang, J. H., et al. (2021). Critical role of neutralizing antibody for SARS-CoV-2 reinfection and transmission. *Emerg. Microb. Infect.* 10, 152–160. doi: 10.1080/22221751.2021.1872352

Kim, Y. S., Aigerim, A., Park, U., Kim, Y., Park, H., Rhee, J. Y., et al. (2021). Sustained responses of neutralizing antibodies against middle east respiratory syndrome Coronavirus (MERS-CoV) in recovered patients and their therapeutic applicability. *Clin. Infect. Dis.* 73, e550–e558. doi: 10.1093/cid/ciaa1345

Lau, E. H. Y., Tsang, O. T. Y., Hui, D. S. C., Kwan, M. Y. W., Chan, W. H., Chiu, S. S., et al. (2021). Neutralizing antibody titres in SARS-CoV-2 infections. *Nat. Commun.* 12:63. doi: 10.1038/s41467-020-20247-4

Le Bert, N., Tan, A. T., Kunasegaran, K., Tham, C. Y. L., Hafezi, M., Chia, A., et al. (2020). SARS-CoV-2-specific T cell immunity in cases of COVID-19 and SARS, and uninfected controls. *Nature* 584, 457–462. doi: 10.1038/s41586-020-2550-z

Legros, V., Denolly, S., Vogrig, M., Boson, B., Siret, E., Rigaill, J., et al. (2021). A longitudinal study of SARS-CoV-2-infected patients reveals a high correlation between neutralizing antibodies and COVID-19 severity. *Cell. Mol. Immunol.* 18, 318–327. doi: 10.1038/s41423-020-00588-2

Lei, Q., Li, Y., Hou, H. Y., Wang, F., Ouyang, Z. Q., Zhang, Y., et al. (2021). Antibody dynamics to SARS-CoV-2 in asymptomatic COVID-19 infections. *Allergy* 76, 551–561. doi: 10.1111/all.14622

Liu, P. P., Zong, Y., Jiang, S. P., Jiao, Y. J., and Yu, X. J. (2021). Development of a nucleocapsid protein-based ELISA for detection of human IgM and IgG antibodies to SARS-CoV-2. *ACS Omega* 6, 9667–9671. doi: 10.1021/acsomega.1c00253

Liu, W., Fontanet, A., Zhang, P. H., Zhan, L., Xin, Z. T., Baril, L., et al. (2006). Two-year prospective study of the humoral immune response of patients with severe acute respiratory syndrome. *J. Infect. Dis.* 193, 792–795. doi: 10.1086/500469

Long, Q. X., Liu, B. Z., Deng, H. J., Wu, G. C., Deng, K., Chen, Y. K., et al. (2020). Antibody responses to SARS-CoV-2 in patients with COVID-19. *Nat. Med.* 26, 845–848. doi: 10.1038/s41591-020-0897-1

Ng, O. W., Chia, A., Tan, A. T., Jadi, R. S., Leong, H. N., Bertoletti, A., et al. (2016). Memory T cell responses targeting the SARS coronavirus persist up to 11 years post-infection. *Vaccine* 34, 2008–2014. doi: 10.1016/j.vaccine.2016.02.063

Ni, L., Ye, F., Cheng, M. L., Feng, Y., Deng, Y. Q., Zhao, H., et al. (2020). Detection of SARS-CoV-2-specific humoral and cellular immunity in COVID-19 convalescent individuals. *Immunity* 52, 971–977.e3. doi: 10.1016/j.immuni.2020.04.023

Payne, D. C., Iblan, I., Rha, B., Alqasrawi, S., Haddadin, A., Al Nsour, M., et al. (2016). Persistence of antibodies against middle east respiratory syndrome Coronavirus. *Emerg. Infect. Dis.* 22, 1824–1826. doi: 10.3201/eid2210.160706

Peng, P., Hu, J., Deng, H. J., Liu, B. Z., Fang, L., Wang, K., et al. (2021). Changes in the humoral immunity response in SARS-CoV-2 convalescent patients over 8 months. *Cell. Mol. Immunol.* 18, 490–491. doi: 10.1038/s41423-020-00605-4

Robbiani, D. F., Gaebler, C., Muecksch, F., Lorenzi, J. C. C., Wang, Z., Cho, A., et al. (2020). Convergent antibody responses to SARS-CoV-2 in convalescent individuals. *Nature* 584, 437–442. doi: 10.1038/s41586-020-2456-9

Rydyznski Moderbacher, C., Ramirez, S. I., Dan, J. M., Grifoni, A., Hastie, K. M., Weiskopf, D., et al. (2020). Antigen-specific adaptive immunity to SARS-CoV-2 in acute COVID-19 and associations with age and disease severity. *Cell* 183, 996–1012.e19. doi: 10.1016/j.cell.2020.09.038

Sandberg, J. T., Varnaite, R., Christ, W., Chen, P., Muvva, J. R., Maleki, K. T., et al. (2021). SARS-CoV-2-specific humoral and cellular immunity persists through 9 months irrespective of COVID-19 severity at hospitalisation. *Clin. Transl. Immunol.* 10:e1306. doi: 10.1002/cti2.1306

Schmidt, F., Weisblum, Y., Muecksch, F., Hoffmann, H. H., Michailidis, E., Lorenzi, J. C. C., et al. (2020). Measuring SARS-CoV-2 neutralizing antibody activity using pseudotyped and chimeric viruses. *J. Exp. Med.* 217:e20201181. doi: 10.1084/jem.20201181

Selvaraj, P., Lien, C. Z., Selvaraj, P., Lien, C. Z., Liu, S., Stauft, C. B., et al. (2021). SARS-CoV-2 infection induces protective immunity and limits transmission in Syrian hamsters. *Life Sci. Allian.* 4:e202000886. doi: 10.26508/lsa.202000886

Sholukh, A. M., Fiore-Gartland, A., Ford, E. S., Miner, M. D., Hou, Y. J., Tse, L. V., et al. (2021). Evaluation of cell-based and surrogate SARS-CoV-2 neutralization assays. *J. Clin. Microbiol.* 59:e0052721. doi: 10.1128/jcm.00527-21

Takahashi, T., Ellingson, M. K., Wong, P., Israelow, B., Lucas, C., Klein, J., et al. (2020). Sex differences in immune responses that underlie COVID-19 disease outcomes. *Nature* 588, 315–320. doi: 10.1038/s41586-020-2700-3

Tan, Y., Liu, F., Xu, X., Ling, Y., Huang, W., Zhu, Z., et al. (2020). Durability of neutralizing antibodies and T-cell response post SARS-CoV-2 infection. *Front. Med.* 14, 746–751. doi: 10.1007/s11684-020-0822-5

Tang, F., Quan, Y., Xin, Z. T., Wrammert, J., Ma, M. J., Lv, H., et al. (2011). Lack of peripheral memory B cell responses in recovered patients with severe acute respiratory syndrome: a six-year follow-up study. *J. Immunol.* 186, 7264–7268. doi: 10.4049/jimmunol.0903490

To, K. K., Tsang, O. T., Leung, W. S., Tam, A. R., Wu, T. C., Lung, D. C., et al. (2020). Temporal profiles of viral load in posterior oropharyngeal saliva samples and serum antibody responses during infection by SARS-CoV-2: an observational cohort study. *Lancet Infect. Dis.* 20, 565–574. doi: 10.1016/s1473-3099(20)30196-1

Wajnberg, A., Amanat, F., Firpo, A., Altman, D. R., Bailey, M. J., Mansour, M., et al. (2020). Robust neutralizing antibodies to SARS-CoV-2 infection persist for months. *Science* 370, 1227–1230. doi: 10.1126/science.abd7728

Wang, H., Yuan, Y., Xiao, M., Chen, L., Zhao, Y., Haiwei, Z., et al. (2021). Dynamics of the SARS-CoV-2 antibody response up to 10 months after infection. *Cell. Mol. Immunol.* 18, 1832–1834. doi: 10.1038/s41423-021-00708-6

Wang, Z., Muecksch, F., Schaefer-Babajew, D., Finkin, S., Viant, C., Gaebler, C., et al. (2021a). Naturally enhanced neutralizing breadth against SARS-CoV-2 one year after infection. *Nature* 595, 426–431. doi: 10.1038/s41586-021-03696-9

Wang, Z., Schmidt, F., Weisblum, Y., Muecksch, F., Barnes, C. O., Finkin, S., et al. (2021b). mRNA vaccine-elicited antibodies to SARS-CoV-2 and circulating variants. *Nature* 592, 616–622. doi: 10.1038/s41586-021-03324-6

Wang, P., Liu, L., Nair, M. S., Yin, M. T., Luo, Y., Wang, Q., et al. (2020). SARS-CoV-2 neutralizing antibody responses are more robust in patients with severe disease. *Emerg. Microb. Infect.* 9, 2091–2093. doi: 10.1080/22221751.2020.1823890

Wang, Y., Zhang, L., Sang, L., Ye, F., Ruan, S., Zhong, B., et al. (2020). Kinetics of viral load and antibody response in relation to COVID-19 severity. *J. Clin. Invest.* 130, 5235–5244. doi: 10.1172/jci138759

World Health Organization [WHO] (2021). *Coronavirus Disease (COVID-19) Dashboard*. Available online at: https://covid19.who.int/ (accessed December 12, 2021).

Yamayoshi, S., Yasuhara, A., Ito, M., Akasaka, O., Nakamura, M., Nakachi, I., et al. (2021). Antibody titers against SARS-CoV-2 decline, but do not disappear for several months. *E Clin. Med.* 32:100734. doi: 10.1016/j.eclinm.2021.100734

Yu, J., Li, Z., He, X., Gebre, M. S., Bondzie, E. A., Wan, H., et al. (2021). Deletion of the SARS-CoV-2 spike cytoplasmic tail increases infectivity in pseudovirus neutralization assays. *J. Virol.* 95:e00044-21. doi: 10.1128/jvi.00044-21

Zhang, J., Lin, H., Ye, B., Zhao, M., Zhan, J., Dong, S., et al. (2021). One-year sustained cellular and humoral immunities of COVID-19 convalescents. *Clin. Infect. Dis.* 2021:ciab884. doi: 10.1093/cid/ciab884

Zhou, R., To, K. K., Wong, Y. C., Liu, L., Zhou, B., Li, X., et al. (2020). Acute SARS-CoV-2 infection impairs dendritic cell and T cell responses. *Immunity* 53, 864–877.e5. doi: 10.1016/j.immuni.2020.07.026

Zhuang, Z., Lai, X., Sun, J., Chen, Z., Zhang, Z., Dai, J., et al. (2021). Mapping and role of T cell response in SARS-CoV-2-infected mice. *J. Exp. Med.* 218:e20202187. doi: 10.1084/jem.20202187

Conflict of Interest: The authors declare that the research was conducted in the absence of any commercial or financial relationships that could be construed as a potential conflict of interest.

Publisher's Note: All claims expressed in this article are solely those of the authors and do not necessarily represent those of their affiliated organizations, or those of the publisher, the editors and the reviewers. Any product that may be evaluated in this article, or claim that may be made by its manufacturer, is not guaranteed or endorsed by the publisher.

frontiers in Microbiology

ORIGINAL RESEARCH
published: 16 March 2022
doi: 10.3389/fmicb.2022.851460

Inflammatory Profiles of Tracheal Biopsies From SARS-CoV-2 Patients

Giacomo Fiacchini[1†], Agnese Proietti[2†], Anello Marcello Poma[3], Miriana Picariello[1], Iacopo Dallan[1], Fabio Guarracino[4], Francesco Forfori[3], Gabriella Fontanini[3] and Luca Bruschini[1]*

[1]Otolaryngology, Audiology and Phoniatric Operative Unit, Department of Surgical, Medical and Molecular Pathology and Critical Care Medicine, University of Pisa, Pisa, Italy, [2]Unit of Pathological Anatomy, University Hospital of Pisa, Pisa, Italy, [3]Department of Surgical, Medical, Molecular Pathology and Critical Area, University of Pisa, Pisa, Italy, [4]Cardiothoracic and Vascular Anaesthesia and Intensive Care, Department of Anaesthesia and Critical Care Medicine, Azienda Ospedaliero-Universitaria Pisana (AOUP), Pisa, Italy

Purpose: An increasing number of laryngotracheal complications in mechanically ventilated COVID-19 patients has been reported in the last few months. Many etiopathogenetic hypotheses were proposed but no clear explanation of these complications was identified. In this paper we evaluated the possibility that the tracheal mucosa could be a high viral replication site that could weaken the epithelium itself.

Methods: Subjects for the COVID-19 group and the control group were selected retrospectively according to specific criteria. Patients' basic and clinical data were recorded and analyzed. Tracheal samples of both groups were collected during surgical tracheostomies and then analyzed from a histological and genetic-transcriptional point of view.

Results: Four COVID-19 patients were enrolled in this study and compared with four non-COVID-19 patients. No laryngotracheal complications were identified in both groups. The SARS-CoV-2 was detected in one out of four COVID-19 samples. A subepithelial inflammatory lymphomonocyte infiltrate was observed in all patients but two cases of the COVID-19 group showed vasculitis of small subepithelial vessels associated with foci of coagulative necrosis. Two gene sets (HALLMARK_INFLAMMATORY_RESPONSE and HALLMARK_ESTROGEN_RESPONSE_LATE) were significantly deregulated in COVID-19 patients compared to the control group.

Conclusion: The altered inflammatory response of the COVID-19 patients could be another possible explanation of the increasing number of laryngotracheal complications.

Keywords: COVID-19, SARS-CoV-2, virus replication, tracheal lesions, prolonged mechanical ventilation

OPEN ACCESS

Edited by:
Jue Liu,
Yangzhou University, China

Reviewed by:
Martha Ann Delaney,
University of Illinois at Urbana-Champaign, United States
Sabine Stegemann-Koniszewski,
University Hospital Magdeburg, Germany

***Correspondence:**
Giacomo Fiacchini
g.fiacchini@gmail.com

†These authors have contributed equally to this work and share first authorship

Specialty section:
This article was submitted to Virology, a section of the journal Frontiers in Microbiology

Received: *09 January 2022*
Accepted: *11 February 2022*
Published: *16 March 2022*

Citation:
Fiacchini G, Proietti A, Poma AM, Picariello M, Dallan I, Guarracino F, Forfori F, Fontanini G and Bruschini L (2022) Inflammatory Profiles of Tracheal Biopsies From SARS-CoV-2 Patients. Front. Microbiol. 13:851460. doi: 10.3389/fmicb.2022.851460

INTRODUCTION

The coronavirus disease 2019 (COVID-19) outbreak has led to a significant and unprecedent increase in laryngotracheal complications and their potential life-threatening sequelae in patients subjected to invasive mechanical ventilation (Fiacchini et al., 2021; Piazza et al., 2021; Sandu, 2021). Many etiopathogenetic hypotheses were proposed such as the pronation maneuvers

which could increase the cuff pressure on the tracheal walls (Crivello et al., 2022), the microvascular injury of laryngo-tracheal mucosa caused by the prothrombotic and antifibrinolytic state of these patients, the use of high dose systemic steroids or more simply due to unreported mistakes or accidents by physically and emotionally exhausted health care professionals. However, to date, no clear explanation was identified but a list of recommendations were proposed to prevent and manage this type of complication (Meister et al., 2021).

Another possible cause of laryngotracheal lesions could be the high viral replication within the laryngotracheal mucosa which could weaken the epithelium itself. In fact, SARS-CoV-2 particles were observed in tracheal epithelial cells and within the extracellular mucus in the tracheal lumen of trachea samples taken during autopsies (Bradley et al., 2020).

In this work, we investigated this last etiopathogenetic hypothesis by performing a histological and genetic-transcriptional analysis of tracheal samples taken during surgical tracheostomies in critically ill COVID-19 patients subjected to mechanical invasive ventilation and comparing them with tracheal samples taken from non-COVID-19 patients.

MATERIALS AND METHODS

Subjects for the COVID-19 group and the control group (non-COVID-19 patients) were selected retrospectively according to the following criteria:

- age from 18 to 75 years;
- admitted to the Intensive Care Units (ICU) of our tertiary referral hospital between November 1 and December 31, 2020 (Italian second wave) and requiring invasive mechanical ventilation for Acute Respiratory Distress Syndrome (ARDS) caused by SARS-CoV-2 (COVID-19 group) or for other pathologies (control group);
- SARS-CoV-2 detected in nasopharyngeal/oropharyngeal swabs (COVID-19 group) or not detected (control group); and
- subjected to open surgical tracheostomy where a small anterior portion of one or two tracheal rings is removed (Cheung and Napolitano, 2014; Brass et al., 2016) and submitted in 4% buffered formalin to the Surgical Pathology Department of our hospital. The decision to perform a percutaneous or an open surgical tracheostomy in COVID-19 patients was taken by the "tracheo-team" (two otolaryngologists and two anesthesiologists) according to internal guidelines derived from the most recent literature (Bassi et al., 2020; Takhar et al., 2020).

Patients' basic and clinical data such as age, sex, COVID-19 status, comorbidities, duration of invasive mechanical ventilation with oro-tracheal tubes before open surgical tracheostomy, surgical complications and pharmacological treatments were recorded and analyzed. Data on comorbidities were collected using the Adult Comorbidity Evaluation 27 index (ACE-27; Piccirillo et al., 2004). This study was approved by the Local Ethics Committee on June 24, 2021. Written informed consent to collect deidentified data was obtained from all patients. This study followed the Strengthening the Reporting of Observational Studies in Epidemiology (STROBE) reporting guideline.

Histological Analysis

One paraffin-embedded inclusion was obtained from each biopsy and three-micrometer thick sections were cut from each sample and stained with Hematoxylin–Eosin (Diapath Spa, Bergamo, Italy).

Immunohistochemistry

Three-micrometer thick sections were cut from each sample, dewaxed, pretreated by cell conditioner at 95°C for 32 min with ULTRA CC1 ready-to-use solution (Ventana Medical Systems, Inc., Oro Valley, AZ, United States), and thereafter incubated with anti-SARS Nucleocapsid Protein Rabbit Polyclonal antibody (Novus Biologicals; dilution 1:500 and at 36°C for 32 min). The antibody–antigen binding has been detected using the OptiView DAB IHC Detection kit (Ventana Medical Systems, Inc., Oro Valley, AZ, United States). Then slides were counterstained with Hematoxylin II and Bluing Reagent (Ventana Medical Systems, Inc., Oro Valley, AZ, United States) for 8 min.

Three-micrometer thick sections were cut from each sample were stained with ready-to-use CONFIRM anti-CD3 (2GV6) Rabbit Monoclonal Primary Antibody, CONFIRM anti-CD20 (L26) Mouse Monoclonal Primary Antibody, CONFIRM anti-CD4 (SP35) Mouse Monoclonal Primary Antibody, CONFIRM anti-CD8 (SP57) Rabbit Monoclonal Primary Antibody, CONFIRM anti-CD68 (KP-1) Mouse Monoclonal Primary Antibody (Roche Diagnostics Ventana Medical Systems, Inc., Oro Valley, AZ, United States), and CONFIRM anti-CD34 (QBEnd/10) Mouse Monoclonal Primary Antibody. The antibody–antigen binding has been detected using the ultraView Universal DAB Detection Kit (Ventana Medical Systems, Inc., Oro Valley, AZ, United States). Staining was done on an automated IHC/ISH slide staining system (BenchMark ULTRA—Ventana Medical Systems, Inc., Oro Valley, AZ, United States).

Gene Expression Analysis and Detection of SARS-CoV-2

Four unstained 10 µm-thick formalin-fixed paraffin-embedded sections were used for RNA isolation using the RNeasy FFPE kit (Qiagen, Hilden, Germany). RNA quality was tested by spectrophotometry (Xpose, Trinean, Gentbrugge, Belgium). About 150 ng of RNA were used for the RT-PCR assay to detect the SARS-CoV-2 using the Easy SARS-CoV-2 WE kit (Diatech Pharmacogenetics, Jesi, Italy). The assay is designed to target the viral nucleocapsid (N) and RNA-dependent RNA Polymerase (RdRp) genes. Viral assays were run in duplicates. A sample was deemed positive when at least one of the targets was amplified, as suggested by the manufacturer. For the gene expression assay, about 150 ng of RNA were hybridized at 65°C for 21 h with capture and reporter probes of the Human Host Response panel (nanoString Technologies, Seattle, WA,

United States). All procedures were performed following the manufacturer's suggestions.

Statistical Analysis

Raw expression counts were normalized using the Advanced Analysis module of the nSover v.4.0 (nanoString Technologies, Seattle, WA, United States). Low count genes (raw numbers below 20 counts) were filtered out, and normalized gene expression levels were log2 transformed. Differentially expressed genes (DEG) between COVID-19 cases and controls were computed by a linear model using control samples as baseline and following the procedures of the Advanced Analysis module of the nSolver software. Values of p were adjusted with the Benjamini-Hochberg method, and false discovery rates (FDR) below 0.05 were considered significant. The ranked gene list was used for the gene set enrichment analysis (GSEA) following the procedures of the clusterProfiler Bioconductor package v.3.13. In detail, the Hallmark collection was used as reference database (Liberzon et al., 2015), and a minimum gene set size cut-off of 10 genes was set. The immune cell abundances were computed using the method described by Middleton et al. (2020) and compared by the Mann–Whitney U test. A value of p of 0.05 was set as significance cut-off. The analyses and plots were done in R environment v.4.1.0 (https://www.r-project.org/, last accessed May 31, 2021), unless otherwise specified.

RESULTS

General Data Analysis

From November 1 to December 31, 2020, 62 patients were admitted to the COVID-19 dedicated ICU of our hospital. Twenty patients were referred for tracheostomy and the "tracheo-team" decided to perform an open surgical tracheostomy in four of them. All four patients were enrolled in this study and all of them got a positive PCR test result for Sars-CoV-2 performed the day before the surgical procedure. Four control patients matched for age and sex were selected according to our criteria in the aforementioned time frame. Patients' basic and clinical data are reported in **Table 1**.

Histological Findings

A predominantly subepithelial inflammatory lymphomonocyte infiltrate was observed in all COVID-19 and non-COVID-19 patients, associated with epithelial erosion. Two cases in the COVID-19 group (case #2 and #4) showed evident lymphocytic vasculitis of small subepithelial vessels associated with foci of coagulative necrosis (**Figure 1**), while granulomas and granulation tissue were not observed in any patient. Squamous metaplasia was identified in patients with a longer duration of intubation (patient #1 and #2). Acute tracheitis was not identified in any tracheal sample. Inflammatory cells, as lymphocyte and macrophages, were detected by immunohistochemical staining in each COVID-patient sample. CD20, CD3, CD4, and CD8 lymphocyte and CD68 macrophages cells were counted in 10 different randomly chosen areas in each processed slide with 40× magnification. Counting was performed blindly by two independent observers.

Detection of the SARS-CoV-2

The SARS-CoV-2 was detected in one out of four COVID-19 samples (case #4) by the RT-PCR assay whereas all tracheal samples were negative at immunohistochemical detection with anti-SARS Nucleocapsid Protein.

COVID-19 Samples Have a Remarkable Gene Expression Alteration

After filtering out low count genes, 664 transcripts were considered for further analyses. Compared to the control group, COVID-19 samples showed marked gene expression changes with a trend toward gene down-regulation. In fact, a statistically significant difference was identified in 332 out of 664 genes (**Figure 2**) but, when adjusting for multiple comparisons, no genes had a false discovery rate (FDR) less than 0.05 due to the low statistical power.

The GSEA showed that two gene sets were significantly deregulated in COVID-19 patients. In details, the HALLMARK_INFLAMMATORY_RESPONSE was activated (FDR = 0.0001, normalized enrichment score (NES) =1.91) and the HALLMARK_ESTROGEN_RESPONSE_LATE was suppressed (FDR = 0.05, NES = −1.82; **Figure 3**).

As regards immune cell abundances, COVID-19 tracheal samples showed higher scores of innate immune cells including macrophages ($p = 0.03$), M2 macrophages ($p = 0.007$), osteoclast-like ($p = 0.01$) and polymorphonuclear neutrophils ($p = 0.03$; **Figure 4**). These results were confirmed by the immunohistochemistry (IHC) analysis; in fact, CD68 macrophages were significantly more abundant in the COVID-19 samples than in samples of the control group ($p = 0.03$; **Figure 5**).

DISCUSSION

Many papers related to acute and late laryngotracheal complications in COVID-19 patients subjected to invasive mechanical ventilation have been published in the last few months (Alturk et al., 2021; Balakrishnan et al., 2021; Fiacchini et al., 2021; Mahmood et al., 2021; Sandu, 2021; Scholfield et al., 2021). In order to explain the increase in the incidence of this particular type of complication, several etiopathogenetic hypotheses have been proposed. However, none of these appear to be more acceptable than others and the cause is likely to be found in a combination of multiple triggers. Among them, the possibility that the laryngotracheal mucosa could be a site of high viral replication intrigued us and led us to investigate in this sense. This hypothesis was corroborated by the findings of Bradley et al. (2020). As a matter of fact, they identified viral particles in the tracheal epithelium of 12 autopsies. Moreover, other authors reported laryngotracheal oedema that might suggest virus-mediated inflammation (McGrath et al., 2020; Oliver et al., 2020; Osbeck Sandblom et al., 2021). For these reasons, the aim of this study was to identify the virus

TABLE 1 | Patients' basic and clinical data.

ID patient	Age	Sex	COVID-19 status	Comorbidities (ACE-27)	Main pathology	IOTI (days)	Laryngo-tracheal complications	Outcome	SBP (mmHg)	DBP (mmHg)	HR (bpm)	Antibiotics	Antivirals	Hydroxy chloroquine	Steroids	Low-molecular-weight heparin
1	65	F	+	Mild	ARDS—Covid-19	18	None	Dead	110	60	55	Yes	No	No	Yes (dexamethasone 8 mg daily)	Yes (prophylactic dosage)
2	60	F	+	Moderate	ARDS - Covid-19	17	None	Discharge	110	65	60	Yes	No	No	Yes (dexamethasone 8 mg daily)	Yes (therapeutic dosage)
3	56	F	+	Mild	ARDS - Covid-19	13	None	Discharge	120	65	60	Yes	No	No	Yes (dexamethasone 8 mg daily)	Yes (therapeutic dosage)
4	48	M	+	None	ARDS - Covid-19	14	None	Discharge	120	70	60	Yes	No	No	Yes (dexamethasone 8 mg daily)	Yes (therapeutic dosage)
5	75	F	–	Moderate	Intracranial Hemorrhage	7	None	Dead	120	70	80	Yes	No	No	No	Yes (prophylactic dosage)
6	62	M	–	None	Trauma	6	None	Discharge	135	75	78	Yes	No	No	Yes (dexamethasone 4 mg daily)	Yes (prophylactic dosage)
7	70	F	–	Mild	Complications of Cardiac Surgery	15	None	Discharge	120	90	90	Yes	No	No	Yes (dexamethasone 8 mg daily)	Yes (therapeutic dosage)
8	65	M	–	Moderate	Complications of Thoracic Surgery	14	None	Discharge	110	60	70	Yes	No	No	No	Yes (prophylactic dosage)

ACE-27, adult comorbidity evaluation 27; ARDS, acute respiratory distress syndrome; DBP, diastolic blood pressure; HR, heart rate; IOTI, invasive oro-tracheal intubation; SBP, systolic blood pressure.

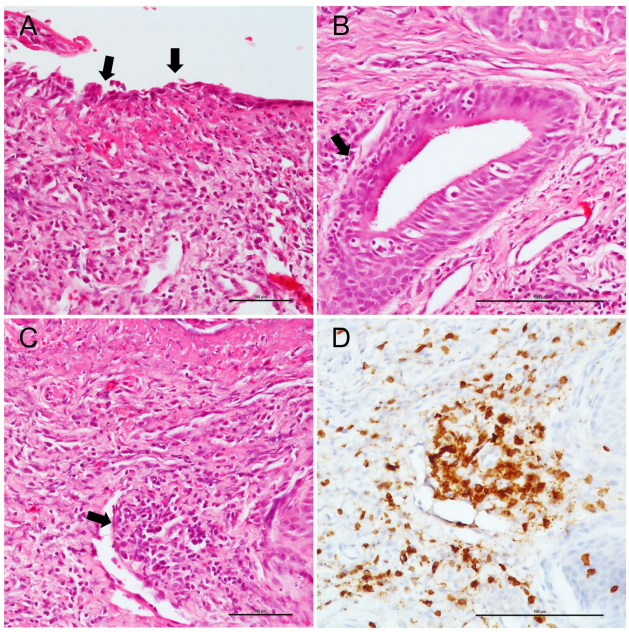

FIGURE 1 | Pathological tracheal alterations in a COVID-19 case. **(A)** epithelial erosion is highlighted by black arrows. **(B)** subepithelial inflammatory lymphomonocyte infiltrate (black arrow). **(C)** hematoxylin and eosin staining shows lymphocytic vasculitis of small subepithelial vessel (black arrow), which is confirmed by CD3 staining. **(D)** Scale bars refer to 100 micrometers.

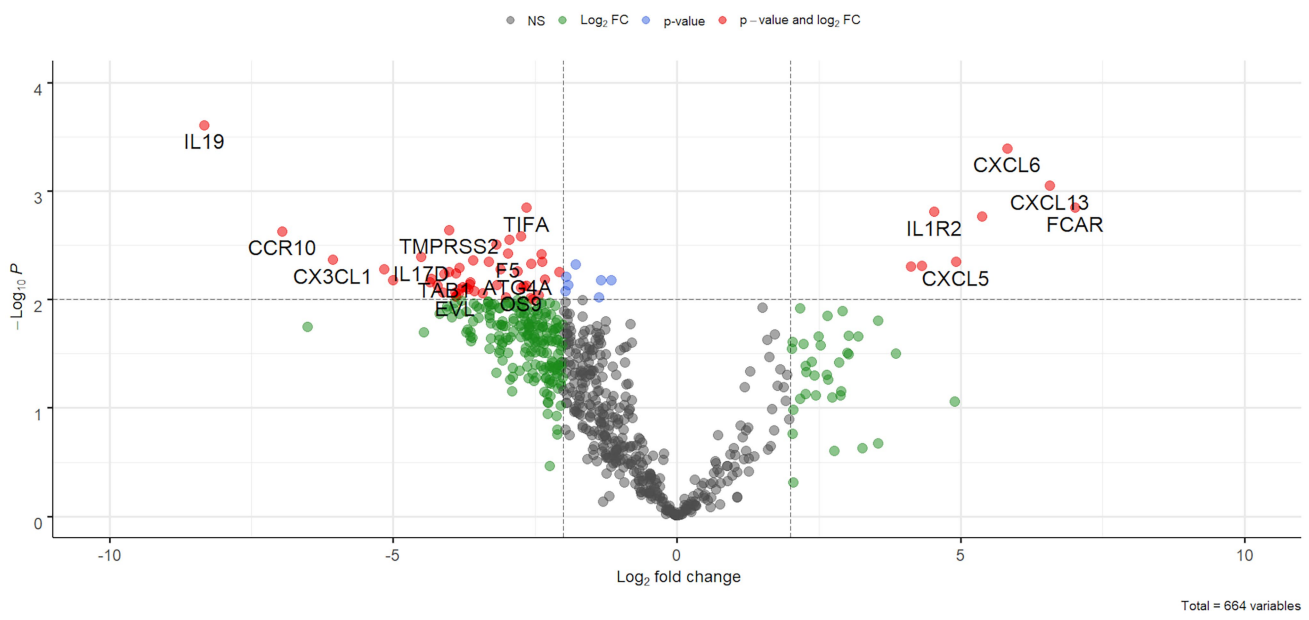

FIGURE 2 | Volcano plot. Results of differential expression analysis were plotted as fold changes (*x*-axis) and -log10 of value of ps (*y*-axis). Dotted lines represent a value of *p* of 0.01 (horizontal line) and a 2-fold absolute value (vertical lines).

particles in the tracheal epithelium of live COVID-19 patients and to evaluate any histological and genetic differences compared to a control group.

Histologic evidence in COVID-19 tracheal biopsies were similar to those observed in other series, with lymphomonocytic subepithelial inflammation and vasculitis, with small foci of coagulative necrosis (Lucchi et al., 2020). However, in our small series, immunohistochemical detection of SARS-CoV-2 was negative, differently from other reports (Martines et al., 2020). This is probably due to the prolonged oro-tracheal intubation

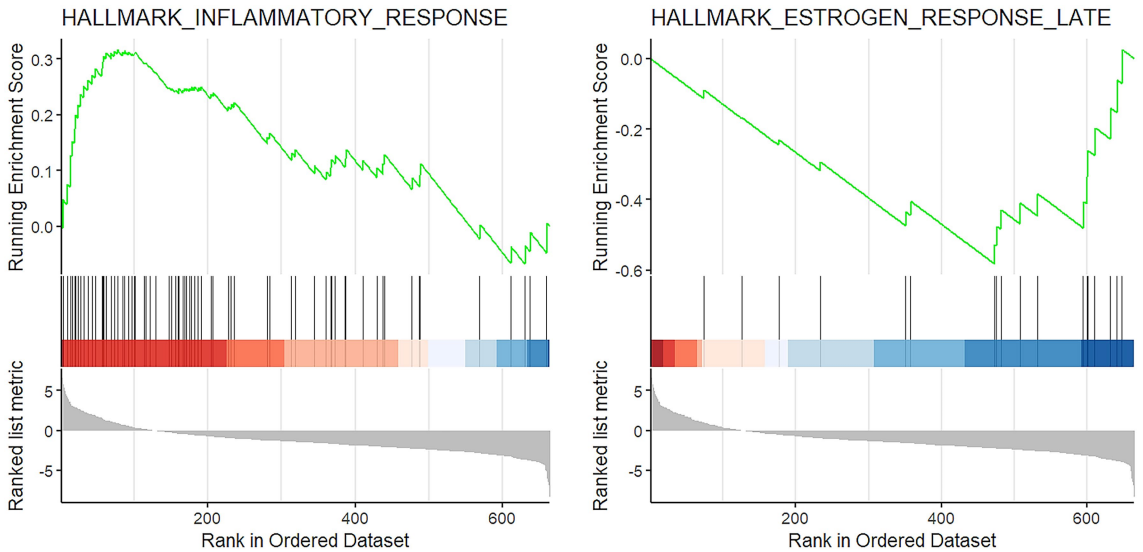

FIGURE 3 | GSEA results. Enrichment plot of the two significantly altered gene sets in COVID-19 cases: activation of inflammatory response (left) and suppression of late estrogen response (right).

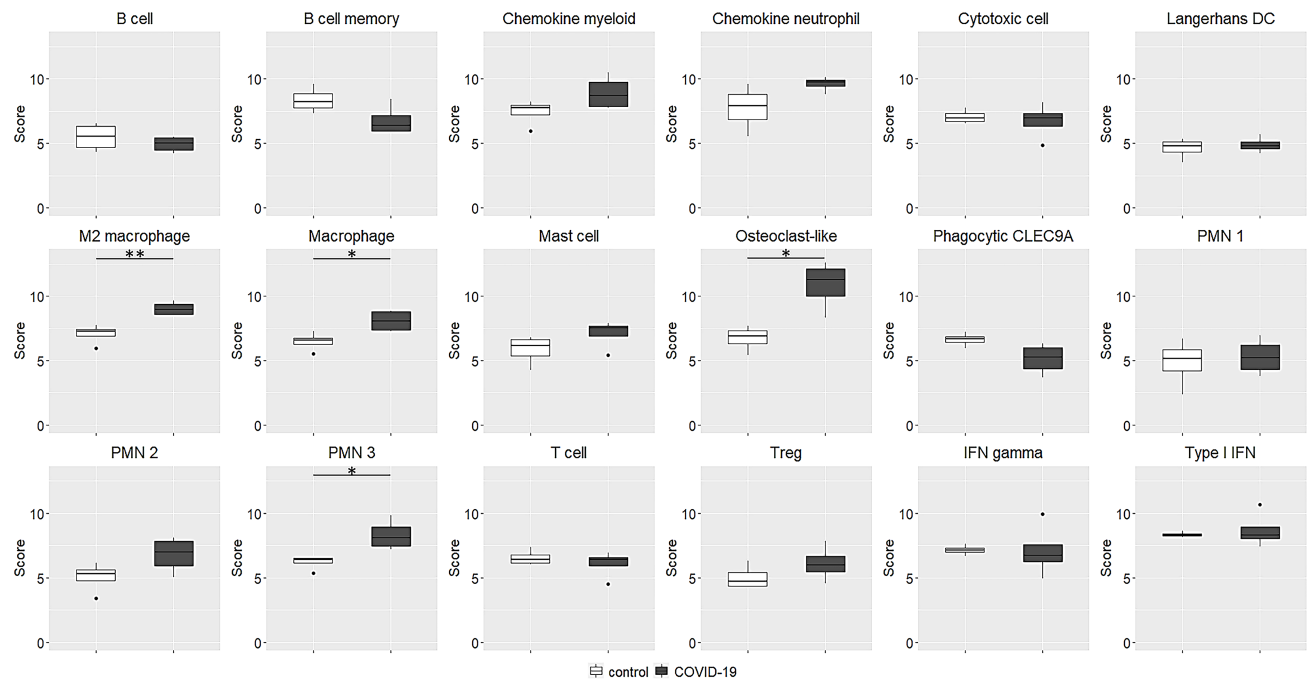

FIGURE 4 | Immune cell abundance estimated by transcriptional data. The abundances are expressed as log2 expression. Macrophage, M2 macrophage, osteoclast-like and polymorphonuclear neutrophils scores were significantly higher in COVID-19 tracheal samples. *$p < 0.05$; **$p < 0.01$. PMN, polymorphonuclear neutrophils; IFN, interferon.

and the use of electrified instruments to perform the tracheostomy that both caused de-epithelialization of the tracheal samples. However, in one case the SARS-CoV-2 genome was detected at very low load. The possibility that positivity of PCR assays represents viral spreading *via* blood/lymphatic vessels rather than specific virus tropism, should also be considered.

COVID-19 samples showed an intense inflammatory response and a strong gene deregulation. In addition, these cases presented a greater infiltration of innate immune cells (mostly macrophages or cells with phagocytic activity), which are coherent with an early phase of immune response. It has been widely discussed that both in patients who eventually died of Severe Adult

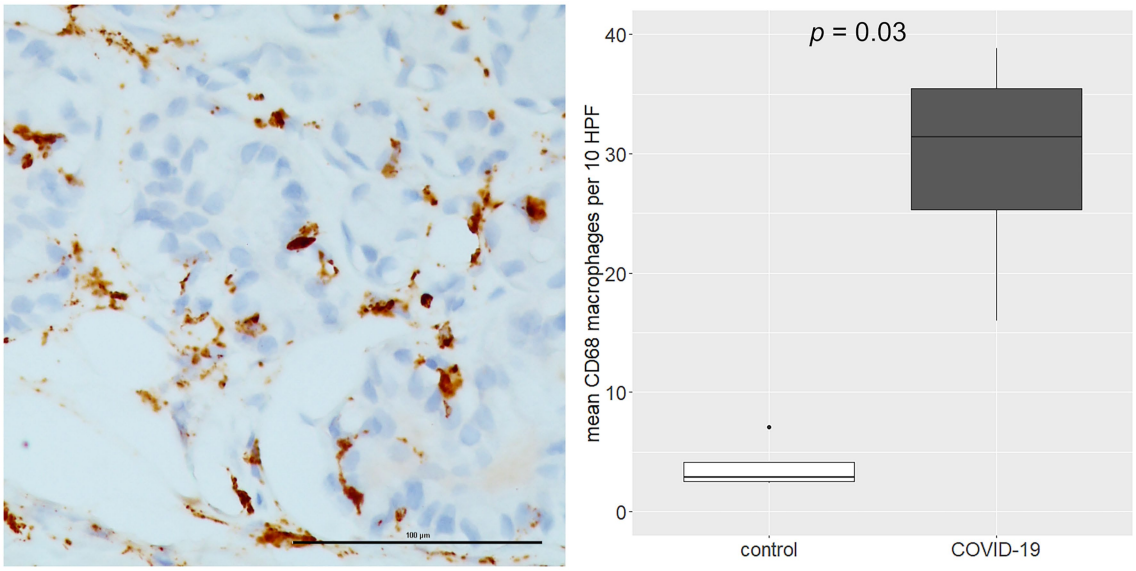

FIGURE 5 | Immunohistochemistry (IHC) analysis of CD68 macrophages (left side). The over-representation of CD68 macrophages was confirmed by IHC analysis (right side). Scale bar refers to 100 μm.

Respiratory Syndrome (SARS) and in animal models, extensive lung damage is associated with high initial viral loads, increased inflammatory monocytes/macrophages accumulation in the lungs and elevated serum proinflammatory cytokines (Nicholls et al., 2003; Perlman and Dandekar, 2005). While much is known about the terminal phase of SARS, little is known about the early immune events during the acute phase of infection.

Monocytes and macrophages may be directly infected by SARS-CoV-2 through ACE2-dependent process or indirectly infected *via* ACE2-independent pathways and phagocytosis of virus-containing apoptotic bodies. SARS-CoV-2 can effectively suppress the anti-viral IFN response in monocytes and macrophages. Upon infection, monocytes migrate to tissues where they become infected resident macrophages, allowing viruses to spread through all organs and tissues. The SARS-CoV-2-infected monocytes and macrophages can produce large amounts of numerous types of pro-inflammatory cytokines and chemokines, which contribute to the local tissue inflammation and dangerous systemic inflammatory response as named cytokine storm (Jafarzadeh et al., 2020).

Interestingly, studies comparing the host response to SARS-CoV-2 and influenza viruses in the upper respiratory tract, observed very low levels of virus but a robust transcriptional response with differential expression of transcripts implicated in two populations of immune cell signatures (Blanco-Melo et al., 2020). The first population included common markers for monocytes and lymphocytes, and the induction of these genes was comparable between SARS-CoV-2 and influenza virus. Consistent with this, they found significant induction of monocyte-associated chemokines such as CCL2 and CCL8. In addition, their data suggest that neutrophils could also contribute to the disease observed in COVID-19 patients, as demonstrated by CXCL2 and CXCL8 induction, differently from influenza virus infection. This is consistent with data showing elevated circulating neutrophil levels among COVID-19 patients (Chen et al., 2020; Qin et al., 2020), which may have prognostic value for identifying individuals at risk for developing severe disease. These data, obtained from the analysis of *in vitro* and *ex vivo* samples, support what we observed in our series, highlighting the multiplicity of disease pathways of SARS-CoV-2.

Herein, we observed also the suppression of estrogen response pathway. It was already reported that sex hormones, including estrogens, may regulate both innate and adaptive immune response (Khan and Ansar Ahmed, 2015). Consequently, estrogen suppression has been involved in autoimmune conditions (Moulton, 2018; Kim et al., 2019). It is interesting to note that, in support of this observation, the groups analyzed show a gender imbalance, with a preponderance of female sex in the COVID-19 group compared to the control group.

This work has several limitations. The first is the small sample size. As a matter of fact, the "tracheo-team" decided to perform an open surgical tracheostomy in only four patients (20%) due to the fact that the percutaneous technique has several advantages, especially in terms of aerosolization. The second is relative to its retrospective and single center nature. Third, we were not able to identify the viral genome in three tracheal samples due to the aforementioned reasons. For all these issues we were not able to draw any definitive conclusions. Anyway, we can take some ideas from these data, especially related to the gene expression alterations. Even without the identifications of SARS-CoV-2 genome and prominent histological differences between the two groups, the gene expression is clearly altered in the COVID-19 group meaning that a different inflammatory response is taking place in these patients. However, it must be considered that the control group was not matched for the main pathology that had caused the ICU hospitalization. In particular, no patient in the control group suffered from ARDS, so all of them may not have an ongoing inflammatory process in the respiratory tract. Certainly, other studies with larger and adequate sample

size are needed to confirm these data, but this could be another piece in the composition of this difficult puzzle of laryngotracheal complications in COVID-19 patients.

In conclusion, we cannot confirm that the trachea is a site of high viral replication. However, the tissue samples of the COVID-19 group showed a significant alteration of gene expression in two gene sets (activation of the HALLMARK_INFLAMMATORY_RESPONSE and suppression of the HALLMARK_ESTROGEN_RESPONSE_LATE) compared to the control group, meaning that the inflammatory response of the COVID-19 patients is completely different. Further studies are warranted to investigate these aspects.

DATA AVAILABILITY STATEMENT

The original contributions presented in the study are included in the article/supplementary material, further inquiries can be directed to the corresponding authors.

ETHICS STATEMENT

This study was approved by the Local Ethics Committee on June 24, 2021. Written informed consent to collect deidentified data was obtained from all patients. This study followed the Strengthening the Reporting of Observational Studies in Epidemiology (STROBE) reporting guideline.

AUTHOR CONTRIBUTIONS

All authors contributed to the study conception and design. Material preparation, data collection and analysis were performed by GiF, AP, AMP, and LB. The first draft of the manuscript was written by GiF and AP and all authors commented on previous versions of the manuscript. Review and editing were performed by GiF, AP, MP, ID, and LB. The methodology of study was supervised by GaF and FG. All authors read and approved the final manuscript.

REFERENCES

Alturk, A., Bara, A., and Darwish, B. (2021). Post-intubation tracheal stenosis after severe COVID-19 infection: a report of two cases. *Ann. Med. Surg.* 67:102468. doi: 10.1016/j.amsu.2021.102468

Balakrishnan, K., Brenner, M. J., and Hillel, A. T. (2021). Laryngeal and tracheal pressure injuries in patients with COVID-19. *JAMA Otolaryngol. Head Neck Surg.* 147, 484–485. doi: 10.1001/jamaoto.2021.0001

Bassi, M., Ruberto, F., Poggi, C., Diso, D., Anile, M., De Giacomo, T., et al. (2020). Is surgical tracheostomy better Than percutaneous tracheostomy in COVID-19-positive patients? *Anesth. Analg.* 131, 1000–1005. doi: 10.1213/ANE.0000000000005100

Blanco-Melo, D., Nilsson-Payant, B. E., Liu, W.-C., Uhl, S., Hoagland, D., Møller, R., et al. (2020). Imbalanced host response to SARS-CoV-2 drives development of COVID-19. *Cell* 181, 1036–1045.e9. doi: 10.1016/j.cell.2020.04.026

Bradley, B. T., Maioli, H., Johnston, R., Chaudhry, I., Fink, S. L., Xu, H., et al. (2020). Histopathology and ultrastructural findings of fatal COVID-19 infections in Washington state: a case series. *Lancet* 396, 320–332. doi: 10.1016/S0140-6736(20)31305-2

Brass, P., Hellmich, M., Ladra, A., Ladra, J., and Wrzosek, A. (2016). Percutaneous techniques versus surgical techniques for tracheostomy. *Cochrane Database Syst. Rev.* 7:CD008045. doi: 10.1002/14651858.CD008045.pub2

Chen, N., Zhou, M., Dong, X., Qu, J., Gong, F., Han, Y., et al. (2020). Epidemiological and clinical characteristics of 99 cases of 2019 novel coronavirus pneumonia in Wuhan, China: a descriptive study. *Lancet* 395, 507–513. doi: 10.1016/S0140-6736(20)30211-7

Cheung, N. H., and Napolitano, L. M. (2014). Tracheostomy: epidemiology, indications, timing, technique, and outcomes. *Respir. Care* 59, 895–915. doi: 10.4187/respcare.02971

Crivello, A., Milazzo, M., La Rosa, D., Fiacchini, G., Danti, S., Guarracino, F., et al. (2022). Experimental assessment of cuff pressures on the walls of a trachea-like model using force sensing resistors: insights for patient management in intensive care unit settings. *Sensors* 22:697. doi: 10.3390/s22020697

Fiacchini, G., Tricò, D., Ribechini, A., Forfori, F., Brogi, E., Lucchi, M., et al. (2021). Evaluation of the incidence and potential mechanisms of tracheal complications in patients With COVID-19. *JAMA Otolaryngol. Head Neck Surg.* 147, 70–76. doi: 10.1001/jamaoto.2020.4148

Jafarzadeh, A., Chauhan, P., Saha, B., Jafarzadeh, S., and Nemati, M. (2020). Contribution of monocytes and macrophages to the local tissue inflammation and cytokine storm in COVID-19: lessons from SARS and MERS, and potential therapeutic interventions. *Life Sci.* 257, 118102–118102. doi: 10.1016/j.lfs.2020.118102

Khan, D., and Ansar Ahmed, S. (2015). The immune system is a natural target for estrogen action: opposing effects of estrogen in two prototypical autoimmune diseases. *Front. Immunol.* 6:635. doi: 10.3389/fimmu.2015.00635

Kim, D.-H., Park, H.-J., Park, H.-S., Lee, J.-U., Ko, C., Gye, M. C., et al. (2019). Estrogen receptor α in T cells suppresses follicular helper T cell responses and prevents autoimmunity. *Exp. Mol. Med.* 51, 1–9. doi: 10.1038/s12276-019-0237-z

Liberzon, A., Birger, C., Thorvaldsdóttir, H., Ghandi, M., Mesirov, J. P., and Tamayo, P. (2015). The molecular signatures database (MSigDB) hallmark gene set collection. *Cell Syst.* 1, 417–425. doi: 10.1016/j.cels.2015.12.004

Lucchi, M., Ambrogi, M., Aprile, V., Ribechini, A., and Fontanini, G. (2020). Laryngotracheal resection for a post-tracheotomy stenosis in a patient with coronavirus disease 2019 (COVID-19). *JTCVS Tech.* 4, 360–364. doi: 10.1016/j.xjtc.2020.08.023

Mahmood, K., Cheng, G. Z., Van Nostrand, K., Shojaee, S., Wayne, M. T., Abbott, M., et al. (2021). Tracheostomy for COVID-19 respiratory failure: multidisciplinary, multicenter data on timing, technique, and outcomes. *Ann. Surg.* 274, 234–239. doi: 10.1097/SLA.0000000000004955

Martines, R. B., Ritter, J. M., Matkovic, E., Gary, J., Bollweg, B. C., Bullock, H., et al. (2020). Pathology and pathogenesis of SARS-CoV-2 associated with fatal coronavirus disease, United States. *Emerg. Infect. Dis.* 26, 2005–2015. doi: 10.3201/eid2609.202095

McGrath, B. A., Wallace, S., and Goswamy, J. (2020). Laryngeal oedema associated with COVID-19 complicating airway management. *Anaesthesia* 75, 972–972. doi: 10.1111/anae.15092

Meister, K. D., Pandian, V., Hillel, A. T., Walsh, B. K., Brodsky, M. B., Balakrishnan, K., et al. (2021). Multidisciplinary safety recommendations After tracheostomy During COVID-19 pandemic: state of the art review. *Otolaryngol. Head Neck Surg.* 164, 984–1000. doi: 10.1177/0194599820961990

Middleton, G., Yang, Y., Campbell, C. D., André, T., Atreya, C. E., Schellens, J. H. M., et al. (2020). BRAF-mutant transcriptional subtypes predict outcome of combined BRAF, MEK, and EGFR blockade with Dabrafenib, Trametinib, and Panitumumab in patients with colorectal cancer. *Clin. Cancer Res.* 26, 2466–2476. doi: 10.1158/1078-0432.CCR-19-3579

Moulton, V. R. (2018). Sex hormones in acquired immunity and autoimmune disease. *Front. Immunol.* 9:2279. doi: 10.3389/fimmu.2018.02279

Nicholls, J., Dong, X.-P., Jiang, G., and Peiris, M. (2003). SARS: clinical virology and pathogenesis. *Respirology* 8, S6–S8. doi: 10.1046/j.1440-1843.2003.00517.x

Oliver, C. M., Campbell, M., Dulan, O., Hamilton, N., and Birchall, M. (2020). Appearance and management of COVID-19 laryngo-tracheitis: two case reports. *F1000Res* 9:310. doi: 10.12688/f1000research.23204.1

Osbeck Sandblom, H., Dotevall, H., Svennerholm, K., Tuomi, L., and Finizia, C. (2021). Characterization of dysphagia and laryngeal findings in COVID-19 patients treated in the ICU-an observational clinical study. *PLoS One* 16:e0252347. doi: 10.1371/journal.pone.0252347

Perlman, S., and Dandekar, A. A. (2005). Immunopathogenesis of coronavirus infections: implications for SARS. *Nat. Rev. Immunol.* 5, 917–927. doi: 10.1038/nri1732

Piazza, C., Filauro, M., Dikkers, F. G., Nouraei, S. A. R., Sandu, K., Sittel, C., et al. (2021). Long-term intubation and high rate of tracheostomy in COVID-19 patients might determine an unprecedented increase of airway stenoses: a call to action from the European laryngological society. *Eur. Arch. Otorhinolaryngol.* 278, 1–7. doi: 10.1007/s00405-020-06112-6

Piccirillo, J. F., Tierney, R. M., Costas, I., Grove, L., and Spitznagel, E. L. (2004). Prognostic importance of comorbidity in a hospital-based cancer registry. *JAMA* 291, 2441–2447. doi: 10.1001/jama.291.20.2441

Qin, C., Zhou, L., Hu, Z., Zhang, S., Yang, S., Tao, Y., et al. (2020). Dysregulation of immune response in patients With coronavirus 2019 (COVID-19) in Wuhan, China. *Clin. Infect. Dis.* 71, 762–768. doi: 10.1093/cid/ciaa248

Sandu, K. (2021). Laryngotracheal complications in intubated COVID-19 patients. *Clin. Med. Insights Case Rep.* 14:11795476211020590. doi: 10.1177/11795476211020590

Scholfield, D. W., Warner, E., Ahmed, J., and Ghufoor, K. (2021). Subglottic and tracheal stenosis associated with coronavirus disease 2019. *J. Laryngol. Otol.* 135, 656–658. doi: 10.1017/S0022215121001134

Takhar, A., Walker, A., Tricklebank, S., Wyncoll, D., Hart, N., Jacob, T., et al. (2020). Recommendation of a practical guideline for safe tracheostomy during the COVID-19 pandemic. *Eur. Arch. Otorhinolaryngol.* 277, 2173–2184. doi: 10.1007/s00405-020-05993-x

Conflict of Interest: The authors declare that the research was conducted in the absence of any commercial or financial relationships that could be construed as a potential conflict of interest.

frontiers in Microbiology

ORIGINAL RESEARCH
published: 28 March 2022
doi: 10.3389/fmicb.2022.831852

The CREB and AP-1–Dependent Cell Communication Network Factor 1 Regulates Porcine Epidemic Diarrhea Virus-Induced Cell Apoptosis Inhibiting Virus Replication Through the p53 Pathway

Hongchao Zhou†, Yuting Zhang†, Jingjing Wang, Yuchao Yan, Yi Liu, Xiaojie Shi, Qi Zhang and Xingang Xu**

College of Veterinary Medicine, Northwest A&F University, Xianyang, China

OPEN ACCESS

Edited by:
Cao Yong Chang,
Sun Yat-sen University, China

Reviewed by:
Zhao-Hua Zhong,
Harbin Medical University, China
Fanfan Zhang,
Jiangxi Academy of Agricultural Sciences (CAAS), China

***Correspondence:**
Qi Zhang
zhangqi77@nwsuaf.edu.cn
Xingang Xu
tiger2003@nwsuaf.edu.cn

† These authors have contributed equally to this work

Specialty section:
This article was submitted to Virology, a section of the journal Frontiers in Microbiology

Received: *09 December 2021*
Accepted: *14 February 2022*
Published: *28 March 2022*

Citation:
Zhou H, Zhang Y, Wang J, Yan Y, Liu Y, Shi X, Zhang Q and Xu X (2022) The CREB and AP-1–Dependent Cell Communication Network Factor 1 Regulates Porcine Epidemic Diarrhea Virus-Induced Cell Apoptosis Inhibiting Virus Replication Through the p53 Pathway. Front. Microbiol. 13:831852. doi: 10.3389/fmicb.2022.831852

Porcine epidemic diarrhea virus (PEDV) infection causes severe diarrhea, dehydration, and high mortality in sick pigs, causing huge economic losses to the pig industry. However, the relationship between cell communication network factor 1 (CCN1) and PEDV infection has not been reported. In this study, we showed that the expression of CCN1 was enhanced by PEDV infection, and we observed that PEDV promotes the CREB and AP-1 activation to promote CCN1 expression. The PKA and p38 inhibitors significantly suppress CCN1 expression, indicating that PEDV-induced CCN1 expression may be through PKA and p38 pathway. Further tests confirmed that CREB and AP-1 are regulated by PKA and p38, respectively. Overexpression of CCN1 decreased the replication of PEDV, whereas knockdown of CCN1 increased the replication of PEDV. We proved that the overexpression of CCN1 increased the phosphorylation level of p53, promoted the expresion of Bax and the cleavage of caspase 9 and caspase 3, and inhibited the production of Bcl-2. CCN1 knockdown decreased the phosphorylation level of p53, inhibited the production of Bax and the cleavage of caspase 9 and caspase 3, and promoted the expression of Bcl-2. The treatment of PFT-α (p53 inhibitor) significantly suppressed the expression of cleaved caspase 9 and caspase 3, leading to the decrease of apoptosis. Together, these studies showed that PEDV promotes the activation of CREB and AP-1 to increase the expression of CCN1. Overexpression of CCN1 promotes apoptosis by elevating p53 protein phosphorylation and inhibits PEDV replication, and knockdown of CCN1 inhibits apoptosis by decreasing p53 protein phosphorylation and promotes PEDV replication. Our study could provide some reference for the molecular mechanisms of PEDV-induced CCN1 induction and supply a new therapeutic target for PEDV.

Keywords: PEDV, CCN1, CREB, AP-1, p53 pathway, apoptosis

INTRODUCTION

Porcine epidemic diarrhea (PED) leads to severe diarrhea and dehydration, intestinal villi atrophy, and high mortality of neonatal piglets, causing enormous economic losses for the pig industry. Porcine epidemic diarrhea virus (PEDV), the etiological agent of PED, is an enveloped, single-stranded positive-sense RNA virus with a genome of approximately 28 kb, belonging to the genus *Alphacoronavirus* family Coronaviridae. The PEDV genome has seven open reading frames (ORFs), which encode two non-structural polyproteins (pp1a and pp1b) (Si et al., 2020; Ye et al., 2020), four structural proteins (S, E, M, and N) (Cochrane et al., 2020), and one virulence accessory protein (ORF3) (Lee, 2016). At present, the pathogenesis of PEDV is not clear. Therefore, it is particularly critical to study the interaction between PEDV and cellular proteins to search for the prevention and treatment mechanisms of PEDV.

Apoptosis is a death program performed by cells that can maintain cell homeostasis by clearing damaged and infected cells. It is mainly regulated by the caspase family protein (Ivanisenko et al., 2020). Apoptosis is activated through three different pathways including the extrinsic pathway, the intrinsic pathway, and the endoplasmic reticulum (ER) pathway (Pan et al., 2018). As a cell defense mechanism, apoptosis can be activated through a series of stimuli, including virus infection. For example, PEDV promotes the release of the mitochondrial pro-apoptosis protein AIF to promote cell apoptosis (Kim and Lee, 2014). The p53-PUMA pathway was activated by PEDV, which induced Vero cell apoptosis (Yang et al., 2021). However, the role of the cell proteins in PEDV-induced apoptosis is still unclear.

Cell communication network factor 1 (CCN1) is a cysteine-rich matrix cell protein, which belongs to one of the CCN family members and consists of four conserved domains: insulin-like growth factor–binding protein homologies domain, von Willebrand growth factor C repeat domain, thrombospondin type I repeat domain, and carboxyl-terminal domain–containing cysteine motif (Zhu et al., 2020). As a multifunctional protein, CCN1 regulates diverse cellular processes such as cell adhesion, migration, proliferation, and apoptosis (Chen and Du, 2007; Lau, 2016). CCN1 induces the apoptosis and senescence of cells through the accumulation of reactive oxygen species (ROS) and CCN1 promotes the cleavage of caspase 9 and caspase 3 through p53-dependent Bax activation in fibroblasts (Todorovic et al., 2005; Lau, 2011), but the role between CCN1 and PEDV-induced apoptosis remains unclear. In addition to regulating the function of apoptosis, CCN1 can also be induced by viruses and regulate virus replication. Previous studies have shown that CCN1 induced by oncolytic virus infection can stimulate type I interferon reaction in glioblastoma cells, thus reducing virus replication (Thorne et al., 2014). Instead, the Zika virus by regulating CCN1 promotes ZIKV replication (Sun et al., 2020). However, it is not clear whether the infection of PEDV can regulate the expression of CCN1 and whether CCN1 affects the replication of PEDV.

In this study, we demonstrated that PEDV promotes transcription factors cAMP response element binding (CREB) and Activator protein 1 (AP-1) phosphorylation into the nucleus through protein kinase A (PKA) and p38 pathways. Activated CREB and Activator protein 1 (AP-1) increase the transcriptional expression of CCN1 by combining with the CCN1 promoter. Overexpression of CCN1 can inhibit the replication of PEDV replication and promote cell apoptosis, whereas knockdown of CCN1 promotes the replication of PEDV and inhibits apoptosis. We demonstrated that the levels of phospho-p53(ser15) and phospho-p53(ser20) protein were elevated during CCN1 overexpression, whereas the levels of phospho-p53(ser15) and phospho-p53(ser20) protein were inhibited during CCN1 knockdown. Moreover, the treatment of Pifithrin-α (PFT-α) inhibited CCN1-induced apoptosis, indicating CCN1-induced apoptosis is dependent on the p53 pathway. In conclusion, our study showed that CREB and AP-1 play dominant roles in PEDV-induced CCN1 expression and disclosed the mechanism by which CCN1 regulates cell apoptosis and PEDV replication.

MATERIALS AND METHODS

Cells Cultures, Virus, Virus Titration, and Infection

African green monkey kidney epithelial cells (Marc-145) and Vero cells, PEDV-permissive cell line, were maintained in Dulbecco's Modified Eagle Medium (Hyclone, Logan, UT, United States) supplemented with 10% fetal bovine serum (PAN-Biotech, Aidenbach, Germany) and culture at 37°C with 5% CO_2. PEDV variant strain CH/SXYL/2016 was originally isolated from intestinal tract contents suffering from PEDV piglets (Sun et al., 2018). The PEDV strain was amplified and titrated in Marc-145 cells. Briefly, 96-well plates were covered with monolayer Marc-145 and then infected with serially dilute PEDV (10^{-1} to 10^{-10}). The virus titer was determined by the Reed-Muench method and transformed into a 50% tissue culture infection dose ($TCID_{50}$). Marc-145 cells were infected with PEDV strain at an multiplicity of infection (MOI) of 1.

Inhibitors and Antibodies

p38 inhibitor SB203580 (10 μM), c-Jun N-terminal kinase (JNK) inhibitor SP600125 (10 μM), extracellular signal-regulated kinase (ERK) inhibitor PD98059 (5 μM), PKA inhibitor H-89 (5 μM), c-Jun inhibitor SR11302 (5 μM), CREB inhibitor EML-425 (5 μM), and p53 inhibitor PFT-α (10 μM) are all purchased from MedChemExpress (Shanghai, China). All inhibitors were configured with dimethyl sulfoxide (DMSO; Solarbio, Beijing, China). Antibodies against Bax, Bcl-2, caspase 3, caspase 8, caspase 9, FasL, Fas, p53, his, phospho-p53(ser15), phospho-p53(ser46), and phospho-p53(ser20) were purchased from Cell Signaling Technology (Danvers, MA, United States). Monoclonal antibodies against CCN1, c-Jun, phospho-c-Jun, c-Fos, phospho-c-Fos, CREB, and phospho-CREB were obtained from ABclonal (Wuhan, China). Antibodies against PEDV (CH/SXYL/2016) N protein were stored in our laboratory (Xu et al., 2019).

Construction of the Cell Communication Network Factor 1 Promoter Expression Vectors and Promoter Deletion Mutants

Extraction of genomic DNA from Marc-145 cells using a DNA extraction kit (Tiangen, Beijing, China). The fragment of the CCN1 gene promoter from −1,994 to 203 bp was cloned and inserted into the luciferase reporter vector pGL4.10-basic to generate the CCN1 promoter reporter plasmid (–1994∼203-Luc). A series of CCN1 promoter truncated mutants were constructed and cloned into a pGL4.10-basic vector at the *Kpn*I and *Nhe*I sites. The CCN1 promoters AP-1, SP1, and CREB element deletion mutants were constructed using the primers listed in **Table 1** and –985∼203-Luc as a template by overlapping PCR. Then, the constructed mutant sequence was verified and cloned into pGL.4.10-basic vector to generate ΔAP-1-Luc, ΔSP1-Luc, and ΔCREB-Luc. The CCN1 promoter primer and truncated mutants of the CCN1 promoter primer were listed in **Table 1**.

Overexpression Plasmid Construction and Transfections

Total RNAs were extracted from Marc-145 cells using TRIzol reagent and reverse-transcribed to cDNA using the FastKing RT Kit with gDNase (Tiangen, Beijing, China). The sequence of the CCN1 gene was amplified through using cDNA as a template. The length of the CCN1 gene was confirmed with DNA sequencing and cloned into the pcDNA3.1-his vector to produce pcDNA3.1-CCN1-his. The Marc-145 cells were seeded on a six-well plate. The next day, the pcDNA3.1-CCN1-his were transfected into Marc-145 cells using lipo8000 (Beyotime Biotechnology, Shanghai, China) according to the manufacturer's instructions. The efficiency of overexpression of CCN1 protein was confirmed by Western blot. The sequences of the CCN1 primer are listed in **Table 1**.

TABLE 1 | Primers for truncated sequence of CCN1 promoter[a].

Primer name[b]	Sequence (5′-3′)[c]
–1994/203-F	CGGGGGTACCTGGATAACAGAGGCAGAA (*Kpn*I)
–1678/203-F	CGGGGTACCCTGTGTACATGTTGGGC (*Kpn*I)
–985/203-F	CGGGGTACCACTGGAATCTGGTTTG (*Kpn*I)
–24/203-F	CGGGGTACCTCCGCCGGCCCATATAA (*Kpn*I)
–1994/203-R	CTAGCTAGCAAGACGCCAACAAGCT (*Nhe*I)
ΔAP-1-F	CGGGGTACCTGGATAACAGAGGCAGAAAAATGTTAA (*Kpn*I)
ΔAP-1-R	CTAGCTAGCAAGACGCCAACAAGCT (*Nhe*I)
ΔAP-1-F_1[d]	TCCCGGAGAACTCCCCGCGTTCGTTTCCTCTC
ΔAP-1-R_1[e]	GCGGGGAGTTCTCCGGGATTCCTCACGGATACAGGA
ΔSP1-F	CGGGGTACCTGGATAACAGAGGCAGAAAAATGTTAA (*Kpn*I)
ΔSP1-R	CTAGCTAGCAAGACGCCAACAAGCT (*Nhe*I)
ΔSP1-F_1	CTCGCGACCCTCCAACCACCATCACCACCATCACA
ΔSP1-R_1	TGGTTGGAGGGTCGCGAGGTCCAGTTCAGAACTTTG
ΔCREB-F	CGGGGTACCTGGATAACAGAGGCAGAAAAATGTTAA (*Kpn*I)
ΔCREB-R	CTAGCTAGCAAGACGCCAACAAGCT (*Nhe*I)
ΔCREB-F_1	GCAACACGCGGCGCCTCCGCCGGCCCATATAAAA
ΔCREB-R_1	GCGGAGGCGCCGCGTGTTGCTCTGTCTGCGCGTT
CCN1-F	TAGAATTCCGCCACCATGAGCTCCCGCATCGC (*Eco*RI)
CCN1-R	CCGCTCGAGGCGTCCCTAAATTTGTGAATGT (*Xho*I)

[a]*Nucleotide 1 represents the site of transcription initiation of the CCN1 promoter.*
[b]*F, forward primer; R, reverse primer.*
[c]*CCN1 promoter gene sequences were downloaded from GenBank.*
[d,e]*Intermediate primer fragment for overlapping PCR overlapping PCR.*

Small Interfering RNAs Knockdown and Transfections

Small interfering RNAs (siRNAs) targeting CCN1 protein and a negative control (siNC) were designed and synthesized by biomics (Biomics, Jiangsu, China). Marc-145 cells were grown in a six-well plate, and the siRNA or siNC was transfected using lipo8000 (Beyotime Biotechnology, Shanghai, China) when density was about 70∼80%. At 48 h post-transfection, cells were infected with PEDV and then collected at different time points by Western blot to evaluate the efficiency of knockdown. The sequences of siCCN1 and siNC are listed in **Table 2**.

One-Step Growth Curve Assay

Marc-145 cells were seeded into six-well plates, and, when the cell density reached 90%, PEDV at MOI of 1 was used to infect cells. The cell supernatant was collected, indicating time to detect $TCID_{50}$.

Quantitative Real-Time PCR

Total mRNA was isolated from Marc-145 cells using TRIzol reagent (Invitrogen, Carlsbad, CA, United States), and 2 μg of total RNA were reverse-transcribed to cDNA using the FastKing RT Kit with gDNase (Tiangen, Beijing, China) according to the manufacturer's protocol. Quantitative real-time PCR (qRT-PCR) was carried out to detect the expression levels of the specific genes. The relative quantities of mRNA were calculated using the $2^{-\Delta\Delta Ct}$ method. The gene-specific primers for qRT-PCR are listed in **Table 3**.

Western Blotting

The treated Marc-145 cells were washed with PBS twice and then treated with RIPA lysate containing protease inhibitor and phenylmethylsulfonyl fluoride. Protein concentrations were determined using the bicinchoninic acid (BCA) protein quantitative kit (Pierce, Rockford, IL, United States). Equivalent amounts of protein samples were separated by sulfate–polyacrylamide gel electrophoresis and transferred onto polyvinylidene difluoride membranes (Millipore Corp, Atlanta, GA, United States). The membranes were blocked for 1 h in 5%

TABLE 2 | Sequences of siRNAs used in this study.

Primer name[a]	Sequence (5′-3′)
siCCN1-1-F	GGCAGACCCUGUGAAUAUADTDT
siCCN1-1-R	UAUAUUCACAGGGUCUGCCDTDT
siCCN1-2-F	GGGAAAGUUUCCAGCCCAADTDT
siCCN1-2-R	UUGGGCUGGAAACUUUCCCDTDT
siCCN1-3-F	CCCGAAUCAGUUAGGUUUADTDT
siCCN1-3-R	UAAACCUAACUGAUUCGGGDTDT
siNC-F	UUCUCCGAACGUGUCACGUTT
siNC-R	ACGUGACACGUUCGGAGAATT

[a]*F, forward primer; R, reverse primer.*

TABLE 3 | List of primers for qRT-PCR.

Primer[a]	Sequence (5′-3′)[b]
PEDV (N)-F	AGATCGCCAGTTTAGCACCA
PEDV (N)-R	GGCAAACCCACATCATCGT
CCN1-F	ACGAGGATAGTGTCAAGGACC
CCN1-R	CAGGGAGCCGCTTCAGT
c-Jun-F	CAGACAGTGCCCGAGATG
c-Jun-R	CCTCATGCGCTTCCTCT
c-Fos-F	TGTGCAACCCACCCTCA
c-Fos-R	CCACTGCTGTAGCCACTCAT
IFN-β-F	ACGGCTCTTTCCATGAGCTAC
IFN-β-R	GTCAATGCAGCGTCCTCCTT
TNF-α-F	TCTGTCTGCTGCACTTTGGAGTGA
TNF-α-R	TTGAGGGTTTGCTACAACATGGGC
IL-6-F	TTACTACAGTGGCAACGAGGATG
IL-6-R	GGAATCAAGGTGCTCAGGTCAT
IL-8-F	GGAACCATCTCGCTCTGTGTAA
IL-8-R	GGTCCACTCTCAATCACTCTCAG
ISG15-F	CACCGTGTTCATGAATCTGC
ISG15-R	CTTTATTTCCGGCCCTTGAT
β-actin-F	CTTAGTTGCGTTACACCCTTTC
β-actin-R	TGTCACCTTCACCGTTCCA

[a] *F, forward primer; R, reverse primer.*
[b] *Monkey gene sequences and PEDV gene sequences were downloaded from GenBank.*

non-fat dry milk or bovine serum albumin at room temperature and incubated overnight at 4°C with the indicated primary antibody. After sufficient washing with PBST, membranes were incubated with appropriate horseradish peroxidase (HRP)-conjugated secondary antibodies at room temperature for 1 h and then subjected to washing. Protein bands were visualized using an ECL reagent (DiNing, Beijing, China).

Dual-Luciferase Reporter Assays

The Marc-145 cells were seeded in a 12-well dish. The following day, cells were transfected with the constructed plasmids (pRL-TK, pGL-4.10-basic, pGL-4.10-CCN1 promoter, and pGL-4.10-CCN1 mutant promoter) using Lipofectamine 8000 (Beyotime Biotechnology, Shanghai, China) according to the manufacturer's protocol. At 24 h post-transfection, cells were treated with or without PEDV at MOI of 1 for 48 h. The cells were harvested and lysed and then analyzed by a dual-luciferase reporter assay kit (Promega, Beijing, China) according to the manufacturer's instructions.

Flow Cytometry

Marc-145 cells were growing at a density of $10^5 \sim 10^6$ cells per well in a six-well plate. The next day, cells were transfected with CCN1 overexpression plasmid or CCN1 interference RNA. At 48 h post-transfection, cells were infected and incubated with PEDV for 24 h. After 24 h, cells were harvested and stained using annexin V/fluorescein isothiocyanate (FITC) apoptosis detection kit (BioVision, Inc., Milpitas, CA, United States) and analyzed by flow cytometry (Becton Dickinson, New York, NY, United States).

Cell Viability Assay

Marc-145 cells were seeded into 96-well plate and added different concentration of signal pathway inhibitor when density was about 90%. Cells were incubated at 37°C for 48 h, and then, 20 μl of 3-(4,5-Dimethylthiazol-2-yl)-2,5-diphenyltetrazolium bromide (MTT) labeling reagent was added to each well and addition incubated for 4 h. After adding 150 μl of solubilizing solution, the absorbance at 550 nm using an enzyme-linked immunosorbent assay reader was measured.

Statistical Analysis

All experiments were performed with at least three independent experiments, group data were presented as means ± SD and were assessed using one-way ANOVA. For each assay, Student's *t*-tests were used to assess differences in GraphPad Prism software. Significance difference was denoted in the figures as follows: $^{*}p \leq 0.05$, $^{**}P \leq 0.01$, and $^{***}p \leq 0.001$.

RESULTS

The Replication of Porcine Epidemic Diarrhea Virus in Marc-145 Cells

To determine the propagation kinetics of PEDV in Marc-145 cells, the mRNA levels and $TCID_{50}$ of PEDV infection at different times were investigated. As shown in **Supplementary Figure 1A**, 24 h after PEDV infection, the N gene increased 300 times compared with the control group. Moreover, the multiplication peak of PEDV appeared at 48 h after infection, and then gradually decreased at 72 h after infection. In addition, the growth-kinetics curve showed that with the increase of infection time, the replication of PEDV was gradually enhanced (**Supplementary Figure 1B**), which was consistent with the results of mRNA. Together, these results indicate that PEDV can infect Marc-145 cells with high efficiency and multiply rapidly.

Porcine Epidemic Diarrhea Virus Infection Promotes Cell Communication Network Factor 1 Expression in Marc-145

Previous studies have determined that CCN1 expression was enhanced when infected with Zika and PRRSV (Park and Chun, 2020; Sun et al., 2020). However, there are few study reports concerning PEDV regulating CCN1 expression in Marc-145 cells. To determine whether the expression of CCN1 was influenced by PEDV, Marc-145 was infected with PEDV and harvested at different times after infection. Then, qRT-PCR and Western blot were used to analyze the expression levels of CCN1 mRNA and protein. The results showed that CCN1 mRNA was elevated gradually at 36 and 48 h after infection (**Figure 1A**); CCN1 protein expression was also increased significantly at 36 and 48 h after PEDV infection (**Figures 1B,C**). Then, the dose dependency of the expression of CCN1 on PEDV was verified. Marc-145 was infected with PEDV at MOIs of 0.1, 1, or 3. The data indicate that the elevation of CCN1 mRNA (**Figure 1D**) and protein (**Figures 1E,F**) by PEDV was in a dose-dependent manner. In addition, we confirm the results in other PEDV-susceptible

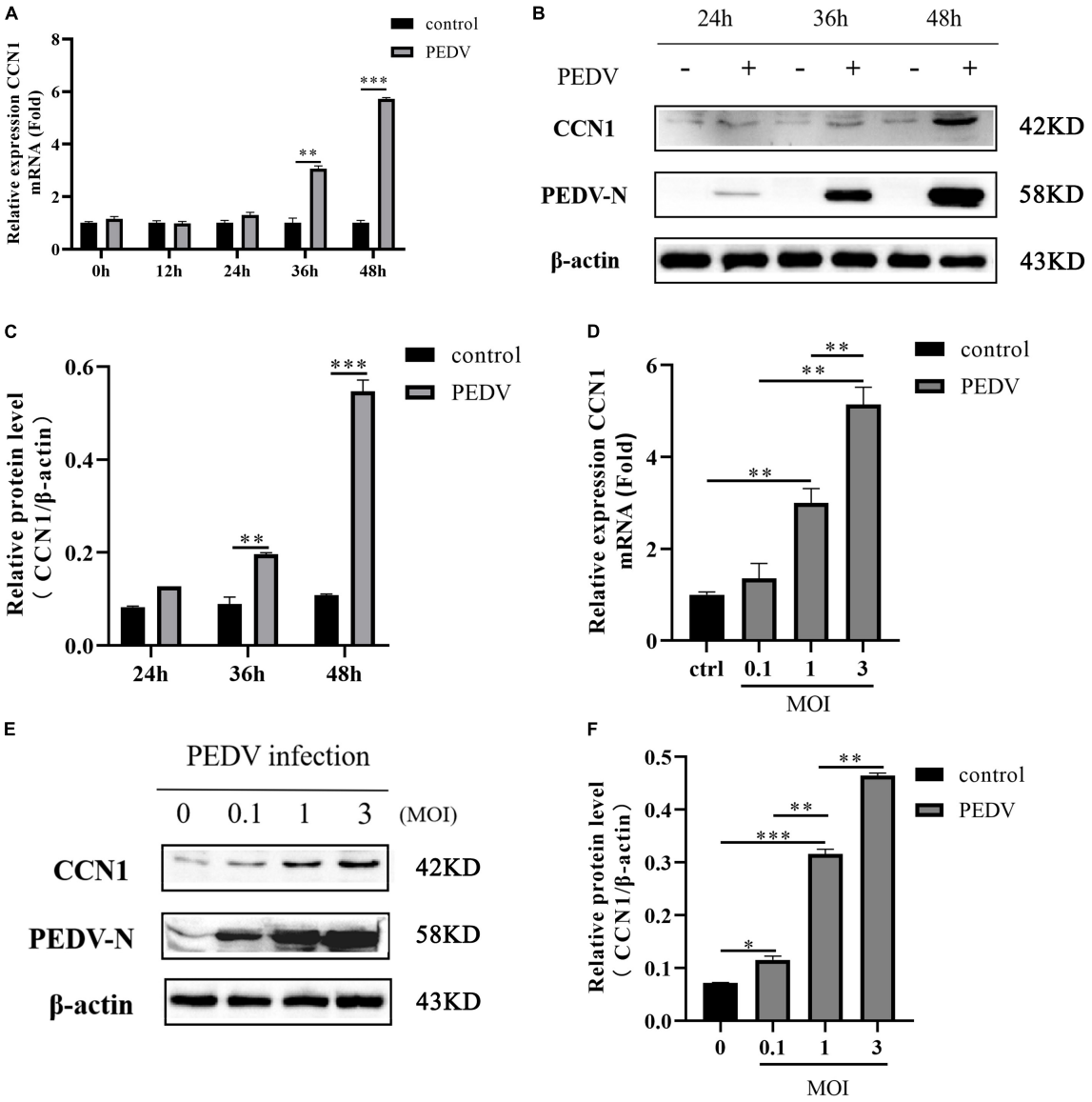

FIGURE 1 | Porcine epidemic diarrhea virus infection induces CCN1 expression in Marc-145 cells. **(A,B)** Marc-145 cells were incubated with PEDV at MOI of 1, and then, the cell was harvested at indicated time point post-infection. Quantitative real-time PCR was used to detect CCN1 expression **(A)** and Western blotting was used to analyze CCN1 protein levels **(B)**. **(C)** Densitometric analysis of CCN1 relative to β-actin using ImageJ. **(D,E)** Marc-145 was infected with PEDV at MOIs of 0.1, 1, and 3 for 48 h, and the cells were collected to analyze CCN1 mRNA levels using real-time PCR **(D)** and CCN1 protein levels by Western blotting **(E)**. **(F)** Densitometric analysis of CCN1 relative to β-actin using ImageJ. The data were performed from three independent experiments. The differences were evaluated using Student's *t*-test, and significance differences were denoted by $*p < 0.05$, $**p < 0.01$, and $***p < 0.001$.

cell lines. We performed similar experiments using Vero cells. The mRNA and protein levels were detected similar results in PEDV-infected Vero cells (**Supplementary Figure 2**). These results suggested that PEDV upregulated the expression of CCN1 at the transcriptional levels and protein levels.

Exploring the Potential Transcription Factor Binding Sequence for the Activation of Cell Communication Network Factor 1 Promoter Activity

To further decipher the transcriptional regulation mechanism of PEDV-induced CCN1 production, the 5′ flanking 2,197-bp regions of the CCN1 gene were cloned. Using bioinformatics approach (Promoter 2.0 and ALGGEN prediction programs) analysis shows that several underlying transcriptional regulatory elements, including CArG (−1,937∼−1,946), OCT (−1,634∼−1,644), and SP1 (−1,211∼−1,221; −273∼−283), AP-1 (−811∼−823), and CREB (−40∼−51), were identified in the CCN1 promoter. To assess the CCN1 promoter activity and find the regions of the CCN1 promoter that respond to PEDV stimulation, a series of CCN1 promoter 5′ flanking region truncation sequences were constructed, cloned, and inserted into a pGL4.10-basic reporter vector (**Figure 2A**). Marc-145 cells were transfected with 1 μg of a variety of constructed plasmid and 0.2 μg of pRL-TK plasmid for 24 h, and then,

the cell was infected with or without the PEDV. Luciferase assay showed that all truncated sequences had higher luciferase activities with or without PEDV stimulation compared to the pGL-4.10 basic, except the construct −24/203-luc (**Figure 2B**). This result indicated that all the constructs have promoter activity, among the –985/203-luc mutants exhibited about 1.5-fold upregulation after PEDV infection. However, the –24/203-luc mutants had no significant difference after PEDV stimulation. Therefore, the –985/203 region of the CCN1 promoter may contain transcription factor binding sites in response to PEDV infection.

AP-1 and CREB Is Essential for Porcine Epidemic Diarrhea Virus to Activate the Cell Communication Network Factor 1 Promoter

Three transcription factor binding sites were found in the −985 to 203 regions of the CCN1 promoter: AP-1 binding site (−811∼−823), Sp1 binding site (−1,211∼−1221), and CREB binding site (−40∼−51). To identify specific transcription factors in the CCN1 promoter, which respond to PEDV infection, three deletion mutants of transcription factor binding sites were constructed (**Figure 3A**). Then, luciferase analysis was used to detect the activity of the mutated CCN1 promoter. The result showed that the deletion of AP-1 and CREB binding sites dramatically impaired the activity of the CCN1 promoter (**Figure 3B**). Moreover, the effect of the CREB binding site is relatively more significant. To further prove that AP-1 and CREB binding sites mediate transcription induction of the CCN1 promoter, SR11302 (AP-1 inhibitor) or EML-425 (CREB inhibitor) was used to block the activity of AP-1 or CREB. The cytotoxicity of different concentration inhibitors was detected by a cell viability assay (**Supplementary Figures 3A,B**). The obtained results are consistent with the analysis of Luciferase report. EML-425 notably inhibited PEDV-induced CCN1 mRNA (**Figure 3C**) and protein (**Figures 3D,E**) expression in a dose-dependent manner. However, the difference of CCN1 mRNA expression was exhibited when the concentration of SR11032 was 5 and 10 μM (**Figure 3F**), and CCN1 protein levels were suppressed significantly with 10 μM SR11302 treatment (**Figures 3G,H**).

To determine whether AP-1 and CREB pathways were activated by PEDV, the phosphorylation levels of AP-1 and CREB were detected. Western blot analysis suggested that the level of CREB phosphorylation was elevated with the increase of infection time (**Figures 3I,J**). AP-1 is a dimeric complex, which consists of c-Jun and c-Fos. By detecting the transcription expression of c-Jun and c-Fos, it was determined that the mRNA levels of c-Jun and c-Fos increased significantly after PEDV infection (**Figure 3K**), and then, we detect the level of c-Jun and c-Fos protein. As shown in **Figures 3L,M**, PEDV infection promoted the expression of c-Jun phosphorylation, and there was a slight increase compared with a mock group at 24 and 36 h post-infection. The level of c-Fos phosphorylation is elevated significantly after PEDV infection (**Figures 3N,O**). Together, all data demonstrated that PEDV infection promotes the expression of CCN1 through AP-1 and CREB binding elements.

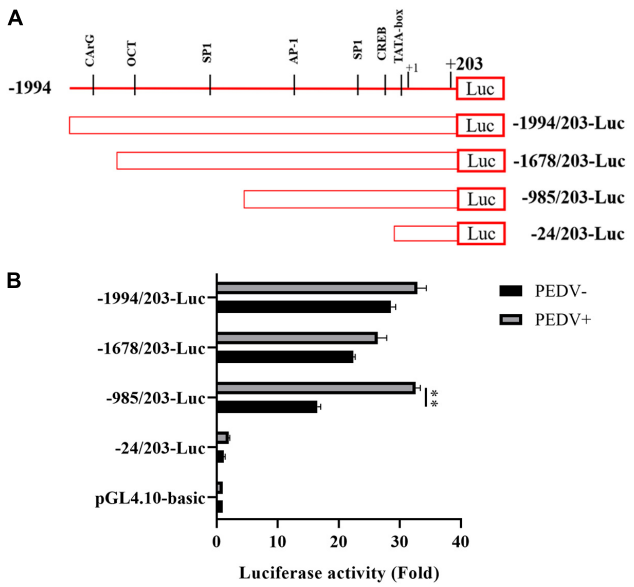

FIGURE 2 | Cell communication network factor 1 promoter sequences were cloned, analyzed, and mapped latent PEDV-responsive regulatory elements. **(A)** Schematic representation of the CCN1 promoter and CCN1 promoter truncated mutants were inserted into pGL4.10-basic vectors, and the constructed vectors were denoted as -1994/203-Luc, -1678/203-Luc, -985/203-Luc, and -24/203-Luc. **(B)** Marc-145 cells were respectively transfected with a variety of constructed plasmid for 24 h and incubated with PEDV. At 48 h post-infection, cells were collected and detected the luciferase activity. The data were performed from three independent experiments. (PEDV−, mock infection group; PEDV+, PEDV infection group). The differences were evaluated using Student's *t*-test, and significance differences were denoted by $^{**}p < 0.01$.

PKA and p38 Signaling Pathways Are Involved in Porcine Epidemic Diarrhea Virus-Induced Cell Communication Network Factor 1 Expression

To dissert the upstream signal molecules that PEDV regulates the expression of CCN1, Marc-145 using inhibitors of the signaling pathways, including PKA, p38, JNK, ERK1/2, were incubated for 1 h and then infected with PEDV. At 48 h post-infection, CCN1 expression was analyzed by RT-PCR. As shown in **Figure 4A**, PEDV-induced CCN1 expression was decreased significantly by the addition of SB203580 (p38 inhibitor) and H-89 (PKA inhibitor), whereas the SP600125 (JNK inhibitor) and PD98059 (ERK1/2 inhibitor) did not affect PEDV-induced CCN1 expression. To further confirm the above results, different concentrations of inhibitors were added to Marc-145 before infecting with PEDV for 48 h. The H-89 (PKA inhibitor) and SB203580 (p38 inhibitor) significantly inhibited the production of CCN1 mRNA induced by PEDV (**Figures 4B,C**). These data suggest that the activation of CCN1 is mediated by PKA and p38 pathways. The concentration of different pathways inhibitors did not affect cell viability (**Supplementary Figure 3C**).

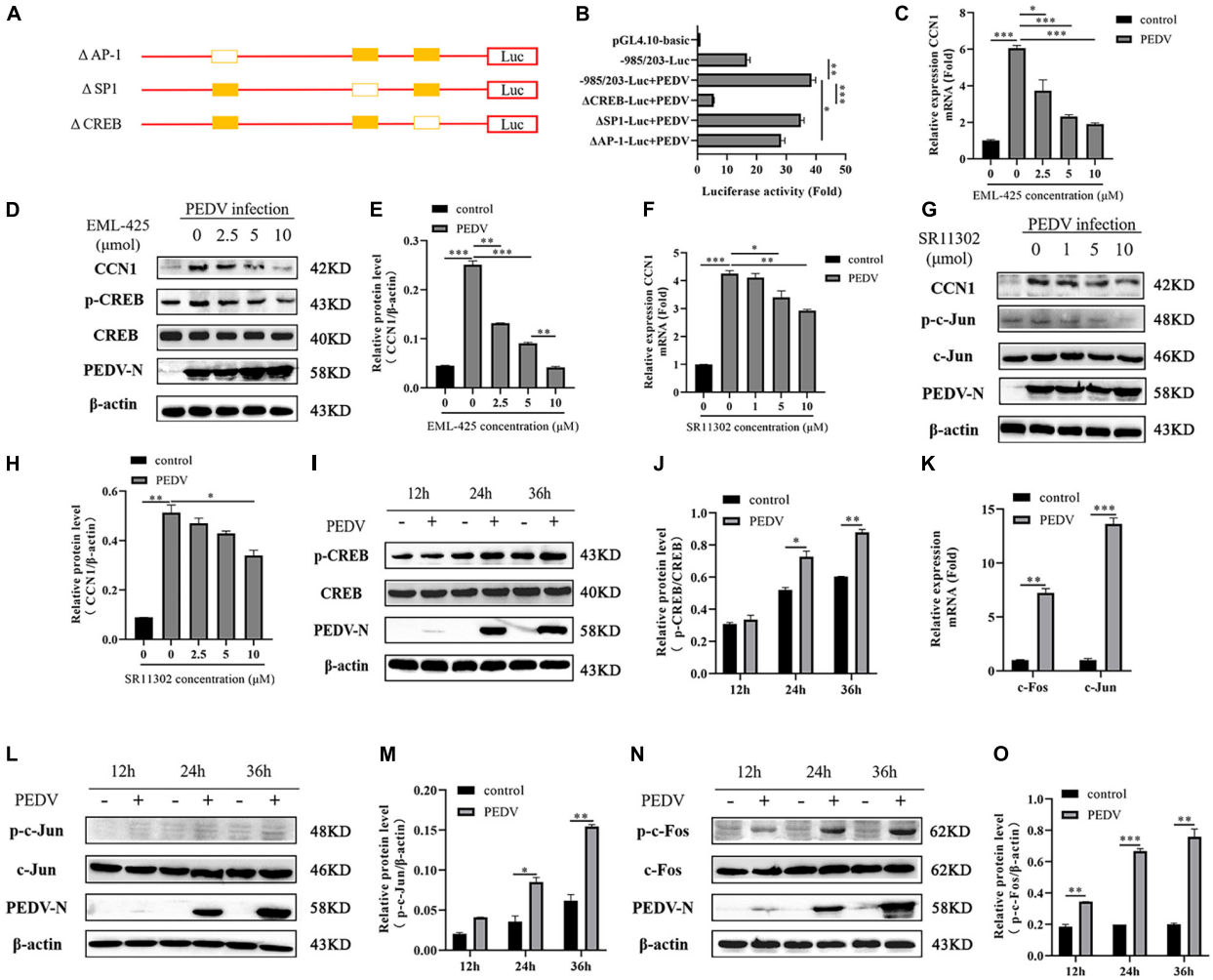

FIGURE 3 | The CREB binding site and AP-1 binding site are indispensable for CCN1 production. **(A)** Schematic diagram represents the –985/203-luc CCN1 promoter deletion mutant vectors. **(B)** The –985/203-luc CCN1 promoter and variety of deletion mutant were transfected into Marc-145 cells for 24 h. The cells were infected with PEDV for 48 h determining the luciferase activity. **(C,D)** Marc-145 cells were treatment using EML-425 (CREB inhibitor) with different concentrations at 1 h and then using PEDV incubated for 48 h. Real-time PCR was used to analyze CCN1 levels **(C)**, and Western blotting was used to analyze the protein expression of CCN1 **(D)**. **(E)** Densitometric analysis of CCN1 relative to β-actin using ImageJ. **(F,G)** Marc-145 cells were treatment using SR11302 (AP-1 inhibitor) at 1 h and then using PEDV incubated for 48 h. Real-time PCR was used to analyze CCN1 levels **(F)**, and Western blotting was used to analyze the protein expression of CCN1 **(G)**. **(H)** Densitometric analysis of CCN1 relative to β-actin using ImageJ. **(I)** Marc-145 cells were incubated with PEDV, and cells were collected at 12, 24, and 36 h. Western blotting was used to examine the level of CREB and phospho-CREB. **(J)** Densitometric analysis of phospho-CREB relative to CREB using ImageJ. **(K)** Marc-145 cells were infected with PEDV, cells were harvested at 48 h, and the mRNA level of c-Jun and c-Fos were analyzed using real-time PCR. **(L)** Marc-145 cells were infected with PEDV, and cells were harvested at 12, 24, and 36 h. Western blotting was used to examine the level of c-Jun and phospho-c-Jun. **(M)** Densitometric analysis of phospho-c-Jun relative to β-actin using ImageJ. **(N)** Marc-145 cells were infected with PEDV, and cells were harvested at 12, 24, and 36 h. Western blotting was used to examine the level of c-Fos and phospho-c-Fos. **(O)** Densitometric analysis of phospho-c-Fos relative to β-actin using ImageJ. The data were performed from three independent experiments. The differences were evaluated using Student's *t*-test, and significance differences were denoted by $^{*}p < 0.05$, $^{**}p < 0.01$, $^{***}p < 0.001$.

Next, the correlation between PKA, p38, and CREB, AP-1 was investigated during PEDV infection. Marc-145 cells were treated with H-89 (PKA inhibitor) and SB203580 (p38 inhibitor) at different concentrations for 1 h before PEDV infection. At 48 h post-infection, cells were harvested to assess the level of CCN1, phospho-CREB, phospho-c-Jun, and phospho-c-Fos using Western blotting. The results showed that H-89 (PKA inhibitor) dramatically impaired PEDV-induced CREB phosphorylation levels in a dose-dependent manner (**Figures 4D,E**), and the expression of CCN1 protein was also suppressed with the increase of the concentration of H-89 (**Figures 4F,G**). The addition of SB203580 (p38 inhibitor) significantly inhibited the c-Jun and c-Fos phosphorylation levels (**Figures 4H–K**). Moreover, CCN1 protein production is also decreased significantly when using the treatment of SB203580 (**Figures 4L,M**). Together, these observations indicate that p38 and PKA signaling pathways are involved in PEDV-mediated induction of CCN1.

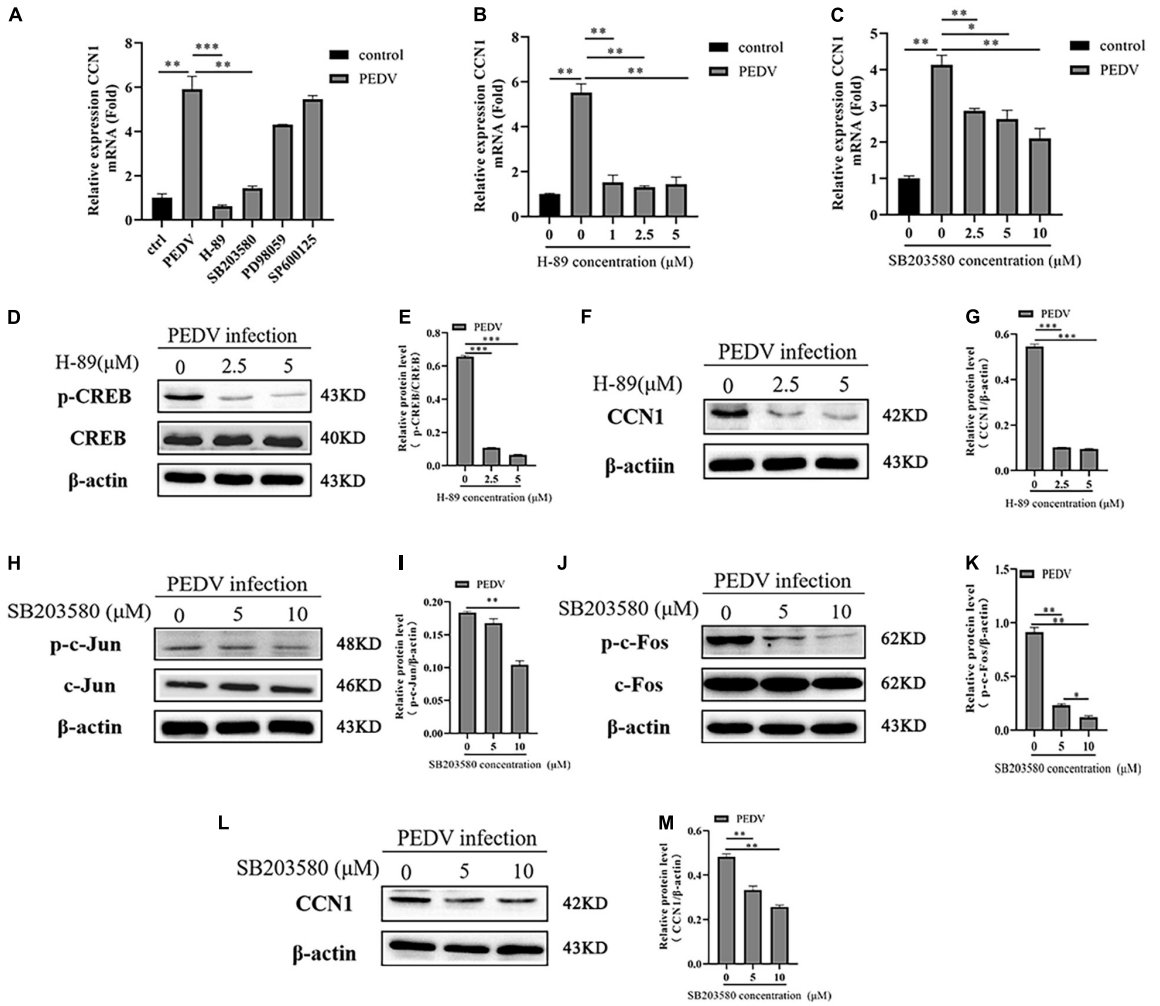

FIGURE 4 | The PKA and P38 pathways are involved in PEDV-mediated the expression of CCN1. **(A)** Marc-145 cells were pretreated using H-89, SB203580, PD98059, and SP600125 for 1 h then infected with PEDV for 48 h, real-time PCR analyzed the mRNA expression of CCN1. **(B)** Marc-145 cells were pretreated using H-89 at doses of 1, 2.5, and 5 for 1 h and then infected with PEDV 48 h; real-time PCR analyzed the mRNA expression of CCN1. **(C)** Marc-145 cells were pretreated using SB203580 at doses of 2.5, 5, and 10 for 1 h and then infected with PEDV for 48 h; real-time PCR analyzed the mRNA expression of CCN1. **(D)** Marc-145 cells were pretreated using H-89 at doses of 0, 2.5, and 5 for 1 h and then infected with PEDV for 48 h; Western blotting assessed the expression level of CREB and phospho-CREB. **(E)** Densitometric analysis of phospho-CREB relative to CREB using ImageJ. **(F)** Marc-145 cells were pretreated using H-89 at doses of 0, 2.5, and 5 μM for 1 h and then infected with PEDV for 48 h; Western blotting assessed the expression level of CCN1. **(G)** Densitometric analysis of CCN1 relative to β-actin using ImageJ. **(H)** Marc-145 cells were pretreated using SB203580 at doses of 0, 5, and 10 μM for 1 h and then infected with PEDV for 48 h; Western blotting assessed the level of c-Jun and phospho-c-Jun. **(I)** Densitometric analysis of phospho-c-Jun relative to β-actin using ImageJ. **(J)** Marc-145 cells were pretreated using SB203580 at doses of 0, 5, and 10 μM for 1 h and then infected with PEDV for 48 h; Western blotting assessed the level of c-Fos and phospho-c-Fos. **(K)** Densitometric analysis of phospho-c-Fos relative to β-actin using ImageJ. **(L)** Marc-145 cells were pretreated using SB203580 at doses of 0, 5, and 10 μM for 1 h and then infected with PEDV for 48 h; Western blotting assessed the level of CCN1. **(M)** Densitometric analysis of CCN1 relative to β-actin using ImageJ. The data were performed from three independent experiments. The differences were evaluated using Student's *t*-test, and significance differences were denoted by $^{*}p < 0.05$, $^{**}p < 0.01$, and $^{***}p < 0.001$.

Effect of Cell Communication Network Factor 1 on Porcine Epidemic Diarrhea Virus Replication

The effect of CCN1 on the virus has rarely been reported. Because PEDV induces significant expression of CCN1 mRNA and protein in Marc-145, we hypothesized that CCN1 might play a crucial role in PEDV replication. To verify the above hypothesis, the pcDNA3.1-his and pcDNA3.1-CCN1-his were transfected, respectively, into Marc-145 and infected with PEDV. As presented in **Figure 5A**, CCN1 can be expressed effectively in Marc-145 cells. As expected, the results showed that compared with the empty vector group, the overexpression of CCN1 significantly downregulated the level of PEDV-N mRNA (**Figure 5B**). In particular, the expression of PEDV-N protein was significantly reduced at 24 h (**Figures 5C,D**). The virus titers were measured by collecting cell supernatants. The data show that it is

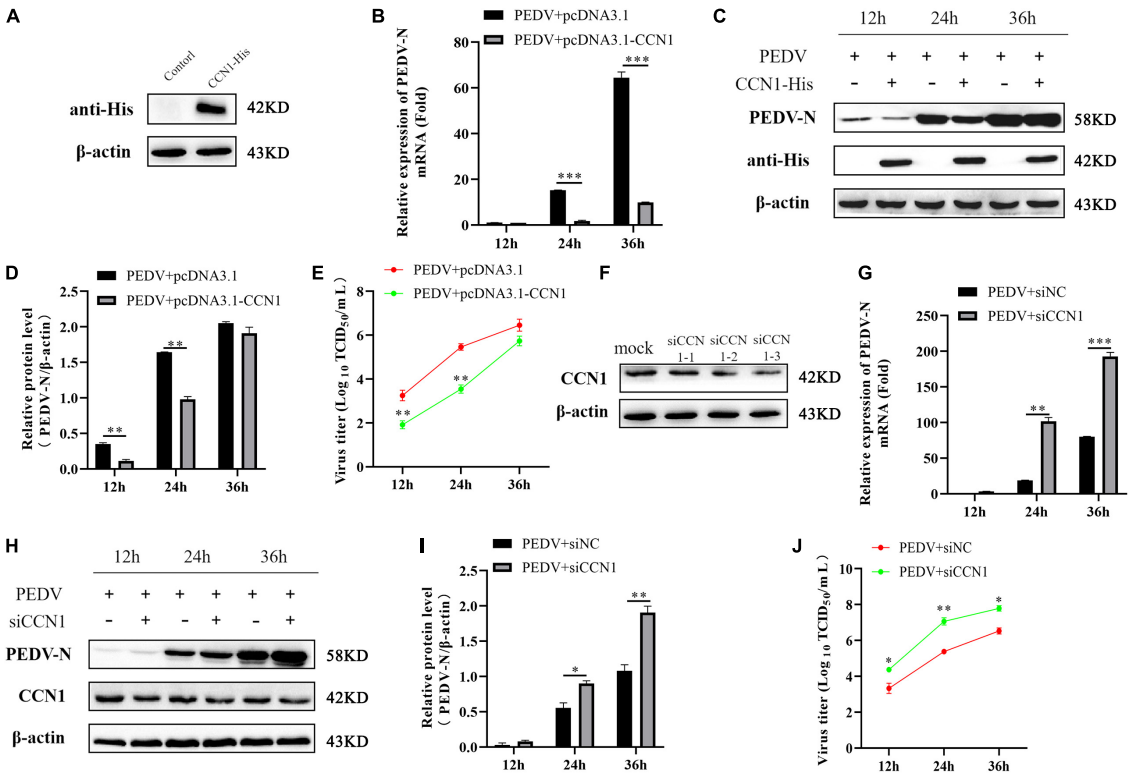

FIGURE 5 | The CCN1 protein to the effect of PEDV replication. **(A)** Marc-145 cells were transfected with pcDNA3.1-CCN1-his or pcDNA3.1-his vector for 36 h. Western blot detected CCN1 expression efficiency. **(B–D)** Marc-145 cells were transfected with pcDNA3.1-CCN1-his or pcDNA3.1-his vector for 36 h. PEDV at MOI 1 was used to infect cell for 1 h. Then, cells and supernatant were harvested to evaluate the mRNA and protein expression level of PEDV-N by real-time PCR **(B)**, Western blot **(C)**, and densitometric analysis **(D)**. **(E)** The supernatant was harvested to assess viral title by $TCID_{50}$. **(F)** Marc-145 cells were transfected with three siRNA for 48 h, and CCN1 knockdown efficiency was assessed. **(G–J)** Marc-145 cells were transfected with siNC or siCCN1 for 48 h, and cells were incubated with PEDV at MOI 1 for 1 h. Then, using real-time PCR and Western blot, respectively, detected PEDV-N mRNA **(G)**, protein expression **(H)**, and densitometric analysis **(I)**. $TCID_{50}$ was used to examine viral title **(J)**. The data were performed from three independent experiments. The data were performed from three independent experiments. The differences were evaluated using Student's *t*-test, and significance differences were denoted by $^{*}p < 0.05$, $^{**}p < 0.01$, and $^{***}p < 0.001$.

consistent with the results of the mRNA and protein (**Figure 5E**). To further verify the relevance of CCN1 in PEDV proliferation, we generated three special siRNAs targeting CCN1. Western blot was performed to assess the interfere efficiency of CCN1 in Marc-145. As presented in **Figure 5F**, siCCN1-3 exhibited a more obvious knockdown efficiency than siCCN1-1 and siCCN1-2. The following experiments were carried out with siCCN1-3. The results showed that CCN1 interference facilitates the expression of PEDV-N mRNA and protein (**Figures 5G–I**) and increased virus titer (**Figure 5J**). Together, the overexpression of CCN1 inhibited the replication of PEDV, whereas interference of CCN1 facilitated the replication of PEDV.

The Effect of Cell Communication Network Factor 1 in Suppressing Porcine Epidemic Diarrhea Virus Does Not Depend on the Expression of Interferon

The above study found that CCN1 overexpression decreases PEDV replication. To study whether CCN1 exerts antiviral function on Marc-145 cells by producing inflammatory cytokines and type I interferon. The CCN1 overexpression plasmids were transfected into Marc-145 cells. The data showed that overexpression of CCN1 promotes PEDV-induced IL-6 (**Figure 6D**) and IL-8 (**Figure 6E**) mRNA levels, whereas did not affect the mRNA expression of ISG15 ubiquitin-like modifier (ISG15) (**Figure 6A**), interferon β (IFN-β) (**Figure 6B**), and tumor necrosis factor α (TNF-α) (**Figure 6C**). It is widely known that IFN-β has a direct antiviral function, but CCN1 has not changed the expression of IFN-β, suggesting that CCN1 suppresses the replication of PEDV maybe through other pathways. Together, the results indicated that the effect of CCN1 in suppressing PEDV does not depend on the expression of interferon.

Cell Communication Network Factor 1 Regulates Porcine Epidemic Diarrhea Virus-Induced Apoptosis

It has previously been reported that CCN1 through (TNF)-related apoptosis-inducing ligand (TRAIL) induces EAC cell apoptosis (Dang and Chai, 2020). To study whether CCN1 is involved in PEDV-induced apoptosis, CCN1 overexpression plasmids and siCCN1 were transfected in Marc-145. At 24 h post-transfection, cells were infected with PEDV and the apoptosis of Marc-145 cells was evaluated by flow cytometry.

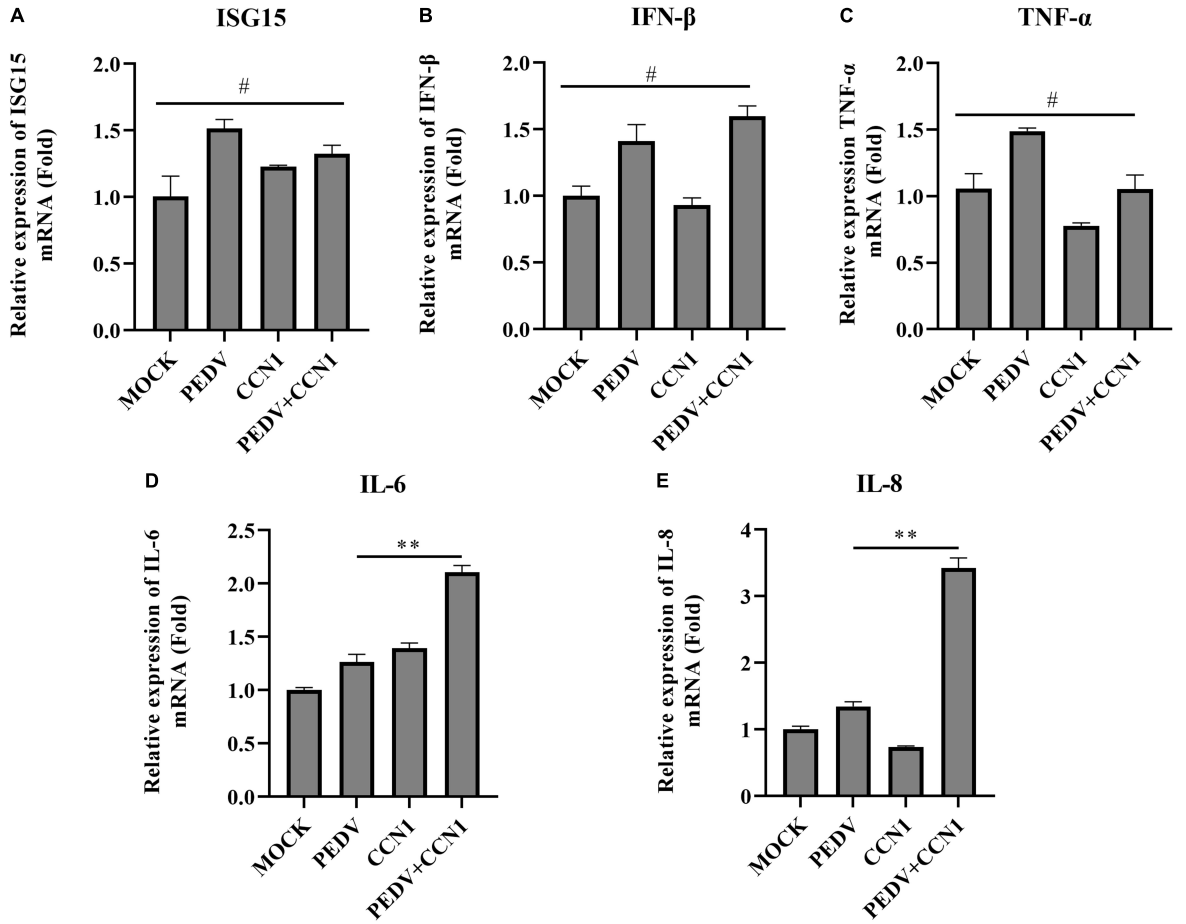

FIGURE 6 | Cell communication network factor 1 has no effect on the expression of interferon. **(A–E)** Marc-145 cells were transfected with pcDNA3.1-CCN1-his or pcDNA3.1-his vector for 36 h and were infected with or without the PEDV strain. At 24 h, cells were collected to analyze the mRNA level of ISG15 **(A)**, IFN-β **(B)**, TNF-α **(C)**, IL-6 **(D)**, and IL-8 **(E)** by real-time PCR assay. The data were performed from three independent experiments. The differences were evaluated using Student's *t*-test, and significance differences were denoted by $^{**}p < 0.01$.

Compared with the empty vector, the apoptotic rate in Marc-145 cells with CCN1 overexpression was notably increased. Moreover, the apoptotic proportion in Marc-145 cells with the CCN1 knockdown vector decreased compared with the negative control cells (**Figure 7A**). To confirm the above results, using Western blot analysis, the cleaved caspase 3 protein levels revealed that, compared with the empty vector group, the cleaved caspase 3 increased in the CCN1 overexpression group (**Figures 7B,C**). Instead, the knockdown of CCN1 attenuated caspase 3 cleavage (**Figures 7D,E**). The results indicate that CCN1 can regulate PEDV-induced apoptosis in Marc-145 cells.

Cell Communication Network Factor 1 Regulated Porcine Epidemic Diarrhea Virus-Induced Apoptosis Through the Mitochondrial Pathway

To gain the specific mechanism of CCN1 involved in the apoptosis induced by PEDV. We measured the protein-related death receptor pathway (Fas/FasL/caspase 8) and the protein-related of the mitochondrial pathway (Bcl-2/Bax/caspase 9). The result showed that overexpression of CCN1 resulted in anti-apoptotic protein Bcl-2 decreased compared with the empty vector group, and pro-apoptotic protein Bax expresses levels increased (**Figures 8A,B**). Moreover, cleaved caspase 9 increased in the CCN1 overexpression groups (**Figures 8A,C**). However, the death receptor-related proteins Fas, FasL, and caspase 8 have no significant difference in pcDNA3.1-CCN1-his–transfected cells (**Figures 8D,E**). Then, CCN1 knockdown was used to investigate Bax, Bcl-2, and caspase 9. The data showed that knockdown of CCN1 decreased the activation of Bax and caspase 9 and increased the expression of Bcl-2 (**Figures 8F–H**). Further studying whether the CCN1 protein itself can induce cell apoptosis, the results show that, when CCN1 is overexpressed or knocked down, it has no effect on the lysis of caspase 3 and caspase 9, and only under the stimulation of the virus, CCN1 can play a role (**Figures 8I–N**). Together, these results showed that CCN1 regulates PEDV-induced apoptosis by regulating the level of Bcl-2 and Bax to activate caspase 9.

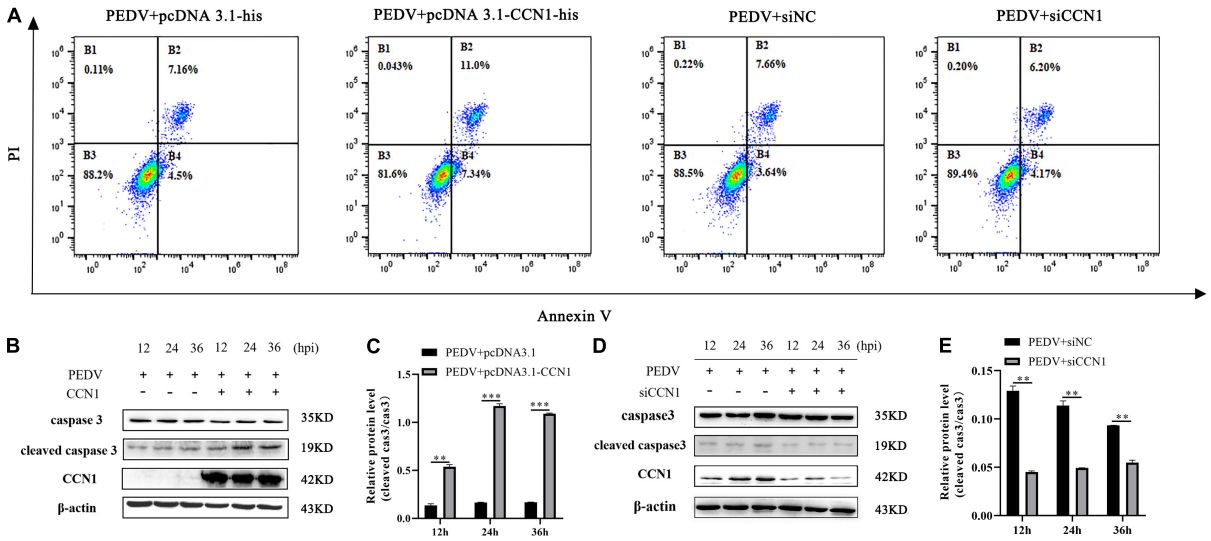

FIGURE 7 | Cell communication network factor 1 regulates PEDV-induced apoptosis in Marc-145 cells. **(A)** Marc-145 cells were transfected with pcDNA3.1-his, pcDNA3.1-CCN1-his, siNC, and siCCN1, stained with annexin V and PI, and apoptosis was detected by flow cytometry. **(B)** Marc-145 cells were transfected with pcDNA3.1-CCN1-his or pcDNA3.1-his vector for 36 h and infected with the PEDV. Cells were harvested at the indicated time, and Western blot was used to assess the expression of the caspase 3 and cleaved caspase 3. **(C)** Densitometric analysis of cleaved caspase 3 relative to caspase 3 using ImageJ. **(D)** Marc-145 cells were transfected with siNC or siCCN1 for 48 h and infected with the PEDV. Cells were harvested at the indicated time, and Western blot was used to assess the expression of the caspase 3 and cleaved caspase 3. **(E)** Densitometric analysis of cleaved caspase 3 relative to caspase 3 using ImageJ. The data were performed from three independent experiments. The differences were evaluated using Student's *t*-test, and significance differences were denoted by $^{**}p < 0.01$, $^{***}p < 0.001$.

Cell Communication Network Factor 1 Regulated Mitochondrial-Mediated Apoptosis Through p53-Dependent Pathway to Inhibit Porcine Epidemic Diarrhea Virus Replication

Tumor suppressor p53 is known to be involved in the regulation of cell senescence and apoptosis (Wawryk-Gawda et al., 2014). Our previous study found that PEDV infection could induce cell apoptosis by activating the p53 signal pathway (Xu et al., 2019). To further determine whether CCN1 has an influence on the p53 pathway, Western blot was used to detect the p53 total protein levels and phosphorylated p53 protein levels. As shown in **Figures 9A,D**, there is no effect on the p53 total protein level of both CCN1 overexpression and CCN1 knockdown. However, the phosphorylated p53 levels had changed significantly. CCN1 overexpression catalyzed phosphorylation of p53 at serine 20 (phospho-p53 ser20) and serine 15 (phospho-p53 ser15) compared to the empty vector group (**Figures 9A–C**). Knockdown of CCN1 suppress phospho-p53(ser15) and phospho-p53(ser20) level (**Figures 9D,E**). These results suggested that there was a close relationship between CCN1 protein and p53 protein phosphorylation.

Next, we used the PFT-α (p53 inhibitor) to further study whether CCN1-mediated apoptosis is through the p53 pathway. The results showed that phosphorylate levels of p53 at ser15, ser20, and ser46 were significantly suppressed by PFT-α (**Figures 9G–I**). Compared with the cell without pretreatment using PFT-α inhibitors, pretreated PFT-α decreases activation of caspase 3 and caspase 9 (**Figures 9K,L**). Besides, the expression of Bax protein was notably inhibited, whereas the expression of Bcl-2 protein was restored (**Figure 9J**). Together, these data indicated that the CCN1-regulated apoptosis mainly depends on the p53 pathway. Moreover, we found that the inhibitory effect of CCN1 on PEDV-N protein expression was weakened by PFT-α. CCN1 can inhibit PEDV replication and can regulate apoptosis through p53 pathway, we hypothesis that the CCN1 suppresses PEDV replication through apoptosis. To prove the relationship, using caspase inhibitor Z-VAD-FMD to inhibit apoptosis, it was found that the inhibitory effect of CCN1 on the PEDV was weakened (**Figures 9M,N**). Therefore, the results showed that CCN1 inhibits PEDV through apoptosis.

DISCUSSION

Porcine epidemic diarrhea virus evolved a variety of strategies to promote its persistent infection in the host cell (Li et al., 2021; Su et al., 2021; Xu et al., 2021). To escape the invasion of the virus, the secretion of antiviral proteins in the host cell was enhanced (Li et al., 2019; Pandey et al., 2019; Wang et al., 2021). CCN1, as a pro-inflammation factor, is regulated by many factors, including cytokines, viruses, and bacteria (Todorovic et al., 2005; Chen and Du, 2007; Kurozumi et al., 2008). It is reported that many viral infections can enhance the expression of CCN1. For example, Zika virus promotes the expression of CCN1 by the CaMKIIα-CREB pathway (Sun et al., 2020). Coxsackieviruses (CVB) and herpes simplex virus-1 (HSV-1) infection increase CCN1 expression in HeLa cell and rat glioma

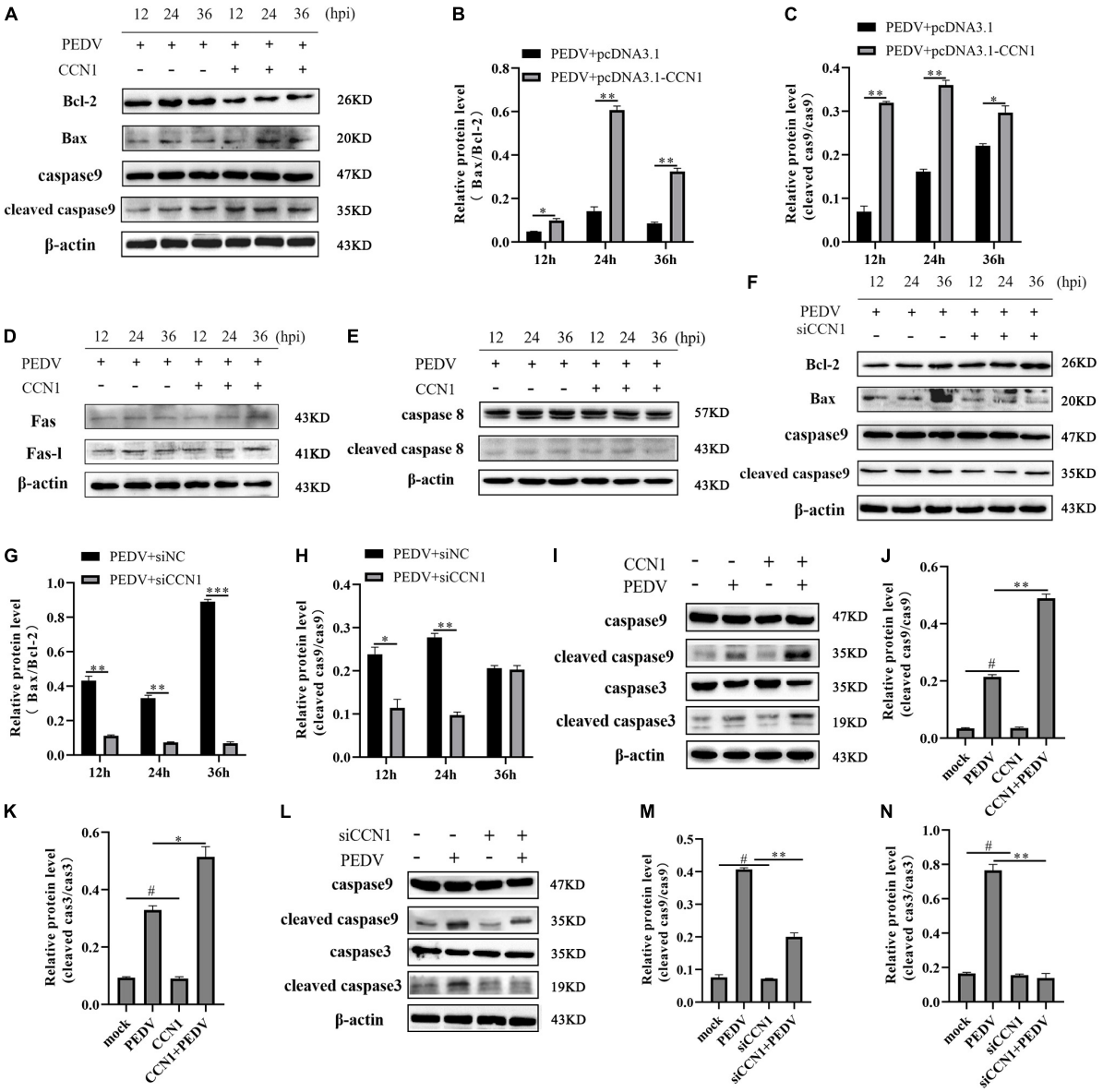

FIGURE 8 | The mitochondrial pathway was involved CCN1 induced apoptosis. **(A–C)** Marc-145 cells were transfected with pcDNA3.1-CCN1-his or pcDNA3.1-his vector for 36 h and infected with the PEDV. Cells were harvested at the indicated time, Western blot was used to assess the expression of the Bcl-2, Bax, caspase 9, and cleaved caspase 9 **(A)**, densitometric analysis of Bax relative to Bcl-2, and cleaved caspase 9 relative to caspase 9 using ImageJ **(B,C)**. Western blot was used to elevate the level of the Fas-L, Fas, caspase 8, and cleaved caspase 8 **(D,E)**. **(F–H)** Marc-145 cells were transfected with siNC or siCCN1 for 48 h and infected with the PEDV. Cells were harvested at the indicated time, Western blot was used to assess the expression of the Bcl-2, Bax, caspase 9, and cleaved caspase 9 **(F)**, densitometric analysis of Bax relative to Bcl-2, and cleaved caspase 9 relative to caspase 9 using ImageJ **(G,H)**. **(I–K)** Marc-145 cells were transfected with pcDNA3.1-CCN1-his or pcDNA3.1-his vector for 36 h and infected with the PEDV. Cells were harvested at 24 h after PEDV infection, Western blot was used to assess the expression of the caspase 9, cleaved caspase 9, caspase 3, and cleaved caspase 3 **(I)**, densitometric analysis of cleaved caspase 9 relative to caspase 9, and cleaved caspase 3 relative to caspase 3 using ImageJ **(J,K)**. **(L–N)** Marc-145 cells were transfected with siNC or siCCN1 for 48 h and infected with the PEDV. Cells were harvested at 24 h after PEDV infection, and Western blot was used to assess the expression of the caspase 9, cleaved caspase 9, caspase 3, and cleaved caspase 3 **(L)**, densitometric analysis of cleaved caspase 9 relative to caspase 9, and cleaved caspase 3 relative to caspase 3 using ImageJ. **(M,N)** The data were performed from three independent experiments. The differences were evaluated using Student's *t*-test, and significance differences were denoted by $^{*}p < 0.05$, $^{**}p < 0.01$, and $^{***}p < 0.001$.

cells (Kim et al., 2004; Kurozumi et al., 2008). In this study, we demonstrated PEDV infection can promote the secretion of CCN1. We speculate that the expression of CCN1 may be related to the proliferation stage of the virus. The virus proliferation curve showed that the logarithmic growth phase of the virus was 36–48 h after infection. The host cell initiates defense by perceiving a large number of replicated viruses and promotes the induction of protein CCN1.

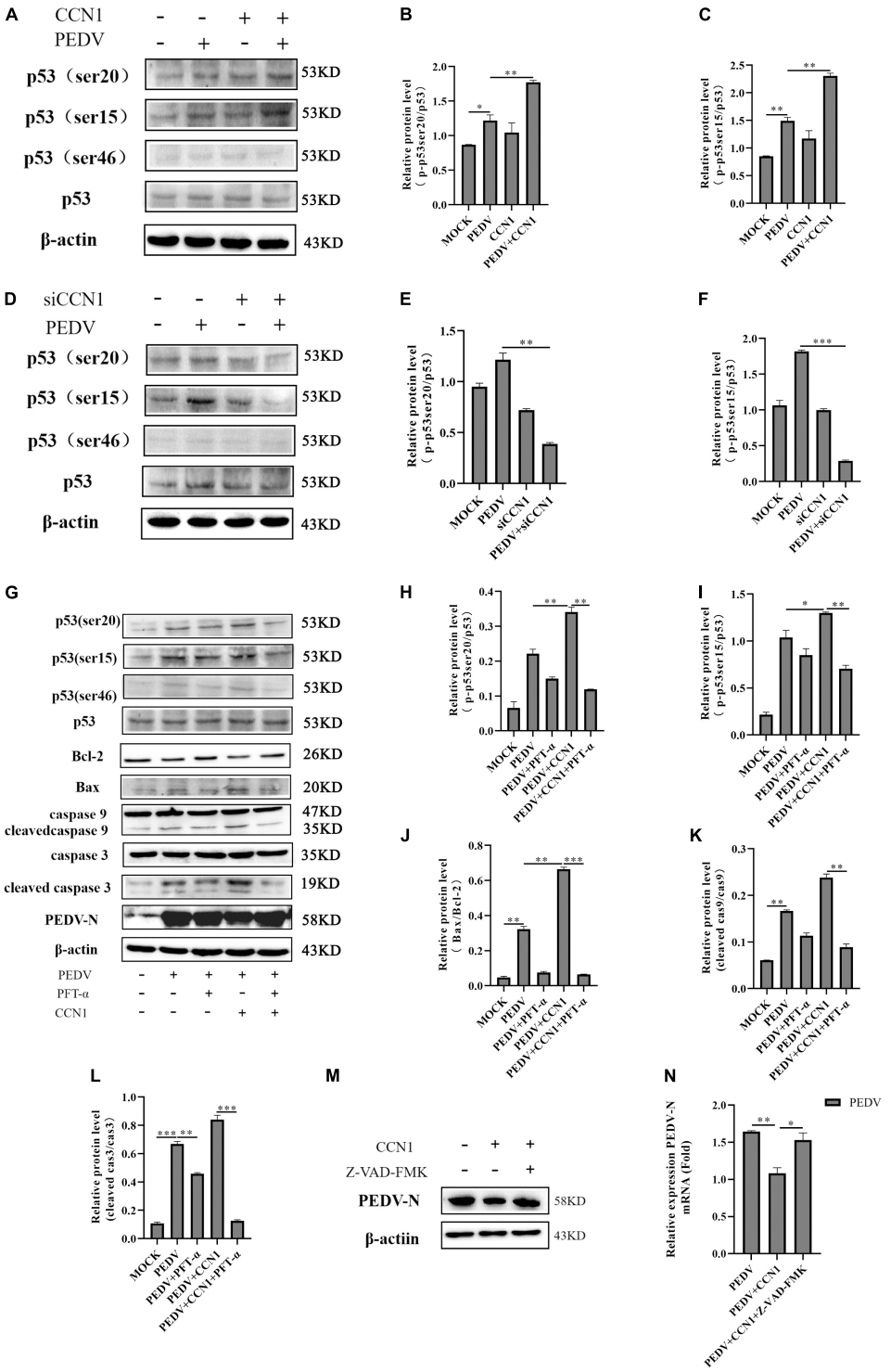

FIGURE 9 | The role of p53 in CCN1-mediated apoptosis. **(A–C)** Marc-145 cells were transfected with pcDNA3.1-CCN1-his or pcDNA3.1-his vector for 36 h and then with or without the PEDV strain to infect cells for 24 h; Western blot was used to detect the abundance of the p53, phospho-p53(ser15), phospho-p53(ser20), and phospho-p53(ser46). **(D–F)** Marc-145 cells were transfected with siNC or siCCN1 for 48 h and then with or without the PEDV strain to infect cells for 24 h; Western blot was used to detect the expression of the p53, phospho-p53(ser15), phospho-p53(ser20), and phospho-p53(ser46). **(G–L)** Marc-145 cells were transfected with pcDNA3.1-CCN1-his or pcDNA3.1-his vector for 36 h, using pretreated PFT-α 1 h before infecting with PEDV; Western blot analyzes caspase 9, cleaved caspase 9, caspase 3, cleaved caspase 3, Bax, Bcl-2, PEDV-N, p53, and phosphorylated p53 expression levels. **(M,N)** Marc-145 cells were transfected with pcDNA3.1-CCN1-his or pcDNA3.1-his vector for 36 h, using pretreated Z-VAD-FMK 1 h before infecting with PEDV; Western blot analyzes PEDV expression levels. The data were performed from three independent experiments. The differences were evaluated using Student's *t*-test, and significance differences were denoted by $^{*}p < 0.05$, $^{**}p < 0.01$, and $^{***}p < 0.001$.

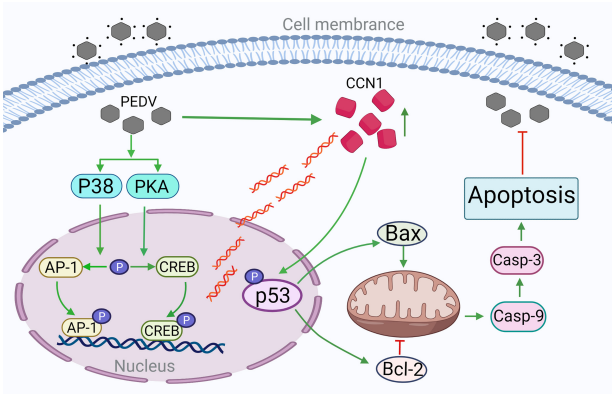

FIGURE 10 | The CREB and AP-1–dependent CCN1 promote PEDV-induced apoptosis through the p53 pathway inhibiting PEDV replication. PEDV infections promote transcription factor CREB and AP-1 phosphorylation, respectively, through PKA and p38 pathways. Phosphorylated CREB and AP-1 binding to CCN1 promoter increase CCN1 expression. CCN1 overexpression increases p53 protein phosphorylation activity. The overexpression of CCN1 promotes Bax expression and inhibits Bcl-2 expression, increases the cleaved of caspase 9 and caspase 3, promotes apoptosis, and inhibits PEDV replication. The addition of p53 inhibitor decreased the occurrence of apoptosis; thus, CCN1 promotes PEDV-induced apoptosis through the p53 pathway. →, activation; ⊥, inhibition.

Cell communication network factor 1 promoter sequences contain a variety of regulatory elements, including CArG, OCT, AP-1, CREB, and SP1 (Kim et al., 2003; Qin et al., 2014; Seefried et al., 2017). Phosphorylated CREB can directly bind to the CCN1 promoters to enhance CCN1 transcriptional expression (Dou et al., 2017). EGF stimulation enhances CREB phosphorylation and activates the expression of CCN1 promoter (Chin et al., 2016). Nuclear translocation of myocardial protein-related transcription factor -A (promotes the expression of CCN 1 by binding to CArG box of CCN 1 promoter (Caires et al., 2007). In addition, the deletion of the AP-1 binding site reduces the activity of the CCN1 promoter by 50% (You et al., 2010). In the study, we confirmed that AP-1 and CREB were essential for the induction of CCN1, and the deletion of CREB and AP-1 binding elements decreased the expression of CCN1. According to previous reports, CREB phosphorylation depends on mitogen- and stress-activated kinases1/2, Ca^{2+}–calmodulin-dependent kinase II (CaMKII), and cAMP-dependent protein kinase (PKA) (De Cesare et al., 1999). CaMKII regulates the expression of CCN1 by regulating CREB phosphorylation has been reported (Sun et al., 2020). In $PKA^{-/-}$ cells, CCN1 promoter activity was not detected (Meyuhas et al., 2008). Thus, we explored whether PKA affects CCN1 expression through regulating CREB. We found that the addition of H-89 (PKA inhibitor) can inhibit about 80% of the mRNA expression of CCN1. The mitogen-activated protein kinase (MAPK) pathway–related protein to regulate CCN1 expression has also been studied. For example, CVB3 enhances CCN1 expression through JNK activation (Kim et al., 2004), Beas2B cells were treated by cigarette smoke extract (CSE)-induced JNK and p38 MAPK phosphorylation–induced CCN1 secretion (Moon et al., 2013), and PRRSV infection suppresses CCN1 transcription by blocking the ERK-AP-1 axis (Park and Chun, 2020). Here, our data show that the addition of SB203580 (p38 inhibitor) can suppress about 50% of the mRNA expression of CCN1 when the concentration of SB203580 was 10 μM, indicating that the PKA and p38 pathways are essential for PEDV-induced CCN1 expression.

Previous research shows that CCN1 plays a role in the replication of many viruses. For example, CCN1 could activate type I IFN antiviral defense response in glioblastoma cells, which is conducive to virus clearance (Thorne et al., 2014). However, Zika-induced CCN1 expression can promote virus replication in human astrocytoma cells (CCF-STTG1) cells (Sun et al., 2020). The current study found that the overexpression of CCN1 inhibited PEDV replication and the knockdown of CCN1 enhanced PEDV replication. The previous investigation reported that CCN1 could induce IL-8 (Wu et al., 2017) and CCL20 induction in keratinocytes (Li et al., 2017), and increased IL-6 expression level in 16HBE cells (Shi et al., 2018). Our results showed that the overexpression of CCN1 upregulated the mRNA expression level of IL-6 and IL-8 in Marc-145 cells during PEDV infection, whereas the mRNA level of IFN-β, ISG15, and TNF-α were not affected. In addition, the only overexpression CCN1 protein does not change the expression of the IL-6 and IL-8, indicating that PEDV infection is essential for the production of the IL-6 and IL-8 induced by CCN1. *In vitro*, IFN-β and ISG15 can directly resist viral infections (Zhao et al., 2020; Liu et al., 2021), whereas pro-inflammation cytokines IL-6 and IL-8 may not have antiviral effects on a single cell. However, pro-inflammation cytokines can play phagocytosis by recruiting macrophages and can also promote the secretion of inflammatory factors to resist the invasion of virus *in vivo*. From the above, we know that the antiviral effect induced by CCN1 may be through other means.

Apoptosis, as a physiological defense mechanism, can regulate viral propagation. However, the specific effect of apoptosis on the virus remains controversial. Some studies have shown that virus invades cells by holding the expression of apoptosis-related proteins to inhibit or delay the occurrence of apoptosis, which is beneficial to the reproduction of virus offspring (Umeshappa et al., 2010). Some studies have shown that, in viral infection, host proteins eliminate the infected cells by enhancing apoptosis and blocking the proliferation of the virus in the body (Barber, 2001). Recently, some evidence has demonstrated that extracellular matrix (ECM) is an associated protein involved in the production of cell apoptosis, rather than cell survival (Li et al., 2016). CCN1, as an ECM protein, reduces intrinsic apoptotic pathway and inhibits the expression of survivin promoting EAV cell apoptosis (Dang et al., 2018). The synergistic treatment of CCN1 and FasL induces cardiomyoblast apoptosis by disrupting caspase inhibitor XIAP (Su and Mo, 2014). The overexpression of CCN1 results in cell apoptosis by inducing ER stress in hepatic stellate cells (Borkham-Kamphorst et al., 2016). In the present study, we found that the overexpression of CCN1 enhanced caspase 3 activation, and the knockdown of CCN1 inhibited caspase 3

activation in Marc-145. Caspase 3 is an executive protein between intrinsic and extrinsic pathways apoptotic pathway (Jorgensen et al., 2017). The combination of apoptosis-related ligand FasL, TNF-α, and corresponding receptors initiates activation of extrinsic apoptosis pathways, whereas intrinsic apoptosis is mainly regulated by Bcl-2 family protein (Pan et al., 2018). For example, the IAV NP interacts with the anti-apoptosis protein clusterin (CLU), which inhibits the intrinsic pathway of apoptosis by binding to Bax protein (Tripathi et al., 2013). Our data clearly suggest that CCN1 is involved in the initiation of the intrinsic apoptosis pathway, CCN1 expression was associated with Bcl-2, Bax, and caspase 9 activation, rather than FasL, Fas, and caspase 8.

P53 protein plays an important role in apoptosis. Under normal circumstances, the p53 protein has low secretion and a short half-life. The p53 protein through phosphorylation levels increase to inhibit the ubiquitin degradation of cellular protein and promote the stability of p53 protein, thereby promoting the induction of its downstream factor involved in apoptosis (Moll and Petrenko, 2003). Phosphorylation of p53 protein exerts cell survival and apoptosis functions by regulating Bcl-2 family proteins (Wang et al., 2021). Previous studies have shown that PEDV infection induced the accumulation of reactive oxygen species (ROS) and enhanced the p53(ser20) phosphorylation and subsequently promoted cell apoptosis (Xu et al., 2019). In this study, we found that the CCN1 regulates apoptosis by promoting the phosphorylation level of phospho-p53(ser15) and phospho-p53(ser20). Moreover, the addition of PFT-α (p53 inhibitor) suppresses the Bax, Bcl-2, and cleaved caspase 9 and caspase 3 expression, confirming that the p53 pathway is essential for CCN1-induced apoptosis. In addition, our research found that PFT-α can restore the effect of CCN1 on PEDV, so apoptosis may be the way for CCN1 to inhibit virus replication.

CONCLUSION

Our study revealed the molecular mechanism of the expression of CCN 1 in Marc-145 cells induced by PEDV and further confirmed the mechanism of CCN 1 inducing apoptosis and inhibiting the replication of PEDV. PEDV activates the transcription factors CREB and AP-1 through the PKA and p38 pathways, respectively. The activated CREB and AP-1 combine with the CCN1 promoter element to promote CCN1 expression. Then, we demonstrated that CCN1 can affect the replication of PEDV and increase pro-inflammation of the IL-6 and IL-8, rather than IFN-β, ISG15, and TNF-α. Further studies clarified that CCN1 promotes p53(ser15) and p53(ser20) phosphorylation to regulate apoptosis and inhibit PEDV replication in Marc-145 (**Figure 10**). Given the detriment of PEDV in the pig industry in recent years, the study possibly provides new insights into the pathogenesis mechanism of PEDV and possibly helps the development of therapeutic targets against PEDV infection.

DATA AVAILABILITY STATEMENT

The original contributions presented in the study are included in the article/**Supplementary Material**, further inquiries can be directed to the corresponding author/s.

AUTHOR CONTRIBUTIONS

HZ and YZ performed the majority of the experiments and were involved in preparation of the manuscript. JW and YY participated in the editing of the manuscript. YL and XS participated in the experimental work. QZ and XX conceived the study, participated in its design and coordination, and revised the manuscript. All authors have read and approved the final manuscript.

FUNDING

This work was supported by grants from the agricultural special fund project of Shaanxi Province (No. 2019SJNYZX45) and the innovation project for agrotechnology of Shaanxi Province (No. 2019NY-081), China.

ACKNOWLEDGMENTS

We thank Kangkang Guo for his valuable review and comments on early drafts of this manuscript.

SUPPLEMENTARY MATERIAL

The Supplementary Material for this article can be found online at: https://www.frontiersin.org/articles/10.3389/fmicb.2022.831852/full#supplementary-material

REFERENCES

Barber, G. N. (2001). Host defense, viruses and apoptosis. *Cell Death Differ.* 8, 113–126. doi: 10.1038/sj.cdd.4400823

Borkham-Kamphorst, E., Steffen, B. T., Van de Leur, E., Haas, U., Tihaa, L., Friedman, S. L., et al. (2016). CCN1/CYR61 overexpression in hepatic stellate cells induces ER stress-related apoptosis. *Cell. Signal.* 28, 34–42. doi: 10.1016/j.cellsig.2015.10.013

Caires, K., de Avila, J., and McLean, D. (2007). Vascular endothelial growth factor-A stimulates germ cell differentiation in bovine testis xenografts. *Biol. Reprod.* 77:198.

Chen, Y., and Du, X. Y. (2007). Functional properties and intracellular signaling of CCN1/Cyr61. *J. Cell Biochem.* 100, 1337–1345. doi: 10.1002/jcb.21194

Chin, L. H., Hsu, S. P., Zhong, W. B., and Liang, Y. C. (2016). Involvement of cysteine-rich protein 61 in the epidermal growth factor-induced migration of human anaplastic thyroid cancer cells. *Mol. Carcinog.* 55, 622–632. doi: 10.1002/mc.22308

Cochrane, R. A., Dritz, S. S., Woodworth, J. C., Stark, C. R., Saensukjaroenphon, M., Gebhardt, J. T., et al. (2020). Assessing the effects of medium-chain fatty acids and fat sources on PEDV infectivity. *Transl. Anim. Sci.* 4:txz179. doi: 10.1093/tas/txz179

Dang, T., and Chai, J. (2020). Molecular dynamics in esophageal adenocarcinoma: who's in control? *Curr. Cancer Drug Targets* 20, 789–801. doi: 10.2174/1568009620666200720011341

Dang, T., Modak, C., Meng, X., Wu, J., Narvaez, R., and Chai, J. (2018). CCN1 induces apoptosis in esophageal adenocarcinoma through p53-dependent downregulation of survivin. *J. Cell Biochem.* 120, 2070–2077. doi: 10.1002/jcb.27515

De Cesare, D., Fimia, G. M., and Sassone-Corsi, P. (1999). Signaling routes to CREM and CREB: plasticity in transcriptional activation. *Trends Biochem. Sci.* 24, 281–285. doi: 10.1016/s0968-0004(99)01414-0

Dou, Q., Hao, F., Sun, L., Xu, X., and Cui, M. Z. (2017). CRE and SRE mediate LPA-induced CCN1 transcription in mouse aortic smooth muscle cells. *Can. J. Physiol. Pharmacol.* 95, 275–280. doi: 10.1139/cjpp-2016-0559

Ivanisenko, N. V., Seyrek, K., Kolchanov, N. A., Ivanisenko, V. A., and Lavrik, I. N. (2020). The role of death domain proteins in host response upon SARS-CoV-2 infection: modulation of programmed cell death and translational applications. *Cell Death Discovery* 6:101. doi: 10.1038/s41420-020-00331-w

Jorgensen, I., Rayamajhi, M., and Miao, E. A. (2017). Programmed cell death as a defence against infection. *Nat. Rev. Immunol.* 17, 151–164. doi: 10.1038/nri.2016.147

Kim, K. H., Min, Y. K., Baik, J. H., Lau, L. F., Chaqour, B., and Chung, K. C. (2003). Expression of angiogenic factor Cyr61 during neuronal cell death *via* the activation of c-Jun N-terminal kinase and serum response factor. *J. Biol. Chem.* 278, 13847–13854. doi: 10.1074/jbc.M210128200

Kim, S. M., Park, J. H., Chung, S. K., Kim, J. Y., Hwang, H. Y., Chung, K. C., et al. (2004). Coxsackievirus B3 infection induces cyr61 activation *via* JNK to mediate cell death. *J. Virol.* 78, 13479–13488. doi: 10.1128/JVI.78.24.13479-13488.2004

Kim, Y., and Lee, C. (2014). Porcine epidemic diarrhea virus induces caspase-independent apoptosis through activation of mitochondrial apoptosis-inducing factor. *Virology* 46, 180–193. doi: 10.1016/j.virol.2014.04.040

Kurozumi, K., Hardcastle, J., Thakur, R., Shroll, J., Nowicki, M., Otsuki, A., et al. (2008). Oncolytic HSV-1 infection of tumors induces angiogenesis and upregulates CYR61. *Mol. Ther.* 16, 1382–1391. doi: 10.1038/mt.2008.112

Lau, L. F. (2011). CCN1/CYR61: the very model of a modern matricellular protein. *Cell. Mol. Life Sci.* 68, 3149–3163. doi: 10.1007/s00018-011-0778-3

Lau, L. F. (2016). Cell surface receptors for CCN proteins. *J. Cell Commun. Signal.* 10, 121–127. doi: 10.1007/s12079-016-0324-z

Lee, C. (2016). Erratum to: porcine epidemic diarrhea virus: an emerging and re-emerging epizootic swine virus. *Virol. J.* 13:19. doi: 10.1186/s12985-016-0465-y

Li, H., Li, H., Huo, R., Wu, P., Shen, Z., Xu, H., et al. (2017). Cyr61/CCN1 induces CCL20 production by keratinocyte *via* activating p38 and JNK/AP-1 pathway in psoriasis. *J. Dermatol. Sci.* 88, 46–56. doi: 10.1016/j.jdermsci.2017.05.018

Li, M., Wu, Y., Chen, J., Shi, H., Ji, Z., Zhang, X., et al. (2021). Innate immune evasion of porcine epidemic diarrhea virus through degradation of F-box and WD repeat domain-containing 7 protein *via* ubiquitin-proteasome pathway. *J. Virol.* doi: 10.1128/JVI.00889-21, Online ahead of print,

Li, Y., Chen, Y. M., Sun, M. M., Guo, X. D., Wang, Y. C., and Zhang, Z. Z. (2016). Inhibition on apoptosis induced by elevated hydrostatic pressure in retinal ganglion cell-5 *via* laminin upregulating beta1-integrin/focal adhesion kinase/protein kinase B signaling pathway. *Chin. Med. J.* 129, 976–983. doi: 10.4103/0366-6999.179785

Li, Y., Wu, Q., Jin, Y., and Yang, Q. (2019). Antiviral activity of interleukin-11 as a response to porcine epidemic diarrhea virus infection. *Vet. Res.* 50:111. doi: 10.1186/s13567-019-0729-9

Liu, Y. C., Mok, B. W., Wang, P., Kuo, R. L., Chen, H., and Shih, S. R. (2021). Cellular 5′-3′ mRNA exoribonuclease XRN1 inhibits interferon beta activation and facilitates influenza a virus replication. *mBio* 12:e0094521. doi: 10.1128/mBio.00945-21

Meyuhas, R., Pikarsky, E., Tavor, E., Klar, A., Abramovitch, R., Hochman, J., et al. (2008). A Key role for cyclic AMP-responsive element binding protein in hypoxia-mediated activation of the angiogenesis factor CCN1 (CYR61) in Tumor cells. *Mol. Cancer Res.* 6, 1397–1409. doi: 10.1158/1541-7786.MCR-07-2086

Moll, U. M., and Petrenko, O. (2003). The MDM2-p53 interaction. *Mol. Cancer Res.* 1, 1001–1008.

Moon, H. G., Zheng, Y., An, C. H., Kim, Y. K., and Jin, Y. (2013). CCN1 secretion induced by cigarette smoking extracts augments IL-8 release from bronchial epithelial cells. *PLoS One* 8:e68199. doi: 10.1371/journal.pone.0068199

Pan, Y., Li, P., Jia, R., Wang, M., Yin, Z., and Cheng, A. (2018). Regulation of apoptosis during porcine circovirus type 2 infection. *Front. Microbiol.* 9:2086. doi: 10.3389/fmicb.2018.02086

Pandey, K., Zhong, S., Diel, D. G., Hou, Y., Wang, Q., Nelson, E., et al. (2019). GTPase-activating protein-binding protein 1 (G3BP1) plays an antiviral role against porcine epidemic diarrhea virus. *Vet. Microbiol.* 236:108392. doi: 10.1016/j.vetmic.2019.108392

Park, I. B., and Chun, T. (2020). Porcine reproductive and respiratory syndrome virus (PRRSV) non-structural protein (NSP)1 transcriptionally inhibits CCN1 and CCN2 expression by blocking ERK-AP-1 axis in pig macrophages *in vitro*. *Res. Vet. Sci.* 132, 462–465. doi: 10.1016/j.rvsc.2020.07.029

Qin, Z., Robichaud, P., He, T., Fisher, G. J., Voorhees, J. J., and Quan, T. (2014). Oxidant exposure induces cysteine-rich protein 61 (CCN1) *via* c-Jun/AP-1 to reduce collagen expression in human dermal fibroblasts. *PLoS One* 9:e115402. doi: 10.1371/journal.pone.0115402

Seefried, L., Muller-Deubert, S., Krug, M., Youssef, A., Schutze, N., Ignatius, A., et al. (2017). Dissection of mechanoresponse elements in promoter sites of the mechanoresponsive CYR61 gene. *Exp. Cell Res.* 354, 103–111. doi: 10.1016/j.yexcr.2017.03.031

Shi, L., Dong, N., Ji, D., Huang, X., Ying, Z., Wang, X., et al. (2018). Lipopolysaccharide-induced CCN1 production enhances interleukin-6 secretion in bronchial epithelial cells. *Cell Biol. Toxicol.* 34, 39–49. doi: 10.1007/s10565-017-9401-1

Si, F., Chen, B., Hu, X., Yu, R., Dong, S., Wang, R., et al. (2020). Porcine epidemic diarrhea virus orf3 protein is transported through the exocytic pathway. *J. Virol.* 94:e00808-20. doi: 10.1128/JVI.00808-20

Su, B. C., and Mo, F. E. (2014). CCN1 enables Fas ligand-induced apoptosis in cardiomyoblast H9c2 cells by disrupting caspase inhibitor XIAP. *Cell. Signal.* 26, 1326–1334. doi: 10.1016/j.cellsig.2014.02.019

Su, M., Shi, D., Xing, X., Qi, S., Yang, D., Zhang, J., et al. (2021). Coronavirus porcine epidemic diarrhea virus nucleocapsid protein interacts with p53 to induce cell cycle arrest in S-phase and promotes viral replication. *J. Virol.* 95:e0018721. doi: 10.1128/JVI.00187-21

Sun, J., Zhang, W., Tan, Z., Zheng, C., Tang, Y., Ke, X., et al. (2020). Zika virus promotes CCN1 expression *via* the CaMKIIalpha-CREB pathway in astrocytes. *Virulence* 11, 113–131. doi: 10.1080/21505594.2020.1715189

Sun, P., Wu, H., Huang, J., Xu, Y., Yang, F., Zhang, Q., et al. (2018). Porcine epidemic diarrhea virus through p53-dependent pathway causes cell cycle arrest in the G0/G1 phase. *Virus Res.* 253, 1–11. doi: 10.1016/j.virusres.2018.05.019

Thorne, A. H., Meisen, W. H., Russell, L., Yoo, J. Y., Bolyard, C. M., Lathia, J. D., et al. (2014). Role of cysteine-rich 61 protein (CCN1) in macrophage-mediated oncolytic herpes simplex virus clearance. *Mol. Ther.* 22, 1678–1687. doi: 10.1038/mt.2014.101

Todorovic, V., Chen, C. C., Hay, N., and Lau, L. F. (2005). The matrix protein CCN1 (CYR61) induces apoptosis in fibroblasts. *J. Cell Biol.* 171, 559–568. doi: 10.1083/jcb.200504015

Tripathi, S., Batra, J., Cao, W., Sharma, K., Patel, J. R., Ranjan, P., et al. (2013). Influenza A virus nucleoprotein induces apoptosis in human airway epithelial cells: implications of a novel interaction between nucleoprotein and host protein Clusterin. *Cell Death Dis.* 4:e562. doi: 10.1038/cddis.2013.89

Umeshappa, C. S., Singh, K. P., Nanjundappa, R. H., and Pandey, A. B. (2010). Apoptosis and immuno-suppression in sheep infected with bluetongue virus serotype-23. *Vet. Microbiol.* 144, 310–318. doi: 10.1016/j.vetmic.2010.02.033

Wang, H., Kong, N., Jiao, Y., Dong, S., Sun, D., Chen, X., et al. (2021). EGR1 suppresses porcine epidemic diarrhea virus replication by regulating IRAV to degrade viral nucleocapsid protein. *J. Virol.* 95:e0064521. doi: 10.1128/JVI.00645-21

Wawryk-Gawda, E., Chylinska-Wrzos, P., Lis-Sochocka, M., Chlapek, K., Bulak, K., Jedrych, M., et al. (2014). P53 protein in proliferation, repair and apoptosis of cells. *Protoplasma* 251, 525–533. doi: 10.1007/s00709-013-0548-1

Wu, P., Ma, G., Zhu, X., Gu, T., Zhang, J., Sun, Y., et al. (2017). Cyr61/CCN1 is involved in the pathogenesis of psoriasis vulgaris *via* promoting IL-8 production by keratinocytes in a JNK/NF-kappaB pathway. *Clin. Immunol.* 174, 53–62. doi: 10.1016/j.clim.2016.11.003

Xu, J., Mao, J., Han, X., Shi, F., Gao, Q., Wang, T., et al. (2021). Porcine epidemic diarrhea virus inhibits hdac1 expression to facilitate its replication *via*

binding of its nucleocapsid protein to host transcription factor Sp1. *J. Virol.* 95:e0085321. doi: 10.1128/JVI.00853-21

Xu, X., Xu, Y., Zhang, Q., Yang, F., Yin, Z., Wang, L., et al. (2019). Porcine epidemic diarrhea virus infections induce apoptosis in Vero cells *via* a reactive oxygen species (ROS)/p53, but not p38 MAPK and SAPK/JNK signalling pathways. *Vet. Microbiol.* 232, 1–12. doi: 10.1016/j.vetmic.2019.03.028

Yang, L., Wang, C., Shu, J., Feng, H., He, Y., Chen, J., et al. (2021). Porcine epidemic diarrhea virus induces vero cell apoptosis *via* the p53-PUMA signaling pathway. *Viruses* 13:1218. doi: 10.3390/v13071218

Ye, G., Wang, X., Tong, X., Shi, Y., Fu, Z. F., and Peng, G. (2020). Structural basis for inhibiting porcine epidemic diarrhea virus replication with the 3C-like protease inhibitor GC376. *Viruses* 12:240. doi: 10.3390/v12020240

You, J. J., Yang, C. M., Chen, M. S., and Yang, C. H. (2010). Regulation of Cyr61/CCN1 expression by hypoxia through cooperation of c-Jun/AP-1 and HIF-1alpha in retinal vascular endothelial cells. *Exp. Eye Res.* 91, 825–836. doi: 10.1016/j.exer.2010.10.006

Zhao, L., Xia, M., Wang, K., Lai, C., Fan, H., Gu, H., et al. (2020). A long non-coding RNA IVRPIE promotes host antiviral immune responses through regulating interferon beta1 and ISG expression. *Front. Microbiol.* 11:260. doi: 10.3389/fmicb.2020.00260

Zhu, Y., Almuntashiri, S., Han, Y., Wang, X., Somanath, P. R., and Zhang, D. (2020). The roles of CCN1/CYR61 in pulmonary diseases. *Int. J. Mol. Sci.* 21:7810. doi: 10.3390/ijms21217810

Conflict of Interest: The authors declare that the research was conducted in the absence of any commercial or financial relationships that could be construed as a potential conflict of interest.

Publisher's Note: All claims expressed in this article are solely those of the authors and do not necessarily represent those of their affiliated organizations, or those of the publisher, the editors and the reviewers. Any product that may be evaluated in this article, or claim that may be made by its manufacturer, is not guaranteed or endorsed by the publisher.

frontiers in Microbiology

ORIGINAL RESEARCH
published: 30 March 2022
doi: 10.3389/fmicb.2022.827818

Singapore Grouper Iridovirus Induces Glucose Metabolism in Infected Cells by Activation of Mammalian Target of Rapamycin Signaling

Xixi Guo[1], Qi Zheng[1], Zanbin Pan[1], Youhua Huang[1], Xiaohong Huang[1] and Qiwei Qin[1,2,3]**

[1] Guangdong Laboratory for Lingnan Modern Agriculture, University Joint Laboratory of Guangdong Province, Hong Kong and Macao Region on Marine Bioresource Conservation and Exploitation, College of Marine Sciences, South China Agricultural University, Guangzhou, China, [2] Southern Marine Science and Engineering Guangdong Laboratory, Zhuhai, China, [3] Laboratory for Marine Biology and Biotechnology, Qingdao National Laboratory for Marine Science and Technology, Qingdao, China

OPEN ACCESS

Edited by:
Cao Yong chang,
Sun Yat-sen University, China

Reviewed by:
Tanmay Majumdar,
National Institute of Immunology (NII), India
Puxian Fang,
Huazhong Agricultural University, China

***Correspondence:**
Xiaohong Huang
huangxh@scau.edu.cn
Qiwei Qin
qinqw@scau.edu.cn

Specialty section:
This article was submitted to Virology, a section of the journal Frontiers in Microbiology

Received: *02 December 2021*
Accepted: *31 January 2022*
Published: *30 March 2022*

Citation:
Guo X, Zheng Q, Pan Z, Huang Y, Huang X and Qin Q (2022) Singapore Grouper Iridovirus Induces Glucose Metabolism in Infected Cells by Activation of Mammalian Target of Rapamycin Signaling. Front. Microbiol. 13:827818. doi: 10.3389/fmicb.2022.827818

Singapore grouper iridovirus (SGIV), a member of the *Iridoviridae* family, is an important marine cultured fish pathogen worldwide. Our previous studies have demonstrated that lipid metabolism was essential for SGIV entry and replication, but the roles of glucose metabolism during SGIV infection still remains largely unknown. In this study, we found that the transcription levels of key enzymes involved in glycolysis were regulated in varying degrees during SGIV infection based on the transcriptomic analysis. Quantitative PCR and western blot analysis also indicated that the expression of both glucose transporters (GLUT1 and GLUT2) and the enzymes of glucose metabolism (hexokinase 2, HK2 and pyruvate dehydrogenase complex, PDHX) were upregulated during SGIV infection *in vivo* or *in vitro*, suggesting that glycolysis might be involved in SGIV infection. Exogenous glucose supplementation promoted the expression of viral genes and infectious virion production, while glutamine had no effect on SGIV infection, indicating that glucose was required for SGIV replication. Consistently, pharmacological inhibition of glycolysis dramatically reduced the protein synthesis of SGIV major capsid protein (MCP) and infectious virion production, and promotion of glycolysis significantly increased SGIV infection. Furthermore, knockdown of HK2, PDHX, or GLUT1 by siRNA decreased the transcription and protein synthesis of SGIV MCP and suppressed viral replication, indicating that those enzymes exerted essential roles in SGIV replication. In addition, inhibition of mTOR activity in SGIV-infected cells effectively reduced the expression of glycolysis key enzymes, including HK2, PDHX, GLUT1, and GLUT2, and finally inhibited SGIV replication, suggesting that mTOR was involved in SGIV-induced glycolysis. Thus, our results not only provided new insights into the mechanism of how SGIV infection affects host cell glycolysis, but also contributed to further understanding of the iridovirus pathogenesis.

Keywords: SGIV, glycolysis, HK2, GLUT1, mTOR signaling

INTRODUCTION

Viruses are obligate intracellular parasites that rely on host cellular metabolic system for the energy and macromolecule synthesis required for their replication. In recent years, with the development of technology, studies have focused on examining how virus infection alters host metabolic system. Understanding how virus infection manipulates cellular metabolism is an emerging and critical field for effective vaccine development and virus treatment. Increasing evidence suggested that both DNA viruses and RNA viruses modulated the host cell metabolic profiles after virus infection, including human cytomegalovirus (HCMV), herpes simplex virus 1 (HSV-1), hepatitis C virus (HCV), influenza A virus, human immunodeficiency virus type 1 (HIV-1), Kaposi's sarcoma-associated herpesvirus (KSHV), vaccinia virus (VACV), Epstein-Barr virus (EBV), infectious spleen and kidney necrosis virus (ISKNV), and so on (Munger et al., 2006, 2008; Diamond et al., 2010; Ritter et al., 2010; Hollenbaugh et al., 2011; Rabinowitz et al., 2011; Roe et al., 2011; Vastag et al., 2011; Delgado et al., 2012; Fontaine et al., 2014; Xiao et al., 2014; Goodwin et al., 2015; Mushtaq et al., 2016; Guo et al., 2019). These reports have revealed numerous dramatic cellular metabolism changes triggered by virus infection. Particularly, the activation of glycolysis has been reported in most of these reports, indicating that glucose is a critical carbon source during virus infection.

Glucose and glutamine are the two main carbon sources for the energetic and biosynthetic needs in cells. In normal cells, glucose is thought to be responsible for cellular ATP generation via glycolysis and the tricarboxylic acid (TCA) cycle. However, in cancer cells, glucose is separated away from the TCA cycle to be used biosynthetically and glutamine serves to anaplerotically replenish the TCA cycle (DeBerardinis et al., 2007, Deberardinis et al., 2008; Wise et al., 2008). For glucose metabolism, exogenous glucose uptake into cells is mediated by glucose transporters (GLUTs), and glucose metabolism was catalyzed by several key enzymes (Adeva-Andany et al., 2016). For example, hexokinases (HKs), which convert glucose to glucose 6-phosphate, is the first and rate-limiting enzyme in glycolytic pathway and the HK2 isoform is a key mediator of aerobic glycolysis (Wolf et al., 2011; Gershon et al., 2013). Pyruvate dehydrogenase complex (PDHX), which provide acetyl-CoA for the TCA cycle, is a multienzyme complex central to aerobic respiration, connecting glycolysis to mitochondrial oxidation of pyruvate (Forsberg et al., 2020).

Iridoviruses are large DNA viruses and result in heavy economic losses in aquaculture industry (Shinmoto et al., 2009). To date, the family Iridoviridae is divided into two subfamilies (*Alphairidovirinae* and *Betairidovirinae*) and categorized into five known genera: *Iridovirus, Chloriridovirus, Lymphocystivirus, Megalocytivirus,* and *Ranavirus* (Chinchar et al., 2017). It has been reported that glucose and glutamine metabolism might play a critical role in the replication of megalocytivirus by producing required energy and metabolites (Fu et al., 2017; Guo et al., 2019). Singapore grouper iridovirus (SGIV) was isolated from diseased grouper (*Epinephelus tauvina*) (Qin et al., 2001, 2003), and characterized as a novel member of the genus *Ranavirus* (Chinchar et al., 2017). The highly lethal and serious systemic disease induced by SGIV infection resulted in great economic losses in aquaculture industry (Gibson-Kueh et al., 2003). The previous studies showed that SGIV infection in host cells evoked non-apoptotic cell death, and mitogen-activated protein kinase (MAPK) signaling pathway involved in SGIV (Huang et al., 2011a,b). During SGIV infection, the level of phosphorylated mammalian target of rapamycin (mTOR) was increased with infection time, suggesting that SGIV inhibited autophagy through decreasing in mTOR activity to some extent (Li et al., 2020). Recently, cellular fatty acid synthesis was demonstrated to exert crucial roles during SGIV infection via regulating virus entry and host immune response (Zheng et al., 2022). Moreover, palmitic acid promoted SGIV replication by suppressing autophagic flux and negatively regulating TANK binding kinase 1 (TBK1)-interferon regulator factor (IRF) 3/7 pathway (Yu et al., 2020). However, the molecular mechanism by which SGIV regulated glucose metabolism still remained largely unknown.

In the present study, the roles of glucose metabolism during SGIV replication was investigated. The expression levels of crucial enzymes of glucose metabolism were examined, and the roles of glycolysis in SGIV infection were investigated using pharmacological inhibitors and siRNA technology. In addition, we also clarified the roles of mTOR in SGIV induced glycolysis. Our results will shed important lights on the mechanism of SGIV pathogenesis, providing new clues to understanding the fish-virus interaction.

MATERIALS AND METHODS

Fish, Cells, and Viruses

Juvenile orange-spotted grouper (weight 30–40 g) were purchased from a local marine fish farm in Hainan Province, China. Fish were maintained in a laboratory recirculating seawater system at 24–28°C and fed twice daily for 2 weeks. Grouper spleen (EAGS) cells were established in our lab (Huang et al., 2009). Grouper head kidney (ELHK) cell used in this study was a new grouper cell line that was established from grouper head kidney (Liu et al., 2021). EAGS and ELHK cells were maintained at 28°C in Leibovitz's L-15 medium (Gibco, United States) supplemented with 10% fetal bovine serum (Gibco, United States). SGIV was stored in our laboratory (Qin et al., 2003). The virus was propagated in EAGS cells at 28°C and the viral titer was determined by a $TCID_{50}$ assay.

Reagents

2-Deoxy-D-glucose (2DG) and Dichloroacetate (DCA) were purchased from Sigma-Aldrich. Rapamycin (Rapa, AY-22989) was purchased from Selleckchem. 2DG and DCA were dissolved in L-15 medium to a stock concentration of 500 mM and 400 mM, respectively. Rapamycin was dissolved in DMSO to a stock concentration of 10 mM. These reagents need to be diluted to a working concentration using L-15 medium (2DG and DCA) or DMSO (Rapamycin) just before use. The mouse monoclonal antibody against SGIV major capsid protein (MCP) was prepared and stored in our laboratory. The rabbit polyclonal antibodies

against HK2, PDHX, GLUT1, and GLUT2 were purchased from Proteintech (United States). The rabbit monoclonal antibody against β-tubulin was purchased from Abcam.

Virus Infection and Transcriptomic Analysis

At 5d postinfection (p.i.), three parallel samples of SGIV-infected or mock-infected groupers were harvested. Transcriptomic profiling was performed on an Illumina Hiseq 2500 platform and the analysis process was conducted by Shanghai OE Biotech Co., Ltd. (Shanghai, China).

Challenge and Samples Collection

A total of 120 healthy Juvenile orange-spotted grouper were randomly divided into two groups, including SGIV- and Mock-infected group (60 fish per group, 20 fish per tank, 3 replicates). The SGIV-infected groups were injected intraperitoneally with 0.1 mL of SGIV ($10^{5.5}$ $TCID_{50}$). The Mock-infected groups were injected with 0.1 mL of PBS. Three fish (one fish each duplicate) were randomly selected from SGIV- and Mock-infected group on the 1st, 2nd, 3rd, 5th, and 7th day post-infection. Then the liver, spleen and kidney tissues were obtained for samples preparation.

Cell Viability

Cell Counting Kit-8 (CCK-8) assay was performed to examine the impact of glucose, glutamine, 2DG and DCA treatment on cell proliferation according to the manufacturer's instructions. In brief, EAGS and ELHK cells cultured in 96-well plates were incubated with glucose (0, 1.0, and 4.5 g/L), glutamine (0, 2.0 mM), 2DG (0, 0.2, 0.5, 1.0, 2.0, and 5.0 mM) and DCA (0, 0.1, 0.2, 0.5, 0.6, and 1.0 mM) for 24 h. Cells were washed with culture medium three times, and then 100 μL of culture medium supplemented with 10 μL Cell Counting Kit-8 (CCK-8, UE) was added into each well and incubated at 28°C for 4 h. The absorbance was measured in Varioskan™ LUX multimode microplate reader (Thermo Fisher Scientific, United States) at 450 nm.

Cell Transfection

Cell transfection was carried out using Lipofectamine 2000 reagent (Invitrogen) according to the manufacturer's protocol. EAGS cells were seeded in 12-well plates at 70–80% confluence for 18–24 h, and cells were transfected with the mixture of 4 μL Lipofectamine 2000 and 100 nM siRNA incubated for 4–6 h. After replacing with fresh normal medium, cells were cultured for further study. The HK2, PDHX, and GLUT1 siRNA was designed by GenePharma. EAGS cells were transfected with HK2, PDHX, and GLUT1 siRNA, respectively, or the same volume of negative control (NC) siRNA for 24 h, and then infected with SGIV for 12 and 24 h.

Virus Titer Assay

Viral titer was assessed in EAGS cells to determine the effect of glucose, glutamine, 2DG, and DCA on SGIV production, respectively. In brief, EAGS cells were pretreated with glucose, glutamine, 2DG and DCA or vehicle for 2 h, and then the cells were infected with SGIV [at multiplicity of infection (MOI) of 1.0] and collected at 24 h p.i. for virus titer assay. The viral titers of cell lysates were evaluated using the 50% tissue culture infectious dose ($TCID_{50}$) assay (Reed and Muench, 1938). The cytopathic effects (CPEs) were observed under a light microscope (Leica, Germany) every day, and each sample was measured in triplicate.

RNA Extraction and Real-Time RT-qPCR (qRT-PCR)

EAGS and ELHK cells were infected with SGIV at MOI of 1.0, respectively. The total RNA isolation was performed using the Cell Total RNA Isolation Kit (FOREGENE, China) according the manufacturer's instructions, and reverse transcription was carried out using ReverTra Ace (TOYOBO, China). Then, qPCR was performed under the ABI Quantstudio™ 5 Real-Time PCR System (Thermo Fisher Scientific, Applied Biosystems, United States). The primers used in this study were listed in **Table 1**. Reactions of SYBR Green were performed in a 10 μL volume containing 5 μL of 2 × SYBR® Premix Ex Taq™, 0.3 μL of each forward and reverse primer (10 μM), 1 μL of cDNA, and 3.4 μL of water. All experiments were performed in triplicate, and the cycling parameters were chosen according to the manufacturer's instructions. The expression levels of viral genes and host glycolysis metabolism genes were detected. The relative expression ratio of the selected gene normalized to β-actin was calculated using the $2^{-\Delta\Delta}$CT method.

Western Blot Analysis

EAGS and ELHK cells were mock- or SGIV-infected at MOI of 1.0, respectively. After the experimental treatments, cells were lysed and solubilized in 50 μL of Pierce IP Lysis Buffer (Thermo Fisher Scientific), containing protease/phosphatase inhibitor cocktail. Samples were boiled for 5 min after mixing with 5 × loading buffer. The equal of proteins were resolved by 10% SDS-PAGE and then electrophoretically transferred to

TABLE 1 | Primers used in this study.

Primer names	Gens names	Sequence (5′–3′)
q-Actin-F	β-Actin	TACGAGCTGCCTGACGGACA
q-Actin-R		GGCTGTGATCTCCTTCTGCA
q-HK2-F	Hexokinase 2	CCCATTGGTTGAGGACTG
q-HK2-R		GTTTCTCGGCTGCTTTGT
q-PDHX-F	Pyruvate dehydrogenase complex	CTGGGTCGTCAAGGGATT
q-PDHX-R		GGGTGACCGAAAGAAGTGT
q-GLUT1-F	Glucose transporter 1	AGGTGTTTGGATTGGAGGTA
q-GLUT1-R		CTGTTGATGAGCAGGAAGC
q-GLUT2-F	Glucose transporter 2	TCTGGGAGCCCTTCTTCATCTGTG
q-GLUT2-R		CGGGGTCATCAACACAGTCTTCAC
q-GLUT4-F	Glucose transporter 4	TGGCGGAGATGAAGGAGGAGAAG
q-GLUT4-R		GCGGTAGAGCGAAGAGCGAAAG
q-MCP-F	MCP	GCACGCTTCTCTCACCTTCA
q-MCP-R		AACGGCAACGGGAGCACTA
q-ICP18-F	ICP18	ATCGGATCTACGTGGTTGG
q-ICP18-R		CCGTCGTCGGTGTCTATTC

0.45 μm TransBlot Turbo PVDF (Minipore). The membranes were blocked with 5% skim milk for 2 h, then incubated with different primary antibodies for 3 h at room temperature or overnight at 4°C. After washing with PBST buffer for 3 times, the membranes were incubated with secondary goat-anti-rabbit or goat-anti-mouse antibody labeled with horseradish peroxidase. Finally, the immunoreactive bands were visualized with Super ECL Plus Kit (UElandy) according to the manufacturer's protocol. The following primary antibodies were used: anti-HK2 (1:1,000 dilution), anti-PDHX (1:1,000 dilution), anti-GLUT1 (1:500 dilution), anti-GLUT2 (1:300 dilution), anti-SGIV-MCP (1:3,000 dilution), and anti-β-Tubulin (1:3,000 dilution). Data were normalized to the mean of β-Tubulin expression.

Determination of Enzyme Activity of Hexokinase 2 and Pyruvate Dehydrogenase Complex in Cells During Singapore Grouper Iridovirus Infection

EAGS cells and ELHK cells were collected at 12 and 24 h after mock- or SGIV infection. HK2 and PDHX activity was measured using Hexokinase Colorimetric Assay Kit (Sigma-Aldrich, MAK091) and Pyruvate Dehydrogenase Activity Assay Kit (Sigma-Aldrich, MAK183) according to the manufacturer's instructions, respectively. The measured activity was normalized to the total of cells.

Statistical Analysis

Each sample was assayed in triplicate and results were reported as mean ± standard deviation (SD). Statistical differences between groups were determined by one-way analysis of variance (ANOVA) using SPSS 21.0 software (IBM, United States). Data were considered statistically significant at $p < 0.05$.

RESULTS

Singapore Grouper Iridovirus Infection Altered Glucose Metabolism

To clarify whether glucose metabolism was involved in SGIV infection, we firstly analyzed the transcriptional changes of key enzymes of glucose metabolism pathway based on the

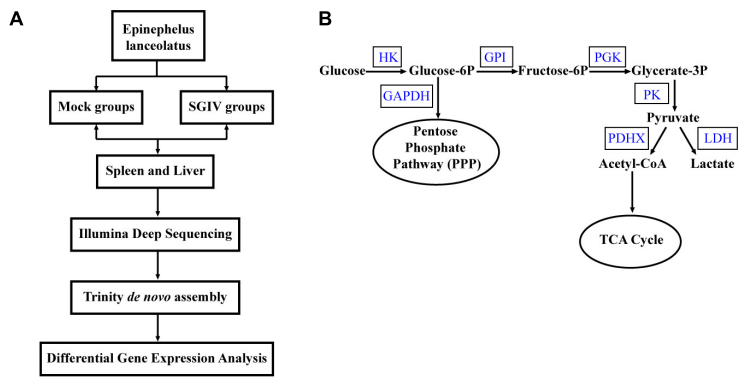

C

Gene Name	SGIV-infected Liver	SGIV-infected Spleen
Phosphoglucomutase (PGM)	**2.17**	**2.69**
Hexokinase (HK)	**3.01**	**2.05**
glucose-6-phosphate isomerase (GPI)	/	**2.37**
glyceraldehyde 3-phosphate dehydrogenase (GAPDH)	-0.37	-0.32
phosphoglycerate kinase (PGK)	/	**2.97**
pyruvate kinase (PK)	**4.96**	**2.13**
pyruvate dehydrogenase E1 component (PDH)	-0.42	-0.27
L-lactate dehydrogenase (LDH)	**24.61**	**8.92**

FIGURE 1 | Glucose metabolism is altered during SGIV infection. Grouper were mock- or SGIV- infected and harvested at 5 d for transcriptomic analysis. **(A)** A work flow of transcriptomic design. **(B)** A schema of glucose metabolism, including some glycolytic enzymes (blue typeface showed the enzymes involved in SGIV infection). **(C)** A table visualization of fold changes in levels of glycolytic enzymes profiled during SGIV infection. Bold red values indicate that the mean values are significantly higher in SGIV infected for that comparison, and black values indicate that the values are significantly lower.

transcriptomic data. As shown in **Figure 1**, the levels of the important glycolytic enzymes were differently expressed in SGIV-infected tissues compared to that in mock-infected tissues. In detail, the transcription levels of phosphoglucomutase (PGM), HK, glucose-6-phosphate isomerase (GPI), phosphoglycerate kinase (PGK), pyruvate kinase (PK) and L-lactate dehydrogenase (LDH) were significantly increased in liver and spleen of SGIV-infected groupers. In contrast, the expressions of the other two glycolytic enzymes, including glyceraldehyde 3-phosphate dehydrogenase (GAPDH) and pyruvate dehydrogenase E1 component (PDH) were decreased (**Figure 1**). Thus, we speculated that SGIV infection *in vivo* caused the alteration in glucose metabolism.

Glucose Was Required During Singapore Grouper Iridovirus Infection

In order to determine the roles of glucose or glutamine in SGIV replication *in vitro*, the effects of glucose and glutamine deprivation on viral infection were examined. EAGS cells were infected with SGIV at MOI of 1.0 and subsequently fed replete medium containing both glucose (1 or 4.5 g/L), glutamine (2 mM) or medium lacking either glucose or glutamine. Depriving EAGS cells of exogenous glucose or glutamine had no significant impact on cell viability for 24 h (**Figures 2A,E**). Firstly, the expression of viral MCP in transcription and protein level was determined by qPCR and western blot when SGIV-infected cells was fed with replete medium or medium lacking glucose or glutamine. Deletion of exogenous glucose in the culture medium significantly inhibited the transcription and expression of viral MCP (**Figures 2B,C**). Furthermore, the virus production was significantly reduced in SGIV-infected exogenous glucose depriving cells. The virus titer in glucose deficient medium was 30 and 50% lower than that in medium containing 1 or 4.5 g/L glucose, respectively (**Figure 2D**). In contrast, deletion of exogenous glutamine in the culture medium had no significant effects on SGIV replication (**Figures 2F–H**). These results suggested that glucose was an essential carbon source for SGIV replication.

Glycolysis Was Activated During Singapore Grouper Iridovirus Infection

It has been reported that exogenous glucose uptake into cells is mediated by glucose transporters (GLUTs), and glucose metabolism is catalyzed by several key enzymes, including HKs and PDHX (Gershon et al., 2013; Adeva-Andany et al., 2016; Forsberg et al., 2020). To determine whether SGIV infection activated glycolysis, the transcription levels of HK2, PDHX, GLUT1, and GLUT2 were firstly examined *in vivo* by qPCR during SGIV infection. The groupers were divided into mock and SGIV infected groups, fish were collected at indicated time points. As shown in **Figure 3**, HK2, PDHX, GLUT1, and GLUT2 were constitutively expressed in all the analyzed tissues. Among them, HK2, GLUT1, and GLUT2 showed similar expression patterns after SGIV infection, and significantly up-regulated than

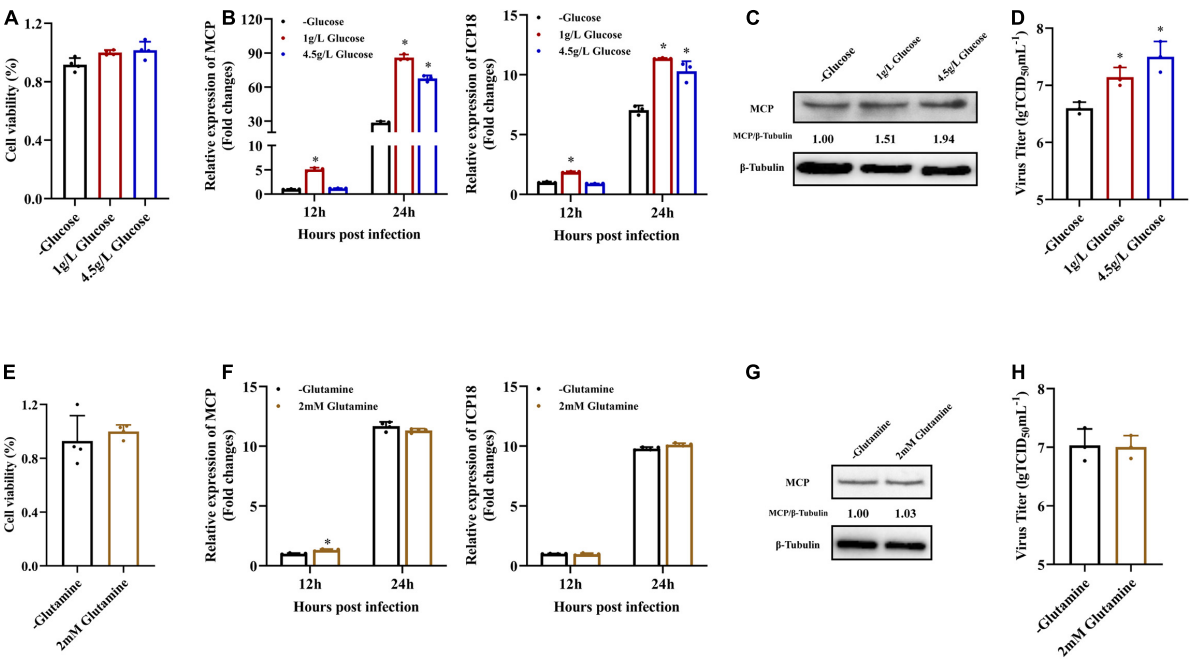

FIGURE 2 | Glucose is necessary for efficient infectious SGIV production. **(A,E)** EAGS cells were cultured in replete medium containing both glucose (1 and 4.5 g/L) and glutamine (2 mM) or medium lacking either glucose or glutamine, and the cell viability was detected by CCK-8 assay at 24 h. EAGS cells were infected with SGIV at MOI of 1.0 and fed replete (1, 4.5 g/L glucose, and 2 mM glutamine), glucose-free, or glutamine-free medium at 2 h. At 12 and 24 h p.i., SGIV was quantified by qRT-PCR **(B,F)**. At 24 h p.i., SGIV was quantified by Western blot **(C,G)** and $TCID_{50}$ **(D,H)**. The data are represented as mean ± SD. The significance level was defined as $^*p < 0.05$.

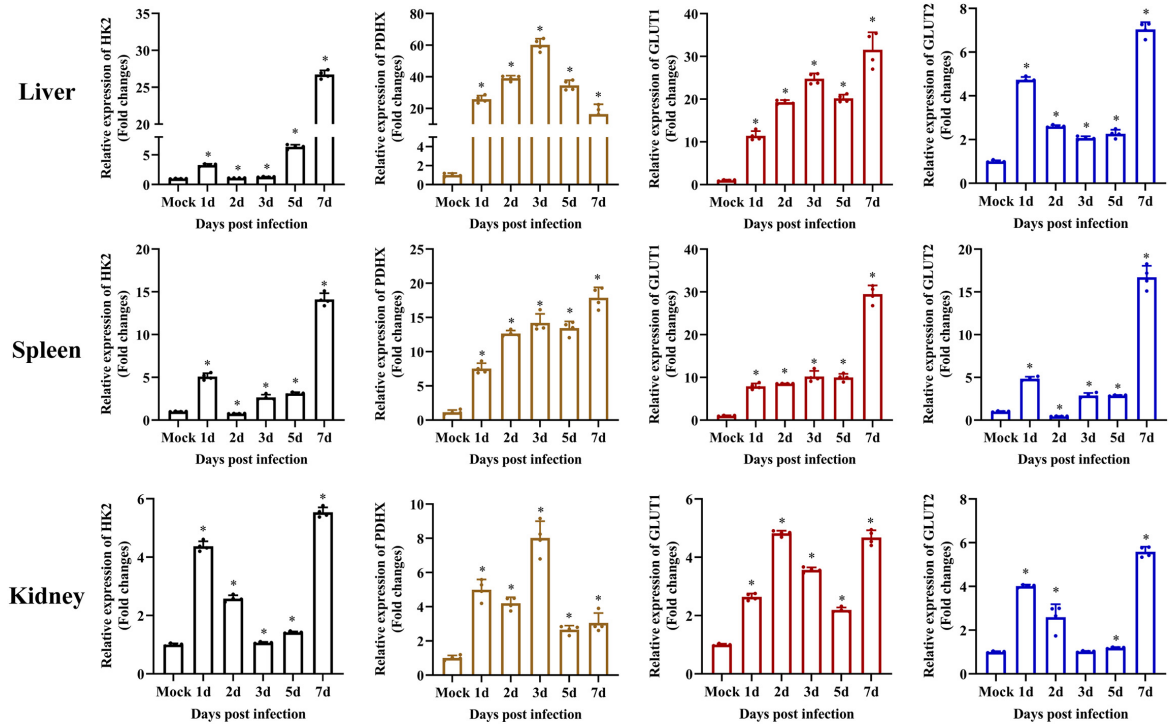

FIGURE 3 | Glycolysis is induced during SGIV infection *in vivo*. The expression of HK2, PDHX, GLUT1, and GLUT2 in grouper tissue (liver, spleen, and kidney). Data were expressed as a ratio to mock expression. The data are represented as mean ± SD. The significance level was defined as $^*p < 0.05$.

mock group, then peaked at 7 days in all the analyzed tissues. Interestingly, the expression of PDHX peaked at 3 days in liver and kidney and at 7 days in spleen. These results suggested that SGIV infection promote glycolysis process *in vivo*.

Furthermore, the protein expressions of those enzymes in mock- and SGIV-infected cells were measured by western blot using specific antibody (**Figure 4A**). The expressions of HK2, PDHX, GLUT1, and GLUT2 increased in SGIV-infected cells compared to that in mock-infected cells at 12 and 24 h p.i. HK2, GLUT1, and GLUT2 expression increased both at 12 and 24 h p.i. after SGIV infection. Whereas, the expression levels of PDHX first increased at 12 h p.i. and then decreased at 24 h p.i. after SGIV infection. Of note, the expression of GLUT2 increased 1.5-fold in SGIV-infected cells at 24 h compared to that in mock-infected cells. In addition, the activities of HK2 and PDHX was significantly increased in SGIV-infected cells compared to mock-infected cells (**Figures 4B,C**). Taken together, our results suggested that glycolysis was activated in response to SGIV infection.

Glycolysis Was Required for Optimal Infectious Singapore Grouper Iridovirus Production

In order to investigate whether glycolysis was involved in SGIV replication, we used specific inhibitors to destroy glycolysis *in vitro*, and then examined the effects of specific inhibitors on SGIV replication. 2DG and DCA are hexokinase inhibitor and pyruvate dehydrogenase kinase (PDK) inhibitor, respectively (Delgado et al., 2010; Kennedy et al., 2019). After determining the cell cytotoxicity of 2DG and DCA on cells (**Figures 5A,D**), non-toxicity concentration of 2DG (0.4 and 0.5 mM) and DCA (0.5 and 0.6 mM) were used to pretreat cells before SGIV infection. Treatment with 2DG significantly inhibited SGIV replication, evidenced by the decreasing in viral MCP synthesis and production of progeny virus (**Figures 5B,C**). Moreover, viral protein level and viral titer increased following DCA treatment (**Figures 5E,F**). The effects of 2DG or DCA on SGIV replication was dose dependent. The similar results also obtained from ELHK cells (**Supplementary Figure 1**), indicating that glycolysis was involved in the SGIV replication. In addition, we further clarify the effects of inhibition of glutamine metabolism on SGIV replication. EAGS cells were treated with BPTES (an inhibitor of glutaminase) and EGCG (an inhibitor of glutamate dehydrogenase). Consistent with the results shown in **Figure 2**, the inhibitors of glutamine metabolism have no significant effects on SGIV production (**Supplementary Figure 2**), indicating that glutamine was not necessary for SGIV replication.

To further explore whether grouper HK2, PDHX, and GLUT1 played roles in SGIV replication, we firstly knocked down HK2, PDHX, and GLUT1 in EAGS cells using specific target siRNA, and examined the potent silencing efficiencies of siRNAs on endogenous HK2, PDHX, and GLUT1, respectively. As shown in **Figure 6A**, the synthesized HK2, PDHX, and GLUT1 protein in siRNA-transfected cells was significantly reduced compared with the negative control siRNA (NC)-transfected

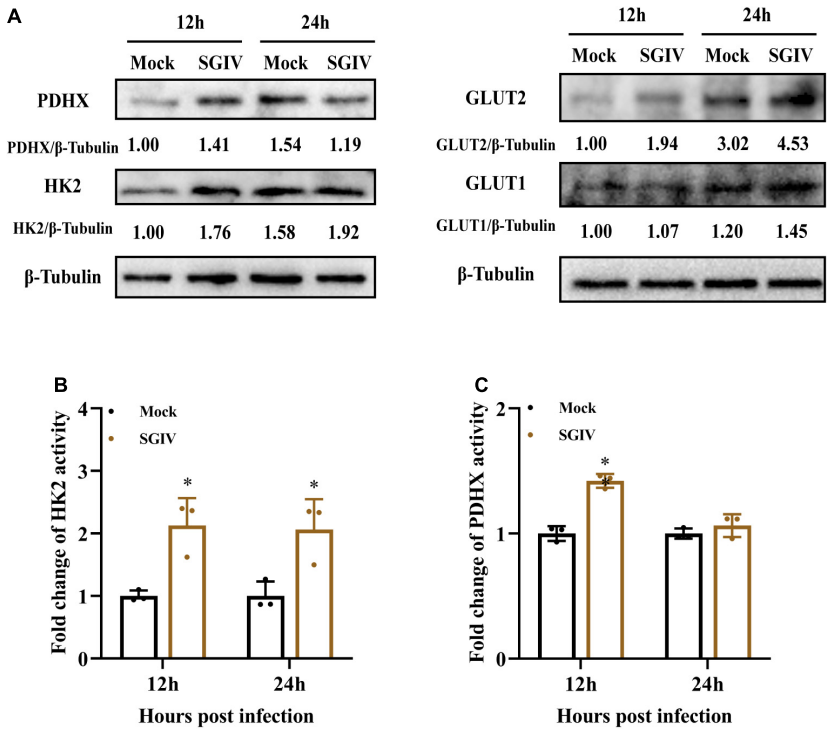

FIGURE 4 | Glycolysis is induced during SGIV infection in EAGS cells. **(A)** Immunoblot analysis of HK2, PDHX, GLUT1, and GLUT2 levels in mock- and SGIV-infected cells. Lysates from cells harvested at 12 and 24 h p.i. were subjected to Western blot analysis using antibodies indicated and β-tubulin was used as the internal control. The values below the lanes indicate the relative intensity of each major band. **(B,C)** The enzyme activity of HK2 and PDHX in SGIV-infected cells compared to mock-infected cells. The data are represented as mean ± SD. The significance level was defined as $^*p < 0.05$.

cells. Then, siRNA2-HK2, siRNA2-PDHX, and siRNA3-GLUT1 were chosen to evaluate the effects of knock down of HK2, PDHX, and GLUT1 on SGIV replication, respectively. The results showed that knock down of HK2, PDHX, and GLUT1 significantly inhibited SGIV infection, demonstrated by the marked reduction in both transcription and protein expression of SGIV MCP (**Figures 6B,C**). Moreover, the virus production in siRNA transfected cells were all significant decreased compared with NC-transfected cells (**Figure 6D**). Thus, our data revealed that HK2, PDHX, and GLUT1 played essential role in SGIV replication.

Inhibition of Mammalian Target of Rapamycin Signaling Blocked Singapore Grouper Iridovirus-Induced Glycolytic Activation and Attenuated Singapore Grouper Iridovirus Viral Replication

Mammalian target of rapamycin (mTOR) signaling plays a critical role in the regulation of energy metabolism, cell growth and proliferation (Mori et al., 2009; Dukhande et al., 2011). To further determine whether mTOR signaling was involved in SGIV-induced activation of glycolysis, we treated SGIV-infected cells with rapamycin, a specific inhibitor of mTOR, and then determined the impact of mTOR inhibition on the expressions of glucose transporters and glycolytic enzymes. As shown in **Figures 7A,B**, rapamycin treatment dramatically reduced transcription and protein level expression of GLUT1, GLUT2, HK2, PDHX in SGIV-infected cells, indicating that the mTOR activation was critical to regulating SGIV-mediated glycolytic activation in the infected EAGS cells. Furthermore, we also detected the effect of rapamycin on SGIV replication. The results showed that there was a significant decrease in protein level expression and virion production in SGIV-infected cells after rapamycin treatment (**Figures 7C,D**). Taken together, our results suggested that mTOR signaling was involved in activation of glycolysis induced by SGIV infection.

DISCUSSION

Viruses hijack host cellular metabolism to provide the building blocks and energy required for successful viral replication. Among them, glucose metabolism is one of an important energy metabolism. During viral infection, the virus can activate glycolysis pathway, which benefit for viral replication. In this study, we examined the alteration of numerous glycolytic enzymes during SGIV infection, and explored the roles of glucose metabolism in SGIV replication. Our transcriptomic results showed that SGIV infection induced the change of numerous glycolytic enzymes, suggesting that glucose metabolism might be involved in the process of SGIV infection. Consistent with

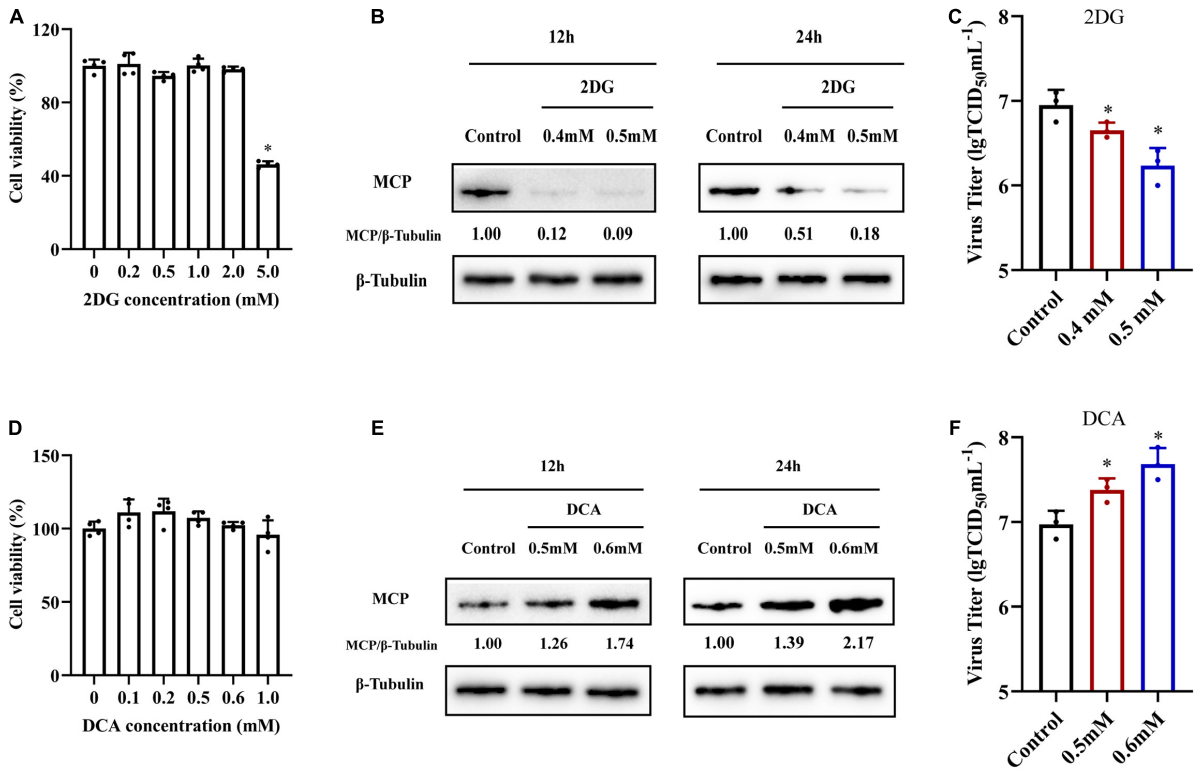

FIGURE 5 | The roles of glycolysis during SGIV replication. **(A,D)** The cytotoxicity of 2DG and DCA on EAGS cells, respectively. **(B,E)** Virus protein level reduced after 2DG treatment and increased after DCA treatment. The level of SGIV-MCP was detected by western blot, and β-tubulin was used as the internal control. **(C,F)** Virus production of SGIV was evaluated. EAGS cells incubated with indicated concentration 2DG and DCA were infected with SGIV and collected at 24 h p.i. Viral titers were determined using the $TCID_{50}$ method. The data are represented as mean ± SD. The significance level was defined as $^*p < 0.05$.

transcriptome data, we found the expression levels of key glycolytic enzymes (HK2 and PDHX) and GLUTs were changed *in vitro and in vivo*, with a concurrent increase in enzymes activity of HK2 and PDHX, providing further evidence that SGIV infection can activate glycolysis. The differential expression levels between tissues might be caused by the progress of SGIV infection in different tissues. It has been reported that virus infection could activate glycolysis using different manners. ISKNV infection activates glycolysis through up-regulating the expression of numerous key glycolytic enzymes in infected cells (Guo et al., 2019). EBV LMP1 prompts aerobic glycolysis in infected cells by up-regulation of HK2, which facilitates proliferation by blocking apoptosis (Xiao et al., 2014). HCV activates glycolytic activity by up-regulating the expression of HK2, which directly interact with HCV NS5A protein for viral replication (Ramiere et al., 2014). Dengue Virus (DENV) induces glycolysis for its replication, alone with the up-regulated expression of GLUT1 and HK2 (Fontaine et al., 2015). In addition, Kaposi's sarcoma herpesvirus (KSHV) infection either induces Warburg effect in the infected cells or employs specific viral microRNAs targeting the key regulators of glucose metabolism and mitochondrial biogenesis in the infected cells to induce glycolytic activity (Delgado et al., 2010, 2012; Yogev et al., 2014). More recently, it was shown that human herpesvirus 6A (HHV-6A) infection increases GLUTs and key glycolytic enzymes expression to prompts glycolysis (Wu et al., 2020). These studies prompted that glucose metabolism may be a common metabolic pathway explored by different viruses to support their replication.

Glucose and glutamine are the two main carbon sources utilized to support the energetic and biosynthetic needs of cells. Viruses utilized glucose or glutamine metabolism to produce required ATP or macromolecule metabolites for virus replication. In our study, we showed that SGIV production was significantly decreased when SGIV-infected cells were deprived of exogenous glucose. In contrast, depriving SGIV-infected cells of exogenous glutamine has no significantly impact on viral yield. The consistent results were obtained when glycolysis was destroyed by specific inhibitors, indicating that exogenous glucose was required for SGIV infection, while glutamine was not. The similar results were reported that Dengue virus required glucose for optimal replication (Fontaine et al., 2015). Differently, Glutamine was required for efficient replication of infectious spleen and kidney necrosis virus (ISKNV) and red-spotted grouper nervous necrosis virus (RGNNV) *in vitro* (Asim et al., 2017; Fu et al., 2017). In addition, white spot syndrome virus (WSSV) induced increased aerobic glycolysis via activation of the PI3K-Akt-mTOR pathway during replications and needed glutamate metabolism to benefit its replication (Su et al., 2014; He et al., 2019). Therefore, activated glycolysis do not represent general host metabolism reprogramming during viral infection,

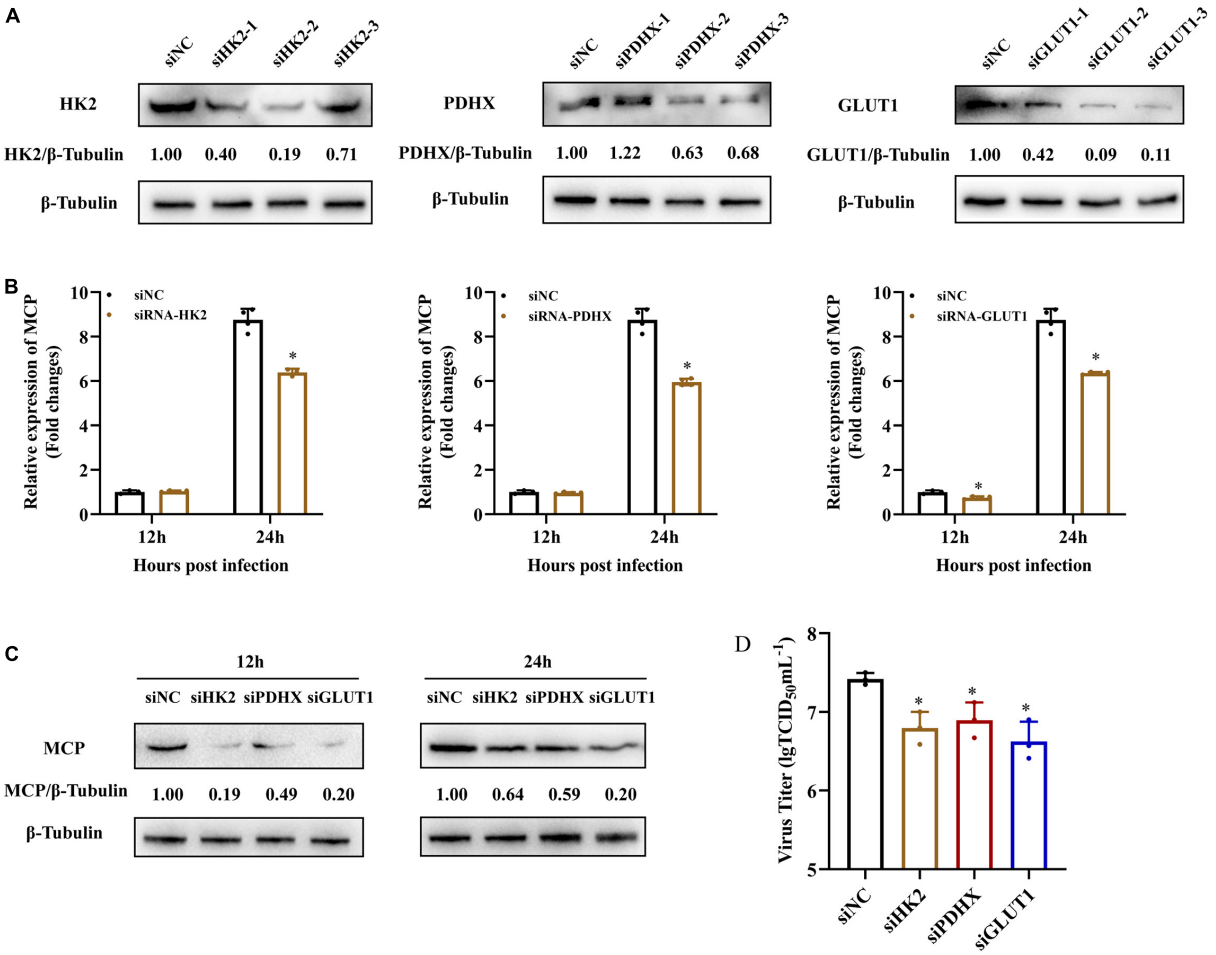

FIGURE 6 | HK2, PDHX, and GLUT1 were essential for SGIV replication. **(A)** The efficacy of different siRNAs targeting grouper HK2, PDHX, and GLUT1 were evaluated by western blotting analysis. Chemically synthesized siRNAs were transfected into grouper cells, and their silencing efficiencies on gene transcription and protein synthesis of HK2, PDHX, and GLUT1 were evaluated by western blotting. **(B–D)** The role of HK2, PDHX, and GLUT1 during SGIV replication. siRNA2-, siRNA2-, and siRNA3- were chosen to evaluate the effect of HK2, PDHX, and GLUT1 silence on SGIV replication, and viral gene transcription and protein synthesis were detected using qPCR, western blotting, and $TCID_{50}$, respectively. Data are expressed as means ± SD. The significance level was defined as $^*p < 0.05$.

it is more likely that certain viruses have evolved to induce glycolysis pathway to finish their life cycles.

Exogenous glucose across the membranes of cells is mediated by glucose transporters (GLUTs), and glucose metabolism is catalyzed by a number of enzymes, such as HKs, PDHX, lactase dehydrogenase (LDH), and et al. (Gershon et al., 2013; Mueckler and Thorens, 2013; Adeva-Andany et al., 2016; Forsberg et al., 2020). HKs, as a rate-limiting enzyme in glycolytic pathway, had been proved to not only be a new innate immune receptor that activated NOD-like receptor protein 3 (NLRP3) (Wolf et al., 2011, 2016), but also sequester MAVS preventing RIG-I signaling to escape immune response during Hepatitis B virus (HBV) infection (Zhou et al., 2021). In our study, we found that SGIV infection promoted HK2 activity and protein expression, and inhibition of HK2 activity resulted in a significant reduction in SGIV production, suggested that HK2 might be involved in SGIV replication. Of note, PDHX activity and protein expression was promoted at 12 h p.i., suggested that SGIV infection induced PDHX activation and promoted pyruvate into TCA cycle at the early stage of infection. Consistent with the inhibitory effect of siPDHX on SGIV replication, DCA activated PDHX resulted in a significant increase, suggested that PDHX was also essential for SGIV infection. In addition, knockdown of GLUT1 also showed significant inhibition on SGIV replication, suggesting that GLUT1 might enhance the cell capacity to transport glucose and meet increased energy demands following SGIV infection. In addition to regulating glucose transport, GLUT1 can function as a receptor for human T-cell leukemia virus type 1 (HTLV) (Manel et al., 2003). The detailed mechanism of these key enzymes of glycolysis in SGIV infection still needed further investigation.

mTOR is a highly conserved serine/threonine kinase that controls cell growth, cell proliferation and energy metabolism (Duvel et al., 2010; Liu et al., 2015). Our previous studies showed that mTOR pathway participated in autophagy during SGIV infection (Li et al., 2020). Here, inhibition of mTOR activity

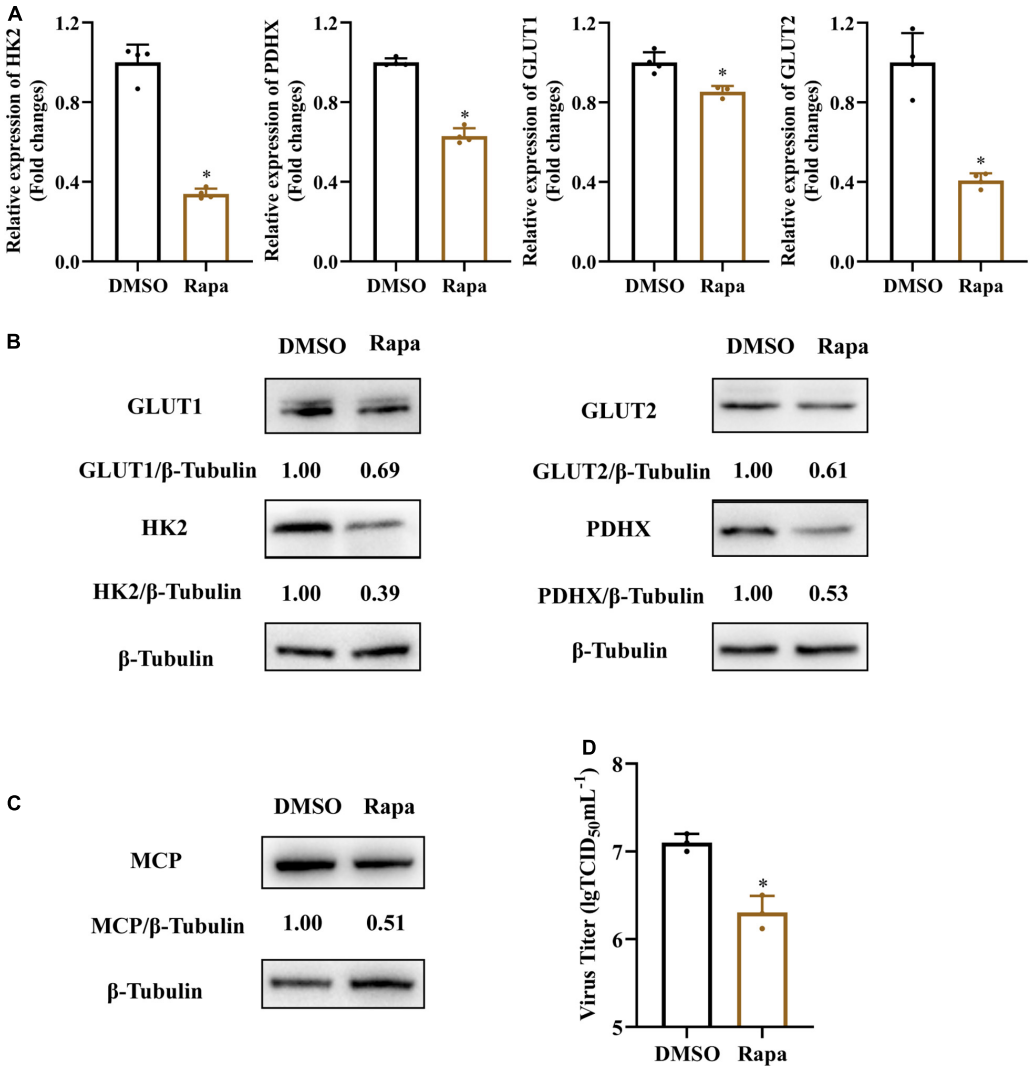

FIGURE 7 | Inhibition of mTOR blocks SGIV-induced glycolytic activation and viral production. Glycolytic enzymes and Gluts expression in SGIV infected EAGS cells with rapamycin treatment for 24 h. **(A)** Total RNA was isolated from the EAGS cells and analyzed by real-time PCR. The expression levels of each gene were normalized to β-actin expression levels and adjusted to the levels in mock-infected EAGS cells. **(B)** The level of glycolytic enzymes and Gluts were detected by western blot, and β-tubulin was used as the internal control. **(C,D)** The impact of mTORC1 on viral protein and, and viral titer using western blotting, and $TCID_{50}$, respectively. Data are expressed as means ± SD. The significance level was defined as $^*p < 0.05$.

not only decreases glycolysis in the SGIV-infected cells but also decreased virus replication, suggesting that SGIV-induced glycolysis activation is mainly dependent on mTOR signaling activation. In the other hand, our results also suggested that mTOR exerted a dual role during SGIV infection, regulating glycolysis activation and inhibiting autophagy. Increased literatures revealed that mTOR pathway plays an important role in virus infection. WSSV infection activates PI3K-Akt-mTOR pathway in the infected cells, which is critical for the WSSV-induced aerobic glycolysis (Su et al., 2014). EBV activates AMPK/mTOR/HIF1 pathway to promote glycolysis and induces angiogenesis in nasopharyngeal carcinoma cells (Zhang et al., 2017; Lyu et al., 2018). HHV-6 activates mTOR signaling to promote glycolysis in infected T cells (Wu et al., 2020). Avian reovirus activates the mTORC1/eIF4E/HIF-1α pathway to enhance glycolysis for virus replication (Chi et al., 2018).

In summary, we investigated the roles of glycolysis during SGIV replication. Several genes related to the glucose metabolism were regulated during SGIV infection, and glycolysis inhibition impaired SGIV replication. Furthermore, inhibition of mTOR signaling blocked SGIV-induced glycolytic activation and attenuated SGIV replication, suggesting mTOR signaling involve the glycolytic activation during SGIV replication. Thus, our study provides new insights into understanding the underlying molecular mechanism of glucose metabolism during SGIV infection, which was critical to the development novel therapeutic strategies to restrain viral replication and may provide new insights for preventing viral infection of fish.

DATA AVAILABILITY STATEMENT

The data presented in the study are deposited in the NCBI public repository under accession number PRJNA804746.

ETHICS STATEMENT

The animal study protocol was approved by the Ethics Committee of Experimental Animals, South China Agricultural University (protocol code 2020g009, 2020.9.8).

AUTHOR CONTRIBUTIONS

XG performed the experiments, analyzed the data, and drafted the manuscript. QZ and ZP participated in the qPCR experiments. YH contributed experimental suggestions. QQ and XH designed the experiments and reviewed the manuscript. All authors read and approved the final manuscript.

FUNDING

This work was supported by grants from the National Natural Science Foundation of China (31930115), the National Key R&D Program of China (2018YFD0900500), and the China Agriculture Research System of MOF and MARA (CARS-47-G16).

SUPPLEMENTARY MATERIAL

The Supplementary Material for this article can be found online at: https://www.frontiersin.org/articles/10.3389/fmicb.2022.827818/full#supplementary-material

Supplementary Figure 1 | The roles of glycolysis during SGIV replication. **(A,D)** The cytotoxicity of 2DG and DCA on ELHK cells, respectively. **(B,E)** Virus protein level reduced after 2DG treatment and increased after DCA treatment. The level of SGIV-MCP was detected by western blot, and β-tubulin was used as the internal control. **(C,F)** Virus production of SGIV was evaluated. ELHK cells incubated with indicated concentration 2DG and DCA were infected with SGIV and collected at 24 h p.i. Viral titers were determined using the TCID50 method. The data are represented as mean ± SD. The significance level was defined as $*p < 0.05$.

Supplementary Figure 2 | The roles of glutamine metabolism during SGIV replication. **(A)** SGIV transcription level not affected after BPTES and EGCG treatment quantified by qRT-PCR. **(B)** Virus protein level not affected after BPTES and EGCG treatment. The level of SGIV-MCP was detected by western blot, and β-tubulin was used as the internal control. **(C)** Virus production of SGIV was evaluated. EAGS cells incubated with indicated concentration BPTES and EGCG were infected with SGIV and collected at 24 h p.i. Viral titers were determined using the TCID50 method. The data are represented as mean ± SD. The significance level was defined as $*p < 0.05$.

REFERENCES

Adeva-Andany, M. M., Perez-Felpete, N., Fernandez-Fernandez, C., Donapetry-Garcia, C., and Pazos-Garcia, C. (2016). Liver glucose metabolism in humans. *Biosci. Rep.* 36:BSR20160385. doi: 10.1042/BSR20160385

Asim, M., Jiang, S., Yi, L., Chen, W., Sun, L., Zhao, L., et al. (2017). Glutamine is required for red-spotted grouper nervous necrosis virus replication via replenishing the tricarboxylic acid cycle. *Virus Res.* 227, 245–248. doi: 10.1016/j.virusres.2016.11.007

Chi, P. I., Huang, W. R., Chiu, H. C., Li, J. Y., Nielsen, B. L., and Liu, H. J. (2018). Avian reovirus sigmaA-modulated suppression of lactate dehydrogenase and upregulation of glutaminolysis and the mTOC1/eIF4E/HIF-1alpha pathway to enhance glycolysis and the TCA cycle for virus replication. *Cell Microbiol.* 20:e12946. doi: 10.1111/cmi.12946

Chinchar, V. G., Waltzek, T. B., and Subramaniam, K. (2017). Ranaviruses and other members of the family Iridoviridae: Their place in the virosphere. *Virology* 511, 259–271. doi: 10.1016/j.virol.2017.06.007

DeBerardinis, R. J., Mancuso, A., Daikhin, E., Nissim, I., Yudkoff, M., Wehrli, S., et al. (2007). Beyond aerobic glycolysis: transformed cells can engage in glutamine metabolism that exceeds the requirement for protein and nucleotide synthesis. *Proc. Natl. Acad. Sci. U S A.* 104, 19345–19350. doi: 10.1073/pnas.0709747104

Deberardinis, R. J., Sayed, N., Ditsworth, D., and Thompson, C. B. (2008). Brick by brick: metabolism and tumor cell growth. *Curr. Opin. Genet. Dev.* 18, 54–61. doi: 10.1016/j.gde.2008.02.003

Delgado, T., Carroll, P. A., Punjabi, A. S., Margineantu, D., Hockenbery, D. M., and Lagunoff, M. (2010). Induction of the Warburg effect by Kaposi's sarcoma herpesvirus is required for the maintenance of latently infected endothelial cells. *Proc. Natl. Acad. Sci. U S A.* 107, 10696–10701. doi: 10.1073/pnas.1004882107

Delgado, T., Sanchez, E. L., Camarda, R., and Lagunoff, M. (2012). Global metabolic profiling of infection by an oncogenic virus: KSHV induces and requires lipogenesis for survival of latent infection. *PLoS Pathog.* 8:e1002866. doi: 10.1371/journal.ppat.1002866

Diamond, D. L., Syder, A. J., Jacobs, J. M., Sorensen, C. M., Walters, K. A., Proll, S. C., et al. (2010). Temporal proteome and lipidome profiles reveal hepatitis C virus-associated reprogramming of hepatocellular metabolism and bioenergetics. *PLoS Pathog.* 6:e1000719. doi: 10.1371/journal.ppat.1000719

Dukhande, V. V., Sharma, G. C., Lai, J. C., and Farahani, R. (2011). Chronic hypoxia-induced alterations of key enzymes of glucose oxidative metabolism in developing mouse liver are mTOR dependent. *Mol. Cell Biochem.* 357, 189–197. doi: 10.1007/s11010-011-0889-z

Duvel, K., Yecies, J. L., Menon, S., Raman, P., Lipovsky, A. I., Souza, A. L., et al. (2010). Activation of a metabolic gene regulatory network downstream of mTOR complex 1. *Mol. Cell* 39, 171–183. doi: 10.1016/j.molcel.2010.06.022

Fontaine, K. A., Camarda, R., and Lagunoff, M. (2014). Vaccinia virus requires glutamine but not glucose for efficient replication. *J. Virol.* 88, 4366–4374. doi: 10.1128/JVI.03134-13

Fontaine, K. A., Sanchez, E. L., Camarda, R., and Lagunoff, M. (2015). Dengue virus induces and requires glycolysis for optimal replication. *J. Virol.* 89, 2358–2366. doi: 10.1128/JVI.02309-14

Forsberg, B. O., Aibara, S., Howard, R. J., Mortezaei, N., and Lindahl, E. (2020). Arrangement and symmetry of the fungal E3BP-containing core of the pyruvate dehydrogenase complex. *Nat. Commun.* 11:4667. doi: 10.1038/s41467-020-18401-z

Fu, X., Hu, X., Li, N., Zheng, F., Dong, X., Duan, J., et al. (2017). Glutamine and glutaminolysis are required for efficient replication of infectious spleen and kidney necrosis virus in Chinese perch brain cells. *Oncotarget* 8, 2400–2412. doi: 10.18632/oncotarget.13681

Gershon, T. R., Crowther, A. J., Tikunov, A., Garcia, I., Annis, R., Yuan, H., et al. (2013). Hexokinase-2-mediated aerobic glycolysis is integral to cerebellar neurogenesis and pathogenesis of medulloblastoma. *Cancer Metab.* 1:2. doi: 10.1186/2049-3002-1-2

Gibson-Kueh, S., Netto, P., Ngoh-Lim, G. H., Chang, S. F., Ho, L. L., Qin, Q. W., et al. (2003). The pathology of systemic iridoviral disease in fish. *J. Comparat. Pathol.* 129, 111–119. doi: 10.1016/S0021-9975(03)00010-0

Goodwin, C. M., Xu, S., and Munger, J. (2015). Stealing the Keys to the Kitchen: Viral Manipulation of the Host Cell Metabolic Network. *Trends Microbiol.* 23, 789–798. doi: 10.1016/j.tim.2015.08.007

Guo, X., Wu, S., Li, N., Lin, Q., Liu, L., Liang, H., et al. (2019). Accelerated Metabolite Levels of Aerobic Glycolysis and the Pentose Phosphate Pathway Are Required for Efficient Replication of Infectious Spleen and Kidney Necrosis Virus in Chinese Perch Brain Cells. *Biomolecules* 9:biom9090440. doi: 10.3390/biom9090440

He, S. T., Lee, D. Y., Tung, C. Y., Li, C. Y., and Wang, H. C. (2019). Glutamine Metabolism in Both the Oxidative and Reductive Directions Is Triggered in Shrimp Immune Cells (Hemocytes) at the WSSV Genome Replication Stage to Benefit Virus Replication. *Front. Immunol.* 10:2102. doi: 10.3389/fimmu.2019.02102

Hollenbaugh, J. A., Munger, J., and Kim, B. (2011). Metabolite profiles of human immunodeficiency virus infected CD4+ T cells and macrophages using LC-MS/MS analysis. *Virology* 415, 153–159. doi: 10.1016/j.virol.2011.04.007

Huang, X., Huang, Y., OuYang, Z., Cai, J., Yan, Y., and Qin, Q. (2011a). Roles of stress-activated protein kinases in the replication of Singapore grouper iridovirus and regulation of the inflammatory responses in grouper cells. *J. Gen. Virol.* 92, 1292–1301. doi: 10.1099/vir.0.029173-0

Huang, X., Huang, Y., Ouyang, Z., Xu, L., Yan, Y., Cui, H., et al. (2011b). Singapore grouper iridovirus, a large DNA virus, induces nonapoptotic cell death by a cell type dependent fashion and evokes ERK signaling. *Apoptosis* 16, 831–845. doi: 10.1007/s10495-011-0616-y

Huang, X., Huang, Y., Sun, J., Han, X., and Qin, Q. (2009). Characterization of two grouper Epinephelus akaara cell lines: Application to studies of Singapore grouper iridovirus (SGIV) propagation and virus–host interaction. *Aquaculture* 292, 172–179. doi: 10.1016/j.aquaculture.2009.04.019

Kennedy, B. E., Murphy, J. P., Clements, D. R., Konda, P., Holay, N., Kim, Y., et al. (2019). Inhibition of Pyruvate Dehydrogenase Kinase Enhances the Antitumor Efficacy of Oncolytic Reovirus. *Cancer Res.* 79, 3824–3836. doi: 10.1158/0008-5472.CAN-18-2414

Li, C., Wang, L., Liu, J., Yu, Y., Huang, Y., Huang, X., et al. (2020). Singapore Grouper Iridovirus (SGIV) Inhibited Autophagy for Efficient Viral Replication. *Front. Microbiol.* 11:1446. doi: 10.3389/fmicb.2020.01446

Liu, C., Chapman, N. M., Karmaus, P. W., Zeng, H., and Chi, H. (2015). mTOR and metabolic regulation of conventional and regulatory T cells. *J. Leukoc Biol.* 97, 837–847. doi: 10.1189/jlb.2RI0814-408R

Liu, Z., Zhang, X., Zhang, Y., Qin, Q., Huang, X., and Huang, Y. (2021). Establishment of a cell line from the head kidney of giant grouper (Epinephelus lanceolatus) and its susceptibility to fish viruses. *Aquacult. Rep.* 21:100899. doi: 10.1016/j.aqrep.2021.100899

Lyu, X., Wang, J., Guo, X., Wu, G., Jiao, Y., Faleti, O. D., et al. (2018). EBV-miR-BART1-5P activates AMPK/mTOR/HIF1 pathway via a PTEN independent manner to promote glycolysis and angiogenesis in nasopharyngeal carcinoma. *PLoS Pathog.* 14:e1007484. doi: 10.1371/journal.ppat.1007484

Manel, N., Kim, F. J., Kinet, S., Taylor, N., Sitbon, M., and Battini, J. L. (2003). The ubiquitous glucose transporter GLUT-1 is a receptor for HTLV. *Cell* 115, 449–459. doi: 10.1016/S0092-8674(03)00881-X

Mori, H., Inoki, K., Munzberg, H., Opland, D., Faouzi, M., Villanueva, E. C., et al. (2009). Critical role for hypothalamic mTOR activity in energy balance. *Cell Metab.* 9, 362–374. doi: 10.1016/j.cmet.2009.03.005

Mueckler, M., and Thorens, B. (2013). The SLC2 (GLUT) family of membrane transporters. *Mol. Aspects Med.* 34, 121–138. doi: 10.1016/j.mam.2012.07.001

Munger, J., Bajad, S. U., Coller, H. A., Shenk, T., and Rabinowitz, J. D. (2006). Dynamics of the cellular metabolome during human cytomegalovirus infection. *PLoS Pathog.* 2:e132. doi: 10.1371/journal.ppat.0020132

Munger, J., Bennett, B. D., Parikh, A., Feng, X. J., McArdle, J., Rabitz, H. A., et al. (2008). Systems-level metabolic flux profiling identifies fatty acid synthesis as a target for antiviral therapy. *Nature Biotechnol.* 26, 1179–1186. doi: 10.1038/nbt.1500

Mushtaq, M., Darekar, S., and Kashuba, E. (2016). DNA Tumor Viruses and Cell Metabolism. *Oxid. Med. Cell Longev.* 2016:6468342. doi: 10.1155/2016/6468342

Qin, Q. W., Chang, S. F., Ngoh-Lim, G. H., Gibson-Kueh, S., Shi, C., and Lam, T. J. (2003). Characterization of a novel ranavirus isolated from grouper Epinephelus tauvina. *Dis. Aquat. Organ.* 53, 1–9. doi: 10.3354/dao053001

Qin, Q. W., Lam, T. J., Sin, Y. M., Shen, H., Chang, S. F., Ngoh, G. H., et al. (2001). Electron microscopic observations of a marine fish iridovirus isolated from brown-spotted grouper, Epinephelus tauvina. *J. Virol. Methods* 98, 17–24. doi: 10.1016/s0166-0934(01)00350-0

Rabinowitz, J. D., Purdy, J. G., Vastag, L., Shenk, T., and Koyuncu, E. (2011). Metabolomics in drug target discovery. *Cold Spring Harb. Symp. Quant. Biol.* 76, 235–246. doi: 10.1101/sqb.2011.76.010694

Ramiere, C., Rodriguez, J., Enache, L. S., Lotteau, V., Andre, P., and Diaz, O. (2014). Activity of hexokinase is increased by its interaction with hepatitis C virus protein NS5A. *J. Virol.* 88, 3246–3254. doi: 10.1128/JVI.02862-13

Reed, L. J., and Muench, H. (1938). A SIMPLE METHOD OF ESTIMATING FIFTY PER CENT ENDPOINTS. *Am. J. Epidemiol.* 27, 493–497. doi: 10.1016/j.jviromet.2005.05.005

Ritter, J. B., Wahl, A. S., Freund, S., Genzel, Y., and Reichl, U. (2010). Metabolic effects of influenza virus infection in cultured animal cells: Intra- and extracellular metabolite profiling. *BMC Syst. Biol.* 4:61. doi: 10.1186/1752-0509-4-61

Roe, B., Kensicki, E., Mohney, R., and Hall, W. W. (2011). Metabolomic profile of hepatitis C virus-infected hepatocytes. *PLoS One* 6:e23641. doi: 10.1371/journal.pone.0023641

Shinmoto, H., Taniguchi, K., Ikawa, T., Kawai, K., and Oshima, S. (2009). Phenotypic diversity of infectious red sea bream iridovirus isolates from cultured fish in Japan. *Appl. Environ. Microbiol.* 75, 3535–3541. doi: 10.1128/AEM.02255-08

Su, M. A., Huang, Y. T., Chen, I. T., Lee, D. Y., Hsieh, Y. C., Li, C. Y., et al. (2014). An invertebrate Warburg effect: a shrimp virus achieves successful replication by altering the host metabolome via the PI3K-Akt-mTOR pathway. *PLoS Pathog.* 10:e1004196. doi: 10.1371/journal.ppat.1004196

Vastag, L., Koyuncu, E., Grady, S. L., Shenk, T. E., and Rabinowitz, J. D. (2011). Divergent effects of human cytomegalovirus and herpes simplex virus-1 on cellular metabolism. *PLoS Pathog.* 7:e1002124. doi: 10.1371/journal.ppat.1002124

Wise, D. R., DeBerardinis, R. J., Mancuso, A., Sayed, N., Zhang, X. Y., Pfeiffer, H. K., et al. (2008). Myc regulates a transcriptional program that stimulates mitochondrial glutaminolysis and leads to glutamine addiction. *Proc. Natl. Acad. Sci. U S A.* 105, 18782–18787. doi: 10.1073/pnas.0810199105

Wolf, A. J., Reyes, C. N., Liang, W., Becker, C., Shimada, K., Wheeler, M. L., et al. (2016). Hexokinase Is an Innate Immune Receptor for the Detection of Bacterial Peptidoglycan. *Cell* 166, 624–636. doi: 10.1016/j.cell.2016.05.076

Wolf, A., Agnihotri, S., Micallef, J., Mukherjee, J., Sabha, N., Cairns, R., et al. (2011). Hexokinase 2 is a key mediator of aerobic glycolysis and promotes tumor growth in human glioblastoma multiforme. *J. Exp. Med.* 208, 313–326. doi: 10.1084/jem.20101470

Wu, Z., Jia, J., Xu, X., Xu, M., Peng, G., Ma, J., et al. (2020). Human herpesvirus 6A promotes glycolysis in infected T cells by activation of mTOR signaling. *PLoS Pathog.* 16:e1008568. doi: 10.1371/journal.ppat.1008568

Xiao, L., Hu, Z. Y., Dong, X., Tan, Z., Li, W., Tang, M., et al. (2014). Targeting Epstein-Barr virus oncoprotein LMP1-mediated glycolysis sensitizes nasopharyngeal carcinoma to radiation therapy. *Oncogene* 33, 4568–4578. doi: 10.1038/onc.2014.32

Yogev, O., Lagos, D., Enver, T., and Boshoff, C. (2014). Kaposi's sarcoma herpesvirus microRNAs induce metabolic transformation of infected cells. *PLoS Pathog.* 10:e1004400. doi: 10.1371/journal.ppat.1004400

Yu, Y., Li, C., Liu, J., Zhu, F., Wei, S., Huang, Y., et al. (2020). Palmitic Acid Promotes Virus Replication in Fish Cell by Modulating Autophagy Flux and TBK1-IRF3/7 Pathway. *Front. Immunol.* 11:1764. doi: 10.3389/fimmu.2020.01764

Zhang, J., Jia, L., Lin, W., Yip, Y. L., Lo, K. W., Lau, V. M. Y., et al. (2017). Epstein-Barr Virus-Encoded Latent Membrane Protein 1 Upregulates Glucose Transporter 1 Transcription via the mTORC1/NF-kappaB Signaling Pathways. *J. Virol.* 91:16. doi: 10.1128/JVI.02168-16

Zheng, Q., Huang, Y., Wang, L., Zhang, Y., Guo, X., Huang, X., et al. (2022). SGIV Induced and Exploited Cellular De Novo Fatty Acid Synthesis for Virus Entry and Replication. *Viruses* 14:v14020180. doi: 10.3390/v14020180

Zhou, L., He, R., Fang, P., Li, M., Yu, H., Wang, Q., et al. (2021). Hepatitis B virus rigs the cellular metabolome to avoid innate immune recognition. *Nat. Commun.* 12:98. doi: 10.1038/s41467-020-20316-8

Conflict of Interest: The authors declare that the research was conducted in the absence of any commercial or financial relationships that could be construed as a potential conflict of interest.

Publisher's Note: All claims expressed in this article are solely those of the authors and do not necessarily represent those of their affiliated organizations, or those of the publisher, the editors and the reviewers. Any product that may be evaluated in this article, or claim that may be made by its manufacturer, is not guaranteed or endorsed by the publisher.

frontiers | Frontiers in Microbiology

REVIEW
published: 08 April 2022
doi: 10.3389/fmicb.2022.870316

The Emerging Role of Hedgehog Signaling in Viral Infections

Yulin Zhou†, Jinhua Huang†, Boxin Jin, Su He, Yongfang Dang, Tiejun Zhao and Zhigang Jin**

College of Chemistry and Life Sciences, Zhejiang Normal University, Jinhua, China

The hedgehog (HH) signaling pathway is one of the key pathways that is indispensable for many developmental processes and postnatal tissue homeostasis. Dysregulated HH signaling could lead to developmental disorders and tumorigenesis in a variety of tissues *via* inherited or sporadic mutation, gene overexpression, and crosstalk with other signaling pathways. Recently, accumulating evidence has shown that HH signaling is targeted by viruses to facilitate viral transcription, immune evasion, and uncontrolled growth, leading to effective viral replication and pathogenesis. In this study, we will summarize recent advances in functional interaction between HH signaling and different types of viruses, particularly focusing on the pathological role of HH signaling in viral infections and related diseases.

Keywords: hedgehog, GLI, virus, viral diseases, pathogenesis

OPEN ACCESS

Edited by:
Jue Liu,
Yangzhou University, China

Reviewed by:
Jian Huang,
Coriell Institute for Medical Research, United States
Zhiqiang Qin,
University of Arkansas for Medical Sciences, United States

****Correspondence:***
Tiejun Zhao
tjzhao@zjnu.cn
Zhigang Jin
zgkin@zjnu.edu.cn

† These authors have contributed equally to this work

Specialty section:
This article was submitted to Virology, a section of the journal Frontiers in Microbiology

Received: *06 February 2022*
Accepted: *07 March 2022*
Published: *08 April 2022*

Citation:
Zhou Y, Huang J, Jin B, He S, Dang Y, Zhao T and Jin Z (2022) The Emerging Role of Hedgehog Signaling in Viral Infections. Front. Microbiol. 13:870316. doi: 10.3389/fmicb.2022.870316

HEDGEHOG SIGNALING PATHWAY

The Components of Hedgehog Signaling

Hedgehog (HH), originally named after the spiny appearance of the cuticle in the *Drosophila* mutant, was discovered as a segment polarity gene that governs segmental pattern along with other components of HH signaling (Nüsslein-Volhard and Wieschaus, 1980). Since then, numerous and rapid progress has been made in realizing the significance of HH signaling to a variety of processes during embryonic development, such as wing development in *Drosophila*, limb development, and neural patterning in vertebrates (Jiang and Hui, 2008; Briscoe and Thérond, 2013; Pak and Segal, 2016; Liu, 2019). The signaling mechanism is evolutionarily conserved ranging from *Drosophila* to human, although some divergences do exist between invertebrate and vertebrate, largely due to gene duplication-caused functional redundancy and extreme reliance on primary cilium as a signaling hub and suppressor of fused (SUFU) as a major repressor in vertebrate (Huangfu and Anderson, 2006; Varjosalo et al., 2006; Kuzhandaivel et al., 2014). The HH gene family encodes secreted proteins that undergo processing, release, spread, and reception, transducing signaling from HH-producing cells to HH-responding cells (Gallet, 2011). HH proteins are usually locally produced and form a concentration gradient that induces differential expression of HH target genes and directs tissue patterning. In mammals, three HH gene homologs have been identified, namely, sonic HH (SHH), Indian HH (IHH), and desert HH (DHH). SHH is broadly expressed and essential for the development of most regions in embryos, including limb and neural tube. IHH is more close to SHH and essential for the development of endochondral bone, whereas DHH regulates gonad development and myelination of peripheral nerves.

In vertebrates, the HH protein family triggers a signaling cascade that leads to alteration of the net balance between the activator form (GLI^A) and the repressor form (GLI^R) of the GLI family

of zinc finger transcription factors, and ultimately regulates the specific expression of GLI^A/GLI^R target genes that defines cell identity (Jiang and Hui, 2008; Briscoe and Thérond, 2013; Pak and Segal, 2016; Liu, 2019). The twelve-span transmembrane protein, Patched 1 (PTCH1), is the major receptor of HH ligands that constitutively represses HH signaling. Smoothened (SMO) is a G protein-coupled receptor (GPCR)-like seven-span transmembrane co-receptor. However, SMO is a potent activator of the HH signaling pathway rather than the GPCR-related signaling pathway. The GLI family transcription factors, including GLI1, GLI2, and GLI3, serve as downstream effectors. GLI2 and GLI3 (GLI2/3) could either activate or suppress the transcription of HH target genes, depending on their GLI^A or GLI^R forms. In contrast, GLI1 serves as a transcriptional activator only and could be transcriptionally activated by HH signaling, forming a positive feedback to consolidate signaling strength and duration. SUFU is a major negative regulator of HH signaling in a vertebrate that functions between SMO and GLI proteins, mainly *via* sequestering GLI proteins in the cytoplasm and repressing transcriptional activity of GLI protein in the nucleus.

Hedgehog Signal Transduction

In the absence of HH ligands, PTCH1 is accumulated in the primary cilium where PTCH1 blocks SMO activity by preventing the translocation of SMO to primary cilium. In this condition, full-length GLI2/3 are retained in the cytoplasm by SUFU (**Figure 1**). Protein kinase A (PKA), casein kinases 1 (CK1), and glycogen synthase kinase 3 (GSK3) preferentially phosphorylate GLI2/3 when they exist as GLI2/3-SUFU complex. Hyperphosphorylated GLI2/3 are recognized by E3 ubiquitin ligase β-transducin repeat-containing protein (β-TrCP), resulting in proteolytic processing by the removal of C-terminal transactivation domain and conversion to the repressor form GLI^R. Proteolytic processing of GLI2/3 is dependent on primary cilium as PKA is highly enriched in the base of primary cilium, which prime phosphorylation of GLI2/3 by GSK3 (Nozawa et al., 2013; Bangs and Anderson, 2017). Finally, GLI^R enters the nucleus and suppresses the transcription of target genes. Alternatively, full-length GLI proteins could also be targeted for complete degradation *via* the ubiquitin-proteasome pathway, which accounts for the labile property of GLI proteins (Huntzicker et al., 2006; Wang et al., 2010; Liu, 2019).

In the presence of HH ligands, PTCH1 is internalized for degradation after binding to HH ligands, which derepresses SMO (**Figure 1**). SMO is phosphorylated by CK1 and G-protein-coupled receptor kinase 2 (GRK2) (Chen et al., 2011). Phosphorylated SMO translocates to primary cilium where SMO is activated. SMO is also activated by cholesterol modification in response to HH (Xiao et al., 2017). Active SMO inhibits PKA-mediated phosphorylation and proteolytic processing of GLI2/3. However, prevention of GLI^R production alone is insufficient to fully activate HH signaling. Active SMO further promotes the recruitment of GLI2/3-SUFU complex to the tip of the primary cilium, where GLI2/3 are dissociated from SUFU and converted into the activator to form GLI^A *via* unknown modification. Although the precise signaling between SMO and GLI2/3 remains largely unclear, studies have shown that phosphorylated SMO forms a complex with two ciliary proteins, Ellis-van Creveld (EVC)/EVC2 upon HH stimulation. EVC/EVC2 activates HH signaling downstream of SMO by facilitating cilia localization of GLI2/3-SUFU complex (Dorn et al., 2012; Yang et al., 2012). Therefore, SMO simultaneously relieves the repression of GLI protein by PKA and SUFU, leading to a switch from GLI^R to GLI^A. Finally, GLI^A enters the nucleus as transcription activators to promote the transcription of target genes, including *GLI1*, *PTCH1*, *MYC*, *Cyclin D1*, and *BCL2*. Meanwhile, GLI^A becomes very labile due to Speckle-type POZ protein (SPOP)-mediated degradation, which might be responsible for the termination of HH signaling (Wang et al., 2010; Shi et al., 2014).

A list of novel components of HH signaling that function in a general or context-dependent manner is continuously growing, such as G protein-coupled receptor 161 (GPR161), inositol polyphosphate 5-phosphatase E (INPP5E), and karyopherin β2 (KAPβ2), SLIT and NTRK-like protein-5 (SLITRK5) (Mukhopadhyay et al., 2013; Garcia-Gonzalo et al., 2015; Han et al., 2017; Sun et al., 2021). We have also found that Daz interacting protein 1 (Dzip1) and RUN and SH3 domain-containing 2 (Rusc2) are involved in the regulation of HH signaling and are required for proper eye development in *Xenopus* (Jin et al., 2011, 2016; Schwend et al., 2013). In addition to the canonical HH signaling, non-canonical HH signaling that GLI proteins are cross-activated by other signaling pathways independent of HH ligands or SMO may also occur, especially in pathological conditions (Pietrobono et al., 2019; Sigafoos et al., 2021).

THE ROLE OF HEDGEHOG SIGNALING

The Physiological Role of Hedgehog Signaling

Owing to the diverse sets of target genes, HH signaling is involved in the control of many cellular responses, including cell proliferation, differentiation, and survival (Jiang and Hui, 2008; Briscoe and Thérond, 2013; Pak and Segal, 2016; Liu, 2019). For example, a concentration gradient of HH in the developing neural tube regulates neural patterning through transcriptional activation of *NK6 homeobox 1* (*NKX6.1*), *oligodendrocyte transcription factor 2* (*OLIG2*), and *NKX2.2*. HH signaling is required for the maintenance of stem or progenitor cells in embryonic and adult tissues *via* targeting cell cycle genes *MYC* and *Cyclin D1* and stemness-associated gene *NANOG* and *SOX2* (Ahn and Joyner, 2005; Po et al., 2010; Briscoe and Thérond, 2013; Iriana et al., 2021). HH signaling promotes cell survival *via* targeting the anti-apoptotic gene *BCL2* (Bigelow et al., 2004). In addition, HH signaling maintains the integrity and function of the blood-brain barrier (BBB) *via* its effector *Netrin-1* (Alvarez et al., 2011; Podjaski et al., 2015). As HH signaling is substantially involved in embryonic development and adult tissue homeostasis, it must be under tight control. Not surprisingly,

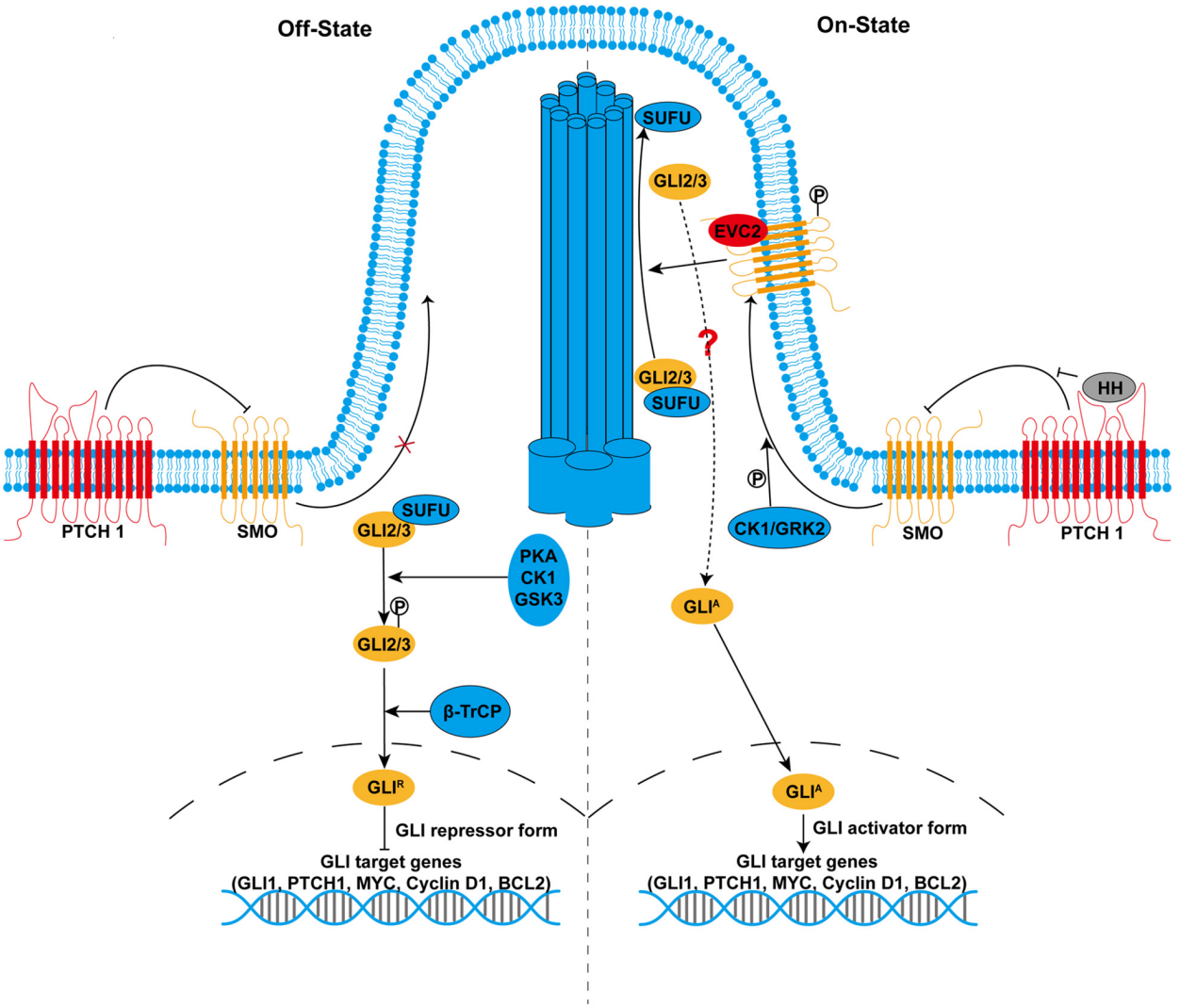

FIGURE 1 | The hedgehog (HH) signaling pathway in mammals. In the absence of HH ligands **(left side)**, smoothened (SMO) is inhibited by primary cilium-localized Patched 1 (PTCH1). With the inactivated SMO, full-length GLI2 and GLI3 (GLI2/3) are retained in the cytoplasm by suppressor of fused (SUFU) and phosphorylated by protein kinase A (PKA), casein kinases 1 (CK1), and glycogen synthase kinase 3 (GSK3). Phosphorylated GLI2/3 are proteolytically processed by E3 ubiquitin ligase β-transducin repeat-containing protein, resulting in the production of the repressor form GLI^R, which enters the nucleus to suppress the transcription of target genes. In the presence of HH ligands **(right side)**, binding of HH to PTCH1 derepresses SMO. SMO is phosphorylated by CK1 and GRK2 and translocates to the primary cilium. Activated SMO not only inhibits proteolytic processing of GLI2/3 but also promotes the recruitment of GLI2/3-SUFU complex to the tip of the primary cilium, leading to their dissociation and production of the activator form GLI^A, a process that might involve Ellis-van Creveld/EVC2. GLI^A enters the nucleus as transcription activators and promotes the transcription of target genes that are important for many cellular processes, including cell proliferation, differentiation, survival, and maintenance of stemness.

aberrant HH signaling caused by genetic or somatic mutations and abnormal expression of HH-related proteins is closely associated with a lot of human diseases, such as developmental disorders and cancer.

Dysregulated Hedgehog Signaling in Developmental Disorders

Dysregulated HH signaling is responsible for many types of developmental disorders. Holoprosencephaly, a common birth defect characterized by incomplete division of the forebrain into two hemispheres, is usually caused by reduced HH signaling due to deletion or mutation in *SHH* and downstream genes (Nieuwenhuis and Hui, 2005; Loo et al., 2021). Compromised HH signaling impairs the eye separation process and induces cyclopia as seen in severe cases of holoprosencephaly, whereas increased HH signaling reduces the eye size (Lee et al., 2014; Jin et al., 2016). Consistently with its important role in limb development, GLI3 is a causative gene mutated in Greig cephalopolysyndactyly syndrome that is characterized by limb defects. Mutations in ciliary genes that affect the proper structure and function of primary or motile cilium could elicit a group of genetic

disorders known as ciliopathies, such as Bardet-Biedl syndrome, Joubert syndrome, and Meckel-Gruber syndrome (Andreu-Cervera et al., 2021; Loo et al., 2021). Since primary cilium is a necessary signaling hub to integrate HH signaling cascade, disruption of HH signaling also underlies the pathogenesis of ciliopathies.

Dysregulated Hedgehog Signaling in Cancer

The relationship between HH signaling and cancer was initially discovered in nevoid basal cell carcinoma syndrome (NBCCS, also known as Gorlin syndrome), a rare developmental disorder that is prone to develop into BCC and medulloblastoma (Hahn et al., 1996). The most common causes of NBCCS are loss-of-function mutations in two repressors of HH signaling, *PTCH1,* and *SUFU*, leading to constitutive activation of HH signaling (Onodera et al., 2020). Elevated HH signaling is a hallmark of many types of human cancer, including BCC and medulloblastoma (Pak and Segal, 2016; Wu et al., 2017; Sigafoos et al., 2021). Loss-of-function mutations in PTCH, SUFU, and gain-of-function mutations in SMO are usually found in the patients of BCC and medulloblastomas. These mutations aberrantly activate HH signaling bypassing HH ligands and the tight regulation of signaling cascade.

In contrast, ligand-dependent activation of HH signaling usually occurs in other types of cancer that rarely contain oncogenic mutations, such as prostate cancer, gastric cancer, and gliomas. In these conditions, elevated HH signaling supports the proliferation and survival of cancer cells in an autocrine way where cancer cells act as both HH-producing and HH-responding cells. Alternatively, a pathway is activated in a paracrine way where HH ligands secreted by cancer-surrounding stromal cells stimulate HH signaling in cancer cells, or HH ligands secreted by cancer cells stimulate HH signaling in stromal cells which in turn release cancer-supporting signals (Pak and Segal, 2016; Wu et al., 2017; Sigafoos et al., 2021). HH signaling also drives cancer initiation and progression by the maintenance of cancer stem cells in an undifferentiated and proliferative state (Cochrane et al., 2015).

HEDGEHOG SIGNALING AND IMMUNOMODULATION

Consistent with the important role of HH signaling in development and homeostasis, selective populations of immature thymocytes and peripheral mature T cells are responsive to HH ligands, and activation of HH signaling is required for fetal and adult T-cell development and peripheral T-cell activation (Crompton et al., 2007; de la Roche et al., 2013). In contrast, HH signaling promotes central nervous system (CNS) immune quiescence by counterbalancing inflammatory events (Alvarez et al., 2011). Thus, HH signaling positively or negatively influences immune response in a context-dependent manner. In recent years, numerous studies have emerged that HH signaling is involved in the evasion of anticancer and antiviral immune response in cancer cells and virus-infected cells, respectively (Hanna and Shevde, 2016; Iriana et al., 2021). It appears that most pathological conditions preferentially switch the outcome of HH signaling toward the suppression of host immunity, especially in cancer and virus-related diseases.

Using T-cell-specific GLI2 transgenic mice, Furmanski et al. (2015) demonstrated that transcription activated by $GLI2^A$ in T cells attenuates T-cell signaling and T-cell activation induced by T-cell receptor (TCR) stimulation. $GLI2^A$ impairs the activation of pro-inflammatory AP-1 and NF-κB signaling. In contrast, $GLI2^R$-mediated transcription repression increases NF-κB activity following TCR stimulation. Thus, HH signaling might skew pro-inflammatory immune responses during inflammation and tissue repair. Indeed, activation of HH signaling increases $CD4^+$ regulatory T-cells (Treg) populations and their immunosuppressive function by activating transforming growth factor-β (TGF-β) production, thereby preventing skin inflammation in the mouse model of atopic dermatitis (Papaioannou et al., 2019). Studies in SMO conditional knockout mice have shown that HH signaling deficiency in $CD4^+$ T cells exacerbates brain-brainstem-cerebellum neuroinflammation (Benallegue et al., 2021). Mechanistically, HH signaling antagonizes $CD4^+$ T-cells-driven neuroinflammation by limiting their production of inflammatory cytokines at the transcriptome level. Notably, intestinal epithelium-derived IHH signals to the stromal cells and maintains immune tolerance of the intestine through suppression of stromal C-X-C motif chemokine ligand 12 (CXCL12), whereas loss of IHH induces a rapid immune response characterized by upregulation of stromal CXCL12 and filtration of immune cells (Westendorp et al., 2018). In the context of the tumor microenvironment, tumor-derived SHH executes immunosuppressive and tumor-supporting functions by promoting Krüppel-like factor 4 (KLF4)-mediated polarization of M2 tumor-associated macrophages (TAMs) and upregulation of PD-L1 expression in TAMs (Petty et al., 2019, 2021). In BCC and medulloblastoma, GLI1 and GLI2 (GLI1/2) directly activate the transcription of suppressor of cytokine signaling 1 (SOCS1) and reduce signal transducer and activator of transcription 1 (STAT1) phosphorylation, imposing a negative effect on Interferon (IFN)-γ/STAT1 signaling and anticancer immunity (Laner-Plamberger et al., 2013). Collectively, HH signaling is deployed by a subset of immune cells and cancer cells to suppress host immunity by expanding Treg population, interfering with immune signaling, and production of cytokines or chemokines.

As HH signaling is substantially involved in cell proliferation, survival, and immunomodulation, it becomes a preferred target for a variety of viruses to evade antiviral immunity and support viral life cycles (**Figure 2**). In most virus-related cancers, HH signaling is abnormally activated by viral proteins to drive the tumor initiation process and metastatic cascade (Hanna and Shevde, 2016; Iriana et al., 2021; Trivedi et al., 2021). Inspired by the elegant review of Smelkinson that sheds light on HH signaling as a pathogenic target (Smelkinson, 2017), in the following sections, we will overview the recent progress on the functional interaction between HH signaling and viruses, in the order of virus types.

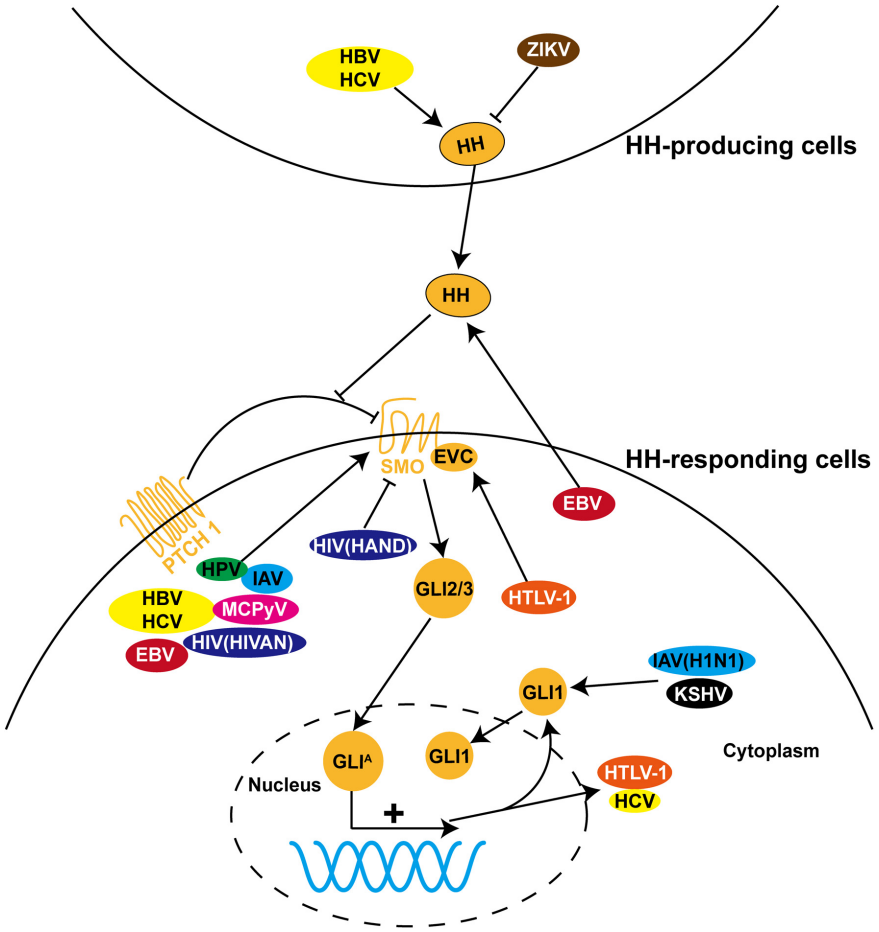

FIGURE 2 | The role of HH signaling in viral infections. HH pathway is dysregulated during infection with a variety of viruses, including hepatitis B virus (HBV), hepatitis C virus (HCV), Epstein-Barr virus (EBV), human papillomavirus (HPV), human immunodeficiency virus (HIV), human T-cell leukemia virus type I (HTLV-1), influenza A virus (IAV), Merkel cell polyomavirus (MCPyV), Zika virus (ZIKV), and Kaposi's sarcoma-associated herpesvirus (KSHV). Most of these viruses induce pathological processes by regulating the expression, protein stability, and subcellular localization of GLI proteins and other components of HH signaling in HH-responding cells. In contrast, dysregulation of HH signaling is triggered in HH-producing cells by ZIKV and in both cells by HBV and HCV. In addition, HTLV-1 and HCV employ HH signaling to facilitate viral transcription and replication.

HEDGEHOG SIGNALING IN VIRAL INFECTIONS

Hepatitis Viruses

Hepatocellular carcinoma (HCC) is one of the leading causes of cancer deaths. About 80% of HCC incidence is associated with chronic infection of hepatitis B virus (HBV) and hepatitis C virus (HCV) (Arzumanyan et al., 2013). HH signaling is maintained at low activity in normal mature hepatocytes but re-activated in the liver of patients with HCC, as illustrated by elevated levels of SHH, SMO, GLI2, and HH target genes in HCC tissues compared to the adjacent normal tissues (Huang et al., 2006; Sicklick et al., 2006; Crompton et al., 2007; Pereira Tde et al., 2010). Chronic infection of HBV or HCV increases the hepatic production of SHH and IHH. Accordingly, the populations of HH-responding cells, including liver myofibroblasts and activated endothelial cells, are expanded, which promotes liver fibrosis and HCC (Pereira Tde et al., 2010). In addition, the expression of SMO directly correlates with HCC tumor size (Sicklick et al., 2006). Virus-induced activation of HH signaling contributes to multiple aspects during the pathogenesis of HCC, including maintenance of cancer stem cells, initiation of epithelial-mesenchymal transition (EMT), metastasis, and drug resistance (Dimri and Satyanarayana, 2020; Zhou et al., 2020; Ding et al., 2021).

As a major cause of HCC, HBV is a small, double-stranded DNA virus but similar to retroviruses in the viral life cycle and genome organization. Integration of viral DNA into the host genome is an important step during the pathogenesis of HBV-induced HCC. HBV integrations are more abundant in HCC tissues than in adjacent normal tissues and HBV integration-targeted genes are significantly enriched in the HH signaling pathway (Yang et al., 2018). However, the effect of HBV integrations on HH signaling and its pathological significance remain to be determined.

HBV-encoded X protein (HBx) is a central pathogenic factor in HCC, which plays an indispensable role in signal transduction, cell cycle progress, protein degradation, apoptosis, and genetic stability (Arzumanyan et al., 2013). Further investigation revealed that HBx accounts for HBV-induced activation of HH signaling. HBx promotes protein stability and nuclear translocation of GLI1/2 by direct protein-protein interaction, concomitant with increased transcriptional activity of GLI1/2 (Kim et al., 2011). HBx expression causes upregulation of HH activity in the liver of patients with HCC infected with HBV and develops HCC phenotypes in HBx transgenic mice (Arzumanyan et al., 2012). Moreover, inhibition of HH signaling by treatment with SMO inhibitor GDC-0449 attenuates cell growth and migration in HCC cell lines and delays tumor development in HBx transgenic mice and xenograft-bearing nude mice. In contrast, GDC-0449 merely affects tumor growth in the nude mice bearing HBx negative HCC cells. Taken together, these findings demonstrate that HBV-mediated pro-tumor function is dependent on HBx-induced activation of HH signaling.

HCV is another leading cause of liver fibrosis and HCC. Unlike HBV, HCV is a positive sense, single-stranded RNA virus. Infection of hepatocytes with HCV significantly increases the expression of SHH mRNA (Pereira Tde et al., 2010). HCV-permissive Huh7.5 HCC cells exhibit enhanced HH activity and mesenchymal identity as compared to parental Huh7 cells that are less permissive for HCV replication (Choi et al., 2011). Interestingly, HCV replication is facilitated in Huh7 cells treated with SHH ligand and SMO agonist SAG, whereas HCV replication is compromised in Huh7.5 cells treated with SMO inhibitor cyclopamine and GDC-0449. In addition, sera of HCV-infected patients increase GLI2 expression and its nuclear accumulation, leading to pro-fibrotic effects, which are antagonized by GLI 1/2 inhibitor GANT 61 (Granato et al., 2016). Collectively, these studies have not only revealed the pathological significance of HH signaling in HCV-induced liver fibrosis and HCC, but also introduced HH pathway inhibitors as a potential therapeutic strategy. However, further investigation is required to address which and how viral proteins target HH signaling for activation during HCV pathogenesis.

Hepatitis D virus (HDV) is a small RNA virus that requires HBV for infection and replication (Farci et al., 2021). Compared to HBV and HCV, the pathogenic process of HDV in HCC is largely unknown. A recent study of transcriptomic profiling identified enrichment of upregulated transcripts of HH signaling pathway in HDV-associated HCC, indicating that activation of HH signaling might be a common mechanism that HBV, HCV, and HDV have evolved to drive HCC progression (Diaz et al., 2018; Farci et al., 2021).

Epstein-Barr Virus

Epstein-Barr virus (EBV) is a member of the herpesvirus family that contributes to about 1.5% of all cases of human cancer, including Hodgkin's lymphoma, nasopharyngeal carcinoma (NPC), and gastric cancer (Farrell, 2019). Dysregulation of the HH signaling pathway plays an important role in the development of EBV-related NPC. A study of microarray profiling found that the expression levels of SHH ligand and HH target genes are upregulated in EBV-infected NPC cell lines and tissues (Port et al., 2013). EBV activates HH signaling in epithelial cells through autocrine induction of SHH ligand, leading to increased expression of stemness-associated genes. This process is recapitulated by overexpression of EBV latent membrane protein 1 (LMP1) and LMP2A but blocked by treatment of GLI1/2 inhibitor GANT 58 or GANT 61, indicating that EBV drives NPC progression through LMP1- and LMP2A-mediated activation of HH signaling. Consistent with dysregulation of HH signaling in EBV infection, HH signaling was identified in the genomic mutation landscape of EBV-positive NPC (Tu et al., 2018). Computational analysis predicted 175 functional interactions between EBV proteins and the known components of HH signaling (Mei and Zhang, 2016).

Abnormal HH signaling is also associated with EBV-related gastric cancer. Downregulation of the human leukocyte antigen (HLA) is one of the common strategies deployed by cancer cells and viruses to evade host immune response. EBV-encoded LMP2A protein downregulates the expression of HLA Class I in gastric cancer cells (Deb Pal and Banerjee, 2015). Mechanistically, LMP2A activates HH signaling in EBV-infected gastric cancer cells, whereas blocking HH signaling by knockdown of GLI1 reverses LMP2A-mediated downregulation of HLA. Thus, EBV suppresses HLA expression to evade host immunity *via* LMP2A-mediated activation of HH signaling. Liang et al. (2014) found that the *IHH* gene is transcriptionally downregulated by EBV-associated hypermethylation in gastric cancer cells infected with EBV. Downregulation of IHH increases cell growth and colony formation ability, suggesting a tumor-suppressive potential of IHH in EBV-related gastric cancer (Liang et al., 2014). These studies imply that HH signaling participates in the occurrence and development of EBV-induced diseases.

Human Papillomavirus

Human papillomavirus (HPV) is a group of related double-stranded DNA viruses known as the primary cause of cervical cancer. HPV 16 and HPV 18 are responsible for at least 70% of cases of cervical cancer, largely dependent on two oncogenes E6 and E7 (Pal and Kundu, 2019). An early link between HH signaling and HPV was discovered in studies, showing that components or target genes of HH signaling are elevated in E7 transgenic mice and patients with cervical cancer (Chaudary et al., 2012; Ibarra Sierra et al., 2012). In agreement with this, inhibition of HH signaling by cyclopamine or GANT 61 reduces the proliferation and survival of cervical cancer cells (Samarzija and Beard, 2012).

A recent study found that GLI1 and E6 stimulate their transcriptional expression reciprocally, resulting in a high level of GLI1 and E6 in cervical cancer stem cells (Vishnoi et al., 2016). The cooperation between GLI1 and E6 maintains the population and stemness of cervical cancer stem cells. Accordingly, simultaneous inhibition of SMO and E6 results in an addictive

anticancer effect. Thus, the crosstalk between GLI1 and E6 might be a strategy utilized by HPV to select a subset of cervical cells for immortalization. The crosstalk between HH signaling and E6 was further confirmed in the mouse model of cervical cancer (Rojo-León et al., 2019). E6/E7 transgenic mice exhibit increased HH signaling activity, which is potentiated in the cervix by treatment of estradiol. E6/E7 oncogenes might cooperate with estradiol to promote uncontrolled growth of the cervix by synergistic activation of HH signaling. Due to the toxicity of SMO inhibitor cyclopamine, a low dose of cyclopamine is used to treat E6/E7 transgenic mice but does not cause an obvious effect on the cervix. Another SMO inhibitor itraconazole reduces growth at an early stage of cervical carcinogenesis but fails to decrease GLI1 activity. Nevertheless, activation of non-canonical HH signaling or canonical HH signaling but downstream of SMO (e.g., loss-of-function mutation of SUFU and gain-of-function mutation of GLI1) might occur during the multistep process of cervical carcinogenesis. If this is the case, GLI1 inhibitor rather than SMO inhibitor would be more suitable for the development of cervical cancer therapy. In conclusion, activation of HH signaling underlies the pathogenesis of HPV-induced cervical cancer. However, the application of HH signaling inhibitor as a candidate therapy for cervical cancer remains to be further explored.

Human Immunodeficiency Virus

Human immunodeficiency virus (HIV) infection is linked to the suppression of protective immune responses and causes acquired immune deficiency syndrome (AIDS). An early study has shown that the expression of immunosuppressive cytokine TGF-β1 is elevated after HIV-1 infection and leads to the development of induced Treg (Furler and Uittenbogaart, 2012). As a main downstream transcription factor of the HH signaling pathway, GLI2 protein enhances the expression of TGF-β1 in naïve $CD4^+$ T cells through activating the human TGF-β1 promoter activity. The HIV-1 encoded viral protein Tat has been implicated as the inducer of TGF-β1 in both *in vitro* and *in vivo*. The identified interaction between Tat and GLI2 raises the possibility that they might synergistically activate TGF-β1 transcription after HIV infection and contribute to immune suppression.

The HIV-associated neurocognitive disorder (HAND) is characterized by the recruitment of infected leukocytes into CNS *via* damaged BBB. As mentioned earlier, HH signaling is essential for the maintenance of BBB integrity (Alvarez et al., 2011). Impaired HH signaling in the CNS correlates with HIV-induced loss of BBB function and neurological injury, whereas re-activation of HH signaling by SAG reduces the viral load in the CNS and rescues BBB integrity and neuroprotection in HIV-infected humanized mice (Singh et al., 2016, 2017). Bohannon et al. (2019) confirmed the disruption of BBB in infected patients with HIV and simian immunodeficiency virus (SIV)-infected rhesus macaques. However, they found the persistent presence of SHH at the BBB. Netrin-1, an important downstream effector of HH signaling, is produced by brain pericytes to fortify BBB (Podjaski et al., 2015). Despite the strong presence of SHH, Netrin-1 and its cellular source pericytes are absent in encephalitic lesions. Therefore, these studies suggest that impaired HH signaling in pericytes might occur downstream of SHH ligand, which contributes to HIV-induced BBB breakdown and neuropathogenesis in HAND.

The HIV-induced EMT of podocytes is an important mechanism of HIV-associated nephropathy (HIVAN). HH signaling is activated in human podocytes infected with HIV and the mouse model of HIVAN (Lan et al., 2017). Treatment with recombinant SHH or overexpression of GLI1 significantly enhances EMT, while blocking HH signaling by GLI1/2 inhibitor GANT 58 attenuates HIV-induced EMT in podocytes, indicating that HIV-induced EMT and kidney injury are dependent on activation of HH signaling. Taken together, these studies reveal that HH signaling plays a key role in the development of HIV-related diseases.

Human T-Cell Leukemia Virus Type 1

Adult T-cell leukemia (ATL) is a peripheral T-lymphocyte malignancy caused by infection of the retrovirus human T-cell leukemia virus type I (HTLV-1). HTLV-1 bZIP factor (HBZ) and Tax play a critical role in leukemogenesis of ATL, and double transgenic mice of HBZ and Tax in $CD4^+$ T cells develop T-cell lymphoma (Zhao et al., 2014; Nosaka and Matsuoka, 2021). HTLV-1-encoded Tax is a potent transcription activator of viral genes dependent on its interaction with a series of host proteins, such as GLI2 (Tanimura et al., 1998; Dan et al., 1999). GLI2 and cyclic AMP response element-binding protein (CREB) form a complex with Tax in the long terminal repeats of HTLV-1 and facilitate Tax-mediated activation of viral transcription.

Tax extensively crosstalks with cellular signaling pathways to subvert cellular functions and suppresses host defense. EVC1 and EVC2, positive modulators of HH signaling that act downstream of SMO, are found to be aberrantly overexpressed in ATL and HTLV-1-infected cells (Takahashi et al., 2014). The upregulation of EVC1 and EVC2 is mediated by Tax *via* epigenetic modification at the EVC loci. Knockdown of EVC1, EVC2, GLI1 or GLI2, or treatment with GLI1/2 inhibitor GANT 61 induces apoptosis of ATL cells, indicating that EVC1/2-mediated activation of HH signaling supports the survival of ATL cells. Thus, HH signaling plays a vital role in ATL pathogenesis and represents a potential therapeutic target of ATL.

Influenza A Viruses

Influenza A viruses (IAVs) are the causative pathogens of seasonal influenza epidemics that affect the upper and lower respiratory tract and represent a wide spectrum of subtypes based on surface proteins hemagglutinin (H) and neuraminidase (N). IAV-encoded non-structural protein NS1 is highly expressed in infected cells. NS1 activates HH signaling *via* direct interaction with transcription factor Ci in *Drosophila* (Smelkinson et al., 2017). The A122 residue of NS1 is critical for establishing interaction and regulation of Ci. Expression of NS1 also exerts an HH-modulating activity in human

TABLE 1 | The pathological role of hedgehog signaling in viral infections and the potential therapeutic strategies.

Viral modulation of HH signaling	Virus	Disease	Pathological outcome	Therapeutic strategy	References
Signaling activation (canonical)	HBV	Viral hepatitis, liver fibrosis, cirrhosis and HCC	Viral replication, tumor development	SMO inhibitor or GLI inhibitor	Pereira Tde et al., 2010; Arzumanyan et al., 2012
	HCV				Choi et al., 2011; Granato et al., 2016
	HDV				Diaz et al., 2018
	EBV	NPC	Tumor development		Port et al., 2013
		Gastric cancer	Immune suppression		Deb Pal and Banerjee, 2015
	HPV	Cervical cancer	Tumor development		Vishnoi et al., 2016; Rojo-León et al., 2019
	HIV	AIDS	Immune suppression		Furler and Uittenbogaart, 2012
		HIVAN	EMT induction		Lan et al., 2017
	IAV	Influenza	Cytokine production		Smelkinson et al., 2017
	MCPyV	MCC	Induction of MCC cell origin		Kervarrec et al., 2020
Signaling activation (non-canonical or downstream of SMO)	HTLV-1	ATL	Viral transcription, cancer cell survival	GLI inhibitor	Tanimura et al., 1998; Takahashi et al., 2014
	IAV(H1N1)	Influenza	Destruction of alveolar barrier		Ruan et al., 2020
	KSHV	KS, PEL	Tumor development		Asha et al., 2020
Signaling reduction	HIV	HAND	BBB breakdown and neuropathogenesis	SMO agonist	Singh et al., 2016; Bohannon et al., 2019
	ZIKV	Microencephaly	Disruption of midbrain development		Thawani et al., 2018

lung epithelial cells and infected mouse lungs. Infection of mice with IAV strongly induces the expression of HH target genes PTCH1 and BMP2 as well as cytokines CXCL10 and IL6 in an autocrine fashion. Surprisingly, IAV with NS1 A122V mutation induces the higher expression of PTCH1 and IL6 and potentiates the lethality in mice, probably due to cytokine storm elicited by other viral factors in the context of virus-infected mice. Thus, NS1 displays a conserved role cross-species in targeting HH signaling for modulation but a divergent output of A122V mutation that might alter influenza virulence.

Influenza is characterized by the destruction of alveolar epithelial and endothelial, which involves IAV-induced activation of non-canonical HH signaling followed by disruption of the epithelial junctions (Ruan et al., 2020). GLI1 is cross-activated by MAPK and PI3K pathways in human lung cells and mice infected with the H1N1 strain. Increased expression of GLI1 induces the expression of SNAIL and SLUG, which downregulate junction proteins Occludin and ZO-1 and increase paracellular permeability of alveolar barrier. GLI1/2 inhibitor GANT 61 specifically suppresses the expression of SNAIL and SLUG in IAV-infected cells but not in uninfected cells. Consequently, the expression of junction proteins and integrity of the alveolar barrier are restored. Collectively, non-canonical activation of GLI1 plays a critical role in disruption of the alveolar barrier during the pathogenesis of IAV.

Merkel Cell Polyomavirus

Merkel cell carcinoma (MCC) is aggressive neuroendocrine skin cancer and its primary cause is Merkel cell polyomavirus (MCPyV). It has been reported that the expression of HH target genes GLI1 and PTCH1 is increased in MCC (Brunner et al., 2010; Gambichler et al., 2021). SHH level is significantly elevated in MCPyV-positive MCC than in MCPyV-negative MCC, indicating that MCPyV activates HH signaling in MCC (Kuromi et al., 2017). MCPyV-encoded small T and large T antigens are recognized as the main driver for the carcinogenesis of MCC. While expression of T antigens or GLI1 alone only induces differentiation of human keratinocytes to the progenitors of Merkel cells, a combination of T antigens and GLI1 gives rise to a mature phenotype of Merkel cells (Kervarrec et al., 2020). As the executor of HH signaling, GLI1 initiates Merkel cell differentiation by induction of SOX2. This study suggests that activation of HH signaling contributes to the initial origin establishment of MCC cells but might be lost during the following tumor development.

Zika Virus

Infection of Zika virus (ZIKV) increases the incidence of microencephaly in fetuses and Guillain-Barre syndrome in adults. The close association between HH signaling with neurodevelopmental disorders raises the possibility that HH signaling might be implicated in ZIKV-induced microencephaly.

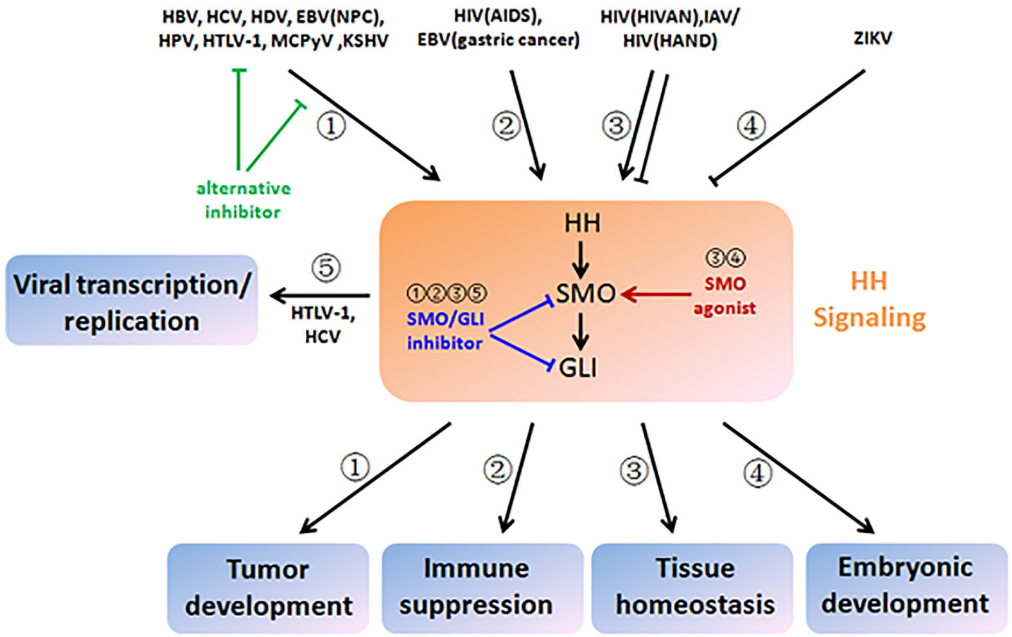

FIGURE 3 | Therapeutic strategies based on viral modulation and pathological outcome of HH signaling. HBV, HCV, HDV, EBV (nasopharyngeal carcinoma), HPV, HTLV-1, MCPyV, and KSHV aberrantly activate HH signaling and drive multistep tumor development (pathway ①). HIV (acquired immune deficiency syndrome) and EBV (gastric cancer) also activate HH signaling, which contributes to immune suppression (pathway ②). HIV (HIV-associated nephropathy), IAV, and HIV (HIV-associated neurocognitive disorder) disturb tissue homeostasis by induction of either increased or decreased HH signaling (pathway ③). ZIKA infection results in disruption of embryonic development by inactivation of HH signaling (pathway ④). HTLV-1 and HCV hijack HH signaling and facilitate viral transcription and replication (pathway ⑤). To reverse viral modulation and restore to the normal activity of HH signaling, SMO/GLI inhibitors could be applied to the scenarios of ①, ②, ③, and ⑤ (blunt arrows in blue), while SMO agonists could be applied to the scenarios of ③ and ③ (sharp arrows in red). Alternatively, chemical inhibitors could also target viral proteins that crosstalk with HH signaling or their interactions for blockage (blunt arrows in green).

Using the developing chicken brains as an animal model, Thawani et al. (2018) found that signaling centers are more sensitive to ZIKV infection. ZIKV strongly infects the midbrain floor plate and causes increased apoptosis and decreased proliferation of SHH-producing cells. Insufficient production of SHH impairs the expression of HH target genes in the adjacent ventral midbrain and consequent neural patterning. Thus, ZIKV-induced deficiency of SHH disrupts midbrain development in a paracrine way, resulting in reduced size of the midbrain.

Kaposi's Sarcoma-Associated Herpesvirus

Kaposi's sarcoma-associated herpesvirus (KSHV), also known as human herpesvirus 8 (HHV8), is a double-stranded DNA virus linked to Kaposi's sarcoma (KS) and primary effusion lymphoma (PEL). Recently, Asha et al. (2020) discovered a significant increase of GLI1 expression in KS skin tissues and PEL cells infected with KSHV, which might be triggered in an HH ligands independent, but AMPK-dependent, manner. GLI1/2 inhibitor GANT 61 regresses the KS tumor formation. Although the precise mechanism involving the viral role in HH signaling activation remains to be investigated, this study uncovered the importance of non-canonical HH signaling to KSHV pathogenesis and its potential as a therapeutic target.

THERAPEUTIC IMPLICATION

Mechanistic insight into HH signaling and the discovery of its chemical modulators are mutually beneficial and co-developing. Since cyclopamine from the plant *Veratrum californicum* was identified as the teratogen responsible for cyclops lambs in 1968 and as the first HH signaling inhibitor in 1998, searching chemical modulators of HH signaling for the therapeutic purpose have attracted numerous research attentions (Lee et al., 2014). These efforts lead to the discovery of current food and drug administration (FDA)-approved SMO inhibitors GDC-0449 (Vismodegib), LDE225 (Sonidegib), and GLI inhibitor arsenic trioxide for cancer treatment, and even more are under investigation (Wu et al., 2017). As HH signaling is also dysregulated during infections of a wide range of viruses (**Figure 2**), a new and promising application of these chemical modulators is to restore dysregulated HH signaling in virus-related diseases. However, caution should be exercised especially in those non-life-threatening diseases due to possible disruption of tissue homeostasis. Importantly, appropriate chemical modulators, including SMO inhibitor,

GLI1/2 inhibitor, and SMO agonist, should be carefully selected according to the diversity and complexity of viral modulations and pathological outcomes of HH signaling (**Table 1** and **Figure 3**, blue and red arrows). An alternative strategy that could be expected is to target viral proteins responsible for modulation of HH signaling or their interactions for blockage (**Figure 3**, green arrows).

CONCLUSION AND PERSPECTIVE

The HH signaling regulates numerous biological processes during embryonic development and postnatal tissue homeostasis. Dysregulation of HH signaling is the important driving force during the initiation and progression of a variety of diseases. In general, HH signaling is aberrantly activated in cancer while reduced in developmental disorders. Recently, accumulating studies have extended the pathological role of HH signaling to viral infections and their related diseases. Similarly, most viral infections that lead to cancer usually activate cellular HH signaling. Viral infections that lead to developmental disorders tend to decrease HH signaling activity, as exampled by ZIKV-induced microencephaly (Thawani et al., 2018). During viral-induced disruption of tissue homeostasis, both positive (IAV-induced disruption of the alveolar barrier) and negative (HIV-induced HAND) modulations of HH signaling are observed (Singh et al., 2016; Ruan et al., 2020). Notably, as a viral niche in host tissues might be different or keep changing after the initial infection, viral modulation of HH signaling and its underlying mechanism might be altered concomitantly. This is the case for HIV which activates HH signaling in the kidney to enhance EMT while inactivating HH signaling in the brain to impair BBB (Singh et al., 2016; Lan et al., 2017). This could even occur in the same viral disease but at different stages, which is implicated by MCPyV-related MCC (Kervarrec et al., 2020). Collectively, these recent advances have not only unveiled the emerging role of HH signaling in viral infections but also evoked the potential of chemical modulator of HH signaling in the treatment of viral diseases. The development of potential new therapies depends on a better understanding of both HH signaling and viral infections to precisely define their interaction along with disease progression.

AUTHOR CONTRIBUTIONS

All authors listed have made a substantial, direct, and intellectual contribution to the work, and approved it for publication.

FUNDING

This work was supported by grants from the National Natural Science Foundation of China (31970755 and 31970173) and the Zhejiang Provincial Natural Science Foundation of China (LY21C120001 and LY21C010001).

REFERENCES

Ahn, S., and Joyner, A. L. (2005). In vivo analysis of quiescent adult neural stem cells responding to Sonic hedgehog. *Nature* 437, 894–897. doi: 10.1038/nature03994

Alvarez, J. I., Dodelet-Devillers, A., Kebir, H., Ifergan, I., Fabre, P. J., Terouz, S., et al. (2011). The Hedgehog pathway promotes blood-brain barrier integrity and CNS immune quiescence. *Science* 334, 1727–1731. doi: 10.1126/science.1206936

Andreu-Cervera, A., Catala, M., and Schneider-Maunoury, S. (2021). Cilia, ciliopathies and hedgehog-related forebrain developmental disorders. *Neurobiol. Dis.* 150:105236. doi: 10.1016/j.nbd.2020.105236

Arzumanyan, A., Reis, H. M., and Feitelson, M. A. (2013). Pathogenic mechanisms in HBV- and HCV-associated hepatocellular carcinoma. *Nat. Rev. Cancer* 13, 123–135. doi: 10.1038/nrc3449

Arzumanyan, A., Sambandam, V., Clayton, M. M., Choi, S. S., Xie, G., Diehl, A. M., et al. (2012). Hedgehog signaling blockade delays hepatocarcinogenesis induced by hepatitis B virus X protein. *Cancer Res.* 72, 5912–5920. doi: 10.1158/0008-5472.can-12-2329

Asha, K., Balfe, N., and Sharma-Walia, N. (2020). Concurrent Control of the Kaposi's Sarcoma-Associated Herpesvirus Life Cycle through Chromatin Modulation and Host Hedgehog Signaling: a New Prospect for the Therapeutic Potential of Lipoxin A4. *J. Virol.* 94, e2177–e2119. doi: 10.1128/jvi.02177-19

Bangs, F., and Anderson, K. V. (2017). Primary Cilia and Mammalian Hedgehog Signaling. *Cold Spring Harb. Perspect. Biol.* 9:a028175. doi: 10.1101/cshperspect.a028175

Benallegue, N., Kebir, H., Kapoor, R., Crockett, A., Li, C., Cheslow, L., et al. (2021). The hedgehog pathway suppresses neuropathogenesis in CD4 T cell-driven inflammation. *Brain* 144, 1670–1683. doi: 10.1093/brain/awab083

Bigelow, R. L., Chari, N. S., Unden, A. B., Spurgers, K. B., Lee, S., Roop, D. R., et al. (2004). Transcriptional regulation of bcl-2 mediated by the sonic hedgehog signaling pathway through gli-1. *J. Biol. Chem.* 279, 1197–1205. doi: 10.1074/jbc.M310589200

Bohannon, D. G., Ko, A., Filipowicz, A. R., Kuroda, M. J., and Kim, W. K. (2019). Dysregulation of sonic hedgehog pathway and pericytes in the brain after lentiviral infection. *J. Neuroinflamm.* 16:86. doi: 10.1186/s12974-019-1463-y

Briscoe, J., and Thérond, P. P. (2013). The mechanisms of Hedgehog signalling and its roles in development and disease. *Nat. Rev. Mol. Cell Biol.* 14, 416–429. doi: 10.1038/nrm3598

Brunner, M., Thurnher, D., Pammer, J., Heiduschka, G., Petzelbauer, P., Schmid, C., et al. (2010). Expression of hedgehog signaling molecules in Merkel cell carcinoma. *Head Neck* 32, 333–340. doi: 10.1002/hed.21191

Chaudary, N., Pintilie, M., Hedley, D., Fyles, A. W., Milosevic, M., Clarke, B., et al. (2012). Hedgehog pathway signaling in cervical carcinoma and outcome after chemoradiation. *Cancer* 118, 3105–3115. doi: 10.1002/cncr.26635

Chen, Y., Sasai, N., Ma, G., Yue, T., Jia, J., Briscoe, J., et al. (2011). Sonic Hedgehog dependent phosphorylation by CK1α and GRK2 is required for ciliary accumulation and activation of smoothened. *PLoS Biol.* 9:e1001083. doi: 10.1371/journal.pbio.1001083

Choi, S. S., Bradrick, S., Qiang, G., Mostafavi, A., Chaturvedi, G., Weinman, S. A., et al. (2011). Up-regulation of Hedgehog pathway is associated with cellular permissiveness for hepatitis C virus replication. *Hepatology* 54, 1580–1590. doi: 10.1002/hep.24576

Cochrane, C. R., Szczepny, A., Watkins, D. N., and Cain, J. E. (2015). Hedgehog Signaling in the Maintenance of Cancer Stem Cells. *Cancers* 7, 1554–1585. doi: 10.3390/cancers7030851

Crompton, T., Outram, S. V., and Hager-Theodorides, A. L. (2007). Sonic hedgehog signalling in T-cell development and activation. *Nat. Rev. Immunol.* 7, 726–735. doi: 10.1038/nri2151

Dan, S., Tanimura, A., and Yoshida, M. (1999). Interaction of Gli2 with CREB protein on DNA elements in the long terminal repeat of human T-cell leukemia

virus type 1 is responsible for transcriptional activation by tax protein. *J. Virol.* 73, 3258–3263. doi: 10.1128/jvi.73.4.3258-3263.1999

de la Roche, M., Ritter, A. T., Angus, K. L., Dinsmore, C., Earnshaw, C. H., Reiter, J. F., et al. (2013). Hedgehog signaling controls T cell killing at the immunological synapse. *Science* 342, 1247–1250. doi: 10.1126/science.1244689

Deb Pal, A., and Banerjee, S. (2015). Epstein-Barr virus latent membrane protein 2A mediated activation of Sonic Hedgehog pathway induces HLA class Ia downregulation in gastric cancer cells. *Virology* 484, 22–32. doi: 10.1016/j.virol.2015.05.007

Diaz, G., Engle, R. E., Tice, A., Melis, M., Montenegro, S., Rodriguez-Canales, J., et al. (2018). Molecular Signature and Mechanisms of Hepatitis D Virus-Associated Hepatocellular Carcinoma. *Mol. Cancer Res.* 16, 1406–1419. doi: 10.1158/1541-7786.mcr-18-0012

Dimri, M., and Satyanarayana, A. (2020). Molecular Signaling Pathways and Therapeutic Targets in Hepatocellular Carcinoma. *Cancers* 12:491. doi: 10.3390/cancers12020491

Ding, J., Li, H. Y., Zhang, L., Zhou, Y., and Wu, J. (2021). Hedgehog Signaling, a Critical Pathway Governing the Development and Progression of Hepatocellular Carcinoma. *Cells* 10:123. doi: 10.3390/cells10010123

Dorn, K. V., Hughes, C. E., and Rohatgi, R. (2012). A Smoothened-Evc2 complex transduces the Hedgehog signal at primary cilia. *Dev. Cell* 23, 823–835. doi: 10.1016/j.devcel.2012.07.004

Farci, P., Niro, G. A., Zamboni, F., and Diaz, G. (2021). Hepatitis D Virus and Hepatocellular Carcinoma. *Viruses* 13:830. doi: 10.3390/v13050830

Farrell, P. J. (2019). Epstein-Barr Virus and Cancer. *Annu. Rev. Pathol.* 14, 29–53. doi: 10.1146/annurev-pathmechdis-012418-013023

Furler, R. L., and Uittenbogaart, C. H. (2012). GLI2 regulates TGF-β1 in human CD4+ T cells: implications in cancer and HIV pathogenesis. *PLoS One* 7:e40874. doi: 10.1371/journal.pone.0040874

Furmanski, A. L., Barbarulo, A., Solanki, A., Lau, C. I., Sahni, H., Saldana, J. I., et al. (2015). The transcriptional activator Gli2 modulates T-cell receptor signalling through attenuation of AP-1 and NFκB activity. *J. Cell Sci.* 128, 2085–2095. doi: 10.1242/jcs.165803

Gallet, A. (2011). Hedgehog morphogen: from secretion to reception. *Trends Cell Biol.* 21, 238–246. doi: 10.1016/j.tcb.2010.12.005

Gambichler, T., Dreißigacker, M., Kasakovski, D., Skrygan, M., Wieland, U., Silling, S., et al. (2021). Patched 1 expression in Merkel cell carcinoma. *J. Dermatol.* 48, 64–74. doi: 10.1111/1346-8138.15611

Garcia-Gonzalo, F. R., Phua, S. C., Roberson, E. C., Garcia, G. III, Abedin, M., Schurmans, S., et al. (2015). Phosphoinositides Regulate Ciliary Protein Trafficking to Modulate Hedgehog Signaling. *Dev. Cell* 34, 400–409. doi: 10.1016/j.devcel.2015.08.001

Granato, M., Zompetta, C., Vescarelli, E., Rizzello, C., Cardi, A., Valia, S., et al. (2016). HCV derived from sera of HCV-infected patients induces pro-fibrotic effects in human primary fibroblasts by activating GLI2. *Sci. Rep.* 6:30649. doi: 10.1038/srep30649

Hahn, H., Wicking, C., Zaphiropoulous, P. G., Gailani, M. R., Shanley, S., Chidambaram, A., et al. (1996). Mutations of the human homolog of Drosophila patched in the nevoid basal cell carcinoma syndrome. *Cell* 85, 841–851. doi: 10.1016/s0092-8674(00)81268-4

Han, Y., Xiong, Y., Shi, X., Wu, J., Zhao, Y., and Jiang, J. (2017). Regulation of Gli ciliary localization and Hedgehog signaling by the PY-NLS/karyopherin-β2 nuclear import system. *PLoS Biol.* 15:e2002063. doi: 10.1371/journal.pbio.2002063

Hanna, A., and Shevde, L. A. (2016). Hedgehog signaling: modulation of cancer properies and tumor mircroenvironment. *Mol. Cancer* 15:24. doi: 10.1186/s12943-016-0509-3

Huang, S., He, J., Zhang, X., Bian, Y., Yang, L., Xie, G., et al. (2006). Activation of the hedgehog pathway in human hepatocellular carcinomas. *Carcinogenesis* 27, 1334–1340. doi: 10.1093/carcin/bgi378

Huangfu, D., and Anderson, K. V. (2006). Signaling from Smo to Ci/Gli: conservation and divergence of Hedgehog pathways from Drosophila to vertebrates. *Development* 133, 3–14. doi: 10.1242/dev.02169

Huntzicker, E. G., Estay, I. S., Zhen, H., Lokteva, L. A., Jackson, P. K., and Oro, A. E. (2006). Dual degradation signals control Gli protein stability and tumor formation. *Genes Dev.* 20, 276–281. doi: 10.1101/gad.1380906

Ibarra Sierra, E., Díaz Chávez, J., Cortés-Malagón, E. M., Uribe-Figueroa, L., Hidalgo-Miranda, A., Lambert, P. F., et al. (2012). Differential gene expression between skin and cervix induced by the E7 oncoprotein in a transgenic mouse model. *Virology* 433, 337–345. doi: 10.1016/j.virol.2012.08.024

Iriana, S., Asha, K., Repak, M., and Sharma-Walia, N. (2021). Hedgehog Signaling: implications in Cancers and Viral Infections. *Int. J. Mol. Sci.* 22:1042. doi: 10.3390/ijms22031042

Jiang, J., and Hui, C. C. (2008). Hedgehog signaling in development and cancer. *Dev. Cell* 15, 801–812. doi: 10.1016/j.devcel.2008.11.010

Jin, Z., Mei, W., Strack, S., Jia, J., and Yang, J. (2011). The antagonistic action of B56-containing protein phosphatase 2As and casein kinase 2 controls the phosphorylation and Gli turnover function of Daz interacting protein 1. *J. Biol. Chem.* 286, 36171–36179. doi: 10.1074/jbc.M111.274761

Jin, Z., Schwend, T., Fu, J., Bao, Z., Liang, J., Zhao, H., et al. (2016). Members of the Rusc protein family interact with Sufu and inhibit vertebrate Hedgehog signaling. *Development* 143, 3944–3955. doi: 10.1242/dev.138917

Kervarrec, T., Samimi, M., Hesbacher, S., Berthon, P., Wobser, M., Sallot, A., et al. (2020). Merkel Cell Polyomavirus T Antigens Induce Merkel Cell-Like Differentiation in GLI1-Expressing Epithelial Cells. *Cancers* 12:1989. doi: 10.3390/cancers12071989

Kim, H. Y., Cho, H. K., Hong, S. P., and Cheong, J. (2011). Hepatitis B virus X protein stimulates the Hedgehog-Gli activation through protein stabilization and nuclear localization of Gli1 in liver cancer cells. *Cancer Lett.* 309, 176–184. doi: 10.1016/j.canlet.2011.05.033

Kuromi, T., Matsushita, M., Iwasaki, T., Nonaka, D., Kuwamoto, S., Nagata, K., et al. (2017). Association of expression of the hedgehog signal with Merkel cell polyomavirus infection and prognosis of Merkel cell carcinoma. *Hum. Pathol.* 69, 8–14. doi: 10.1016/j.humpath.2017.05.011

Kuzhandaivel, A., Schultz, S. W., Alkhori, L., and Alenius, M. (2014). Cilia-mediated hedgehog signaling in Drosophila. *Cell Rep.* 7, 672–680. doi: 10.1016/j.celrep.2014.03.052

Lan, X., Wen, H., Cheng, K., Plagov, A., Marashi Shoshtari, S. S., Malhotra, A., et al. (2017). Hedgehog pathway plays a vital role in HIV-induced epithelial-mesenchymal transition of podocyte. *Exp. Cell Res.* 352, 193–201. doi: 10.1016/j.yexcr.2017.01.019

Laner-Plamberger, S., Wolff, F., Kaser-Eichberger, A., Swierczynski, S., Hauser-Kronberger, C., Frischauf, A. M., et al. (2013). Hedgehog/GLI signaling activates suppressor of cytokine signaling 1 (SOCS1) in epidermal and neural tumor cells. *PLoS One* 8:e75317. doi: 10.1371/journal.pone.0075317

Lee, S. T., Welch, K. D., Panter, K. E., Gardner, D. R., Garrossian, M., and Chang, C. W. (2014). Cyclopamine: from cyclops lambs to cancer treatment. *J. Agric. Food Chem.* 62, 7355–7362. doi: 10.1021/jf5005622

Liang, Q., Yao, X., Tang, S., Zhang, J., Yau, T. O., Li, X., et al. (2014). Integrative identification of Epstein-Barr virus-associated mutations and epigenetic alterations in gastric cancer. *Gastroenterology* 147, 1350.e–1362.e. doi: 10.1053/j.gastro.2014.08.036

Liu, A. (2019). Proteostasis in the Hedgehog signaling pathway. *Semin. Cell Dev. Biol.* 93, 153–163. doi: 10.1016/j.semcdb.2018.10.009

Loo, C. K. C., Pearen, M. A., and Ramm, G. A. (2021). The Role of Sonic Hedgehog in Human Holoprosencephaly and Short-Rib Polydactyly Syndromes. *Int. J. Mol. Sci.* 22:9854. doi: 10.3390/ijms22189854

Mei, S., and Zhang, K. (2016). Computational discovery of Epstein-Barr virus targeted human genes and signalling pathways. *Sci. Rep.* 6:30612. doi: 10.1038/srep30612

Mukhopadhyay, S., Wen, X., Ratti, N., Loktev, A., Rangell, L., Scales, S. J., et al. (2013). The ciliary G-protein-coupled receptor Gpr161 negatively regulates the Sonic hedgehog pathway via cAMP signaling. *Cell* 152, 210–223. doi: 10.1016/j.cell.2012.12.026

Nieuwenhuis, E., and Hui, C. C. (2005). Hedgehog signaling and congenital malformations. *Clin. Genet.* 67, 193–208. doi: 10.1111/j.1399-0004.2004.00360.x

Nosaka, K., and Matsuoka, M. (2021). Adult T-cell leukemia-lymphoma as a viral disease: subtypes based on viral aspects. *Cancer Sci.* 112, 1688–1694. doi: 10.1111/cas.14869

Nozawa, Y. I., Lin, C., and Chuang, P. T. (2013). Hedgehog signaling from the primary cilium to the nucleus: an emerging picture of ciliary localization, trafficking and transduction. *Curr. Opin. Genet. Dev.* 23, 429–437. doi: 10.1016/j.gde.2013.04.008

Nüsslein-Volhard, C., and Wieschaus, E. (1980). Mutations affecting segment number and polarity in Drosophila. *Nature* 287, 795–801. doi: 10.1038/287795a0

Onodera, S., Nakamura, Y., and Azuma, T. (2020). Gorlin Syndrome: recent Advances in Genetic Testing and Molecular and Cellular Biological Research. *Int. J. Mol. Sci.* 21:7559. doi: 10.3390/ijms21207559

Pak, E., and Segal, R. A. (2016). Hedgehog Signal Transduction: key Players, Oncogenic Drivers, and Cancer Therapy. *Dev. Cell* 38, 333–344. doi: 10.1016/j.devcel.2016.07.026

Pal, A., and Kundu, R. (2019). Human Papillomavirus E6 and E7: the Cervical Cancer Hallmarks and Targets for Therapy. *Front. Microbiol.* 10:3116. doi: 10.3389/fmicb.2019.03116

Papaioannou, E., Yánez, D. C., Ross, S., Lau, C. I., Solanki, A., Chawda, M. M., et al. (2019). Sonic Hedgehog signaling limits atopic dermatitis via Gli2-driven immune regulation. *J. Clin. Invest.* 129, 3153–3170. doi: 10.1172/jci125170

Pereira Tde, A., Witek, R. P., Syn, W. K., Choi, S. S., Bradrick, S., Karaca, G. F., et al. (2010). Viral factors induce Hedgehog pathway activation in humans with viral hepatitis, cirrhosis, and hepatocellular carcinoma. *Lab. Invest.* 90, 1690–1703. doi: 10.1038/labinvest.2010.147

Petty, A. J., Dai, R., Lapalombella, R., Baiocchi, R. A., Benson, D. M., Li, Z., et al. (2021). Hedgehog-induced PD-L1 on tumor-associated macrophages is critical for suppression of tumor-infiltrating CD8+ T cell function. *JCI Insight* 6:e146707. doi: 10.1172/jci.insight.146707

Petty, A. J., Li, A., Wang, X., Dai, R., Heyman, B., Hsu, D., et al. (2019). Hedgehog signaling promotes tumor-associated macrophage polarization to suppress intratumoral CD8+ T cell recruitment. *J. Clin. Invest.* 129, 5151–5162. doi: 10.1172/jci128644

Pietrobono, S., Gagliardi, S., and Stecca, B. (2019). Non-canonical Hedgehog Signaling Pathway in Cancer: activation of GLI Transcription Factors Beyond Smoothened. *Front. Genet.* 10:556. doi: 10.3389/fgene.2019.00556

Po, A., Ferretti, E., Miele, E., De Smaele, E., Paganelli, A., Canettieri, G., et al. (2010). Hedgehog controls neural stem cells through p53-independent regulation of Nanog. *EMBO J.* 29, 2646–2658. doi: 10.1038/emboj.2010.131

Podjaski, C., Alvarez, J. I., Bourbonniere, L., Larouche, S., Terouz, S., Bin, J. M., et al. (2015). Netrin 1 regulates blood-brain barrier function and neuroinflammation. *Brain* 138(Pt 6), 1598–1612. doi: 10.1093/brain/awv092

Port, R. J., Pinheiro-Maia, S., Hu, C., Arrand, J. R., Wei, W., Young, L. S., et al. (2013). Epstein-Barr virus induction of the Hedgehog signalling pathway imposes a stem cell phenotype on human epithelial cells. *J. Pathol.* 231, 367–377. doi: 10.1002/path.4245

Rojo-León, V., García, C., Valencia, C., Méndez, M. A., Wood, C., and Covarrubias, L. (2019). The E6/E7 oncogenes of human papilloma virus and estradiol regulate hedgehog signaling activity in a murine model of cervical cancer. *Exp. Cell Res.* 381, 311–322. doi: 10.1016/j.yexcr.2019.05.024

Ruan, T., Sun, J., Liu, W., Prinz, R. A., Peng, D., Liu, X., et al. (2020). H1N1 Influenza Virus Cross-Activates Gli1 to Disrupt the Intercellular Junctions of Alveolar Epithelial Cells. *Cell Rep.* 31:107801. doi: 10.1016/j.celrep.2020.107801

Samarzija, I., and Beard, P. (2012). Hedgehog pathway regulators influence cervical cancer cell proliferation, survival and migration. *Biochem. Biophys. Res. Commun.* 425, 64–69. doi: 10.1016/j.bbrc.2012.07.051

Schwend, T., Jin, Z., Jiang, K., Mitchell, B. J., Jia, J., and Yang, J. (2013). Stabilization of speckle-type POZ protein (Spop) by Daz interacting protein 1 (Dzip1) is essential for Gli turnover and the proper output of Hedgehog signaling. *J. Biol. Chem.* 288, 32809–32820. doi: 10.1074/jbc.M113.512962

Shi, Q., Li, S., Li, S., Jiang, A., Chen, Y., and Jiang, J. (2014). Hedgehog-induced phosphorylation by CK1 sustains the activity of Ci/Gli activator. *Proc. Natl. Acad. Sci. U.S.A.* 111, E5651–E5660. doi: 10.1073/pnas.1416652111

Sicklick, J. K., Li, Y. X., Jayaraman, A., Kannangai, R., Qi, Y., Vivekanandan, P., et al. (2006). Dysregulation of the Hedgehog pathway in human hepatocarcinogenesis. *Carcinogenesis* 27, 748–757. doi: 10.1093/carcin/bgi292

Sigafoos, A. N., Paradise, B. D., and Fernandez-Zapico, M. E. (2021). Hedgehog/GLI Signaling Pathway: transduction, Regulation, and Implications for Disease. *Cancers* 13:3410. doi: 10.3390/cancers13143410

Singh, V. B., Singh, M. V., Gorantla, S., Poluektova, L. Y., and Maggirwar, S. B. (2016). Smoothened Agonist Reduces Human Immunodeficiency Virus Type-1-Induced Blood-Brain Barrier Breakdown in Humanized Mice. *Sci. Rep.* 6:26876. doi: 10.1038/srep26876

Singh, V. B., Singh, M. V., Piekna-Przybylska, D., Gorantla, S., Poluektova, L. Y., and Maggirwar, S. B. (2017). Sonic Hedgehog mimetic prevents leukocyte infiltration into the CNS during acute HIV infection. *Sci. Rep.* 7:9578. doi: 10.1038/s41598-017-10241-0

Smelkinson, M. G. (2017). The Hedgehog Signaling Pathway Emerges as a Pathogenic Target. *J. Dev. Biol.* 5:14. doi: 10.3390/jdb5040014

Smelkinson, M. G., Guichard, A., Teijaro, J. R., Malur, M., Loureiro, M. E., Jain, P., et al. (2017). Influenza NS1 directly modulates Hedgehog signaling during infection. *PLoS Pathog.* 13:e1006588. doi: 10.1371/journal.ppat.1006588

Sun, J., Shin, D. Y., Eiseman, M., Yallowitz, A. R., Li, N., Lalani, S., et al. (2021). SLITRK5 is a negative regulator of hedgehog signaling in osteoblasts. *Nat. Commun.* 12:4611. doi: 10.1038/s41467-021-24819-w

Takahashi, R., Yamagishi, M., Nakano, K., Yamochi, T., Yamochi, T., Fujikawa, D., et al. (2014). Epigenetic deregulation of Ellis Van Creveld confers robust Hedgehog signaling in adult T-cell leukemia. *Cancer Sci.* 105, 1160–1169. doi: 10.1111/cas.12480

Tanimura, A., Dan, S., and Yoshida, M. (1998). Cloning of novel isoforms of the human Gli2 oncogene and their activities to enhance tax-dependent transcription of the human T-cell leukemia virus type 1 genome. *J. Virol.* 72, 3958–3964. doi: 10.1128/jvi.72.5.3958-3964.1998

Thawani, A., Sirohi, D., Kuhn, R. J., and Fekete, D. M. (2018). Zika Virus Can Strongly Infect and Disrupt Secondary Organizers in the Ventricular Zone of the Embryonic Chicken Brain. *Cell Rep.* 23, 692–700. doi: 10.1016/j.celrep.2018.03.080

Trivedi, P., Patel, S. K., Bellavia, D., Messina, E., Palermo, R., Ceccarelli, S., et al. (2021). When Viruses Cross Developmental Pathways. *Front. Cell Dev. Biol.* 9:691644. doi: 10.3389/fcell.2021.691644

Tu, C., Zeng, Z., Qi, P., Li, X., Guo, C., Xiong, F., et al. (2018). Identification of genomic alterations in nasopharyngeal carcinoma and nasopharyngeal carcinoma-derived Epstein-Barr virus by whole-genome sequencing. *Carcinogenesis* 39, 1517–1528. doi: 10.1093/carcin/bgy108

Varjosalo, M., Li, S. P., and Taipale, J. (2006). Divergence of hedgehog signal transduction mechanism between Drosophila and mammals. *Dev. Cell* 10, 177–186. doi: 10.1016/j.devcel.2005.12.014

Vishnoi, K., Mahata, S., Tyagi, A., Pandey, A., Verma, G., Jadli, M., et al. (2016). Cross-talk between Human Papillomavirus Oncoproteins and Hedgehog Signaling Synergistically Promotes Stemness in Cervical Cancer Cells. *Sci. Rep.* 6:34377. doi: 10.1038/srep34377

Wang, C., Pan, Y., and Wang, B. (2010). Suppressor of fused and Spop regulate the stability, processing and function of Gli2 and Gli3 full-length activators but not their repressors. *Development* 137, 2001–2009. doi: 10.1242/dev.052126

Westendorp, B. F., Büller, N., Karpus, O. N., van Dop, W. A., Koster, J., Versteeg, R., et al. (2018). Indian Hedgehog Suppresses a Stromal Cell-Driven Intestinal Immune Response. *Cell Mol. Gastroenterol. Hepatol.* 5, 67.e–82.e. doi: 10.1016/j.jcmgh.2017.08.004

Wu, F., Zhang, Y., Sun, B., McMahon, A. P., and Wang, Y. (2017). Hedgehog Signaling: from Basic Biology to Cancer Therapy. *Cell Chem. Biol.* 24, 252–280. doi: 10.1016/j.chembiol.2017.02.010

Xiao, X., Tang, J. J., Peng, C., Wang, Y., Fu, L., Qiu, Z. P., et al. (2017). Cholesterol Modification of Smoothened Is Required for Hedgehog Signaling. *Mol. Cell* 66, 154.e–162.e. doi: 10.1016/j.molcel.2017.02.015

Yang, C., Chen, W., Chen, Y., and Jiang, J. (2012). Smoothened transduces Hedgehog signal by forming a complex with Evc/Evc2. *Cell Res.* 22, 1593–1604. doi: 10.1038/cr.2012.134

Yang, L., Ye, S., Zhao, X., Ji, L., Zhang, Y., Zhou, P., et al. (2018). Molecular Characterization of HBV DNA Integration in Patients with Hepatitis and Hepatocellular Carcinoma. *J. Cancer* 9, 3225–3235. doi: 10.7150/jca.26052

Zhao, T., Satou, Y., and Matsuoka, M. (2014). Development of T cell lymphoma in HTLV-1 bZIP factor and Tax double transgenic mice. *Arch. Virol.* 159, 1849–1856. doi: 10.1007/s00705-014-2099-y

Zhou, X. T., Ding, J., Li, H. Y., Zuo, J. L., Ge, S. Y., Jia, H. L., et al. (2020). Hedgehog signalling mediates drug resistance through targeting TAP1 in hepatocellular carcinoma. *J. Cell Mol. Med.* 24, 4298–4311. doi: 10.1111/jcmm.15090

Conflict of Interest: The authors declare that the research was conducted in the absence of any commercial or financial relationships that could be construed as a potential conflict of interest.

frontiers | Frontiers in Microbiology

ORIGINAL RESEARCH
published: 04 May 2022
doi: 10.3389/fmicb.2022.829241

Endoplasmic Reticulum Aminopeptidase 1 Is Involved in Anti-viral Immune Response of Hepatitis B Virus by Trimming Hepatitis B Core Antigen to Generate 9-Mers Peptides

Huanhuan Liu[1], Bingqi Hu[1], Junfeng Huang[1], Qin Wang[1], Feier Wang[2], Faming Pan[2] and Liwen Chen[1]**

[1] Department of Laboratory Medicine, Second Hospital of Anhui Medical University, Hefei, China, [2] Department of Epidemiology and Biostatistics, School of Public Health, Anhui Medical University, Hefei, China

OPEN ACCESS

Edited by:
Jue Liu,
Yangzhou University, China

Reviewed by:
Irini Evnouchidou,
Inovarion, France
Dmitry Kostyushev,
Federal State Budgetary Institution National Medical Research Center of Phthisiopulmonology and Infectious Diseases, Russia

***Correspondence:**
Faming Pan
famingpan@ahmu.edu.cn
Liwen Chen
chenliwen@ahmu.edu.cn

Specialty section:
This article was submitted to Virology, a section of the journal Frontiers in Microbiology

Received: *05 December 2021*
Accepted: *17 March 2022*
Published: *04 May 2022*

Citation:
Liu H, Hu B, Huang J, Wang Q, Wang F, Pan F and Chen L (2022) Endoplasmic Reticulum Aminopeptidase 1 Is Involved in Anti-viral Immune Response of Hepatitis B Virus by Trimming Hepatitis B Core Antigen to Generate 9-Mers Peptides. Front. Microbiol. 13:829241. doi: 10.3389/fmicb.2022.829241

Endoplasmic reticulum aminopeptidase 1 (ERAP1) is a processing enzyme of antigenic peptides presented to major histocompatibility complex (MHC) class I molecules. ERAP1-dependent trimming of epitope repertoire determines an efficacy of adoptive $CD8^+$ T-cell responses in several viral diseases; however, its role in hepatitis B virus (HBV) infection remains unknown. Here, we show that the serum level of ERAP1 in patients with chronic hepatitis B (CHB) (n = 128) was significantly higher than that of healthy controls (n = 44) (8.78 ± 1.82 vs. 3.52 ± 1.61, $p < 0.001$). Furthermore, peripheral ERAP1 level is moderately correlated with HBV DNA level in patients with CHB (r = 0.731, $p < 0.001$). HBV-transfected HepG2.2.15 cells had substantially increased ERAP1 expression and secretion than the germline HepG2 cells ($p < 0.001$). The co-culture of ERAP1-specific inhibitor ERAP1-IN-1 pretreated HepG2.2.15 cells or *ERAP1* knockdown HepG2.2.15 cells with $CD8^+$ T cells led to 14–24% inhibition of the proliferation of $CD8^+$ T cells. Finally, liquid chromatography tandem mass spectrometry (LC-MS/MS) test demonstrated that ERAP1-IN-1 blocks completely the production of a 9-mers peptide (30–38, LLDTASALY) derived from Hepatitis B core antigen (HBcAg). The predictive analysis by NetMHCpan-4.1 server showed that human leukocyte antigen (HLA)-C*04:01 is a strong binder for the 9-mers peptide in HepG2.2.15 cells. Taken together, our results demonstrated that ERAP1 trims HBcAg to produce 9-mers LLDTASALY peptides for binding onto HLA-C*04:01 in HepG2.2.15 cells, facilitating the potential activation of $CD8^+$ T cells.

Keywords: hepatitis B, endoplasmic reticulum aminopeptidase 1, major histocompatibility complex class I, antigen presentation, immune response

INTRODUCTION

World Health Organization (WHO) Global hepatitis report, 2017 has shown that in 2015, 257 million people were estimated who have been chronically infected with hepatitis B virus (HBV) and more than 887,000 patients die annually due to chronic HBV infection (CHB)-related diseases worldwide (World Health Organization, 2018; Stinco et al., 2021). The risk of CHB after acute

infection is reduced to < 5% for immunocompetent adults (Chen and Tian, 2019). A vigorous $CD8^+$ T-cell response that exhibits antiviral activity by producing interferon-γ (IFN-γ) and tumor necrosis factor-α (TNF-α) or by directly killing the infected hepatocytes is generated to control and clear HBV (Guidotti et al., 1999; Maini et al., 2000; Guidotti and Chisari, 2001; Thimme et al., 2003).

A fundamental component of host immunity against viral infection relies on the presentation of endogenously derived peptides by major histocompatibility complex class I (MHC-I) molecules (Watts and Powis, 1999). These peptide MHC-I (pMHC-I) complexes are presented on the cell surface and recognized by $CD8^+$ cytotoxic T lymphocytes (CTLs) (Chang et al., 2005; Cresswell, 2019; Weimershaus et al., 2019). Antigenic peptides are generated by the degradation of proteasome, translocation into the endoplasmic reticulum (ER) lumen by the transporter associated with antigen processing (TAP), and trimming of excess N-terminal amino acids by aminopeptidases (Alvarez-Navarro and Lopez de Castro, 2014). The endoplasmic reticulum aminopeptidase 1 (ERAP1) belongs to the oxytocinase subfamily of M1 zinc metallopeptidases and trims the N-terminus of peptides to the optimal size of 8–9 amino acids for loading onto MHC-I (Hammer et al., 2007). pMHC-I complexes are then shuttled to the cell surface for antigen presentation, which triggers antigen-specific cytolytic and effector T-cell responses. The regulation of ERAP1 expression has been shown to substantially affect the presentation of immunodominant epitopes, thereby altering the MHC I immunopeptidome profiling (York et al., 2006; Hammer et al., 2007; Cifaldi et al., 2011). However, whether ERAP1 is involved in HBV-specific immune response, namely, the antigenic peptide presentation remains unknown. In this study, we analyzed ERAP1 expression in HBV-transfected HepG2.2.15 cells and peripheral ERAP1 level in patients with CHB. We further explored the enzymatic activity of ERAP1 in HepG2.2.15 cells by the specific ERAP1 inhibitor ERAP1-IN-1, especially its effects on HBV-derived peptides and $CD8^+$ T-cell stimulation. Finally, the binding of ERAP1-trimmed HBV-derived peptides with MHC class I molecules was predicted.

MATERIALS AND METHODS

Patients and Serum Samples

Serum samples were obtained from patients with CHB (n = 128) and healthy controls (HC) (n = 44) in the Second Hospital of Anhui Medical University from June 2018 to July 2021. The baseline and laboratory data of patients with CHB and health controls are shown in **Table 1**. CHB was defined as the persistent presence of serum hepatitis B surface antigen (HBsAg) for > 6 months, and serum tests were performed before receiving any anti-HBV treatment. The exclusion criteria were as follows: (1) coinfection with other hepatotropic viruses (hepatitis A/C/D/E virus) or human immunodeficiency virus (HIV); (2) the coexistence of autoimmune hepatitis, alcoholic liver disease, non-alcoholic fatty liver disease, drug hepatitis, primary biliary cirrhosis, or hepatocellular carcinoma. The study was conducted in the principles of the Declaration of Helsinki and was approved by the Ethics Committee for the Second Hospital of Anhui Medical University, and all patients have signed informed consent.

TABLE 1 | Baseline and laboratory data of patients with CHB and health controls (HC).

Characteristic	CHB (n = 128)	HC (n = 44)	p-value
Age (year)	38 ± 5	39 ± 7	0.136
Gender (Male/Female)	86/42	30/14	0.986
ALT (U/L)	75 (48, 119)	31 (19, 73)	<0.001
AST (U/L)	50.30 (32.00, 75.00)	21.90 (19.35, 24.80)	<0.001
TBIL (μmol/L)	25.70 (15.40, 52.10)	13.00 (7.94, 18.00)	<0.001
ALB (g/L)	41.13 ± 6.23	47.52 ± 3.06	0.035
GGT (IU/L)	57.92 ± 7.64	23.56 ± 4.17	<0.001
HBV genotype		–	–
A	0		
B	31	–	–
C	97	–	–
D	0		
HBV DNA (Log_{10} IU/ml)	2.31 (2.27, 3.70)	–	–
HBsAg (IU/ml)	2,576 (739, 6,881)	–	–
HBeAg (S/CO)	743.52 (236.19, 3286.50)	–	–

Routine Laboratory Tests

Fasting serum level of alanine aminotransferase (ALT, IU/L), aspartate aminotransferase (AST, IU/L), total bilirubin (TBIL, μmol/L), albumin (ALB, g/L), and gamma-glutamyl transpeptidase (GGT, IU/L) was detected by AU5800 biochemistry analyzer (Beckman Coulter, CA, United States). HBV genotyping was based on line probe assays and genotype-specific PCR (Fosun Long March Medical Science, Shanghai, China) according to the manufacturer's instructions. The supernatants from HepG2 and HepG2.2.15 cells treated or left untreated with ERAP1-IN-1 (50 μm) (HY-133125, MedChem Express, New Jersey, United States) were collected 72 h later. HBsAg and HBeAg in the sera and supernatants were measured using commercially available kits with chemiluminescence apparatus (ARCHITECT i2000SR; Abbott diagnostics, IL, United States). HBV viral loads in the sera and supernatants were measured using the real-time polymerase chain reaction (Mx3000p, Agilent Technologies, CA, United States) according to the manufacturer's instructions.

In vitro Enzymatic Assay

The inhibitory potency of ERAP1-IN-1 for ERAP1 was determined using an established fluorogenic assay as previously described (Papakyriakou et al., 2013).

Cell Culture

HepG2. 2.15 cells that are characterized by having stable HBV expression and replication and the germline HepG2 cells were purchased from Shanghai Fuheng Biotechnology. Both cell lines were cultured in Dulbecco's modified eagle medium (DMEM)

containing stable glutamine, supplemented with 10% heat-inactivated fatal bovine serum (FBS) (Gibco) and penicillin (100 IU/ml)/streptomycin (100 μg/ml), and incubated at 37°C, 5% CO_2. Both cell lines were authenticated using short tandem repeat (STR) analysis in combination with sex-typing gene amelogenin detection and compared with DSMZ STR cell line profiles before the use.

Western Blotting

HepG2 and HepG2.2.15 cells were lysed in a radio immunoprecipitation assay (RIPA) buffer supplemented with proteinase inhibitors. About 40 μg of proteins was loaded and separated on sodium dodecyl sulfate–polyacrylamide gel electrophoresis (SDS-PAGE). The protein was then transferred onto a polyvinylidene fluoride (PVDF) membrane, blocked in 5% (w/v) non-fat milk, and incubated with the primary antibodies. The source of the primary antibody was anti-ARTS1/ERAP1 antibody (Abcam, ab124669) and secondary antibody was the Goat Anti-rabbit antibody (Abcam, ab6721). Finally, the protein blots were visualized using enhanced chemiluminescent (ECL) system (Thermo Fisher Scientific, United States). The expression levels of ERAP1 were assessed using ImageJ software (v1.8.0, National Institutes of Health) and were normalized against β-actin.

Enzyme-Linked Immunosorbent Assay

The peripheral ERAP1 was detected using enzyme-linked immunosorbent assay (ELISA) kits (OM534481, Omni mAbs, United States) according to the manufacturer's instructions.

Gene Silencing of Endoplasmic Reticulum Aminopeptidase 1

The small interfering RNA target ERAP1 (Si-ERAP1) and the negative control siRNA (SiControl) oligos were synthesized by Jima Biotechnology (Shanghai, China). The sequences of the siRNA-ERAP1 were as follows: siERAP1 #1, 5′-GGG CGA GUC UCA UUA ACA ATT-3′ and siERAP1 #2, 5′-UUG UUA AUG AGA CUC GCC CTT-3′. The siControl oligos were as follows: siControl #1, 5′-UUC UCC GAA CGU GUC ACG UTT-3′ and siControl #2, 5′-ACG UGA CAC GUU CGG AGA ATT-3′. Lipofectamine 3,000 reagent (L3000015, Invitrogen, United States) was used to perform transfection according to the manufacturer's protocol. The siRNA-transfected and mock HepG2.2.15 cells were incubated at 37°C in 5% CO_2, and ERAP1 knockdown was verified at 48 h post-transfection *via* western blotting analysis.

$CD8^+$ T-Cell Isolation

Peripheral blood mononuclear cells (PBMCs) were prepared from the heparinized venous blood of healthy volunteers by Ficoll-paque plus (GE, United States) density gradient centrifugation. Human naïve $CD8^+$ T cells were sorted by positive magnetic-activated cell sorting (MACS, Miltenyi Biotec, United States) according to the manufacturer's instructions. The cell purity was confirmed by flow cytometry using an anti-mouse CD8 antibody (eBioscience, CA, United States).

Co-culture of $CD8^+$ T Lymphocytes With HepG.2.2.15 Cells

HepG2.2.15 cells were treated or left untreated by ERAP1-IN-1 (50 μm) for 72 h followed by the treatment with mitomycin C (10 μg/ml) for 2.5 h. Cells were washed 5 times with PBS to remove residual ERAP1-IN-1 and mitomycin C and resuspended in DMEM at a final concentration of 1×10^4/ml. The isolated $CD8^+$ T lymphocytes and HepG2.2.15 cells (10:1) were seeded in the 96-well plate, supplemented with recombinant human IL-2 (200 U/ml), and cultured for 14 days. The proliferation of $CD8^+$ T cells was determined by WST-8/CCK-8 at 0, 3, 5, 7, 10, and 14 days. Briefly, 10 μl of the WST-8/CCK-8 solution (Biosharp, Shanghai, China) was added to each well and incubated for 4 h. Finally, the absorbance was measured at 450 nm.

ERAP1-IN-1 Cytotoxicity Assay

To evaluate ERAP1-IN-1 cytotoxicity against HepG2.2.15 cells, 100 μl (10^4/ml) cell suspension was dispensed into 96-well plate, and varying concentrations (0, 20, 40, 60, 80, and 100 μm) of ERAP1-IN-1 was added and cultured for 72 h. About 10 μl of the WST-8/CCK-8 solution (Biosharp, Shanghai, China) was added to each well and incubated for 4 h, and the absorbance was measured at 450 nm. All experiments were performed at least three times and the relative cell viability (%) was expressed as a percentage relative to untreated control cells. Cell viability (%) = OD value of ERAP1-IN-1 group/OD value of control group × 100%.

Protein Extraction and Digestion

After 72 h of treatment with ERAP1-IN-1, HepG2.2.15 cells were harvested for peptidome analysis. SDS with DTT (SDT) buffer (4% SDS, 100 mM Tris-HCL, 1 mM DTT, pH7.6) was used for cell lysis and protein extraction. The extracted protein was quantified with the BCA (bicinchoninic acid) Protein Assay Kit (Bio-Rad, United States). The protein suspensions were digested with 4 μg trypsin (Promega, Madison, United States) in 40 μl 25 mM NH_4HCO_3 buffer overnight at 37°C. The digested peptides of each sample were desalted on C18 Cartridges (Empore^{TM} SPE Cartridges C18, Sigma), concentrated by vacuum centrifugation, and reconstituted in 40 μl of 0.1% (v/v) formic acid.

Mass Spectrometry Analysis

Liquid chromatography tandem mass spectrometry analysis was performed on a timsTOF Pro mass spectrometer (Bruker) that was coupled to Nanoelute (Bruker Daltonics). Peptides were separated using a linear gradient of buffer (84% acetonitrile and 0.1% formic acid) for 120 min at a flow rate of 300 nl/min and a Thermo Scientific reverse-phase nano Easy-spray column (Thermo Scientific PepMap C18, 2 μm particle size, 100 A pore size, 75 μm i.d). The mass spectrometer was operated in positive ion mode. The mass spectrometer collected ion mobility MS spectra over a mass range of m/z 100–1,700 and 1/k0 of 0.6–1.6 and then performed 10 cycles of PASEF MS/MS with a

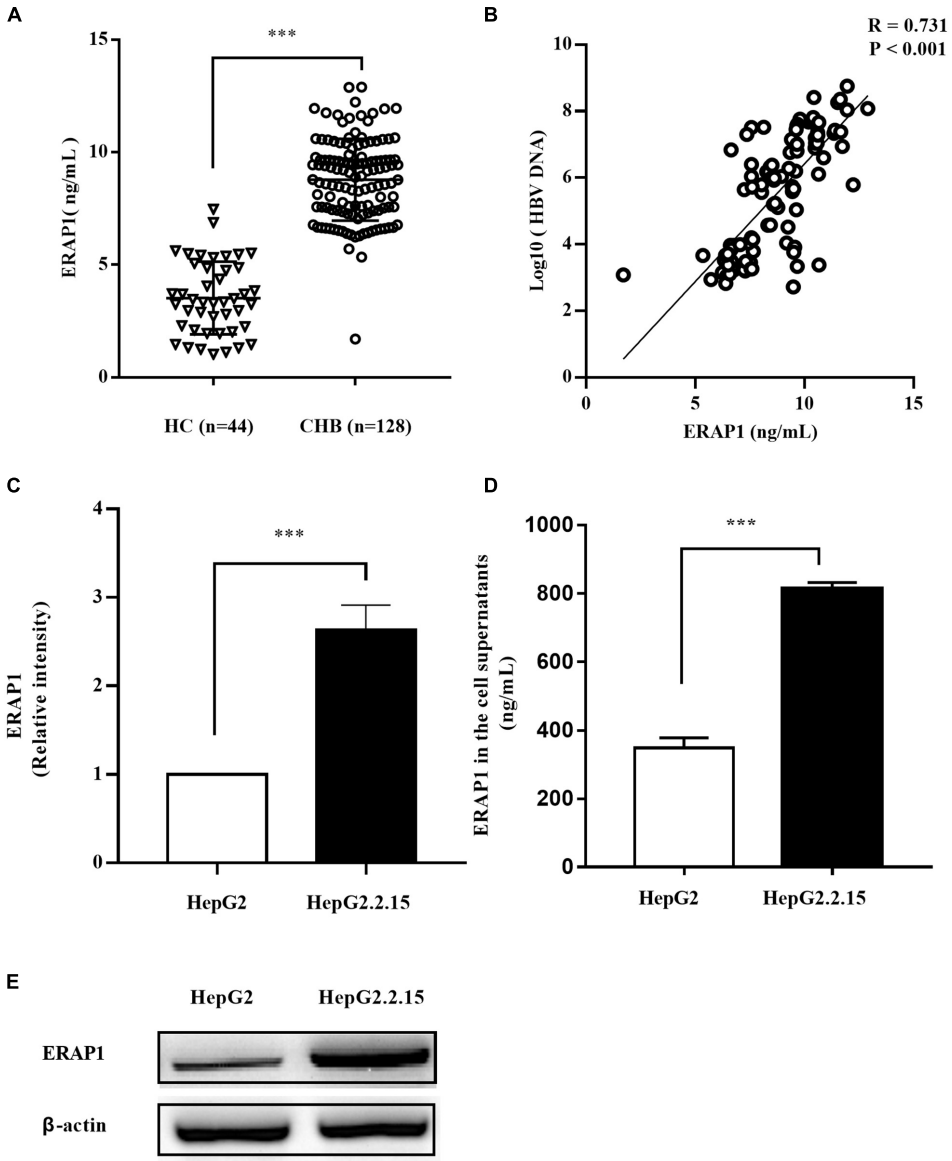

FIGURE 1 | HBV infection promotes ERAP1 expression and secretion. **(A)** the peripheral level of ERAP1 in patients with CHB (n = 128) and HC (n = 44) was detected by ELISA. **(B)** Pearson's correlation analysis between sera ERAP1 and HBV DNA of patients with CHB. **(C,E)** ERAP1 expression and quantitative analysis in HepG2.2.15 cells and the germline HepG2 cells. **(D)** The amounts of ERAP1 in supernatants ofHepG2.2.15 cells and the germline HepG2 cells. Data are presented as the mean ± SD of three independent experiments. CHB, chronic hepatitis B; HC, healthy control. ***$p < 0.001$.

target intensity of 1.5 k and a threshold of 2,500. The dynamic exclusion was set to 24 s. The MS raw data for each sample were combined and searched using the MaxQuant (1.5.3.17) software for the identification and quantitation analysis. The integration of each peptide and protein signal on the LC-MS was calculated by the chromatography based on MS1. Precursor ion mass and fragment mass tolerance was set to 20 ppm, FDR was set to 0.01, peptide-spectrum matching FDR was set to 0.01, and oxidation (Met) was used as the variable modifications. Any identification from the reverse database and known contaminants was eliminated. The mass spectrometry proteomics data have been deposited to the ProteomeXchange Consortium[1] *via* the iProX partner repository with the dataset identifier PXD031858.

Affinity of Peptides to Major Histocompatibility Complex Class I Molecules Predicted by NetMHCpan

We adopted NetMHCpan-4.1 server[2] to predict the binding of peptides to any MHC molecule of known sequence using artificial neural networks (ANNs). The protein sequence of

[1]http://proteomecentral.proteomexchange.org

[2]http://www.cbs.dtu.dk/services/NetMHCpan/

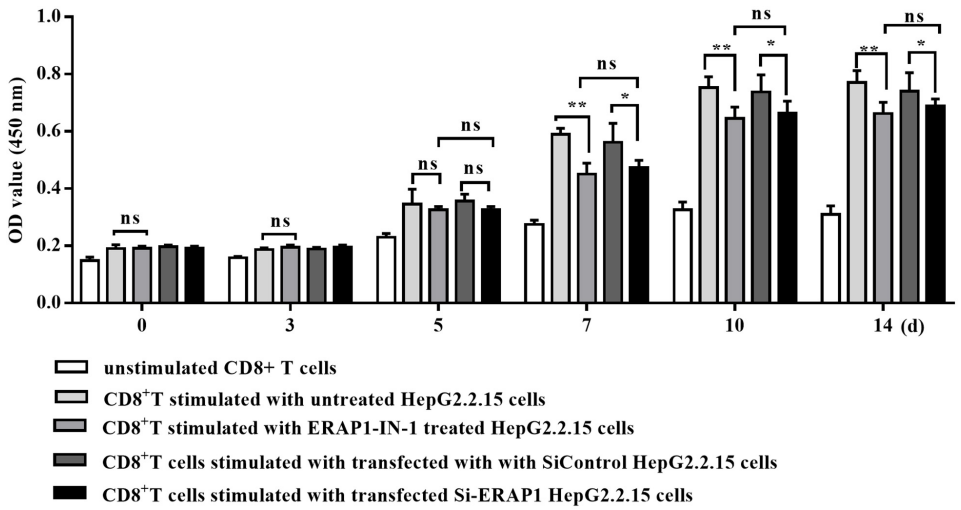

FIGURE 2 | ERAP1-IN-1 or EARP1 knockdown restrains the stimulating ability of HepG2.2.15 cells to $CD8^+$ T cells. HepG2.2.15 cells were pretreated with ERAP1-IN-1 (50 μm) for 72 h, or siERAP1 HepG2.2.15 cells were treated with mitomycin C (10 μg/ml) for further 2.5 h and then co-cultured with isolated $CD8^+$ T cells (1:10). The proliferation of $CD8^+$ T cells was detected by CCK-8 (OD 450 nm) 0, 3, 5, 7, 10, and 14 days later after co-culturing. ERAP1-IN-1 untreated or mock HepG2.2.15 cells were used as stimulator control, and unstimulated $CD8^+$ T cells were used as negative control. ns, no significance; $^*P < 0.05$; $^{**}p < 0.01$.

HBcAg (GenBank: AXM44938.1, 185aa) was inputted in FASTA format and peptide length of 9-mers was selected for analysis. Being an automated method, NetMHCpan-4.1 is trained on a combination of more than 850,000 quantitative binding affinities (BA) and mass spectrometry eluted ligands (EL) peptides. The prediction outputs used for each MHC allele include score_EL and % Rank_EL. The former is raw prediction score, whereas % Rank_EL denotes the rank of the predicted binding score compared to a set of random natural peptides. This measure is not affected by an inherent bias of certain molecules toward higher or lower predicted affinities. The bind level includes strong binder (SB) and weak binder (WB). Strong binders are defined as having % Rank_EL < 0.5 and weak binders with % Rank_EL < 2.

Statistical Analysis

All data were processed and analyzed by SPSS 24.0 and GraphPad Prism 7.0. Normal data were described with mean and standard deviation (SD), and comparisons between two groups were performed using two-tailed Student's *t*-tests. Data of abnormal distribution were expressed as a median with a range of lower–upper quartiles (between 25th and 75th percentiles) and analyzed by Mann–Whitney U test. Correlations between variables were evaluated using the Spearman's rank correlation test. *p*-value < 0.05 was considered as significantly different.

RESULTS

Hepatitis B Virus Infection Upregulates Endoplasmic Reticulum Aminopeptidase 1 Expression

Endoplasmic reticulum aminopeptidase 1 is usually retained in the lumen of ER and was therefore named for the localization. However, it could be secreted into the extracellular milieu in response to inflammatory stimuli, although the precise molecular mechanisms behind the secretion remain unclear (Tsujimoto et al., 2020). We therefore analyzed peripheral ERAP1 level in patients with CHB. As shown in **Figure 1A**, the serum level of ERAP1 in patients with CHB (n = 128) was significantly higher than that of healthy controls (n = 44) (8.78 ± 1.82 ng/ml vs. 3.52 ± 1.61 ng/ml, $p < 0.001$). Furthermore, peripheral ERAP1 level was moderately correlated with HBV DNA levels in patients with CHB (**Figure 1B**, $r = 0.731$, $p < 0.001$). HBV-transfected HepG2.2.15 cells had substantially increased ERAP1 expression than the germline HepG2 cells ($p < 0.0001$, two-tailed unpaired Student's *t*-tests) (**Figures 1C,E**). Meanwhile, ERAP1 level in the cell supernatants was detected by ELISA. We found that the ERAP1 secretion was also considered excessive when the intracellular ERAP1 protein levels were elevated (**Figure 1D**). These results indicate that HBV infection upregulates ERAP1 expression from cellular to organismic level.

Endoplasmic Reticulum Aminopeptidase 1 Promotes Hepatitis B Virus-Specific $CD8^+$ T-Cell Proliferation

Endoplasmic reticulum aminopeptidase 1 acts as a final processing enzyme of antigenic peptides presented to MHC class I molecules (Wearsch and Cresswell, 2008). We therefore investigated the effects of HBV-induced ERAP-1 upregulation on $CD8^+$ T lymphocytes. We used ERAP1-IN-1, a recently discovered non-peptide compound, which competitively inhibits ERAP1 activity toward a nonamer peptide suitable for MHC class I presentation (Maben et al., 2020). The inhibitory effect of ERAP1-IN-1 is dose-dependent, and we choose the working concentration at 50 μm that exhibited specific inhibition of peptide presentation in the cellular context (Maben et al., 2020).

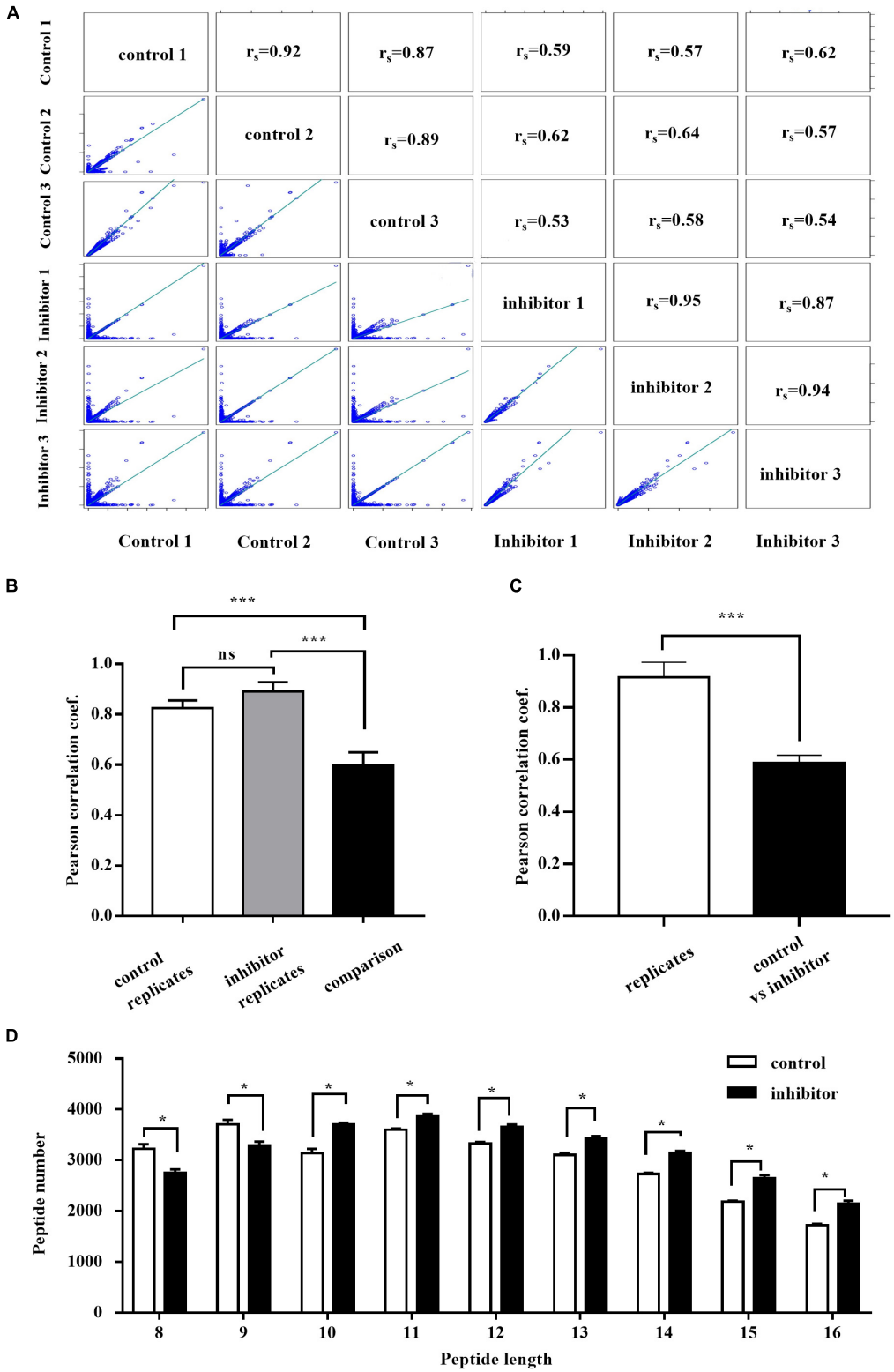

FIGURE 3 | ERAP1-IN-1 treatment affects (8–16)-mers peptides distribution in HepG2.2.15 cells. **(A)** Peptide intensity correlations between different experiments and replicates. The calculated Pearson coefficient is indicated in each panel. **(B)** Average Pearson coefficient of correlations between control replicates, inhibitor replicates, and control vs. inhibitor experiments. **(C)** Average Pearson coefficient of correlations between replicates of the same condition and control vs. inhibitor. **(D)** The peptide length distribution of 8–16 residues in the control and inhibitor groups detected by LC/LC-MS. LFQ, label-free quantification. $^{*}P < 0.05$; $^{***}P < 0.001$.

The cell viability of HepG2.2.15 cells was not affected by ERAP1-IN-1 at 50 μm for 72 h, even though a significant decrease was observed both at 80 and 100 μm (**Supplementary Figure 1**). In this study, we also demonstrated dose-dependent inhibition of ERAP1-IN-1 on the *in vitro* enzymatic activity of recombinant ERAP1 (**Supplementary Figure 2**). Additionally, being a newly reported inhibitor, the effects of ERAP1-IN-1 on HBV replication need to be assessed. Our results showed that HBsAg, HBeAg, and HBV-DNA in the supernatants of HepG2.2.15 treated with ERAP1-IN-1 (50 μm for 72 h) have no significant difference with that of HepG2.2.15 cells left untreated (**Supplementary Figure 3**). Besides, *ERAP1* knockdown HepG2.2.15 cells were used paralleled to ERAPI-IN-1 to verify the effects of the inhibitor.

The co-culture of ERAP1-IN-1 pretreated or ERAP1 knockdown HepG2.2.15 cells with $CD8^+$ T cells significantly reduced proliferation of $CD8^+$ T cells after time periods of 7, 10, and 14 days in culture, as compared to untreated and mock HepG2.2.15 cells, respectively (**Figure 2**). The percent inhibition calculated for $CD8^+$ T cells ranged from 14% to 24%. These results strongly suggested that ERAP1 promotes anti-HBV immune response in the context of the presentation of antigenic peptides by MHC class I molecules to stimulate $CD8^+$ T lymphocytes.

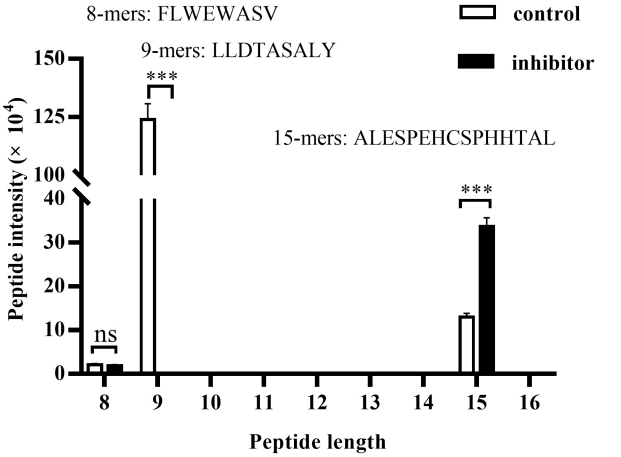

FIGURE 4 | ERAP1 trims HBcAg-specific peptides in HepG2.2.15 cells. HepG2.2.15 cells were treated with ERPA1-IN-1 (50 μM) for 72 h. Cells were lysed, and the extracted protein was then analyzed by LC-MS/MS. The LFQ intensity of 8–16-mers residues was calculated and the peptides origin was identified by the MaxQuant (1.5.3.17) software *via* sequence-specific annotations based on the UniProt databases. ns, no significance; $^{***}p < 0.001$.

Endoplasmic Reticulum Aminopeptidase 1 Regulates Peptide Distribution in Hepatitis B Virus-Infected HepG2.2.15 Cells

It has been well characterized that ERAP1 has length specificity unique among aminopeptidases, efficiently trimming longer (9–16 residues) peptides to 8–9 residues that match the length preferences of MHC-I (Chang et al., 2005). Thus, we analyzed the distribution of the peptide with size range of 8–16 by LC-MS/MS in HepG2.2.15 cells treated with ERAP1-IN-1 (50 μm) for 72 h. To have sufficient statistical power to define the inhibitor-induced changes, we performed three biological replicates for each condition. The cross-correlation analysis revealed the Pearson's correlation coefficients of $r > 0.85$ and $r < 0.65$ between the same condition replicates and between cross-pairs (inhibitor vs. control), respectively (**Figures 3A–C**). Among the total peptides identified, ERAP1-IN-1-treated group had 6.24% and 4.32% reduction of the numbers of peptides with 8 and 9 residues, respectively. In contrast, all peptides > 9-mers have a number increased by a range from 3.01% to 27.14% (**Figure 3D**). Thus, our results demonstrated that ERAP1 regulates peptide numbers of different segments in HBV-infected HepG2.2.15 cells, leading to a significant shift of the peptides length distribution.

Endoplasmic Reticulum Aminopeptidase 1 Trims HBcAg-Specific Peptides in Hepatitis B Virus-Infected Cells

The total kinds of peptides with size range of 8–16 detected by LC/MS in HepG2.2.15 cells are more than 5,000, which derived from more than 20,000 kinds of total peptides. However, only three kinds of 8–16 residues peptides are derived from HBV genome. The peptide distribution includes one kind of 8-mers (161–168, FLWEWASV) peptide which is cleaved from HBsAg and two kinds of peptides enzymatically cut from HBcAg, 9-mers (30–38, LLDTASALY) and 15-mers (41–55, ALESPEHCSPHHTAL) (**Figure 4**). We further compared the intensity of the three peptides between HepG2.2.15 cells treated or left untreated with ERAP1-IN-1. The inhibitor produced a complete block of 9-mers peptide and a substantial increment of 15-mers peptide while having no remarkable effect on 8-mers. Taken together, these results suggested that ERAP1 trims HBcAg-specific peptides in HBV-infected cells.

Prediction of the Binding of 9-mers LLDTASALY Peptide With HLA Class I Molecules

The Expert Protein Analysis System (ExPASy) databases provide a detailed description of HLA allotypes expressed by the HepG2 cells.[3] **Table 2** shows the bind level output of six HLA I alleles with HBcAg-derived 9-mers at Pos 30 (residue number (starting from 0) of the peptide in the protein sequence), namely, the 9-mers core sequence LLDTASALY. Also, the prediction data of 9-mers sequence at Pos 29 (shifted forward by one peptide, DLLDTASAL) and Pos 31 (shifted backward by one peptide, LDTASALYR) were outputted as control. The score_EL of HLA-A*02:01, HLA-A*24:02, HLA-B*35:14, HLA-B*51:01, HLA-C*04:01, and HLA-C*16:02 with 9-mers at Pos 30 was 0.0264, 0.002041, 0.092112, 0.000118, 0.127962, and 0.013707, respectively. The % Rank_EL was 3.287, 8.205, 1.516, 50.286, 0.483, and 4.84, respectively. As a result, the bind level of HLA-B*35:14 and HLA-C*04:01 with 9-mers at Pos 30 was WB and

[3]https://web.expasy.org/cellosaurus/CVCL_0027

TABLE 2 | Binding affinity prediction of 9-mers peptide with MHC-I molecules in HepG2.2.15 cells.

Pos	HLA alleles	Peptide	Core	Of	Gp	G1	IP	I1	Icore	Identity	% Rank_EL	Bind level
29	HLA-A*02:01	DLLDTASAL	DLLDTASAL	0	0	0	0	0	DLLDTASAL	Sequence	3.402	
30	HLA-A*02:01	LLDTASALY	LLDTASALY	0	0	0	0	0	LLDTASALY	Sequence	4.592	
31	HLA-A*02:01	LDTASALYR	LDTASALYR	0	0	0	0	0	LDTASALYR	Sequence	65	
29	HLA-A*24:02	DLLDTASAL	DLLDTASAL	0	0	0	0	0	DLLDTASAL	Sequence	13.027	
30	HLA-A*24:02	LLDTASALY	LLDTASALY	0	0	0	0	0	LLDTASALY	Sequence	8.205	
31	HLA-A*24:02	LDTASALYR	LDTASALYR	0	0	0	0	0	LDTASALYR	Sequence	60	
29	HLA-B*35:14	DLLDTASAL	DLLDTASAL	0	0	0	0	0	DLLDTASAL	Sequence	1.812	≤ WB
30	HLA-B*35:14	LLDTASALY	LLDTASALY	0	0	0	0	0	LLDTASALY	Sequence	1.516	≤ WB
31	HLA-B*35:14	LDTASALYR	LDTASALYR	0	0	0	0	0	LDTASALYR	Sequence	52.143	
29	HLA-B*51:01	DLLDTASAL	DLLDTASAL	0	0	0	0	0	DLLDTASAL	Sequence	3.802	
30	HLA-B*51:01	LLDTASALY	LLDTASALY	0	0	0	0	0	LLDTASALY	Sequence	13.068	
31	HLA-B*51:01	LDTASALYR	LDTASALYR	0	0	0	0	0	LDTASALYR	Sequence	50.286	
29	HLA-C*04:01	DLLDTASAL	DLLDTASAL	0	0	0	0	0	DLLDTASAL	Sequence	3.417	
30	**HLA-C*04:01**	**LLDTASALY**	**LLDTASALY**	**0**	**0**	**0**	**0**	**0**	**LLDTASALY**	**Sequence**	**0.48**	**≤ SB**
31	HLA-C*04:01	LDTASALYR	LDTASALYR	0	0	0	0	0	LDTASALYR	Sequence	42.8	
29	HLA-C*16:02	DLLDTASAL	DLLDTASAL	0	0	0	0	0	DLLDTASAL	Sequence	13.719	
30	HLA-C*16:02	LLDTASALY	LLDTASALY	0	0	0	0	0	LLDTASALY	Sequence	4.84	
31	HLA-C*16:02	LDTASALYR	LDTASALYR	0	0	0	0	0	LDTASALYR	Sequence	41.25	

*Pos, Residue number (starting from 0) of the peptide in the protein sequence. MHC, specified MHC molecule/allele name. Peptide, amino acid sequence of the potential ligand. Core, the minimal 9 amino acid binding core directly in contact with the MHC. Of, the starting position of the Core within the Peptide (if > 0, the method predicts a N-terminal protrusion). Gp, position of the deletion, if any. Gl, length of the deletion, if any. Ip, position of the insertion, if any. Il, length of the insertion, if any. Icore, interaction core. This is the sequence of the binding core including eventual insertions of deletions. Identity, Protein identifier, i.e., the name of the FASTA entry. Score_EL, The raw prediction score. % Rank_EL, Rank of the predicted binding score compared to a set of random natural peptides. This measure is not affected by inherent bias of certain molecules toward higher or lower mean predicted affinities. Strong binders are defined as having % rank < 0.5, and weak binders with % rank < 2. We advise to select candidate binders based on % Rank rather than score bind level: (SB, strong binder; WB, weak binder). The peptide will be identified as a strong binder if the % Rank is below the specified threshold for the strong binders (by default, 0.5%). The peptide will be identified as a weak binder if the % Rank is above the threshold of the strong binders but below the specified threshold for the weak binders (by default, 2%). The bold value indicates that HLA-C*04:01 is a strong binder (SB) for the screened 9-mers peiptde.*

SB, respectively. In contrast, only HLA-B*35:14 is a weak binder for 9-mers at Pos 29, which has the score_EL and % Rank_EL of 0.074915 and 1.812, respectively. Taken together, these results indicate that the 9-mers peptide LLDTASALY is enzymatically trimmed by ERAP-1 and followed by the presentation of predominantly HLA-C*04:01 molecule in HepG2.2.15 cells.

DISCUSSION

The previous studies have shown that ERAP1 is dysregulated in autoimmune diseases (Burton et al., 2007), cancer (Wearsch and Cresswell, 2008; Cifaldi et al., 2011; James et al., 2013; Koumantou et al., 2019), and several types of viral disease including HIV (Tenzer et al., 2009), lymphocytic choriomeningitis virus (LCMV) (York et al., 2006), and human cytomegalovirus (HCMV) (Kim et al., 2011). In this study, both upregulation of ERAP1 and its secretion were observed in HBV-transfected HepG2.2.15 cells in contrast to germline HepG2 cells. Furthermore, the serum level of ERAP1 was significantly upregulated and moderately correlated with HBV DNA levels in patients with CHB. These results suggest that HBV infection results in ERAP1 expression both at cellular and organismic level. It is to be noted that both upregulation of ERAP1 and its secretion from the ER are induced by IFN-γ (Saric et al., 2002; Goto et al., 2011). However, it seems unlikely that ERAP1 upregulation in this study is elicited by IFN-γ as HBV infection has been reported to induce type-III but not type-I or type-II interferon. Furthermore, HBV has evolved various mechanisms to suppress IFN signaling (Mani and Andrisani, 2019). On the other hand, the previous study (Goto et al., 2011) has shown a supporting role of the secreted ERAP1 as it enhances the phagocytic activity of macrophages through the generation of active peptides. Thus, the intracellular and extracellular ERAP1 are functionally complementary and proportionally increased, as we have shown in **Figures 1C,D**. Collectively, these results suggested that HBV-mediated upregulation of ERAP-1 is involved in HBV-induced immune responses.

The proliferation of $CD8^+$ T cells decreased significantly upon stimulated by HepG2.2.15 cells pretreated with ERAP1-IN-1 or ERAP1 gene knockdown (**Figure 2**). Furthermore, ERAP1-IN-1 treatment resulted in 6.24% and 4.32% reduction of the total numbers of peptides with 8 and 9 residues (**Figure 3D**), the length specific and predominant for ERAP1 trimming. These results indicated that ERAP1 promotes $CD8^+$ T-specific antiviral immune response in the context of antigenic peptides presentation by MHC class I molecules. In contrast, the number of all peptides > 9-mers increased at the same time in comparison with the untreated group. These results were consistent with the previous observations in LCMV, HCMV, and vaccinia infection which showed an increase in the length of the viral peptides in the absence of ERAP1. Furthermore, a lack of antigen processing by ERAP1 profoundly altered the immune responses to LCMV, HCMV, and vaccinia virus, characterized by the decreased frequency of $CD8^+$ T cells specific for viral epitopes (York et al., 2006; Blanchard et al., 2010). Overall, these results confirm the unique enzymatic properties of ERAP1 in HBV-infected HepG2.2.15 cells, leading to precise trimming of longer peptides

to 8–9-mers length. Furthermore, the final peptides trimmed by ERAP1 were presented by MHC class I molecule to induce $CD8^+$ T-cell-mediated antiviral immune responses.

As the present studies demonstrate, three kinds of 8–16 residues peptides derived from two HBV antigens, HBsAg and HBcAg, were observed in HepG2.2.15 cells. The 8-mers (161–168, FLWEWASV) peptide is cleaved from HBsAg, and the 9-mers (30–38, LLDTASALY) and 15-mers (41–55, ALESPEHCSPHHTAL) peptides were enzymatically cut from HBcAg. The inhibitor ERAP1-IN-1 produced a complete block of 9-mers and a substantial increment of 15-mers while having no remarkable effect on 8-mers, suggesting that ERAP1 trims HBcAg-specific peptides in HBV-infected cells. The HBV C gene contains two in-phase initiation codons, the C region and the pre-C sequence, which directs the synthesis of HBcAg (185 aa) and of a pre-core protein which upon processing results in the secretion of HBeAg (159 aa) (Jean-Jean et al., 1989, p. 30). Multiple copies of HBcAg dimers, mainly the N-terminal 155 aa, form HBV nucleocapsids which endow the viral particles with high immunogenicity (Gallina et al., 1989). The previous study has shown that 4 mutants at position A11-E8, L37-A41, R39-L31, and A41-E43 of HBcAg were not able to assemble detectable amounts of capsids in co-transfected HuH7 cells (Koschel et al., 2000). Thus, it is very likely that capsid formation is a prerequisite for trimming of HBcAg by ERAP1 since the 9-mers (30-38, LLDTASALY) peptide is located within the above-mentioned mutation region. Immunization studies have demonstrated that HBsAg and HBcAg are capable of eliciting distinct, humoral, and cell-mediated immune responses, respectively (Hoofnagle et al., 1975). Apparently, the HBcAg-derived 9-mers peptide is loaded in the ER by MHC class I molecules, which are eventually presented as peptide-MHC I (pMHC I) complexes on the cell surface to induce $CD8^+$ T-cell-mediated antiviral immune responses. On the other hand, we also observed a substantial increment of 15-mers peptide upon ERAP1-IN-1 treatment. However, the 8–9-mers enzymatic fragments of the increased peptide were not observed in untreated control. It will be useful to determine whether hyper-editing of the 15-mers peptide happened as a proportion of peptides that enter the ER are destroyed by ERAP1 to below the minimal size needed for presentation on MHC class I molecules (Hammer et al., 2007; Georgiadou and Stratikos, 2009; Chen and Tian, 2019). Therefore, ERAP1 functions in a paradoxical manner as an interrupter limiting antigen presentation while it is still an ideal aminopeptidase to generate the final optimal length of peptides for pMHC I presentation (York et al., 2002).

The predictive analysis by the NetMHCpan-4.1 server showed that HLA-C*04:01 molecule is a strong binder for the 9-mers peptide LLDTASALY, which is enzymatically trimmed by ERAP-1 in HepG2 cells. In addition, HLA-B*35:14 was observed to be a weak binder for both 9-mers at Pos 30 and Pos 29. The previous study has shown that HLA-C*04:01 is one of the most frequent HLA class I alleles in Cameroonian infected with HBV, with a frequency of 37.5% in patients with HBV compared with that of 25.5% in healthy populations (Yengo et al., 2020). In addition, HLA-C*04:01 was also observed to be in association with poor viral control of HIV (Olvera et al., 2015) and severe clinical course of COVID-19 (Weiner et al., 2021). However, the genome-wide association study (GWAS) findings highlighted the importance of HLA-C in the clearance of HBV infection in addition to HLA-DP and HLA-DQ (Hu et al., 2013). Thus, accurate functional and genetic study is needed to ascertain the correlation between HLA-C*04:01 and HBV infection.

CONCLUSION

In conclusion, our findings identify a previously unknown viral antigen peptides presentation-based immune response mechanism that targets a key step in the MHC class I antigen-processing pathway.

DATA AVAILABILITY STATEMENT

The data presented in the study are deposited in the ProteomeXchange Consortium repository (http://proteomecentral.proteomexchange.org), accession number PXD031858.

ETHICS STATEMENT

The studies involving human participants were reviewed and approved by Ethics Committee for the Second Affiliated Hospital of Anhui Medical University. The patients/participants provided their written informed consent to participate in this study.

AUTHOR CONTRIBUTIONS

HL and LC: conceptualization. HL and BH: data curation. JH, QW, and FW: formal analysis. HL, BH, and JH: investigation. HL: writing—original draft. LC and FP: writing, reviewing, and editing. All authors have read and agreed to the published version of the manuscript.

FUNDING

This study was supported by the Natural Science Foundation of Anhui Province (grant no. 1808085MH229) and the Key Research and Development Program of Anhui Province (grant no. 202004j07020027).

ACKNOWLEDGMENTS

We are grateful to the Department of Epidemiology and Biostatistics, School of Public Health, Anhui Medical University who provide assistance in data processing.

SUPPLEMENTARY MATERIAL

The Supplementary Material for this article can be found online at: https://www.frontiersin.org/articles/10.3389/fmicb.2022.829241/full#supplementary-material

Supplementary Figure 1 | ERAP1-IN-1 displays no toxicity to HepG2.2.15 cells at working concentration (50 μm). Cell viability of HepG2.2.15 cells treated with gradient concentrations of ERAP1-IN-1 was assayed by WST-8/CCK-8, and the positive control group (cells left untreated) was normalized to 100%.

Supplementary Figure 2 | Titration of ERAP1-IN-1 inhibits recombinant ERAP1 activity *in vitro*.

Supplementary Figure 3 | The level of HBsAg, HBeAg, and HBV-DNA in the supernatants of HepG2.2.15 cells treated or left untreated with ERAP1-IN-1 for 72 h.

REFERENCES

Alvarez-Navarro, C., and Lopez de Castro, J. A. (2014). ERAP1 structure, function and pathogenetic role in ankylosing spondylitis and other MHC-associated diseases. *Mol. Immunol.* 57, 12–21. doi: 10.1016/j.molimm.2013.06.012

Blanchard, N., Kanaseki, T., Escobar, H., Delebecque, F., Nagarajan, N. A., Reyes-Vargas, E., et al. (2010). Endoplasmic reticulum aminopeptidase associated with antigen processing defines the composition and structure of MHC class I peptide repertoire in normal and virus-infected cells. *J. Immunol.* 184, 3033–3042. doi: 10.4049/jimmunol.0903712

Burton, P. R., Clayton, D. G., Cardon, L. R., Craddock, N., Deloukas, P., Duncanson, A., et al. (2007). Association scan of 14,500 nonsynonymous SNPs in four diseases identifies autoimmunity variants. *Nat. Genet.* 39, 1329–1337. doi: 10.1038/ng.2007.17

Chang, S. C., Momburg, F., Bhutani, N., and Goldberg, A. L. (2005). The ER aminopeptidase, ERAP1, trims precursors to lengths of MHC class I peptides by a "molecular ruler" mechanism. *Proc Natl Acad Sci U.S.A.* 102, 17107–17112. doi: 10.1073/pnas.0500721102

Chen, Y., and Tian, Z. (2019). HBV-induced immune imbalance in the development of HCC. *Front. Immunol.* 10:2048. doi: 10.3389/fimmu.2019.02048

Cifaldi, L., Lo Monaco, E., Forloni, M., Giorda, E., Lorenzi, S., Petrini, S., et al. (2011). Natural killer cells efficiently reject lymphoma silenced for the endoplasmic reticulum aminopeptidase associated with antigen processing. *Cancer Res.* 71, 1597–1606. doi: 10.1158/0008-5472.CAN-10-3326

Cresswell, P. (2019). A personal retrospective on the mechanisms of antigen processing. *Immunogenetics* 71, 141–160. doi: 10.1007/s00251-018-01098-2

Gallina, A., Bonelli, F., Zentilin, L., Rindi, G., Muttini, M., and Milanesi, G. (1989). A recombinant hepatitis B core antigen polypeptide with the protamine-like domain deleted self-assembles into capsid particles but fails to bind nucleic acids. *J. Virol.* 63, 4645–4652. doi: 10.1128/JVI.63.11.4645-4652.1989

Georgiadou, D., and Stratikos, E. (2009). Cellular Mechanisms that Edit the Immunopeptidome. *Curr. Proteomics* 6, 13–24. doi: 10.2174/157016409787847439

Goto, Y., Ogawa, K., Hattori, A., and Tsujimoto, M. (2011). Secretion of endoplasmic reticulum aminopeptidase 1 is involved in the activation of macrophages induced by lipopolysaccharide and interferon-gamma. *J. Biol. Chem.* 286, 21906–21914. doi: 10.1074/jbc.M111.239111

Guidotti, L. G., and Chisari, F. V. (2001). Noncytolytic control of viral infections by the innate and adaptive immune response. *Annu. Rev. Immunol.* 19, 65–91. doi: 10.1146/annurev.immunol.19.1.65

Guidotti, L. G., Rochford, R., Chung, J., Shapiro, M., Purcell, R., and Chisari, F. V. (1999). Viral clearance without destruction of infected cells during acute HBV infection. *Science* 284, 825–829. doi: 10.1126/science.284.5415.825

Hammer, G. E., Kanaseki, T., and Shastri, N. (2007). The final touches make perfect the peptide-MHC class I repertoire. *Immunity* 26, 397–406. doi: 10.1016/j.immuni.2007.04.003

Hoofnagle, J. H., Gerety, R. J., and Barker, L. F. (1975). Hepatitis B core antigen and antibody. *Dev. Biol. Stand.* 30, 175–185.

Hu, Z., Liu, Y., Zhai, X., Dai, J., Jin, G., Wang, L., et al. (2013). New loci associated with chronic hepatitis B virus infection in Han Chinese. *Nat. Genet.* 45, 1499–1503. doi: 10.1038/ng.2809

James, E., Bailey, I., Sugiyarto, G., and Elliott, T. (2013). Induction of protective antitumor immunity through attenuation of ERAAP function. *J. Immunol.* 190, 5839–5846. doi: 10.4049/jimmunol.1300220

Jean-Jean, O., Levrero, M., Will, H., Perricaudet, M., and Rossignol, J. M. (1989). Expression mechanism of the hepatitis B virus (HBV) C gene and biosynthesis of HBe antigen. *Virology* 170, 99–106. doi: 10.1016/0042-6822(89)90356-5

Kim, S., Lee, S., Shin, J., Kim, Y., Evnouchidou, I., Kim, D., et al. (2011). Human cytomegalovirus microRNA miR-US4-1 inhibits CD8(+) T cell responses by targeting the aminopeptidase ERAP1. *Nat. Immunol.* 12, 984–991. doi: 10.1038/ni.2097

Koschel, M., Oed, D., Gerelsaikhan, T., Thomssen, R., and Bruss, V. (2000). Hepatitis B virus core gene mutations which block nucleocapsid envelopment. *J. Virol.* 74, 1–7. doi: 10.1128/jvi.74.1.1-7.2000

Koumantou, D., Barnea, E., Martin-Esteban, A., Maben, Z., Papakyriakou, A., Mpakali, A., et al. (2019). Editing the immunopeptidome of melanoma cells using a potent inhibitor of endoplasmic reticulum aminopeptidase 1 (ERAP1). *Cancer Immunol. Immunother.* 68, 1245–1261. doi: 10.1007/s00262-019-02358-0

Maben, Z., Arya, R., Rane, D., An, W. F., Metkar, S., Hickey, M., et al. (2020). Discovery of selective inhibitors of endoplasmic reticulum aminopeptidase 1. *J. Med. Chem.* 63, 103–121. doi: 10.1021/acs.jmedchem.9b00293

Maini, M. K., Boni, C., Lee, C. K., Larrubia, J. R., Reignat, S., Ogg, G. S., et al. (2000). The role of virus-specific CD8(+) cells in liver damage and viral control during persistent hepatitis B virus infection. *J. Exp. Med.* 191, 1269–1280. doi: 10.1084/jem.191.8.1269

Mani, S. K. K., and Andrisani, O. (2019). Interferon signaling during Hepatitis B Virus (HBV) infection and HBV-associated hepatocellular carcinoma. *Cytokine* 124:154518. doi: 10.1016/j.cyto.2018.08.012

Olvera, A., Perez-Alvarez, S., Ibarrondo, J., Ganoza, C., Lama, J. R., Lucchetti, A., et al. (2015). The HLA-C*04: 01/KIR2DS4 gene combination and human leukocyte antigen alleles with high population frequency drive rate of HIV disease progression. *AIDS* 29, 507–517. doi: 10.1097/QAD.0000000000000574

Papakyriakou, A., Zervoudi, E., Theodorakis, E. A., Saveanu, L., Stratikos, E., and Vourloumis, D. (2013). Novel selective inhibitors of aminopeptidases that generate antigenic peptides. *Bioorg. Med. Chem. Lett.* 23, 4832–4836. doi: 10.1016/j.bmcl.2013.07.024

Saric, T., Chang, S. C., Hattori, A., York, I. A., Markant, S., Rock, K. L., et al. (2002). An IFN-gamma-induced aminopeptidase in the ER, ERAP1, trims precursors to MHC class I-presented peptides. *Nat. Immunol.* 3, 1169–1176. doi: 10.1038/ni859

Stinco, M., Rubino, C., Trapani, S., and Indolfi, G. (2021). Treatment of hepatitis B virus infection in children and adolescents. *World J. Gastroenterol.* 27, 6053–6063. doi: 10.3748/wjg.v27.i36.6053

Tenzer, S., Wee, E., Burgevin, A., Stewart-Jones, G., Friis, L., Lamberth, K., et al. (2009). Antigen processing influences HIV-specific cytotoxic T lymphocyte immunodominance. *Nat. Immunol.* 10, 636–646. doi: 10.1038/ni.1728

Thimme, R., Wieland, S., Steiger, C., Ghrayeb, J., Reimann, K. A., Purcell, R. H., et al. (2003). CD8(+) T cells mediate viral clearance and disease pathogenesis during acute hepatitis B virus infection. *J. Virol.* 77, 68–76. doi: 10.1128/jvi.77.1.68-76.2003

Tsujimoto, M., Aoki, K., Ohnishi, A., and Goto, Y. (2020). Endoplasmic reticulum aminopeptidase 1 beyond antigenic peptide-processing enzyme in the endoplasmic reticulum. *Biol. Pharm. Bull.* 43, 207–214. doi: 10.1248/bpb.b19-00857

Watts, C., and Powis, S. (1999). Pathways of antigen processing and presentation. *Rev. Immunogenet.* 1, 60–74.

Wearsch, P. A., and Cresswell, P. (2008). The quality control of MHC class I peptide loading. *Curr. Opin. Cell Biol.* 20, 624–631. doi: 10.1016/j.ceb.2008.09.005

Weimershaus, M., Evnouchidou, I., Li, L., van Endert, P., and Bouvier, M. (2019). Trimming of MHC class I ligands by ERAP aminopeptidases. *Methods Mol. Biol.* 1988, 31–43. doi: 10.1007/978-1-4939-9450-2_3

Weiner, J., Suwalski, P., Holtgrewe, M., Rakitko, A., Thibeault, C., Muller, M., et al. (2021). Increased risk of severe clinical course of COVID-19 in carriers of HLA-C*04:01. *EClinicalMedicine* 40:101099. doi: 10.1016/j.eclinm.2021.101099

World Health Organization (2018). *Hepatitis B*. Geneva: World Health Organization.

Yengo, C. K., Torimiro, J., Kowo, M., Lebon, P. A., Tiedeu, B. A., Luma, H., et al. (2020). Variation of HLA class I (-A and -C) genes in individuals infected with hepatitis B or hepatitis C virus in Cameroon. *Heliyon* 6:e05232. doi: 10.1016/j.heliyon.2020.e05232

York, I. A., Brehm, M. A., Zendzian, S., Towne, C. F., and Rock, K. L. (2006). Endoplasmic reticulum aminopeptidase 1 (ERAP1) trims MHC class I-presented peptides *in vivo* and plays an important role in immunodominance. *Proc. Natl. Acad. Sci. U.S.A.* 103, 9202–9207. doi: 10.1073/pnas.0603095103

York, I. A., Chang, S. C., Saric, T., Keys, J. A., Favreau, J. M., Goldberg, A. L., et al. (2002). The ER aminopeptidase ERAP1 enhances or limits antigen presentation by trimming epitopes to 8-9 residues. *Nat. Immunol.* 3, 1177–1184. doi: 10.1038/ni860

Conflict of Interest: The authors declare that the research was conducted in the absence of any commercial or financial relationships that could be construed as a potential conflict of interest.

frontiers | Frontiers in Microbiology

ORIGINAL RESEARCH
published: 09 May 2022
doi: 10.3389/fmicb.2022.880394

Identification of Cytoplasmic Chaperone Networks Relevant for Respiratory Syncytial Virus Replication

*Victor Latorre and Ron Geller**

Viral Biology Group, Institute for Integrative Systems Biology (I2SysBio), Universitat de València-Consejo Superior de Investigaciones Científicas (CSIC), Paterna, Spain

RNA viruses have limited coding capacity and must therefore successfully subvert cellular processes to facilitate their replication. A fundamental challenge faced by both viruses and their hosts is the ability to achieve the correct folding and assembly of their proteome while avoiding misfolding and aggregation. In cells, this process is facilitated by numerous chaperone systems together with a large number of co-chaperones. In this work, we set out to define the chaperones and co-chaperones involved in the replication of respiratory syncytial virus (RSV). Using an RNAi screen, we identify multiple members of cellular protein folding networks whose knockdown alters RSV replication. The reduced number of chaperones and co-chaperones identified in this work can facilitate the unmasking of specific chaperone subnetworks required for distinct steps of the RSV life cycle and identifies new potential targets for antiviral therapy. Indeed, we show that the pharmacological inhibition of one of the genes identified in the RNAi screen, valosin-containing protein (VCP/p97), can impede the replication of RSV by interfering with the infection cycle at multiple steps.

Keywords: respiratory syncytial virus, chaperones, valosin-containing protein, antivirals, *Mononegavirales*

OPEN ACCESS

Edited by:
Yongqun Oliver He,
University of Michigan, United States

Reviewed by:
Yves Gaudin,
Centre National de la Recherche Scientifique (CNRS), France
Melinda Ann Brindley,
University of Georgia, United States

***Correspondence:**
Ron Geller
ron.geller@uv.es

Specialty section:
This article was submitted to Virology, a section of the journal Frontiers in Microbiology

Received: *21 February 2022*
Accepted: *04 April 2022*
Published: *09 May 2022*

Citation:
Latorre V and Geller R (2022) Identification of Cytoplasmic Chaperone Networks Relevant for Respiratory Syncytial Virus Replication. Front. Microbiol. 13:880394. doi: 10.3389/fmicb.2022.880394

INTRODUCTION

The majority of RNA viruses have small genomes and encode only a few proteins. Nevertheless, RNA viruses are able to perform an astonishing number of functions with their limited proteome, including disarming antiviral defenses, replicating the viral genome, producing new virions, and spreading to new cells and/or hosts. To a large part, this is achieved by masterfully interacting with, and coopting, cellular processes to favor viral replication at each step of the virus life cycle.

Among the key challenges faced by viruses and cells alike is the successful translation of their genome to a functional proteome. In cells, this process is facilitated by a large number of dedicated protein-folding factors, termed chaperones, that help maintain cellular homeostasis (proteostasis) together with the protein degradation machinery (Kim et al., 2013; Balchin et al., 2016). To perform their functions, chaperones are organized into networks that cooperate to support folding from the

time the polypeptide emerges from the ribosome, through maturation and assembly into larger protein complexes, as well as at later points, when proteins become misfolded or aggregated (Kim et al., 2013; Balchin et al., 2016; Bar-Lavan et al., 2016). The major chaperone systems in human cells are comprised of numerous isoforms of Hsp70/HSPA, a constitutive and a stress-inducible isoform of Hsp90/HSPC, and the oligomeric chaperone complex TRiC/CCT (Kim et al., 2013; Balchin et al., 2016; Bar-Lavan et al., 2016; Radons, 2016a,b). To facilitate client protein folding and maturation, these chaperones employ ATP-hydrolysis to drive conformational changes in their client proteins. These major chaperone systems are regulated by a much larger cohort of co-chaperones that provide client-protein specificity and interconnect different chaperone systems. For example, the binding of client proteins to Hsp70 and the chaperone cycle are regulated by > 50 DNAJ/Hsp40 proteins and nucleotide exchange factors, such as BAG domain proteins (Kampinga and Craig, 2010; Bracher and Verghese, 2015). Similarly, Hsp90 activity is regulated by numerous co-chaperones that regulate client-protein binding and release (Schopf et al., 2017). Finally, the activity of both the Hsp70 and Hsp90 chaperones systems are linked via interaction with a large set of proteins containing tetratricopeptide repeat (TPR) domains (Balchin et al., 2016). Aside from these central systems, a set of small heat shock proteins (HSPBs) form part of the cellular response to combat protein aggregation, and the prefoldin chaperone participates in early folding events en route to the central chaperone systems (Balchin et al., 2016).

While chaperones are mainly involved in protein folding, they participate in the degradation of terminally misfolded proteins via both the proteasomal and autophagy pathways (Edkins, 2015; Ciechanover and Kwon, 2017). This is accomplished by co-chaperones that help link individual chaperones with the degradation machinery. For example, the C-terminus of Hsc70-interacting protein (CHIP) is an E3 ubiquitin ligase that ubiquitinates misfolded proteins to tag them for proteasomal degradation. Via its TPR domain, CHIP interacts with both Hsp70 and Hsp90, linking these chaperone systems to the cellular degradation machinery (Edkins, 2015; Dikic, 2017). Additionally, valosin-containing protein (VCP)/p97 is an ATP-dependent multifunctional protein that assists in the remodeling of protein complexes as well as in the extraction of proteins across membranes, as in ER-associated degradation (ERAD) (Dikic, 2017; Ye et al., 2017; Huryn et al., 2020). While VCP/p97 is frequently involved in facilitating the degradation of proteins, it can also act to disassemble complexes (Ye et al., 2017).

As is the case with cellular proteins, the proteins of RNA viruses are folded by cellular chaperone systems. Indeed, pharmacological inhibition of Hsp70 and Hsp90 has revealed that many RNA viruses are not only dependent on these central chaperone systems for their replication but are in fact hypersensitive to changes in their levels compared to host cells (Mayer, 2005; Geller et al., 2012; Wang et al., 2017; Aviner and Frydman, 2019). Accordingly, reductions in the activity of these chaperones at levels that are not toxic to cells are highly detrimental to viral replication, making chaperone inhibitors broad-spectrum antivirals (Mayer, 2005; Geller et al., 2012; Wang et al., 2017; Aviner and Frydman, 2019). However, a more general understanding of chaperone networks utilized by particular viruses is largely lacking. Recently, different components of the Hsp70 chaperone system were shown to play distinct roles at different stages of the replication cycle of both Dengue virus and ZIKA virus (Taguwa et al., 2015, 2019).

In this work, we aimed to obtain a general picture of chaperones utilized by a medically relevant human RNA virus, respiratory syncytial virus (RSV). RSV is among the most important respiratory infections in the pediatric setting and causes significant morbidity in the elderly population (Griffiths et al., 2017; Bergeron and Tripp, 2021). RSV belongs to the *Mononegavirales* order, harboring a single-stranded, negative-sense RNA genome, and encodes 11 different proteins. Hence, RSV represents a relatively simple model with which to begin to untangle cellular protein folding networks. While prior work has shown Hsp70 and Hsp90 to play a key role in the replication of RSV (Radhakrishnan et al., 2010; Geller et al., 2013; Munday et al., 2015; Huong et al., 2016; Latorre et al., 2018), general information about additional chaperone systems and/or co-chaperones is lacking. To this end, we conducted an RNAi screen for a large number of cytoplasmic chaperones and co-chaperones in human cells. We identify numerous players in the protein-folding network to modulate RSV replication. This information can be used as a starting point to map specific chaperone subnetworks required for distinct steps of the RSV infection cycle. In addition, some of the identified factors can present potential targets for antiviral therapy. Indeed, we show that pharmacological inhibition of one of the identified genes, the VCP/p97 protein, can block the replication of RSV as well as an additional member of the *Mononegavirales*, supporting its potential as a broad-spectrum antiviral target.

MATERIALS AND METHODS

Cell Lines, Viruses, and Reagents

HeLa-H1 (CRL-1958), HEp2 (CCL-23), HEK-293 (CRL-1573), and A549 (CCL-185) cells were obtained from ATCC. All cells were maintained in DMEM with 10% FBS, 100 IU/mL penicillin, and 100 μg/mL streptomycin at 5% CO_2 and 37°C. RSV expressing the fluorescent protein mKate2 (RSV-mKate2) was generated by transfection of the infectious clone system obtained from BEI Resources (NIAID, NIH: Bacterial artificial chromosome plasmid pSynkRSV-I19F containing antigenomic cDNA from respiratory syncytial virus (RSV) A2-Line19F, NR-3646). This was done by transfection of HEK-293 cells with an optimized T7 plasmid (Addgene, United States, 65974) together with the antigenomic plasmid, N, P, M2-1, and L plasmids at a ratio of 4:2:2:2:1 using Lipofectamine 2000 (Thermo Fisher Scientific, United States). Cells were transfected in 6 well plates and subsequently transferred to T25 flasks with Hep2 cells until cytopathic effect (CPE) was observed. For the generation of RSV encoding nanoluciferase (RSV-nanoLuc), the mKate2 open reading frame was replaced with that of the nanoluciferase gene from pNL1.2[NlucP] (Promega) and the virus was generated as indicated above. Passage 0 stocks were

amplified 3 additional times and titrated using TCID50 (RSV-nanoLuc) and plaque assay (RSV-mKate2; see below). Vesicular stomatitis virus (VSV) encoding mCherry was kindly provided by Dr. Rafael Sanjuan (University of Valencia). CVB3 was generated as previously described (Mattenberger et al., 2021). The VCP/p97 inhibitor CB-5083 (CAS: 1542705-92-9; Cayman Chemicals, United States) and the hsp90 inhibitor 17-DMAG (CA 467214-20-6; LC Laboratories) were dissolved in DMSO and resazurin (CAS: 62758-13-8; Sigma-Aldrich, United States) was dissolved in water.

Virus Quantification

Plaque assays were used to measure RSV, VSV, and CVB3 infectious virus production. For this, serial dilutions of the virus were used to infect confluent HeLa-H1 cells in 6 well plates for 2 h (RSV-mKate2) or 45 min (VSV-mCherry and CVB3). Subsequently, the virus was removed and cells overlaid with DMEM containing 2% FBS and either 0.6% agarose for RSV-mKate2 and VSV-mCherry or 0.8% agarose for CVB3 during 24 h. Finally, RSV-mKate2 plaques were assessed by examining fluorescence using a live-cell microscope (IncuCyte S3; Sartorius), while VSV-mCherry and CVB3 plaques were visualized using crystal violet staining following fixation with 1% formaldehyde. For the TCid50 assay, confluent Hep2 cells in a 96 well plate were infected with serial dilutions of RSV-nanoLuc (8 replicates) in DMEM containing 2% FBS. Seven days after the infection, cells were fixed with 1% formaldehyde and stained with crystal violet. To quantify intracellular virus replication, the mean fluorescence signal in each well resulting from the expression of the viral encoded fluorescent protein (mKate2 or mCherry) was obtained using a live-cell microscope.

RNAi Screening

Genes were selected for evaluation based on a list of the human chaperone network (Brehme et al., 2014), which was filtered to exclude non-cytoplasmic chaperones and those not expressed in A549 cells or lung tissue based on data from the human protein atlas.[1] This list was inspected individually, and missing known chaperone/co-chaperone genes were included (**Supplementary Table 1**). We then ordered endoribonuclease prepared siRNA (MISSION esiRNA, Sigma-Aldrich, United States) for all genes for which esiRNA were available (**Supplementary Table 3**). For the primary screen, A549 cells were reverse transfected with 20 uM of esiRNA using the MISSION siRNA Transfection Reagent (Sigma-Aldrich, United States) following the manufacturer protocol in white-bottom 96 well plates. After 48 h, cells were infected with RSV-nanoLuc at a multiplicity of infection (MOI) of 0.01. Finally, RSV replication was evaluated by reading nano-luciferase activity with the Nano-Glo Luciferase Assay system (Promega) on a Tecan Spark plate reader. All experiments were performed in 6 replicates on 6 independent plates. The strictly standardized mean difference (SSMD) relative to infected wells that were transfected with a control esiRNA targeting firefly luciferase was calculated using the UMVUE estimate of SSMD (formula A5 in Table 3 in Zhang, 2011). Finally, *p*-values were converted to *q*-values to correct for multiple testing using the R package *q*-value (version 3.14). For the secondary validation, esiRNAs targeting a different region of the gene were employed (esiSec; Sigma-Aldrich, United States; see **Supplementary Table 3**). Two different esiRNAs targeting CryAB and PFD2 were tested, of which only 1 resulted in knockdown and was analyzed (HU-01337-3 for PFD2 and HU-01732-2 for CRYAB). The experiment was performed similarly, except that all six replicates for each esiRNA were performed in the same plate, and RSV-mKate2 was used. Virus replication was assessed at 24 hpi by quantifying the average red fluorescence in each well using a live cell microscope (Incucyte S3, Sartorius).

[1] https://www.proteinatlas.org/

Evaluation of Gene Knockdown

A549 cells were reverse transfected as indicated above. Following 72 h, gene expression was measured by qPCR. For this, RNA was extracted from A549 cells using RNAzol RT (Sigma-Aldrich, United States) following the manufacturer's protocol. The cDNA was then synthesized from 500 ng of RNA and used to evaluate gene expression by qPCR using the primers listed in **Supplementary Table 4** and the M-MuLV Reverse Transcriptase (NZYtech, Portugal) in a QuantStudio3 machine using the PowerUp SYBR green qPCR master mix (Applied Biosystems, United States). Knockdown efficiency was calculated by standardizing target gene expression to that of GAPDH in esiRNA transfected cells vs. control-esiRNA transfected cells using the $\Delta\Delta$Ct method. For a few esiRNA, high expression levels were observed in knockdown cells and these were retested individually and the strongest gene knock-down level was taken as the knockdown value.

Toxicity Evaluation

To assess esiRNA toxicity, cells were transfected in triplicate as indicated above and incubated at 37°C for 72 h. Subsequently, the medium was replaced by fresh DMEM containing a final concentration of 44 μM resazurin. After a 1-h incubation period, fluorescence was read using excitation/emission filters of 535/595 nm using a microplate reader (Tecan Spark). Toxicity was compared by standardizing to the average signal obtained from cells transfected with the control esiRNA. To assess CB-5083 toxicity, cells were treated with increasing concentrations of the inhibitor for 24 h before the addition of resazurin as indicated above.

Drug Treatments

Cells were treated with different concentrations of the VCP/p97 inhibitor CB-5083 for 2 h. Subsequently, cells were infected at an MOI of 1 for 2 h in the presence of the drug. Following infection, the virus inoculum was removed and fresh media containing the indicated inhibitor concentration was added. Twenty-four hours later, the supernatant was collected and used for measuring virus production via a plaque assay as indicated below.

Analysis of VSV-Glycoprotein Surface Expression

Hela-H1 cells were transfected with a plasmid encoding the VSV-G gene (pMD2.G; Addgene, United States #12259) using Lipofectamine 2000. Twenty-four hours later, 1 μM CB-5083 or

DMSO were added to the media for an additional 24 h. Finally, cells were trypsinized, stained with a primary anti-VSV antibody (Cuevas et al., 2017) (kind gift of Dr. Rafael Sanjuán), followed by a FITC labeled secondary goat anti-mouse IgG (Thermo Fisher Scientific, United States) and analyzed on a FACSVerse (BD Biosciences).

Statistical Analysis

All statistical tests were performed with R (version 4.1.2) and graphs produced with the ggpubr (version 0.4.0) package. All tests were two-tailed, and the individual test employed is indicated in the main text. *Q*-values were obtained using the *q*-value package (version. 3.14). Statistical significant was set at $p < 0.05$ or $q < 0.05$.

RESULTS

RNAi Screen to Identify Chaperones Involved in the Replication of Respiratory Syncytial Virus

In order to define which cytoplasmic chaperones are involved in the RSV replication cycle, we selected a list of cytoplasmic cellular molecular chaperones as well as key modulators of proteostasis that are expressed in the lung (see section "Materials and Methods"; **Supplementary Table 1**). From this list, endoribonuclease-prepared siRNA (esiRNA) were commercially available for 114 (**Supplementary Table 2**). These included a total of 37 chaperones genes from all major cytoplasmic chaperone families (Hsp70, Hsp90, TRiC/CCT, Prefoldin, and small heat shock proteins), 73 co-chaperones (e.g., Hsp40s, proteins containing TPR domain), a central player in the protein degradation machinery that cooperates with different chaperone systems (VCP/p97), and three genes from transcription factors involved in the cellular heat shock response (HSF; see **Supplementary Table 2**).

To identify cytoplasmic chaperones relevant to RSV infection, we used the human lung adenocarcinoma cell line A549 as a model for the alveolar type II pulmonary epithelium. We first assessed the effects of chaperone depletion on cell viability. A549 cells were transfected with the different esiRNAs and cell viability was assessed 3 days following transfection using the Alamar Blue (resazurin reduction) assay (**Supplementary Figure 1A** and **Supplementary Table 2**). Most esiRNA transfections resulted in low or no toxicity, with greater than two-thirds of genes maintaining cell viability above 70% relative to non-targeting control transfection (77 of 114 genes). Strong toxicity was only observed for 5% of esiRNAs, which reduced viability > 50% (**Supplementary Table 2**). We next evaluated the effect of ∼60% of the esiRNAs (69 of the 114) for their knockdown efficiency using qPCR to measure target gene expression. A median reduction of 70% was observed, with greater than two-thirds (47/69) of the genes showing less than 50% expression, suggesting gene-specific knockdown is achieved using the esiRNA transfection (**Supplementary Figure 1B** and **Supplementary Table 2**).

We next evaluated the effect of chaperone depletion on RSV replication (**Figure 1A**). To this end, cells were transfected with esiRNA targeting the different chaperones or a control esiRNA targeting firefly luciferase. Following 48 h, cells were infected with an RSV strain carrying a nano-luciferase reporter (RSV-nanoLuc) at a low multiplicity of infection for 24 h. Finally, nanoLuc activity was measured to quantify virus entry and intracellular replication and the results were standardized to that of control transfected conditions. Hits were evaluated using the strictly standardized mean difference (SSMD) and its associated significance value following multiple testing correction (*q*-value) (Zhang, 2011). SSMD provides a measure of effect size that takes into account variability in both experimental and control conditions, with positive values indicating increased replication and negative values indicating reduced replication. In total, 24 genes showing a knockdown efficiency of at least 20% had a statistically significant effect on RSV replication ($q < 0.05$) that was classified as at least moderate (absolute SSMD score of > 1.28; **Figure 1B** and **Supplementary Table 5**). The effect on RSV replication was not significantly associated with viability ($p = 0.13$, Spearman's $\rho = -3.2$), suggesting the results are likely to stem from specific effects on RSV replication rather than toxicity. Within this dataset, genes belonging to all major chaperone systems were observed (e.g., Hsp70/HSPA, Hsp90/HSPC, TRiC/CCT, prefoldin), the multifunctional VCP/p97 protein, master regulators of the transcriptional response to stress (Heat Shock Factor; HSF1), and co-chaperones regulating the activity of Hsp70 and Hsp90 (**Figure 1B** and **Supplementary Table 5**). Nearly all of the identified chaperones resulted in reduced replication following their depletion, indicating a supportive role in the RSV replication cycle; however, the replication of RSV increased following the depletion of two chaperones, SGTB and DNAJC12, suggesting these could be detrimental to RSV replication under normal conditions (**Figure 1B** and **Supplementary Table 5**). Importantly, we identify isoforms of both the Hsp70 and Hsp90 chaperones to inhibit RSV replication, as has been previously reported using pharmacological inhibitors (Geller et al., 2013; Munday et al., 2015; Latorre et al., 2018), confirming the ability of the screen to identify relevant chaperones.

To validate the results of the primary screen, we obtained esiRNA targeting alternative regions in 15 genes that showed a significant reduction in RSV replication when depleted (**Supplementary Table 5**). Moreover, to account for any effects the chaperones could have on the nanoLuc reporter rather than RSV replication, we used an RSV strain encoding a red fluorescent gene (RSV-mKate2) for the validation test. From the 15 genes analyzed, 80% significantly reduced RSV replication ($q < 0.05$; 12/15 genes) without strong toxicity (viability > 70%; **Figure 1C** and **Supplementary Table 5**) supporting the validity of the primary screen. For two of the three genes that did not show a significant effect on replication in the secondary screen, lower knockdown levels were observed (approximately two and sixfold lower for CCT2 and PFDN2, respectively), which could underlie the lack of effect. For the third gene, CDC37, a similar reduction in gene expression was observed in both the primary and secondary screens, indicating this gene is not likely

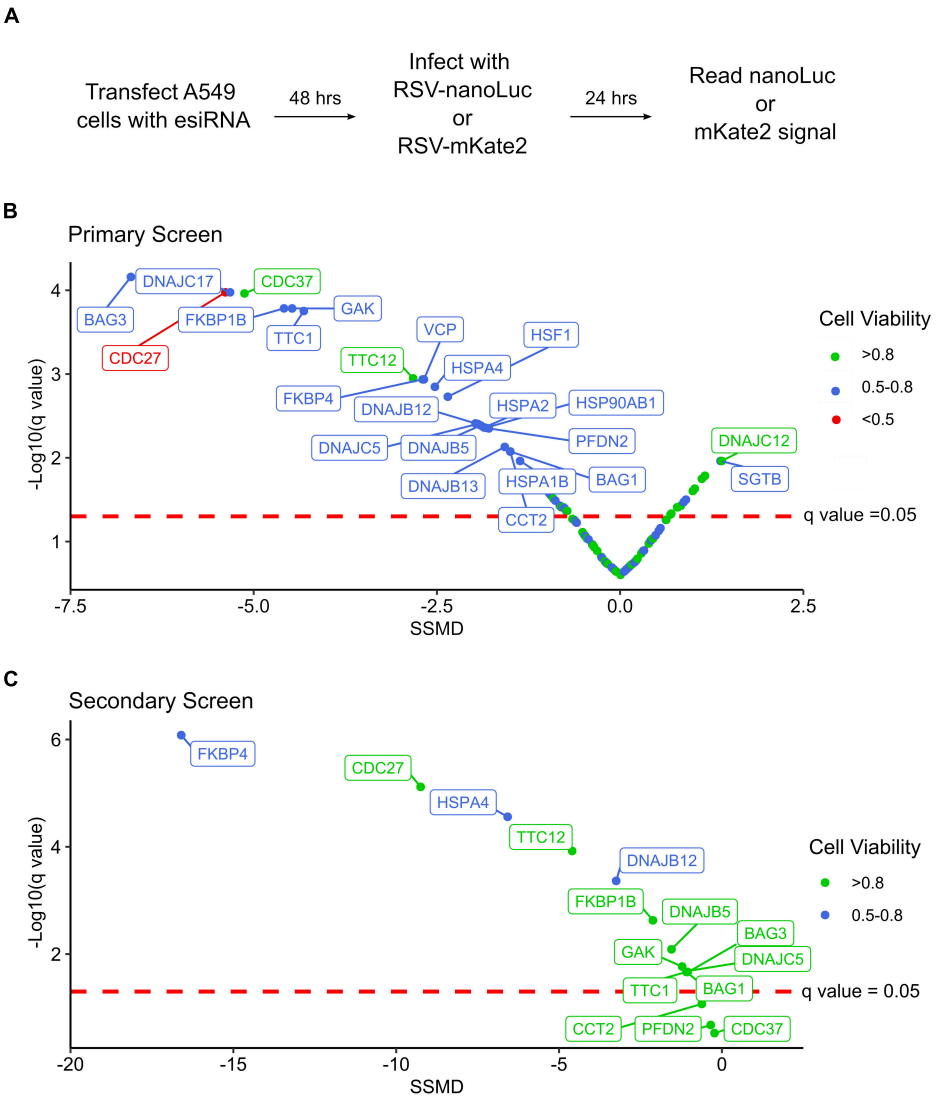

FIGURE 1 | An RNAi screen for chaperones and co-chaperones involved in RSV replication. **(A)** Overview of the experimental approach. **(B)** Results of the primary screening, showing the strictly standardized mean deviation (SSMD) and the statistical significance (*q*-value). *n* = 6. **(C)** Results of the secondary screening, showing the SSMD and statistical significance. *n* = 6.

to represent a real hit. A very strong reduction in RSV replication was observed for FKBP4, a cis-trans prolyl isomerase from the immunophilin family that interacts with Hsp70 and Hsp90, the Hsp70 nucleotide exchange factor HSPA4, and the Hsc70 co-chaperone DNAJB12 (**Figure 1C** and **Supplementary Table 5**).

Valosin-Containing Protein Inhibition Reduces the Replication of Respiratory Syncytial Virus and Vesicular Stomatitis Virus

Pharmacological inhibitors of cellular factors provide a direct means to assess the relevance of the targeted protein in viral infection. Indeed, Hsp70 and Hsp90 inhibitors have been used to demonstrate the relevance of these chaperones in the viral replication cycle (Geller et al., 2012, 2013; Aviner and Frydman, 2019; Yang et al., 2020). We therefore chose to validate the antiviral role of VCP/p97, which was identified in the primary screen (**Figure 1B**), using a selective inhibitor that prevents ATP binding to VCP/p97, CB-5083 (Zhou et al., 2015; Huryn et al., 2019). We first evaluated the toxicity of CB-5083 in A549 cells. Concentrations of up to 0.5 μM resulted in low toxicity (~90% viability), while higher concentrations resulted in significant toxicity (~50% viability at 2 μM; **Figure 2A**). Next, we assessed the effect of VCP/p97 inhibition on RSV production. For this, cells were infected in the presence of VCP/p97 and RSV production was quantified following 24 h. At CB-5083 concentrations of 0.5 μM, RSV production was reduced by ~90% ($p < 0.01$ by Mann-Whitney test), while concentrations of 1μM resulted in a > 99% reduction but showed higher toxicity

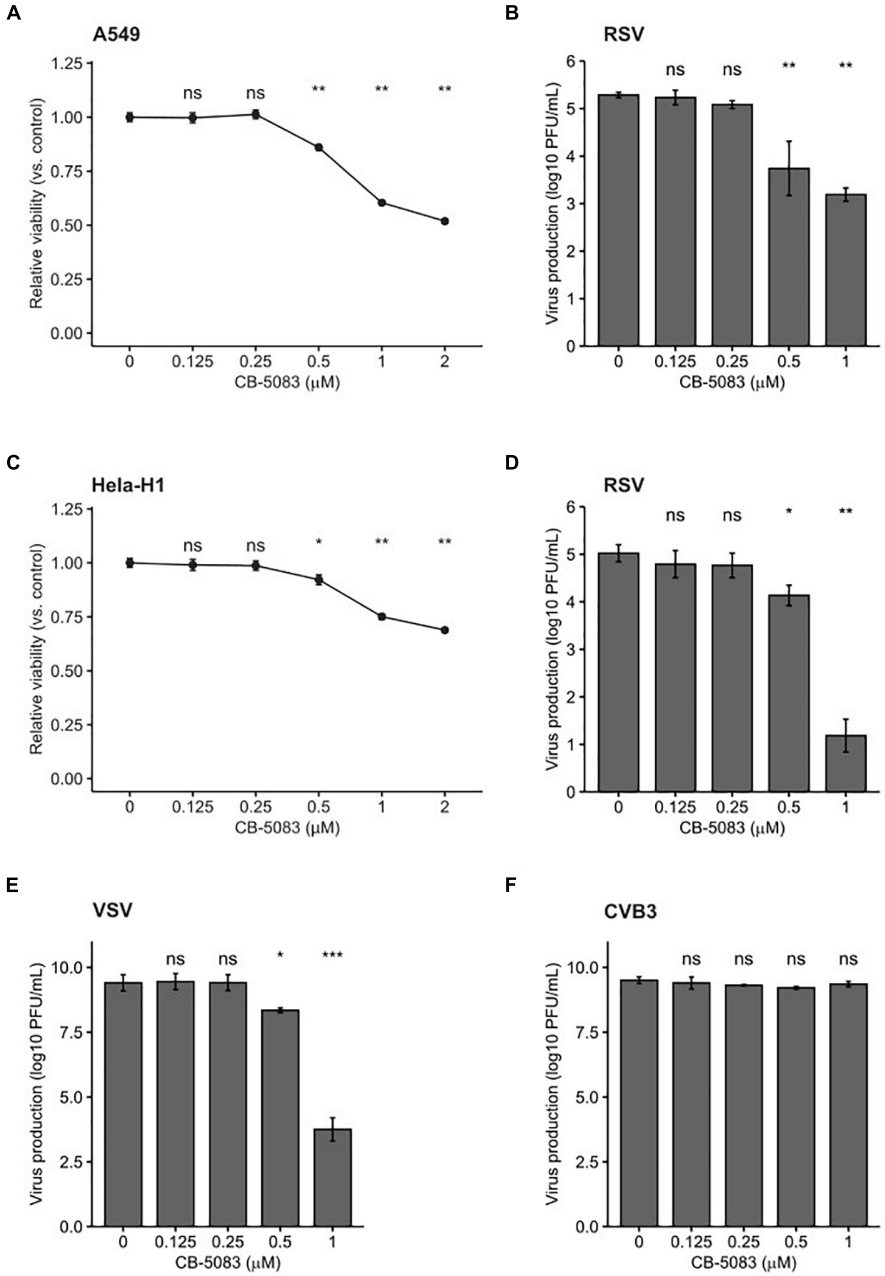

FIGURE 2 | VCP/p97 inhibition reduces RSV and VSV production. **(A)** The effect of the VCP/p97 inhibitor CB-5083 on A549 cell viability ($n = 6$). **(B)** The effect of CB-5083 on RSV virus production in A549 ($n = 6$). **(C)** The effect of the VCP/p97 inhibitor CB-5083 on Hela-H1 cell viability ($n = 6$). **(D,E)** The effect of CB-5083 on RSV ($n = 7$) **(D)**, vesicular stomatitis virus (VSV) ($n = 7$) **(E)**, or coxsackievirus B3 (CVB3) production ($n = 4$). **(F)** Virus production in Hela-H1 cells. Results indicate the mean and SEM. $^{ns}p > 0.05$; $^{*}p < 0.05$; $^{**}p < 0.01$; $^{***}p < 0.001$ by a two-tail, unpaired Mann-Whitney test/Wilcoxon rank sum exact test.

($p < 0.01$ by Mann-Whitney test; **Figures 2A,B**). To ensure the effect was not cell-specific, we repeated the experiments in Hela-H1 cells. At concentrations that did not alter cell viability strongly (> 92% viability at 0.5 μM; **Figure 2C**), RSV production was reduced by 84% ($p < 0.05$ by Mann-Whitney test; **Figure 2D**). Interestingly, VCP/p97 inhibition also reduced the production of an unrelated member of the *Mononegavirales* order, vesicular stomatitis virus (VSV), by 98% at the same concentration ($p < 0.05$ by Mann-Whitney test; **Figure 2E**). Inhibitor concentrations showing higher toxicity (25% toxicity; 1 μM) had profound antiviral activity, reducing RSV and VSV production by > 3 and > 5 logs, respectively ($p < 0.01$ and $p < 0.001$ by Mann-Whitney test for RSV and VSV, respectively; **Figures 2D,E**). Importantly, these antiviral effects are not the result of toxicity, as the replication of a positive-strand RNA virus, coxsackievirus B3 (CVB3), was not affected at inhibitor

concentrations up to 1 μM ($p > 0.05$ by Mann-Whitney test; **Figure 2F**), as has been previously reported (Arita et al., 2012).

Valosin-Containing Protein Is Not Involved in the Early Steps of Viral Infection

To determine whether VCP/p97 is involved in the early steps of viral replication, namely entry and uncoating, we performed a time-of-addition study. Specifically, we added the VCP/p97 inhibitor CB-5083 at 1 μM to HeLa-H1 cells either 1 h before infection, following infection, or 2 h post-infection, when binding, entry, and uncoating are complete. We then used the fluorescence intensity of the viral-encoded reporter proteins to measure effects on viral replication. For RSV we observed an 87, 82, and 79% reduction in fluorescence intensity when the drug was added 1 h before infection, at the time of infection, or 2 h post-infection, respectively, compared with the DMSO-treated cells ($p < 0.01$ for all vs. DMSO by *t*-test on log-transformed data; **Figure 3A**). Similarly, VSV replication was reduced by 99.7, 99.8, and 99.9% when added 1 h before infection, at the time of infection, or 2 h post-infection, respectively, compared with the DMSO-treated cells ($p < 0.01$ for all conditions vs. DMSO by *t*-test on log-transformed data; **Figure 3B**), with no appreciable reduction in effectivity when the drug was added at a stage following entry and uncoating. As the effect of VCP/p97 inhibition on the replication of both RSV and VSV was similar when added prior to infection or after completion of the entry process, VCP/p97 likely acts downstream of these early steps in the viral infection cycle.

Valosin-Containing Protein Is Involved in Multiple Steps of the Viral Replication Cycle

The final steps in the viral replication cycle are the formation of mature virions and egress from the cell. To investigate whether VCP/p97 plays a role in these late stages of viral replication, we evaluated how CB-5083 affected intracellular viral replication compared to infectious particle formation in HeLa-H1. We reasoned that observing a stronger effect on the quantity of released infectious particles compared to intracellular replication will support an additional role for VCP/p97 in the late stages of viral replication. As a control, we tested the effects of an Hsp90 inhibitor, 17-DMAG (Egorin et al., 2002), under the same conditions. Hsp90 is known to be required for the folding and maturation of the RNA-dependent RNA polymerase of both RSV (Geller et al., 2013) and VSV (Connor et al., 2007). As polymerase function is required for replication but is not involved in late stages of the viral cycle, blocking Hsp90 should show a similar effect on both intracellular replication and virus production.

As in previous experiments (**Figures 2B,D**), both RSV intracellular viral replication, as measured by the quantification of viral encoded fluorescent protein, and virus production were significantly reduced by VCP/p97 inhibition at 1 μM (**Figures 4A,B**). However, virus production was reduced by ∼4-logs ($p < 0.0001$ by *t*-test on log-transformed data; **Figure 4A**), while intracellular replication was only reduced by ∼1-log when blocking VCP/p97 function ($p < 0.001$ by *t*-test on log-transformed data; **Figure 4B**). When standardizing the effect of VCP/p97 inhibition in each assay to control-treated cells, virus production was > 1,000 times more affected by VCP/p97 inhibition than intracellular replication ($p < 0.05$ by *t*-test on log-transformed data; **Figure 4C**). In contrast, while Hsp90 inhibition also reduced both RSV virus production ($p < 0.001$ by *t*-test on log-transformed data; **Figure 4A**) and intracellular viral replication ($p < 0.001$ by *t*-test on log-transformed data; **Figure 4B**), the relative effect on each one was similar (average standardized effect of intracellular replication vs. virus production of 3.44 ± 1.12; $p < 0.05$ by *t*-test on log-transformed data; **Figure 4C**). This is consistent with no additional role of the Hsp90-dependent viral RNA-dependent RNA polymerase in the late stages of replication. Similarly, for VSV, CB-5083 treatment diminished virus production by ∼6 logs ($p < 0.0001$ by *t*-test on log-transformed data; **Figure 4D**) and intracellular replication by ∼3 logs, respectively, ($p < 0.0001$ by *t*-test on log-transformed data; **Figure 4E**). As for RSV, virus production was > 1,000 times more affected by VCP/p97 inhibition than intracellular replication ($p < 0.0001$ by *t*-test on log-transformed

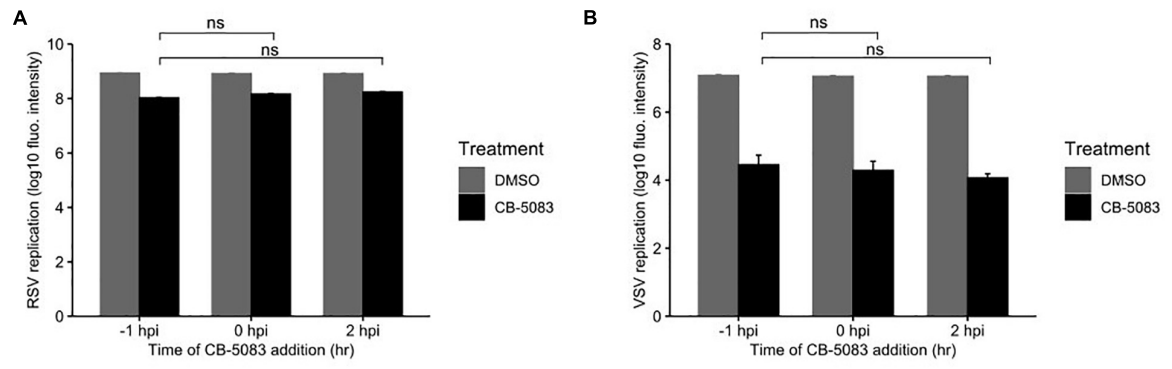

FIGURE 3 | VCP/p97 is not involved in the early steps of infection. The VCP/p97 inhibitor CB-5083 was added at the indicated time point relative to infection (hours post-infection, hpi) with RSV **(A)** or VSV **(B)** and virus production was quantified. Data represent the mean and SEM of three replicates. ns, $p > 0.05$ by *t*-test on log-transformed data vs. drug treatment 1 h prior to infection (–1 hpi).

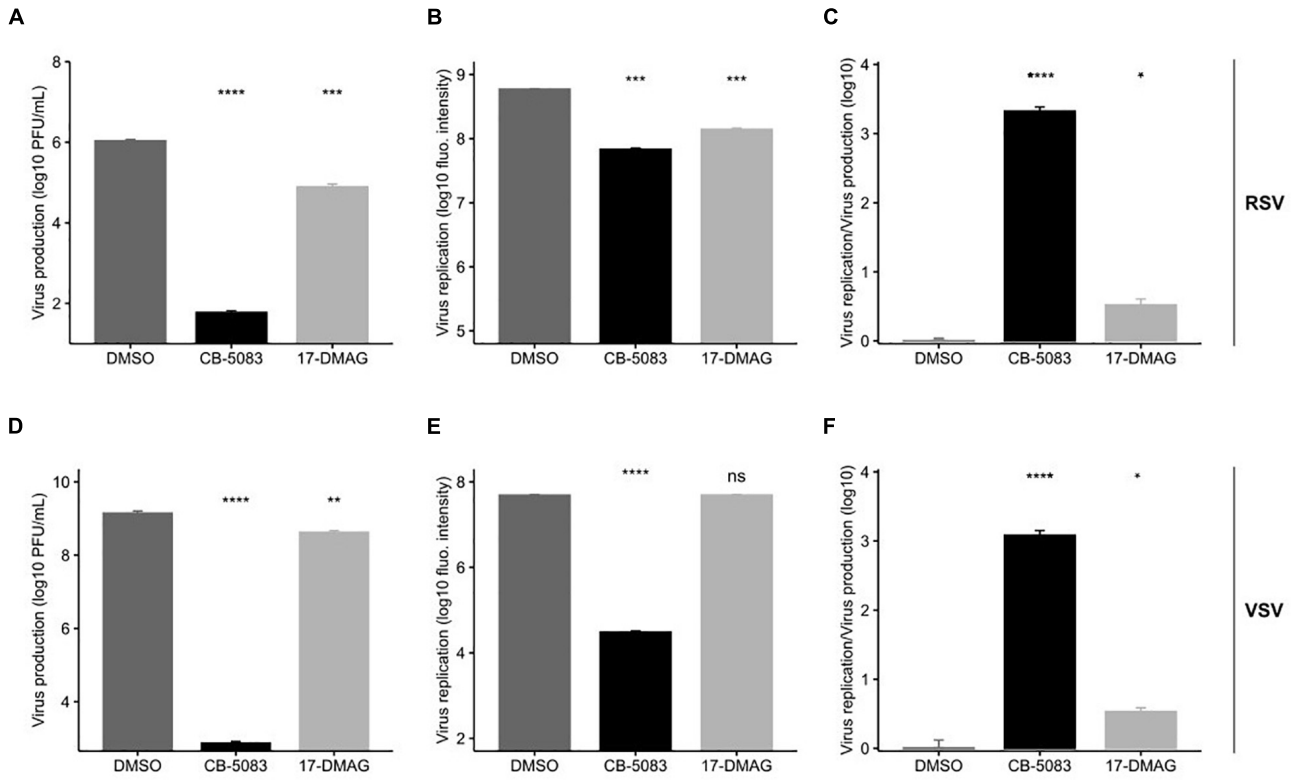

FIGURE 4 | VCP/p97 is involved in multiple steps of the RSV and VSV infection cycle. Cells were treated with the VCP/p97 inhibitor CB-5083 or the Hsp90 inhibitor 17-DMAG and infected with RSV (top row) or VSV (bottom row). Subsequently, virus production was measured by plaque assay **(A,D)** and intracellular replication was measured by the expression of a reporter protein **(B,E)**. The ratio of the antiviral effect observed for virus replication compared to virus production **(C,F)**. Plotted are the means and SEM for three replicates. $^{ns}p > 0.05$; $^{*}p < 0.05$; $^{**}p < 0.01$; $^{***}p < 0.001$; $^{****}p < 0.0001$ by *t*-test on log-transformed data.

data; **Figure 4F**). Hsp90 inhibition showed only mild inhibition of VSV virus production in our assay conditions, with a threefold reduction observed for virus production ($p < 0.01$ by *t*-test on log-transformed data; **Figure 4C**), and the effect on intracellular replication was not significant ($p > 0.05$ by *t*-test on log-transformed data; **Figure 4D**), potentially due to the late time point of infection at which we examined intracellular replication (24 h). Again, Hsp90 inhibition affected both VSV virus production and intracellular replication in a similar manner, indicating no specific role in late events (average standardized effect of intracellular replication vs. virus production of 3.47 ± 0.73; $p < 0.05$ by *t*-test on log-transformed data; **Figure 4F**).

Valosin-Containing Protein Inhibition Does Not Affect Trafficking to the Cell Surface

Both RSV and VSV encode glycoproteins that require translation, folding, and trafficking in the endoplasmic reticulum (ER). Since VCP/p97 is a key player in ER quality control and ER-associated degradation (van den Boom and Meyer, 2018; Hänzelmann et al., 2019; Huryn et al., 2019), we examined whether the translation of the VSV glycoprotein (VSV-G) was affected by VCP/p97 inhibition. For this, cells were transfected with a plasmid encoding VSV-G and subsequently treated with CB-5083 (1 μM) or DMSO for 24 h prior to assessing VSV-G surface expression by flow cytometry. Surprisingly, CB-5083 treatment resulted in a slightly enhanced expression of the VSV-G protein on the cell surface ($p < 0.01$ by *t*-test; **Figure 5**). Hence, the antiviral activity of VCP/p97 inhibition is not due to reduced translation or trafficking in the ER. However, it is important to note that these experiments do not assess whether the VSV-G protein is properly folded and functional.

DISCUSSION

Cellular proteostasis is maintained through highly interconnected networks of chaperones, co-chaperones, and components of the degradation machinery (Kim et al., 2013; Balchin et al., 2016; Bar-Lavan et al., 2016). The complexity of these interactions makes it challenging to define cellular proteostasis networks for particular proteins and/or cellular functions. As RNA viruses utilize the cellular proteostasis machinery but encode only a few proteins, they could provide a simplified system with which to define such proteostasis networks.

To date, very limited information is available on the cellular proteostasis machinery involved in RSV replication. Prior work

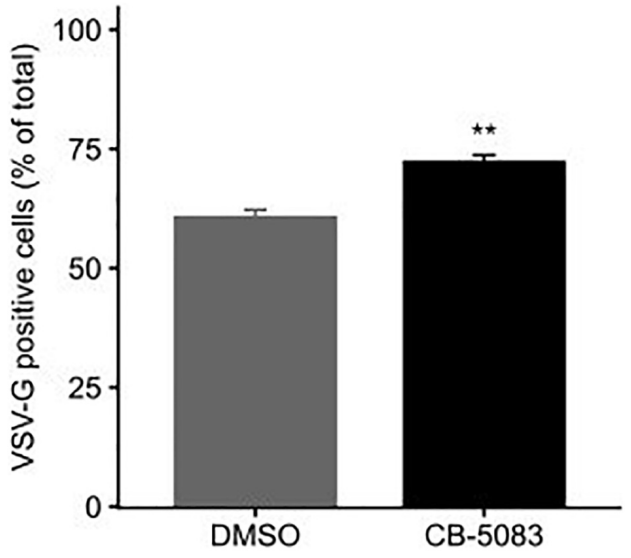

FIGURE 5 | VCP/p97 treatment does not block the trafficking of viral glycoproteins to the surface. Cells were transfected with a plasmid encoding the VSV glycoprotein (VSV-G). Following 24 h, cells were either treated or mock-treated with the VCP/p97 inhibitor CB-5083. Following an additional 24 h, VSV-G expression was assessed by flow cytometry. Data represent the mean and SEM of three replicates. $^{**}p < 0.01$ by *t*-test.

has demonstrated a dependence on both Hsp70 and Hsp90 chaperone systems (Radhakrishnan et al., 2010; Geller et al., 2013; Munday et al., 2015; Latorre et al., 2018), largely for polymerase function, but has not defined which isoform of these chaperones is of relevance, nor the co-chaperones that are involved. In this work, we set out to begin to define the cellular protein folding networks utilized by RSV during replication. We assessed a total of 114 genes belonging to all major chaperone systems using an RNAi screen and identified a total of 24 cellular genes that significantly impacted RSV replication, having at least a moderate effect (absolute SSMD > 1.28; **Figure 1B**). To validate the primary screening, we used RNAi targeting a different site in 15 hits from the primary screen. Overall, the knockdown of 12 genes reduced RSV replication significantly (**Figure 1C**). For two of the three genes that did not reach significance (CCT2 and PFD2), reduced levels of gene knockdown efficiency relative to the primary screen could underlie the lack of effect (**Supplementary Table 5**). Finally, we validated the role of one of the genes identified in the primary screen, VCP/p97, using a pharmacological approach (**Figure 2**). Hence, of the 24 genes identified in the primary screening, we validated 12/15 by RNAi, one by pharmacological inhibition (VCP/p97), and three were implicated in previous studies (two Hsp70 isoforms and one Hsp90 isoform), suggesting > 80% of the genes are likely to represent true hits.

Overall, numerous genes involved in the Hsp70 chaperone cycle were identified to alter RSV replication with at least a moderate effect (absolute SSMD > 1.28): Two of nine Hsp70 chaperones (HSPA1B and HSPA2), three of nine Hsp70 nucleotide exchange factors (BAG1, BAG3, and HSPA4), and seven of the 24 Hsp70 co-chaperones (**Supplementary Table 5**). Previously, the constitutive Hsp70 isoform, Hsc70/HSPA8, was shown to be involved in RSV replication (Radhakrishnan et al., 2010). Indeed, we observe the depletion of this gene to significantly reduce RSV replication in our screen (q-value < 0.05) although its effect was relatively weak (SSMD = –0.79), as was the case for two additional Hsp70 isoforms (HSPA1A and HSPA12B; **Supplementary Table 2**). Overall, our results reduce the complexity of the Hsp70 system to 12 genes of the 42 genes analyzed. Similarly, we identified one of the two Hsp90 isoforms (HSP90AB1) and two of the fourteen Hsp90 co-chaperones analyzed (FKBP1B and FKBP4) to be involved in the replication of RSV, reducing the members of this chaperone family to three out of 16 genes. Moreover, four of nineteen Hsp70-Hsp90 co-chaperones containing TPR domains were identified (CDC27, TTC1, TTC12, and SGTB). These results suggest that despite numerous chaperones and co-chaperones in each family, individual proteins have specific functions that cannot be compensated by other isoforms. This is in agreement with the results of previous work characterizing the role of different components of the Hsp70 chaperone system in the replication of Dengue virus and Zika virus (Taguwa et al., 2015, 2019). The results of the current work can facilitate the identification of specific chaperone subnetworks involved in individual steps of the RSV infection cycle.

Previous work has shown that pharmacological inhibition of Hsp70 and Hsp90 can constitute a broad-spectrum antiviral approach (Geller et al., 2007, 2012; Latorre et al., 2018; Aviner and Frydman, 2019). As a clinically evaluated pharmacological inhibitor (CB-5083) was available for one of the identified hits from the RNAi screen, VCP, we evaluated its potential as an antiviral. We found CB-5083 to inhibit RSV replication in both A549 and Hela-H1 cells (**Figures 2B,D**), as well as to block the replication of VSV (**Figure 2E**). These results further support VCP/p97 as a general target for antiviral therapy against different viruses (Das and Dudley, 2021). To gain insights into the step of the replication cycle where VCP/p97 acts, we examined the effect of adding CB-5083 before or after viral entry. We found no difference in the antiviral effect of CB-5083 if added post-entry, suggesting a role in downstream aspects of viral replication (**Figure 3**). In contrast, the effect of CB-5083 was observed for both intracellular replication and virus release, with the latter being significantly more affected (**Figure 4**). Nevertheless, this is unlikely to stem from effects on viral glycoprotein expression, as blocking of VCP/p97 did not reduce the expression of the VSV glycoprotein (**Figure 5**). Hence, it is likely that VCP/p97 acts at multiple steps of the replication of RSV and VSV.

DATA AVAILABILITY STATEMENT

The original contributions presented in the study are included in the article/**Supplementary Material**, further inquiries can be directed to the corresponding author/s.

AUTHOR CONTRIBUTIONS

VL performed the work and analyzed the data. RG performed the work, analyzed the data, obtained funding, and wrote the manuscript. Both authors contributed to the article and approved the submitted version.

FUNDING

This research was funded by a grant from the Conselleria de Educación, Investigación, Cultura y Deporte (SEJI/2017/006) and 2017 Research Grant by the European Society of Clinical Microbiology and Infectious Diseases (ESCMID) to RG.

ACKNOWLEDGMENTS

We would like to thank Beatriz Alvarez-Rodriguez for her critical reading of the manuscript.

SUPPLEMENTARY MATERIAL

The Supplementary Material for this article can be found online at: https://www.frontiersin.org/articles/10.3389/fmicb.2022.880394/full#supplementary-material

Supplementary Figure 1 | Evaluation of the toxicity and knockdown efficiency for the esiRNAs used in the primary screen. **(A)** The relative viability of cells transfected with esiRNAs targeting cellular proteostasis components was compared to that of cells transfected with non-targeting esiRNA. **(B)** The expression of the targeted genes following esiRNA transfection was compared to that in cells transfected with non-targeting esiRNA.

Supplementary Table 1 | Description of the genes selected for evaluation.

Supplementary Table 2 | Results of the toxicity, knockdown efficiency, and SSMD for evaluated genes.

Supplementary Table 3 | esiRNA information for screened genes.

Supplementary Table 4 | Primer sequences for evaluation of gene knockdown using qPCR.

Supplementary Table 5 | Significant hits from the primary and secondary screen RNAi screens.

REFERENCES

Arita, M., Wakita, T., and Shimizu, H. (2012). Valosin-containing protein (VCP/p97) is required for poliovirus replication and is involved in cellular protein secretion pathway in poliovirus infection. *J. Virol.* 86, 5541–5553. doi: 10.1128/JVI.00114-12

Aviner, R., and Frydman, J. (2019). Proteostasis in Viral Infection: Unfolding the Complex Virus–Chaperone Interplay. *Cold Spring Harb. Perspect. Biol.* 12:a034090. doi: 10.1101/cshperspect.a034090

Balchin, D., Hayer-Hartl, M., and Hartl, F. U. (2016). In vivo aspects of protein folding and quality control. *Science* 353:aac4354. doi: 10.1126/science.aac4354

Bar-Lavan, Y., Shemesh, N., and Ben-Zvi, A. (2016). Chaperone families and interactions in metazoa. *Essays Biochem.* 60, 237–253. doi: 10.1042/EBC20160004

Bergeron, H. C., and Tripp, R. A. (2021). Immunopathology of rsv: An updated review. *Viruses* 13:2478. doi: 10.3390/v13122478

Bracher, A., and Verghese, J. (2015). GrpE, Hsp110/Grp170, HspBP1/Sil1 and BAG domain proteins: nucleotide exchange factors for Hsp70 molecular chaperones. *Subcell Biochem.* 78, 1–33. doi: 10.1007/978-3-319-11731-7_1

Brehme, M., Voisine, C., Rolland, T., Wachi, S., Soper, J. H., Zhu, Y., et al. (2014). A chaperome subnetwork safeguards proteostasis in aging and neurodegenerative disease. *Cell Rep.* 9, 1135–1150. doi: 10.1016/j.celrep.2014.09.042

Ciechanover, A., and Kwon, Y. T. (2017). Protein quality control by molecular chaperones in neurodegeneration. *Front. Neurosci.* 11:185. doi: 10.3389/fnins.2017.00185

Connor, J. H., McKenzie, M. O., Parks, G. D., and Lyles, D. S. (2007). Antiviral activity and RNA polymerase degradation following Hsp90 inhibition in a range of negative strand viruses. *Virology* 362, 109–119. doi: 10.1016/j.virol.2006.12.026

Cuevas, J. M., Durán-Moreno, M., and Sanjuán, R. (2017). Multi-virion infectious units arise from free viral particles in an enveloped virus. *Nat. Microbiol.* 2:17078. doi: 10.1038/nmicrobiol.2017.78

Das, P., and Dudley, J. P. (2021). How viruses use the VCP/p97 atpase molecular machine. *Viruses* 13:1881. doi: 10.3390/v13091881

Dikic, I. (2017). Proteasomal and Autophagic Degradation Systems. *Annu. Rev. Biochem.* 86, 193–224. doi: 10.1146/annurev-biochem-061516-044908

Edkins, A. L. C. H. I. P. (2015). a co-chaperone for degradation by the proteasome. *Subcell Biochem.* 78, 219–242. doi: 10.1007/978-3-319-11731-7_11

Egorin, M. J., Lagattuta, T. F., Hamburger, D. R., Covey, J. M., White, K. D., Musser, S. M., et al. (2002). Pharmacokinetics, tissue distribution, and metabolism of 17-(dimethylaminoethylamino)- 17-demethoxygeldanamycin (NSC 707545) in CD 2f 1 mice and fischer 344 rats. *Cancer Chemother Pharmacol.* 49, 7–19. doi: 10.1007/s00280-001-0380-8

Geller, R., Andino, R., and Frydman, J. (2013). Hsp90 inhibitors exhibit resistance-free antiviral activity against respiratory syncytial virus. *PLoS One* 8:e56762. doi: 10.1371/journal.pone.0056762

Geller, R., Taguwa, S., and Frydman, J. (2012). Broad action of Hsp90 as a host chaperone required for viral replication. *Biochim. Biophys. Acta* 1823, 698–706. doi: 10.1016/j.bbamcr.2011.11.007

Geller, R., Vignuzzi, M., Andino, R., and Frydman, J. (2007). Evolutionary constraints on chaperone-mediated folding provide an antiviral approach refractory to development of drug resistance. *Genes. Dev.* 21, 195–205. doi: 10.1101/gad.1505307

Griffiths, C., Drews, S. J., and Marchant, D. J. (2017). Respiratory Syncytial Virus: Infection, Detection, and New Options for Prevention and Treatment. *Clin. Microbiol. Rev.* 30, 277–319. doi: 10.1128/CMR.00010-16

Hänzelmann, P., Galgenmüller, C., and Schindelin, H. (2019). Structure and Function of the AAA+ ATPase p97, a Key Player in Protein Homeostasis. *Subcell. Biochem.* 93 221–272. doi: 10.1007/978-3-030-28151-9_7

Huong, T. N., Tan, B. H., and Sugrue, R. J. A. (2016). Proteomic-Based Workflow Using Purified Respiratory Syncytial Virus Particles to Identify Cellular Factors as Drug Targets. *Methods Mol. Biol.* 1442, 175–194. doi: 10.1007/978-1-4939-3687-8_13

Huryn, D. M., Kornfilt, D. J. P., and Wipf, P. (2019). p97: An Emerging Target for Cancer, Neurodegenerative Diseases, and Viral Infections. *J. Med. Chem.* 63, 1892–1907. doi: 10.1021/acs.jmedchem.9b01318

Huryn, D. M., Kornfilt, D. J. P., and Wipf, P. (2020). P97: An Emerging Target for Cancer, Neurodegenerative Diseases, and Viral Infections. *J. Med. Chem.* 63, 1892–1907.

Kampinga, H. H., and Craig, E. A. (2010). The HSP70 chaperone machinery: J proteins as drivers of functional specificity. *Nat. Rev. Mol. Cell Biol.* 11, 579–592. doi: 10.1038/nrm2941

Kim, Y. E., Hipp, M. S., Bracher, A., Hayer-Hartl, M., and Hartl, F. U. (2013). Molecular chaperone functions in protein folding and proteostasis. *Annu Rev Biochem.* 82:323–55. doi: 10.1146/annurev-biochem-060208-092442

Latorre, V., Mattenberger, F., and Geller, R. (2018). Chaperoning the Mononegavirales: Current Knowledge and Future Directions. *Viruses* 10:699. doi: 10.3390/v10120699

Mattenberger, F., Latorre, V., Tirosh, O., Stern, A., and Geller, R. (2021). Globally defining the effects of mutations in a picornavirus capsid. *Elife* 10:e64256. doi: 10.7554/eLife.64256

Mayer, M. P. (2005). Recruitment of Hsp70 chaperones: a crucial part of viral survival strategies. *Rev. Physiol. Biochem. Pharmacol.* 153, 1–46. doi: 10.1007/s10254-004-0025-5

Munday, D. C., Wu, W., Smith, N., Fix, J., Noton, S. L., Galloux, M., et al. (2015). Interactome Analysis of the Human Respiratory Syncytial Virus RNA

Polymerase Complex Identifies Protein Chaperones as Important Cofactors That Promote L-Protein Stability and RNA Synthesis. *J. Virol.* 89, 917–930. doi: 10.1128/JVI.01783-14

Radhakrishnan, A., Yeo, D., Brown, G., Myaing, M. Z., Iyer, L. R., Fleck, R., et al. (2010). Protein analysis of purified respiratory syncytial virus particles reveals an important role for heat shock protein 90 in virus particle assembly. *Mol. Cell. Proteomics* 9, 1829–1848. doi: 10.1074/mcp.M110.001651

Radons, J. (2016a). The Hsp90 Chaperone Machinery: An Important Hub in Protein Interaction Networks. *Br. J. Med. Med. Res.* 14, 1–32. doi: 10.9734/BJMMR/2016/24631

Radons, J. (2016b). The human HSP70 family of chaperones: where do we stand? *Cell Stress Chaperones* 21, 379–404. doi: 10.1007/s12192-016-0676-6

Schopf, F. H., Biebl, M. M., and Buchner, J. (2017). The HSP90 chaperone machinery. *Nat. Rev. Mol. Cell Biol.* 18, 345–360. doi: 10.1038/nrm.2017.20

Taguwa, S., Maringer, K., Li, X., Bernal-Rubio, D., Rauch, J. N., Gestwicki, J. E., et al. (2015). Defining Hsp70 Subnetworks in Dengue Virus Replication Reveals Key Vulnerability in Flavivirus Infection. *Cell* 163, 1108–1123. doi: 10.1016/j.cell.2015.10.046

Taguwa, S., Te Yeh, M., Rainbolt, T. K., Nayak, A., Shao, H., Gestwicki, J. E., et al. (2019). Zika Virus Dependence on Host Hsp70 Provides a Protective Strategy against Infection and Disease. *Cell Rep.* 26, 906.e–920.e. doi: 10.1016/j.celrep.2018.12.095

van den Boom, J., and Meyer, H. V. C. P. (2018). /p97-Mediated Unfolding as a Principle in Protein Homeostasis and Signaling. *Mol. Cell* 69, 182–194. doi: 10.1016/j.molcel.2017.10.028

Wang, Y., Jin, F., Wang, R., Li, F., Wu, Y., Kitazato, K., et al. (2017). HSP90: a promising broad-spectrum antiviral drug target. *Arch. Virol.* 162, 3269–3282. doi: 10.1007/s00705-017-3511-1

Yang, J., Xu, Y., Yan, Y., Li, W., Zhao, L., Dai, Q., et al. (2020). Small Molecule Inhibitor of ATPase Activity of HSP70 as a Broad-Spectrum Inhibitor against Flavivirus Infections. *ACS Infect. Dis.* 6, 832–843. doi: 10.1021/acsinfecdis.9b00376

Ye, Y., Tang, W. K., Zhang, T., and Xia, D. A. (2017). mighty "protein extractor" of the cell: Structure and function of the p97/CDC48 ATPase. *Front. Mol. Biosci.* 4:39. doi: 10.3389/fmolb.2017.00039

Zhang, X. D. (2011). Illustration of SSMD, z score, SSMD*, z* score, and t statistic for hit selection in RNAi high-throughput screens. *J. Biomol. Screen* 16, 775–785. doi: 10.1177/1087057111405851

Zhou, H.-J., Wang, J., Yao, B., Wong, S., Djakovic, S., Kumar, B., et al. (2015). Discovery of a First-in-Class, Potent, Selective, and Orally Bioavailable Inhibitor of the p97 AAA ATPase (CB-5083).J Med Chem. 58, 9480–97. doi: 10.1021/acs.jmedchem.5b01346

Conflict of Interest: The authors declare that the research was conducted in the absence of any commercial or financial relationships that could be construed as a potential conflict of interest.

Publisher's Note: All claims expressed in this article are solely those of the authors and do not necessarily represent those of their affiliated organizations, or those of the publisher, the editors and the reviewers. Any product that may be evaluated in this article, or claim that may be made by its manufacturer, is not guaranteed or endorsed by the publisher.

frontiers | Frontiers in Microbiology

ORIGINAL RESEARCH
published: 08 June 2022
doi: 10.3389/fmicb.2022.931043

A Novel Rabies Vaccine Based on a Recombinant Bovine Herpes Virus Type 1 Expressing Rabies Virus Glycoprotein

Caiquan Zhao[1,2†], Jie Gao[1†], Yongzhi Wang[1†], Lina Ji[1], Hui Qin[1], Wei Hu[1] and Yang Yang[1*]*

[1] The State Key Laboratory of Reproductive Regulation and Breeding of Grassland Livestock, School of Life Sciences, Inner Mongolia University, Hohhot, China, [2] School of Biological Science and Technology, Baotou Teachers' College, Baotou, China

Rabies is a highly prevalent zoonotic disease and a public health threat worldwide. Currently licensed rabies vaccines are effective but less is known which would protect cattle. This study describes the construction of a novel recombinant bovine herpes virus type I (BHV-1) expressing rabies virus glycoprotein (RABV G) instead of its gE glycoprotein (gE) by CRISPR-Cas9 and homologous recombination technology (BHV-1-ΔgE-G). Insertion of the RABV G gene is stable after 20 rounds of *in vitro* passaging and the recombinant virus replicates to high titers in MDBK cells. The RABV G expresses in the recombinant virus-infected cells and on the virion surface of BHV-1-ΔgE-G. One single immunization with BHV-1-ΔgE-G-activated dendritic cells (DCs) and B cells furthermore induced a protective immune response in mice against severe lethal challenge infection. A protective level of RABV-specific virus-neutralizing antibody (VNA) was detected in intramuscular immunized mice and cattle without any clinical symptoms. This research demonstrated that the BHV-1 vector-based RABV vaccine is a potential candidate for cattle.

Keywords: rabies virus, bovine herpesvirus type I, vaccine, glycoprotein, dendritic cell, virus-neutralizing antibody

OPEN ACCESS

Edited by:
Cao Yong Chang,
Sun Yat-sen University, China

Reviewed by:
Yanrong Zhou,
Huazhong Agricultural University, China
Xing Liu,
Nanjing Agricultural University, China

***Correspondence:**
Wei Hu
huw@imu.edu.cn
Yang Yang
yang55797961@163.com

†These authors have contributed equally to this work

Specialty section:
This article was submitted to Virology, a section of the journal Frontiers in Microbiology

Received: *28 April 2022*
Accepted: *09 May 2022*
Published: *08 June 2022*

Citation:
Zhao C, Gao J, Wang Y, Ji L, Qin H, Hu W and Yang Y (2022) A Novel Rabies Vaccine Based on a Recombinant Bovine Herpes Virus Type 1 Expressing Rabies Virus Glycoprotein. Front. Microbiol. 13:931043. doi: 10.3389/fmicb.2022.931043

INTRODUCTION

According to the World Health Organization (WHO) estimates, rabies is endemic in more than 150 countries worldwide, and about 59,000 people die from rabies every year (World Health Organization., 2013). Due to the limitation of effective control in animal reservoirs in developing regions, rabies in stray dogs, cattle, goats, camels, and wild animals have increased in the north part of China, provincial regions, where rabies had rarely been reported previously (Shao et al., 2011; Liu et al., 2016; Feng et al., 2020; Li et al., 2020). Although the canine rabies vaccine has been recommended for cattle by the World Organization for Animal Health and successfully performed in rabies endemic countries (Yakobson et al., 2015), it is still costly and uncertain that local rabies vaccine could block the spread of infection in cattle.

Efficacious rabies vaccines are for safety and commercial purposes. Worldwide, human rabies vaccines are based on the fixed strains of RABVs that are grown in cell culture, which contain inactivated virus and adjuvant (DiStefano et al., 2013). Usually, these vaccines need to be given three to five times in a prophylactic immunization to achieve protective immunity (Zhou et al., 2006). On the other hand, SAD-modified live RV vaccines used in wild animals have effectively reduced the incidence of fox-derived rabies in Western Europe (Freuling et al., 2013). However,

these recombinant RABV vaccines are still based on the RABVs genome, which raises the possibility of recombination between the vaccine RABVs and wild-type RABVs resulting in unpredictable possibilities.

Rabies virus is a single-stranded negative-strand RNA virus with a total genome length of about 12 kb, encoding five structural proteins: nucleoprotein (N), phosphoprotein (P), matrix protein (M), glycoprotein (G), and large transcription protein (L). Among them, RABV G is a trimeric transmembrane protein, expressed on the surface of the RABV virus, and it has specific recognition sites for B cells and T cells on its surface, which can cause an immune response and is a key protein that induces the production of VNA. Therefore, RABV G protein is often used in the construction of recombinant rabies vaccines. To vaccinate livestock in developing countries, a low-cost vaccine with one injection would be ideal. Live recombinant viral vectors which induced excellent humoral and cellular immunity are considered to be effective vaccine candidates to deliver antigens derived from pathogens. Various vector rabies vaccines have been constructed with different viral vectors, such as Parapoxvirus, Newcastle disease virus, Sindbis virus, parainfluenza virus, herpes virus, adenovirus, and baculovirus. Moreover, a safe and effective rabies vaccine especially for cattle still needs to be further developed.

Bovine herpes virus type I (BHV-1) is a double-stranded DNA virus belonging to the family Herpesviridae, subfamily Aphaherpesvirinae, with a total genome length of about 138 kb, and 10 of the proteins it encodes are envelope glycoproteins. Among them, gE glycoprotein, as a transmembrane glycoprotein, is a non-essential protein for virus replication. The current BHV-1 live vaccine in which gE is deleted has been widely used in Europe, so BHV-1 lacking the gE gene is safe as a vector for constructing recombinant rabies virus (Petrini et al., 2019). A similar construct using BHV type 5 for cattle has been developed to protect the animals in Latin America both against BHV-5 and rabies (bats-transmitted rabies) (Ana et al., 2002). Also, recombinant Canine Herpesviruses expressing RABV G have been tested as immune-contraceptive vaccines for carnivores (Chen et al., 2019). Furthermore, the herpesvirus genome is substantial enough to tolerate the insertion of large foreign genes and have a stable genome and technologies for the construction of recombinants that are well-established. For instance, recombinant BHV-1 or BHV-4 expressed other viral antigens have developed in animals and have good immunogenicity (Schrijver et al., 1997; Kweon et al., 1999; Macchi et al., 2018; Pedrera et al., 2020; Chowdhury et al., 2021). These characteristics above suggest that BHV-1 may be a potential vaccine candidate for preventing rabies in cattle and other ruminants.

Here, we used CRISPR-Cas9 and homologous recombination technology to construct a recombinant BHV-1 expressing RABV G and evaluated the replication of BHV-1-ΔgE-G, the expression of RABV G, genetic stability *in vitro*, attenuation, immune response, and immunogenicity in animal models. Our results show that a single dose of BHV-1-ΔgE-G induces a protective level of RABV VNA in cattle serum and BHV-1-ΔgE-G provides complete protection against the lethal challenge of RABV in mice.

MATERIALS AND METHODS

Cells, Viruses, Antibodies, and Plasmids

Madin–Darby bovine kidney (MDBK) cells, human embryonic kidney 293T (HEK293T), and African green monkey kidney cells (VERO-E6) were kept in our lab and cultured in Dulbecco's modified eagle's medium (DMEM, Gibco, CA, USA) containing 10% fetal bovine serum (FBS, Gibco, CA, USA), and mouse neuroblastoma (NA) cells were maintained in Roswell Park Memorial Institute (RPMI) 1640 medium (Gibco, CA, USA) supplemented with 10% FBS. In brief, DCs isolated from mouse bone marrow and cultured in RPMI 1640 supplemented with 10% FBS and 20 ng/ml granulocyte-macrophage colony-stimulating factor (GM-CSF, PeproTech, USA) for 7 days as previously described (Yang et al., 2015). The parent BHV-1 (named NM14, GenBank No. of gE gene is MK035760.1) was isolated from bovine and stored in our lab as described previously (Mu et al., 2018). Challenge virus standard CVS-24 strain of rabies virus was bred in the sucking mice brain and a neuro attenuated rabies virus SAD-L16 was bred in the NA cells (Morimoto et al., 1999). Fluorescein isothiocyanate (FITC)-conjugated antibodies against the RABV N protein were purchased from FujiRab (Melvin, PA).

Animals

ICR mice were purchased from Charles River (Beijing Vital River Laboratory Animal Technology Co., Ltd.). Experimental infectious studies were approved by the Ethics Committee of Inner Mongolia University (IMU-MO-2020-031). All healthy male cattle (6–8 months old) were obtained by the pasture, and their BHV-1 antigen and antibody tests were negative. All cattle were divided into three groups and immunized with BHV-1-ΔgE-G, SAD, or DMEM by intramuscular injection, and bovine serum was collected at 1, 2, 3, 6, 12, 18 weeks. The above immunization experiments were carried out entirely with the permission of the rancher. All efforts were made to minimize the suffering of the animals.

Donor Plasmids and sgRNA CRISPR/Cas9 Plasmids Construction

Figure 1A is a schematic of the generation of the recombinant viral vector. sgRNAs were designed using the online CRISPR Design Tool (https://zlab.bio/guide-design-resources), and the guide RNAs were cloned into the pSpCas9(BB)-2A-Puro (PX459) V2.0 vector (Addgene, Cambridge, MA, USA, Plasmid #62988) as previously described (Cong et al., 2013). All primers are used in the present study list in **Table 1**. The primer pairs of gE-sgRNA1-F/gE-sgRNA1-R and gE-sgRNA2-F/gE-sgRNA2-R were targeted to gE of BHV-1, and the primer pairs of EGFP-sgRNA1-F/EGFP-sgRNA1-R and EGFP-sgRNA2-F/EGFP-sgRNA2-R were targeted to EGFP to delete EGFP from EGFP positive recombinant BHV-1. The pcDNA3.1 (+) expression vector (Clontech, PaloAlto, CA, USA) was used as a backbone to construct the donor template. The gE homologous arms were amplified using PCR from BHV-1 with left homologous arms primer pairs (LgE-F and LgE-R) and

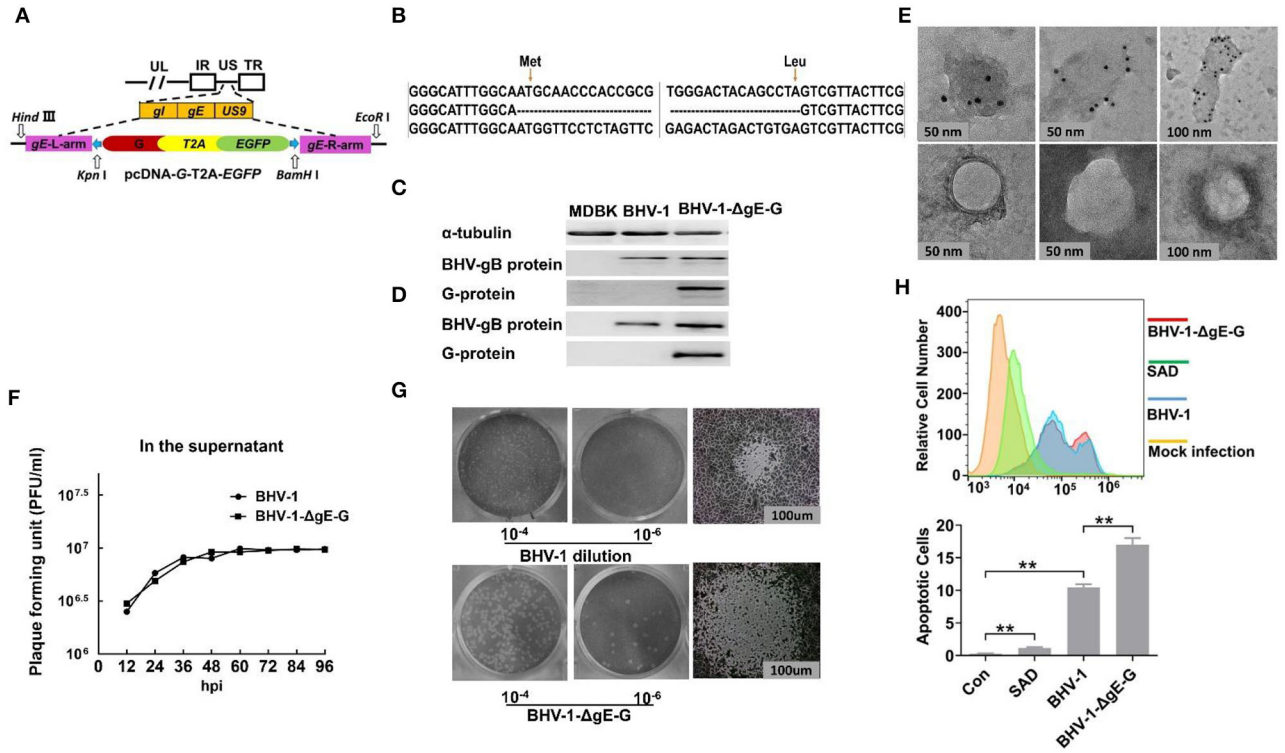

FIGURE 1 | Construction and characterization of BHV-1-ΔgE-G. **(A)** Schematic on the generation of a recombinant viral vector. The pcDNA3.1 expression vector is used as a backbone to construct the donor template. gE homologous arms were amplified using PCR from BHV-1 with the primer pairs L-ge and R-ge, the RABV G gene was amplified using PCR from SAD with primer pairs G-F and G-R, and the T2A and EGFP genes were amplified using PCR from pCAG-EGFP with primer pairs T2A-EGFP-F and T2A-EGFP-R. These PCR products were digested with enzyme sets HindIII & EcoR I, Kpn I & Not I, and Not I & BamH I, and then ligated into pcDNA3.1 plasmid vector (pcDNA-LgE-G-EGFP-RgE), respectively. **(B)** Viral genome DNA isolated from BHV-1-ΔgE-G infected MDBK cells was used to carry out PCR and sequencing. **(C)** The RABV G expressed in MDBK infected with BHV-1-ΔgE-G at 24 hpi was detected by Western blot. **(D)** The RABV G incorporated in virion of BHV-1-ΔgE-G was purified by sucrose gradient ultracentrifuge and detected by Western blot. **(E)** The RABV G incorporated in virion of BHV-1-ΔgE-G was purified by sucrose gradient ultracentrifuge and analyzed by EM. **(F)** Multistep growth curves of BHV-1-ΔgE-G and BHV-1 in MDBK cells. MDBK cells were infected with the indicated viruses at an MOI of 0.01, and the virus titers in infected cell supernatants were determined at indicated time point. **(G)** The plaque diameter of BHV-1-ΔgE-G and BHV-1 was analyzed by the viral plaque assay using a Nikon ECLIPSE TS100 microscope. **(H)** The prorogation of apoptotic cells infected by BHV-1-ΔgE-G, BHV-1, and RABV was determined with BD Accuri C6 Flow Cytometer, and the data were analyzed with FlowJo software (TreeStar, San Carlos, CA). Significance was assessed using Student's *t*-test. $^{**}P \leq 0.01$.

right homologous arms primer pairs (RgE-F and RgE-R), the RABV G gene was amplified using PCR from SAD-L16 with primer pairs G-F and G-R, and the T2A and EGFP gene were amplified using PCR from pCAG-EGFP (Addgene, Cambridge, MA, USA, Plasmid #89684) with primer pairs T2A-EGFP-F and T2A-EGFP-R. These PCR products were digested with the enzyme sets HindIII & EcoR I, Kpn I & Not I, and Not I & BamH I, and then ligated into pcDNA3.1 plasmid vector (pcDNA-LgE-G-EGFP-RgE), respectively. The pcDNA-LgE-G-EGFP-RgE plasmid was verified by sequencing with primer pairs (BHV-1-gE-F and BHV-1-gE-R).

Virus Recombination and Plaque Purification

The sgRNA/Cas9 vectors and donor vectors were co-transfected into VERO-E6 cells with 1 μg of sgRNA/Cas9 plasmid and 4 μg of pcDNA-LgE-G-EGFP-RgE plasmid using Lipofectamine 3000 (Invitrogen, CA, USA) according to the manufacturer's instructions. After 6-h transfection, the parent BHV-1 was infected at a multiplicity of infection (MOI) of 0.01 and the culture medium was changed to DMEM with 2% FBS, and cells were collected at 48-h post-infection (hpi). After three rounds of freeze and thaw, the cell lysate was centrifuged for 5 min at 10,000 rpm/min. The supernatant was used for the next propagation or stored at −80°C. The first-generation recombinant virus was purified by fluorescence-activated cell sorting. For recombinant virus purification, the infected MDBK cells (MOI = 0.01) were covered by 1% low melting-point agarose. After 72 h of infection, well-separated plaques with positive EGFP or negative EGFP were picked up by pipette tip and stored in microtubes containing 200 μl serum-free DMEM. The rescued virus was subjected to at least 10 rounds of plaque purification assay. All plaque purified viruses were passaged 20 rounds on MDBK cells and then evaluated by PCR, flow cytometry, viral plaque assay, and Western blot as described below.

TABLE 1 | Primers used in the study.

Primer	Sequence (5′ to 3′)	Restriction enzyme sites
gE-sgRNA1-F	CACCGCGAGCCCGGGGTTTCGGTCGCGG	BbsI
gE-sgRNA1-R	AAACCCGCGACCGAAACCCCGGGCTCGC	BbsI
gE-sgRNA2-F	CACCGCCACGTCGGTGAAGCACTCGCGG	BbsI
gE-sgRNA2-R	AAACCCGCGAGTGCTTCACCGACGTGGC	BbsI
EGFP-sgRNA1-F	CACCGGTCGCCCTCGAACTTCACCT	BbsI
EGFP-sgRNA1-R	AAACAGGTGAAGTTCGAGGGCGACC	BbsI
EGFP-sgRNA2-F	CACCGGTTGGGGTCTTTGCTCAGGG	BbsI
EGFP-sgRNA2-R	AAACCCCTGAGCAAAGACCCCAACC	BbsI
G-F	CGGGGTACCTCTTGGATGTGAAAAAAACTATTAAC	KpnI
G-R	AAGGAAAAAAGCGGCCGCCAGTCTGGTCTCACCCCCACTCTTG	NotI
T2A-EGFP-F	AAGGAAAAAAGCGGCCGCGCAAAAAAGAAAAAGGA	NotI
T2A-EGFP-R	CTAGGGATCCGCAACTAGAAGGCACAG	BamHI
LgE- F	CGAAAGCTTTCGCCTCCTGCCCGCG	HindIII
LgE-R	TTTGGTACCCTCTCGCGTGCGC	KpnI
RgE-F	AAAGGATCCAGTCGTTACTTCGGACCGTTTGGTG	BamHI
RgE-R	AAGGAATTCCAGCGCCTCGATAGTTTTCGTTGAC	EcoRI
BHV-1-gE-F	CGCCGGGTTGTTAAATGGGTCTCG	_
BHV-1-gE-R	GGGGCGCGTCCTCGATGGTG	_

Underlined are restriction sites.

Purification of Recombinant BHV-1 by Fluorescence-Activated Cell Sorting

The fluorescence-activated cell sorting was performed as previously described with slight modifications (Di Lullo et al., 2010). The fluorescence-activated cell sorting was performed on BD FACSAria cell sorter (BD Biosciences, USA) with 488 nm lasers. MDBK cells were infected with the first-generation recombinant BHV-1 at an MOI of 0.01. At 48 hpi, cells were washed, trypsinized, washed again, resuspended in a culture medium, and kept on ice. The MDBK cells expressing EGFP were sorted into a 96-well plate with 5,000 cells per well.

Plaque Assay for BHV-1

BHV-1 was titrated on MDBK cells by viral titering-Plaque Assay. MDBK cells were cultured in 12-well plates for 12 h and then infected with 10-fold dilutions of BHV-1. After 2 h of incubation, cells were washed with PBS and then cultured in DMEM with 1% FBS and 4% sodium carboxymethyl cellulose (Sigma, USA). After 2 days of incubation at 37°C, cells were fixed with 10% formaldehyde and stained with crystal violet. The number of plaques was recorded and the plaque-forming unit per ml (PFU/mL) was calculated as follows: Virus titer (PFU/mL) = (number of plaques per well × virus dilution factor)/virus inoculation per mL).

Western Blotting

MDBK cells extract or purified virions were lysed in hot Laemmli sample buffer (BIO-RAD, USA) and boiled for 5 min. All samples were resolved by 10% sodium dodecyl sulfate-polyacrylamide gel electrophoresis (SDS-PAGE) and transferred onto a polyvinylidene difluoride (PVDF) membrane. PVDF blocked with tris-buffered saline (TBS) contained 1% bovine serum albumin (BSA) and then incubated with respective primary antibodies at room temperature for 2 h, followed by horseradish peroxidase-conjugated secondary antibodies (Sigma) for 1 h at room temperature. Proteins were detected by west pico chemiluminescent substrate (Thermo Fisher Scientific, United States). Band signals corresponding to immunoreactive proteins were developed by exposure in the Tanon 5200 imaging system (Tanon Science and Technology, Beijing, China) using Tanon MP software. An anti-BHV-1 gB antibody was purchased from VMRD INC. (WA, USA) and anti-RABV G (G53) monoclonal antibody was prepared as previously described (Jiang et al., 2010).

Electron Microscopy and Immunogold Labeling for BHV-1-ΔgE-G

Viruses are purified by 3K Ultra-15 Centrifugal Filter Units (Millipore, USA). The G in BHV-1-ΔgE-G was labeled with 10-nm immunogold and evaluated by transmission electron microscopy (TEM) as described previously with minor modification (Li et al., 2019). In brief, viruses were absorbed onto parlodion-coated nickel grids for 30 min followed by fixation with 2.5% glutaraldehyde for 30 min. Grids were then washed with a drop of TBS, pH 7.4, three times for 5 min, followed by floating on a drop of RABV G-specific monoclonal antibody (G53) diluted to 1:300 in TBS containing 1% BSA for 1 h. After washing with TBS three times, samples were incubated for 1 h with Goat Anti-Mouse IgG H&L (10 nm Gold), and preadsorbed (Abcam, USA) and diluted at 1:10 in TBS containing 1% BSA. Grids were again washed with TBS and then stained with 2% phosphotungstic acid (pH 7.0) for 30 s. The grids were then observed under an FEI Tecnai G^2 F20 S-Twin transmission electron microscope (Thermo Fisher, USA).

Flow Cytometry

For immune cells activation analysis, inguinal lymph nodes of mice were taken out after administration and slowly added to a 100-μm cell filter (Sigma-Aldrich) with a pipette gun for filtration and centrifuged the obtained filtrate at room temperature at 400 g for 5 min. Samples were resuspended with PBS buffer containing 2% FBS and 20 nM EDTA. The above steps were repeated twice. Cells were stained with fluorescent-labeled differential markers CD4, CD11c, CD86, CD80, and CD138, major histocompatibility complex class II (MHC-II), IL-17, Foxp3 antibodies, and an isotype control for 1 h and washed twice, then measured by flow cytometry. All the antibodies used in the flow cytometry above were purchased from BD biosciences (USA). For apoptosis assay, MDBK cells were infected with BHV-1, BHV-1-ΔgE-G, or SAD virus for 48 h at MOI of 0.01, respectively. Cells were collected at 48 hpi and detected the apoptosis using FITC Annexin V Apoptosis Detection Kit I (BD biosciences, USA) by flow cytometry. Cells were suspended with PBS containing 1% FBS and 2 μM EDTA solutions, washed twice with cold PBS, and resuspended cells in 1X Binding Buffer at a concentration of 10^6 cells/ml. Transfer 100 μl of the solution (1×10^5 cells) to a 1.5-ml centrifuge tube. Add 5 μl of FITC Annexin V and 5 μl PI to cells undergoing apoptosis (FITC Annexin V positive and PI negative). Gently vortex the cells and incubate for 15 min at RT (25°C) in the dark. Add 400 μl of 1X Binding Buffer to each tube and analyze by flow cytometry within 1 h. Flow cytometry was performed on BD AccuriTM C6 flow cytometry (BD Bioscience), and data were analyzed by BD FACSDiva (BD Pharmingen) and FlowJo software (TreeStar, San Carlos, CA), and finally, GraphPad Prism 5.0 software was used to plot the analyzed data.

Statistics Analysis

Statistical significance of the differences between groups was determined using student's *t*-test with *** indicating a $p < 0.001$, ** a $p < 0.01$, and *a $p < 0.05$ using Graph Pad prism software (GraphPad Software, Inc., CA). The statistical significance of survival rates was determined by the log-rank test and Kaplan–Meier survival analysis.

Ethics Statement

All animal procedures were approved by the Ethics Committee of Inner Mongolia University (IMU-MO-2020-031). All efforts were made to minimize animal suffering. The animal experiments involving the infection with RABV were carried out in the animal facility with ABSL-2 level at Inner Mongolia University.

RESULTS

Construction and Characterization of Recombinant BHV-1 Expressing RABV G

Our lab's previous report indicated that EGFP inserted between the gI and US9 genes of BHV-1 was expressed well in MDBK cells (Mu et al., 2018). The safety and immunogenicity of recombinant BHV-1 have also been approved in the last decades (Kaashoek et al., 1994). To explore the potential of BHV-1 as a live prophylactic vaccination candidate for protection from rabies, the RABV G gene was used instead of the partial gE gene (amino acid position of gE, 136 Met to 513 Leu) for constructing a recombinant BHV-1. To avoid false genetic recombination caused by green fluorescent gene expression in the homologous recombination donor template, the expressions of RABV G and EGFP were driven by the endogenous viral promoter without other specific promoters, which occurs only after precise DNA homologous recombination (**Figure 1A**). The recombinant virus, BHV-1-ΔgE-G, was established with two steps of CRISPR/Cas9 and DNA homologous recombination and purified with FACS technique as specifically described in Materials and Methods section. First, the gE gene of BHV-1 was replaced with RABV G and EGFP by CRISPR Cas9-mediated homologous recombination. Next, the EGFP in the recombinant was deleted by CRISPR Cas9-mediated homologous recombination. After 20 rounds of virus passage in the MDBK cells, the stability of the inserted gene was confirmed by PCR analysis and sequencing (**Figure 1B**). Expression of the G protein was detected by Western blot in BHV-1-ΔgE-G-infected MDBK cells. At 24 hpi, specific expression of RABV G in MDBK was detectable (**Figure 1C**). The BHV-1-ΔgE-G was purified by sucrose gradient ultracentrifuge and the G incorporated into the virions was analyzed by Western blot (**Figure 1D**). A RABV G band was detected in the BHV-1-ΔgE-G virions, whereas no RABV G band was found in the parental BHV-1 virions. To visually observe the expression of RABV G on BHV-1-ΔgE-G, the virus particles of BHV-1-ΔgE-G were analyzed using RABV G-specific antibodies and examined with an electron microscope (EM). RABV G was detected on the surface of BHV-1-ΔgE-G which indicated that RABV G is incorporated into the recombinant BHV-1 particles (**Figure 1E**).

MDBK cells were infected with parental BHV-1 or BHV-1-ΔgE-G at an MOI of 0.01, and the supernatants were quantified by viral plaque assay in MDBK cells. As shown in **Figure 1F**, BHV-1-ΔgE-G had similar initial growth kinetics, and both the virus titers of parental and recombinant BHV-1 reach $10^{6.5}$ FFU at 48 hpi. The viral plaque morphology was also observed under the microscope. The plaque diameter of BHV-1-ΔgE-G was almost twice the diameter of parental BHV-1 (**Figure 1G**). Previous studies have reported that the RABV G induces cell apoptosis (Sarmento et al., 2005). To investigate whether the stronger cytopathic effect (CPE) of BHV-1-ΔgE-G is induced by the apoptosis, MDBK cells were infected with BHV-1, BHV-1-ΔgE-G, or SAD for 48 h at an MOI of 0.01, respectively (**Figure 1H**). The prorogation of apoptotic cells infected by BHV-1-ΔgE-G (17.0%) was higher than BHV-1 (10.4%) and RABV (1.2%).

Clinical Observations and VNA Persistence of BHV-1-ΔgE-G in Mice

To estimate any adverse effects on mice that might induce by BHV-1 infection, 2-week-old ICR mice and 6-week-old female ICR mice were administered with 10^6 FFU of BHV-1, BHV-1-ΔgE-G, SAD, or mock-infected with DMEM via

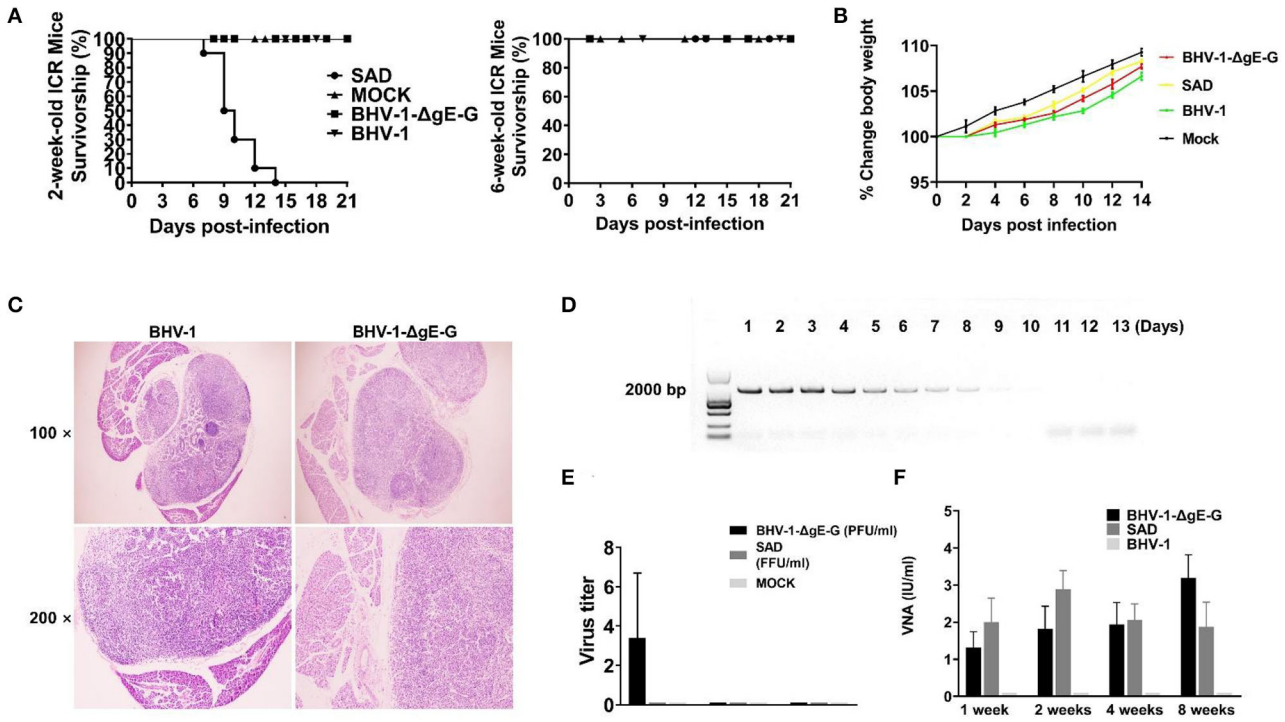

FIGURE 2 | Clinical observations and VNA persistence in mice that administrated SAD and BHV-1-ΔgE-G via the IM route. **(A)** The survivorship of 2-week-old and 6-week-old female ICR mice inoculated with the indicated virus via IM route. **(B)** Body weight change (%) was evaluated in mice which were injected with the indicated virus via the IM route. **(C)** Inguinal lymph nodes were obtained from immunized mice and subjected to HE staining. **(D)** The gB gene expression in mice inguinal lymph nodes that were immunized with BHV-1-ΔgE-G was detected by PCR and analyzed with electrophoresis. **(E)** The inguinal lymph nodes were obtained from mice immunized with the indicated virus and evaluated the virus titer. **(F)** The serum of mice inoculated with the indicated virus was subjected to RFFIT for the analysis of VNA.

intramuscularly (IM) route. All the 2-week-old mice injected with SAD succumbed to infection within 15 days. In contrast, all mice infected with BHV-1-ΔgE-G or BHV-1 were non-lethal mice (**Figure 2A**). As previously reported, the SAD and its derivatives remained pathogenic for young rodents (Rasalingam et al., 2005).

For 6-week-old mice, RABVs were non-pathogenic. All mice ($n = 10$) were observed daily for 2 weeks with body weight change and clinical symptoms. After 4 days of immunization, the body weight of all mice increased gradually as normal mice (**Figure 2B**). None of the clinical symptoms were observed in the mice after administration with any of the viruses mentioned above. To determine whether the BHV-1 infection in mice was reflected in the pathological change of inguinal lymph nodes, surrounding tissues were collected from mice for histopathology. There was no significant histological change between BHV-1-ΔgE-G immunized mice and mock-immunized mice (**Figure 2C**). The gB of BHV-1 can be detected from 1 day to 9 days after immunization in mice inguinal lymph nodes, and the expression level of gB was decreased from 5 days post-immunization (**Figure 2D**). The live BHV-1-ΔgE-G in mice inguinal lymph nodes can be detected within 1 week and the virus titer was lower than 10 PFU/ml (**Figure 2E**). To evaluate the persistence of the VNA against RABV, the mice sera were collected at 1, 2, 4, and 8 weeks after IM immunization and the VNA in serum was estimated by the fluorescent antibody virus neutralization (FAVN) test. As expected, BHV-1-ΔgE-G induced a persistent and high level of VNA in mice serum, 1 week after immunization until 8 weeks, and the VNA level was higher than 1 IU (**Figure 2F**). The VNA level of BHV-1-ΔgE-G immunized mice was similar to the SAD-immunized mice, both of which were higher than 0.5 IU, which was the minimum protective antibody level in carnivores (Cliquet et al., 1998).

BHV-1-ΔgE-G Enhances the Activation of DC and B Cell

To determine the immune effect of recombinant virus BHV-1-ΔgE-G, 6-week-old ICR mice were immunized via IM route with 2×10^5 PFU of BHV-1-ΔgE-G, 2×10^5 FFU of SAD, or mock-immunized control group (DMEM), respectively. Seven days and 14 days post-immunization, single-cell suspensions were prepared from inguinal lymph nodes of mice, and activation of DCs, Th17 cells, and B cells in lymph nodes were analyzed by flow cytometry. As shown in **Figure 3A**, the activation of DC cells (CD11c high expression and CD86 high expression) in the lymph nodes of mice which were immunized with the BHV-1-ΔgE-G were significantly higher than SAD and mock-immunized group. In addition, the number of Th17 cells and

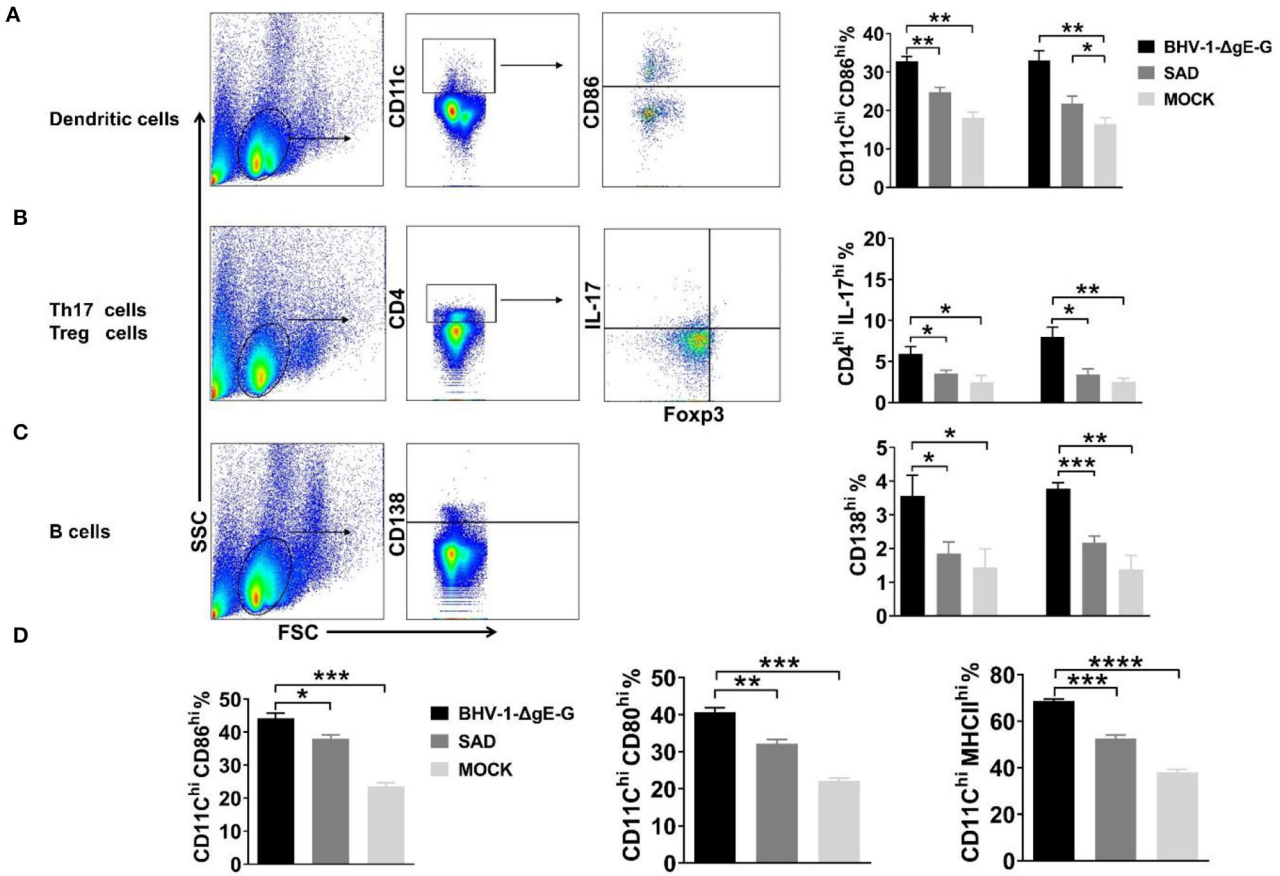

FIGURE 3 | BHV-1-ΔgE-G induces early activation of immune cells. **(A–C)** Flow cytometric analysis of activation status of DCs, Th 17 cells, and B cells in mice inguinal lymph nodes which were immunized with the indicated virus via the IM route. **(D)** Flow cytometric analysis of CD11c, CD86, or MHCII expression level of DCs infected with 0.1 MOI of indicated virus at 48 hpi. Significance was assessed using Student's *t*-test. $^{*}P \leq 0.05$; $^{**}P \leq 0.01$; $^{***}P \leq 0.001$; $^{****}P \leq 0.0001$.

B lymphocytes in the recombinant virus BHV-1-ΔgE-G group increased significantly, which was higher than that in SAD and mock-immunized groups, indicating that the recombinant virus promoted the increase of Th17 cells and B lymphocytes and activated humoral immunity (**Figures 3B,C**). To further confirm the activation of DC, whether it is directly induced by the BHV-1-ΔgE-G, the bmDCs were infected with 0.1 MOI of BHV-1, 0.1 MOI of BHV-1-ΔgE-G, 0.1 MOI of SAD, or mock-infected control group (DMEM), respectively. At 48 hpi, DCs were evaluated by FACS, and the number of $CD11c^{hi}$ & $CD86^{hi}$ cells, $CD11c^{hi}$ & $CD80^{hi}$ cells, and $CD11c^{hi}$ & MHC II^{hi} cells in BHV-1-ΔgE-G-infected group were significantly higher than other groups (**Figure 3D**). These results suggest that the recombinant virus BHV-1-ΔgE-G can activate the DCs *in vivo* and *in vitro*, and further maturated T cells and B cells.

Induction of Protective Immune Response in Mice

To determine the immune protection rate of BHV-1-ΔgE-G via IM route, mice were immunized with 2×10^5 PFU of BHV-1-ΔgE-G and 2×10^5 FFU of SAD virus on days 1 and 14, respectively, and DMEM was injected as the mock immunization group. Seven days post the boost, rabies virus Challenge Virus Standard (CVS-24) with 50 of LD50 was used to infect the above mice. The clinical symptoms and survival rate of the mice were observed until 21 days post-infection. As shown in **Figure 4A**, the survival rates of mice injected with BHV-1-ΔgE-G and SAD were 90 and 100%, respectively. While in the mock-immunization group, all mice died within 11 days after CVS-24 challenge. These results indicate that the recombinant virus BHV-1-ΔgE-G can produce effective immune protection efficiency in mice by intramuscular injection.

In mice that succumbed to rabies, an average virus titer in mice brain reached $10^{4.5}$ FFU/ml, while the virus titer in mice brain that protected by vaccine is nearly to 0 FFU/ml (**Figure 4B**). In mice immunized with BHV-1-ΔgE-G or SAD, the average VNA production of 2.25 IU/ml or 3.00 IU/ml was detected, respectively (**Figure 4C**). Therefore, the immune protection efficiency of BHV-1-ΔgE-G group was same as the SAD, and the recombinant virus BHV-1-ΔgE-G is an ideal vaccine candidate.

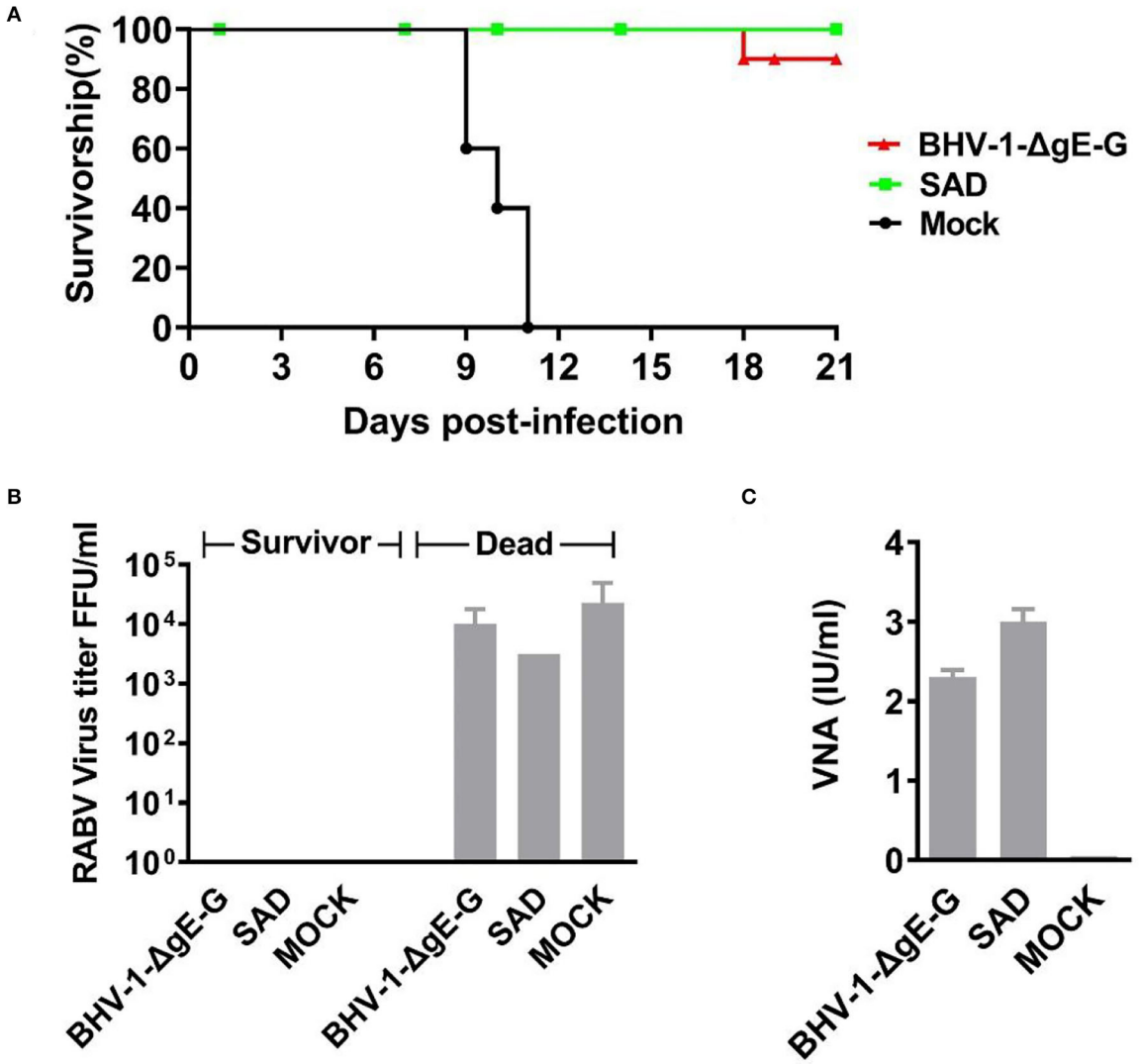

FIGURE 4 | Survival rate and VNA of mice post-challenge. **(A)** Six-week-old female ICR mice were randomly divided into three groups, and each group included 10 mice. Each group of mice was inoculated once with 10^5 PFU of BHV-1-ΔgE-G, 10^5 FFU of SAD or medium control, respectively. Each mice was inoculated with 20 μl of virus, 10 μl for each hind leg. All mice received a challenge with 50 LD50 CVS-24 via an IM route at 21 days post-immunization. Mice were seen to be moribund or that had lost more than 30% of their starting body weight were humanely euthanized. The number of euthanized mice and the corresponding days of death were observed, and the results were graphed by GraphPad Prism 5.0 software. **(B)** Virus titers in the brains of surviving and dead mice. **(C)** VNA in the serum of dead and surviving mice.

Clinical Observations and Antibody Response of Cattle Immunized With BHV-1-ΔgE-G *via* IM Route

To test whether the BHV-1-ΔgE-G is a potential vaccine candidate in cattle, we test the safety, virus persistence period, and RABV-specific VNA in cattles' serum after IM injection. Each group of five cattle was immunized via IM route with a single dose of 10^7 PFU of BHV-1-ΔgE-G or 10^7 FFU of SAD virus on day 1, and DMEM was taken as a control group. Clinical symptoms and VNA in cattle serum were observed after being immunized for another 12 weeks without challenge. None of these cattle developed any clinical signs during the observation period. Serum samples were collected at 1, 6, 12, and 18 weeks and subjected to virus titration and VNA analysis. In addition, none of the live SAD and BHV-1-ΔgE-G in cattle's serum was detected within 18 weeks. As shown in **Figure 5**, both BHV-1-ΔgE-G and SAD vaccinated cattle produce productive serum VNA. The VNA titers of BHV-1-ΔgE-G immunized cattle were 0.8, 1.05, 2.0, and 1.7 IU/ml at 1-, 6-, 12-, and 18-weeks post-immunization, and the VNA titers of SAD-vaccinated cattle were 1.85, 2.0, 2.4, and 2.0 IU/ml at 1-, 6-, 12-, and 18-weeks post-immunization, respectively. Furthermore, to test whether the recombinant virus produced specific immunity to BHV-1, bovine serum was collected on the 14th and 21st days after IM injection,

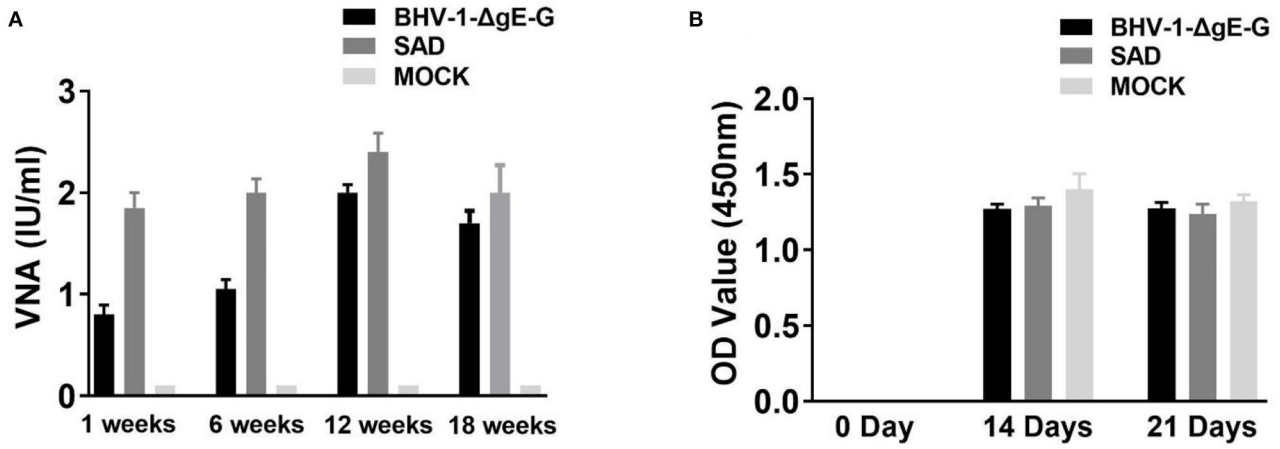

FIGURE 5 | VNA level of cattle immunized with BHV-1-ΔgE-G via IM route. **(A)** Five cattle immunized with a single dose of 10^7 PFU of BHV-1-ΔgE-G, 10^7 PFU of SAD, or DMEM. Serum samples were collected at 1, 6, 12, and 18 weeks and subjected RFFIT for VNA analysis. **(B)** Serum samples were collected on 0 day, 14 days, and 21 days and performed ELISA for gB antibody for BHV-1.

and OD values of gB specific antibodies were detected in the serum by gB antibody ELISA kit (IDEXX, USA). As shown in **Figure 5B**, OD values of BHV-1-ΔgE-G immunized cattle were 1.273 and 1.276 on 14- and 21-days post-immunization, and OD values of BHV-1-ΔgE-G-immunized cattle were 1.291 and 1.238 on 14- and 21-days post-immunization, indicating that the recombinant virus could produce specific immunity to BHV-1.

DISCUSSION

The existing rabies vaccine used in animals still has several disadvantages to be improved, such as, reducing the cost of vaccinations, increasing cellular immune response, prolonging the immune protection period, distinguishing wild-type virus infection from vaccine immunization, and decreasing potential pathogenicity. There are four possible ways to further improve the above problems. First, combining several antigens into a multivalent vaccine is a traditional approach used to provide broad coverage of protection for different diseases and reduce the cost of immunization. Second, for the development of immune responses specific to RABV infection, our lab previously constructed several recombinant RABVs that expressed cytokine or chemokine to enhance innate and adaptive immune responses (Wen et al., 2011; Li et al., 2017). Third, the risk of pathogenicity enhancement in RABV-based live rabies vaccines used in animals needs to be seriously considered (Hostnik et al., 2014; Vuta et al., 2016). A recombinant virus vector expressed that RABV G might be a possible way to solve this problem. And several other virus-based vectors may also induce a higher and long-lasting immunoreaction. Fourth, due to the live-rabies virus used in wildlife, any RABV isolated from animals in a vaccination region needs a rapid characterized method using monoclonal antibodies or molecular techniques to distinguish vaccine RABVs from wild-type RABV. A recombinant rabies vaccine containing molecular markers would be a good solution.

In the present study, BHV-1 was shown to induce a rapid and stronger immune response by recruiting and activating DCs, which also maturate B cells and result in secreting of VNA against RABV. IM vaccination of BHV-1-ΔgE-G induced a protective level of VNA response in mice and cattle. Furthermore, a single dose of BHV-1-ΔgE-G could protect mice from 50 LD50 of CVS-24 RABV challenge, and IM-immunized cattle developed a RABV-specific serum antibody titers higher than 0.5 IU/ml within 14 days. A key characteristic of herpes virus infection is that they persist and induce durable immune responses in their infected hosts. Previous studies reported that replication-defective herpes viruses have been used as vectors for gene therapy (Burton et al., 2005) or for vaccine, including Simian immunodeficiency virus (SIV) (Kaur et al., 2007), Influenza virus, Dengue virus (DENV) (Bischof et al., 2017), Porcine circovirus type 2 (PCV2) virus (Chi et al., 2014), Bovine viral diarrhea virus (BVDV) (Chowdhury et al., 2021), Bovine respiratory syncytial virus (BRSV) (Schrijver et al., 1997), Peste des petits ruminants virus (PPRV) (Macchi et al., 2018), and Nipah Virus (Pedrera et al., 2020). Furthermore, Canine Herpesviruses and BHV-5 have been validated safety and effective for a rabies vaccine vector. On the other hand, cellular apoptosis can activate innate and adaptive immunity that may prevent and treat infectious diseases and cancer (Restifo, 2000). As well, large numbers of apoptotic cells entirely triggered DC maturation and processed intracellular antigens from apoptotic cells (Rovere et al., 1998). Previous studies reported that apoptosis in rabies may block virus replication and apoptosis in inflammatory cells and promote the elimination of the virus by the host inflammatory response (Suja et al., 2011). In our study, the G of BHV-1-ΔgE-G was specifically expressed intracellular and on the virion. Moreover, the BHV-1-ΔgE-G induced a stronger apoptosis response than parent BHV-1 or RABV. In particular, almost all cattle will be immunized with the BHV-1 vaccine in most areas of China, especially in the grazing areas where the BHV-1-ΔgE-G will also effectively block rabies transmitted by wild animals. Meanwhile,

it can reduce the cost and inconvenience of reimmunization against rabies.

The safety of the novel vaccine vector is considered the most important feature, but it is hard to evaluate the vaccine in all nature host animals. Therefore, we examined the safety of BHV-1-ΔgE-G in cells, mice, and cattle. The RABV G gene was inserted between the gI and US9 genes of BHV-1 strain NM14 and was correctly expressed in good amounts, which did not detectably alter the growth characteristics of parental BHV-1, and the RABV G was stably inherited after 20 rounds of passage in cells, as similarly reported after expression of BVDV envelope protein and PPRV envelope glycoprotein in a BHV-4 vector (Kweon et al., 1999; Macchi et al., 2018). Furthermore, in immunized mice that are non-permissive for BHV-1, only early BHV-1 genes are expressed, and live BHV-1 cannot detect after 14 days inoculation in blood of mice and consequently cannot induce efficient anti-BHV-1 specific immunity. Previous research reported that a replication-deficient HSV-1 vector also provided a good immune response (Samaniego et al., 1998); hence, we will construct a replication-deficient BHV-1 vaccine vector to enhance the safety in the next step of the experiment.

Previous herpes virus-based vaccine was constructed by homologous recombination, which requires to pick hundreds of virus plaques to get one recombinant virus. We combined highly efficient DNA virus recombinant systems in BHV-1 construction, CRISPR/Cas9, and single cell FACS technology to increase the viral gene editing efficiency and virus purification efficiency. Our previous study also reported that BHV-1 gene recombination efficiency in VERO-E6 cells is significantly higher than other cells and using a pair of gRNAs can promote homologous recombination efficiency. Therefore, we can obtain recombinant BHV-1 by a simple plaque purification procedure.

In the present study, we constructed a recombinant BHV-1 that expressed RABV G (BHV-1-ΔgE-G) using CRISPR-Cas9 and estimate the safety and immunogenicity as a multivalent vaccine against animals' rabies in cattle. Animal experiments demonstrated that BHV-1 did not cause any adverse clinical syndromes in mice and cattle, and this vaccine might have a potential to control the cattle and other ruminants derived rabies epidemic in China and some developing countries.

DATA AVAILABILITY STATEMENT

The original contributions presented in the study are included in the article/Supplementary Material, further inquiries can be directed to the corresponding authors.

ETHICS STATEMENT

The animal study was reviewed and approved by Ethics Committee of Inner Mongolia University (IMU-MO-2020-031). Written informed consent was obtained from the owners for the participation of their animals in this study.

AUTHOR CONTRIBUTIONS

YY and WH: writing—review and editing. YY and JG: writing—original draft preparation. CZ: methodology. JG: supervision. LJ and HQ: data curation. YW: visualization. All authors have read and agreed to the published version of the manuscript.

FUNDING

This research was funded by the National Natural Science Foundation of China (Grant 32072900 to YY), the Program for Young Talents of Science and Technology in Universities of Inner Mongolia Autonomous Region (No. NJYT22106 to YY), the Science and Technology Major Project of Inner Mongolia Autonomous Region of China (Nos. 2020ZD0008, 2021ZD0013, and 2021ZD0048), and the High-Level Talent Scientific Research Startup Fund for Baotou Teachers' College (No: BTTCRCQD2020-004 to CZ).

REFERENCES

Ana, C., Franciscus,. A., and Paulo, M. (2002). "Bovine herpesvirus mutant type 5, vaccine directed against bovine viral encephalitis (bhv-5) and the rabies virus and vaccine preparation method." in *Google Patents*, eds National Center for Biotechnology Information. Brazil: UNIV FED DO RIO GRANDE DO SUL (BR).

Bischof, G. F., Magnani, D. M., Ricciardi, M., Shin, Y. C., Domingues, A., Bailey, V. K., et al. (2017). Use of a recombinant gamma-2 herpesvirus vaccine vector against dengue virus in rhesus monkeys. *J. Virol.* 91:e00525–17. doi: 10.1128/JVI.00525-17

Burton, E. A., Fink, D. J., and Glorioso, J. C. (2005). Replication-defective genomic HSV gene therapy vectors: design, production and CNS applications. *Curr. Opin. Mol. Ther.* 7, 326–336. doi: 10.1016/j.copbio.2005.07.002

Chen, T., Zhou, X., Qi, Y., Mi, L., Sun, X., Zhang, S., et al. (2019). Feline herpesvirus vectored-rabies vaccine in cats: a dual protection. *Vaccine* 37, 2224–2231. doi: 10.1016/j.vaccine.2019.03.008

Chi, J. N., Wu, C. Y., Chien, M. S., Wu, P. C., Wu, C. M., and Huang, C. (2014). The preparation of porcine circovirus type 2 (PCV2) virus-like particles using a recombinant pseudorabies virus and its application to vaccine development. *J. Biotechnol.* 181, 12–19. doi: 10.1016/j.jbiotec.2014.04.006

Chowdhury, S. I., Pannhorst, K., Sangewar, N., Pavulraj, S., Wen, X., Stout, R. W., et al. (2021). BoHV-1-Vectored BVDV-2 subunit vaccine induces BVDV cross-reactive cellular immune responses and protects against BVDV-2 challenge. *Vaccines* 9:46. doi: 10.3390/vaccines 9010046

Cliquet, F., Aubert, M., and Sagne, L. (1998). Development of a fluorescent antibody virus neutralisation test (FAVN test) for the quantitation of rabies-neutralising antibody. *J. Immunol. Methods* 212, 79–87. doi: 10.1016/S0022-1759(97)00212-3

Cong, L., Ran, F. A., Cox, D., Lin, S., Barretto, R., Habib, N., et al. (2013). Multiplex genome engineering using CRISPR/Cas systems. *Science* 339, 819–823. doi: 10.1126/science.1231143

Di Lullo, G., Soprana, E., Panigada, M., Palini, A., Agresti, A., Comunian, C., et al. (2010). The combination of marker gene swapping and fluorescence-activated cell sorting improves the efficiency of recombinant modified vaccinia virus Ankara vaccine production for human use. *J. Virol. Methods* 163, 195–204. doi: 10.1016/j.jviromet.2009.09.016

DiStefano, D., Antonello, J. M., Bett, A. J., Medi, M. B., and Casimiro DR, and ter Meulen J. (2013). Immunogenicity of a reduced-dose whole killed rabies vaccine is significantly enhanced by ISCOMATRIX adjuvant, Merck amorphous aluminum hydroxylphosphate sulfate (MAA) or a

synthetic TLR9 agonist in rhesus macaques. *Vaccine* 31, 4888–4893. doi: 10.1016/j.vaccine.2013.07.034

Feng, Y., Wang, Y., Xu, W., Tu, Z., Liu, T., Huo, M., et al. (2020). Animal rabies surveillance, China, 2004-2018. *Emerg. Infect. Dis.* 26, 2825–2834. doi: 10.3201/eid2612.200303

Freuling, C. M., Hampson, K., Selhorst, T., Schroder, R., Meslin, F. X., Mettenleiter, T. C., et al. (2013). "The elimination of fox rabies from Europe: determinants of success and lessons for the future. *Philos. Trans. R. Soc. Lond. B. Biol. Sci.* 368:20120142. doi: 10.1098/rstb.2012.0142

Hostnik, P., Picard-Meyer, E., Rihtaric, D., Toplak, I., and Cliquet, F. (2014). Vaccine-induced rabies in a red fox (Vulpes vulpes): isolation of vaccine virus in brain tissue and salivary glands. *J. Wildl. Dis.* 50, 397–401. doi: 10.7589/2013-07-183

Jiang, Y., Luo, Y., Michel, F., Hogan, R. J., He, Y., and Fu, Z. F. (2010). Characterization of conformation-specific monoclonal antibodies against rabies virus nucleoprotein. *Arch. Virol.* 155, 1187–1192. doi: 10.1007/s00705-010-0709-x

Kaashoek, M. J., Moerman, A., Madic, J., Rijsewijk, F. A., Quak, J., Gielkens, A. L., et al. (1994). A conventionally attenuated glycoprotein E-negative strain of bovine herpesvirus type 1 is an efficacious and safe vaccine. *Vaccine* 12, 439–444. doi: 10.1016/0264-410X(94)90122-8

Kaur, A., Sanford, H. B., Garry, D., Lang, S., Klumpp, S. A., Watanabe, D., et al. (2007). Ability of herpes simplex virus vectors to boost immune responses to DNA vectors and to protect against challenge by simian immunodeficiency virus. *Virology* 357, 199–214. doi: 10.1016/j.virol.2006.08.007

Kweon, C. H., Kang, S. W., Choi, E. J., and Kang, Y. B. (1999). Bovine herpes virus expressing envelope protein (E2) of bovine viral diarrhea virus as a vaccine candidate. *J. Vet. Med. Sci.* 61, 395–401. doi: 10.1292/jvms.61.395

Li, C., Wang, Y., Liu, H., Zhang, X., Baolige, D., Zhao, S., et al. (2020). Change in the single amino acid site 83 in rabies virus glycoprotein enhances the BBB permeability and reduces viral pathogenicity. *Front. Cell Dev. Biol.* 8:632957. doi: 10.3389/fcell.2020.632957

Li, C., Zhang, H., Ji, L., Wang, X., Wen, Y., Li, G., et al. (2019). Deficient incorporation of rabies virus glycoprotein into virions enhances virus-induced immune evasion and viral pathogenicity. *Viruses* 11:218. doi: 10.3390/v11030218

Li, Y., Zhou, M., Luo, Z., Zhang, Y., Cui, M., Chen, H., et al. (2017). Overexpressin of Interleukin-7 extends the humoral immune response induced by rabies vaccination. *J. Virol.* 91, e02324–16. doi: 10.1128/JVI.02324-16

Liu, Y., Zhang, H. P., Zhang, S. F., Wang, J. X., Zhou, H. N., Zhang, F., et al. (2016). Rabies outbreaks and vaccination in domestic camels and cattle in Northwest China. *PLoS Negl. Trop. Dis.* 10:e0004890. doi: 10.1371/journal.pntd.0004890

Macchi, F., Rojas, J. M., Verna, A. E., Sevilla, N., Franceschi, V., Tebaldi, G., et al. (2018). Bovine Herpesvirus-4-Based vector delivering peste des petits ruminants virus hemagglutinin ORF Induces both neutralizing antibodies and cytotoxic T cell responses. *Front. Immunol.* 9:421. doi: 10.3389/fimmu.2018.00421

Morimoto, K., Hooper, D. C., Spitsin, S., Koprowski, H., and Dietzschold, B. (1999). Pathogenicity of different rabies virus variants inversely correlates with apoptosis and rabies virus glycoprotein expression in infected primary neuron cultures. *J. Virol.* 73, 510–518. doi: 10.1128/JVI.73.1.510-518.1999

Mu, Y. X., J., Zhang, L., C., Liu Y, H l, I. U., R, Y Wen, J., et al. (2018). Construction of BHV-1 gE deletion strain based on CRISPR/Cas9 technique and preliminary identification of its immunobiological characteristics. *J. Agric. Biotechnol.* 26, 2003–2016. doi: 10.3969/j.issn.1674-7968.2018.12.001

Pedrera, M., Macchi, F., McLean, R. K., Franceschi, V., Thakur, N., Russo, L., et al. (2020). Bovine Herpesvirus-4-Vectored delivery of nipah virus glycoproteins enhances T cell immunogenicity in pigs. *Vaccines* 8:115. doi: 10.3390/vaccines8010115

Petrini, S., Iscaro, C., and Righi, C. (2019). Antibody responses to Bovine Alphaherpesvirus 1 (BoHV-1) in passively immunized calves. *Viruses* 11:23. doi: 10.3390/v11010023

Rasalingam, P., Rossiter, J. P., and Jackson, A. C. (2005). Recombinant rabies virus vaccine strain SAD-l16 inoculated intracerebrally in young mice produces a severe encephalitis with extensive neuronal apoptosis. *Can. J. Vet. Res.* 69, 100–105. doi: 10.1080/03079450500059032

Restifo, N. P. (2000). Building better vaccines: how apoptotic cell death can induce inflammation and activate innate and adaptive immunity. *Curr. Opin. Immunol.* 12, 597–603. doi: 10.1016/S0952-7915(00)00148-5

Rovere, P., Vallinoto, C., Bondanza, A., Crosti, M. C., Rescigno, M., Ricciardi-Castagnoli, P., et al. (1998). Bystander apoptosis triggers dendritic cell maturation and antigen-presenting function. *J. Immunol.* 161, 4467–4471.

Samaniego, L. A., Neiderhiser, L., and DeLuca, N. A. (1998). Persistence and expression of the herpes simplex virus genome in the absence of immediate-early proteins. *J. Virol.* 72, 3307–3320. doi: 10.1128/JVI.72.4.3307-3320.1998

Sarmento, L., Li, X. Q., Howerth, E., Jackson, A. C., and Fu, Z. F. (2005). Glycoprotein-mediated induction of apoptosis limits the spread of attenuated rabies viruses in the central nervous system of mice. *J. Neurovirol.* 11, 571–581. doi: 10.1080/13550280500385310

Schrijver, R. S., Langedijk, J. P., Keil, G. M., Middel, W. G., Maris-Veldhuis, M., Van Oirschot, J. T., et al. (1997). Immunization of cattle with a BHV1 vector vaccine or a DNA vaccine both coding for the G protein of BRSV. *Vaccine* 15, 1908–1916. doi: 10.1016/S0264-410X(97)00129-1

Shao, X. Q., Yan, X. J., Luo, G. L., Zhang, H. L., Chai, X. L., Wang, F. X., et al. (2011). Genetic evidence for domestic raccoon dog rabies caused by Arctic-like rabies virus in Inner Mongolia, China. *Epidemiol. Infect.* 139, 629–635. doi: 10.1017/S0950268810001263

Suja, M. S., Mahadevan, A., Madhusudana, S. N., and Shankar, S. K. (2011). Role of apoptosis in rabies viral encephalitis: a comparative study in mice, canine, and human brain with a review of literature. *Patholog. Res. Int.* 2011:374286. doi: 10.4061/2011/374286

Vuta, V., Picard-Meyer, E., Robardet, E., Barboi, G., Motiu, R., Barbuceanu, F., et al. (2016). Vaccine-induced rabies case in a cow (*Bos taurus*): molecular characterisation of vaccine strain in brain tissue. *Vaccine* 34, 5021–5025. doi: 10.1016/j.vaccine.2016.08.013

Wen, Y., Wang, H., Wu, H., Yang, F., Tripp, R. A., Hogan, R. J., et al. (2011). Rabies virus expressing dendritic cell-activating molecules enhances the innate and adaptive immune response to vaccination. *J. Virol.* 85, 1634–1644. doi: 10.1128/JVI.01552-10

World Health Organization. (2013). *WHO Expert Consultation on Rabies*. Second report. *World Health Organ Tech Rep Ser* (982). p. 1–139, back cover.

Yakobson, B., Taylor, N., Dveres, N., Rozenblut, S., Tov, B. E., Markos, M., et al. (2015). Cattle rabies vaccination–A longitudinal study of rabies antibody titres in an Israeli dairy herd. *Prev. Vet. Med.* 121, 170–175. doi: 10.1016/j.prevetmed.2015.05.004

Yang, Y., Huang, Y., Gnanadurai, C. W., Cao, S., Liu, X., Cui, M., et al. (2015). The inability of wild-type rabies virus to activate dendritic cells is dependent on the glycoprotein and correlates with its low level of the *de novo*-synthesized leader RNA. *J. Virol.* 89, 2157–2169. doi: 10.1128/JVI.02092-14

Zhou, D., Cun, A., Li, Y., Xiang, Z., and Ertl, H. C. (2006). A chimpanzee-origin adenovirus vector expressing the rabies virus glycoprotein as an oral vaccine against inhalation infection with rabies virus. *Mol. Ther.* 14, 662–672. doi: 10.1016/j.ymthe.2006.03.027

Conflict of Interest: The authors declare that the research was conducted in the absence of any commercial or financial relationships that could be construed as a potential conflict of interest.

Publisher's Note: All claims expressed in this article are solely those of the authors and do not necessarily represent those of their affiliated organizations, or those of the publisher, the editors and the reviewers. Any product that may be evaluated in this article, or claim that may be made by its manufacturer, is not guaranteed or endorsed by the publisher.

frontiers | Frontiers in Microbiology

ORIGINAL RESEARCH
published: 30 June 2022
doi: 10.3389/fmicb.2022.894356

EGFR Activation Impairs Antiviral Activity of Interferon Signaling in Brain Microvascular Endothelial Cells During Japanese Encephalitis Virus Infection

Ya-Ge Zhang[1,2,3,4], *Hao-Wei Chen*[1,2,3,4], *Hong-Xin Zhang*[1,2,3,4], *Ke Wang*[1,2,3,4], *Jie Su*[1,2,3,4], *Yan-Ru Chen*[1,2,3,4], *Xiang-Ru Wang*[1,2,3,4], *Zhen-Fang Fu*[1,2,3,4] *and Min Cui*[1,2,3,4]*

[1] State Key Laboratory of Agricultural Microbiology, College of Veterinary Medicine, Huazhong Agricultural University, Wuhan, China, [2] Key Laboratory of Preventive Veterinary Medicine in Hubei Province, The Cooperative Innovation Center for Sustainable Pig Production, Wuhan, China, [3] Key Laboratory of Development of Veterinary Diagnostic Products, Ministry of Agriculture of the People's Republic of China, Wuhan, China, [4] International Research Center for Animal Disease, Ministry of Science and Technology of the People's Republic of China, Wuhan, China

OPEN ACCESS

Edited by:
Jue Liu,
Yangzhou University, China

Reviewed by:
Bin Zhou,
Nanjing Agricultural University, China
Jianzhong Zhu,
Yangzhou University, China

***Correspondence:**
Min Cui
cuimin@mail.hzau.edu.cn

Specialty section:
This article was submitted to Virology, a section of the journal Frontiers in Microbiology

Received: 11 March 2022
Accepted: 24 May 2022
Published: 30 June 2022

Citation:
Zhang Y-G, Chen H-W, Zhang H-X, Wang K, Su J, Chen Y-R, Wang X-R, Fu Z-F and Cui M (2022) EGFR Activation Impairs Antiviral Activity of Interferon Signaling in Brain Microvascular Endothelial Cells During Japanese Encephalitis Virus Infection. Front. Microbiol. 13:894356. doi: 10.3389/fmicb.2022.894356

The establishment of Japanese encephalitis virus (JEV) infection in brain microvascular endothelial cells (BMECs) is thought to be a critical step to induce viral encephalitis with compromised blood–brain barrier (BBB), and the mechanisms involved in this process are not completely understood. In this study, we found that epidermal growth factor receptor (EGFR) is related to JEV escape from interferon-related host innate immunity based on a STRING analysis of JEV-infected primary human brain microvascular endothelial cells (hBMECs) and mouse brain. At the early phase of the infection processes, JEV induced the phosphorylation of EGFR. In JEV-infected hBMECs, a rapid internalization of EGFR that co-localizes with the endosomal marker EEA1 occurred. Using specific inhibitors to block EGFR, reduced production of viral particles was observed. Similar results were also found in an EGFR-KO hBMEC cell line. Even though the process of viral infection in attachment and entry was not noticeably influenced, the induction of IFNs in EGFR-KO hBMECs was significantly increased, which may account for the decreased viral production. Further investigation demonstrated that EGFR downstream cascade ERK, but not STAT3, was involved in the antiviral effect of IFNs, and a lowered viral yield was observed by utilizing the specific inhibitor of ERK. Taken together, the results revealed that JEV induces EGFR activation, leading to a suppression of interferon signaling and promotion of viral replication, which could provide a potential target for future therapies for the JEV infection.

Keywords: Japanese encephalitis virus, human brain microvascular endothelial cells, epidermal growth factor receptor, interferon, ERK

INTRODUCTION

Japanese encephalitis virus (JEV) is an arbovirus that remains the leading cause of Flavivirus-based mosquito-borne viral encephalitis worldwide. The epidemic of Japanese encephalitis (JE) is mainly observed in Asia, but the western Pacific and northern Australia are also exposed to the risk of JEV infection nowadays (Turtle and Driver, 2018; Kuwata et al., 2020). Approximately, one-third of patients hospitalized with JE die due to the lack of approved therapies and antiviral drugs in endemic areas, which is thought to be a high case fatality rate (Griffiths et al., 2014).

Japanese encephalitis is usually accompanied by the disruption of the blood–brain barrier (BBB), which is a highly specialized structure as the first immune barrier and helps in the maintenance of the homeostasis of the central nervous system (CNS) microenvironment by restricting the invasion of pathogens (Saunders et al., 2008; Burkhart et al., 2015; Chen and Li, 2021). Among the cells composing BBB, brain microvascular endothelial cells (BMECs) are the crucial components that space out neurons from blood circulation (Sweeney et al., 2019). The release of the viral particles from JEV-infected BMECs has been considered to be one of the mechanisms by which the JEV penetrates the BBB (Lai et al., 2012; Al-Obaidi et al., 2017). Apart from JEV, it has been reported that the Zika virus (ZIKV) can continuously establish infection and is released basolaterally from human brain microvascular endothelial cells (hBMECs) (Mladinich et al., 2017). The endothelial cells of the BBB expressed all of the recognized HCV entry receptors and supported HCV infection, which contributed to changed endothelial permeability (Fletcher et al., 2012). In terms of immune activation of BBB, previous studies provide little information on the antiviral ability of BMECs directly against JEV. Nevertheless, immune response featuring pro-inflammatory and anti-inflammatory signaling could be initiated in BMECs in response to pathogens or external stimuli (Chen and Li, 2021). A previous study showed that a robust interferon-β (IFN-β) response was induced in endothelial cells during Nipah virus (NiV) infection (Lo et al., 2010). Li's report also has revealed that the antiviral factors released from immune-activated hBMECs inhibit the infection of HIV in macrophages (Li et al., 2013). Besides, in hBMECs, productive JEV infection has been reported, which causes IFN-β and tumor necrosis factor-α (TNF-α) production (Shwetank et al., 2013). Without a doubt, exposure to pathogens like JEV could profoundly affect the immune function of BMECs.

The epidermal growth factor receptor is a tyrosine kinase receptor that belongs to the ERBB family, whose activation involves the specific ligands including epidermal growth factor (EGF), transforming growth factor-α (TGFα), betacellulin (BTC), heparin-binding EGF-like growth factor (HB-EGF), epiregulin (EREG), epigen (EPGN), and amphiregulin (AREG) (Cataldo et al., 2011; Liebmann, 2011; Freed et al., 2017). The activation of EGFR has been proved to be decisive in many diseases (Linggi and Carpenter, 2006; Finigan et al., 2012; Chen et al., 2017; Martin et al., 2017). Recent studies have demonstrated that activated EGFR in hBMECs contributes to bacteria-mediated disruption of BBB and causes neuroinflammation (Wang et al., 2016; Yang et al., 2016). The activation of EGFR and its downstream cascade are also essential in restricting the host's innate immunity against virus infection (Lupberger et al., 2011; Ueki et al., 2013). For example, impaired activation of EGFR by prostasin causes a decreased dengue virus (DENV) propagation through the downregulation of cyclooxygenase/prostaglandin-E2 (COX-2/PGE2) (Lin et al., 2019). EGFR signaling suppresses the production of IFN response genes to weaken the host antiviral effect in HCV infection (Lupberger et al., 2013). Similarly, Yang et al. have reported that infection by porcine epidemic diarrhea virus (PEDV) activates EGFR and its downstream STAT3, and the treatment with the inhibitor of either EGFR or STAT3 decreases virus production by the upregulation of type I interferon (IFN-I) (Yang et al., 2018). Moreover, during influenza A virus (IAV) infection, the EGFR/mitogen-activated protein kinase/extracellular signal-regulated kinase (MAPK/ERK)/specificity protein 1 (Sp1) signaling cascade was found to participate in the production of the epithelial cell-derived mucin MUC5AC, which provides a protective barrier against pathogenic challenges (Barbier et al., 2012). In the case of JEV, attachment of the virus to host cells induces the activation of EGFR signaling, thereby leading to RhoA activation, which promotes the activation of caveolin-1 and Rac1, thus resulting in caveolin-associated viral internalization (Xu et al., 2016). In hBMECs, activated EGFR has been reported not only to prompt the invasion of meningitic *Escherichia coli* (*E. coli*) but also to cause neuroinflammation in *Streptococcus suis* (*S. suis*) meningitis (Yang et al., 2016; Fu et al., 2018). However, to the best of our knowledge, whether EGFR is involved in the JEV infection of hBMECs is still obscure.

In the present study, we validated the specific role of EGFR on JEV propagation in brain microvascular endothelial cells. JEV infection activated EGFR and its downstream cascades. Using specific inhibitors and knocking out the endogenous EGFR, it was confirmed that EGFR assists the replication and virion production of JEV by negatively regulating the antiviral efficacy of interferon signaling, but does not affect viral attachment or entry. Together with the knowledge of the roles of EGFR in virus infection, the work presented here revealed the mechanism of how JEV exploits EGFR signaling to prompt virus replication, which is likely to provide insights into JEV-induced CNS invasion.

Abbreviations: JEV, Japanese encephalitis virus; EGFR, epidermal growth factor receptor; BBB, blood–brain barrier; BMECs, brain microvascular endothelial cells; hBMECs, human brain microvascular endothelial cells; CNS, central nervous system; RNA-Seq, RNA sequencing; qRT-PCR, quantitative reverse transcription-polymerase chain reaction; PPIs, protein–protein interactions; DMEM, Dulbecco's Modified Eagle's Medium; FBS, fetal bovine serum; PFU, plaque-forming units; IFN, interferon; MOI, multiplicity of infection; IF, immunofluorescence; WB, Western blotting; hpi, hours post-infection; ISGs, interferon-stimulated genes.

MATERIALS AND METHODS

Viruses and Cell Culture

The JEV P3 strain was generated and harvested in mice brains according to the protocol in the previous study

(Li et al., 2015). The heat-inactivated JEV P3 (heated-JEV P3) was acquired via incubating at 94°C for 15 min (Chang et al., 2015). The ZIKV MR766 was generated in the Vero cell line and collected for experiments. The hBMEC and hBMEC EGFR knockout (EGFR-KO) cell lines were kindly provided by Dr. Xiangru Wang (Huazhong Agricultural University, Wuhan, China) and subcultured in flasks with 10% heat-inactivated fetal bovine serum (FBS), 2 mM L-glutamine, 1 mM sodium pyruvate, vitamins, essential amino acids, nonessential amino acids, and 100 U/ml penicillin-streptomycin in RPMI 1640 medium, and maintained in a humidified incubator (37°C, 5% CO_2) (Wang et al., 2016). The Vero and BHK-21 cells were cultured in Dulbecco's Modified Eagle's Medium (DMEM) (Gibco) plus 10% FBS and 1% penicillin/streptomycin. The cells were starved in a serum-free medium for 12∼16 h and subjected to further experimentation when cells were 90∼95% confluent.

Reagents, Antibodies, and Inhibitors

Human EGF recombinant protein (rhEGF) was purchased from Life Technologies (Gaithersburg, MD USA). Proteinase K, phenylmethylsulfonyl fluoride (PMSF), and Cell Counting Kit (CCK-8) assay were all obtained from Biosharp (Anhui, China). HighGene Transfection reagent (RM09014) was purchased from ABclonal (Wuhan, Hube, China). The EGFR inhibitor AG1478 (HY-13524), Gefitinib inhibitor (HY-50895), ERK inhibitor U0126 (HY-12031), and HSP90/STAT3 inhibitor 17-AAG (HY-10211) were purchased from MedChem Express (Shanghai, China). Antibodies used for Western blotting, anti-phospho-EGFR (Tyr1068), and anti-EGFR antibodies (both rabbit polyclonal antibodies) were obtained from Cell Signaling Technology (Danvers, MA, USA). Anti-phospho-STAT3 (Tyr705) and anti-STAT3 (both rabbit) were purchased from Abcam (Cambridge, MA, USA). Anti-phospho-ERK-T202/Y204 and anti-ERK antibodies (both rabbit) were purchased from ABclonal (Wuhan, Hubei, China). An anti-β-actin antibody was purchased from Proteintech (Chicago, IL, USA). Monoclonal antibodies of JEV envelope (E) and ZIKV non-structural protein 5 (NS5) were courtesy of Dr. Shengbo Cao (Huazhong Agricultural University, Wuhan, China). For immunofluorescence, mouse anti-EGFR antibody was obtained from Abcam and rabbit anti-EEA1 antibody was from Cell Signaling Technology, while Alexa Fluor 488 or Cy3-labeled secondary antibodies and DAPI were obtained from Thermo Fisher Scientific (San José, CA, USA).

Drug Treatments and Virus Infection

When cells reached 100% confluence, hBMECs and Vero cells were serum-starved for 12∼16 h before rhEGF was added. After that, cells were washed to prepare for the subsequent experiments. For the inhibition experiment, hBMECs were treated with the inhibitors AG1478, gefitinib, U0126, 17-AAG, or the vehicle control dimethyl sulfoxide (DMSO) at various concentrations for the corresponding times as previously described (András et al., 2005; Maruvada and Kim, 2012). For the virus infection procedure, hBMECs and Vero cells were infected with the JEV at a multiplicity of infection (MOI) of 1 at various times. All virus infection experiments were executed using the above-described procedure unless otherwise stated. The treated cells were then acquired for the following analysis.

RNA Extraction and Quantitative Real-Time PCR

Total RNA from treated cells was extracted with TRIzol reagent following the manufacturer's instructions (Invitrogen, Grand Island, NY). The RNA was reverse-transcribed into cDNA using the ReverTra Ace qPCR RT kit (Toyobo, Japan). SYBR Green 2× mix (Invitrogen) was utilized to perform quantitative real-time PCR using a 7500 Real-Time PCR System (Applied Biosystems). The transcriptional levels of the target mRNA were normalized to β-actin except for the JEV-C gene and ZIKV-NS5 gene. A standard curve was generated to quantify the viral copy numbers, and the pcDNA3.0-HA/JEV-C gene plasmid or the pcDNA3.0-HA/ZIKV-NS5 gene plasmid was used as a template. All amplifications were performed in triplicate, and primers employed for the quantitative real-time PCR are listed in **Table 1**.

Immunofluorescence (IF) and Western Blotting (WB)

Immunofluorescence staining of the cells cultured in the 12-well plate was performed to determine virus replication. In brief, the cells were rinsed with 1× PBS and fixed in 4% paraformaldehyde. The fixed cells were subsequently permeabilized and blocked with 0.2% Triton X-100 and 5% bovine serum albumin (BSA) in 1× PBS for 2 h at room temperature, followed by incubation with mouse anti-JEV-E or mouse anti-ZIKV-NS5 monoclonal antibody (1:1,000) in a humidified chamber overnight at 4°C. After three washes with 1× PBS, the cells were incubated with fluorescently labeled anti-mouse IgG for 1 h at room temperature. Then, the cell nuclei were stained with DAPI. Finally, immunostained samples were visualized under fluorescence microscopy or laser confocal microscopy (Nikon STORM).

For Western blotting analyses, briefly, cells were washed with ice-cold 1 × PBS and then whole cell extracts were prepared using 60 μl of RIPA buffer containing protease inhibitor cocktail (Roche) and phosphatase inhibitor cocktail (Roche). Then the lysates were centrifuged and quantified for protein concentration using a BCA protein assay kit (Beyotime, China). Protein samples were separated by sodium dodecyl sulfate-polyacrylamide gel electrophoresis (12%) and then transferred to PVDF membranes using a wet transfer system. The membranes were blocked in 5% BSA in Tris-buffered saline with Tween 20 (TBST) for 1 h at room temperature and were incubated with primary antibodies overnight at 4°C with shaking. After washing thrice with TBST, the membrane was incubated with a horseradish peroxidase (HRP)-labeled secondary antibody and finally visualized.

Plaque Assay and CCK-8 Assay

Plaque assays were performed on BHK-21 cells utilizing the 24-well culture plate. The supernatants were collected from virus-infected cells at indicated time intervals and stored at −80°C after removing cellular debris. The clarified supernatant was subjected to serial dilution and added into confluent BHK-21 cells for 1.5 h,

TABLE 1 | Primers used for qPCR in this study.

Gene	Forward (5′ - 3′)	Reverse (5′ - 3′)	Species
β-actin	AGCGGGAAATCGTGCGTGAC	GGAAGGAAGGCTGGAAGAGTG	Human
EGFR	TACAGACCCAAGAGCAGCA	AGCCGTACATAGATCCAGAA	Human
IFN-α	FCTTGTGCCTGGGAGGTTGTC	TAGCAGGGGTGAGAGTCTTTG	Human
IFN-β	GACGCCGCATTGACCATCTA	TTGGCCTTCAGGTAATGCAGAA	Human
IFN-λ1	CACATTGGCAGGTTCAAATCTCT	CCAGCGGACTCCTTTTTGG	Human
IFN-λ2,3	CTGACGCTGAAGGTTCTGGAG	CGGAAGAGGTTGAAGGTGACAG	Human
ISG15	CGCAGATCACCCAGAAGATCG	TTCGTCGCATTTGTCCACCA	Human
JEV-C	GGCTCTTATCACGTTCTTCAAGTTT	TGCTTTCCATCGGCCYAAAA	
ZIKV-NS5	TGCTCTCAACACATTCACCAACTTG	CATCTCCACTGACCGCCATTCG	

and then the cells were overlaid with DMEM containing 1.5% carboxymethylcellulose (Sigma-Aldrich) for 5 days. Finally, the plaques were counted to calculate viral titers.

The CCK-8 assay was performed to determine cell viability. Briefly, the hBMECs were plated into a 96-well plate at a density of 5,000 cells per well for 24 h and starved for 12∼16 h with a serum-free medium. The inhibitor of various concentrations was added into cells for 2 h, and CCK-8 solutions were subsequently added to each well and continuously incubated for approximately 45 min. Finally, the absorbance of the samples was measured at a wavelength of 450 nm in a Spectrophotometer reader (Bio-Rad, CA, USA).

Measurement of Virus Attachment and Entry

The hBMECs were seeded in the 24-well plate until reaching 100% confluence, and the incubation medium was replaced with serum-free DMEM for 12∼16 h. Then, the cells were incubated with JEV of indicated MOI at 4°C for 1 h (attachment assay). For entry assay, the plate was shifted to 37°C containing 5% CO_2 for 2 h, proteinase K (1 mg/ml) was used to remove non-internalized virions, and then 2 mM PMSF in 1× PBS with 3% bovine serum albumin was applied to inactivated proteinase K as previously described (Dejarnac et al., 2018).

Statistical Analysis

The statistical data are presented as the mean ± SEMs values, with at least three replicates for each treatment. Student's *t*-test, one-way analysis of variance (ANOVA), or two-way ANOVA were applied to analyze the statistical significance of the differences by using GraphPad Prism (v7.0; GraphPad, La Jolla, CA, USA). A value of $p < 0.05$ (*) was considered statistically significant, while values of $p < 0.01$ (**), $p < 0.001$ (***), and $p < 0.0001$ (****) indicated extremely significant differences.

RESULTS

JEV Induced EGFR Activation at the Early Phase of Infection

According to the IFN-related genes identified to be markedly altered in succession at three time points in our unpublished hBMECs RNA-seq data and similar results in Li's report on RNA-seq of JEV-infected mouse brain (**Supplementary Figure S1A**) (Li et al., 2017), a protein to protein interaction (PPI) network was constructed by STRING, from which the emergence of EGFR caught our attention (**Supplementary Figure S1B**). Nevertheless, in the monolayer of hBMECs, there was no significant difference both in transcription and translation levels of EGFR at 12, 36, and 72 h post-infection (hpi) (**Supplementary Figure S1C**). Many viruses activate EGFR through phosphorylation at the early stage of infection, including ZIKV, PEDV, and IAV (Yang et al., 2018; Sabino et al., 2021; Wang et al., 2021). To figure out whether EGFR could be activated by JEV through phosphorylation, phosphorylation on tyrosine sites of EGFR in hBMECs at the early phase of JEV infection was examined. hBMECs were treated with JEV, heat-inactivated JEV (heated-JEV), and DMEM, respectively, and phosphorylated EGFR was determined by Western blotting at 0, 10, 20, 30, 60, and 120 min post-treatment. Simultaneously, the total EGFR expression levels were also measured. The accumulation of phosphorylated EGFR appeared at 10 min and was sustained for at least 2 h in JEV-infected hBMECs but not in heated-JEV or mock-infected hBMECs (**Figure 1A**). The inactivation of heated-JEV was verified by plaque assay, in which no live virus particles were detected (data not shown). Next, Vero cells were utilized to determine whether the activation of EGFR occurred in other cell types besides hBMECs. It was observed that the phosphorylation level of EGFR was also boosted in Vero cells, which is similar to the result in hBMECs (**Figure 1B**). These results demonstrated that JEV but not heated-JEV could induce the phosphorylation of EGFR with no remarkable effect on the expression of total EGFR. EGF, one of the ligands of EGFR, was utilized as a positive stimulator in the activation of EGFR (Yang et al., 2018; Kim et al., 2020). To determine if cells are responsive to EGF, cells were treated with rhEGF, which could prompt the receptor dimerization, autophosphorylation, and activation of EGFR (Herbst, 2004; Xiong et al., 2020). The phosphorylation of EGFR was induced at 10 min and reached the peak at 30 min in hBMECs, but the highest level was around 10 min in Vero cells, and the total EGFR showed no noticeable change over time (**Figures 1C,D**). The divergence of the highest levels of phosphorylated EGFR in hBMECs and Vero cells is probably owing to the different biological characteristics of the two cell types, while both

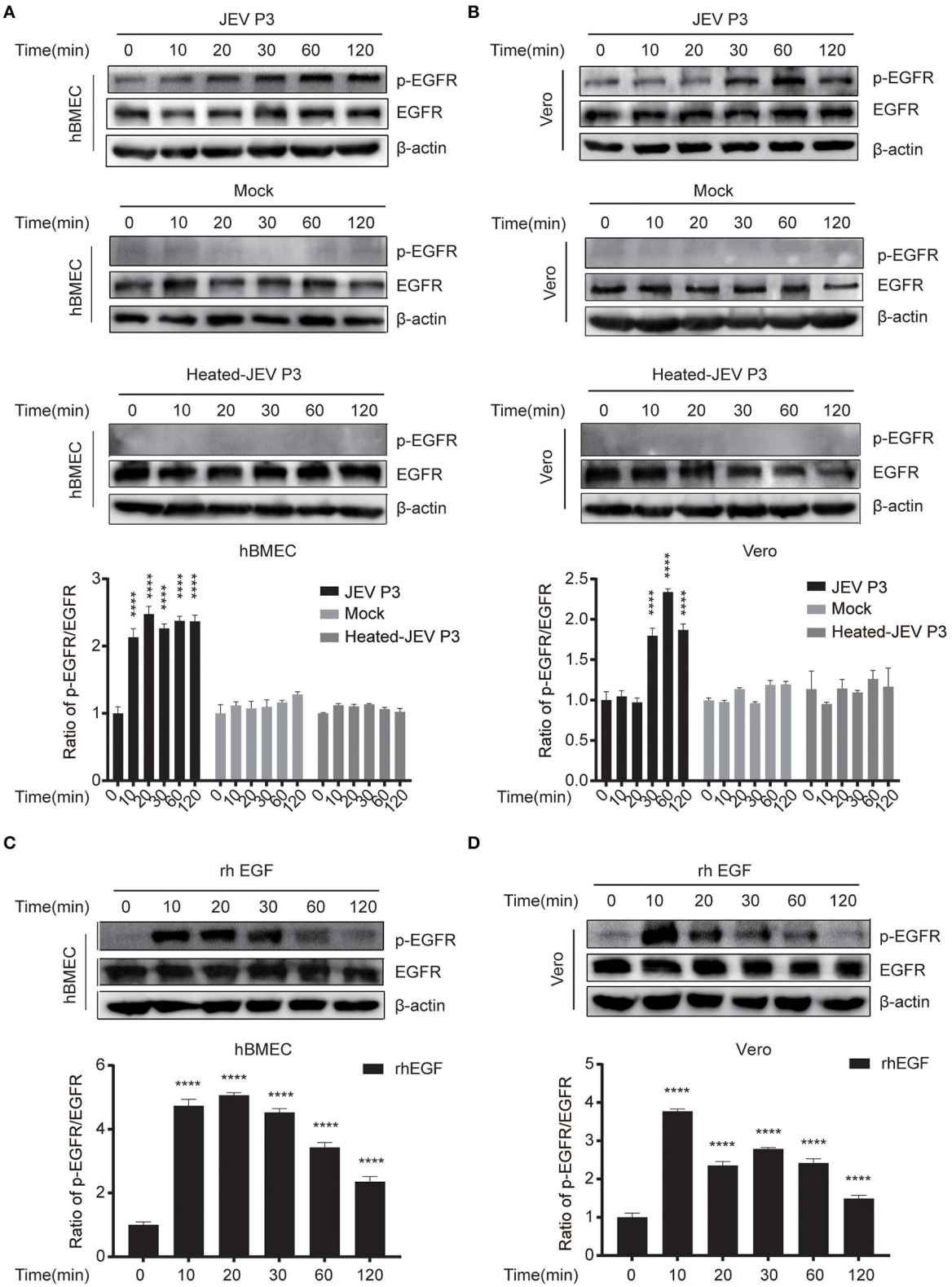

FIGURE 1 | JEV infection induces EGFR phosphorylation. **(A,B)** hBMECs and Vero cells were infected with JEV P3 (MOI = 1) or heated-inactivated JEV P3 (heated-JEV P3, 94°C, 15 min, MOI = 1) for 0, 10, 20, 30, 60, and 120 min, and the cells treated with DMEM were used as control. Cell lysates were harvested and

(Continued)

FIGURE 1 | subsequently examined by Western blotting using the antibodies of p-EGFR, EGFR, and β-actin. Quantification of phosphorylated levels of EGFR relative to the total EGFR levels was performed. **(C,D)** rhEGF-treated cells showed increased phosphorylation of EGFR in a time-dependent manner. About 10 ng/ml rhEGF was added into hBMECs and Vero cells for indicated times in a 37°C humidified incubator after serum-starved for 12∼16 h, then the cells were collected and prepared for Western blotting. Quantification of phosphorylated levels of EGFR relative to the total levels was analyzed with ImageJ and presented as percent of the control samples. The results are represented as mean ± SEM values from three independent experiments. ****, $p < 0.0001$.

cells are consistent with the previous report that prolonged stimulation with EGF leads to the degradation of ligand-induced phosphorylated EGFR (Schlessinger, 1986; Sorkin, 2001). Taking all these observations together, these results suggested that JEV infection activates EGFR through phosphorylation at the early stage of infection.

JEV Triggers EGFR Internalization in HBMECs

To explore whether the intracellular localization of EGFR could be affected by JEV, hBMECs were infected with JEV at an MOI of 1. Simultaneously, hBMECs were treated with rhEGF as a positive control. The specific antibodies of EGFR (red) and EEA1 (endosome marker, green) were utilized to determine the localization of EGFR under JEV infection, which was observed by confocal laser scanning microscopy. As shown in **Figure 2A**, compared to hBMECs in the mock group, both in JEV- and rhEGF-treated hBMECs, cell membrane EGFR substantially decreased and EGFR in cell cytoplasm and nucleus increased and presented as intracellular dot-like structures, which is concomitant with the increasing co-localization of EGFR and endosomal marker EEA1 (**Figure 2A**). Thereafter, the infection of JEV in hBMECs was measured with JEV E-specific antibody (green) by confocal laser scanning microscopy (**Figure 2B**). These results suggested that EGFR is internalized after JEV infection. Previous data demonstrated that EGFR localization might be changed at the early stage of JEV infection. To further confirm the result, hBMECs were infected with JEV at an MOI of 10, and then images were captured by confocal microscopy. The majority of the EGFR is located at the plasma membrane in uninfected hBMECs, while contrastingly, the dot-like structures near the cytoplasm and nucleus appeared at 30 min and persisted up to 120 min after JEV infection (**Figure 2C**). The altered subcellular localization of EGFR in hBMECs indicates that EGFR is internalized at the early phase of JEV infection.

The Inhibition of EGFR Phosphorylation Restricts the Production of Viral Particles in HBMECs

For further study, two EGFR tyrosine kinase inhibitors, AG1478 and gefitinib, were applied, which were functionally approved in the previous research (Dhar et al., 2018; Li et al., 2021). To determine the toxic effects of the inhibitors, the cell viability of hBMECs was assessed upon inhibitor treatment. The hBMECs were seeded in 96-well plates and treated with AG1478 or gefitinib with concentrations from 0.5 to 100 μM for 48 h. In gefitinib-treated hBMECs, there were still more than 70% of cells that remained viable at the dose of 50 μM; for AG1478 treatment, in the concentration of 50 μM, 90% of cells remained viable. Hence, based on the CC_{50} (cell cytotoxicity at 50%), 25 μM was chosen as the highest dose of treatment in the following study for both inhibitors (**Figure 3A**). Afterward, hBMECs and Vero cells were pretreated with AG1478 or gefitinib in different concentrations. It was observed that the tyrosine phosphorylation of EGFR abrogated markedly after pretreatment, which confirmed that AG1478 and gefitinib could be used as inhibitors of EGFR phosphorylation in both hBMECs and Vero cells (**Figure 3B**).

Previous studies gave evidence that the EGFR pathway plays a role in producing various viruses, such as DENV, ZIKV, etc (Ueki et al., 2013; Lin et al., 2019; Chuang et al., 2020). To explore whether EGFR is involved in the JEV infection process, cells were pretreated with AG1478 or gefitinib in different concentrations. It was observed that the level of viral RNA (JEV-C gene) was dramatically decreased in hBMECs treated with 0.5 μM of AG1478, 1 μM of gefitinib, or higher doses (**Figure 3C**). Further study demonstrated that both 10 μM AG1478 and 25 μM gefitinib memorably inhibited viral replication at 24 h and 48 h after JEV infection (**Figure 3D**). Consistent with the transcription levels, viral protein (JEV-E) expression was downregulated in cells treated with 10 μM AG1478 or 25 μM gefitinib at 24 hpi (**Figure 3E**). As shown in the immunofluorescence assay, the number of JEV-positive cells was significantly less in AG1478- or gefitinib-treated hBMECs than in a mock-treated control group (**Figure 3F**). Furthermore, the plaque assay illustrated that the production of viral particles was markedly reduced with inhibitor treatment in hBMECs (**Figure 3G**). Then, we investigated whether activated EGFR could also affect the infection of other CNS-invading flaviviruses in hBMECs. It was reported that ZIKV persistently infects hBMECs, and another report revealed that EGFR is related to the ZIKV life cycle (Mladinich et al., 2017; Sabino et al., 2021). Thus, the replication of ZIKV was determined in AG1478- and gefitinib-treated hBMECs. The result showed a significant reduction in the expression of ZIKV protein (NS5) in the inhibitor-treated groups compared to that in the mock group, which is consistent with the result of JEV infection (**Supplementary Figures S2A,B**). Taken together, the results demonstrated that activated EGFR is associated with the infection of JEV and ZIKV in hBMECs.

Viral Infection Is Impaired in Endogenous EGFR Knockout HBMECs

The above-mentioned results showed a positive correlation between the activated EGFR and viral infection in hBMECs. To further evaluate the function of EGFR in JEV infection, EGFR knockout (KO) hBMEC cell lines were utilized, which were previously generated by using clustered regularly interspaced

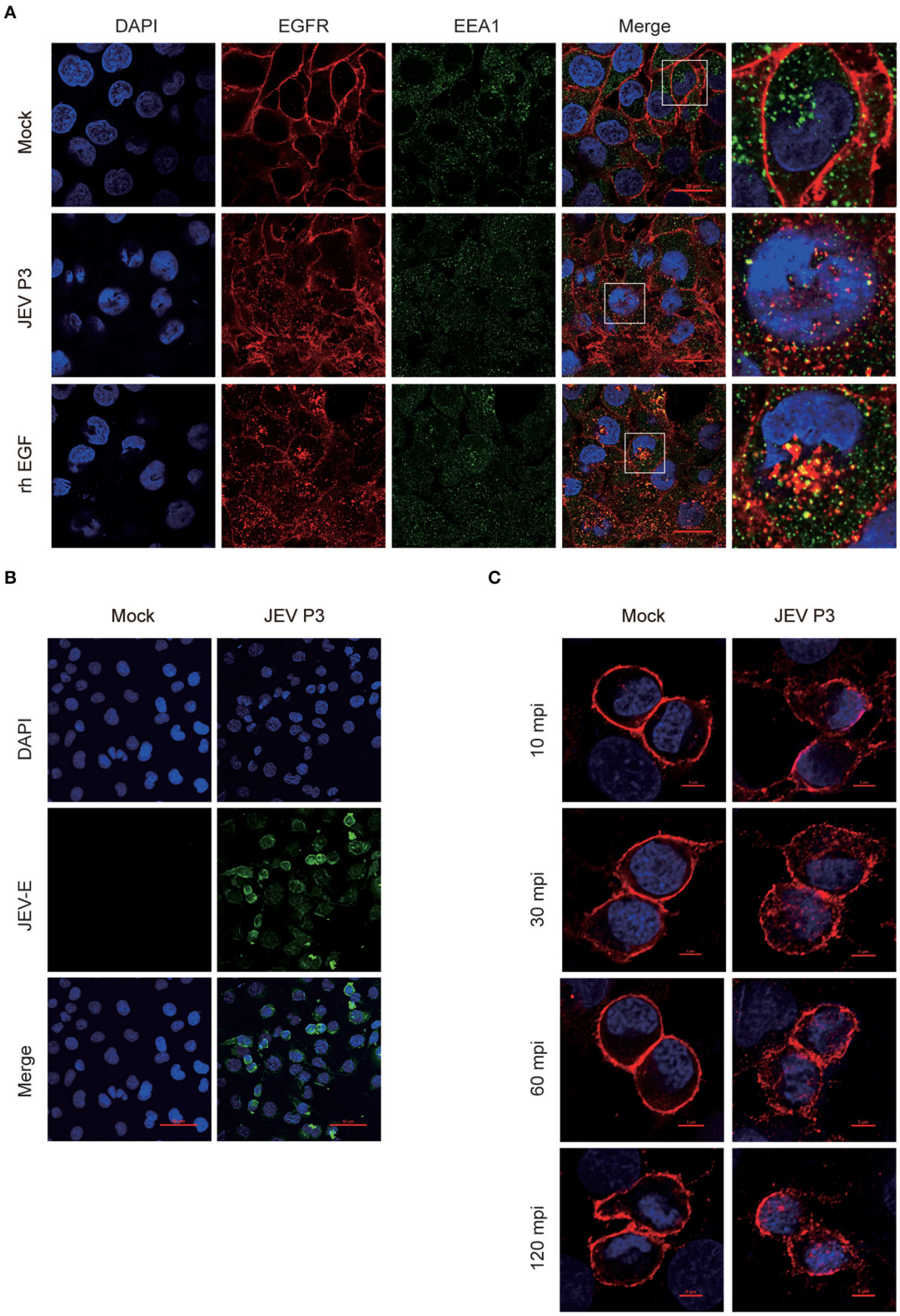

FIGURE 2 | Internalization of EGFR in JEV-infected hBMECs. hBMECs were infected with JEV P3 (MOI = 1) for 16 h, and then images were captured by confocal laser scanning microscopy. **(A)** Uninfected cells and rhEGF-stimulated cells (10 ng/ml rhEGF for 30 min) were utilized as negative and positive controls, respectively.

(Continued)

FIGURE 2 | Cells were fixed and stained with specific antibodies (EGFR and EEA1), and nuclei were stained with DAPI. Bar, 20 μm. **(B)** Negative control was presented with uninfected cells. Nuclei were stained with DAPI, and JEV-E protein was visualized with a JEV envelope protein monoclonal antibody. Bar, 50 μm. **(C)** hBMECs were exposed to JEV P3 (MOI = 10) or mock-treated for 60 min at 4°C and then transferred to a 37°C incubator for 10, 30, 60, and 120 min. Uninfected cells were used as a negative control. Nuclei were stained with DAPI, and EGFR was visualized with a specific antibody. Bar, 5 μm. The results are represented as mean ± SEM values from three independent experiments.

short palindromic repeat (CRISPR)/Cas9-mediated gene editing method (Fu et al., 2018). First, the expression of EGFR was confirmed in EGFR-KO cells by Western blotting (**Figure 4A**). The viral infection was drastically reduced in EGFR-KO cells both in RNA and protein levels in a time-dependent manner compared to that observed in wild-type (WT) hBMECs (**Figures 4B,C**). As shown in the immunofluorescence assay, the number of JEV-positive cells was significantly decreased in EGFR-KO hBMECs than in WT hBMECs (**Figure 4D**). Additionally, the plaque assay showed the viral titer was much lower in the supernatant of EGFR-KO hBMECs than that of WT hBMECs at 24, 48, and 72 hpi, which is consistent with the result of RNA and protein levels (**Figure 4E**). Furthermore, similar to JEV infection, the depression of ZIKV infection was also found in EGFR-KO hBMECs (**Supplementary Figures S3A–C**). These findings support the proposition that EGFR is crucial in mediating Flaviviridae infection in hBMECs.

EGFR Is Related to the Antiviral Response of Interferon Signaling

As EGFR is positively correlated with viral infection in hBMECs, the underlying specific mechanism needs to be further elucidated. The previous report had identified EGFR as a critical regulator in JEV entry into human neuronal cells (Xu et al., 2016). Here, RT-qPCR was performed to validate whether EGFR is related to JEV entry into hBMECs. However, pretreatment with EGFR inhibitor AG1478 or gefitinib did not change either the attachment or entry of JEV to hBMECs compared to the control group treated with DMSO (**Figure 5A**). Additionally, consistent with inhibitor treatment, no significant difference was observed in viral attachment and entry between EGFR-KO hBMECs and WT hBMECs (**Figure 5B**). Since EGFR does not affect JEV attachment and entry in hBMECs, how does EGFR facilitate JEV infection in hBMECs? It has been widely reported that EGFR participates in the regulation of host innate immunity during viral infection (Lupberger et al., 2013; Qiu et al., 2020; Wang et al., 2021). For example, respiratory virus (RSV) induced EGFR phosphorylation, which inhibited interferon regulatory factor 1 (IRF1)-regulate interferon-lambda (IFN-λ) production and breakdown of airway epithelium antiviral response (Kalinowski et al., 2018). Besides, in COVID-19 therapy, EGFR signaling inhibitors potentiated the IFN-I response, thereby considered to be an attractive therapeutic strategy (Matsuyama et al., 2020). On the other hand, regarding the tight correlation between interferon response and JEV infection, it was also reported that interferon signaling affects the inoculation dose-independent mortality in JEV attacked mice (Aoki et al., 2014). Besides, restricted viral propagation was observed when IFN-β production was enabled by neutralizing miR-301a in mouse neurons (Hazra and Kumawat, 2017), *In vitro*, porcine IFN-α inhibited JEV replication, and the overexpression of ISG15 showed antiviral activity against JEV infection (Hsiao et al., 2010; Liu et al., 2013). Based on the studies and previous PPI analysis (**Supplementary Figure S1B**), we speculated that EGFR might serve as a regulator in interferon signaling of host innate immune response in JEV-infected hBMECs. Hence, the expression of several interferons and interferon-stimulated genes (ISGs) was measured. The result showed that the gene expression of type I IFNs (IFN-α and IFN-β), type III IFNs (IFN-λ1, and IFN-λ2, 3), and ISG15 were significantly increased in EGFR-KO hBMECs compared to the WT hBMECs under JEV infection (**Figure 5C**). Collectively, these data demonstrated the negative correlation between EGFR and interferon signaling in JEV-infected hBMECs.

ERK Is Downstream of EGFR in Regulating Interferon Signaling During JEV Infection

Next, the downstream signaling of EGFR stimulated by JEV was investigated. As previously reported, the phosphorylation of ERK or signal transducers and activators of transcription 3 (STAT3) signaling was downstream of EGFR cascade to virus infection (Kung et al., 2011; Xu et al., 2013; Ding et al., 2017). Therefore, the phosphorylation of STAT3 and ERK was measured by Western blotting in hBMECs treated with JEV, rhEGF, or DMEM. Phosphorylation levels of STAT3 and ERK were increased in the hBMECs treated with JEV and rhEGF but not DMEM (**Figure 6A**). The decreased phosphorylation of STAT3 and ERK was observed at 30 min post-infection with the treatment of the inhibitor AG1478 and gefitinib, but not at 10 min (**Figure 6B**). It was assumed that the effects of EGFR on STAT3 and ERK may be induced later. Thus, the phosphorylation of STAT3 and ERK in hBMECs was determined at 60 and 120 min with the treatment of AG1478 or gefitinib. Decreased phosphorylation of STAT3 and ERK appeared in EGFR inhibitor-treated hBMECs and EGFR-KO hBMECs compared to the WT hBMECs (**Figures 6C,D**).

The use of 17-AAG, an inhibitor of heat shock protein 90 (HSP90), or U0126, an ERK inhibitor, has been shown to disrupt the phosphorylation of STAT3 or ERK, respectively, in hBMECs (Maruvada and Kim, 2012; Zhao et al., 2017). To further verify that STAT3 and ERK are related to virus replication during JEV infection, these two inhibitors were applied to the cells to inhibit phosphorylation of STAT3 or ERK (**Figure 6E**). When compared to mock-treated cells, a markedly impaired production of JEV viral RNA and E protein, as well as viral particles in U0126, was observed, but this change was not noticed in 17-AAG-treated hBMECs (**Figures 6F–H**). Previous reports have demonstrated that ERK negatively regulates the interferon

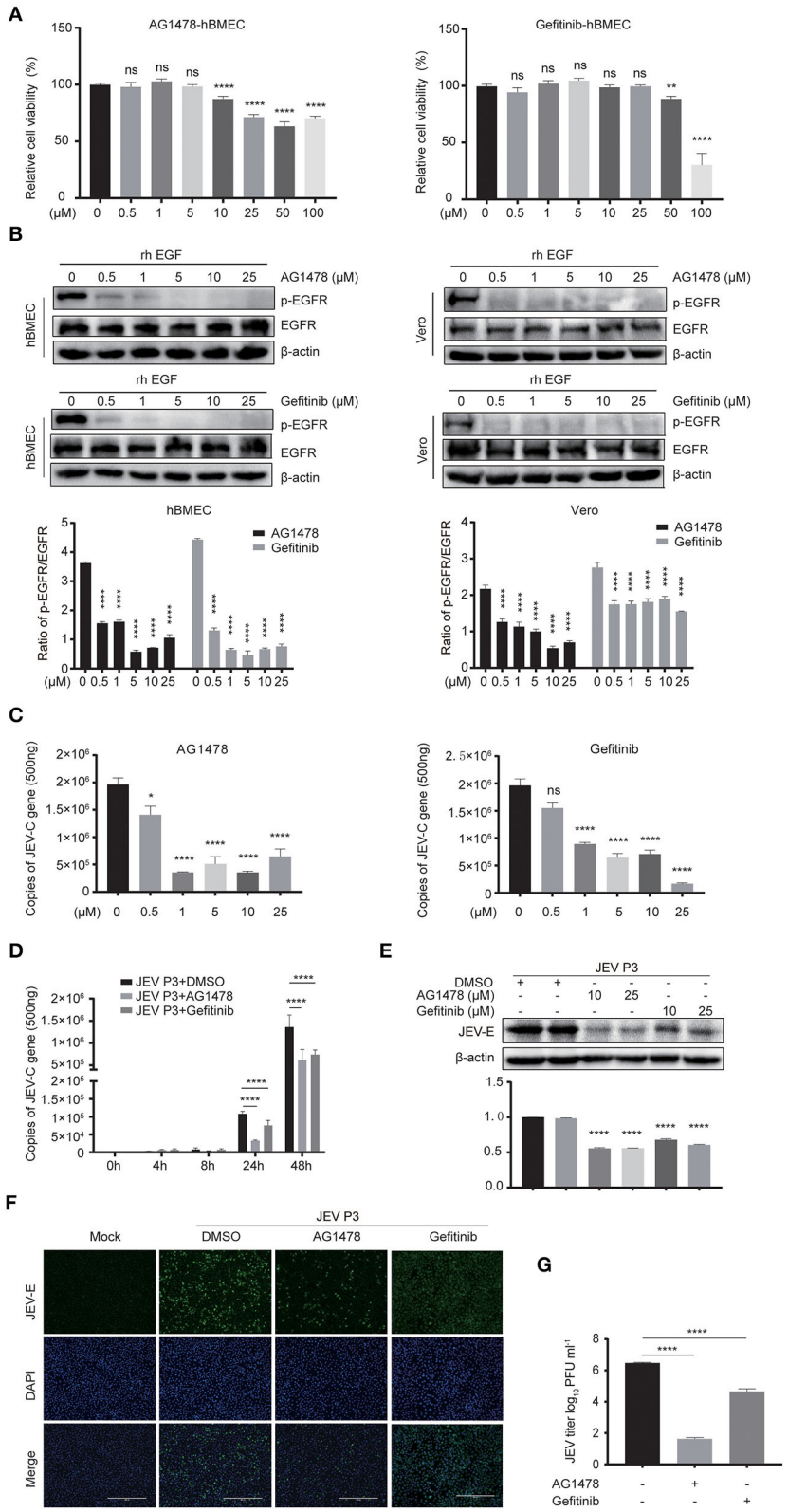

FIGURE 3 | EGFR inhibitors reduce JEV infection in hBMECs. **(A)** Cell cytotoxicity of the EGFR inhibitors. hBMECs were treated with the carrier control DMSO, AG1478, or gefitinib at various concentrations for 48 h, and cell cytotoxicity was analyzed with the CCK-8 assay. **(B)** The inhibitory effect of AG1478 and gefitinib in rhEGF-treated cells. The hBMECs and Vero cells were treated with corresponding concentrations of AG1478 and gefitinib for 2 h and then rhEGF was added for

(Continued)

FIGURE 3 | another 30 min for hBMECs and 10 min for Vero cells, and subsequently, the lysed cells were subjected to Western blotting. hBMECs were pretreated with DMSO, AG1478, or gefitinib for 2 h followed by virus (MOI = 1) infection for corresponding times. Results were quantified. **(C,E)** The verification of the JEV P3 replication in RNA and protein levels treated with indicated concentrations of AG1478 and gefitinib for 24 h. Results were quantified. **(D)** The effects of 10 μM AG1478 or 25 μM gefitinib on JEV P3 replication in hBMECs over time with quantitative real-time PCR. **(F)** The immunofluorescence (IF) assay was performed to determine JEV P3 infection in hBMECs at 24 h after being treated with 10 μM AG1478 or 25 μM gefitinib. Cells were fixed and stained with a specific antibody (JEV-E protein monoclonal antibody), and nuclei were stained with DAPI. Scale bar, 400 μm. **(G)** Supernatants in JEV P3-infected hBMECs with different treatments were collected, and the viral titer was detected in BHK-21 cells with plaque assay. The results are represented as mean ± SEM values from three independent experiments. * $p < 0.05$; ** $p < 0.01$; ****, $p < 0.0001$; ns, not significant.

signaling-mediated antiviral response (Yang and Ding, 2019; Freed et al., 2021). Therefore, the expression of interferons and ISGs was also measured with U0126 treatment in JEV-infected hBMECs. The expression levels of genes ISG15, IFN-α, IFN-β, IFN-λ1 and IFN-λ2, 3 were significantly increased in U0126-treated hBMECs compared to control during JEV infection, which probably is responsible for the dropped replication of JEV in hBMECs (**Figure 6I**). These findings support that the involvement of the EGFR-ERK pathway represses the host interferon signaling, leading to an acceleration of viral replication in hBMECs.

DISCUSSION

As the physical barrier between CNS and circulatory system, BMECs are the first line of BBB controlling the trafficking of JEV and/or JEV-infected cells into the CNS. The infection of BMECs by JEV is thought to be a pivotal step in causing the leakage of BBB, leading to brain infection and encephalitis (Lai et al., 2012; Al-Obaidi et al., 2017). Though BMECs have been largely known to compose BBB, their distinct antimicrobial and antiviral properties are also essential. In the present work, for the first time, the activation of the EGFR/ERK pathway was found, which negatively regulates the antiviral response of interferon signaling, promoting JEV replication in hBMECs.

As a member of the tyrosine kinase family, the biological significance of EGFR has been well studied in tumorigenesis. In recent years, the activated EGFR also appeared in response to viral infection, including IAV, PEDV, ZIKV, and severe acute respiratory syndrome coronavirus 2 (SARS-CoV-2) (Yang et al., 2018; Klann et al., 2020; Sabino et al., 2021; Wang et al., 2021). The activation of EGFR might build a favorable cellular environment to prompt viral entry or replication (Oshiumi et al., 2015; Fukano et al., 2021). In the case of JEV infection, the activated EGFR-PI3K signaling cascade was reported to play a crucial role in caveolin-1-mediated JEV entry into human neuronal cells (Xu et al., 2016). In the present study, the activated EGFR and its downstream signaling also appeared in the early phase of JEV-infected hBMECs. EGFR internalization has been identified in ZIKV-, HBV-, IAV-, and TGEV-infected cells, which assisted in efficient viral entry (Eierhoff et al., 2010; Hu et al., 2018; Iwamoto et al., 2019; Sabino et al., 2021). The internalized EGFR was confirmed by changed subcellular distribution and co-localization with EEA1, while no effect on the viral entry of internalized EGFR was found in JEV-infected hBMECs. The inconsistent result of EGFR in different virus infections is not surprising, which also appeared in the previous study. During human cytomegalovirus (HCMV) infection, Wang et al. indicated that EGFR is a necessary cellular receptor for viral entry (Wang et al., 2003). In contrast, others hold an inconsistent view that EGFR is not an essential factor for cellular invasion or virus-induced signaling (Soroceanu et al., 2008). These inconsistencies might be due to the distinct cell types or differential infection conditions, and more work is needed to address this topic.

Repressed DENV replication was observed in human monocytes in utilizing the EGFR-specific inhibitor gefitinib (Duran et al., 2017), which demonstrates a positive correlation between activated EGFR and viral infection. Moreover, the consistent result of reduced viral infection was also acquired in hBMECs with the use of EGFR-specific inhibitors AG1478 or gefitinib. Notably, in the early phase of *S. suis*-infected hBMECs, the AG1478 caused dephosphorylation of EGFR, which may provide specific protection for the brain from inflammatory cytokine/chemokine-induced BBB disruption (Yang et al., 2016). Further evidence for a decreased production of virions was provided by the EGFR-KO hBMECs with the boosted response of interferon signaling when compared to the WT hBMECs in JEV infection, which showed that activated EGFR weakens the antiviral defense via restraining interferon signaling. Moreover, and not coincidentally, activated EGFR has also been identified to be involved in the production of interferon signaling molecules in other cases, such as cancer and viral infections (Kalinowski et al., 2014; Liu and Han, 2019). The expression of interferon regulatory factor 1 (IRF1) was downregulated by the activation of EGFR signaling in EGFR-mutated non–small cell lung cancer (Sugiyama and Togashi, 2020). In PEDV infection, the activation of EGFR signaling negatively regulates the antiviral activity of interferon (Yang et al., 2018). Even in COVID-19 treatment, targeting EGFR signaling was considered to be an attractive strategy, as its inhibitors may synergistically potentiate the anti-SARS-CoV-2 activity of IFN-I (Matsuyama et al., 2020). Moreover, the IAV-induced activation of EGFR can suppress the production of IFN-λ (Ueki et al., 2013). The result supports the notion, herein, that JEV induced the activation of EGFR, which negatively regulated the production of interferon and helped the virus escape from the antiviral immunity of host cells.

Currently, the EGFR downstream cascade in JEV-infected hBMECs is still enigmatic. Activated EGFR recruits several major downstream signaling pathways during viral infection. Yang et al. elucidated that the depleted EGFR strengthens

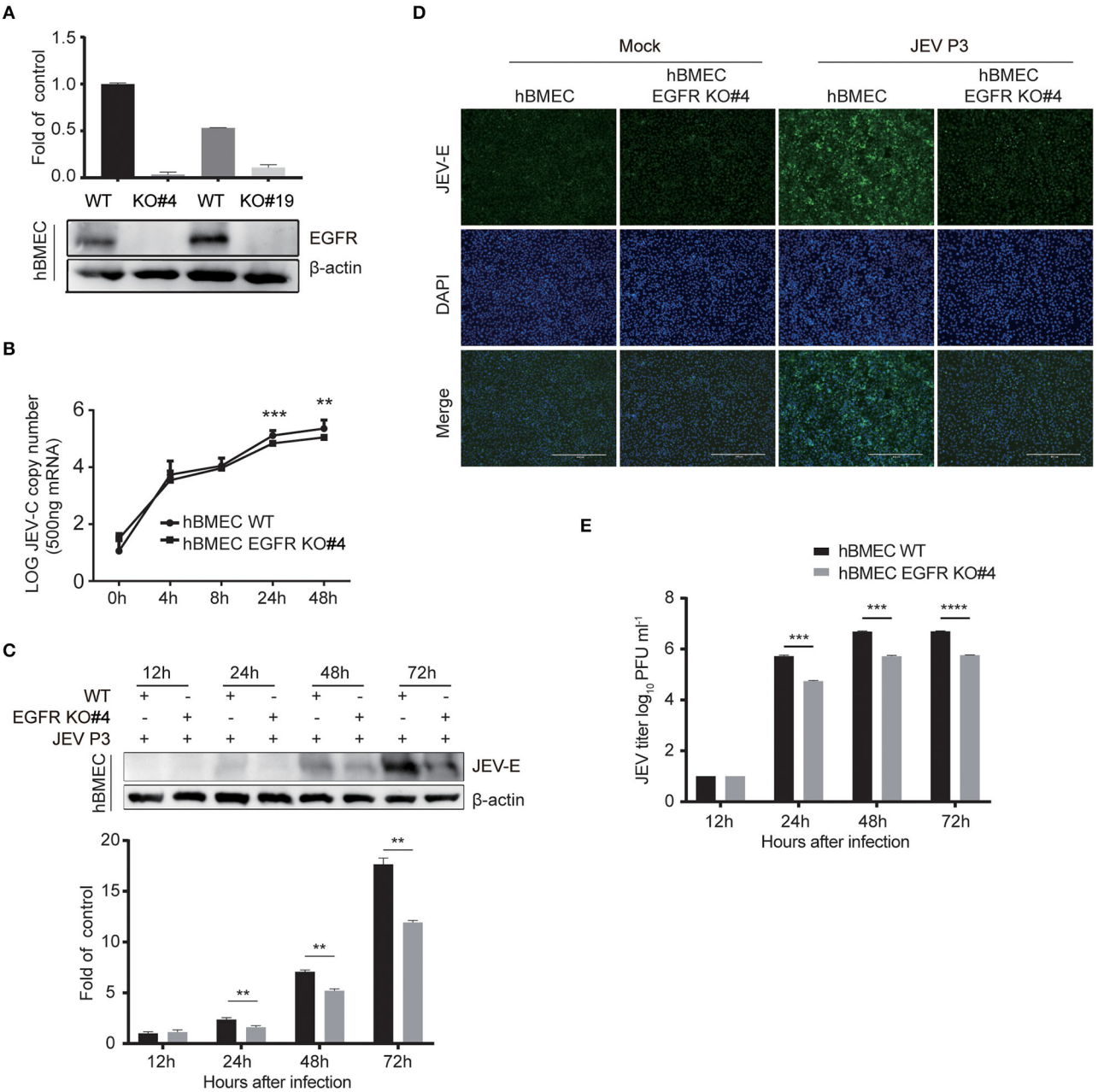

FIGURE 4 | Viral infection was reduced in EGFR knockout hBMECs. **(A)** The verification of the EGFR knockout was measured with Western blotting in hBMECs. Results were quantified. **(B)** The comparison of JEV P3 replication between wild-type and EGFR-KO hBMECs over time by quantitative real-time PCR. **(C)** Western blotting assay was performed to determine the expression of JEV-E protein at different times in wild-type and EGFR-KO hBMECs. Results were quantified. **(D)** Wild-type and EGFR-KO hBMECs were infected with JEV P3 for 24 h, and then immunofluorescence (IF) staining was performed to detect JEV-E protein with JEV-E protein monoclonal antibody. Nuclei were stained with DAPI. Scale bar, 400 μm. **(E)** Supernatants in JEV P3-infected wild-type and EGFR-KO hBMECs were collected over time, and the viral titer was detected in BHK-21 cells by plaque assay. The results are represented as mean ± SEM values from three independent experiments. **, $p < 0.01$; ***, $p < 0.001$; ****, $p < 0.0001$.

the host antiviral activity, which requires attenuated STAT3 signaling (Yang et al., 2018). A more recent model indicated that ZIKV infection induces the activation of EGFR and further transduction of the MAPK/ERK signaling cascade (Sabino et al., 2021). Intriguingly, the phosphorylation of STAT3 and ERK was noticed in both JEV- and rhEGF-treated hBMECs. Therefore, the question arises as to which of the two proteins acts as the downstream effector of EGFR. As a previous study reported, EGF induces the activation of transcription factor TAZ via EGFR and downstream factors STAT3 and

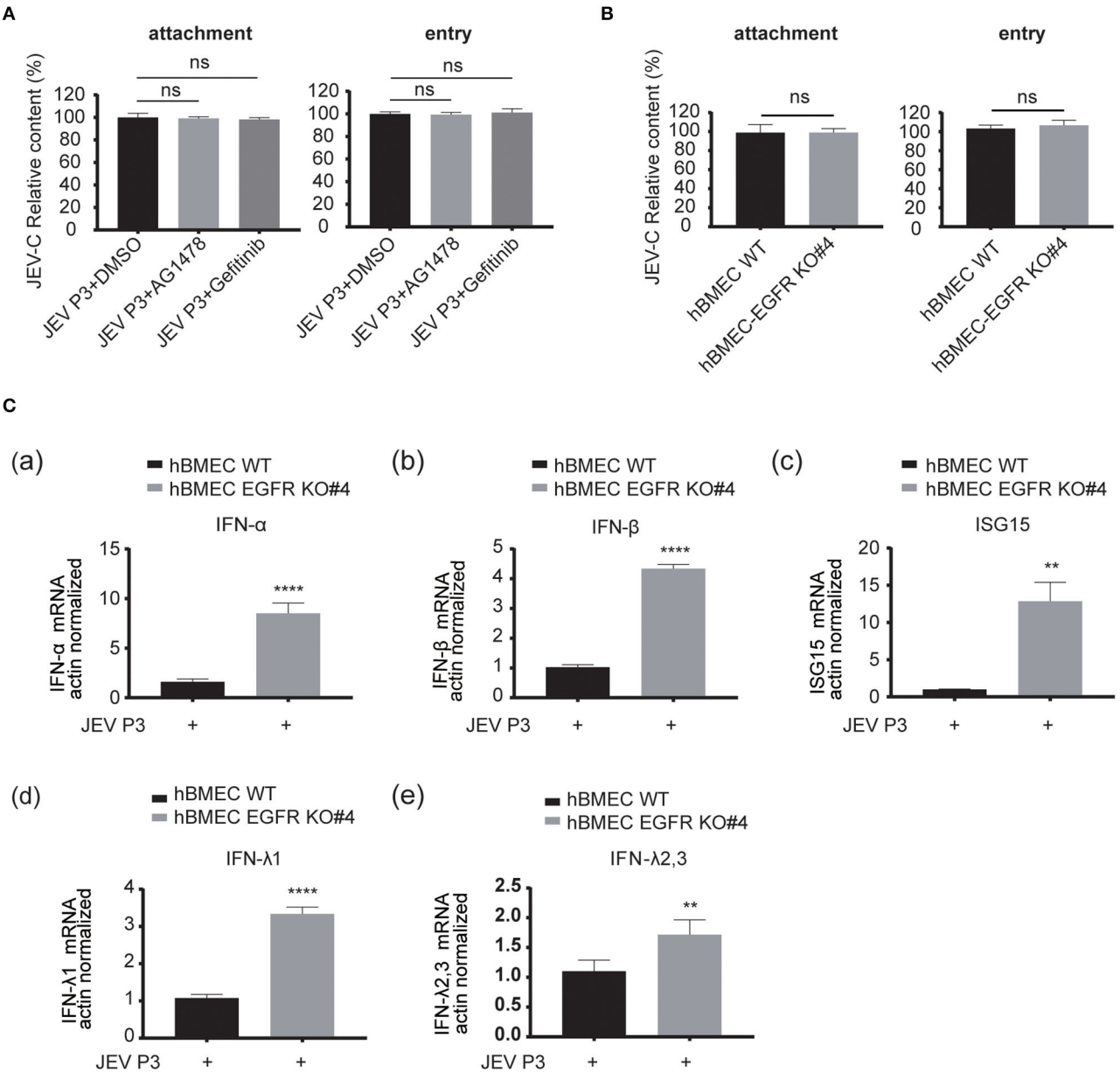

FIGURE 5 | EGFR is involved in the antiviral response of interferon signaling. **(A)** The hBMECs were treated with AG1478, gefitinib, or vehicle control DMSO, and then bound with JEV P3 (MOI = 10) at 4°C for 1 h for attachment. The cells were transferred to a 37°C incubator for 1 h for entry, and total RNA was extracted to determine the RNA copy numbers of JEV P3 with quantitative real-time PCR. **(B)** The hBMECs and EGFR-KO hBMECs were infected with JEV P3 (MOI = 10) at 4°C for 1 h. After washing thrice with PBS containing proteinase k, the cells were then transferred to a 37°C incubator for 1 h to allow virus entry. **(C)** Comparison between hBMECs and EGFR-KO hBMECs in mRNA levels of IFN (IFN-α, IFN-β, IFN-λ1, and IFN-λ2, 3) and ISG15 production in the presence or absence of JEV P3 infection. The hBMECs and EGFR-KO hBMECs were infected with JEV P3 (MOI = 1) for 8 h, and total RNA was extracted and quantitative real-time PCR was performed. The results are represented as mean ± SEM values from three independent experiments. **, $p < 0.01$; ****, $p < 0.0001$; ns, not significant.

ERK (Gao et al., 2021). By comparing the phosphorylation levels of STAT3 and ERK from cells with or without the treatment of EGFR-specific inhibitors, both STAT3 and ERK were identified as the downstream cascade (Xu et al., 2017), which was further evidenced by utilizing EGFR-KO hBMECs in our study. Then, we explored which downstream factor, STAT3 or ERK, is involved in the host's innate immunity in resisting JEV infection. Inhibition of STAT3 by 17-AAG in hBMECs efficiently impaired JEV infection, which was not observed in MAPK/ERK inhibition by U0126, supporting that the MAPK/ERK pathway could contribute to the JEV life cycle, which is similar to the result in ZIKV infection

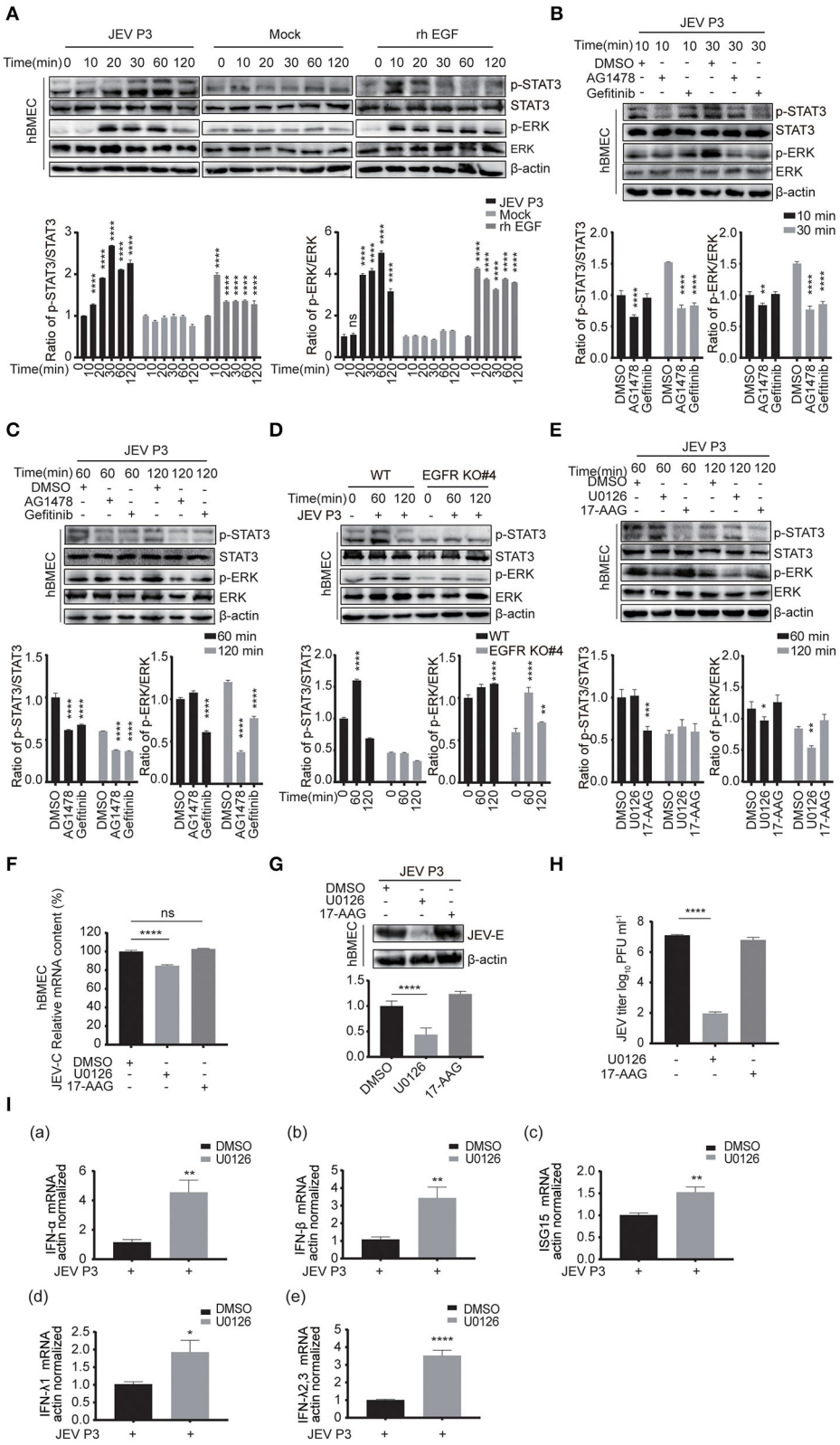

FIGURE 6 | ERK signaling participated in EGFR-regulated host antiviral response by activating interferon signaling. **(A)** Both JEV P3 and rhEGF induced the phosphorylation of ERK and STAT3 in hBMECs. hBMECs were treated with JEV P3, rhEGF, or DMEM for 0, 10, 20, 30, 60, and 120 min. The expression of p-ERK, ERK, p-STAT3, and STAT3 were determined by Western blotting analysis with specific antibodies, while the expression of β-actin was detected as a loading control.

(Continued)

FIGURE 6 | Results were quantified. **(B,C)** hBMECs were pretreated with 10 μM AG1478, 25 μM gefitinib, or DMSO for 2 h, followed by JEV P3 infection (MOI = 1) for corresponding times, and the cell lysis was harvested. Western blotting assay was performed to detect the expression of p-EGFR, EGFR, p-STAT3, STAT3, p-ERK, and ERK. Results were quantified. **(D)** The hBMECs and EGFR-KO hBMECs were infected with JEV P3 (MOI = 1) for corresponding times, and the protein expression was examined using indicated antibodies. Results were quantified. **(E)** hBMECs were pretreated with U0126 (10 μM, ERK inhibitor), 17-AAG (1 μM, STAT3 inhibitor), or DMSO, and then infected with JEV P3 (MOI = 1) for 60 or 120 min. The proteins were analyzed with indicated antibodies by Western blotting. (F-H) hBMECs were pretreated with U0126 (10 μM), 17-AAG (1 μM), or DMSO followed by JEV P3 (MOI = 1) infection for 24 h, and the viral RNA levels **(F)**, the protein levels **(G)**, and the production of viral particles **(H)** were detected with quantitative real-time PCR, Western blotting, and plaque assay, respectively. Results were quantified. **(I)** hBMECs were pretreated with 10 μM U0126, followed by JEV P3 (MOI = 1) infection for 8 h, and then total RNA was collected and subjected to quantitative real-time PCR for assessing the expression levels of IFN (IFN-α, IFN-β, IFN-λ1, and IFN-λ2, 3) and ISG15. The results are shown as mean ± SEM values. Data are representative of three independent experiments. *, $p < 0.05$; **, $p < 0.01$; ***, $p < 0.001$; ****, $p < 0.0001$, ns, not significant.

(Sabino et al., 2021). The previous report demonstrated that the MEK1/2-ERK pathway negatively regulates interferon production in plasmacytoid dendritic cells (Janovec et al., 2018). In human microvascular endothelial cells, ERK was considered a contributor to rosiglitazone-inhibited IFN-γ production (Lombardi et al., 2008). Similar results in U0126-treated hBMECs illustrated a noticeable increase in IFNs and ISGs, which hinders immune escape to JEV in this study. Consistently, activation of the ERK pathway impaired the antiviral activity of IFN-α in resisting HCV infection, indicating a complex relationship between ERK and IFNs (Zhao et al., 2015). The treatment of AG1478 or U0126 was also demonstrated to lighten bile acid prompted HCV replication and recover the anti-HCV effects by inducing IFN-α in replicon-harboring cells (REF) (Patton et al., 2011). In IAV infection, activated EGFR/ERK signaling was also evidenced to suppress type I and type III interferon-mediated host antiviral innate immunity (Wang et al., 2021). Thus, the EGFR/ERK signaling pathway hijacked by viruses might be a common immune escape strategy for viral infection.

In conclusion, our result in this study for the first time provides new insight into the mechanism that JEV-induced activation of EGFR-ERK signaling cascade contributes to viral escape from host innate immunity by suppressing the interferon signaling response in hBMECs. JEV infection induced EGFR activation, manifesting in promoting the phosphorylated form of EGFR and further contributing to EGFR internalization. Indeed, blockade of EGFR signaling with EGFR inhibitors reduced JEV replication and impeded viral particle production. Further study demonstrated that the positive correlation between EGFR phosphorylation and viral replication was mainly dependent on ERK phosphorylation. The ERK inhibitor substantially alleviated the constraint of interferons and ISGs and lowered viral replication. Taken together, it is worthwhile to consider EGFR as a potential target for antiviral strategies in the future.

DATA AVAILABILITY STATEMENT

The original contributions presented in the study are included in the article/**Supplementary Material**, further inquiries can be directed to the corresponding author.

AUTHOR CONTRIBUTIONS

Y-GZ conceived and performed the experiments, analyzed the data, and drafted the manuscript. H-WC, H-XZ, and KW analyzed the data and revised the manuscript. Y-RC and JS assisted to complete the experiment. X-RW and Z-FF provided the material and technological support. MC conceived the experiments and revised the manuscript. All authors contributed to the article and approved the submitted version.

FUNDING

The authors are grateful for the financial support provided by the National Natural Sciences Foundation of China (Grant No. 31872455) and the Natural Sciences Foundation of Hubei Province (2019CFA010).

ACKNOWLEDGMENTS

Practical suggestions of confocal capture given by Dr. Hu Zhe of State Key Laboratory of Agricultural Microbiology, College of Veterinary Medicine, Huazhong Agricultural University, are acknowledged.

SUPPLEMENTARY MATERIAL

The Supplementary Material for this article can be found online at: https://www.frontiersin.org/articles/10.3389/fmicb.2022.894356/full#supplementary-material

REFERENCES

Al-Obaidi, M. M. J., Bahadoran, A., Har, L. S., Mui, W. S., Rajarajeswaran, J., Zandi, K., et al. (2017). Japanese encephalitis virus disrupts blood-brain barrier and modulates apoptosis proteins in THBMEC cells. *Virus Res.* 233, 17–28. doi: 10.1016/j.virusres.2017.02.012

András, I. E., Pu, H., Tian, J., Deli, M. A., Nath, A., Hennig, B., et al. (2005). Signaling mechanisms of HIV-1 Tat-induced alterations of claudin-5 expression i.n brain endothelial cells. *J Cereb. Blood Flow. Metab.* 25, 1159–1170. doi: 10.1038/sj.jcbfm.9600115

Aoki, K., Shimada, S., Simantini, D. S., Tun, M. M., Buerano, C. C., Morita, K., et al. (2014). Type-I interferon response affects an inoculation dose-independent mortality in mice following Japanese encephalitis virus infection. *Virol. J.* 11, 105. doi: 10.1186/1743-422X-11-105

Barbier, D., Garcia-Verdugo, I., Pothlichet, J., Khazen, R., Descamps, D., Rousseau, K., et al. (2012). Influenza A induces the major secreted airway mucin MUC5AC in a protease-EGFR-extracellular regulated

kinase-Sp1-dependent pathway. *Am. J. Respir. Cell Mol. Biol.* 47, 149–157. doi: 10.1165/rcmb.2011-0405OC

Burkhart, A., Thomsen, L. B., Thomsen, M. S., Lichota, J., Fazakas, C., Krizbai, I., et al. (2015). Transfection of brain capillary endothelial cells in primary culture with defined blood-brain barrier properties. *Fluids Barriers CNS* 12, 19. doi: 10.1186/s12987-015-0015-9

Cataldo, V. D., Gibbons, D. L., Pérez-Soler, R., and Quintás-Cardama, A. (2011). Treatment of non-small-cell lung cancer with erlotinib or gefitinib. *N. Engl. J. Med.* 364, 947–955. doi: 10.1056/NEJMct0807960

Chang, C. Y., Li, J. R., Chen, W. Y., Ou, Y. C., Lai, C. Y., Hu, Y. H., et al. (2015). Disruption of in vitro endothelial barrier integrity by Japanese encephalitis virus-Infected astrocytes. *Glia* 63, 1915–1932. doi: 10.1002/glia.22857

Chen, Y., Peng, F. F., Jin, J., Chen, H. M., Yu, H., and Zhang, B. F. (2017). Src-mediated ligand release-independent EGFR transactivation involves TGF-β-induced Smad3 activation in mesangial cells. *Biochem. Biophys. Res. Commun.* 493, 914–920. doi: 10.1016/j.bbrc.2017.09.121

Chen, Z., and Li, G. (2021). Immune response and blood-brain barrier dysfunction during viral neuroinvasion. *Innate Immun.* 27, 109–117. doi: 10.1177/1753425920954281

Chuang, F. K., Liao, C. L., Hu, M. K., and Chiu, Y. L. (2020). Antiviral activity of compound L3 against dengue and zika viruses in vitro and in vivo. 21. doi: 10.3390/ijms21114050

Dejarnac, O., Hafirassou, M. L., Chazal, M., Versapuech, M., Gaillard, J., Perera-Lecoin, M., et al. (2018). TIM-1 ubiquitination mediates dengue virus entry. *Cell Rep.* 23, 1779–1793. doi: 10.1016/j.celrep.2018.04.013

Dhar, D., Antonucci, L., Nakagawa, H., Kim, J. Y., Glitzner, E., Caruso, S., et al. (2018). Liver Cancer initiation requires p53 Inhibition by CD44-enhanced growth factor signaling. *Cancer Cell 33(6)* 1061-1077.e1066. doi: 10.1016/j.ccell.2018.05.003

Ding, D., Huang, H., Jiang, W., Yu, W., Zhu, H., Liu, J., et al. (2017). Reticulocalbin-2 enhances hepatocellular carcinoma proliferation via modulating the EGFR-ERK pathway. *Oncogene* 36, 6691–6700. doi: 10.1038/onc.2017.230

Duran, A., Valero, N., Mosquera, J., Fuenmayor, E., and Alvarez-Mon, M. (2017). Gefitinib and pyrrolidine dithiocarbamate decrease viral replication and cytokine production in dengue virus infected human monocyte cultures. *Life Sci.* 191, 180–185. doi: 10.1016/j.lfs.2017.10.027

Eierhoff, T., Hrincius, E. R., Rescher, U., Ludwig, S., and Ehrhardt, C. (2010). The epidermal growth factor receptor (EGFR) promotes uptake of influenza A viruses (IAV) into host cells. *PLoS Pathog.* 6, e1001099. doi: 10.1371/journal.ppat.1001099

Finigan, J. H., Downey, G. P., and Kern, J. A. (2012). Human epidermal growth factor receptor signaling in acute lung injury. *Am. J. Respir. Cell Mol. Biol.* 47, 395–404. doi: 10.1165/rcmb.2012-0100TR

Fletcher, N. F., Wilson, G. K., Murray, J., Hu, K., Lewis, A., Reynolds, G. M., et al. (2012). Hepatitis C virus infects the endothelial cells of the blood-brain barrier. *Gastroenterology 142(3)* 634-643.e636. doi: 10.1053/j.gastro.2011.11.028

Freed, D. M., Bessman, N. J., Kiyatkin, A., Salazar-Cavazos, E., Byrne, P. O., Moore, J. O., et al. (2017). EGFR ligands differentially stabilize receptor dimers to specify signaling kinetics. *Cell 171(3)* 683-695.e618. doi: 10.1016/j.cell.2017.09.017

Freed, S. M., Baldi, D. S., Snow, J. A., Athen, S. R., Guinn, Z. P., Pinkerton, T. S., et al. (2021). MEK/ERK MAP kinase limits poly I:C-induced antiviral gene expression in RAW264.7 macrophages by reducing interferon-beta expression. *–No match found–*595, 2665–2674. doi: 10.1002/1873-3468.14200

Fu, J., Li, L., Yang, X., Yang, R., Amjad, N., Liu, L., et al. (2018). Transactivated Epidermal Growth Factor Receptor Recruitment of α-actinin-4 From F-actin Contributes to Invasion of Brain Microvascular Endothelial Cells by Meningitic Escherichia coli. *Front Cell Infect Microbiol* 8, 448. doi: 10.3389/fcimb.2018.00448

Fukano, K., Oshima, M., Tsukuda, S., and Aizaki, H. (2021). NTCP Oligomerization Occurs Downstream of the NTCP-EGFR Interaction during Hepatitis B Virus Internalization. *J. Virol.* 95, e0093821. doi: 10.1128/JVI.00938-21

Gao, M., Fu, Y., Zhou, W., Gui, G., Lal, B., Li, Y., et al. (2021). EGFR activates a TAZ-driven oncogenic program in glioblastoma. *Cancer Res.* 81, 3580–3592. doi: 10.1158/0008-5472.CAN-20-2773

Griffiths, M. J., Turtle, L., and Solomon, T. (2014). Japanese encephalitis virus infection. *Handb. Clin. Neurol.* 123, 561–576. doi: 10.1016/B978-0-444-53488-0.00026-2

Hazra, B., and Kumawat, K. L. (2017). The host microRNA miR-301a blocks the IRF1-mediated neuronal innate immune response to Japanese encephalitis virus infection. *Sci. Signal.* 10, eaaf5185. doi: 10.1126/scisignal.aaf5185

Herbst, R. S. (2004). Review of epidermal growth factor receptor biology. *Int. J. Radiat. Oncol. Biol. Phys.* 59, 21–26. doi: 10.1016/j.ijrobp.2003.11.041

Hsiao, N. W., Chen, J. W., Yang, T. C., Orloff, G. M., Wu, Y. Y., Lai, C. H., et al. (2010). ISG15 over-expression inhibits replication of the Japanese encephalitis virus in human medulloblastoma cells. *Antiviral Res.* 85, 504–511. doi: 10.1016/j.antiviral.2009.12.007

Hu, W., Zhang, S., Shen, Y., and Yang, Q. (2018). Epidermal growth factor receptor is a co-factor for transmissible gastroenteritis virus entry. *Virology.* 521, 33–43. doi: 10.1016/j.virol.2018.05.009

Iwamoto, M., Saso, W., Sugiyama, R., Ishii, K., Ohki, M., Nagamori, S., et al. (2019). Epidermal growth factor receptor is a host-entry cofactor triggering hepatitis B virus internalization. *Proc. Natl. Acad. Sci. U S A.* 116, 8487–8492. doi: 10.1073/pnas.1811064116

Janovec, V., Aouar, B., Font-Haro, A., Hofman, T., Trejbalova, K., Weber, J., et al. (2018). The MEK1/2-ERK pathway inhibits type I IFN production in plasmacytoid dendritic cells. *Front. Immunol.* 9, 364. doi: 10.3389/fimmu.2018.00364

Kalinowski, A., Galen, B. T., Ueki, I. F., Sun, Y., Mulenos, A., Osafo-Addo, A., et al. (2018). Respiratory syncytial virus activates epidermal growth factor receptor to suppress interferon regulatory factor 1-dependent interferon-lambda and antiviral defense in airway epithelium. *Mucosal. Immunol.* 11, 958–967. doi: 10.1038/mi.2017.120

Kalinowski, A., Ueki, I., Min-Oo, G., Ballon-Landa, E., Knoff, D., Galen, B., et al. (2014). EGFR activation suppresses respiratory virus-induced IRF1-dependent CXCL10 production. *Am. J. Physiol. Lung Cell. Mol. Physiol.* 307, L186–196. doi: 10.1152/ajplung.00368.2013

Kim, J. M., Ji, J. H., Kim, Y. S., Lee, S., and Oh, S. Y. (2020). rhEGF treatment improves EGFR inhibitor-induced skin barrier and immune defects. *Cancers (Basel).* 12. doi: 10.3390/cancers12113120

Klann, K., Bojkova, D., Tascher, G., Ciesek, S., Münch, C., and Cinatl, J. (2020). Growth factor receptor signaling inhibition prevents SARS-CoV-2 replication. *Mol Cell.* 80, 164–174.e164. doi: 10.1016/j.molcel.2020.08.006

Kung, C. P., Meckes, D. G. Jr., and Raab-Traub, N. (2011). Epstein-Barr virus LMP1 activates EGFR, STAT3, and ERK through effects on PKCdelta. *J. Virol.* 85, 4399–4408. doi: 10.1128/JVI.01703-10

Kuwata, R., Torii, S., Shimoda, H., Supriyono, S., Phichitraslip, T., Prasertsincharoen, N., et al. (2020). Distribution of Japanese Encephalitis Virus, Japan and Southeast Asia, 2016-2018. *Emerging Infect. Dis.* 26, 125–128. doi: 10.3201/eid2601.190235

Lai, C. Y., Ou, Y. C., Chang, C. Y., Pan, H. C., Chang, C. J., Liao, S. L., et al. (2012). Endothelial Japanese encephalitis virus infection enhances migration and adhesion of leukocytes to brain microvascular endothelia via MEK-dependent expression of ICAM1 and the CINC and RANTES chemokines. *J. Neurochem.* 123, 250–261. doi: 10.1111/j.1471-4159.2012.07889.x

Li, F., Wang, Y., Yu, L., Cao, S., Wang, K., Yuan, J., et al. (2015). Viral infection of the central nervous system and neuroinflammation precede blood-brain barrier disruption during japanese encephalitis virus infection. *J. Virol.* 89, 5602–5614. doi: 10.1128/JVI.00143-15

Li, J., Chen, X., Zhu, L., Lao, Z., Zhou, T., Zang, L., et al. (2021). SOX9 is a critical regulator of TSPAN8-mediated metastasis in pancreatic cancer. *Oncogene*. 40, 4884–4893. doi: 10.1038/s41388-021-01864-9

Li, J., Wang, Y., Wang, X., Ye, L., Zhou, Y., Persidsky, Y., et al. (2013). Immune activation of human brain microvascular endothelial cells inhibits HIV replication in macrophages. *Blood.* 121, 2934–2942. doi: 10.1182/blood-2012-08-450353

Li, Y., Zhang, H., Zhu, B., Ashraf, U., Chen, Z., Xu, Q., et al. (2017). Microarray Analysis Identifies the Potential Role of Long Non-Coding RNA in Regulating Neuroinflammation during Japanese Encephalitis Virus Infection. *Front. Immunol.* 8, 1237. doi: 10.3389/fimmu.2017.01237

Liebmann, C. (2011). EGF receptor activation by GPCRs: an universal pathway reveals different versions. *Mol. Cell. Endocrinol.* 331, 222–231. doi: 10.1016/j.mce.2010.04.008

Lin, C. K., Tseng, C. K., Wu, Y. H., Lin, C. Y., Huang, C. H., Wang, W. H., et al. (2019). Prostasin impairs epithelial growth factor receptor activation to suppress dengue virus propagation. *J. Infect. Dis.* 219, 1377–1388. doi: 10.1093/infdis/jiy677

Linggi, B., and Carpenter, G. (2006). ErbB receptors: new insights on mechanisms and biology. *Trends Cell Biol.* 16, 649–656. doi: 10.1016/j.tcb.2006.10.008

Liu, K., Liao, X., Zhou, B., Yao, H., Fan, S., Chen, P., et al. (2013). Porcine alpha interferon inhibit Japanese encephalitis virus replication by different ISGs in vitro. *Res. Vet. Sci.* 95, 950–956. doi: 10.1016/j.rvsc.2013.08.008

Liu, Z., and Han, C. (2019). Hypofractionated EGFR tyrosine kinase inhibitor limits tumor relapse through triggering innate and adaptive *Immunity*. 4. doi: 10.1126/sciimmunol.aav6473

Lo, M. K., Miller, D., Aljofan, M., Mungall, B. A., Rollin, P. E., Bellini, W. J., et al. (2010). Characterization of the antiviral and inflammatory responses against Nipah virus in endothelial cells and neurons. *Virology*. 404, 78–88. doi: 10.1016/j.virol.2010.05.005

Lombardi, A., Cantini, G., Piscitelli, E., Gelmini, S., Francalanci, M., Mello, T., et al. (2008). A new mechanism involving ERK contributes to rosiglitazone inhibition of tumor necrosis factor-alpha and interferon-gamma inflammatory effects in human endothelial cells. *Arterioscler. Thromb. Vasc. Biol.* 28, 718–724. doi: 10.1161/ATVBAHA.107.160713

Lupberger, J., Duong, F. H., Fofana, I., Zona, L., Xiao, F., Thumann, C., et al. (2013). Epidermal growth factor receptor signaling impairs the antiviral activity of interferon-alpha. *Hepatology*. 58, 1225–1235. doi: 10.1002/hep.26404

Lupberger, J., Zeisel, M. B., Xiao, F., Thumann, C., Fofana, I., Zona, L., et al. (2011). EGFR and EphA2 are host factors for hepatitis C virus entry and possible targets for antiviral therapy. *Nat. Med.* 17, 589–595. doi: 10.1038/nm.2341

Martin, L. J., Smith, S. B., Khoutorsky, A., Magnussen, C. A., Samoshkin, A., Sorge, R. E., et al. (2017). Epiregulin and EGFR interactions are involved in pain processing. *J. Clin. Invest.* 127, 3353–3366. doi: 10.1172/JCI87406

Maruvada, R., and Kim, K. S. (2012). IbeA and OmpA of Escherichia coli K1 exploit Rac1 activation for invasion of human brain microvascular endothelial cells. *Infect. Immun.* 80, 2035–2041. doi: 10.1128/IAI.06320-11

Matsuyama, T., Kubli, S. P., Yoshinaga, S. K., and Pfeffer, K. (2020). An aberrant STAT pathway is central to COVID-19. *Cell Death Differ.* 27, 3209–3225. doi: 10.1038/s41418-020-00633-7

Mladinich, M. C., Schwedes, J., and Mackow, E. R. (2017). Zika virus persistently infects and is basolaterally released from primary human brain microvascular endothelial cells. *mBio.* 8. doi: 10.1128/mBio.00952-17

Oshiumi, H., Miyashita, M., Okamoto, M., Morioka, Y., Okabe, M., Matsumoto, M., et al. (2015). DDX60 is involved in RIG-I-dependent and independent antiviral responses, and its function is attenuated by virus-induced EGFR activation. *Cell Rep.* 11, 1193–1207. doi: 10.1016/j.celrep.2015.04.047

Patton, J. B., George, D., and Chang, K. O. (2011). Bile acids promote HCV replication through the EGFR/ERK pathway in replicon-harboring cells. *Intervirology*. 54, 339–348. doi: 10.1159/000321452

Qiu, W., Chang, L., He, Y., and Zhu, L. (2020). The role of epidermal growth factor receptor signaling pathway during bovine herpesvirus 1 productive infection in cell. *Culture*. 12(9). doi: 10.3390/v12090927

Sabino, C., Bender, D., Herrlein, M. L., and Hildt, E. (2021). The epidermal growth factor receptor is a relevant host factor in the early stages of the Zika virus life cycle in vitro. *J. Virol.* 95, e0119521. doi: 10.1128/JVI.01195-21

Saunders, N. R., Ek, C. J., Habgood, M. D., and Dziegielewska, K. M. (2008). Barriers in the brain: a renaissance? *Trends Neurosci.* 31, 279–286. doi: 10.1016/j.tins.2008.03.003

Schlessinger, J. (1986). Allosteric regulation of the epidermal growth factor receptor kinase. *J. Cell Biol.* 103, 2067–2072. doi: 10.1083/jcb.103.6.2067

Shwetank, D.ate, O. S., Kim, K. S., and Manjunath, R. (2013). Infection of human endothelial cells by Japanese encephalitis virus: increased expression and release of soluble HLA-E. *PLoS ONE.* 8, e79197. doi: 10.1371/journal.pone.0079197

Sorkin, A. (2001). Internalization of the epidermal growth factor receptor: role in signalling. *Biochem. Soc. Trans.* 29, 480–484. doi: 10.1042/bst0290480

Soroceanu, L., Akhavan, A., and Cobbs, C. S. (2008). Platelet-derived growth factor-alpha receptor activation is required for human cytomegalovirus infection. *Nature.* 455, 391–395. doi: 10.1038/nature07209

Sugiyama, E., and Togashi, Y. (2020). Blockade of EGFR improves responsiveness to PD-1 blockade in EGFR-mutated non-small cell lung *Cancer*. 5. doi: 10.1126/sciimmunol.aav3937

Sweeney, M. D., Zhao, Z., Montagne, A., Nelson, A. R., and Zlokovic, B. V. (2019). Blood-brain barrier: from physiology to disease and back. *Physiol. Rev.* 99, 21–78. doi: 10.1152/physrev.00050.2017

Turtle, L., and Driver, C. (2018). Risk assessment for Japanese encephalitis vaccination. *Hum. Vaccin. Immunother.* 14, 213–217. doi: 10.1080/21645515.2017.1380756

Ueki, I. F., Min-Oo, G., Kalinowski, A., Ballon-Landa, E., Lanier, L. L., Nadel, J. A., et al. (2013). Respiratory virus-induced EGFR activation suppresses IRF1-dependent interferon λ and antiviral defense in airway epithelium. *J. Exp. Med.* 210, 1929–1936. doi: 10.1084/jem.20121401

Wang, Q., Pan, W., Wang, S., Pan, C., Ning, H., Huang, S., et al. (2021). Protein tyrosine phosphatase SHP2 suppresses host innate immunity against influenza A virus by regulating EGFR-mediated. *Signaling*. 95. doi: 10.1128/JVI.02001-20

Wang, X., Huong, S. M., Chiu, M. L., Raab-Traub, N., and Huang, E. S. (2003). Epidermal growth factor receptor is a cellular receptor for human cytomegalovirus. *Nature.* 424, 456–461. doi: 10.1038/nature01818

Wang, X., Maruvada, R., Morris, A. J., Liu, J. O., and Wolfgang, M. J. (2016). Sphingosine 1-phosphate activation of EGFR as a novel target for meningitic escherichia coli penetration of the blood-brain barrier. *PLoS Pathog.* 12, e1005926. doi: 10.1371/journal.ppat.1005926

Xiong, Y., Yuan, L., Chen, S., Xu, H., Peng, T., and Ju, L. (2020). WFDC2 suppresses prostate cancer metastasis by modulating EGFR signaling inactivation. *Cell Death Dis.* 11, 537. doi: 10.1038/s41419-020-02752-y

Xu, Q., Cao, M., Song, H., Chen, S., Qian, X., Zhao, P., et al. (2016). Caveolin-1-mediated Japanese encephalitis virus entry requires a two-step regulation of actin reorganization. *Future Microbiol.* 11, 1227–1248. doi: 10.2217/fmb-2016-0002

Xu, X., Wang, J., Yang, R., Dong, Z., and Zhang, D. (2017). Genetic or pharmacologic inhibition of EGFR ameliorates sepsis-induced AKI. *Oncotarget.* 8, 91577–91592. doi: 10.18632/oncotarget.21244

Xu, Y., Shi, Y., Yuan, Q., Liu, X., Yan, B., Chen, L., et al. (2013). Epstein-Barr Virus encoded LMP1 regulates cyclin D1 promoter activity by nuclear EGFR and STAT3 in CNE1 cells. *J. Exp. Clin. Cancer Res.* 32, 90. doi: 10.1186/1756-9966-32-90

Yang, L., and Ding, J. L. (2019). MEK1/2 Inhibitors Unlock the Constrained Interferon Response in Macrophages Through IRF1 Signaling. *Front. Immunol.* 10, 2020. doi: 10.3389/fimmu.2019.02020

Yang, L., Xu, J., Guo, L., Guo, T., Zhang, L., Feng, L., et al. (2018). Porcine Epidemic Diarrhea Virus-Induced Epidermal Growth Factor Receptor Activation Impairs the Antiviral Activity of Type I Interferon. *J. Virol.* 92(8). doi: 10.1128/JVI.02095-17

Yang, X. P., Fu, J. Y., Yang, R. C., Liu, W. T., Zhang, T., Yang, B., et al. (2016). EGFR transactivation contributes to neuroinflammation in Streptococcus suis meningitis. *J. Neuroinflammation.* 13, 274. doi: 10.1186/s12974-016-0734-0

Zhao, L. J., Wang, W., Wang, W. B., Ren, H., and Qi, Z. T. (2015). Involvement of ERK pathway in interferon alpha-mediated antiviral activity against hepatitis C virus. *Cytokine.* 72, 17–24. doi: 10.1016/j.cyto.2014.11.031

Zhao, M., Zhang, L., Lv, S., Zhang, C., Wang, L., Chen, H., et al. (2017). IQGAP1 mediates Hcp1-promoted escherichia coli meningitis by stimulating the MAPK pathway. *Front. Cell Infect. Microbiol.* 7, 132. doi: 10.3389/fcimb.2017.00132

Conflict of Interest: The authors declare that the research was conducted in the absence of any commercial or financial relationships that could be construed as a potential conflict of interest.

Publisher's Note: All claims expressed in this article are solely those of the authors and do not necessarily represent those of their affiliated organizations, or those of the publisher, the editors and the reviewers. Any product that may be evaluated in this article, or claim that may be made by its manufacturer, is not guaranteed or endorsed by the publisher.

frontiers | Frontiers in Microbiology

ORIGINAL RESEARCH
published: 04 July 2022
doi: 10.3389/fmicb.2022.931922

Porcine Epidemic Diarrhea Virus Infection Subverts Arsenite-Induced Stress Granules Formation

Xiaozhen Guo[1†], Kejian Yu[2†], Zhonghao Xin[2], Liping Liu[1], Yuehua Gao[1], Feng Hu[1], Xiuli Ma[1], Kexiang Yu[1], Yufeng Li[1], Bing Huang[1], Zhengui Yan[2] and Jiaqiang Wu[2,3,4*]*

[1] Shandong Key Laboratory of Immunity and Diagnosis of Poultry Diseases, Institute of Poultry Science, Shandong Academy of Agricultural Sciences, Jinan, China, [2] Shandong Provincial Key Laboratory of Animal Biotechnology and Disease Control and Prevention, College of Animal Science and Technology, Shandong Agricultural University, Taian, China, [3] Shandong Key Laboratory of Disease Control and Breeding, Institute of Animal Science and Veterinary Medicine, Shandong Academy of Agricultural Science, Jinan, China, [4] Shandong Key Laboratory of Animal Resistant Biology, College of Life Sciences, Shandong Normal University, Jinan, China

OPEN ACCESS

Edited by:
Cao Yong Chang,
Sun Yat-sen University, China

Reviewed by:
Bibo Zhu,
University of Virginia, United States
Wentao Li,
Huazhong Agricultural University, China

***Correspondence:**
Zhengui Yan
sdauyan@sdau.edu.cn
Jiaqiang Wu
wujiaqiang2000@sina.com

[†] These authors have contributed equally to this work

Specialty section:
This article was submitted to Virology, a section of the journal Frontiers in Microbiology

Received: 29 April 2022
Accepted: 09 June 2022
Published: 04 July 2022

Citation:
Guo X, Yu K, Xin Z, Liu L, Gao Y, Hu F, Ma X, Yu K, Li Y, Huang B, Yan Z and Wu J (2022) Porcine Epidemic Diarrhea Virus Infection Subverts Arsenite-Induced Stress Granules Formation. Front. Microbiol. 13:931922. doi: 10.3389/fmicb.2022.931922

Stress granules (SGs) are dynamic cytoplasmic protein-RNA structures that form in response to various stress conditions, including viral infection. Porcine epidemic diarrhea virus (PEDV) variant-related diarrhea has caused devastating economic losses to the swine industry worldwide. In this study, we found that the percentage of PEDV-infected cells containing SGs is nearly 20%; meanwhile, PEDV-infected cells were resistant to sodium arsenite (SA)-induced SGs formation, as demonstrated by the recruitment of SGs marker proteins, including G3BP1 and TIA1. Moreover, the formation of SGs induced by SA treatment was suppressed by PEDV papain-like protease confirmed by confocal microscopy. Further study showed that PEDV infection disrupted SGs formation by downregulating G3BP1 expression. Additionally, PEDV replication was significantly enhanced when SGs' assembly was impaired by silencing G3BP1. Taken together, our findings attempt to illuminate the specific interaction mechanism between SGs and PEDV, which will help us to elucidate the pathogenesis of PEDV infection in the near future.

Keywords: PEDV replication, stress granules, sodium arsenite, papain-like protease, interaction mechanism

INTRODUCTION

Porcine epidemic diarrhea (PED) caused by the porcine epidemic diarrhea virus (PEDV) variant is characterized by acute enteric infection and high mortality in suckling piglets and occasional endemics, leading to significant economic losses to the global swine industry (Lee, 2015; Niederwerder and Hesse, 2018). PEDV is an enveloped, single-stranded positive-sense RNA virus belonging to the genus Alphacoronavirus in the family Coronaviridae of the order Nidovirales (Li et al., 2012). The viral genome is ∼28 kb and encodes at least seven open reading frames (ORFs). The two largest ORFs (ORF1a and ORF1b) located in the two-thirds of the genome downstream of the 5′UTR are further processed into 16 non-structural proteins, nsp1 to nsp16. The other one-third genome encodes the structural and accessory proteins including spike (S) glycoprotein, small envelope (E) protein, membrane (M) protein, nucleocapsid (N) protein, and accessory protein (ORF3). A better understanding of the interactions between PEDV and host might contribute to the development of more effective control measures (Guo et al., 2017).

Stress granules (SGs) are dynamic cytoplasmic protein-RNA structures that form in response to various stress conditions including viral infection (Anderson and Kedersha, 2009). The major components of SGs are untranslated mRNAs, mainly including Ras GTPase-activating protein-binding protein 1 (G3BP1), T-cell internal antigen 1 (TIA1), eukaryotic translation initiation factors (eIF), and TIA1-related protein (TIAR) (Panas et al., 2016). G3BP1 and TIA-1 are usually used as SGs markers to identify SGs formation. Accumulating evidence has shown that SGs play an important role in regulating viral replication. For example, several viruses, such as a respiratory syncytial virus (RSV), have been reported to benefit from SGs formation (Lindquist et al., 2010). However, SGs are also considered as an indication of an antiviral innate response to many viruses (Onomoto et al., 2014; Yoneyama et al., 2016). Many viruses have evolved strategies to overcome the antiviral effect of SGs by degrading or sequestering its key components, such as G3BP1 or TIA-1/TIAR to prevent the formation of SGs (Humoud et al., 2016; Le Sage et al., 2017). It was documented that Infectious Bronchitis Virus (IBV) antagonized the formation of SGs by nsp15 *via* reducing the viral dsRNA accumulation and sequestering/depleting the critical component of SGs (Gao et al., 2021). Foot-and-mouth disease virus (FMDV) leader protease cleaves G3BP1 and G3BP2 to inhibit SG formation (Visser et al., 2019). A previous study reported that PEDV infection induced caspase-8 mediated G3BP1 cleavage to subvert SG formation (Sun et al., 2021). However, in addition to the above-mentioned mechanisms, whether there is another mechanism to inhibit SG formation during PEDV infection remains largely unknown.

In the present study, we demonstrated that PEDV infection disrupted SA-induced SGs formation *via* downregulating G3BP1 expression. Further study indicated that PEDV papain-like protease could subvert SGs formation. Moreover, impairment of SG formation dramatically enhanced PEDV replication. Collectively, this study will lay the foundation for further investigation of PEDV infection and SG formation from the perspective of the protein encoded by the virus itself.

MATERIALS AND METHODS

Cells and Viruses

The kidney cell lines of the African green monkey, Vero-E6 cells, were cultured and maintained in Dulbecco's modified Eagle's medium (DMEM), supplemented with 10% fetal bovine serum (Invitrogen, Carlsbad, CA, USA), 100 U/mL penicillin, and 100 μg/mL streptomycin sulfate in a humidified 37°C, 5% CO_2 incubator. The PEDV variant strain SDSX16 (Accession no. MH117940.1) was isolated from a suckling piglet with acute diarrhea in our lab.

Virus Infection

Vero cells were cultured for nearly 24 h for 80% confluence and washed twice with serum-free medium. Then, the cells were mock-infected or infected with PEDV at a multiplicity of infection (MOI) of 0.1 and incubated with serum-free DMEM containing 8 μg/mL trypsin (Invitrogen) for 12 h, and then were treated with 5 mM SA for 30 min.

TABLE 1 | Primer sequences used in this experiment.

Primer name	Primer sequence
PEDV-PLP1-F	CCCATCGATATCTCACAGGATCTGCT
PEDV-PLP1-R	ACCCCCGGGTCAAGCAGCATCATAAAAGTT
PEDV-PLP2-F	CAAGAATTCGTATCCACACCTGATGAT
PEDV-PLP2-R	CCCGGTACCCTACTCTGAGACGACAACATTT
PEDV-NSP5-F	AAAGAATTCGCTGGCTTGCGTAAGATGGC
PEDV-NSP5-R	CCCGCATGCTTACTGAAGATTAACGCCATACATTTGA
PEDV-M-F	CGTACAGGTAAGTCAATTAC
PEDV-M-R	GATGAAGCATTGACTGAA
β-actin-F	TTAGTTGCGTTACACCCTTTC
β-actin-R	ACCTTCACCGTTCCAGTT

TABLE 2 | siRNA sequences used in this experiment.

Gene name	siRNA sequence(5′-3′)	siRNA sequence(3′-5′)
G3BP1	UCAACAUGGCGAAUC UUGGUGUGGC	GCCACACCAAGAUUC GCCAUGUUGA
NC	CAAGAUGCAGCAGUAU GUAUGUGAA	UUCACAUACAUACUGCU GCAUCUUG

Plasmid Construction

cDNA encoding PEDV PLP1, PLP2, and nsp5 were amplified by RT-PCR from total RNA of PEDV using specific primers (**Table 1**), and the three genes were cloned into pCAGGS-HA vector, respectively. All constructs were validated by DNA sequencing.

Reagent, siRNA, and Cell Transfection

Sodium arsenite (SA) was obtained from Sigma-Aldrich (St. Louis, MO, USA) and used at a concentration of 5 mM. The siRNAs targeting monkey G3BP1 gene or negative control siRNA were purchased from GenePharma and used at a concentration of 50 nM using Lipofectamine 3000 reagent (Invitrogen) according to the manufacturer's instructions. The siRNA sequences used in this study are listed in **Table 2**.

Antibody

Rabbit poly antibodies (pAbs) against TIA1, G3BP1, eIF3B, mouse monoclonal antibody (mAb) against β-actin, horseradish peroxidase (HRP)-conjugated goat anti-rabbit, and HRP-conjugated goat anti-mouse IgG were all purchased from ABclonal Technology Co., Ltd. (Wuhan, China). Mouse mAb against HA-tag was purchased from Medical & Biological Laboratories Co., Ltd (MBL). Mouse mAb against PEDV S protein was generated by our laboratory. Alexa Fluor 488-conjugated goat anti-mouse IgG and Fluor Cy5-conjugated goat anti-rabbit IgG were obtained from Servicebio Biotechnology Co., Ltd. (Wuhan, China).

Confocal Fluorescence Microscopy

Vero cells were seeded on coverslips and transfected with PCAGGS-HA associated expression plasmids or G3BP1 siRNA,

or were infected with PEDV alone for the indicated time points. The cells were then fixed with cold 4% paraformaldehyde for 10 min. After permeabilization and blocking, the cells were then incubated with mouse mAbs directed against the HA-tag or S protein, or rabbit pAbs against TIA1, G3BP1, and eIF3B, respectively for 1 h, and were then inoculated with Alexa Fluor 488-conjugated goat anti-mouse IgG or Fluor Cy5-conjugated goat anti-rabbit IgG antibody for 30 min. Cell nuclei were counterstained with 0.01% 4′,6-diamidino-2-phenylindole (DAPI, Invitrogen). The fluorescent images were examined under a confocal laser scanning microscope (LSM 510 Meta, Carl Zeiss, Munich, Germany).

Western Blot Assay

The PEDV-infected and mock-infected cells were harvested and lysed at 12 hpi. The protein concentration was quantified by the BCA protein assay kit, and equal amounts of protein samples from each sample were mixed with 5× sample loading buffer and boiled for 10 min and then separated by 12% sodium dodecyl sulfate polyacrylamide gel electrophoresis (SDS-PAGE). The proteins were electro-transferred to 0.45 μm PVDF membranes (Millipore, Mississauga, ON, Canada). Membranes were blocked with 5% (w/v) skim milk-TBST at room temperature for 2 h and then incubated overnight at 4°C with primary antibody to G3BP1 and mouse mAb against β-actin, respectively. The membranes were washed with TBST and then incubated with horseradish peroxidase (HRP) conjugated goat anti-rabbit IgG or goat anti-mouse IgG (ABclonal, Wuhan, China) at 37°C for 1 h. The protein bands were visualized using the Clarity™ Western ECL Blotting Substrate (Bio-Rad, Hercules, CA, USA). The protein blots were quantified by Image J software (National Institutes of Health, Bethesda, MD, USA).

Quantitative Real-Time PCR

Total RNA was extracted from PEDV-infected or mock-infected cells using Simply P Total RNA Extraction Kit (BioFlux, Europe) according to the manufacturer's protocol. A total of 1 μg RNA from each sample was subsequently reverse-transcribed to cDNA by using oligo (dT) as the primer (Roche, Mannheim, Germany). The relative quantitative real-time PCR was performed in an Applied Biosystems ViiA 7 real-time PCR system (Applied Biosystems, Foster City, CA, USA) as previously described (Guo et al., 2017). The primers are listed in **Table 1**.

Quantification of SGs Formation

For the quantification of SGs formation, more than 10 high-powered fields (HPFs) were randomly obtained for each sample. PEDV-S protein was used to detect PEDV infection. HA-tag was used to monitor the effective expression of PLP1, PLP2, and nsp5, respectively. The number of SG-positive cells was counted by the results of staining for the presence of G3BP1, TIA1, or eIF3B proteins. The relative percentage of cells with SGs was calculated by: cells positive with G3BP1, TIA1, or eIF3B individually, and PEDV-S or HA tag divided by cells positive with PEDV-S or HA tag ×100% (Zhou et al., 2017; Gao et al., 2021).

Statistical Analysis

Data of three independent experiments were expressed as the means with SEM. The student's *t*-test was applied for the statistical analyses. A $p < 0.05$ was considered as statistically significant.

RESULTS

PEDV Infection Does Not Trigger SGs Formation in Most Infected Cells

The immunofluorescence analysis of G3BP1 was performed to detect SGs formation. A monoclonal antibody specific for PEDV-S protein was used to detect PEDV infection. The SGs were examined at 12 h after PEDV infection. Cells treated with SA, a potent SG-inducer, served as the positive control. Meanwhile, the mock-infected cells were regarded as the negative control. Unsurprisingly, the percentage of SGs positive cells reached more than 80% in SA-treated cells, while no obvious SGs were observed in mock-infected cells (**Figure 1A**). The percentage of PEDV-infected cells containing SGs is nearly 20% (**Figure 1B**), which is consistent with a previous report (Gao et al., 2021). These data suggest that PEDV infection cannot effectively trigger SGs formation in most infected Vero cells.

PEDV-Infected Cells Are Resistant to SA Induced SGs Formation

To investigate whether PEDV-infection interferes with the formation of SGs induced by SA treatment, Vero cells were infected with PEDV for 12 h and then treated with SA for 30 min prior to immunofluorescence staining. As expected, SGs appeared in non-infected cells treated with SA, whereas PEDV-infected cells showed fewer SGs, and no specific SGs were detected by G3BP1 in syncytial cells. The percentage of cells with SGs was above 90% in mock-treated cells after SA treatment, while the percentage of SGs was below 40% in PEDV-infected cells (**Figure 2A**). In addition, the SGs' positive rate is close to 100% when only treated with SA and decreased to about 60% after PEDV infection detected by TIA1 (**Figure 2B**). Surprisingly, SGs formation treatment with SA detected by eIF3B was not influenced by PEDV infection (**Figure 2C**). In conclusion, it was proposed that PEDV infection could induce SGs, and PEDV-infected cells are resistant to SA-induced SGs formation.

PEDV Papain-Like Protease Participate in Suppressing SGs Formation

To investigate how PEDV-infected cells are resistant to SA-induced SGs formation, PEDV protease PLP1, PLP2, and nsp5 were successfully expressed in Vero cells. We found that PEDV PLP1 or PLP2, which have L protease activities, suppressed the SGs formation induced by SA treatment, as demonstrated by the recruitment of SGs marker proteins, including G3BP1 and TIA1. Conversely, PEDV nsp5 which has 3C-like protease activities showed remarkable effect on SGs formation indicated by TIA1, not G3BP1 (**Figures 3A,B**).

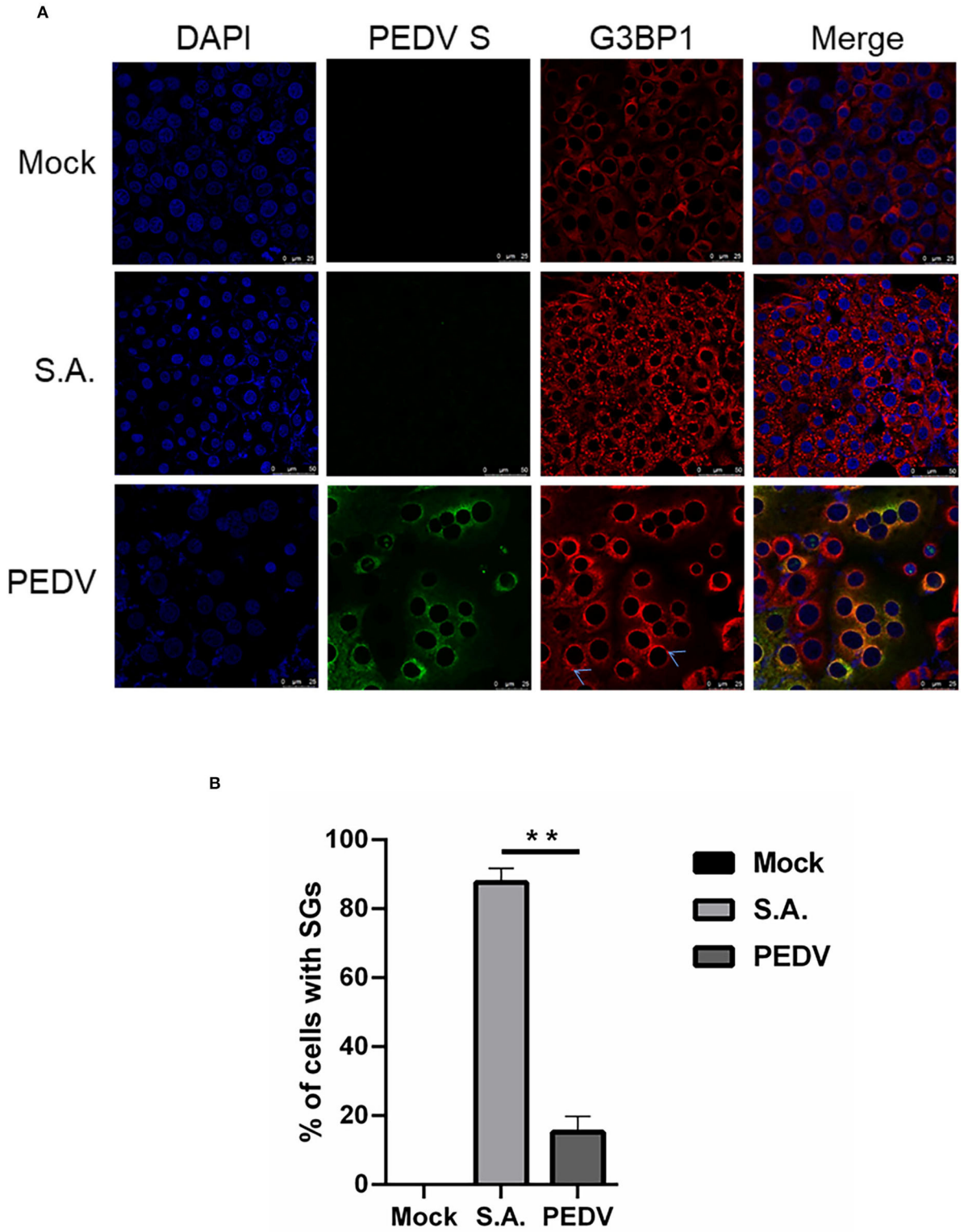

FIGURE 1 | PEDV infection prevents SGs formation in most infected cells. **(A)** Vero cells were mock-infected or infected with PEDV for 12 h. Vero cells treated with 5 mM SA for 30 min served as the positive control. Then the cells were fixed and analyzed by confocal microscopy. Mouse mAb specific for PEDV S was used to detect PEDV infection (green). Rabbit pAb specific for G3BP1 (red) was used to detect SGs. Nuclei were stained with DAPI (blue). **(B)** The number of cells infected with PEDV and cells containing SGs were counted. The relative percentage of cells with SGs was calculated by: cells positive with G3BP1 and PEDV-S divided by cells positive with PEDV-S × 100%. The data were presented as mean ± SEM of three independent experiments (*t*-test, $^{**}p < 0.01$).

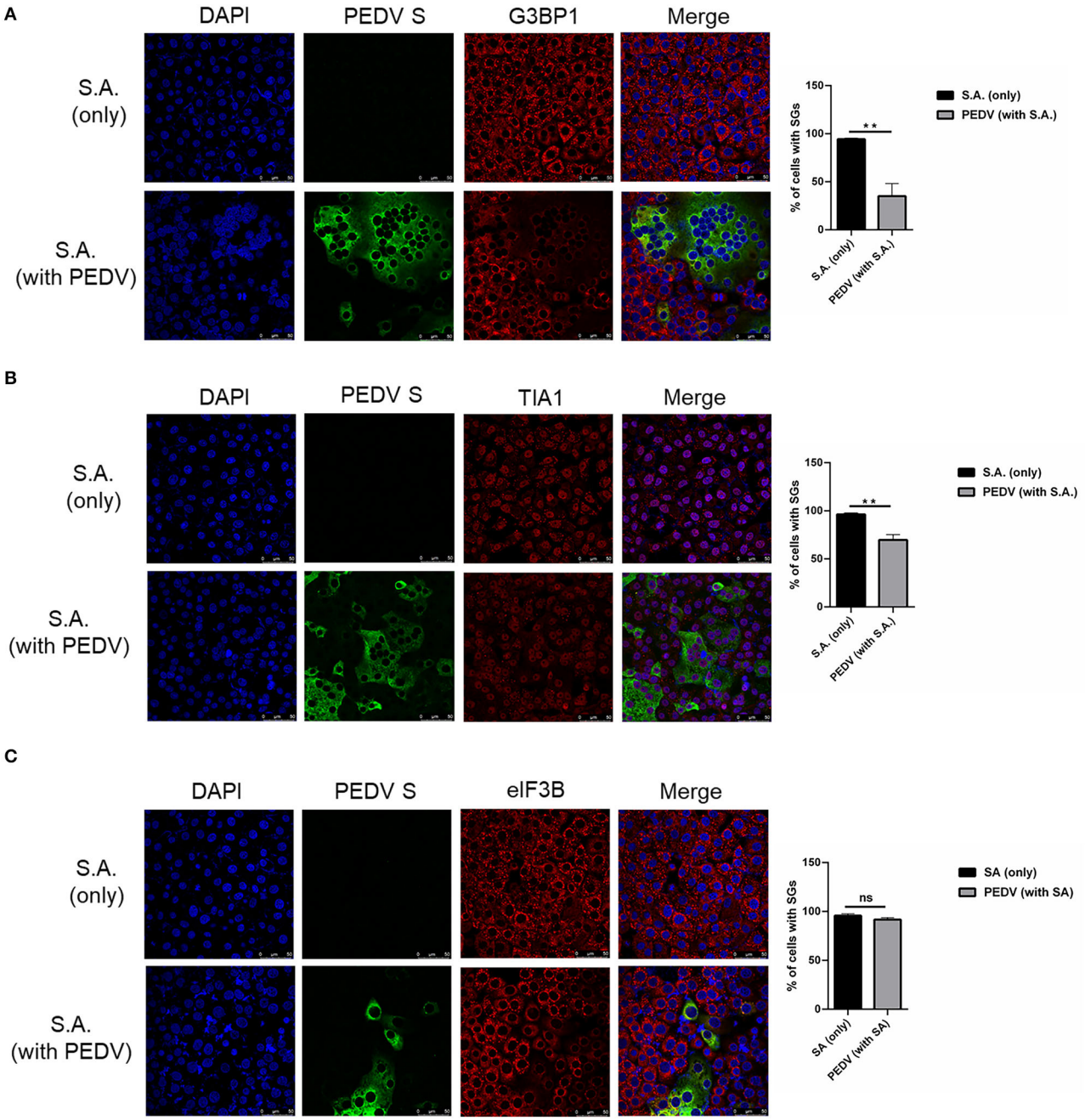

FIGURE 2 | PEDV replication inhibits SGs formation induced by SA treatment. **(A–C)** Vero cells were mock-infected or infected with PEDV for 12 h and then treated with SA for 30 min. Cells were fixed and analyzed by confocal microscopy. Rabbit pAb specific for G3BP1 (**A**: red), TIA1 (**B**: red) or eIF3B (**C**: red) were used to detect SGs. Nuclei were stained with DAPI (blue). The percentage of SGs-positive cells detected by G3BP1, TIA1 or eIF3B was quantified. Error bars show standard deviations. The data were presented as mean ± SEM of three independent experiments (*t*-test, $^{**}p < 0.01$).

Meanwhile, we found that not only PEDV PLP1 and PLP2 but also nsp5 has inconspicuous effect on SGs detected by eIF3B (**Figure 3C**). These results indicated that PEDV proteases PLP1 and PLP2 play an important part in suppressing SA-induced SGs.

PEDV Infection Disrupted SGs Formation by Downregulating G3BP1 Expression

It is well known that G3BP1 is proposed to be key for the nucleation of SG assembly. As shown in **Figure 2A**, a loss of G3BP1 has been found in PEDV-infected cells treatment

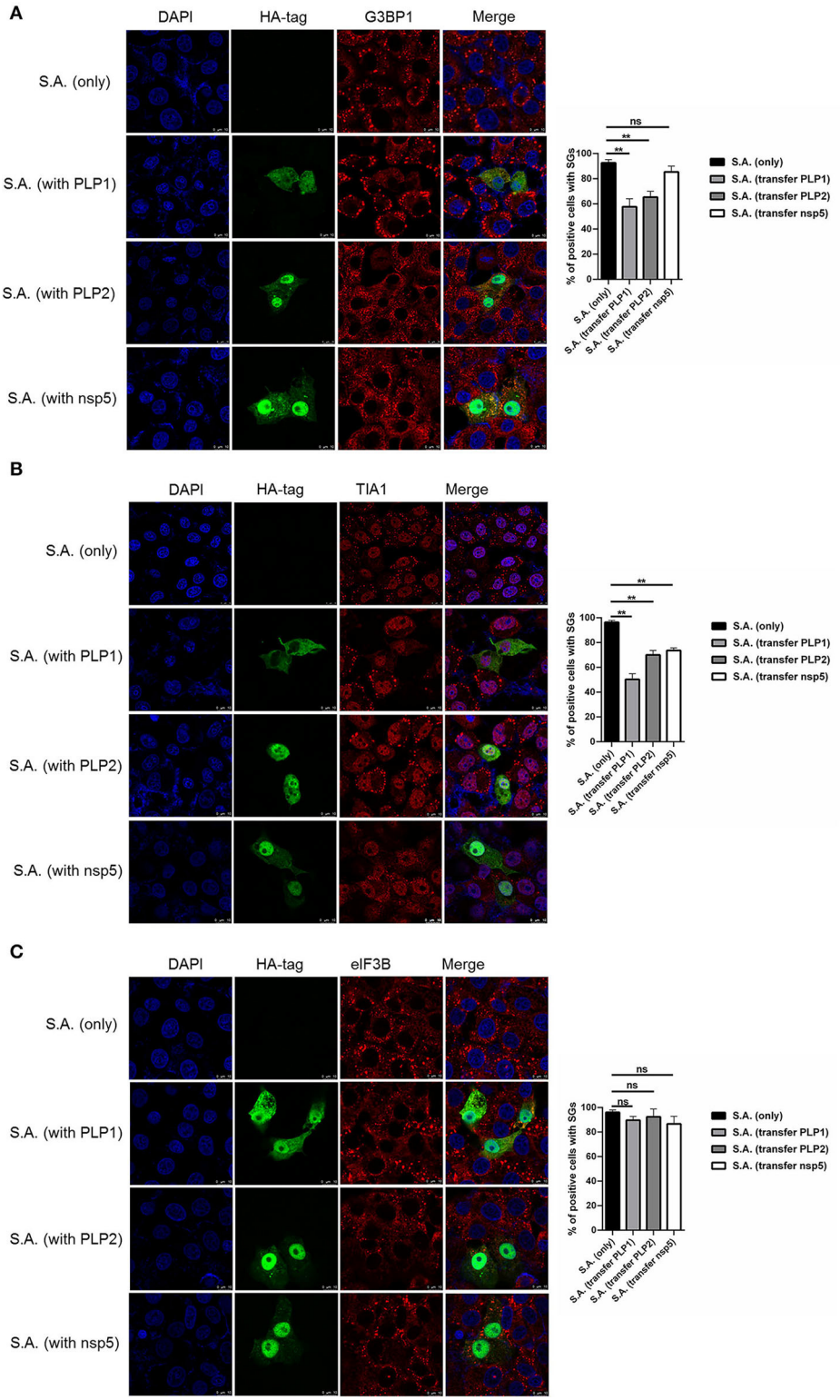

FIGURE 3 | PEDV papain-like protease participate in suppressing SGs formation. **(A–C)** Vero cells were respectively transfected with an expression vector containing PLP1, PLP2,or nsp5 for 24 h and then treated with 5mM SA for 30 min. Rabbit pAb specific for G3BP1 (**A**: red), TIA1 (**B**: red), or eIF3B (**C**: red) was used to detect SGs. Mouse mAb specific for HA-tag was used to detect protein expression. Nuclei were stained with DAPI (blue). The percentage of SG-positive cells detected by G3BP1, TIA1, or eIF3B was quantified. Error bars show standard deviations. The data were presented as mean ± SEM of three independent experiments (*t*-test, $^{**}p < 0.01$).

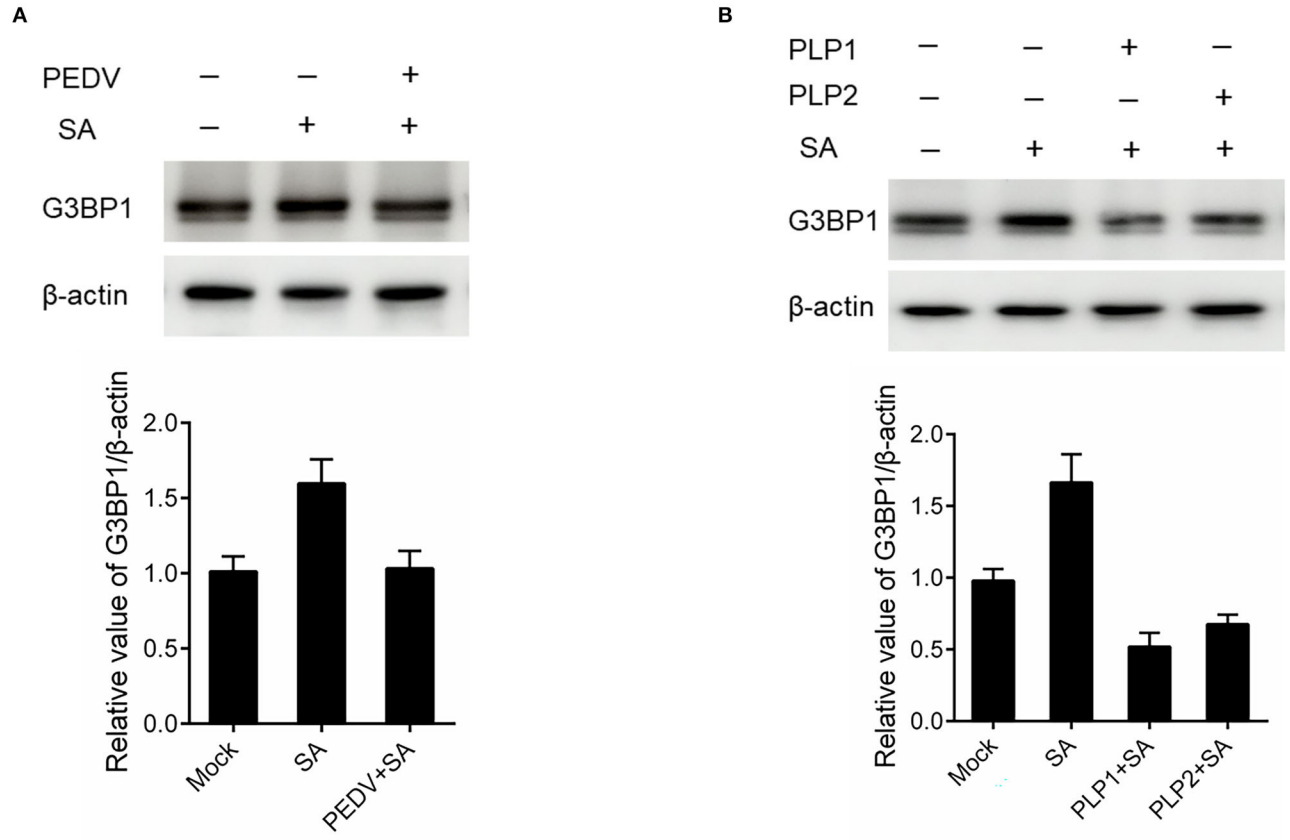

FIGURE 4 | PEDV infection disrupted SGs formation by downregulating G3BP1 expression. **(A)** Vero cells were infected with PEDV for 12 h and treated with SA for 30 min. **(B)** Vero cells were respectively transfected with an expression vector containing PLP1 or PLP2 for 24 h and then treated with 5 mM SA for 30 min. The level of G3BP1 was analyzed by western blot. The expression of β-actin served as a control. The relative value of G3BP1/β-actin was analyzed by using Image J Software.

with SA than non-infected. These data led us to further investigate whether PEDV infection could downregulate G3BP1 expression by western blot. As shown in **Figure 4A**, the content of G3BP1 was increased in mock-infected cells treatment with SA compared with no treatment, while the protein level of G3BP1 was decreased in PEDV-infected cells treatment with SA. Meanwhile, we found that PEDV papain-like protease could suppress SA-induced SGs formation. Next, we determined the expression of G3BP1 in cells transfected with PEDV papain-like protease. As expected, the expression of G3BP1 was also decreased in PLP1 or PLP2-containing cells treatment with SA compared with cells lacking PLP1 or PLP2 (**Figure 4B**). It was speculated that PEDV infection might subvert SGs formation by downregulating the expression of G3BP1, which might depend on PEDV papain-like protease.

Silencing G3BP1 Expression Had a Positive Influence on PEDV Replication

To assess whether SGs are associated with PEDV replication, we tried to impair SG formation by silencing G3BP1 expression. Specific siRNA was designed, and the knockdown efficiency was demonstrated by the results of real-time RT-qPCR and western blot assays (**Figure 5A**). The specific siRNA targeting G3BP1 was transfected into Vero cells, followed by PEDV infection. The formation of SGs monitored by immunostaining decreased by 50% in G3BP1-silenced cells compared with NC-treated cells, while the fluorescence signal of PEDV infection was enhanced in G3BP1-silenced cells (**Figure 5B**). These data indicated that the downregulation of G3BP1 can affect the formation of PEDV-induced SGs. Data from **Figure 5C** further demonstrated that the suppression of G3BP1 expression obviously increased the viral titer and virus copy number compared to the control group. All the aforementioned data prompted us to draw the conclusion that SGs formation had a negative influence on PEDV replication.

DISCUSSION

Research on SGs induced by virus infection has rapidly advanced in recent years. Here, we observed that PEDV infection does not induce SGs formation in most infected Vero cells. Meanwhile, the downregulation of G3BP1 enhanced PEDV replication, which was consistent with previous studies (Pandey et al., 2019). It is proposed that SGs exert specific antiviral activities by providing a

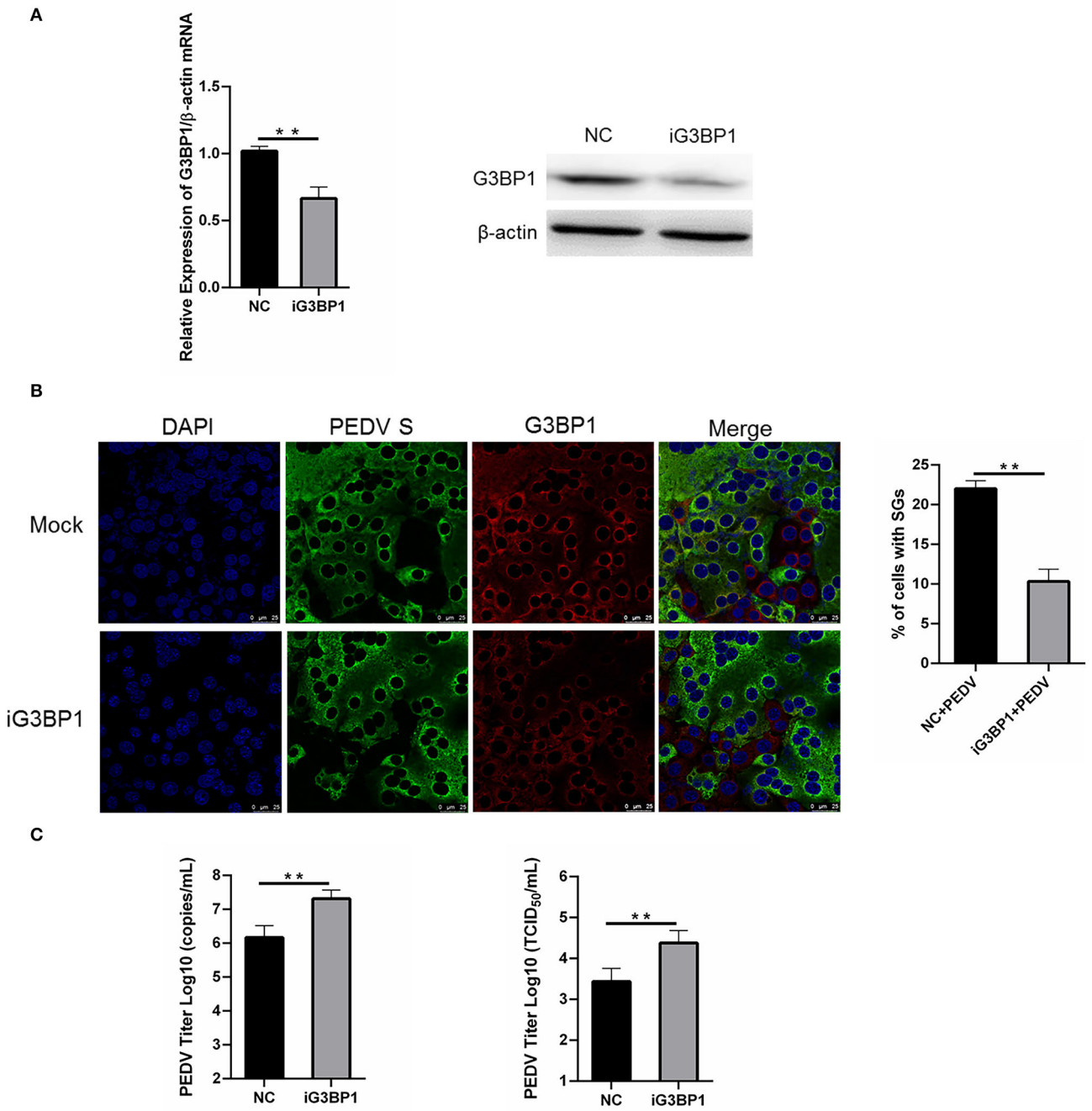

FIGURE 5 | Silencing G3BP1 expression had positive influence on PEDV replication. **(A)** Vero cells were transfected with siRNA G3BP1 or NC for 24 h. The resulting mRNA and protein level of G3BP1 were determined by qRT-PCR and western blot. **(B)** Vero cells were infected with PEDV for another 12 h after transfection with siRNA G3BP1 or NC for 24 h and then the cells were fixed and analyzed by confocal microscopy. Mouse mAb specific for PEDV S was used to detect PEDV infection (green). Rabbit pAb specific for G3BP1 (red) was used to detect SGs formation. Nuclei were stained with DAPI (blue). The percentage of SG-positive cells was quantified as described in the Materials and Methods. The data were presented as mean ± SEM of three independent experiments (*t*-test, $^{**}p < 0.01$). **(C)** Vero cells were treated as **(B)**. PEDV titer was determined by qRT-PCR and $TCID_{50}$. The data was presented as mean ± SEM of three independent experiments (*t*-test, $^{**}p < 0.01$).

platform for interaction between antiviral proteins and non-self RNA (Gao et al., 2021). Similar observations were reported for other coronaviruses, including mouse hepatitis virus (MHV), transmissible gastroenteritis virus (TGEV), and severe acute respiratory syndrome coronavirus 2 (SARS-CoV-2) (Raaben et al., 2007; Sola et al., 2011; Cascarina and Ross, 2020). Whether

it is a common feature of coronaviruses to modulate SGs requires future works.

Stress granules subversion during virus infection is observed in many viruses. Different viruses disrupt SG-related proteins by various approaches. For example, the foot-and-mouth disease virus (FMDV) L^{pro} cleaves the known SG scaffold proteins G3BP1 and G3BP2 to inhibit SGs formation (Visser et al., 2019). Middle East Respiratory Syndrome Coronavirus (MERS-CoV) can inhibit SGs *via* accessory protein 4a and lead to efficient viral replication (Rabouw et al., 2016; Nakagawa et al., 2018). In this study, we found PEDV-infected cells were resistant to SA-induced SGs formation. Further research indicated that PEDV infection disrupted SGs formation by downregulating G3BP1 expression. It was reported that the activation of the antioxidant pathway by the virus might mediate the inhibition of SGs formation induced by SA treatment since virus infection typically induced both ROS and antioxidant response simultaneously (Basu et al., 2017; Pandey et al., 2019). Although current research reported that PEDV infection induced caspase-8 mediated G3BP1 cleavage and subverted SGs to promote viral replication (Sun et al., 2021), the concrete mechanism of PEDV to circumvent the formation of anti-viral SGs induced by SA treatment needs further investigation.

Previous studies showed that viral protease protein 3C protease (3Cpro) and L protease (Lpro) participated in SGs' disassembly (White et al., 2007; Visser et al., 2019). As is known, PEDV produces two proteases (Nsp3 papain-like protease and Nsp5 3C-like protease) (Wang et al., 2016; Sun et al., 2021). In the present study, we found that PEDV PLP1 or PLP2 which have L protease activities suppressed the SGs formation induced by SA treatment indicated by TIA1 or G3BP1, whereas nsp5 did not show such effect. It was well documented that PEDV impaired SG assembly by targeting G3BP1 *via* the host proteinase caspase-8. In addition, it was reported that coronaviruses antagonized the formation of SGs by nsp15 *via* reducing the viral dsRNA accumulation and sequestering/depleting the critical components of SGs (Gao et al., 2021). Our further research demonstrated that papain-like proteases suppressed SGs formation induced by SA treatment *via* downregulating G3BP1 expression. It is well-known that PEDV papain-like proteases have DUB activity and host interferon antagonistic activity in addition to protease activity (Xing et al., 2013; Chu et al., 2022). It has been reported that ubiquitination is not required for SA-induced SG formation (Gwon and Maxwell, 2021), and Vero cells are interferon-deficient cells (Emmott et al., 2010). Therefore, we speculate that papain-like proteases might inhibit SG formation by exerting its proteolytic function. The elaborate mechanisms of papain-like proteases in suppressing SGs induced by SA treatment are currently under investigation in our laboratory. It will be tremendously valuable to obtain the data about PEDV and SGs interaction from porcine intestinal epithelial cells (IPEC-J2), since Vero cells are not natural host cells for PEDV (Guo et al., 2016).

In conclusion, we provided convincing evidence that PEDV infection does not induce SGs formation in most infected Vero cells. Silencing G3BP1 significantly enhanced PEDV replication. Further research indicated that PEDV might subvert SGs formation *via* downregulating G3BP1 expression dependent on PEDV papain-like proteases. A better understanding of the molecular events involved in the formation of SGs and PEDV infection will undoubtedly help us to elucidate the molecular mechanism of PEDV pathogenesis.

DATA AVAILABILITY STATEMENT

The raw data supporting the conclusions of this article will be made available by the authors, without undue reservation.

AUTHOR CONTRIBUTIONS

BH, ZY, and JW designed the experiments. XG, KejY, ZX, LL, YG, FH, XM, KexY, and YL carried out the experiments. XG and KejY analyzed the data and wrote the paper. XG checked and finalized the manuscript. All authors read and approved the final manuscript.

FUNDING

This research was funded by Shandong Provincial Natural Science Foundation Youth Project (ZR2021QC054), Shandong Provincial Modern Agricultural Industry and Technology System (SDAIT-08-01), Great Scientific and Technological Innovation Projects in Shandong Province (2020CXGC010801), the Shandong Key Provincial Research and Development Program (2019GNC106044), the National Natural Science Funds (Nos. 32070178 and 32002286), and Agricultural Scientific and Technological Innovation Project of Shandong Academy of Agricultural Sciences (CXGC2021A12 and CXGC2021A39).

REFERENCES

Anderson, P., and Kedersha, N. (2009). Stress granules. *Curr. Biol.* 19, R397–R398. doi: 10.1016/j.cub.2009.03.013

Basu, M., Courtney, S. C., and Brinton, M. A. (2017). Arsenite-induced stress granule formation is inhibited by elevated levels of reduced glutathione in West Nile virus-infected cells. *PLoS Pathog.* 13, e1006240. doi: 10.1371/journal.ppat.1006240

Cascarina, S. M., and Ross, E. D. (2020). A proposed role for the SARS-CoV-2 nucleocapsid protein in the formation and regulation of biomolecular condensates. *FASEB J.* 34, 9832–9842. doi: 10.1096/fj.202001351

Chu, H. F., Cheng, S. C., Sun, C. Y., Chou, C. Y., Lin, T. H., and Chen, W. Y. (2022). Structural and biochemical characterization of porcine epidemic diarrhea virus papain-like protease 2. *J. Virol.* 96, e0137221. doi: 10.1128/jvi.01372-21

Emmott, E., Rodgers, M. A., Macdonald, A., McCrory, S., Ajuh, P., and Hiscox, J. A. (2010). Quantitative proteomics using stable isotope labeling with amino acids in cell culture reveals changes in the cytoplasmic, nuclear, and nucleolar proteomes in Vero cells infected with the coronavirus infectious bronchitis virus. *Mol. Cell Proteomics* 9, 1920–1936. doi: 10.1074/mcp.M900345-MCP200

Gao, B., Gong, X., Fang, S., Weng, W., and Wang, H. (2021). Inhibition of anti-viral stress granule formation by coronavirus endoribonuclease

nsp15 ensures efficient virus replication. *PLos Pathog.* 17, e1008690. doi: 10.1371/journal.ppat.1008690

Guo, X., Hu, H., Chen, F., Li, Z., Ye, S., Cheng, S., et al. (2016). iTRAQ-based comparative proteomic analysis of Vero cells infected with virulent and CV777 vaccine strain-like strains of porcine epidemic diarrhea virus. *J Proteomics* 130, 65–75. doi: 10.1016/j.jprot.2015.09.002

Guo, X., Zhang, M., Zhang, X., Tan, X., Guo, H., Zeng, W., et al. (2017). Porcine epidemic diarrhea virus induces autophagy to benefit its replication. *Viruses* 9, 53. doi: 10.3390/v9030053

Gwon, Y., and Maxwell, B. A. (2021). Ubiquitination of G3BP1 mediates stress granule disassembly in a context-specific manner. *Scienece* 372, eabf6548. doi: 10.1126/science.abf6548

Humoud, M. N., Doyle, N., Royall, E., Willcocks, M. M., Sorgeloos, F., van Kuppeveld, F., et al. (2016). Feline calicivirus infection disrupts assembly of cytoplasmic stress granules and induces G3BP1 cleavage. *J. Virol.* 90, 6489–6501. doi: 10.1128/jvi.00647-16

Le Sage, V., Cinti, A., McCarthy, S., Amorim, R., Rao, S., Daino, G. L., et al. (2017). Ebola virus VP35 blocks stress granule assembly. *Virology* 502, 73–83. doi: 10.1016/j.virol.2016.12.012

Lee, C. (2015). Porcine epidemic diarrhea virus: an emerging and re-emerging epizootic swine virus. *Virol. J.* 12, 193. doi: 10.1186/s12985-015-0421-2

Li, W., Li, H., Liu, Y., Pan, Y., Deng, F., Song, Y., et al. (2012). New variants of porcine epidemic diarrhea virus, China, 2011. *Emerg. Infect Dis.* 18, 1350–1353. doi: 10.3201/eid1808.120002

Lindquist, M. E., Lifland, A. W., Utley, T. J., Santangelo, P. J., and Crowe, J. E. Jr. (2010). Respiratory syncytial virus induces host RNA stress granules to facilitate viral replication. *J. Virol.* 84, 12274–12284. doi: 10.1128/jvi.00260-10

Nakagawa, K., Narayanan, K., Wada, M., and Makino, S. (2018). Inhibition of stress granule formation by middle east respiratory syndrome coronavirus 4a accessory protein facilitates viral translation, leading to efficient virus replication. *J. Virol.* 92, e00902-18. doi: 10.1128/jvi.00902-18

Niederwerder, M. C., and Hesse, R. A. (2018). Swine enteric coronavirus disease: a review of 4 years with porcine epidemic diarrhoea virus and porcine deltacoronavirus in the United States and Canada. *Transbound Emerg. Dis.* 65, 660–675. doi: 10.1111/tbed.12823

Onomoto, K., Yoneyama, M., Fung, G., Kato, H., and Fujita, T. (2014). Antiviral innate immunity and stress granule responses. *Trends Immunol.* 35, 420–428. doi: 10.1016/j.it.2014.07.006

Panas, M. D., Ivanov, P., and Anderson, P. (2016). Mechanistic insights into mammalian stress granule dynamics. *J. Cell Biol.* 215, 313–323. doi: 10.1083/jcb.201609081

Pandey, K., Zhong, S., Diel, D. G., Hou, Y., Wang, Q., Nelson, E., et al. (2019). GTPase-activating protein-binding protein 1 (G3BP1) plays an antiviral role against porcine epidemic diarrhea virus. *Vet. Microbiol.* 236, 108392. doi: 10.1016/j.vetmic.2019.108392

Raaben, M., Groot Koerkamp, M. J., Rottier, P. J., and de Haan, C. A. (2007). Mouse hepatitis coronavirus replication induces host translational shutoff and mRNA decay, with concomitant formation of stress granules and processing bodies. *Cell Microbiol.* 9, 2218–2229. doi: 10.1111/j.1462-5822.2007.00951.x

Rabouw, H. H., Langereis, M. A., Knaap, R. C., and Dalebout, T. J. (2016). Middle east respiratory coronavirus accessory protein 4a inhibits PKR-mediated antiviral stress responses. *PLoS Pathog.* 12, e1005982. doi: 10.1371/journal.ppat.1005982

Sola, I., Galán, C., Mateos-Gómez, P. A., Palacio, L., Zúñiga, S., Cruz, J. L., et al. (2011). The polypyrimidine tract-binding protein affects coronavirus RNA accumulation levels and relocalizes viral RNAs to novel cytoplasmic domains different from replication-transcription sites. *J. Virol.* 85, 5136–5149. doi: 10.1128/jvi.00195-11

Sun, L., Chen, H., Ming, X., Bo, Z., Shin, H. J., Jung, Y. S., et al. (2021). Porcine epidemic diarrhea virus infection induces caspase-8-mediated G3BP1 cleavage and subverts stress granules to promote viral replication. *J. Virol.* 95, e02344-20. doi: 10.1128/jvi.02344-20

Visser, L. J., Medina, G. N., Rabouw, H. H., de Groot, R. J., Langereis, M. A., de Los Santos, T., et al. (2019). Foot-and-mouth disease virus leader protease cleaves G3BP1 and G3BP2 and inhibits stress granule formation. *J. Virol.* 93, e00922-18. doi: 10.1128/jvi.00922-18

Wang, D., Fang, L., Shi, Y., Zhang, H., Gao, L., Peng, G., et al. (2016). Porcine epidemic diarrhea virus 3C-like protease regulates its interferon antagonism by cleaving NEMO. *J. Virol.* 90, 2090–2101. doi: 10.1128/jvi.02514-15

White, J. P., Cardenas, A. M., Marissen, W. E., and Lloyd, R. E. (2007). Inhibition of cytoplasmic mRNA stress granule formation by a viral proteinase. *Cell Host Microbe* 2, 295–305. doi: 10.1016/j.chom.2007.08.006

Xing, Y., Chen, J., Tu, J., Zhang, B., Chen, X., Shi, H., et al. (2013). The papain-like protease of porcine epidemic diarrhea virus negatively regulates type I interferon pathway by acting as a viral deubiquitinase. *J. Gen. Virol.* 94(Pt 7), 1554–1567. doi: 10.1099/vir.0.051169-0

Yoneyama, M., Jogi, M., and Onomoto, K. (2016). Regulation of antiviral innate immune signaling by stress-induced RNA granules. *J. Biochem.* 159, 279–286. doi: 10.1093/jb/mvv122

Zhou, Y., Fang, L., Wang, D., Cai, K., Chen, H., and Xiao, S. (2017). Porcine reproductive and respiratory syndrome virus infection induces stress granule formation depending on protein kinase R-like endoplasmic reticulum kinase (PERK) in MARC-145 cells. *Front. Cell Infect. Microbiol.* 7, 111. doi: 10.3389/fcimb.2017.00111

Conflict of Interest: The authors declare that the research was conducted in the absence of any commercial or financial relationships that could be construed as a potential conflict of interest.

Publisher's Note: All claims expressed in this article are solely those of the authors and do not necessarily represent those of their affiliated organizations, or those of the publisher, the editors and the reviewers. Any product that may be evaluated in this article, or claim that may be made by its manufacturer, is not guaranteed or endorsed by the publisher.

frontiers | Frontiers in Microbiology

TYPE Original Research
PUBLISHED 08 August 2022
DOI 10.3389/fmicb.2022.947112

OPEN ACCESS

EDITED BY
Yongqun Oliver He,
University of Michigan, United States

REVIEWED BY
Boli Hu,
Zhejiang University, China
Fuzhou Xu,
Beijing Academy of Agriculture and Forestry Sciences, China

*CORRESPONDENCE
Xiaolong Xu
xiaolong_xu3013@126.com
Qingquan Liu
liuqingquan_2003@126.com

†These authors have contributed equally to this work

SPECIALTY SECTION
This article was submitted to Virology, a section of the journal Frontiers in Microbiology

RECEIVED 18 May 2022
ACCEPTED 15 July 2022
PUBLISHED 08 August 2022

CITATION
Liu M, Liu T, Wang X, Yu C, Qin T, Li J, Zhang M, Li Z, Cui X, Xu X and Liu Q (2022) Cangma Huadu granules attenuate H1N1 virus-induced severe lung injury correlated with repressed apoptosis and altered gut microbiome. *Front. Microbiol.* 13:947112. doi: 10.3389/fmicb.2022.947112

Cangma Huadu granules attenuate H1N1 virus-induced severe lung injury correlated with repressed apoptosis and altered gut microbiome

Mingjiang Liu[1,2†], Tengwen Liu[3†], Xuerui Wang[4,5,6†], Chenglong Yu[1,2], Tao Qin[1,2], Jingui Li[1,2], Mina Zhang[4,5], Zhenxuan Li[4,5], Xuran Cui[4,5,6], Xiaolong Xu[4,5,6*†] and Qingquan Liu[4,5,6*†]

[1]College of Veterinary Medicine, Yangzhou University, Yangzhou, China, [2]Jiangsu Co-innovation Center for Prevention and Control of Important Animal Infectious Diseases and Zoonoses, Yangzhou, China, [3]Chengdu University of Traditional Chinese Medicine, Basic Medical College, Chengdu, China, [4]Beijing Hospital of Traditional Chinese Medicine, Capital Medical University, Beijing, China, [5]Beijing Key Laboratory of Basic Research With Traditional Chinese Medicine on Infectious Diseases, Beijing, China, [6]Beijing Institute of Chinese Medicine, Beijing, China

Severe influenza A virus infection leads to overwhelming inflammatory responses and cellular apoptosis, which causes lung injury and contributes to high mortality and morbidity. The gut microbiome altered in response to the infection might influence the disease progression and the treatment outcome. Cangma Huadu (CMHD) granules, an in-hospital preparation of traditional Chinese medicine, have been shown to be favorable in the clinical treatment of influenza. However, the effects and mechanisms of CMHD granules on severe influenza pneumonia and its mechanisms are not well-known. In this study, a lethal influenza A (H1N1) A/Puerto Rico/8/34 virus (PR8)-infected mice model was established, and the 16S ribosomal RNA (16S rRNA) V3–V4 region sequencing of the intestinal microbiome was conducted. We revealed that the oral administration of CMHD granules protects mice against higher mortality, enhanced weight loss, overwhelmed interferon-γ concentration, lung viral titers, and severe lung pathological injury in PR8-infected mice. CMHD granules' administration downregulated the levels of interleukin (IL)-1β, tumor necrosis factor-α, and malondialdehyde, while it upregulated the levels of IL-10, superoxide dismutase, and glutathione peroxidase. Subsequently, it decreased the protein ratio of B-cell lymphoma-2/Bcl-2-associated X and the expression of cleaved caspase-3. The diversity and compositions of the gut microbes were altered profoundly after the administration of CMHD granules in PR8-infected mice. A higher abundance of *Bifidobacterium*, *Parasutterella*, *Bacteroides*, and *Faecalibaculum* was observed in the CMHD group, and a higher abundance of *Lactobacillus* and *Turicibacter* was observed in the positive drug Ribavirin group. The linear discriminant analysis effect size also revealed a higher proportion of

Bacteroides and *Bifidobacterium_pseudolongum* characterized in the CMHD group. These results demonstrated that CMHD granules are a promising strategy for managing severe influenza and attenuating severe lung damage *via* reducing viral titer, inflammatory responses, and oxidative stress. The mechanisms are involved in repressed Bcl-2-regulated apoptosis and altered composition and diversity of the gut microbiome.

KEYWORDS

influenza A virus, gut microbiota, apoptosis, anti-influenza effect, traditional Chinese medicine, Cangma Huadu

Introduction

Over the past decades, RNA viruses have caused huge global impacts on economic chaos, global public health resources, and, most importantly, human health. Influenza is an acute contagious viral infection with both seasonal and pandemic modes in humans (Bridges et al., 2003; Morens and Taubenberger, 2019). It is reported that seasonal influenza affects up to 10% of the adult population and 20% of children annually and shows a substantial incidence (Peteranderl et al., 2016). The continuing challenges of the influenza A virus (IAV) pandemic include the emergence of the H1N1 pandemic in 2009, human infection with H7N9 avian influenza in 2013, and the sporadic infection of highly pathogenic H5N1 avian influenza. The IAV can affect organs and manifests as an acute febrile illness with variable degrees of systemic and respiratory symptoms (Krammer et al., 2018). Considering the disease progression of IAV infection, two outcomes should be given due attention. First, IAV enters host cells and causes acute lung injury, leading to hospitalization. Second, uncontrolled lung injury leads to secondary bacterial pneumonia, which turns the patient's condition into a severe situation (Klomp et al., 2021). Although the IAV is one of the most deeply studied pathogens, the existing control schemes need further improvement. Influenza vaccines must be updated regularly because of the continuous antigen drift and sporadic antigen transfer in the virus surface glycoprotein. At present, IAV infection treatment is limited to neuraminidase inhibitors; therefore, there is an urgent need for new drugs and vaccine methods.

In terms of mechanism, infected epithelial cells started apoptosis and necroptosis, representing the primary form of damage to the epithelium during the early stages of IAV infection. Damaged cells in the apoptotic cascade promote the activation of caspases and further trigger immune and inflammatory response (Chung et al., 2006). Moreover, virus-infected epithelial cells release chemokines, which recruit a large number of myeloid and lymphoid cells to the lung tissue. The excessive inflammatory response in IAV-infected lungs can lead to acute respiratory distress syndrome, leading to severe lung injury and respiratory failure (Kalil and Thomas, 2019; Stegelmeier et al., 2019). Thus, modulating the apoptosis and inflammatory response can prevent the occurrence and development of lung injury. Traditional Chinese medicine (TCM) has been reported to elicit anti-inflammatory and anti-apoptosis effects in those who underwent diseases. Our previous studies reported that herbal treatment altered microglial polarization from M1 phenotype to M2 phenotype to reduce the pro-inflammatory cytokine production (Wang et al., 2020) and prevented apoptosis by suppressing endoplasmic reticulum- and mitochondria-associated pathways in animal models of lethal infection (Xu et al., 2018). The mechanisms of TCM in the treatment of viral infection have also been proved to be related to the reduction of cytokine storm caused by hyper-release of interferon (IFN), interleukins (IL), tumor-necrosis factors (TNF), chemokines, and cytokines (Huang et al., 2021).

The microbiota plays an essential role in the host disequilibrium transition from homeostasis to disease. Disrupted intestinal bacterial composition is associated with various diseases and dysfunctions, including autoimmunity, inflammatory disorders, and infectious diseases (Cho and Blaser, 2012). Accumulating evidence showed that balanced gut microbiota plays a protective role in the body against infections such as IAV (Stefan et al., 2020), *Klebsiella pneumonia* (Sequeira et al., 2020), *Staphylococcus aureus* (Hu et al., 2020), and *Streptococcus pneumonia* (Schuijt et al., 2016). The natural resistant mechanisms of the gut microbiota after IAV infection have been proved to be related to type I interferon signaling pathways (Steed et al., 2017; Bradley et al., 2019) and the activation of the inflammasome and T lymphocytes (Ichinohe et al., 2011). Gut commensal microbes are essential for the decomposition of nutritional products and critical producers of essential metabolites (Valdes et al., 2018). As one of the natural characteristics of TCM, only partial components can be absorbed directly into the blood; the secondary digestion and decomposition of the active ingredients by gut microbiota are indispensable (Wang et al., 2021a). TCM nutraceuticals, such as indigestive carbohydrates/polysaccharides, polyphenols, alkaloids, could pass through the stomach and reach the

intestine and are frequently fermented or converted by the local gut microbiota to form bioactive and bioavailable metabolites (Lin et al., 2021). Therefore, exploring the interaction between TCM components and gut microbiota may better clarify its mechanisms under diseases.

Historically, TCM has worked well in treating infectious diseases (Huang et al., 2021). During the IAV pandemic in 2009, four anti-flu TCM prescriptions with outstanding clinical efficacy were recommended by the Chinese government to treat H1N1 influenza (Ge et al., 2010; Li et al., 2016). Cangma Huadu (CMHD) granules are a new TCM prescription approved in 2020 by the Beijing Food and Drug Administration (Z20200008000) for the clinical treatment of RNA virus infections, including influenza and SARS-CoV-2. We previously reported that CMHD granules protect mice from mild IAV infection (Cui et al., 2022). However, the underlying mechanism and molecular effects of CMHD granules on lethal influenza remain unclear. In this study, we established an animal model of IAV-induced lethal pneumonia, and the protective effects of CMHD granules on severe lung injury and excessive inflammatory response were investigated. Moreover, we assessed the regulation of CMHD granules on the microbiota of IAV-infected mice. Our findings provide evidence to support the use of CMHD granules for the treatment of IAV infection and gain insights into its underlying regulatory role in the host and microbe.

Materials and methods

Animals

Male ICR mice (18–22 g) were obtained from the Comparative Medicine Center of Yangzhou University [Jiangsu, China Certificate Number: SYXK(E)2017-0044]. All animals were housed under specific pathogen-free conditions (23 ± 1°C; 50 ± 10% humidity, 12 h light/dark cycle) with free access to standard food and water. All animal experiments were conducted under the Animal Care and Use Committee of Yangzhou University. All experimental animal ethics are approved by the Experimental Animal Ethics Committee of Yangzhou University (No. 202103-009).

Influenza A virus infection

The mouse-adapted A/Puerto Rico/8/34(H1N1) influenza virus strain (referred to as PR8) was preserved in the College of veterinary medicine, Yangzhou University, China. Mice were anesthetized with pentobarbital sodium (40 mg/kg) by intraperitoneal injection. When sufficient depth of anesthesia was confirmed and breathing occurred at 2–3-s intervals, mice were intranasally inoculated with 50 μL $10^{4.4}$ EID50 PR8 virus.

Preparation of Cangma Huadu granules

Cangma Huadu granules contain 8 Chinese herbs, including 30 g Cangzhu (*Rhizoma atractylodis*) (30/106), 10 g Mahuang (*Herba ephedra*) (10/106), 10 g Huoxiang (*Herba Agastache*) (10/106), 15 g Shegan (*Rhizoma belamcandae*) (15/106), 10 g Shandougen (*Radix sophora tonkinensis*) (10/106), 10 g Ercha (*Acacia catechu*) (10/106), 15 g Jindenglong [*Physalisalkengi L.var.franchetii (Mast.) Makino*] (15/106), and 6 g Shenggancao (*Glycyrrhiza uralensis Fisch*) (6/106). All the herbs were provided by the pharmacy of Beijing Hospital of Traditional Chinese Medicine, China. A total of 106 g of crude drugs were soaked and decocted using distilled water for 30 min and then concentrated to a low dosage of 0.5 g/mL (CMHD-L groups), a medium dosage of 1 g/mL (CMHD-M groups), and a high dosage of 2 g/mL (CMHD-H groups) as final dosages.

Treatment protocols

The mice were randomized and divided into six groups as follows: the control (Con), the model (Mod), the CMHD low dosage (CMHD-L), the CMHD medium dosage (CMHD-M), the CMHD high dosage (CMHD-L), and the Ribavirin group (RBV). At 1 day post-infection (dpi), CMHD-L, CMHD-M, and CMHD-H groups were orally administrated with 0.2 mL decoction of 0.5, 1, and 2 g/mL CMHD granules, respectively, one time daily for seven continuous days. The mice in the RBV group were orally administrated with 0.2 mL of 0.075 g/kg Ribavirin (Zhejiang Chengyi Pharmaceutical Co., Ltd, Wenzhou, China) that dissolved in dd H2O, one time daily from 1 dpi for seven continuous days. Mice in the Con and Mod groups were orally administrated with 0.2 mL of dd H_2O one time daily from 1 dpi for seven continuous days. The weight of mice in each group was monitored every day for 7 days. On 7 dpi, lung tissue and fecal samples of mice were collected for weighing, pathology, and 16S rRNA sequencing, respectively.

Lung index

Lungs were directly excised surgically and weighed. The lung index is the ratio of organ/body weight and was calculated according to the following formula: Lung index = (Lung weight/Body weight) × 100%.

Histopathological examination

For histopathological analysis, the lung tissues of mice were harvested, fixed in 4% formaldehyde for 24 h, embedded in paraffin, and then sliced into 4 μm-thick sections with a

slicer (LEICA RM2255, Germany). The sections were stained with hematoxylin and eosin. An Olympus microscope (BX53F, Tokyo, Japan) was used for histological observation.

Lung viral titration

Lung viral titration was evaluated by the PR8 mRNA expression of Real-time quantitative polymerase chain reaction (Real-time PCR). Total RNA was extracted using Trizol (Vazyme, China) reagent according to the instructions. Its quantity was detected by the nanodrop spectrophotometer (Thermo Scientific, Wilmington, DE, United States), and cDNA was synthesized using Hiscript II QRT supermax (Vazyme, China). Finally, the real-time PCR was performed using a CFX96^{TM} connected real-time PCR system (Bio-Rad, United States) with SYBR Green PCR Master Mix (Vazyme, China). The cycle conditions were as follows: an initial denaturation step at 95°C for 30 s, 40 cycles of denaturation for 5 s at 95°C, and annealing and extension for 30 s at 60°C. The quantification results were calculated using the $2-\Delta\Delta CT$ method compared to GAPDH as the reference mRNA. Primers for real-time PCR were from Tsingke Biotechnology, China. Their sequences were listed below as follows: PR8: F-3′ TAGCATGCATGCTATCGGTACGT5′, R-3′TAGCTATCTAGC TAGCTAGCTA5′, and GAPDH: F-3′GGTGAAGGTCGGTG TGAACG5′, R-3′CTCGCTCCTGGAAGATGGTG5′.

Inflammatory cytokines and oxidative stress measurement

Mouse ELISA kits for IL-1β (RK00006), IL-10 (RK00006), TNF-α (RK00027), and IFN-γ (RK00019) were all purchased from ABclonal Biotechnology Co., Ltd., China. The oxidative stress kits of superoxide dismutase (SOD), glutathione peroxidase (GSH-Px), and malondialdehyde (MDA) were all purchased from Nanjing Jiancheng Bioengineering Institute, China. All measurements were carried out according to the manufacturer's instructions.

Western blotting analysis

The primary antibodies against B-cell lymphoma-2 (Bcl-2) (3498), Bcl-2-associated X (Bax) (2772), cleaved-caspase-3 (Asp175) (9661), and β-actin (4970) were all from Cell Signaling Technology (Danvers, MA, United States). Total protein was extracted from the left lower lobe using the ice-cold RIPA buffer (APPLYGEN). After protein was quantified with a BCA protein assay kit (Beyotime Institute of Biotechnology, China) and boiled with loading buffer (Solarbio, China), equal amounts of protein in each sample (100 μg) were prepared for electrophoresis on 8–12% SDS-PAGE and then electro-blotted onto PVDF membranes (Merck Millipore, United States). The membrane was incubated with 5% skim milk for 1 h at room temperature (RT), followed by incubation overnight with primary antibodies at 4°C (all antibodies were diluted following instructions). After the primary antibody was incubated, it was washed three times with TBST and then incubated with species-specific horseradish peroxidase-conjugated secondary antibodies (diluted 1:5,000) at RT for 1 h. After three washes with TBST, protein signal bands were visualized on a Chemidoc XRS (Bio-Rad, Marnes-la-Coquette, France) by an enhanced Chemiluminescence kit. Densitometry quantification of immunoblot signals was performed using ImageJ software. Each experiment was performed in triplicate.

DNA extraction and high-throughput 16S rRNA sequencing

Fresh fecal pellets were collected, stored in liquid nitrogen, and then immediately stored in a refrigerator at −80°C before extraction of total DNA. The 16S rRNA gene comprising V3–V4 regions was amplified using the standard primer pair and quality-controlled using the common primer pair and the microbial diversity analysis. Bacteria primers: 341F, CTAYGGGBRGCASCAG; 806R, GGACTACNNGGGTATCTAAT. Fungal ITS1-2 regions were sample barcodes and sequencing adaptors. Fungal primers: ITS1-1F-F, CTTGGTCATTTAGAGGAAGTAA; ITS1-1F-R, GCTGCGTTCTTCATCGATGC. Briefly, the raw sequences were quality-controlled using QIIME with default parameters and then demultiplexed and clustered into species-level (97% similarity) operational taxonomic units (OTUs). Species annotation analysis was performed using the Mothur method and SILVA138's SSUrRNA database (set threshold 0.8∼1). α-Diversity and β-diversity analyses were performed using QIIME. Discriminative taxa were determined using LEfSe (LDA Effect Size). The 16S rRNA gene sequence of the entire prokaryote genome was extracted from the KEGG database and compared with the SILVA SSU Ref NR database (BLAST bitscore > 1500). The correlation matrix was established and the whole genome functional information of prokaryotes annotated by UProc and PAUDA in the KEGG database corresponded to the SILVA databases so that OTU clustering of functional annotation sequencing samples in SSU was achieved.

Statistical analyses

The experimental data were analyzed using SPSS 25.0 statistic software. Diagrams were performed by using GraphPad Prism 8.0 software. The results were compared using the one-way analysis of variance (ANOVA). The differences were

considered significant at a P-value < 0.05. All the experimental data were presented as the mean ± SEM.

Results

Cangma Huadu granules reduced the mortality of influenza A virus infection

To verify the effects of CMHD granules on the mortality of lethal influenza, a nasal drip of a 50 μL $10^{4.4}$ EID50 mouse-adapted influenza A/Puerto Rico/8/1934 H1N1 (PR8) lethal dose virus was used to establish a pneumonia model, and the mortality of animals in each group was observed for 7 days. As seen in **Figure 1A**, all sham animals survived throughout the 7 days. Compared with the control group, the mortality of mice in the model group was significantly higher (7-day mortality 0 vs. 40%, median death time > 7 days vs. 6.25 ± 0.92 days). Compared with the model group, low, medium, and high doses of CMHD granules significantly reduced the mortality of infected mice and prolonged the median death time to 7 days or more. As a positive drug control, Ribavirin significantly reduced the mortality of infected mice compared with the model group. There were no significant differences in mortality and median time of death between CMHD granules and Ribavirin administration.

Cangma Huadu granules attenuated weight loss and virus titer after influenza A virus infection

To further verify the therapeutic effect of CMHD granules on lethal influenza pneumonia, the body weight and viral load of mice in each group were measured. As seen in **Figure 1B**, the weight of the control group mice increased slowly from 0 to 7 dpi. Compared with the control group, the weight in the model group turned and began to decrease at 3 dpi. Compared with the model group, the low, medium, and high doses of CMHD granules groups showed less weight loss. The body weight of the model group decreased significantly compared with the control group. The weight loss was significantly improved after the administration of low, medium, and high doses of CMHD granules compared to the model group. Ribavirin showed no effect on attenuating weight loss after IAV infection.

As seen in **Figure 1C**, the pulmonary viral load in the model group was significantly higher than that of the control group at 7 dpi. The viral load was significantly decreased after low, medium, and high doses of CMHD granules administration compared to the model group. Ribavirin showed the best effect on reducing the viral load among all the groups. The levels of IFN-γ, a key restriction component during IAV replication and transmission, were also detected (**Figure 1D**). The content of IFN-γ in the lung tissue of the model group increased significantly compared with the control group. Low, medium, and high doses of CMHD granules administration showed a similar effect as Ribavirin on decreasing the level of IFN-γ .

Cangma Huadu granules alleviated severe lung damage during influenza A virus airway infection

We further evaluated the effect of CMHD granules on lung damage after IAV infection. As the general morphology of lungs displayed in **Figure 2A**, significant changes, including larger volume, increased edema, and bleeding, were observed in mice after IAV infection compared to the control. Low, medium, and high doses of CMHD granules or Ribavirin administration significantly improved the lung injury after infection, including reduced volume, edema, and bleeding. The alternation of lung index was consistent with the trends of the general morphology (**Figure 2B**). Compared with the control group, the lung index in the model group was significantly higher. Different doses of CMHD granules or Ribavirin administration significantly reduced the lung index caused by infection. HE staining showed that the pathological morphology of lung tissue in the control group was normal. Compared with the control group, the alveolar structure of the model group was incomplete. Cell necrosis, expansion of airspaces, and infiltration of the inflammatory cells were displayed. After administration with different doses of CMHD granules or Ribavirin, the destruction of the alveolar structure was attenuated, with less necrosis and inflammatory cell infiltration than the model group (**Figure 2C**).

Cangma Huadu granules regulated the inflammatory cytokine secretion and oxidative stress upon influenza A virus infection

To better explore the mechanism of CMHD granules in reducing the mortality of infected mice, we detected the secretion of inflammatory cytokines and the alteration of oxidative stress in the lung tissue at 7 dpi. As seen in **Figures 3A–C**, IAV-infected mice demonstrated considerably higher levels of IL-1β and TNF-α and reduced levels of IL-10 compared to the control group. Different dosages of CMHD granules or Ribavirin administration showed similar effects in reducing the levels of IL-1β and TNF-α and increasing the level of IL-10 in lung tissue compared to the model group.

As seen in **Figures 3D,F**, the SOD and GSH-Px activities of the lung tissue in the model group were significantly higher than that in the control group. The administration of CMHD granules or Ribavirin significantly improved the upregulation of SOD and GSH-Px activities caused by infection.

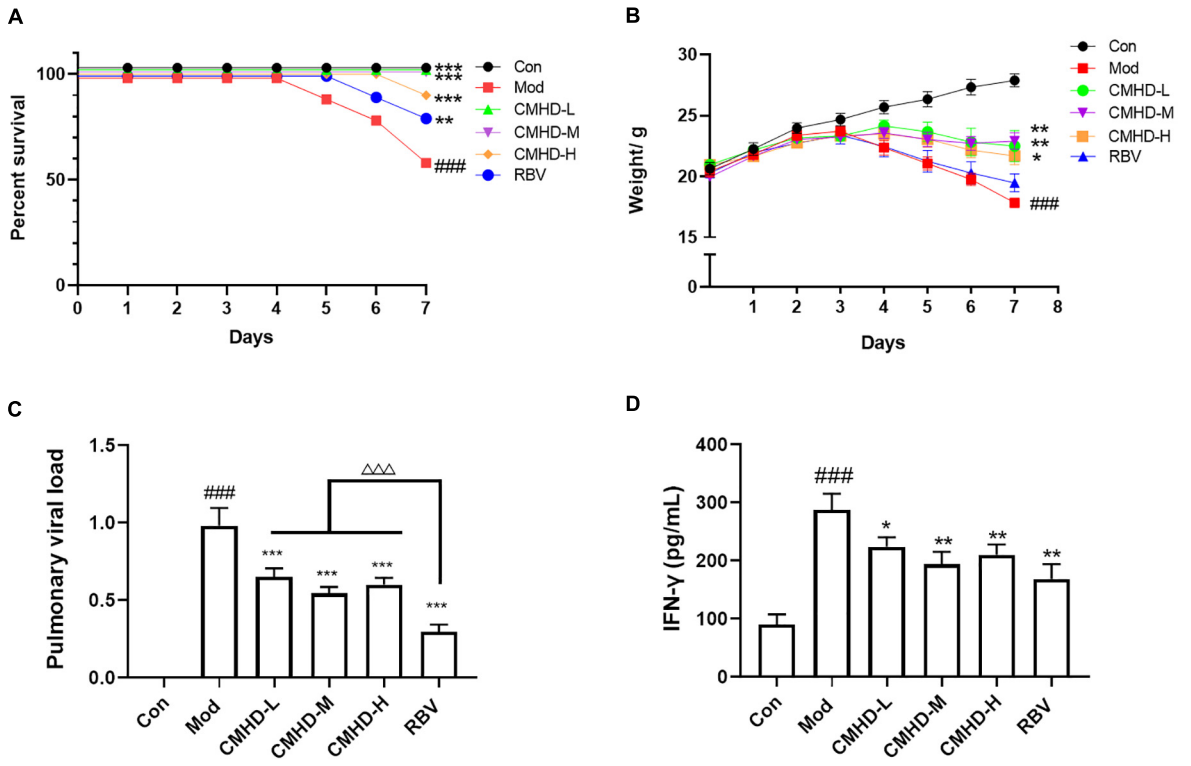

FIGURE 1
CMHD granules attenuated weight loss and virus titer after IAV infection. ICR mice were infected with 50 μL $10^{4.4}$ EID50 influenza A/Puerto Rico/8/1934 H1N1 (PR8) virus following treatment with dd H2O (0.2 ml, oral administration) (Mod), CMHD granule (0.5 g/ml, 0.2 ml, oral administration) (CMHD-L), CMHD granule (1 g/ml, 0.2 ml, oral administration) (CMHD-M), CMHD granule (2 g/ml, 0.2 ml, oral administration) (CMHD-H), or Ribavirin (0.2 Ml, 0.075 g/kg, oral administration) (RBV) per day for seven consecutive days. Mice in the control group (Con) were not infected with a virus and perfused with dd H2O (0.2 ml, oral administration) per day for even consecutive days. **(A)** Kaplan–Meier curves for 7 days. **(B)** Body weight for 7 days. **(C)** Comparison of pulmonary viral load among different groups at 7 dpi. **(D)** Comparison of interferon–γ content in lung tissues among different groups at 7 dpi. Values are mean ± SEM of 10 animals per group. #Compared with Con, *compared with Mod, △compared with RBV. *$p < 0.05$, **$p < 0.01$, ***$p < 0.001$ of each symbol, respectively.

As shown in Figure 3E, the MDA level in the lung tissue of the model group was significantly lower than that in the control group. The administration of CMHD granules or Ribavirin significantly reduced the MDA level compared to the model group. Therefore, CMHD granules have specific anti-inflammatory and anti-oxidative effects under IAV infection.

Effects of Cangma Huadu granules on the Bcl-2/Bax/caspase-3 signaling pathway in influenza A virus-infected mice

To further explore the mechanism of CMHD granule on lethal IAV infection, we detected the protein levels of the Bcl-2 family, including Bcl-2 and Bax, and the level of cleaved-caspase-3, which are related to the regulation of apoptosis in lung tissues (Figure 4A). Compared with the control, the relative protein expression of cleaved-caspase-3 and the ratio of Bax/Bcl-2 were significantly increased in the lung tissue of infected mice (Figure 4B,C). Compared with the model group, low, medium, and high doses of CMHD granule or Ribavirin administration significantly downregulated the protein expression of cleaved-caspase-3 and Bax/Bcl-2 ratio. These results revealed that CMHD administration might inhibit apoptosis after IAV infection in a manner associated with the regulation of the Bcl-2/Bax/caspase-3 signaling pathway.

Cangma Huadu granules altered gut microbial structural diversity

The α-diversity, including Ace, Chao1, and Shannon, indexes were evaluated to determine the ecological diversity within a microbial community after CMHD granules or Ribavirin administration in IAV-infected mice. As seen in Figures 5A–C, ACE and Chao1 indexes in the model group tended to increase, but there was no significant difference in Ace, Chao1, and Shannon indexes of the model group

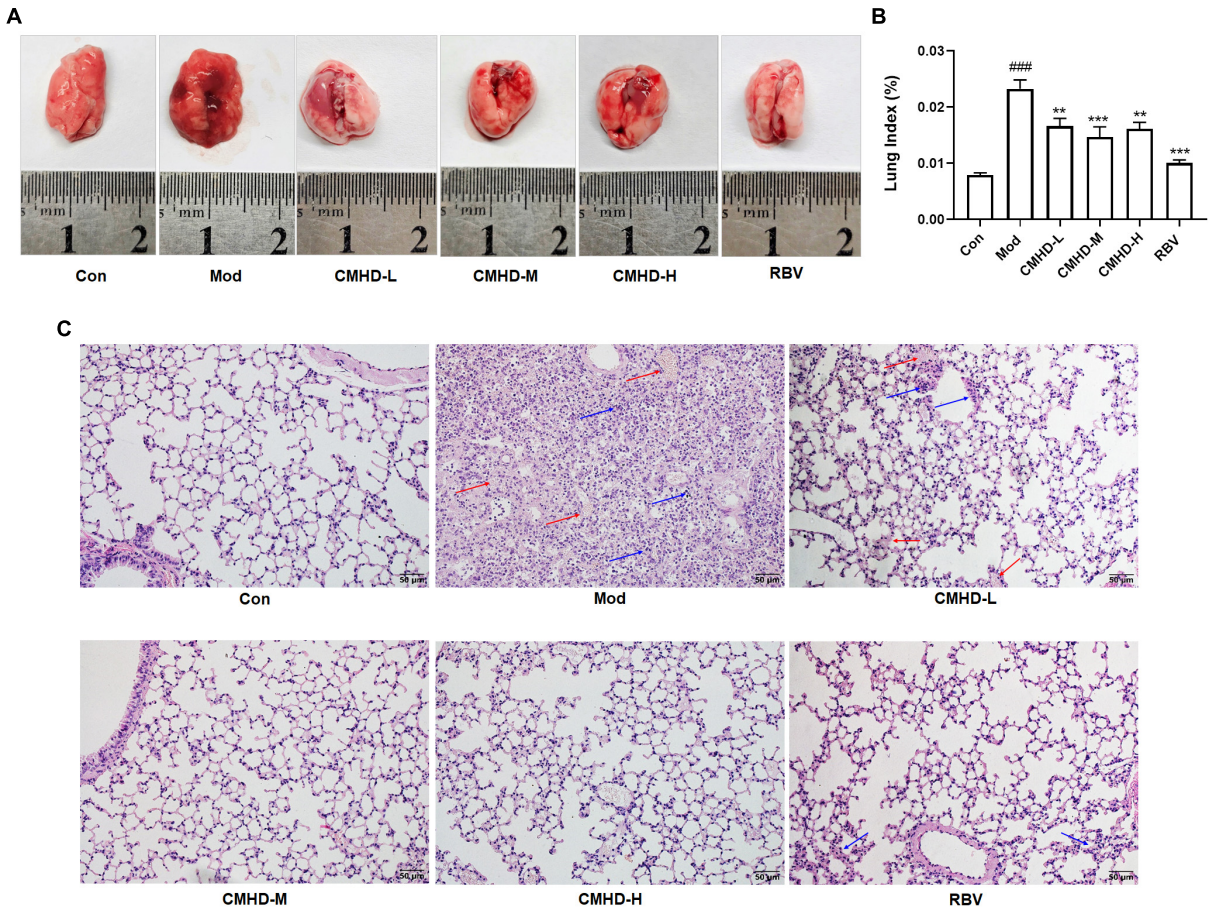

FIGURE 2
CMHD granules alleviated severe lung damage during IAV airway infection. **(A)** The general morphology of lung tissue and **(B)** lung index in uninfected or infected mice following the administration of CMHD granules or Ribavirin at 7 dpi. **(C)** Histopathological injury of representative lung sections in each group at 7 dpi with 400 × magnification (Bar = 50 μm). The blue arrow indicates inflammatory cell infiltration and the red arrow indicates erythrocyte exudation. Values are mean ± SEM of 10 animals per group. #Compared with Con, *compared with Mod. $^{**}p < 0.01$, $^{***}p < 0.001$ of each symbol, respectively.

compared with the control group. Ace and Chao1 indexes in the Ribavirin group were significantly higher than those in the control group. Compared with the model group, the Shannon index of the CMHD group was significantly higher. The ACE index in the Ribavirin group was higher than that in the CMHD group. The β-diversity was measured by the principal coordinate analysis (PCoA) (Figure 5D) and the non-metric multidimensional scaling (NMDS) analysis (Figure 5E). PCoA based on the Bray–Curtis dissimilarity index showed a significant difference among the control, the model, the CMHD, and the Ribavirin groups (ANOSIM $P < 0.001$). NMDS analysis intuitively reflected the difference in distance within and among the groups. The control group and the CMHD group were distributed below NMDS2 0.0, while the model group and the Ribavirin group were distributed above NMDSs2 0.0. The NMDA Stress is 0.12 (less than 0.2), which indicates that the model is reliable. Overall, CMHD granules or Ribavirin administration significantly altered the structural microbial diversity of the intestine in IAV-infected mice.

Cangma Huadu granules altered the dominant bacteria after influenza A virus infection

As seen in Figure 6A, Bacteroidota, Firmicutes, Verrucomicrobiota, Proteobacteria, and unidentified Bacteria were the dominant phyla microbiota (relative abundance > 1%) in the four groups. In addition, Actinobacteria was a dominant phyla microbiota in the model, the CMHD, and the Ribavirin groups. Deferribacteres was a dominant phyla microbiota in the Ribavirin group. The average abundance of Bacteroidota and unidentified Bacteria showed significant differences among the four groups using one-way ANOVA.

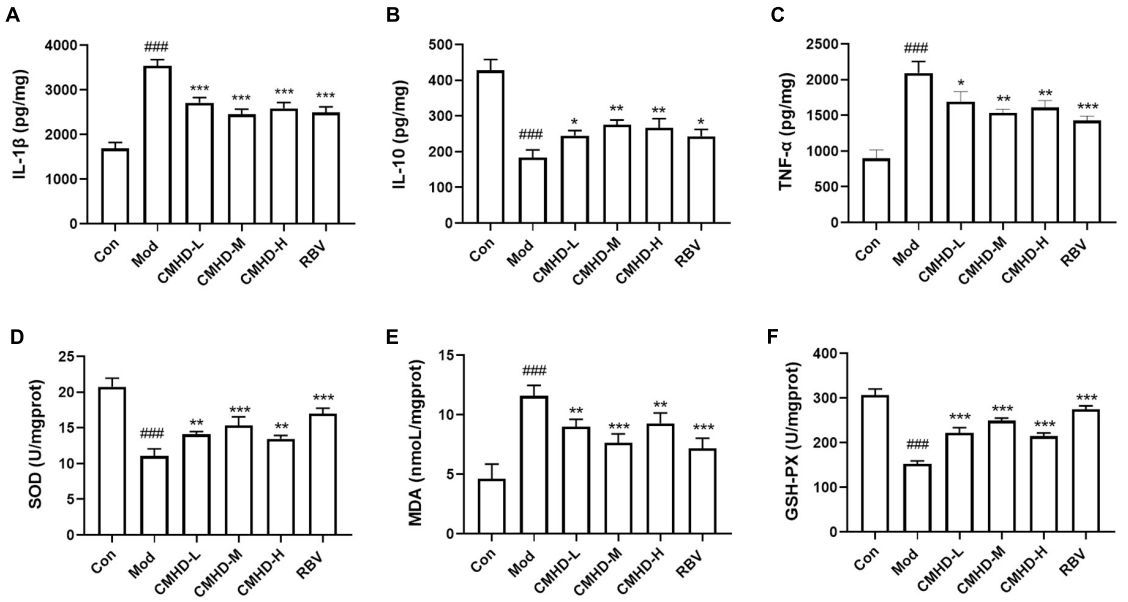

FIGURE 3
CMHD Granules regulated the inflammatory cytokine secretion and oxidative stress upon IAV infection. Lung tissue levels of **(A)** Interleukin-1β (IL-1β), **(B)** interleukin-10 (IL-10), **(C)** tumor necrosis factor-α (TNF-α), **(D)** superoxide dismutase (SOD) activity, **(E)** malondialdehyde (MDA), and **(F)** glutathione peroxidase reactive (GSH-Px) activity detected from uninfected or infected mice following the administration of CMHD granules or Ribavirin at 7 dpi. Values are mean ± SEM of 10 animals per group. #Compared with Con,*compared with Mod. *$p < 0.05$, **$p < 0.01$, ***$p < 0.001$ of each symbol, respectively.

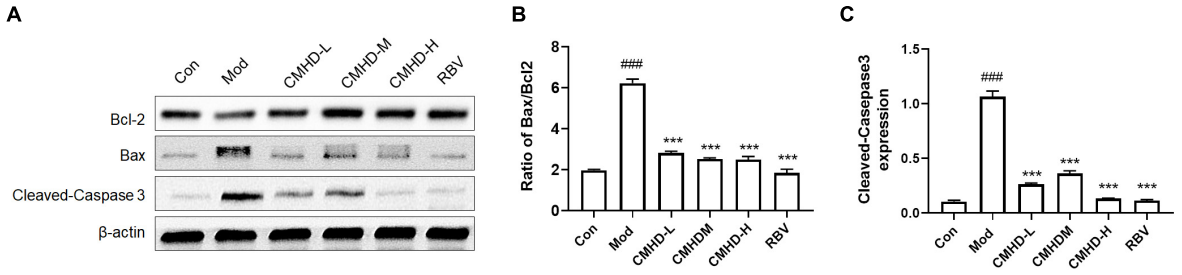

FIGURE 4
Effects of CMHD granules on the Bcl-2/Bax/caspase-3 signaling pathway in IAV-infected mice. **(A)** Representative Western Blots of B-cell lymphoma-2 (Bcl-2) family, including Bcl-2 and Bcl-2-associated X (Bax), and cleaved caspase-3 in lung tissues of uninfected or infected mice following the administration of CMHD granules or Ribavirin at 7 dpi. The same membranes were probed with β-actin. **(B)** Densitometric analysis of Bax/Bcl-2 ratio on protein levels, **(C)** and the expression of cleaved caspase-3. Values are mean ± SEM of 10 animals in each group. #Compared with Con, *compared with Mod. ***$p < 0.001$ of each symbol, respectively.

As seen in Figure 6B, the top 3 predominant genera were *Akkermansia* (17.7%), *Alistipes* (13.4%), and *Alloprevotella* (8.8%) in the control group; *Akkermansia* (35.9%), *Lactobacillus* (10.4%), and *Alistipes* (9.0%) in the model group; *Akkermansia* (15.4%), *Alistipes* (12.3%), and *Bacteroides* (11.7%) in the CMHD group; and *Akkermansia* (16.9%), *Lactobacillus* (13.2%), and *Alistipes* (10.9%) in the Ribavirin group, respectively. The average abundance of *Lactobacillus*, *Parasutterella*, *Turicibacter*, *Bacteroides*, *Faecalibaculum*, and *Bifidobacterium* showed significant differences among the four groups using one-way ANOVA.

Cangma Huadu granules altered fecal microflora composition after influenza A virus infection

As seen in Figure 6C, in the phylum, the abundance of Bacteroidota decreased in the model group compared with the control group, increased in the CMHD group compared with the model group, and decreased in the Ribavirin group compared with the CMHD group, respectively. As seen in Figure 6D, the abundance of unidentified Bacteria increased in the model group compared with the control

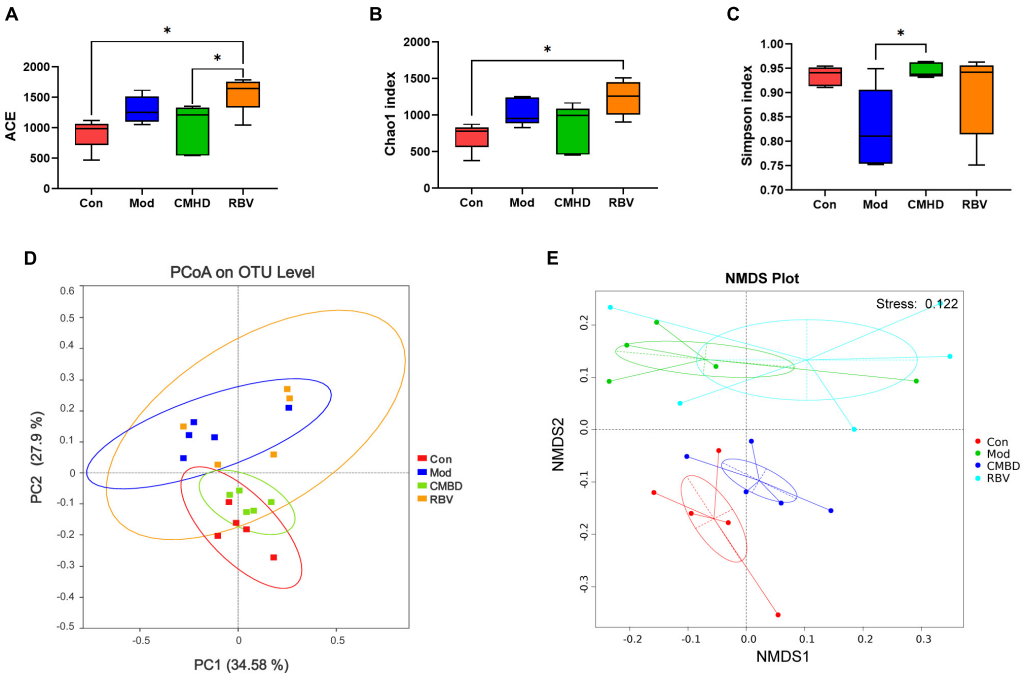

FIGURE 5
CMHD granules altered fecal microbial diversity in IAV-infected mice. 16S rRNA sequencing of the fecal samples in the control (Con), the model (Mod), the CMHD granules administration (CMHD), and the Ribavirin administration groups (RBV) were detected at 8 dpi (5 animals per group). α-Diversity was evaluated based on the Ace **(A)**, Chao1 **(B)**, and Simpson **(C)** indices of the operational taxonomic unit (OTU) levels. $^{*}P < 0.05$. β-Diversity was evaluated based on the principal coordinate analysis (PCoA) **(D)** and non-metric multi-dimensional scaling (NMDS) analysis **(E)** of the OTU levels.

group. As seen in **Figures 6E–J**, in the genera, the abundance of bacterium including *Bifidobacterium*, *Parasutterella*, *Bacteroides*, and *Faecalibaculum* was increased in the CMHD group compared with the model group. The abundance of bacterium including *Bifidobacterium*, *Parasutterella*, *Bacteroides*, and *Faecalibaculum* was decreased, while the bacterium *Lactobacillus* and *Turicibacter* were increased in the Ribavirin group compared with the CMHD group.

Moreover, LEfSe was used to generate a cladogram to identify the specific bacteria in each group. Using a logarithmic LDA score cutoff of 3.5, we identified 40 bacteria as key discriminants (**Figure 7**). Higher proportions of bacterium including Bacteroidota, *Alloprevotella*, and *Atopostipes* were identified in the control group, while a higher proportion of *Pseudomonadale* was identified in the model group. A higher proportion of genera including *Paeasutterlla*, *Bacteroides*, and *Bifidobacterium_pseudolongum* were identified in the CMHD group, while a higher proportion of unidentified_Bacteria and *Nitrospirota* were identified in the Ribavirin group.

Discussion

The development of influenza infection into a severity situation is mainly caused by excessive lung injury and secondary pneumonia (Herold et al., 2015). Two factors are responsible for the exacerbation of the disease and mortality, including lung tissue damage and overwhelming inflammatory response (McCullers and Bartmess, 2003). We previously found that CMHD has therapeutic effects on mild IAV infection by using a non-lethal dose of 35 μL 14LD50 H1N1/FM1 virus infection mouse model (Cui et al., 2022). This study established a lethal influenza model using a dosage of 50 μL $10^{4.4}$ EID50 H1N1/PR8 virus. According to our data, 7-day mortality of the pneumonia model is about 40%, indicating a lethal infection. Treatment with CMHD granules at different doses could decrease the mortality of infected mice. Besides, we noticed that CMHD granules attenuated the weight loss induced by a virus infection, indicating an improvement in the condition. Considering the severity of this model, CMHD granules possess a promising therapeutic effect on preventing severe pneumonia caused by IAV. Anti-viral drug Ribavirin showed similar therapeutic efficacy in the mice with lethal infections. However, based on our understanding, the anti-viral effect of TCM medicine is usually not as effective as designed in western medicine. Therefore, we detected the viral titer in mice of the model group and the treatment group. Not surprisingly, the direct anti-viral property of CMHD granules is inferior to Ribavirin. Taken above, we hypothesize that the curative effect

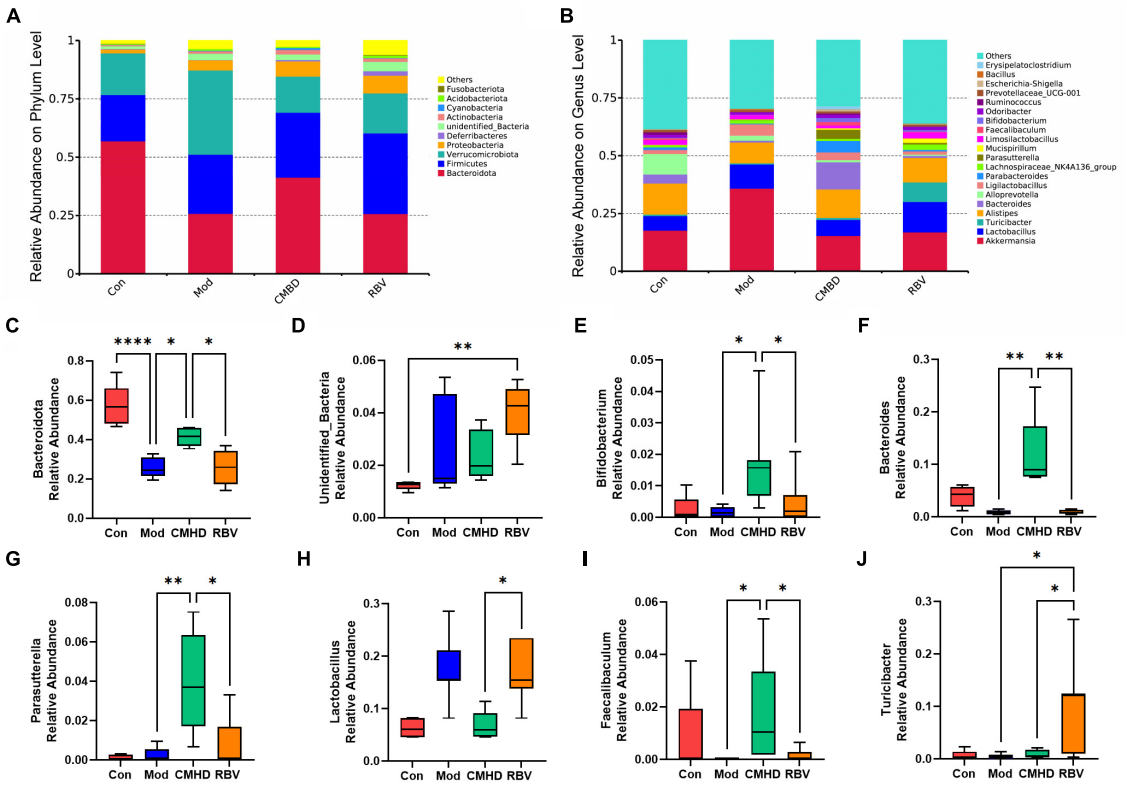

FIGURE 6
CMHD granules altered the dominant bacteria and microbiota composition in IAV-infected mice. The percentage of community abundance at the phylum **(A)** and genus **(B)** levels in the control (Con), the model (Mod), the CMHD granules administration (CMHD), and the Ribavirin administration groups (RBV). Data were shown as relative abundance (%) of the top 10 abundant phylum and top 20 abundant genera in each group. **(C–J)** Significant different bacterium among the Con, Mod, CMHD, and RBV groups. Statistical analysis was performed using the one-way ANOVA. $^{*}P < 0.05$, $^{**}P < 0.01$, $^{****}P < 0.0001$.

of CMHD granules is associated with its regulatory role in either inflammatory response or lung injury.

Previous studies showed that TCM has anti-inflammatory and antioxidant effects in RNA virus infections. Yang et al. reported that different TCM compounds have inhibitory effects on the gene levels of the pro-inflammatory cytokine, including TNF-α, IL-6, CCL-2, and IFN-γ in coronavirus (SARS-CoV-2) infection (Runfeng et al., 2020; Ma et al., 2021). Our study demonstrated that CMHD granules inhibit the release of pro-inflammatory factors, including TNF-α, IL-1β, and IFN-γ, promote the release of anti-inflammatory factor IL-10, and reduce oxidative stress after IAV infection. The increased levels of inflammatory cytokines and reactive oxygen species after IAV infection activate apoptosis and autophagy *in vivo* (Mehrbod et al., 2019). Thus, the endogenous apoptosis pathways, which are strictly controlled by Bcl-2 gene family of proteins, were also evaluated in this study. We found that the ratio of cell death agonists, Bax, vs. cell death antagonists, Bcl-2, decreased after CMHD and Ribavirin administration, alongside the decreased level of executioner caspases, caspase-3. However, as a previous study pointed out that the gut bacteria are necessary for the initiation and maintenance of tissue repair but are unnecessary for the rapid drug-mediated apoptosis as a chemotherapeutic drug's mechanisms (Rigby et al., 2016), and whether the regulation of apoptosis and gut bacteria after CMHD administration is in a parallel or causal relationship needs to be verified in the future.

The influence of the gut microbiota on the pathogenicity of the influenza virus is profound as it can not only affect viral infections in the gastrointestinal system but also produce metabolites or influence different lymphocytes to modulate influenza infections in the lung (Ivanov et al., 2009). Studies have proved the protective effects of gut microbiota against respiratory and systemic infection, especially after influenza virus infection (Brown et al., 2017). In our study, it is notable that the shifted microbiota diversity and composition after CMHD administration tended to be similar to the control. In contrast, the alternation after Ribavirin administration was similar to those in the model group, particularly in the NMDA analysis. We found no statistical difference in the α-diversity between infected and uninfected mice, which is consistent with previous studies. However, they have pointed out the

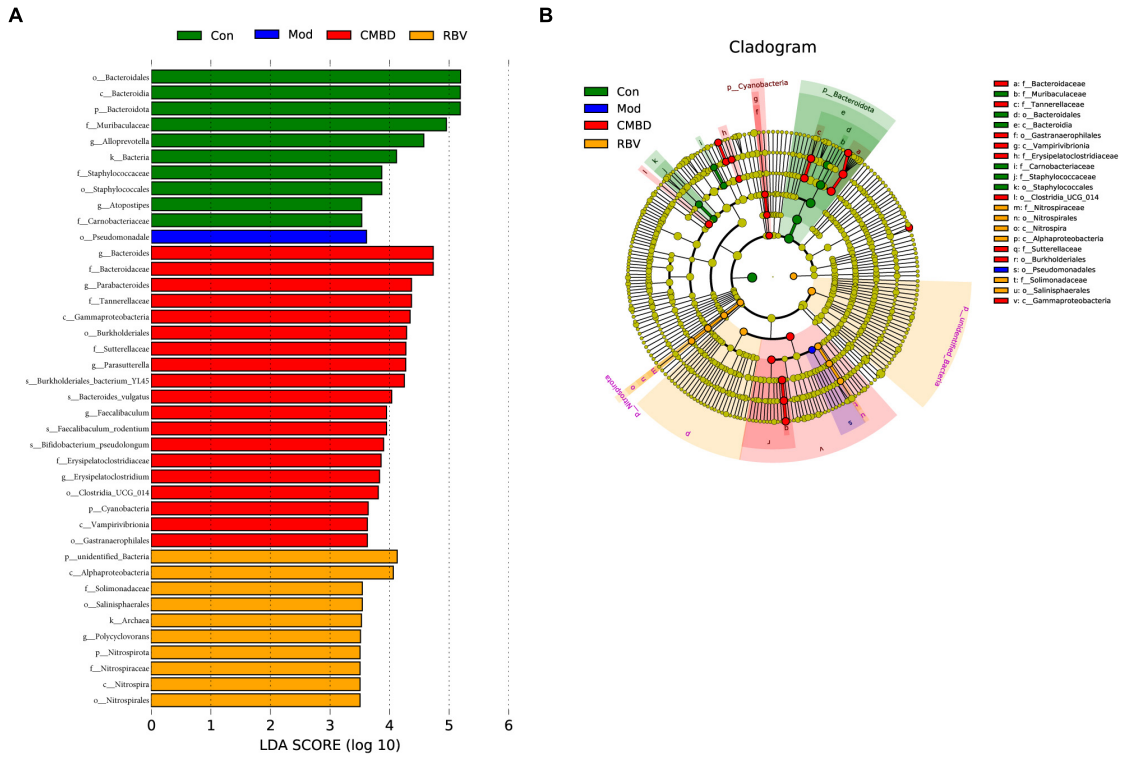

FIGURE 7
Linear discriminant analysis (LDA) integrated with effect size (LEfSe). **(A)** The differences in abundance among the control (Con), the model (Mod), the CMHD granules administration (CMHD), and the Ribavirin administration groups (RBV). **(B)** Cladogram indicating the phylogenetic distribution of microbiota correlated with each group.

reduction of commensal community richness (Yildiz et al., 2018) and the different α-diversity between the IAV infected-death and infected-survival mice (Zhang et al., 2020). Although the ACE index of α-diversity increased after Ribavirin compared with CMHD administration, this is likely due to the increased abundance of unidentified_Bacteria rather than the beneficial commensal community.

We identified a series of genera characteristics of gut microbes that are closely related to CMHD or Ribavirin administration in IAV-infected mice, including *Bifidobacteria*, *Lactobacillus*, *Bacteroides*, *Parasutterella*, *Faecalibaculum*, and *Turicibacter*. *Bifidobacteria* and *Lactobacillus* are common probiotic strains, which have been successfully applied in the food and pharmaceutical industries. Several of them confirmed to have protective effects on IAV infection, including *Bifidobacterium animalis* (Zhang et al., 2020), *Bifidobacterium longum* (Kawahara et al., 2015), and *Lactobacillus rhamnosus* (Villena et al., 2012). The gut population of endogenous *B. animalis* expanded to enhance host influenza resistance during lethal influenza infection. Oral administration of *B. animalis* alone or with *B. pseudolongum* combination significantly increased the survival rate of infected mice (Zhang et al., 2020). Li et al. demonstrated through fecal transplantation experiments that part of the mechanisms of immune regulation of TCM after influenza virus infection is *via* gut microbiota (Deng et al., 2021). Apparently, the significant upregulation of *Bifidobacterium* and *Bifidobacterium_pseudolongum* abundance by CMHD administration was beneficial, which might be one of its mechanisms in treating IAV infection. However, Ribavirin has a better effect on the upregulation of *Lactobacillus* abundance than CMHD. We also found a higher abundance of *Bacteroides*, *Parasutterella*, and *Faecalibaculum* after CMHD administration. *Bacteroides* are beneficial bacteria, which metabolize polysaccharides and oligosaccharides and provide nutrition and vitamins to the host (Zafar and Saier, 2021). A previous study reported preferentially deleted *Bacteroides* in IAV infection mice, which was speculated to be a reason for superinfection sensitivity following IAV infection (Yildiz et al., 2018). There are limited reports on the role of *Parasutterella* and *Faecalibaculum* in influenza infection. However, under other disease conditions, *Parasutterella*, as a succinate producer, played an important role in bile acid maintenance and cholesterol metabolism (Ju et al., 2019), and *Faecalibaculum*, as a short-chain fatty acids producer, reduced tumor growth (Zagato et al., 2020). The effect of Ribavirin on the increase of the bacterial abundance of *Turicibacter* was more significant than

that of CMHD. *Turicibacter* is a common genus of Firmicutes, which is closely related to lipid and carbohydrate metabolism. As a potential beneficial genus, studies showed that *Turicibacter* protects the host from chronic and inflammatory diseases (Wang et al., 2021b). Based on these aforementioned findings, we speculated that the mechanism of CMHD granules is related to the alternation of the microbiota structure and some specific microbiota in the intestine.

Conclusion

Our study provided a novel and effective TCM compound, CMHD granules, for treating lethal influenza. Although the administration of the positive drug Ribavirin showed an excellent effect in reducing viral load, CMHD granules exhibited similar effects on reducing mortality and alleviating lung injury after IAV infection. Our study further underlined the crucial mechanisms of CMHD granules, including reducing virus load, overwhelmed inflammatory responses, oxidative stress, and apoptosis. In addition to these, CMHD granules displayed pronounced beneficial effects on regulating the diversity and composition of gut microbiota after IAV infection. Noteworthy, bacterium protecting hosts against extraintestinal infections, including *Bifidobacterium*, *Bifidobacterium_pseudolongum*, and *Bacteroides*, became more abundant after CMHD granules administration. Nevertheless, Ribavirin showed a better effect on up-regulating the abundance of *Lactobacillus* and some potentially beneficial bacteria, such as *Turicibacter*. In general, this promising example of TCM compound protected hosts against severe influenza, which is comparable to Ribavirin.

Data availability statement

The data presented in this study are deposited in the SRA database, accession number PRJNA860266.

Ethics statement

The animal study was reviewed and approved by the Experimental Animal Ethics Committee of Yangzhou University (No. 202103-009).

Author contributions

XX and QL designed the research. ML, TL, XW, CY, TQ, and JL performed the experiments. MZ, ZL, and XC analyzed the data. ML, TL, and XW wrote the manuscript. All authors contributed to the article and approved the submitted version.

Funding

This work was supported by the special project of National Natural Science Foundation of China (82141202), the National Interdisciplinary Innovation Team of TCM under the State Administration of TCM (ZYYCXTD-D-202201), the financial project of Beijing Municipal Health Commission (No. 11000022T000000425863), and the Priority Academic Program Development of Jiangsu Higher Education Institutions (PAPD).

Acknowledgments

We thank the pharmacy of Beijing Hospital of TCM for providing the herbs in this study.

Conflict of interest

The authors declare that the research was conducted in the absence of any commercial or financial relationships that could be construed as a potential conflict of interest.

Publisher's note

References

Bradley, K. C., Finsterbusch, K., Schnepf, D., Crotta, S., Llorian, M., Davidson, S., et al. (2019). Microbiota-Driven tonic interferon signals in lung stromal cells protect from influenza virus infection. *Cell Rep.* 28, 245–256.e4. doi: 10.1016/j.celrep.2019.05.105

Bridges, C. B., Kuehnert, M. J., and Hall, C. B. (2003). Transmission of influenza: implications for control in health care settings. *Clin. Infect. Dis.* 37, 1094–1101. doi: 10.1086/378292

Brown, R. L., Sequeira, R. P., and Clarke, T. B. (2017). The microbiota protects against respiratory infection via GM-CSF signaling. *Nat. Commun.* 8:1512. doi: 10.1038/s41467-017-01803-x

Cho, I., and Blaser, M. J. (2012). The human microbiome: at the interface of health and disease. *Nat. Rev. Genet.* 13, 260–270. doi: 10.1038/nrg3182

Chung, E. Y., Kim, S. J., and Ma, X. J. (2006). Regulation of cytokine production during phagocytosis of apoptotic cells. *Cell Res.* 16, 154–161. doi: 10.1038/sj.cr.7310021

Cui, X. R., Guo, Y. H., and Liu, Q. Q. (2022). Cangma Huadu granules, a new drug with great potential to treat coronavirus and influenza infections, exert its efficacy through anti-inflammatory and immune regulation. *J. Ethnopharmacol.* 287:114965. doi: 10.1016/j.jep.2021.114965

Deng, L., Shi, Y., Liu, P., Wu, S., Lv, Y., Xu, H., et al. (2021). GeGen QinLian decoction alleviate influenza virus infectious pneumonia through intestinal flora. *Biomed. Pharmacother.* 141:111896. doi: 10.1016/j.biopha.2021.111896

Ge, H., Wang, Y. F., Xu, J., Gu, Q., Liu, H. B., Xiao, P. G., et al. (2010). Anti-influenza agents from traditional chinese medicine. *Nat. Prod. Rep.* 27, 1758–1780. doi: 10.1039/c0np00005a

Herold, S., Becker, C., Ridge, K. M., and Budinger, G. R. (2015). Influenza virus-induced lung injury: pathogenesis and implications for treatment. *Eur. Respir. J.* 45, 1463–1478. doi: 10.1183/09031936.00186214

Hu, X., Guo, J., Zhao, C., Jiang, P., Maimai, T., Yanyi, L., et al. (2020). The gut microbiota contributes to the development of *Staphylococcus aureus*-induced mastitis in mice. *ISME J.* 14, 1897–1910. doi: 10.1038/s41396-020-0651-1

Huang, K., Zhang, P., Zhang, Z., Youn, J. Y., Wang, C., Zhang, H., et al. (2021). Traditional Chinese Medicine (TCM) in the treatment of COVID-19 and other viral infections: Efficacies and mechanisms. *Pharmacol. Ther.* 225:107843. doi: 10.1016/j.pharmthera.2021.107843

Ichinohe, T., Pang, I. K., Kumamoto, Y., Peaper, D. R., Ho, J. H., Murray, T. S., et al. (2011). Microbiota regulates immune defense against respiratory tract influenza A virus infection. *Proc. Natl. Acad. Sci. U.S.A.* 108, 5354–5359. doi: 10.1073/pnas.1019378108

Ivanov, I. I., Atarashi, K., Manel, N., Brodie, E. L., Shima, T., Karaoz, U., et al. (2009). Induction of intestinal Th17 cells by segmented filamentous bacteria. *Cell* 139, 485–498. doi: 10.1016/j.cell.2009.09.033

Ju, T., Kong, J. Y., Stothard, P., and Willing, B. P. (2019). Defining the role of Parasutterella, a previously uncharacterized member of the core gut microbiota. *ISME J.* 13, 1520–1534. doi: 10.1038/s41396-019-0364-5

Kalil, A. C., and Thomas, P. G. (2019). Influenza virus-related critical illness: pathophysiology and epidemiology. *Crit. Care* 23:258. doi: 10.1186/s13054-019-2539-x

Kawahara, T., Takahashi, T., Oishi, K., Tanaka, H., Masuda, M., Takahashi, S., et al. (2015). Consecutive oral administration of *Bifidobacterium longum* MM-2 improves the defense system against influenza virus infection by enhancing natural killer cell activity in a murine model. *Microbiol. Immunol.* 59, 1–12. doi: 10.1111/1348-0421.12210

Klomp, M., Ghosh, S., Mohammed, S., and Nadeem Khan, M. (2021). From virus to inflammation, how influenza promotes lung damage. *J. Leukoc. Biol.* 110, 115–122. doi: 10.1002/JLB.4RU0820-232R

Krammer, F., Smith, G. J. D., Fouchier, R. A. M., Peiris, M., Kedzierska, K., Doherty, P. C., et al. (2018). Influenza. *Nat. Rev. Dis. Primers* 4:3. doi: 10.1038/s41572-018-0002-y

Li, J. H., Wang, R. Q., Guo, W. J., and Li, J. S. (2016). Efficacy and safety of traditional Chinese medicine for the treatment of influenza A (H1N1): a meta-analysis. *J. Chin. Med. Assoc.* 79, 281–291. doi: 10.1016/j.jcma.2015.10.009

Lin, T. L., Lu, C. C., Lai, W. F., Wu, T. S., Lu, J. J., Chen, Y. M., et al. (2021). Role of gut microbiota in identification of novel TCM-derived active metabolites. *Protein Cell* 12, 394–410. doi: 10.1007/s13238-020-00784-w

Ma, Q., Xie, Y., Wang, Z., Lei, B., Chen, R., Liu, B., et al. (2021). Efficacy and safety of ReDuNing injection as a treatment for COVID-19 and its inhibitory effect against SARS-CoV-2. *J. Ethnopharmacol.* 279:114367. doi: 10.1016/j.jep.2021.114367

McCullers, J. A., and Bartmess, K. C. (2003). Role of neuraminidase in lethal synergism between influenza virus and *Streptococcus pneumoniae*. *J. Infect. Dis.* 187, 1000–1009. doi: 10.1086/368163

Mehrbod, P., Ande, S. R., Alizadeh, J., Rahimizadeh, S., Shariati, A., Malek, H., et al. (2019). The roles of apoptosis, autophagy and unfolded protein response in arbovirus, influenza virus, and HIV infections. *Virulence* 10, 376–413. doi: 10.1080/21505594.2019.1605803

Morens, D. M., and Taubenberger, J. K. (2019). Making universal influenza vaccines: lessons from the 1918 Pandemic. *J. Infect. Dis.* 219, S5–S13. doi: 10.1093/infdis/jiy728

Peteranderl, C., Herold, S., and Schmoldt, C. (2016). Human influenza virus infections. *Semin. Respir. Crit. Care Med.* 37, 487–500. doi: 10.1055/s-0036-1584801

Rigby, R. J., Carr, J., Orgel, K., King, S. L., Lund, P. K., and Dekaney, C. M. (2016). Intestinal bacteria are necessary for doxorubicin-induced intestinal damage but not for doxorubicin-induced apoptosis. *Gut Microbes* 7, 414–423. doi: 10.1080/19490976.2016.1215806

Runfeng, L., Yunlong, H., Jicheng, H., Weiqi, P., Qinhai, M., Yongxia, S., et al. (2020). Lianhuaqingwen exerts anti-viral and anti-inflammatory activity against novel coronavirus (SARS-CoV-2). *Pharmacol. Res.* 156:104761. doi: 10.1016/j.phrs.2020.104761

Schuijt, T. J., Lankelma, J. M., Scicluna, B. P., de Sousa e Melo, F., Roelofs, J. J., de Boer, J. D., et al. (2016). The gut microbiota plays a protective role in the host defence against *Pneumococcal* pneumonia. *Gut* 65, 575–583. doi: 10.1136/gutjnl-2015-309728

Sequeira, R. P., McDonald, J. A. K., Marchesi, J. R., and Clarke, T. B. (2020). Commensal Bacteroidetes protect against *Klebsiella pneumoniae* colonization and transmission through IL-36 signalling. *Nat. Microbiol.* 5, 304–313. doi: 10.1038/s41564-019-0640-1

Steed, A. L., Christophi, G. P., Kaiko, G. E., Sun, L., Goodwin, V. M., Jain, U., et al. (2017). The microbial metabolite *Desaminotyrosine* protects from influenza through type I interferon. *Science* 357, 498–502. doi: 10.1126/science.aam5336

Stefan, K. L., Kim, M. V., Iwasaki, A., and Kasper, D. L. (2020). Commensal microbiota modulation of natural resistance to virus infection. *Cell* 183, 1312.e–1324.e. doi: 10.1016/j.cell.2020.10.047

Stegelmeier, A. A., van Vloten, J. P., Mould, R. C., Klafuric, E. M., Minott, J. A., Wootton, S. K., et al. (2019). Myeloid cells during viral infections and inflammation. *Viruses* 11:168. doi: 10.3390/v11020168

Valdes, A. M., Walter, J., Segal, E., and Spector, T. D. (2018). Role of the gut microbiota in nutrition and health. *BMJ* 361:k2179. doi: 10.1136/bmj.k2179

Villena, J., Chiba, E., Tomosada, Y., Salva, S., Marranzino, G., Kitazawa, H., et al. (2012). Orally administered *Lactobacillus rhamnosus* modulates the respiratory immune response triggered by the viral pathogen-associated molecular pattern poly(I:C). *BMC Immunol.* 13:53. doi: 10.1186/1471-2172-13-53

Wang, X., Xu, X., Chen, Y., Li, Z., Zhang, M., Zhao, C., et al. (2021a). Liu shen capsule alters airway microbiota composition and metabolite profiles in healthy humans. *Front. Pharmacol.* 12:824180. doi: 10.3389/fphar.2021.824180

Wang, X., Ye, P., Fang, L., Ge, S., Huang, F., Polverini, P. J., et al. (2021b). Active smoking induces aberrations in digestive tract microbiota of rats. *Front. Cell Infect. Microbiol.* 11:737204. doi: 10.3389/fcimb.2021.737204

Wang, X., Xu, X., Guo, Y., Huang, P., Ha, Y., Zhang, R., et al. (2020). Qiang xin 1 formula suppresses excessive pro-inflammatory cytokine responses and microglia activation to prevent cognitive impairment and emotional dysfunctions in experimental sepsis. *Front. Pharmacol.* 11:579. doi: 10.3389/fphar.2020.00579

Xu, X., Liu, Q., He, S., Zhao, J., Wang, N., Han, X., et al. (2018). Qiang-Xin 1 formula prevents sepsis-induced apoptosis in murine *Cardiomyocytes* by Suppressing Endoplasmic Reticulum- and Mitochondria-Associated Pathways. *Front. Pharmacol.* 9:818. doi: 10.3389/fphar.2018.00818

Yildiz, S., Mazel-Sanchez, B., Kandasamy, M., Manicassamy, B., and Schmolke, M. (2018). Influenza A virus infection impacts systemic microbiota dynamics and causes quantitative enteric dysbiosis. *Microbiome* 6:9. doi: 10.1186/s40168-017-0386-z

Zafar, H., and Saier, M. J. (2021). Gut *Bacteroides* species in health and disease. *Gut Microbes* 13, 1–20. doi: 10.1080/19490976.2020.1848158

Zagato, E., Pozzi, C., Bertocchi, A., Schioppa, T., Saccheri, F., Guglietta, S., et al. (2020). Endogenous murine microbiota member *Faecalibaculum rodentium* and its human homologue protect from intestinal tumour growth. *Nat. Microbiol.* 5, 511–524. doi: 10.1038/s41564-019-0649-5

Zhang, Q., Hu, J., Feng, J. W., Hu, X. T., Wang, T., Gong, W. X., et al. (2020). Influenza infection elicits an expansion of gut population of endogenous *Bifidobacterium animalis* which protects mice against infection. *Genome Biol.* 21:99. doi: 10.1186/s13059-020-02007-1

frontiers | Frontiers in Microbiology

TYPE Original Research
PUBLISHED 09 August 2022
DOI 10.3389/fmicb.2022.973278

OPEN ACCESS

EDITED BY
Bhupesh K. Prusty,
Julius Maximilian University of Würzburg, Germany

REVIEWED BY
Jianqiang Ye,
Yangzhou University, China
Liu Sidang,
Shandong Agricultural University, China

*CORRESPONDENCE
Yongqing Li
chunyudady@sina.com

SPECIALTY SECTION
This article was submitted to Virology, a section of the journal Frontiers in Microbiology

RECEIVED 20 June 2022
ACCEPTED 25 July 2022
PUBLISHED 09 August 2022

CITATION
Jiang B, Wang J, Liu W, Cheng J, Xu J, Cao M and Li Y (2022) Comparative transcriptome analysis of MDBK cells reveals that BoIFN-γ augmented host immune responses to bovine herpesvirus 1 infection.
Front. Microbiol. 13:973278.
doi: 10.3389/fmicb.2022.973278

Comparative transcriptome analysis of MDBK cells reveals that BoIFN-γ augmented host immune responses to bovine herpesvirus 1 infection

Bo Jiang[1], Jing Wang[1], Wenxiao Liu[1], Jing Cheng[1], Jian Xu[2], Mengyao Cao[1,3] and Yongqing Li[1]*

[1]Institute of Animal Husbandry and Veterinary Medicine, Beijing Academy of Agricultural and Forestry Sciences, Beijing, China, [2]Lanzhou Veterinary Research Institute, Chinese Academy of Agricultural Sciences, Lanzhou, China, [3]Animal Science and Technology College, Beijing University of Agriculture, Beijing, China

Bovine herpesvirus 1 (BoHV-1) is an alphaherpesvirus that causes infectious bovine rhinotracheitis and infectious pustular vulvovaginitis in cattle. Interferon-gamma (IFN-γ) is a pleiotropic cytokine with antiviral activity that modulates the innate and adaptive immune responses. In this study, we prepared high-purity bovine interferon gamma (BoIFN-γ) dimer protein using prokaryotic expression system and affinity chromatography. We subsequently investigated the effect of BoIFN-γ on BoHV-1 infection in Madin-Darby bovine kidney (MDBK) cells. The results showed that BoIFN-γ pre-treament not only decreased the production of BoHV-1 but also reduced the cytopathic effect of the virus. Differential gene expression profiles of BoHV-1 infected MDBK cells were then analysed through high-throughput RNA sequencing. The data showed that BoIFN-γ pre-treatment reduced lipid metabolism disorder and DNA damage caused by BoHV-1 infection. Furthermore, BoIFN-γ treatment upregulated the transcription of interferon regulatory transcription factors (IRF1 and GBP5) and interferon-stimulated genes (ISGs) of MDBK cells. Additionally, BoIFN-γ promotes expression of cellular protein involved in complement activation and coagulation cascades response as well as antigen processing and presentation process, while BoHV-1 infection dramatically downregulates transcription of these immune components including C3, C1r, C1s, PLAT, ITGB2, PROCR, BoLA, CD74, B2M, PA28, BoLA-DRA, and TAPBP. Collectively, our findings revealed that BoIFN-γ pre-treatment can improve host resistance to BoHV-1 infection and regulate transcription or expression of host protein associated with cellular metabolism and innate immune response. This provides insights into the development of prophylactic agents for prevention and control of BoHV-1 infection.

KEYWORDS

bovine herpesvirus 1, interferon-gamma, RNA-Seq, pathogen–host interactions, immune response

Introduction

Bovine herpesvirus-1 (BoHV-1), a member of the *Alphaherpesvirinae* subfamily, causes immunosuppression and rhinotracheitis, encephalitis and genital lesions and has led to significant economic loss to the cattle industry worldwide (Muylkens et al., 2007; Rola et al., 2017; Thakur et al., 2017). One key characteristic of BoHV-1 infection is the establishment of latency. Latent viruses are reactivated after cattle are exposed to natural stimuli or corticosteroid treatment. Although vaccination can offer effective protection against the clinical disease, it is difficult to prevent the excretion of recrudescent viruses from latent status (Biswas et al., 2013). BoHV-1 is a successful pathogen because it impairs intrinsic and innate immune responses through encoding genes related to immune-evasion (Jones, 2019). For instance, bICP0 encoded by the IEtu1 promoter plays a role as early interferon antagonist (Saira et al., 2007, 2009). bICP27 is manifested as an inhibitor of IFN-β promoter activation phenomenally (da Silva et al., 2012). Late protein VP8 is a potent IFN antagonist that can disrupt host innate immune responses in the absence of viral protein synthesis (Afroz et al., 2016). gG and UL49.5 would also further antagonise immune-recognition. Since BoHV-1 inhibits immune responses in hosts, it can result in secondary bacterial infection and vaccine breaks (Jones, 2019). Therefore, the severity of disease caused by BoHV-1 is more complicated than its clinical manifestation.

It has previously been demonstrated that the bovine immune response is crucial for the regulation of BoHV-1 latency reactivation (Jones, 2019). BoHV-1 infection stimulates innate and adaptive immune cells to secrete cytokines and antibodies (Decman et al., 2005). One of these is interferon-γ (IFN-γ) which induces or inhibits a number of cellular functions by directly affecting gene expression in many cell types. IFN-γ is important in immune modulation and broad-spectrum pathogen defence, and was originally identified as a secretory factor interfering with viral replication (Kang et al., 2018). Basic components of IFN-γ signalling pathway are defined, activation of IFN-γ signals mainly *via* the Janus kinase (JAK)—signal transducer and activator of transcription (STAT) intracellular signal transduction. Once IFN-γ binds to the receptor, the tyrosine kinases JAK1 and JAK2 phosphorylate the transcription factor (TF) signal transducer and activator of transcription 1 (STAT1), result in nuclear translocation and regulate transcriptions of IFN-γ-inducible genes (Muller et al., 1993; Hu et al., 2021). The activation of the JAK–STAT signalling pathway by IFNs leads to the upregulation of a series of interferon-stimulated genes (ISGs), many of which exert antiviral effect on infected cells (Ezeonwumelu et al., 2021). Increasingly, evidence confirms that IFN-γ acts as a pivotal factor in host defence against double-stranded DNA viruses. Host-derived IFN-γ interferes with viral replication by inhibiting transcription and translation of viral genes (Malmgaard, 2004; Schoenborn and Wilson, 2007). For example, in human papillomavirus (HPV) infection, IFN-γ reduces proteolysis of leucocyte L1 protein, leading to retention of the minor capsid protein L2/genome complex in the late endosome, subsequently inhibiting translocation of the dissociated L2/genome complex into the nucleus for genome replication (Day et al., 2017). Induction of nitric oxide synthase by IFN-γ, and consequent nitric oxide production, was shown to mediate the blocking of vaccinia virus replication after early gene expression (Harris et al., 1995). IFN-γ restricts herpes simplex virus type 1 (HSV-1) reactivation by direct and indirect mechanisms. IFN-γ inhibits HSV-1 mRNA accumulation and the subsequent steps of the viral life cycle including early and late gene expression, viral DNA synthesis and viral replication (Pierce et al., 2005). $CD8^+$ T cells producing IFN-γ have been shown to directly suppress immediate early (IE) gene expression and prevent HSV-1 reactivation from latency in neurons (Decman et al., 2005). Accordingly, IFN-γ plays a protective role in acute infection with DNA viruses, especially herpesviruses, but little is known about the role of BoIFN-γ in BoHV-1 infection.

In the present study, we prepared and purified the BoIFN-γ protein in *Escherichia coli* and analysed how pre-treatment with recombinant BoIFN-γ affected BoHV-1 replication in MDBK cells. We further explored the antiviral mechanisms of BoIFN-γ by differential gene expression (DGE) profile to compare gene expression in BoHV-1 infected MDBK cells with and without IFN-γ pre-treatment. The results revealed that BoIFN-γ effectively alleviated MDBK cells from alteration of cellular proteins involved in DNA damage, lipid metabolism disorder and immunocompromise caused by BoHV-1 infection.

Materials and methods

High purity BoIFN-γ production

The Bovine IFN-γ (BoIFN-γ) gene encoding 122 amino acids was synthesised by Shenggong Life Technologies (Shanghai) according to the sequence released in GenBank (EU276066, nucleotides 24–390) and ligated into the pET-21a(+) vector (Novagen, Merck KGaA, Darmstadt, Germany) and transformed into Escherichia coli strain BL21 (DE3; Supplementary Table 1). The soluble Bovine IFN-γ protein was prepared as described previously with some modifications (Chen et al., 2010). The BoIFN-γ inclusion bodies were gradually dissolved in the refolding buffer (100 mM Tris–HCl, 2 mM EDTA, 400 mM l-arginine-HCl, 0.5 mM oxidised glutathione and 5 mM reduced glutathione pH 8.0). The soluble BoIFN-γ was purified by gel filtration using a Superdex 200 size exclusion column (GE Healthcare) and anion-exchange chromatography using Resource-Q (GE Healthcare).

Plaque reduction test of BoIFN-γ

MDBK cell was purchased from the American Type Culture Collection (Manassas, VA, United States). MDBK Cells seeded

into 6-well plates at 1×10^6 cells/well were incubated overnight at 37°C, treated with BoIFN-γ in 0.5 μg/well for 12 h and infected with 2 ml BoHV-1 ($400TCID_{50}$/ml) incubated at 37°C and 5% CO_2 for 1.5 h. An agarose overlay was added to the infected cell monolayer after the virus mixture was removed. The cells were further incubated for 48 h after the layer solidified. When viral plaques became visible, 4% formaldehyde was added to the plate, and viral plaques were counted using 0.1% toluidine blue in saline.

Cytotoxicity of BoIFN-γ to MDBK cells

MDBK cells were seeded in 6-well plates and cultured to 70% confluency at 37°C for 18–24 h. Then, 1 ml of BoIFN-γ with different concentrations (10, 100, 1,000 U/ml) was added to the culture medium, respectively. Followed by cultivation at 37°C for 12 h, we change the medium containing BoIFN-γ to fresh maintenance medium. Cell proliferation was tested with the CellTiter 96 Aqueous One Solution Cell Proliferation Assay (MTS) Kit (Promega) according to the manufacturer's instructions, and the OD490 values of the test wells were read with a microplate reader. All tests were performed in triplicate.

Antiviral activity of BoIFN-γ

The cytopathic inhibition assay was employed to test the antiviral activity of BoIFN-γ on the MDBK cell line. Briefly, Monolayers of MDBK cells were prepared in 96-well plates. The cells were pre-treated with tenfold serial dilutions of the purified BoIFN-γ and incubated 12 h at 37°C 5% CO2 with the maintenance medium (DMEM with 2% foetal bovine serum). The medium containing BoIFN-γ diluent was removed and cells were washed twice with the DMEM medium.100 TCID50 of BoHV-1 was added to cells and absorbed for 1.5 h at 37°C, then the inoculum was removed and cells were washed twice with PBS. And fresh maintenance medium was added to each well and incubated as before (37°C in a CO2 incubator) for 2–3 days. Subsequently, viral CPEs were observed and recorded under an inverted microscope. The unit of antiviral activity was calculated based on the highest dilution that 50% CPE in the cell sheet was inhibited. Each dilution of purified BoIFN-γ was determined in 8 repeats.

Replication dynamics of BoHV-1 in MDBK pre-treated by BoIFN-γ

After treated with different doses of BoIFN-γ for 12 h, the MDBK cells seeded in 6-well plates were infected with 2 × 105TCID50 of BoHV-1, and viral DNA was isolated from cell and supernatants at different time points. Each experiment was repeated three times. The fluorescence quantitative PCR (FQ-PCR) was performed to calculate DNA copy numbers of BoHV-1in cells using SYBR Green PCR master mix based on gB gene as template (gB PF: 5-GCGAGGAAGAGGAGGAGT-3; gB PR: 5-CATCGGAAGCTGCTGGTAC-3). Viral end-point titration was performed to measure progeny virus titre from supernatants. 50% tissue culture infective dose (TCID50) was determined by Reed–Muench method.

High-throughput RNA-sequencing

After pre-treatment with 1,000 U/ml BoIFN-γ for 12 h, MDBK cells seeded in 6-well plates were incubated with 2 × 105TCID50 BoHV-1 for 1.5 h and then cultured for 24 h in a maintained medium. Cells from four experimental groups were harvested at 24 h post BoHV-1 infection: Group MIV is infected with BoHV-1 only, group MgIV is pre-treated with BoIFN-γ for 12 h and then infected with BoHV-1, group Mg is pre-treated with BoIFN-γ without BoHV-1 infection and group Mock is control group. Following the instructions of TRIzol Reagent (Life Technologies; Carlsbad, CA, United States), total RNA was extracted from MDBK cells at 24 h post infection of BoHV-1, which were pre-treated with or without BoIFN-γ. The purity and fragment length of RNA was assessed using the NanoDrop spectrophotometer (Peqlab, United States) and Agilent 2,100 Bioanalyzer (Agilent Technologies; Böblingen, Germany). Oligo (dT) magnetic beads were used to enrich RNA. Following the first single strand of cDNA was synthesised, double-stranded cDNAs were purified and selected by AMPure XP beads (Beckman Coulter, Krefeld, Germany) and then construct the cDNA library. The insertion fragment size and the effective concentration were detected and accurately quantified by Agilent 2,100 Q-PCR to achieve the highest quality library standards. RNA-seq was obtained by using the Illumina high-throughput sequencing platform (NovaSeq 6,000) by the Beijing Allwegene Technology Company Limited (Beijing, China). Tophat2 software was utilised to compare the obtained sequence with the genome reference sequence. Fragments per kilobase of exon model per million mapped reads (FPKM) of each gene were analysed on the basis of length of the gene and read count mapped to this gene. Differential expression analysis was accomplished by employing DESeq. Each experiment was repeated 3 times.

Bioinformatics analysis of differentially expressed gene sets

GO enrichment analysis was performed by using Goseq software (v1.22). KEGG database (Kyoto Encyclopedia of Genes and Genomes)[1] was applied to study genes and expression information as a whole network, which contains biochemical metabolic pathway and signal transduction pathway. The pathway

1 http://www.kegg.jp

enrichment analysis of DGEs was analysed by KOBAS software (v2.0) on the KEGG database.[2]

Relative quantification of differentially expressed genes by quantitative reverse transcriptase PCR

The RNA used for detecting DGEs was further reverse transcribed into cDNA utilising the FastKing RT Kit (with DNase). The target gene expression levels were normalised to the β-actin gene as reference. A detailed list containing primers for target genes and β-actin is shown in Supplementary Table 2. The quantitative PCR (qPCR) was performed with the following conditions utilising the iTaq universal SYBR Green Supermix and CFX96 real-time system (Bio-Rad): initial denaturation was performed at 95°C for 1 min, followed by 40 cycles of denaturation at 95°C for 15 s and annealing/extension at 60°C for 1 min, with endpoint melting-curve analysis.

Statistical analysis

The data were statistically analysed using GraphPad Prism. The results were expressed as the mean ± SD or the mean ± SEM, as indicated. Statistical significance between experimental groups was assessed by one-way ANOVA with unpaired two-tailed t test or one-way ANOVA, *p*-value significance codes: ***0.001, **0.01, or *0.05.

Results

BoIFN-γ inhibits the replication of BoHV-1 in MDBK cells

A total of 6.68 mg of protein was obtained after refolding a 50 mg BoIFN-γ inclusion body. The refolding efficiency of BoIFN-γ inclusion bodies was 10%–13%. Considering the molecular mass of the BoIFN-γ monomer (14.2 kDa), peak 1 (about 28.4 kDa) from size-exclusion chromatography corresponded to a BoIFN-γ dimer (Figure 1A). The protein was then purified by Resource-Q anion-exchange chromatography and the specific peak appeared at a NaCl concentration of 12%–15% (Figure 1A). About 12% SDS-PAGE gel analysis showed a single band corresponding to the expressed BoIFN-γ (14.2 kDa; Figure 1A, inset).

Results of plaque reduction test revealed that BoIFN-γ pre-treatment significantly reduced the number of plaques formed by BoHV-1 in MDBK cells ($p < 0.01$) (Figures 1B,C). The antiviral (BoHV-1) activity of BoIFN-γ in MDBK cells was 4.73 × 105 U/mg (Supplementary Table 3). When compared with the control group treated with phosphate-buffered saline (PBS), MDBK cells treated with three different concentrations of BoIFN-γ (10, 100, and 1,000 U/ml) displayed no obvious cytotoxicity (Supplementary Figure 1).

In order to investigate the replication dynamics of BoHV-1 when inhibited by different doses of BoIFN-γ, MDBK cells seeded in 6-well plates were pre-treated with BoIFN-γ or PBS and infected with 2 × 105TCID50 BoHV-1 for 48 h. Viruses were then isolated from cells and supernatants were obtained at different time points. We subsequently determined DNA copy numbers and titrations. As shown in Figures 1D,E, when compared with the control group, BoHV-1 replication trends were significantly reduced by BoIFN-γ in a dose-dependent manner, especially at 24 h post infection (Figure 1F). These results were verified by examination of the cytopathic effects under light microscopy (Figure 1G).

Evaluation of transcriptome sequencing data

At least 6.37 GB of clean data were obtained from each sample by transcriptome sequencing. After quality control, the data were further analysed for expression level by using the Illumina NovaSeq 6,000 platform. The Q30 percentages of clean data for all samples were higher than 91.54%, and the GC contents of the clean data for all samples ranged from 46.54% to 58.39% (Table 1). More than 41,496,306 clean reads were obtained from the Mock group, 45,106,246 clean reads from the MIV group, 35,438,468 clean reads from the MgIV group and 47,224, 594 clean reads from the Mg group. At least 92.43% of the clean reads from each panel without BoHV-1 and 63.15% from panels with BoHV-1 were successfully mapped to the bovine reference genome database. In addition, over 90.93% of the clean reads from each panel without BoHV-1 and 61.67% from panels with BoHV-1 were uniquely mapped to the bovine reference genome database. After FPKM standardisation, most of the unique clean reads show only 1 FPKM. Clean reads of more than 60 FPKM were 3–6% of each panel. The construction of DGE libraries is outlined in Table 2.

Identification of differentially expressed genes

Differentially expressed genes (DEGs) were identified from the different experimental panels (padj < 0.05, |Log2FC| > 1). BoHV-1 infection led to 3,566 upregulated and 3,328 downregulated genes compared to Mock. BoIFN-γ pre-treatment resulted in only 944 upregulated and 625 downregulated genes compared to Mock, and there were 2,925 DEGs in the MgIV to Mock comparison including 1,357

2 http://www.genome.jp/kegg

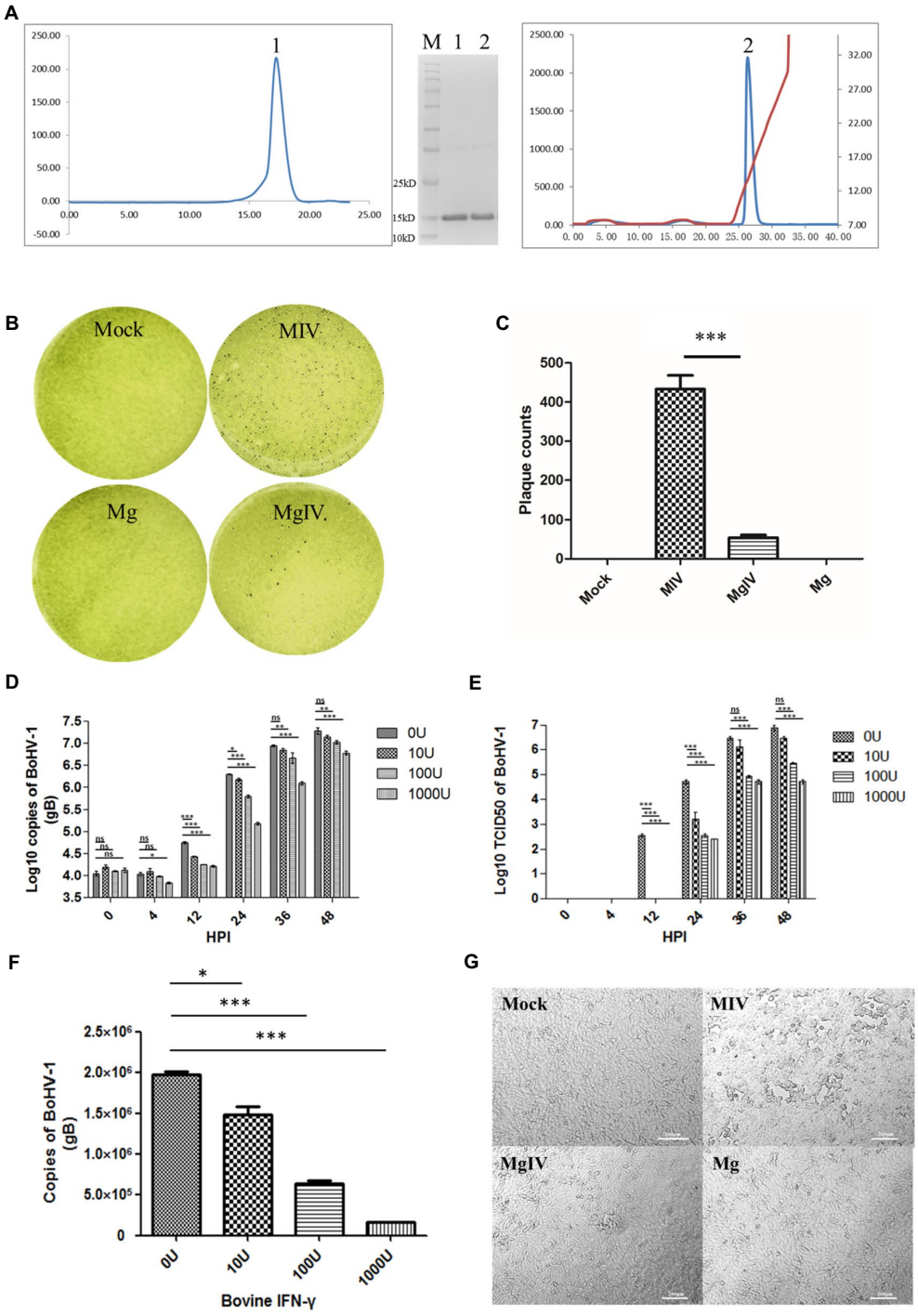

FIGURE 1
Preparation and antiviral activity of BoIFN-γ. **(A)** The expression and purification of BoIFN-γ, Left, Gel-filtration profile of the BoIFN-γ. Right, Results of further purification of the folded BoIFN-γ by anion-exchange chromatography. The protein was eluted at NaCl concentration of 12.0%–15.0%. Inset, reduced SDS-PAGE gel (15%) of the corresponding purified protein (14.2kDa). Lane M contains molecular-weight markers (labelled in kDa). **(B,C)** Plaque reduction test of the BoIFN-γ. Mock represents uninfected MDBK cells, MIV represents MDBK cells infected with BoHV-1 and pre-treated with PBS, Mg represents MDBK cells pre-treated with BoIFN-γ only, MgIV represents MDBK cells infected with BoHV-1 and pre-treated with BoIFN-γ. Viral plaques were counted using 0.1% toluidine blue in saline, and reverse the colour to show plaques more clearly. The data were analysed using SPSS software and one-way ANOVA, and the graph was made using GraphPad Prism 5.0. *** represented statistically statistically differences ($p<0.001$). ** represents statistically significant differences ($p<0.01$). * represents statistically very significant differences ($p<0.05$). **(D)** Replication curves of BoHV-1 in MDBK cells pre-treated with different doses of BoIFN-γ (10, 100, and 1,000U/ml) detected use FQ-PCR. **(E)** Replication curves of BoHV-1 in MDBK cells supernatants pre-treated with different doses of IFN-γ (10, 100, and 1,000U/ml) detected use $TCID_{50}$. **(F)** Replication of BoHV-1 in MDBK cells at 24h poster infection pre-treated with different doses of BoIFN-γ (10, 100, and 1,000U/ml) detected use FQ-PCR. **(G)** Changes in cellular morphology at 24 HPI. MIV is MDBK infected with BoHV-1 only, MgIV is MDBK pre-treated 1,000U/ml BoIFN-γ 12h and then infected BoHV-1, Mg is MDBK pre-treated BoIFN-γ without BoHV-1 infection, Mock is MDBK cell control.

TABLE 1 Summary statistics for sequence quality control and mapped data of sample.

Sample	Raw reads	Raw bases	Clean reads	Clean bases	Error rate	Q20 (%)	Q30 (%)	GC content	Total mapped	Multiple mapped	Uniquely mapped
Mock1	45,480,366	6.82G	44,378,466	6.66G	0.03%	97.95	93.85	51.30%	43,026,488 (96.95%)	555,090 (1.25%)	42,471,398 (95.7%)
Mock2	43,160,072	6.47G	41,496,306	6.22G	0.03%	97.89	93.64	50.56%	40,053,918 (96.52%)	552,862 (1.33%)	39,501,056 (95.19%)
Mock3	44,746,074	6.71G	42,915,262	6.44G	0.03%	97.80	93.38	46.54%	41,087,942 (95.74%)	608,852 (1.42%)	40,479,090 (94.32%)
MIV1	51,231,662	7.68G	45,106,246	6.77G	0.03%	97.53	93.65	53.06%	32,950,636 (73.05%)	407,372 (0.90%)	32,543,264 (72.15%)
MIV2	61,096,760	9.16G	58,418,608	8.76G	0.03%	96.56	91.82	50.74%	50,157,320 (85.86%)	581,446 (1.00%)	49,575,874 (84.86%)
MIV3	66,870,482	10.03G	59,595,576	8.94G	0.03%	97.41	93.22	51.08%	44,931,266 (75.39%)	537,322 (0.90%)	44,393,944 (74.49%)
Mg1	48,128,268	7.21G	47,224,594	7.08G	0.03%	96.80	91.54	48.18%	43,649,800 (92.43%)	709,602 (1.50%)	42,940,198 (90.93%)
Mg2	56,131,542	8.41G	55,139,968	8.27G	0.03%	97.74	93.41	51.71%	52,950,122 (96.03%)	886,668 (1.61%)	52,063,454 (94.42%)
Mg3	51,216,264	7.68G	50,164,130	7.52G	0.03%	97.76	93.43	51.75%	48,275,374 (96.23%)	787,168 (1.57%)	47,488,206 (94.67%)
MgIV1	48,724,732	7.30G	45,307,390	6.80G	0.03%	96.75	92.00	53.80%	35,637,234 (78.66%)	460,964 (1.02%)	35,176,270 (77.64%)
MgIV2	50,299,172	7.54G	45,154,366	6.77G	0.03%	96.88	92.41	54.28%	34,538,518 (76.49%)	467,382 (1.04%)	34,071,136 (75.45%)
MgIV3	42,525,170	6.37G	35,438,468	5.32G	0.03%	96.80	92.79	58.39%	22,380,332 (63.15%)	526,234 (1.48%)	21,854,098 (61.67%)

TABLE 2 Statistical table of the number of genes in different expression levels (fpkm.stat).

FPKM interval	Mock1	Mock2	Mock3	MIV1	MIV2	MIV3	Mg1	Mg2	Mg3	MgIV1	MgIV2	MgIV3
0~1	15,899 (55.11%)	15,730 (54.52%)	15,816 (54.82%)	15,812 (54.81%)	15,848 (54.93%)	15,808 (54.79%)	15,839 (54.90%)	16,035 (55.58%)	15,910 (55.15%)	15,597 (54.06%)	15,874 (55.02%)	17,479 (60.58%)
1~3	1984 (6.88%)	2024 (7.02%)	2,137 (7.41%)	2,768 (9.59%)	2,790 (9.67%)	2,785 (9.65%)	2,202 (7.63%)	2,195 (7.61%)	2,132 (7.39%)	2,626 (9.10%)	2,550 (8.84%)	2,406 (8.34%)
3~15	5,087 (17.63%)	5,204 (18.04%)	5,154 (17.86%)	5,613 (19.46%)	5,594 (19.39%)	5,655 (19.60%)	5,220 (18.09%)	5,102 (17.68%)	5,073 (17.58%)	5,406 (18.74%)	5,411 (18.75%)	4,749 (16.46%)
15~60	4,354 (15.09%)	4,393 (15.23%)	4,248 (14.72%)	3,744 (12.98%)	3,676 (12.74%)	3,697 (12.81%)	4,042 (14.01%)	3,920 (13.59%)	4,110 (14.25%)	4,096 (14.20%)	3,946 (13.68%)	2,944 (10.20%)
>60	1,527 (5.29%)	1,500 (5.20%)	1,496 (5.19%)	914 (3.17%)	943 (3.27%)	906 (3.14%)	1,548 (5.37%)	1,599 (5.54%)	1,626 (5.64%)	1,126 (3.90%)	1,070 (3.71%)	1,273 (4.41%)

upregulated and 1,386 downregulated genes. When compared with BoHV-1 infection only, BoIFN-γ pre-treated BoHV-1 infection generated nine upregulated genes and only 1 downregulated gene. Meanwhile, there were 1,448 upregulated and only 1,942 downregulated genes detected in the MgIV and Mg comparisons (Table 3). 1,291 upregulated genes were conserved in the BoHV-1 infected cells with and without BoIFN-γ pre-treatment, and 2,275 upregulated genes were specific for BoHV-1 infected, whereas only 66 upregulated genes were specific for the MgIV group. Correspondingly, 1,483 downregulated genes were shared by both samples with and without BoIFN-γ pre-treatment, 1,845 downregulated genes were specific for MIV group and only 85 downregulated genes were specific for MgIV group. Furthermore, 148 upregulated genes and 164 downregulated genes were common to the experimental groups MgIV and Mg. About 1,290 upregulated genes and 1,404 downregulated genes were specific for the experimental group MgIV and 796 upregulated genes and 461 downregulated genes were specific for the Mg group (Figure 2).

TABLE 3 Number of differentially expressed genes of samples.

Criteria	Groups				
	MIV vs. Mock	Mg vs. Mock	MgIV vs. Mock	MgIV vs. MIV	MgIV vs. Mg
padj < 0.05	Up: 4,502 Down: 4,156 Total: 8,658	Up: 1,350 Down: 1,055 Total: 2,405	Up: 1,357 Down: 1,568 Total: 2,925	Up: 9 Down: 1 Total: 10	Up: 1,488 Down: 1,942 Total: 3,430
padj < 0.05 $\lvert Log_2FC \rvert > 1$	Up: 3,566 Down: 3,328 Total: 6,894	Up: 944 Down: 625 Total: 1,569	Up: 1,357 Down: 1,568 Total: 2,925	Up: 9 Down: 1 Total: 10	Up: 1,488 Down: 1,942 Total: 3,430
padj < 0.05 $\lvert Log_2FC \rvert > 1.5$	Up: 1,248 Down: 1,424 Total: 2,672	Up: 579 Down: 216 Total: 795	Up: 1,248 Down: 1,424 Total: 1,672	Up: 9 Down: 1 Total: 10	Up: 1,318 Down: 1,694 Total: 3,012

Enrichment analysis of GO terms and KEGG pathway

To determine the functions related to DEGs, we analysed both the GO terms and KEGG pathways. GO classification revealed that the gene expressions altered by BoHV-1 infection were involved in many metabolic processes and cellular components including metabolic process, organic substance metabolic process, cellular metabolic process, organelle organisation, cytoplasm, nucleus, nucleoplasm, mitochondrion, and protein complexes associated with energy supply, such as the inner mitochondrial membrane protein complex and respiratory chain complex and other cellular components-related classifications (Figure 3A). This suggests that viral replication severely affects normal cell metabolism and composition, which is consistent with the cytopathic changes observed. DEGs in the MgIV group significantly enriched not only in metabolic processes and cellular components but also in many of the defence-related processes responsible for maintaining a steady state. These include the regulation of metabolic processes, responses to stress, apoptotic processes, the oxidation–reduction process and responses to cytokine and cellular respiration (Figure 3B). Although BoIFN-γ pre-treatment reduced visible cytopathic changes of MDBK caused by BoHV-1, cell metabolism and cellular component disorders still exist. As expected, regulated DEGs of the Mg group are almost all involved in the host defence-related response, including regulation of the stress response, response to stress, immune system process, response to external stimulus, immune response, innate immune response, interspecies interaction between organisms, extracellular region and major histocompatibility (MHC) protein complex, etc. (Figure 3C). In the comparison between MgIV and Mg groups, not only the metabolism-related processes and cellular components (i.e., metabolic process, organic substance metabolic process, cellular metabolic process, intracellular, organelle and intracellular organelle) were changed, but also many biological processes and cellular components associated with immune responses such as antigen processing and presentation, antigen processing and presentation of peptide antigen, MHC protein complex and MHC class II protein complex. The variety of processes may be seen in Figure 3D. Notably, in the comparison MIV group, MgIV primarily regulated GO terms related to cell cycle-related biology processes such as cell cycle, cell cycle process, mitotic cell cycle and regulation cell cycle process (Figure 3E).

The analysis of KEGG pathways revealed that the host response pathways were considerably (p value <0.05) affected in all comparison groups 24, 24, 31, 36, and 27 significantly DEG-enriched KEGG pathways were identified in comparison groups MIV vs. Mock, MgIV vs. Mock, Mg vs. Mock, MgIV vs. Mg, and MgIV vs. MIV, respectively, (Supplementary Tables 4–8). The MIV vs. Mock comparison group mainly consisted of pathways focusing on thermogenesis, taste transduction, ribosome biogenesis in eukaryotes, ribosome, propanoate metabolism, phagosome, oxidative phosphorylation, non-alcoholic fatty liver disease (NAFLD), Parkinson disease, metabolism, fatty acid metabolism, carbon metabolism and fatty acid metabolism, lysosomes, eukaryotic ribosome biogenesis, cellular senescence, valine, leucine and isoleucine degradation and antiviral defence pathway including toxoplasmosis, herpes simplex virus 1 and human T-cell leukaemia virus 1 infection (Figure 4A; Supplementary Table 4). The comparison group MgIV vs. Mock pathways primarily included valine, leucine and isoleucine degradation, toxoplasmosis, ribosome biogenesis in eukaryotes, propanoate metabolism metabolic, metabolic pathways, melanoma, fatty acid metabolism, glutathione metabolism, carbon metabolism and some antiviral defence pathways such as the MAPK signalling pathway, FoxO signalling pathway and human T-cell leukaemia virus 1 infection (Figure 4B; Supplementary Table 5). The Mg vs. Mock comparison group primarily included pathways associated with viral myocarditis, type I diabetes mellitus, toxoplasmosis, Th1 and Th2 cell differentiation, staphylococcus aureus infection, rheumatoid arthritis, phagosome, leishmaniasis, antigen processing and presentation, allograft rejection, inflammatory bowel disease, herpes simplex virus 1 infection, human T-cell leukaemia virus 1 infection and toxoplasmosis complement and coagulation cascades, the p53 and NOD-like receptor signalling pathways (Figure 4C; Supplementary Table 6). The MgIV vs. MIV comparison group pathways primarily included staphylococcus aureus infection, leishmaniasis, phagosome, asthma, antigen processing and presentation, Th1 and Th2 cell differentiation, herpes simplex virus 1 infection, cell adhesion molecules and complement and coagulation cascades (Supplementary Table 7). The MgIV vs. Mg comparison group pathways included antigen processing and presentation, graft-versus-host disease, lysosome, valine, leucine and isoleucine degradation, phagosome, metabolic pathways, Epstein–Barr virus infection, type I diabetes mellitus and some immune-related pathways such as Th1 and Th2 cell differentiation,

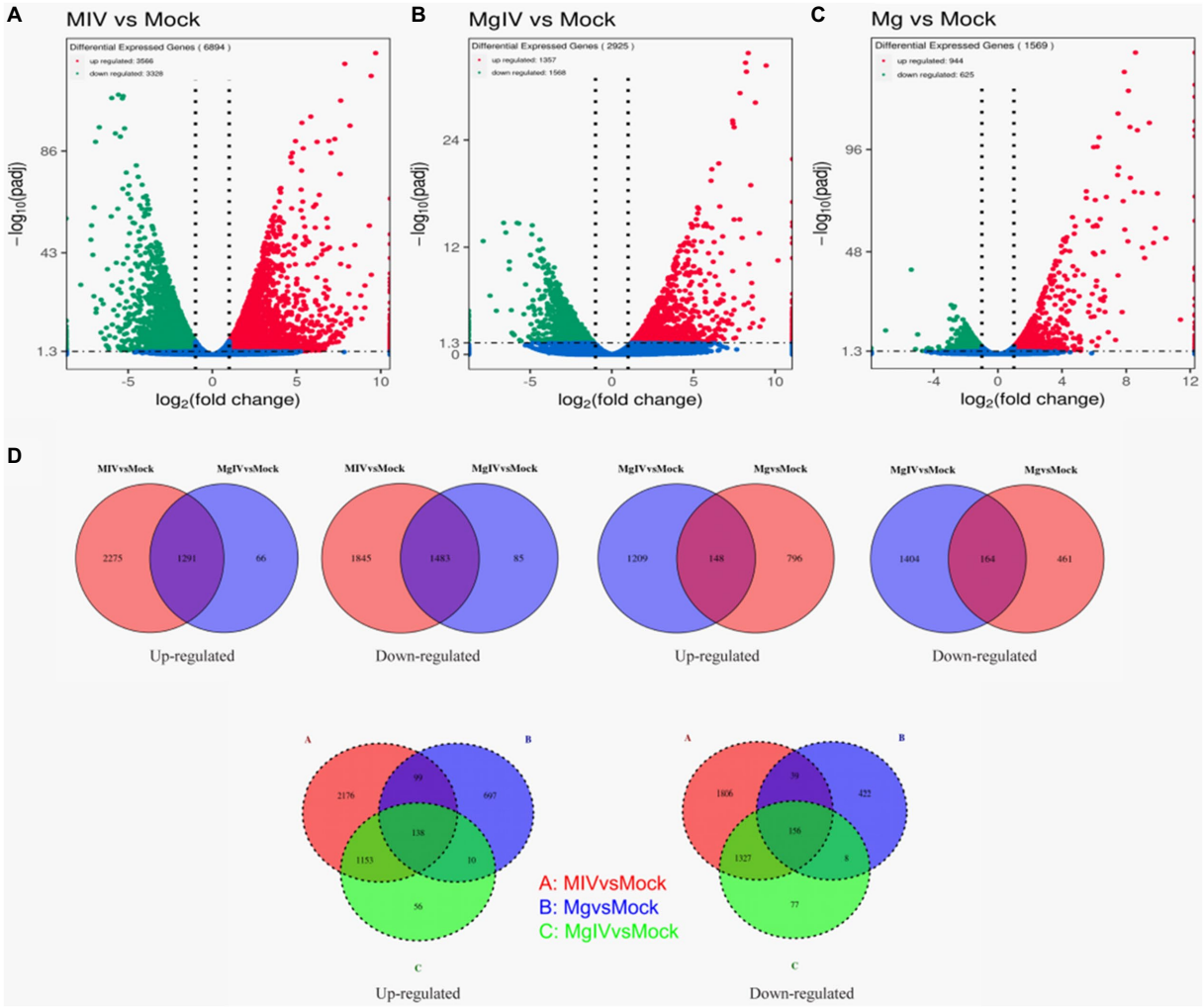

FIGURE 2
Volcano plot and Venn image of global DEGs in different comparison groups. Volcano plot of global DEGs in different comparison groups. **(A)** MIV vs. Mock. **(B)** MgIV vs. Mock. **(C)** Mg vs. Mock. **(D)** Venn diagrams representing the genes in common among treatment groups. (The statistical criteria are padj < 0.05, |Log2FC| > 1.)

Th17 cell differentiation, human T-cell leukaemia virus 1 infection and p53 signalling pathway (Supplementary Table 8). The KEGG pathways that were significantly enriched in both BoHV-1 infection groups (MgIV and MIV) included metabolic pathways, lysosomes, eukaryotic ribosome biogenesis, carbon metabolism, fatty acid metabolism, valine, leucine and isoleucine degradation and human T-cell leukaemia virus 1 infection. In the BoIFN-γ pre-treated groups (MgIV and Mg), the significantly enriched KEGG pathways included glutathione metabolism, toxoplasmosis and human T-cell leukaemia virus 1 infection.

Differential expression of representative functional genes

According to Go and KEGG analysis results, the metabolic response of host cells was significantly disturbed during BoHV-1 infection. Combined with differences in gene transcription levels, we found some DEGs associated with lipid synthesis and metabolism, including ACSS2, FDFT1, HMGCS1, SERBF2, SQLE, FADS1, and FADS2, were significantly downregulated in both comparison group MIV vs. Mock and comparison group MgIV vs. Mock, but transcriptional inhibition of these genes was less in the MgIV group. The results showed that the lipid metabolism disorder caused by virus infection could be improved by BoIFN-γ pre-treatment and the remission of cell cytopathic effects (Figure 5A). Additionally, the genes (BRCA1, BRCA2, ATM, BRIP1, CLSPN, ZBTB1, RAD51, and RAD54L) involved in DNA damage were upregulated in the MIV group, indicating that this occurred as a result of BoHV-1 infection. However, upregulation of these genes in the MgIV group was less with BoIFN-γ pre-treatment, possibly due to inhibition of viral DNA replication by BoIFN-γ (Figure 5B). Compared with the

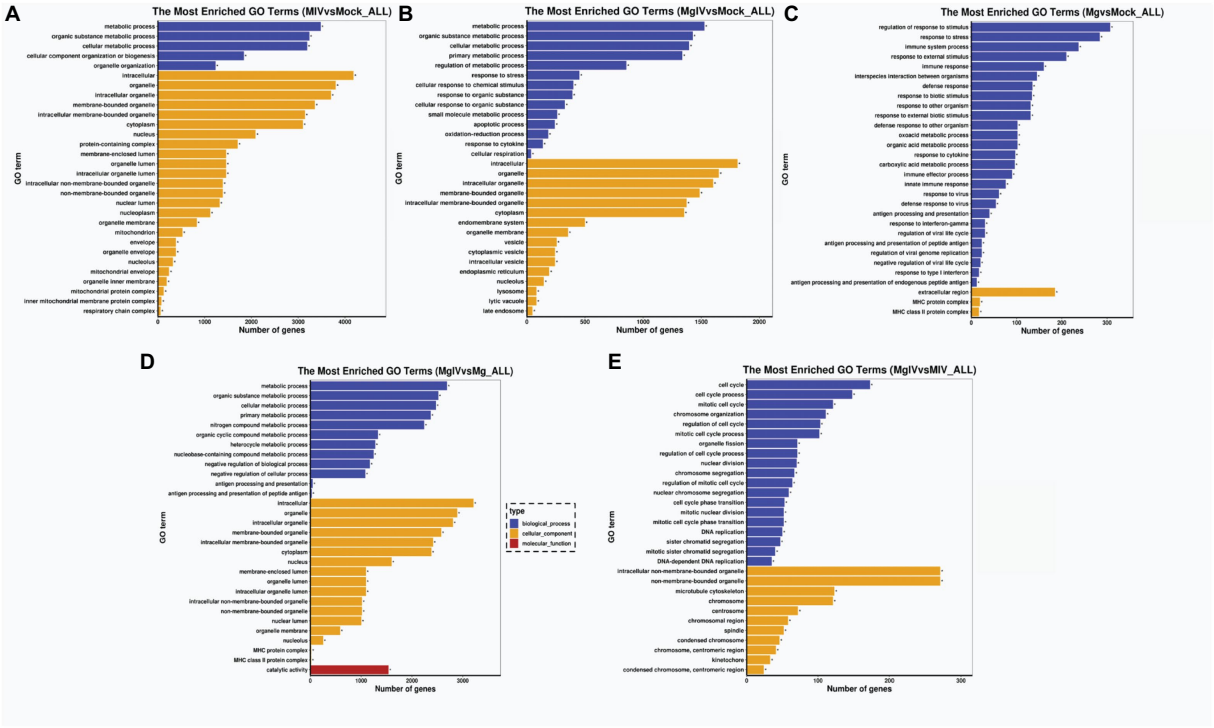

FIGURE 3
GO enrichment analysis of DEGs in different comparison groups. **(A)** MIV vs. Mock. **(B)** MgIV vs. Mock. **(C)** Mg vs. Mock. **(D)** MgIV vs. Mg. **(E)** MgIV vs. MIV. $p<0.05$; |Log2FC|>1. GO terms are on the y-axis. Enrichment ratio of genes shown as GO terms for BP, CC and MF. * means GO categories with significant enrichment.

Mock group, BoHV-1 infection (MIV) drastically reduced the transcriptional levels of the gene coding for complement components C3, C1r, C1s, PLAT (TPA), ITGB2 (CD18), and PROCR (EPCR), but gene transcriptional was significantly induced by BoIFN-γ treatment (Mg). Simultaneously, BoIFN-γ pre-treated cells (MgIV) demonstrated significant resistance to negative regulation of these complement-associated genes by BoHV-1 infection (Figure 5C). Furthermore, expression of the BoLA, CD74, B2M, PA28, BoLA-DRA, and TAPBP genes involved in the antigen presentation process of the acquired immune response was suppressed by BoHV-1 infection but also improved by BoIFN-γ pre-treatment (Figure 5D). As expected, transcription of interferon stimulated genes (ISGs), including MX1, OAS1Y, OAS1X, ADAR, BST2, HNRNPA0, and EIF2AK2, was increased by both BoIFN-γ treatment and BoHV-1 infection. Daxx and Sp100, important components of PML-nuclear bodies, were also upregulated both directly by BoIFN-γand indirectly by viral infection (Figure 5E). Furthermore, both cGAS and IRF7 were upregulated in MIV and MgIV groups, suggesting that the type 1 interferon pathway was activated due to the transcription of cGAS and IRF7 triggered in response to viral infection. Meanwhile, the NF-κB pathway was activated by BoHV-1 infection and the transcription of pro-inflammatory cytokines IL6, IL12, and TNF-α was upregulated in the MIV group (Figure 5F).

Quantitative real-time PCR analysis

Comparisons of transcriptome sequencing data revealed that BoHV-1 infection caused cell metabolism disorder, DNA damage and immunosuppression, while BoIFN-γ pre-treatment enhanced expression of the genes responsible for immune defence and partially inhibited the gene expression involved in apoptosis. To validate the DEGs from our transcriptome sequencing, real-time PCR (RT-qPCR) was used to quantitatively measure the mRNA transcription of 34 selected genes related to lipid metabolism, DNA damage and repair, complement and coagulation signalling cascade responses, antigen processing and presentation, interferon stimulation genes, some cytokines and chemokines and some other immune-related genes, including ACSS2, FDFT1, HMGCS1, SQLE, BACA1, BACA2, ATM, BRIP1, CLSPN, ZBTB, RAD51, RAD54L, C3, C1S, ITGB2, BoLA, CD74, B2M, PA28, BoLA-DRA, TAPBP, MX1, ADAR, EIF2AK2, TNF, IL6, IL6R, ERN1, BCL2L11, GADD34, MAPK8, MAP3K5, ATF4, and CXCL3 (Figure 5; Supplementary Figure 2).

The correlation between RNA-Seq and RT-qPCR results was measured by a scatter plot of the log2 fold-changes. RNA-Seq results were highly correlated with RT-qPCR data, with a correlation coefficient (R2) as high as 0.8243 (Figure 6). In summary, RT-qPCR analysis validated the transcriptional changes of the DEG data from RNA-Seq.

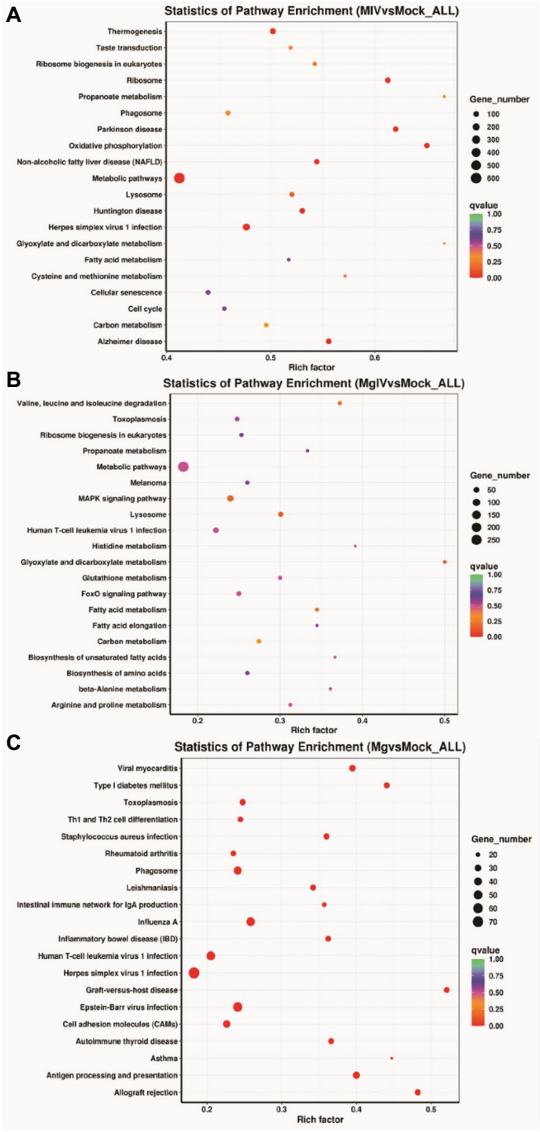

FIGURE 4
KEGG Pathway enrichment analysis of DEGs in different comparison groups. **(A)** MIV vs. Mock. **(B)** MgIV vs. Mock. **(C)** Mg vs. Mock. The name of KEGG pathways are on the y-axis. q-value (range 0–1) is the *p*-value that was corrected by multiple hypothesis tests. The closer the q-value is to zero, the more significant the enrichment of the KEGG pathway.

Discussion

BoHV-1 is a tactical pathogen with various strategies to impair innate and adaptive immune responses throughout productive infection (Jones, 2019). IFN-γ, a pleiotropic cytokine that modulates both innate and adaptive immune networks, was first discovered as a soluble macromolecule with antiviral activity. IFN-γ not only indirectly inhibits virus replication by inducing type I IFNs but also displays type I IFN-independent antiviral activity (Kropp et al., 2011; Hwang et al., 2012; Prestwood et al., 2012). As MDBK cell lines have been widely used to investigate interactions between the host and BoHV-1 and to evaluate novel antiviral approaches, a BoHV-1/MDBK system was employed in this study to investigate the anti-BoHV-1 activity of BoIFN-γ (Wang et al., 2021). The results showed that purified BoIFN-γ significantly reduced the cytopathic effect of productive BoHV-1 infection (Figures 1B,C,G). Furthermore, we evaluated the replication kinetics of BoHV-1 in MDBK cells pre-treated with BoIFN-γ and found that BoIFN-γ halted the replication speed of BoHV-1 in a dose-dependent manner (Figures 1D–F). In order to determine the molecular mechanisms by which BoIFN-γ helps establish an antiviral state in the host, we analysed the differences in gene expression between groups of MDBK cells by RNA-Seq. Transcriptome analysis of MDBK cells revealed that BoHV-1 infection destroyed many biological processes leading to cell death, such as lipid metabolic processes and DNA damage processes. Furthermore, BoHV-1 infection suppressed the transcriptions of these immune components related to complement activation and coagulation cascades response as well as antigen processing and presentation process. However, BoIFN-γ pre-treated cells (MgIV) displayed clearly alleviative injury caused by BoHV-1 infection, which suggests that BoIFN-γ pre-treatment strengthened the resistance of MDBK to BoHV-1 infection.

Replication and infectivity of viruses rely on obtaining all energy and raw materials from the host cell (Cvirkaite-Krupovic et al., 2015). Herpesviruses such as HCMV and HSV-1 actively hijack the metabolic pathways of host cells to create suitable intracellular microenvironments for their life cycle (Vastag et al., 2011; Strating and van Kuppeveld, 2017). In this study, results of enrichment analysis of GO terms and KEGG pathway demonstrated that BoHV-1 infection led to severe metabolic dysfunction. Combined with DEGs significant difference and pathway enrichment analysis, we found that expressions of the genes ACSS2, FDFT1, HMGCS1, SERBF2, SQLE, FADS1, and FADS2, all related to lipid metabolism, were significantly downregulated during BoHV-1 infection. However, these genes were downregulated to a lesser degree by viral infection in BoIFN-γ pre-treated cells (Figure 5F). HMGCS1 is a key ketogenesis enzyme for regulating sterol biosynthesis and cholesterol metabolism and, together with ACSS2, plays an important role in cell growth and progression and cattle growth performance (Wang et al., 2016; Xu et al., 2018). SQLE and SCD are considered rate-limiting enzymes in lipid metabolism that catalyse the synthesis of monounsaturated fatty acids (MUFAs) and inhibitors of the cell death process of ferroptosis (Trapani et al., 2012; Yuan et al., 2020). FDFT1 synthesises squalene *via* condensation of two molecules of farnesyl pyrophosphate, and is critical for metabolic reprogramming, cell proliferation and virus propagation (Park et al., 2014; Ha and Lee, 2020). SREBP2 maintains lipid homeostasis by regulating cholesterol and fatty acid metabolism (Song et al., 2017). Thus, dramatic downregulation of these gene transcriptions indicates that host lipid metabolism was disturbed by BoHV-1 infection, making the

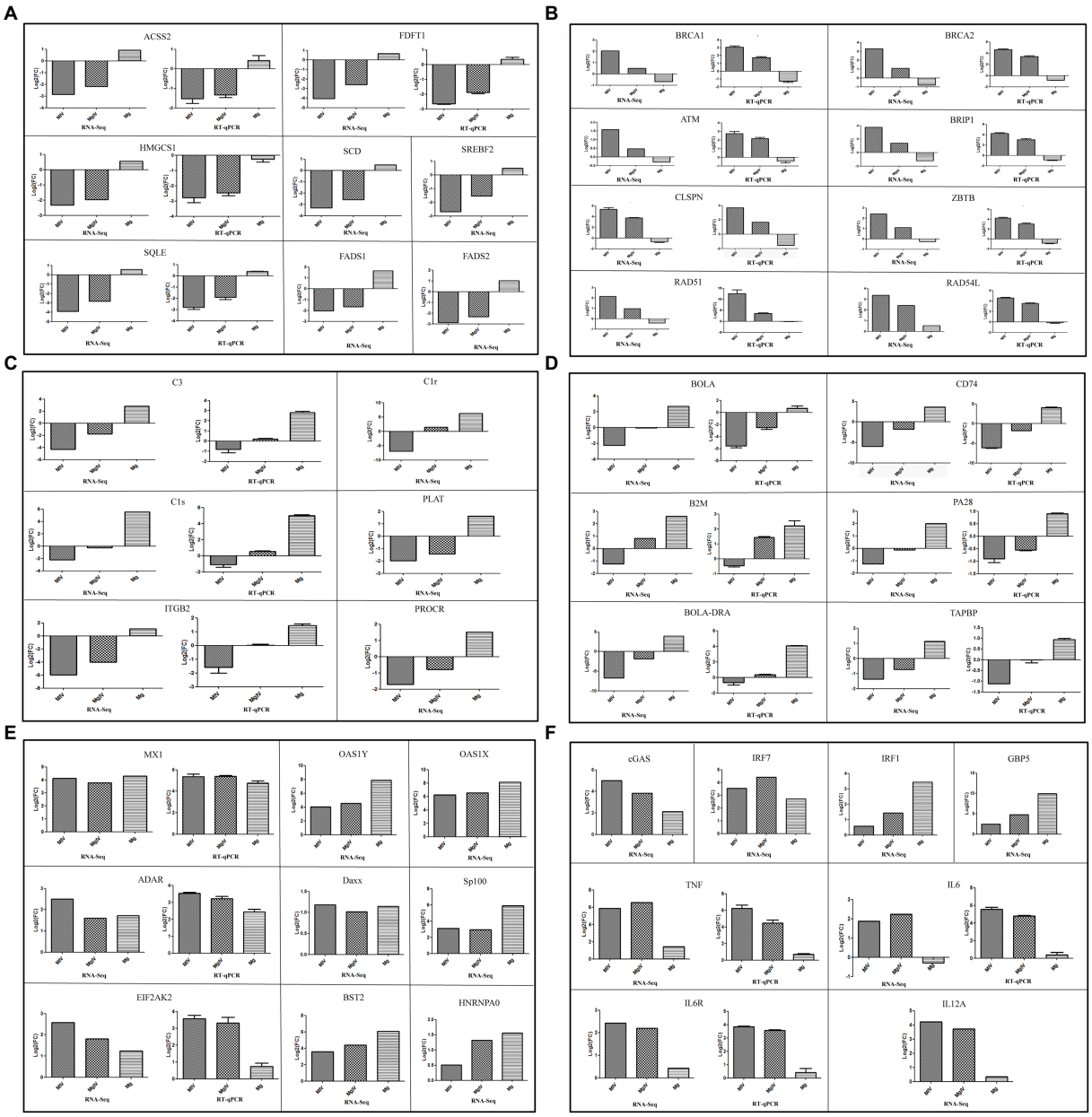

FIGURE 5
Expression level of genes related to lipid metabolism, DNA damage and repair, interferon stimulation genes, complement and coagulation signalling cascades, antigen processing and presentation, interferon regulatory factors and pro-inflammatory cytokines. ACSS2, FDFT1, HMGCS1, SQLE, BACA1, BACA2, ATM, BRIP1, CLSPN, ZBTB, RAD51, RAD54L, C3, C1S, ITGB2, BoLA, CD74, B2M, PA28, BoLA-DRA, TAPBP, MX1, ADAR, EIF2AK2, TNF, IL6, and IL6R validated by RT-qPCR. **(A)** Expression level of genes related to lipid metabolism. **(B)** Expression level of genes related to DNA damage. **(C)** Expression level of genes related to complement and coagulation signalling cascade. **(D)** Expression level of antigen processing and presentation. **(E)** Expression level of genes related to interferon stimulated genes. **(F)** Expression level of genes related to some interferon regulatory factors and pro-inflammatory cytokines. β-actin gene was used as an internal control and relative quantity of gene expression (fold change) of each gene was calculated with the comparative $2^{-\Delta\Delta CT}$ method. Values (RT-qPCR) shown were mean with SD.

normal cell cycle difficult to maintain. Nevertheless, such injuries can be significantly lessened by BoIFN-γ pre-treatment.

As part of the host's immune surveillance, viral replication is recognised by infected cells as DNA damage leading to apoptosis. In the process of DNA virus replication, exogenous viral DNA structures trigger DNA damage and repair responses in cells (Afroz et al., 2018). In our study, DEGs involved in DNA damage and repair, including BRCA1, BRCA2, BRIP1, ZBTB1, RAD51, RAD54L, ATM, and CLSPN, were significantly upregulated by BoHV-1 infection, but regulation of these genes was relatively improved in group MgIV (Figure 5D). BRCA1 and BRCA2 are required for maintaining chromosomal stability to protect the

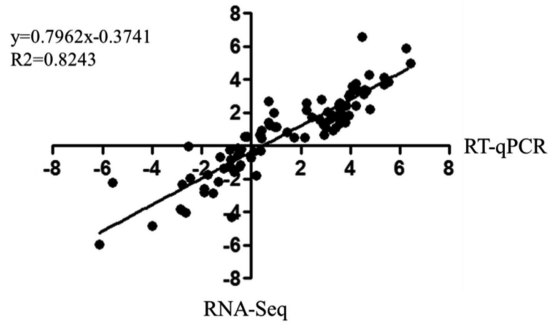

FIGURE 6
Correlation of fold change analysed by data obtained using RT-qPCR (x-axis) with RNA-Seq platform (y-axis). Correlation analysis was performed using GraphPad software 6.0 (San Diego, CA).

genome from damage and to transcriptionally regulate some of the genes involved in DNA repair (Yoshida and Miki, 2004). BRIP1 interacts with numerous proteins associated with the regulation of DNA damage responses and signal checkpoints which are vital for retaining chromosomal and genomic constancy (Khan and Khan, 2021). ZBTB1 is a critical upstream regulator of translesion DNA synthesis and promotes chromatin remodelling and translesion DNA for DNA repair (Kim et al., 2014; Zhang et al., 2020). RAD51 and RAD54 are key elements in homologous recombination which is a versatile DNA damage repair pathway. The strand exchange protein RAD51 promotes genome stability by repairing DNA double strand breaks and damaged replication forks. RAD54L acts with RAD51 to promote recombinational DNA repair (Mason et al., 2015; Mun et al., 2020). Upregulation of RAD51 mRNA expression inhibits the STING-mediated innate immune response (Bhattacharya et al., 2017). As a primary regulator in the DNA damage response, ATM activates many signal pathways associated with cell cycle checkpoints, DNA damage repair, transcription regulation, immune response and metabolism (Jackson and Bartek, 2009; Afroz et al., 2018; Xiao et al., 2019). Additionally, ATM has a positive role in V(D)J-recombination through end-tethering and end-processing, ensuring proper end-joining. There is some evidence that ATM promotes survival in developing lymphocytes undergoing V(D)J-recombination (Weitering et al., 2021). Our results demonstrated that BoHV-1 infection upregulated ATM expression leading to activation of the acquired immune response by V(D)J-recombination. Thus, upregulation of gene transcription in the MIV group is sufficient to indicate that BoHV-1 infection can induce DNA damage and further upregulates programmed cell death. The transcriptional levels of these genes in the MgIV group were more like those of the Mock group than those of the MIV group, suggesting that BoIFN-γ pre-treatment not only inhibited viral replication but also alleviated cellular DNA damage. The mechanism by which BoIFN-γ ameliorates DNA damage caused by BoHV-1 infection remains to be further studied.

C1r, C1s and C1q together form C1, the complex which triggers the classical complement pathway. The downregulated expression of C1 and C3 can inhibit activation of the complement system (Flyvbjerg, 2017). C3, C1r, C1s, PLAT (TPA), ITGB2 (CD18), and PROCR (EPCR), which are enriched in complement and coagulation cascade pathways, were downregulated during BoHV-1 infection but exhibited normal levels with BoIFN-γ pre-treatment (Figure 5C). These findings showed that BoHV-1 inhibits the complement system, facilitating replication during the early stages of infection. The same result, that the expression levels of genes belonging to the complement and coagulation signalling cascades were downregulated during BVDV infection, has been previously reported (Liu et al., 2019). However, this inhibitory effect was greatly reduced in our study *via* BoIFN-γ pre-treatment. This suggests that BoIFN-γ can activate innate immunity by inducing the complement system to inhibit virus replication in the early stages of BoHV-1 infection.

Additionally, DEG analyses revealed that BoHV-1 infection significantly inhibited transcription of genes in the antigen processing and presentation pathway including BoLA, BoLA-DRA, TAPBP, CD74, B2M, and PA28. However, this negative regulation caused by BoHV-1 infection is very mild in MDBK pre-treated with BoIFN-γ. It has been reported that BoHV-1 can inhibit antigen processing and presentation in many ways. Koppers' research show that BoHV-1 interferes with TAP-dependent peptide transport and intracellular trafficking of MHC class I molecules to inhibit CD8+ T cell responses in human cells (Koppers-Lalic et al., 2003; Jones, 2009). BoHV-1 glycoprotein B can also affect CD4+ cell activation by retarding HLA-DR export to the plasma membrane (Grabowska et al., 2020). Previous study reported that IFN-γ could enhance the cytotoxicity of peripheral blood mononuclear leukocytes from immune cattle to BoHV-1-infected cells *in vitro* cytotoxic activity, which is in concert with our transcriptional data that BoIFN-γ initiated transcription of genes in the antigen processing and presentation pathway to CD8+ T cells through MHC I molecule (Campos et al., 1989). Moreover, similar to our results, Fu's work indicated that transcription of MHC I and II molecules was stimulated by IFN-γ in PK15, suggesting that IFN-γ may strengthen CD4, CD8 and NK cell responses *in vivo* (Fu et al., 2016). This is the first report of BoHV-1 suppressing antigen processing and presentation by inhibiting transcription of related genes in MDBK, although further experiments are required to confirm the effect *in vivo*.

ISGs products, including OAS1, OAS2, MX1, ADAR, and EIF2AK2, are major players in innate immune defence against viral infection. Their expression was upregulated by both BoHV-1 infection and BoIFN-γ pre-treatment in the present study (Figure 5B), indicating that BoIFN-γ provoked the transcription of ISGs to confront BoHV-1 replication in MDBK cells. The type 1 interferon pathway was activated due to the transcription of cGAS and IRF7 triggered in response to BoHV-1 infection. Therefore, transcription of ISGs is activated in experimental

groups treated with BoIFN-γ and MDBK infected BoHV-1. Interferon regulatory transcription factors, IRF1 and GBP5, were activated by BoIFN-γ stimuli rather than BoHV-1 infection (Supplementary Figure 2). The transcription level of IRF1 was significantly higher in group MgIV than in group MIV. Previous studies have shown that IRF1 is an early-target gene downstream of IFN-γ signalling and plays a crucial antiviral role in HSV-1 infection (Irving et al., 2020). GBP5 functions as an activator of NLRP3 inflammasome assembly and is important to the innate immune system and in pathogen-inhibiting inflammation (Krapp et al., 2016). Positive regulation of IRF1 and GBP5 transcription in BoHV-1 infected MDBK cells pre-treated with BoIFN-γ was more pronounced than in group MIV. The promoter of IRF1 contains a GAS element which could be activated by STAT1 homodimers induced by the binding of IFN-γ to its receptor (Feng et al., 2021). IRF1 is an activating factor in pathogen defence and contributes to the activation of innate immune responses induced by pathogen sensors such as RLRs, TLRs, or cGAS. As described by IRF1 promotes the innate immune response to viral infection and exhibits antiviral activity both in DNA and RNA virus infection (Wang et al., 2020; Feng et al., 2021). GBP5 is mainly induced by IFN-γ and is involved in innate immunity against a wide variety of microbial pathogens. GBP5 is reported as the major effector of the anti-RSV activity of IFN-γ treatment and potently restricts HIV-1 and other retroviruses (Krapp et al., 2016; Li et al., 2020). Considering the above evidence, we speculate that the activation of IRF1 and GBP5 may play an important role in BoIFN-γ inhibition of viral replication and cytopathic effect relief. Transcription of pro-inflammatory cytokines TNF-α, IL6, IL6 receptor (IL6R) and IL12 was upregulated by BoHV-1 infection, whereas transcription of these genes is almost unaffected by BoIFN-γ treatment (Supplementary Figure 2). However, these pro-inflammatory cytokines still play critical roles in the host antiviral response.

Conclusion

In this study, we found that pre-treatment with BoIFN-γ significantly inhibits the replication and cytopathic effects of BoHV-1 in MDBK. Tanscriptome analysis revealed that BoIFN-γ upregulated ISG transcriptions and interferon regulatory transcription factors IRF1 and GBP5 associated with the host immune response against BoHV-1 infection. In addition, BoIFN-γ promotes expression of cellular components involved in complement activation and coagulation cascades response as well as antigen processing and presentation process. Furthermore, BoIFN-γ significantly alleviated the disorder of gene transcription involved in metabolism and DNA repair caused by BoHV-1 infection. Taken together, BoIFN-γ pre-treatment can improve host cell resistance to BoHV-1 infection, probably due to regulation of gene transcriptions related to cellular metabolism and innate immune response. Although further studies are needed to confirm whether these regulatory effects of BoIFN-γ directly or indirectly inhibit BoHV-1 replication, our findings provide insights into the development of prophylactic agents for prevention and control of BoHV-1 infection.

Data availability statement

The datasets presented in this study can be found in online repositories. The names of the repository/repositories and accession number(s) can be found at: https://www.ncbi.nlm.nih.gov/sra/PRJNA849906.

Author contributions

YL and BJ conceived and designed the experiments, analysed the data, and wrote the paper. BJ, JW, WL, JC, JX, and MC performed the experiments. WL, JC, and JX contributed reagents, materials, and analysis tools. All authors contributed to the article and approved the submitted version.

Funding

This work was supported by a grant from National Natural Science Foundation of China (grant no. 32172818), Beijing Agricultural Forestry Academy Youth Fund (grant no. QNJJ201930), and Beijing Innovation Team of Technology Systems in the Dairy Industry (grant no. BAIC06-2022).

Conflict of interest

The authors declare that the research was conducted in the absence of any commercial or financial relationships that could be construed as a potential conflict of interest.

Publisher's note

Supplementary material

The Supplementary Material for this article can be found online at: https://www.frontiersin.org/articles/10.3389/fmicb.2022.973278/full#supplementary-material

References

Afroz, S., Brownlie, R., Fodje, M., and Hurk, S. (2016). VP8, the major tegument protein of bovine Herpesvirus 1, interacts with cellular STAT1 and inhibits interferon Beta signaling. *J. Virol.* 90, 4889–4904. doi: 10.1128/JVI.00017-16

Afroz, S., Garg, R., Fodje, M., and Hurk, S. (2018). The major tegument protein of bovine Herpesvirus 1, VP8, interacts with DNA damage response proteins and induces apoptosis. *J. Virol.* 92:e00773-18. doi: 10.1128/JVI.00773-18

Bhattacharya, S., Srinivasan, K., Abdisalaam, S., Su, F., Raj, P., Dozmorov, I., et al. (2017). RAD51 interconnects between DNA replication, DNA repair and immunity. *Nucleic Acids Res.* 45, 4590–4605. doi: 10.1093/nar/gkx126

Biswas, S., Bandyopadhyay, S., Dimri, U., and Patra, P. H. (2013). Bovine herpesvirus-1 (BHV-1) - a re-emerging concern in livestock: a revisit to its biology, epidemiology, diagnosis, and prophylaxis. *Vet. Q.* 33, 68–81. doi: 10.1080/01652176.2013.799301

Campos, M., Ohmann, H. B., Hutchings, D., Rapin, N., Babiuk, L. A., and Lawman, M. J. (1989). Role of interferon-gamma in inducing cytotoxicity of peripheral blood mononuclear leukocytes to bovine herpesvirus type 1 (BHV-1)-infected cells. *Cell. Immunol.* 120, 259–269. doi: 10.1016/0008-8749(89)90193-7

Chen, W., Gao, F., Chu, F., Zhang, J., Gao, G. F., and Xia, C. (2010). Crystal structure of a bony fish beta2-microglobulin: insights into the evolutionary origin of immunoglobulin superfamily constant molecules. *J. Biol. Chem.* 285, 22505–22512. doi: 10.1074/jbc.M109.095000

Cvirkaite-Krupovic, V., Carballido-Lopez, R., and Tavares, P. (2015). Virus evolution toward limited dependence on nonessential functions of the host: the case of bacteriophage SPP1. *J. Virol.* 89, 2875–2883. doi: 10.1128/JVI.03540-14

da Silva, L. F., Sinani, D., and Jones, C. (2012). ICP27 protein encoded by bovine herpesvirus type 1 (bICP27) interferes with promoter activity of the bovine genes encoding beta interferon 1 (IFN-beta1) and IFN-beta3. *Virus Res.* 169, 162–168. doi: 10.1016/j.virusres.2012.07.023

Day, P. M., Thompson, C. D., Lowy, D. R., and Schiller, J. T. (2017). Interferon gamma prevents infectious entry of human papillomavirus 16 via an L2-dependent mechanism. *J. Virol.* 91:e00168-17. doi: 10.1128/JVI.00168-17

Decman, V., Kinchington, P. R., Harvey, S. A., and Hendricks, R. L. (2005). Gamma interferon can block herpes simplex virus type 1 reactivation from latency, even in the presence of late gene expression. *J. Virol.* 79, 10339–10347. doi: 10.1128/JVI.79.16.10339-10347.2005

Ezeonwumelu, I. J., Garcia-Vidal, E., and Ballana, E. (2021). JAK-STAT pathway: A novel target to tackle viral infections. *Viruses* 13:2379. doi: 10.3390/v13122379

Feng, H., Zhang, Y. B., Gui, J. F., Lemon, S. M., and Yamane, D. (2021). Interferon regulatory factor 1 (IRF1) and anti-pathogen innate immune responses. *PLoS Pathog.* 17:e1009220. doi: 10.1371/journal.ppat.1009220

Flyvbjerg, A. (2017). The role of the complement system in diabetic nephropathy. *Nat. Rev. Nephrol.* 13, 311–318. doi: 10.1038/nrneph.2017.31

Fu, Y., Zhu, Z., Chang, H., Liu, Z., Liu, J., and Chen, H. (2016). Comparative transcriptome analyses indicate enhanced cellular protection against FMDV in PK15 cells pretreated with IFN-gamma. *Gene* 586, 206–215. doi: 10.1016/j.gene.2016.03.027

Grabowska, K., Wachalska, M., Graul, M., Rychlowski, M., Bienkowska-Szewczyk, K., and Lipinska, A. D. (2020). Alphaherpesvirus gB homologs are targeted to extracellular vesicles, but they differentially affect MHC class II molecules. *Viruses* 12:429. doi: 10.3390/v12040429

Ha, N. T., and Lee, C. H. (2020). Roles of Farnesyl-Diphosphate Farnesyltransferase 1 in tumour and tumour microenvironments. *Cell* 9:2352. doi: 10.3390/cells9112352

Harris, N., Buller, R. M., and Karupiah, G. (1995). Gamma interferon-induced, nitric oxide-mediated inhibition of vaccinia virus replication. *J. Virol.* 69, 910–915. doi: 10.1128/JVI.69.2.910-915.1995

Hu, X., Li, J., Fu, M., Zhao, X., and Wang, W. (2021). The JAK/STAT signaling pathway: from bench to clinic. *Signal Transduct. Target. Ther.* 6:402. doi: 10.1038/s41392-021-00791-1

Hwang, S., Maloney, N. S., Bruinsma, M. W., Goel, G., Duan, E., Zhang, L., et al. (2012). Nondegradative role of Atg5-Atg12/Atg16L1 autophagy protein complex in antiviral activity of interferon gamma. *Cell Host Microbe* 11, 397–409. doi: 10.1016/j.chom.2012.03.002

Irving, A. T., Zhang, Q., Kong, P. S., Luko, K., Rozario, P., Wen, M., et al. (2020). Interferon regulatory factors IRF1 and IRF7 directly regulate gene expression in bats in response to viral infection. *Cell Rep.* 33:108345. doi: 10.1016/j.celrep.2020.108345

Jackson, S. P., and Bartek, J. (2009). The DNA-damage response in human biology and disease. *Nature* 461, 1071–1078. doi: 10.1038/nature08467

Jones, C. (2009). Regulation of innate immune responses by bovine Herpesvirus 1 and infected cell protein 0 (bICP0). *Viruses* 1, 255–275. doi: 10.3390/v1020255

Jones, C. (2019). Bovine Herpesvirus 1 counteracts immune responses and immune-surveillance to enhance pathogenesis and virus transmission. *Front. Immunol.* 10:1008. doi: 10.3389/fimmu.2019.01008

Kang, S., Brown, H. M., and Hwang, S. (2018). Direct antiviral mechanisms of interferon-gamma. *Immune Netw* 18:e33. doi: 10.4110/in.2018.18.e33

Khan, U., and Khan, M. S. (2021). Prognostic value estimation of BRIP1 in breast cancer by exploiting Transcriptomics data Through bioinformatics approaches. *Bioinform. Biol. Insights* 15:11779322211055892. doi: 10.1177/11779322211055892

Kim, H., Dejsuphong, D., Adelmant, G., Ceccaldi, R., Yang, K., Marto, J. A., et al. (2014). Transcriptional repressor ZBTB1 promotes chromatin remodeling and translesion DNA synthesis. *Mol. Cell* 54, 107–118. doi: 10.1016/j.molcel.2014.02.017

Koppers-Lalic, D., Rychlowski, M., van Leeuwen, D., Rijsewijk, F. A., Ressing, M. E., Neefjes, J. J., et al. (2003). Bovine herpesvirus 1 interferes with TAP-dependent peptide transport and intracellular trafficking of MHC class I molecules in human cells. *Arch. Virol.* 148, 2023–2037. doi: 10.1007/s00705-003-0142-5

Krapp, C., Hotter, D., Gawanbacht, A., McLaren, P. J., Kluge, S. F., Sturzel, C. M., et al. (2016). Guanylate binding protein (GBP) 5 is an interferon-inducible inhibitor of HIV-1 infectivity. *Cell Host Microbe* 19, 504–514. doi: 10.1016/j.chom.2016.02.019

Kropp, K. A., Robertson, K. A., Sing, G., Rodriguez-Martin, S., Blanc, M., Lacaze, P., et al. (2011). Reversible inhibition of murine cytomegalovirus replication by gamma interferon (IFN-gamma) in primary macrophages involves a primed type I IFN-signaling subnetwork for full establishment of an immediate-early antiviral state. *J. Virol.* 85, 10286–10299. doi: 10.1128/JVI.00373-11

Li, Z., Qu, X., Liu, X., Huan, C., Wang, H., Zhao, Z., et al. (2020). GBP5 is an interferon-induced inhibitor of respiratory syncytial virus. *J. Virol.* 94:e01407-20. doi: 10.1128/JVI.01407-20

Liu, C., Liu, Y., Liang, L., Cui, S., and Zhang, Y. (2019). RNA-Seq based transcriptome analysis during bovine viral diarrhoea virus (BVDV) infection. *BMC Genomics* 20:774. doi: 10.1186/s12864-019-6120-4

Malmgaard, L. (2004). Induction and regulation of IFNs during viral infections. *J. Interferon Cytokine Res.* 24, 439–454. doi: 10.1089/1079990041689665

Mason, J. M., Dusad, K., Wright, W. D., Grubb, J., Budke, B., Heyer, W. D., et al. (2015). RAD54 family translocases counter genotoxic effects of RAD51 in human tumor cells. *Nucleic Acids Res.* 43, 3180–3196. doi: 10.1093/nar/gkv175

Muller, M., Briscoe, J., Laxton, C., Guschin, D., Ziemiecki, A., Silvennoinen, O., et al. (1993). The protein tyrosine kinase JAK1 complements defects in interferon-alpha/beta and-gamma signal transduction. *Nature* 366, 129–135. doi: 10.1038/366129a0

Mun, J. Y., Baek, S. W., Park, W. Y., Kim, W. T., Kim, S. K., Roh, Y. G., et al. (2020). E2F1 promotes progression of bladder cancer by modulating RAD54L involved in homologous recombination repair. *Int. J. Mol. Sci.* 21:9025. doi: 10.3390/ijms21239025

Muylkens, B., Thiry, J., Kirten, P., Schynts, F., and Thiry, E. (2007). Bovine herpesvirus 1 infection and infectious bovine rhinotracheitis. *Vet. Res.* 38, 181–209. doi: 10.1051/vetres:2006059

Park, E. M., Nguyen, L. N., Lim, Y. S., and Hwang, S. B. (2014). Farnesyl-diphosphate farnesyltransferase 1 regulates hepatitis C virus propagation. *FEBS Lett.* 588, 1813–1820. doi: 10.1016/j.febslet.2014.03.043

Pierce, A. T., DeSalvo, J., Foster, T. P., Kosinski, A., Weller, S. K., and Halford, W. P. (2005). Beta interferon and gamma interferon synergize to block viral DNA and virion synthesis in herpes simplex virus-infected cells. *J. Gen. Virol.* 86, 2421–2432. doi: 10.1099/vir.0.80979-0

Prestwood, T. R., Morar, M. M., Zellweger, R. M., Miller, R., May, M. M., Yauch, L. E., et al. (2012). Gamma interferon (IFN-gamma) receptor restricts systemic dengue virus replication and prevents paralysis in IFN-alpha/beta receptor-deficient mice. *J. Virol.* 86, 12561–12570. doi: 10.1128/JVI.06743-11

Rola, J., Larska, M., Socha, W., Rola, J. G., Materniak, M., Urban-Chmiel, R., et al. (2017). Seroprevalence of bovine herpesvirus 1 related alphaherpesvirus infections in free-living and captive cervids in Poland. *Vet. Microbiol.* 204, 77–83. doi: 10.1016/j.vetmic.2017.04.006

Saira, K., Zhou, Y., and Jones, C. (2007). The infected cell protein 0 encoded by bovine herpesvirus 1 (bICP0) induces degradation of interferon response factor 3 and, consequently, inhibits beta interferon promoter activity. *J. Virol.* 81, 3077–3086. doi: 10.1128/JVI.02064-06

Saira, K., Zhou, Y., and Jones, C. (2009). The infected cell protein 0 encoded by bovine herpesvirus 1 (bICP0) associates with interferon regulatory factor 7 and consequently inhibits beta interferon promoter activity. *J. Virol.* 83, 3977–3981. doi: 10.1128/JVI.02400-08

Schoenborn, J. R., and Wilson, C. B. (2007). Regulation of interferon-gamma during innate and adaptive immune responses. *Adv. Immunol.* 96, 41–101. doi: 10.1016/S0065-2776(07)96002-2

Song, Y., Du, Z., Chen, B., Ren, M., Yang, Q., Sui, Y., et al. (2017). Association of SREBP2 gene polymorphisms with the risk of osteonecrosis of the femoral head relates to gene expression and lipid metabolism disorders. *Mol. Med. Rep.* 16, 7145–7153. doi: 10.3892/mmr.2017.7473

Strating, J. R., and van Kuppeveld, F. J. (2017). Viral rewiring of cellular lipid metabolism to create membranous replication compartments. *Curr. Opin. Cell Biol.* 47, 24–33. doi: 10.1016/j.ceb.2017.02.005

Thakur, V., Kumar, M., and Rathish, R. L. (2017). Seroprevalence of bovine herpesvirus-1 antibodies in bovines in five districts of Uttarakhand. *Vet. World* 10, 140–143. doi: 10.14202/vetworld.2017.140-143

Trapani, L., Segatto, M., and Pallottini, V. (2012). Regulation and deregulation of cholesterol homeostasis: The liver as a metabolic "power station". *World J. Hepatol.* 4, 184–190. doi: 10.4254/wjh.v4.i6.184

Vastag, L., Koyuncu, E., Grady, S. L., Shenk, T. E., and Rabinowitz, J. D. (2011). Divergent effects of human cytomegalovirus and herpes simplex virus-1 on cellular metabolism. *PLoS Pathog.* 7:e1002124. doi: 10.1371/journal.ppat.1002124

Wang, P., Huang, S., Hao, C., Wang, Z., Zhao, H., Liu, M., et al. (2021). Establishment of a suspension MDBK cell line in serum-free medium for production of bovine Alphaherpesvirus-1. *Vaccines* 9:1006. doi: 10.3390/vaccines9091006

Wang, J., Li, H., Xue, B., Deng, R., Huang, X., Xu, Y., et al. (2020). IRF1 promotes the innate immune response to viral infection by enhancing the activation of IRF3. *J. Virol.* 94:e01231-20. doi: 10.1128/JVI.01231-20

Wang, F., Xiang, H., Fischer, G., Liu, Z., Dupont, M. J., Hogan, Q. H., et al. (2016). HMG-CoA synthase isoenzymes 1 and 2 localize to satellite glial cells in dorsal root ganglia and are differentially regulated by peripheral nerve injury. *Brain Res.* 1652, 62–70. doi: 10.1016/j.brainres.2016.09.032

Weitering, T. J., Takada, S., Weemaes, C. M. R., van Schouwenburg, P. A., and van der Burg, M. (2021). ATM: translating the DNA damage response to adaptive immunity. *Trends Immunol.* 42, 350–365. doi: 10.1016/j.it.2021.02.001

Xiao, J., Liu, M., Qi, Y., Chaban, Y., Gao, C., Pan, B., et al. (2019). Structural insights into the activation of ATM kinase. *Cell Res.* 29, 683–685. doi: 10.1038/s41422-019-0205-0

Xu, H., Luo, J., Ma, G., Zhang, X., Yao, D., Li, M., et al. (2018). Acyl-CoA synthetase short-chain family member 2 (ACSS2) is regulated by SREBP-1 and plays a role in fatty acid synthesis in caprine mammary epithelial cells. *J. Cell. Physiol.* 233, 1005–1016. doi: 10.1002/jcp.25954

Yoshida, K., and Miki, Y. (2004). Role of BRCA1 and BRCA2 as regulators of DNA repair, transcription, and cell cycle in response to DNA damage. *Cancer Sci.* 95, 866–871. doi: 10.1111/j.1349-7006.2004.tb02195.x

Yuan, X., Hu, S., Li, L., Liu, H., He, H., and Wang, J. (2020). Metabolomic analysis of SCD during goose follicular development: implications for lipid metabolism. *Genes* 11:1001. doi: 10.3390/genes11091001

Zhang, P., Yang, Y., Qian, K., Li, L., Zhang, C., Fu, X., et al. (2020). A novel tumor suppressor ZBTB1 regulates tamoxifen resistance and aerobic glycolysis through suppressing HER2 expression in breast cancer. *J. Biol. Chem.* 295, 14140–14152. doi: 10.1074/jbc.RA119.010759

frontiers | Frontiers in Microbiology

TYPE Original Research
PUBLISHED 06 September 2022
DOI 10.3389/fmicb.2022.975223

OPEN ACCESS

EDITED BY
Jue Liu,
Yangzhou University, China

REVIEWED BY
Jawhar Gharbi,
King Faisal University, Saudi Arabia
Hongxing Shen,
Jiangsu University, China

*CORRESPONDENCE
Wenran Zhao
zhaowr@hrbmu.edu.cn
Yan Wang
wangyan@hrbmu.edu.cn
Zhaohua Zhong
zhongzh@hrbmu.edu.cn

†These authors have contributed equally to this work

SPECIALTY SECTION
This article was submitted to Virology, a section of the journal Frontiers in Microbiology

RECEIVED 22 June 2022
ACCEPTED 01 August 2022
PUBLISHED 06 September 2022

CITATION
Qin Y, Lin L, Yang S, Dai Z, Zhang C, Huang J, Deng F, Yue X, Ren L, Fei Y, Zhao W, Wang Y and Zhong Z (2022) Circular RNA circ_0076631 promotes coxsackievirus B3 infection through modulating viral translation by sponging miR-214-3p. *Front. Microbiol.* 13:975223. doi: 10.3389/fmicb.2022.975223

Circular RNA circ_0076631 promotes coxsackievirus B3 infection through modulating viral translation by sponging miR-214-3p

Ying Qin[1†], Lexun Lin[1†], Shulong Yang[2†], Zongmao Dai[1], Congcong Zhang[1], Jingjing Huang[1], Fengzhen Deng[1], Xinxin Yue[1], Long Ren[3], Yanru Fei[1], Wenran Zhao[4*], Yan Wang[1*] and Zhaohua Zhong[1*]

[1]Department of Microbiology, Harbin Medical University, Harbin, China, [2]Department of Pediatric Surgery, The Second Affiliated Hospital of Harbin Medical University, Harbin, China, [3]Translational Medicine Research and Cooperation Center of Northern China, Heilongjiang Academy of Medical Sciences, Harbin, China, [4]Department of Cell Biology, Harbin Medical University, Harbin, China

Coxsackievirus B (CVB), a member of *Enterovirus* genus of *Picornaviridae*, is the leading pathogen of viral myocarditis and dilated cardiomyopathy. The pathogenesis of CVB-induced myocarditis has not been completely elucidated, and no specific antiviral measurement is available presently. Circular RNAs (circRNAs) have been reported to be able to modulate viral replication and infection through bridging over non-coding RNAs (ncRNAs) and coding messenger RNAs (mRNAs). To date, the role of circRNAs in CVB infection is largely unknown. In this study, we found that hsa_circ_0076631 (circ_0076631) significantly promoted CVB type 3 (CVB3) replication. Further study showed that the underneath mechanism was circ_0076631 indirectly interacting with CVB3 through sponging miR-214-3p, which targeted the 3D-coding region of CVB3 genome to suppress viral translation. Knocking down circ-0076631 caused a suppression of CVB3 infection; thus, circ-0076631 may be a potential target for anti-CVB therapy.

KEYWORDS

coxsackievirus B3, circRNA, miR-214-3p, 3D polymerase, viral replication

Introduction

Coxsackievirus group B (CVB) belongs to the human *Enterovirus* B species of *Picornaviridae* (Garmaroudi et al., 2015). Six serotypes have been identified in CVB (CVB1—CVB6). Among them, CVB1—CVB5 are the major pathogens of human viral myocarditis and dilated cardiomyopathy (DCM), and CVB3 is frequently used serotype

for studying myocardial pathogenesis of CVB (Tian et al., 2018). CVB is also the pathogen of pancreatitis and aseptic encephalitis (Ye et al., 2013). Currently, there are no specific measurement to treat and prevent CVB infection. CVB genome is a positive single-strand RNA (+ssRNA). The genome is about 7.4 kb in length, including three functional regions: 5′ untranslated region (5′-UTR), a long open reading frame (ORF), and 3′-UTR (Souii et al., 2013; Honkimaa et al., 2020). The ORF is translated into a large polyprotein, which is cleaved into four structural and seven non-structural proteins by the viral proteinases 2A and 3C (Ben M'hadheb et al., 2015; Huang et al., 2017). The non-structural protein 3D plays as RNA-dependent RNA polymerase (RdRp) and is vital for CVB replication (Turkki et al., 2020).

The interaction between viral components and host cellular factor plays a key role in the pathogenesis of CVB (Kim et al., 2022). MiRNAs have been implicated in many viral infections via their mRNAs binding action (Trobaugh et al., 2017). Our previous studies showed that a variety of miRNAs can affect CVB pathogenesis. For example, miR-10a* can promote CVB replication (Tong et al., 2013), while miR-146a modulates the inflammatory response to CVB infection (Fei et al., 2020). Pyroptosis is a cell death process that is induced by proinflammatory signals. Our previous study demonstrated that pyroptosis is involved in the pathogenesis of CVB3 infections (Wang Y. et al., 2018).

Circular RNAs (circRNAs) are highly conserved non-coding RNAs in mammals with a length varied from fewer 100 to thousands of nucleotides (nt) (Pamudurti et al., 2017). CircRNA does not own 5′-cap structure and 3′-poly(A) structures and usually forms a closed circle (Beermann et al., 2016). CircRNA can bind to and "sponge" miRNA, and relieve the suppression of the miRNA on its target mRNAs and thereafter the gene expression (Beermann et al., 2016). Studies have shown that circRNAs are involved a variety of diseases, including cancer, inflammation, fibrosis, and viral infection (Memczak et al., 2013; Zhang H. D. et al., 2018; Zhang Z. et al., 2018; Yang et al., 2019; Xie et al., 2021). CircRNAs have been shown to regulate viral replication, viral pathogenesis, and antiviral immune response and thus may be candidate biomarkers and antiviral target for viral infection (Chen et al., 2017; Li et al., 2017; Sekiba et al., 2018; Tagawa et al., 2018; Wang S. et al., 2018; Yu et al., 2019; Zhao et al., 2019; Lu et al., 2020; Zhang and Wang, 2020). To date, the involvement of circRNAs in CVB replication remains unknown. Only hsa_circ_0000367 (circSIAE) has been reported to inhibit CVB3 replication by targeting cellular TAOK2 (thousand and one amino-acid kinase 2) through sponge adsorption of miR-331-3p (Yang et al., 2022).

Circ_0076631 has been reported to regulate the pyroptosis process of diabetic cardiomyopathy (Yang et al., 2019). In the present study, we found that circ_0076631 could promote the biosynthesis and replication of CVB3 by sponging miR-214-3p, suggesting that circ_0076631 may be a potential therapeutic target against CVB3 infection.

Results

Circ_0076631 abundance increases siginificantly in the CVB3-infected cells

As previously noted, circ_0076631 regulated caspase-1 to mediate pyroptosis of diabetic cardiomyopathy (Yang et al., 2019). According to our previous study, pyroptosis is involved in the pathogenesis of both CVB3 and enterovirus A71 (EV-A71) (Wang Y. et al., 2018). Therefore we speculated that circ_0076631 may play role in regulating CVB3 replication. To clarify the source of hsa_circ_0076631 in human genome (hereafter simplified as circ_0076631), sequence analysis showed that circ_0076631 was originated from the transcript RNA of SLC29A1 between 155 nt (exon 3) and 1264 nt (exon 12) (**Figure 1A**). Ring formation validation indicated that circ_0076631 could form a ring, as indicated by the amplification curve and dissolution curve (**Figure 1B**). Upon real-time quantitative PCR (RT-qPCR) detection in the CVB3-infected cells for 6 h, the levels of circ_0076631 were increased, suggesting that circ_0076631 may be involved in CVB3 infection (**Figure 1C**).

Circ_0076631 knockdown reduces CVB3 replication

To evaluate the role of circ_0076631 in CVB3 infection, three siRNA against circ-0076631 (si-1, si-2, and si-3) were designed to knock down circ_0076631. RT-qPCR showed that three siRNAs worked out to knock circ_0076631 and si-2 demonstrated the highest efficiency (**Figure 2A**). In the cells transfected with si-2, after infection with CVB3 (MOI = 10) for 6 h, RT-qPCR (**Figure 2B**), immunofluorescence staining (**Figures 2C,D**), and western blotting (**Figure 2E**) showed that the levels of CVB3 3D RNA and protein were both decreased, suggesting that inhibition of circ_0076631 reduces CVB3 replication.

Bioinformatics prediction of circ_0076631-binding miRNAs

To elucidate the mechanism of circ_0076631 regulating CVB3 replication, we searched for miRNAs that is capable of binding to circ_0076631 in the ENCORI database[1] and found that 38 miRNAs could bind to circ_0076631 and the top 20 miRNAs were shown in **Figure 3A**. Then, we searched for miRNAs related to the inflammatory pathway and viral infection

1 https://starbase.sysu.edu.cn/agoClipRNA.php?source=lncRNA

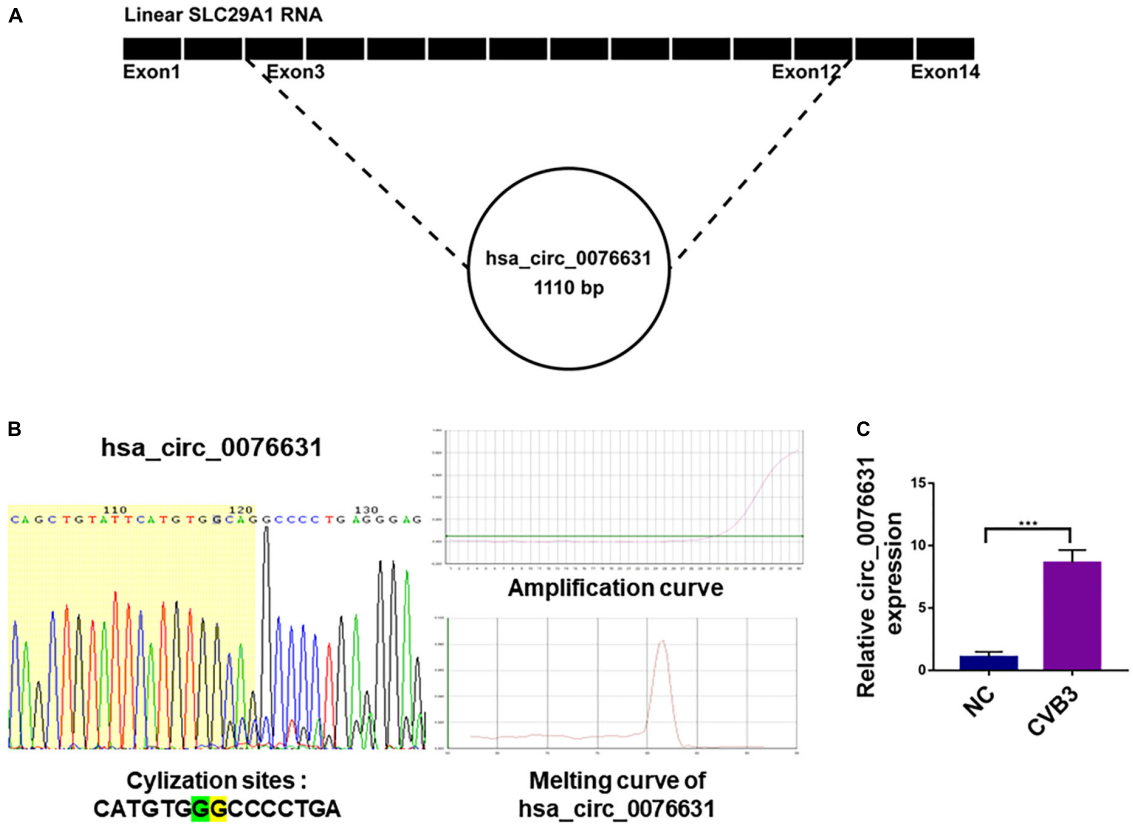

FIGURE 1
The source of circ_0076631 and association with CVB3 infection. **(A)** The genomic location of circ_0076631 in the transcript of SLC29A1 gene. **(B)** Ring formation by circ_0076631 was performed on the basis of the amplification curve and dissolution curve, which are shown. **(C)** HeLa cells were infected with CVB3 (MOI = 10) and incubated for 6 h. Circ_0076631 levels were analyzed by RT-qPCR. $n = 3$, $^{***}P < 0.01$.

in the miRNAs database and mirPath v.3[2] (Figures 3B,C). Three miRNAs were at the intersection of circ_0076631 binding, inflammation, and viral infection (Figure 3D). The detection of these miRNAs in HeLa cells infected with CVB3 showed that these miRNAs downregulated. Among them, miR-214-3p decreased most significantly (Figure 3E).

Circ_0076631 can interact with miR-214-3p

To detect the effect of CVB3 infection on the cellular localization of circ_0076631 and miR-214-3p, induced by CVB3, fluorescence *in situ* hybridization (FISH) assay demonstrated that circ_0076631 was in nucleus and cytoplasm, while miR-214-3p was in the cytoplasm of the non-infected cells. However, the distribution of circ_0076631 in the nucleus increased, while the distribution of miR-214-3p in cytoplasm of the CVB3-infected cells decreased (Figure 4A). To verify the interaction between circ_0076631 and miR-214-3p, the circ_0076631 cDNA was inserted into the 3′-UTR of *Renilla* luciferase (Rluc) gene of plasmid psiCHECK-2, denoted as WT-circ_0076631. Another plasmid with a mutated circ-007631 in which miR-214-3p-targeting site was removed was also prepared similarly and denoted as Mut-circ_0076631. HEK293T cells were transfected with the two plasmids respectively. Dual luciferase assay showed that the relative Rluc/Luc ratio was significantly decreased in the cells transfected with WT-circ_0076631 + miR-213-3p mimic, and increased in the cells transfected with WT-circ_0076631 + AMO-214-3p. No apparent change was observed in the cells with Mut-circ_0076631 treated with mimic or antisense miR-214-3p (AMO-214-3p), confirming that circ_0076631 can interact with miR-214-3p (Figure 4B).

MiR-214-3p can target the 3D-coding sequence of CVB3

Using miRNA target prediction tool RNAhybrid, miR-214-3p showed a strong binding capability to the 3D-coding

2 https://dianalab.e-ce.uth.gr/html/mirpathv3/index.php?r=mirpath

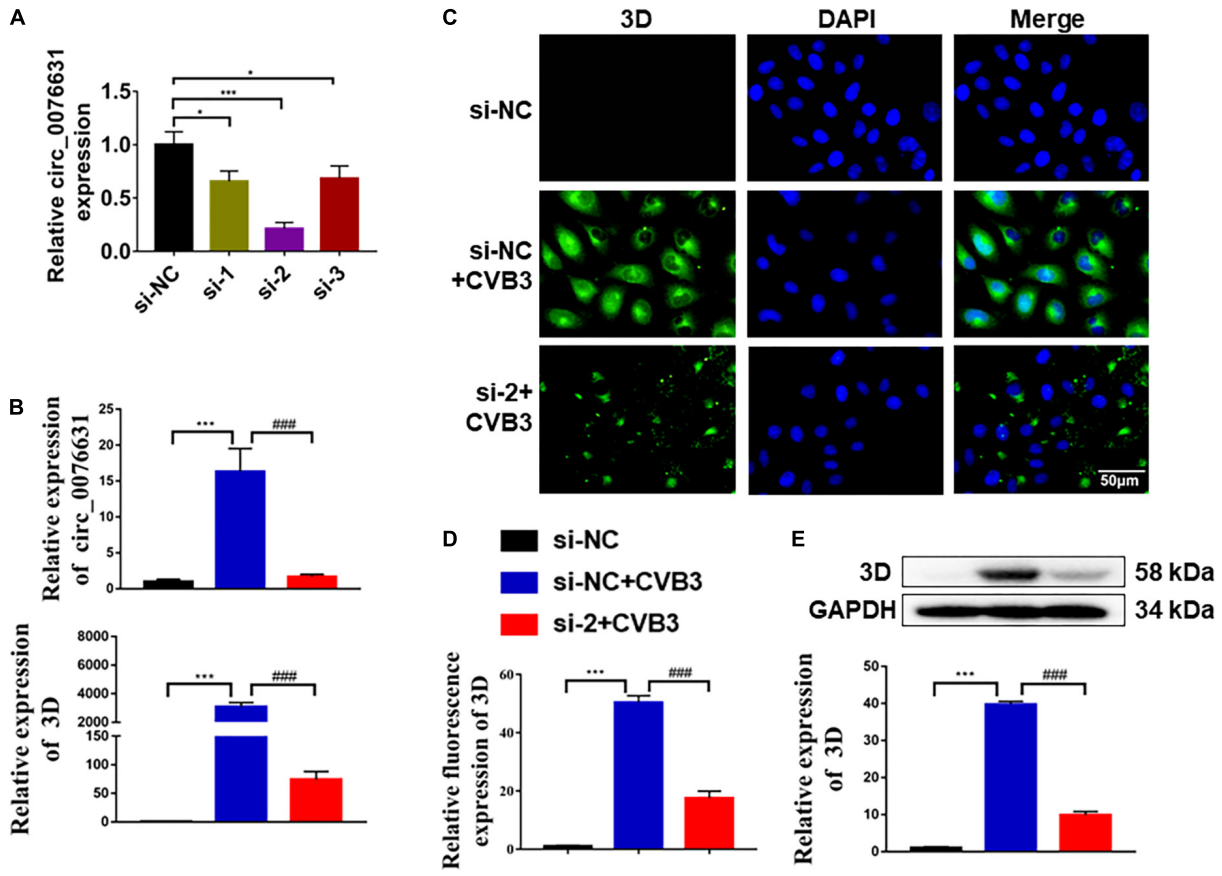

FIGURE 2
Circ_0076631 knockdown suppresses CVB3 replication. **(A)** HeLa cells were transfected with circ_0076631 siRNA (si-1, si-2, si-3) and cultured for 24 h. The abundance level of circ_0076631 was assayed by RT-qPCR. $n = 3$. $^{*}P < 0.05$, $^{***}P < 0.001$. **(B–E)** HeLa cells were transfected separately with si-NC and si-circ-0076631 for 24 h. After infection with CVB3 (MOI = 10) for 6 h. **(B)** The relative abundance level of circ_0076631 and CVB3 3D-coding RNA detected by RT-qPCR. **(C,D)** Immunofluorescence staining was performed to detect the level of CVB3 3D protein. **(E)** The relative level of CVB3 3D protein was detected by western blotting. $n = 3$. $^{**}P < 0.01$, $^{***}P < 0.001$ compared with the si-NC. $^{\#}P < 0.05$, $^{\#\#}P < 0.01$, $^{\#\#\#}P < 0.001$ compared with the si-NC + CVB3 group.

sequence of CVB3 based on the minimum free energy hybridization (Figure 5A). Strong binding capability to the 3D-coding sequences of CVB1, CVB2, CVB3, CVB4, CVB6, and EV-A71 was also predicted (Figure 5A). According to the binding sequence, we constructed two dual luciferase reporter plasmids fused with a wildtype (WT-CVB3-3D) or a mutant (Mut-CVB3-3D) 3D-coding sequences of CVB3, respectively (Figure 5B). In the HEK293T cells transfected with WT-CVB3-3D, the relative Rluc/Luc ratio was significantly reduced when miR-214-3p mimics (miR-214-3p) was co-transfected, whereas the relative Rluc/Luc ratio remarkably increased when AMO-214-3p was given. The relative Rluc/Luc ratio remained no obvious change in the cells with Mut-CVB3-3D + miR-214-3p or Mut-CVB3-3D + AMO-214-3p (Figure 5B). To verify the target of miR-214-3p in the 3D-coding sequence of CVB3, HEK293T cells were co-transfected with miR-214-3p and a 3D-expressing plasmid (denoted as EGFP-3D) or a miR-214-3p binding-site mutated 3D-expressing plasmid (denoted as EGFP-3D^{mut}). The EGFP-3D expression was almost invisible in the cells transfected with miR-214-3p, while EGFP-3D^{mut} expression was not affected by miR-214-3p transfection (Figure 5C).

Circ_0076631 facilitates CVB3 infection through interacting with miR-214-3p

To evaluate the effect of circ_0076631 on CVB3 infection through miR-214-3p, HeLa cells were transfected with si-2 and infected with CVB3 (MOI = 10) for 6 h, RT-qPCR (Figures 6A–C), immunofluorescence staining (Figures 6D,E) and western blotting (Figure 6F) showed that the levels of CVB3 RNA and 3D protein were both decreased. The downregulation effect of si-2 could be mostly reversed by introducing AMO-214-3p. The data suggest that circ_0076631 facilitates CVB3 infection through interacting with miR-214-3p.

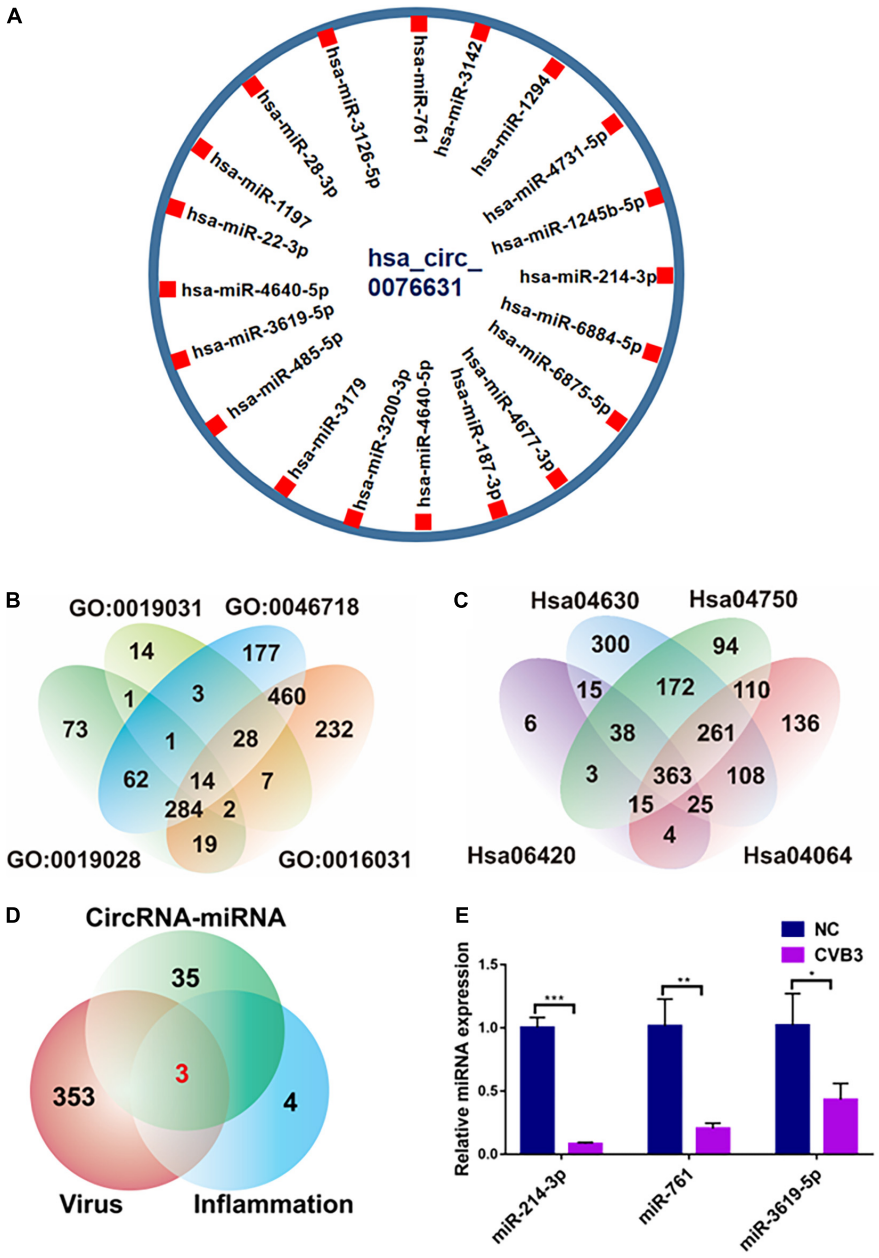

FIGURE 3
Prediction of miRNAs that may bind to targeting circ_0076631. **(A)** Screening the potential miRNAs that may bind to circ_0076631. **(B,C)** Screening of the miRNAs related to the inflammatory pathway and viral infection. **(D)** Comprehensive analysis of the three aforementioned screening results. **(E)** HeLa cells were infected with CVB3 (MOI = 10) for 6 h, and the abundance of miRNAs was measured by RT-qPCR. $n = 3$. $^{*}P < 0.05$, $^{**}P < 0.01$, $^{***}P < 0.001$.

Discussion

CircRNAs play critical roles in various disorders, including cancer, inflammation, fibrosis, and viral infection (Memczak et al., 2013; Zhang H. D. et al., 2018; Zhang Z. et al., 2018; Yang et al., 2019; Xie et al., 2021). Although there are studies reported that circRNAs participate in regulating viral infections (Chen et al., 2017; Li et al., 2017; Sekiba et al., 2018; Tagawa et al., 2018; Wang S. et al., 2018; Yu et al., 2019; Zhao et al., 2019; Lu et al., 2020; Zhang and Wang, 2020), it is unknown whether circRNA directly involves in regulating CVB infection. In this study, we found that circRNA circ_0076631 can promote CVB3 infection by interacting with miR-214-3p, possibly through miRNA sponging mechanism.

Over thousands of circRNAs have been identified in cells (Pamudurti et al., 2017; He et al., 2021). It is hard to select

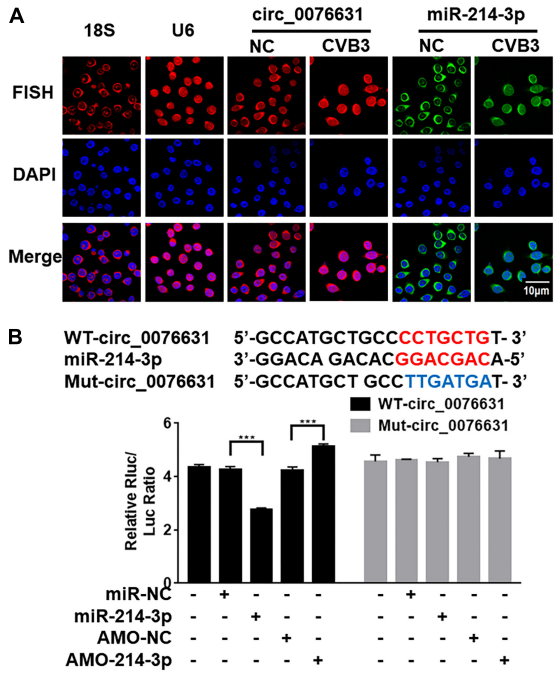

FIGURE 4
Verification of miR-214-3p binding to circ_0076631. **(A)** FISH assay was performed to observe the cellular localization of circ_0076631 in HeLa cells with CVB3 infection. Circ_0076631, 18S rRNA, U6 are showed in red. Nuclei are stained with DAPI (blue). **(B)** The miR-214-3p-binding sequence in wild-type circ_0076631 and the mutated circ_0076631. Plasmids expressing *Renilla* luciferase (Rluc) fused with wide-type circ_0076631 (containing miR-214-3p-targeting site, WT-circ_0076631) or with mutated circ_0076631 (without miR-214-3p-targeting site, Mut-circ_0076631) sequence were co-transfected with miR-214-3p mimic (miR-214-3p), miR-NC, AMO-miR-214-3p (AMO-214-3p), or AMO-miR-NC (AMO-NC) into HEK293T cells, respectively. Luciferase activity was detected with dual luciferase assay. The activity of Rluc was normalized with luciferase (Luc). $n = 3$. $^{***}P < 0.001$.

a single circRNA which may be functional in certain types of viral infections from such a large body of non-coding RNAs. In this study, we selected circ_0076631 based on our previous identification of circ_0076631 as a regulator of pyroptosis in diabetic cardiomyopathy (Yang et al., 2019).

Recent studies demonstrate that miRNAs are highly associated with CVB infection. MiR-10a*, miR-342-5p, miR-142-3p, miR-23b, and miR-296-5p can directly target enterovirus genomic RNA to promote or inhibit enterovirus replication (Kelly et al., 2010; Wang et al., 2012; Tong et al., 2013; Wen et al., 2013; Zheng et al., 2013). MiRNAs can also indirectly affect CVB infection, for example, miR-155 is recognized as a proinflammatory factor in CVB infection, knocking down miR-155 can improve the survival rate and cardiac function of the CVB-infected mice (Corsten et al., 2012). MiR-21 and miR-146b also participate in CVB infection, knocking down miR-21 and miR-146b can alleviate the CVB infection-related cardiac injury by decreasing the proportion of Th17 cells (Liu et al., 2013). We recently recognized miR-146a as an anti-inflammatory miRNA. MiR-146a expresses increasingly upon CVB infection and works as a host's negative regulator on inflammation so as to restrain the inflammatory injury to an adequate scale (Fei et al., 2020). In this study, we found that miR-214-3p could directly interfere CVB3 replication by targeting the 3D-coding region. Though the target site is not in the 3′UTR, which miRNAs target most frequently, our loss-of-function test validated it as a viable target for miR-214-3p. Given that miR-10a*, miR-324-5p, miR-142-3p, and miR-296-5p, miR-23b are all target the coding region of enterovirus genome, it seems a common feature for enteroviruses that the coding region of enterovirus genome can be effectively targeted by miRNAs.

According to this study and a miRNA expression profiling we did previously (data not shown), miR-214-3p abundance undergoes a conversion from high abundant in the normal control cells to low abundant in the CVB-infected cells. Given the suppressing role of miR-214-3p to CVB, the conversion will favor CVB to replicate in the host cells. On the other hand, if the abundance of miR-214-3p can be artificially elevated, it may work as a therapeutic strategy against CVB infection.

The decrease of miR-214-3p abundance in the CVB-infected cells can be an outcome of failures such as downregulated transcription of primary miRNA, impedimental maturation process, and removal by degradation or sponge absorption. CircRNAs can sponge miRNAs to reduce their availability and thus reduce their binding to target mRNAs. The possibility of sponge absorption led us to probe the potential role of circRNAs. Through a bioinformatics searching for circRNAs that may interact with miR-214-3p, circ_0076631 was selected because it owns an 8-nt complemental sequence to miR-214-3p, and it became abundant in the cells with CVB3 infection. Our further evaluation supported that miR-214-3p can bind to circ_0076631. Knockdown of circ_0076631 could inhibit CVB3 infection. The inhibition could be relieved by AMO-214-3p. Taken together, we hypothesize that CVB3 infection upregulates the expression of circ_0076631, which then sponges

TABLE 1 PCR primer sequences.

Primer		Sequence
hsa_circ_0076631	Forward	5′-CGGAGCCTCACAGCTGTATTC-3′
	Reverse	5′-CCCAGACCCAGCATGAAGAAG-3′
miR-214-3p	Forward	5′-TATACATCAAACAGCAGGCACA-3′
	Reverse	5′-CATTCGATCTTCTCCACAGTCTC-3′
CVB 3D	Forward	5′-TCATGACACCAGCAGACAAA-3′
	Reverse	5′-TCCTTGGTCCATCTGATTGA-3′
GAPDH	Forward	5′-ATCACTGCCACCCAGAAGAC-3′
	Reverse	5′-TTTCTAGACGGCAGGTCAGG-3′
U6	Forward	5′-CTCGCTTCGGCAGCACATATACT-3′
	Reverse	5′-ACGCTTCACGAATTTGCGTGTC-3′

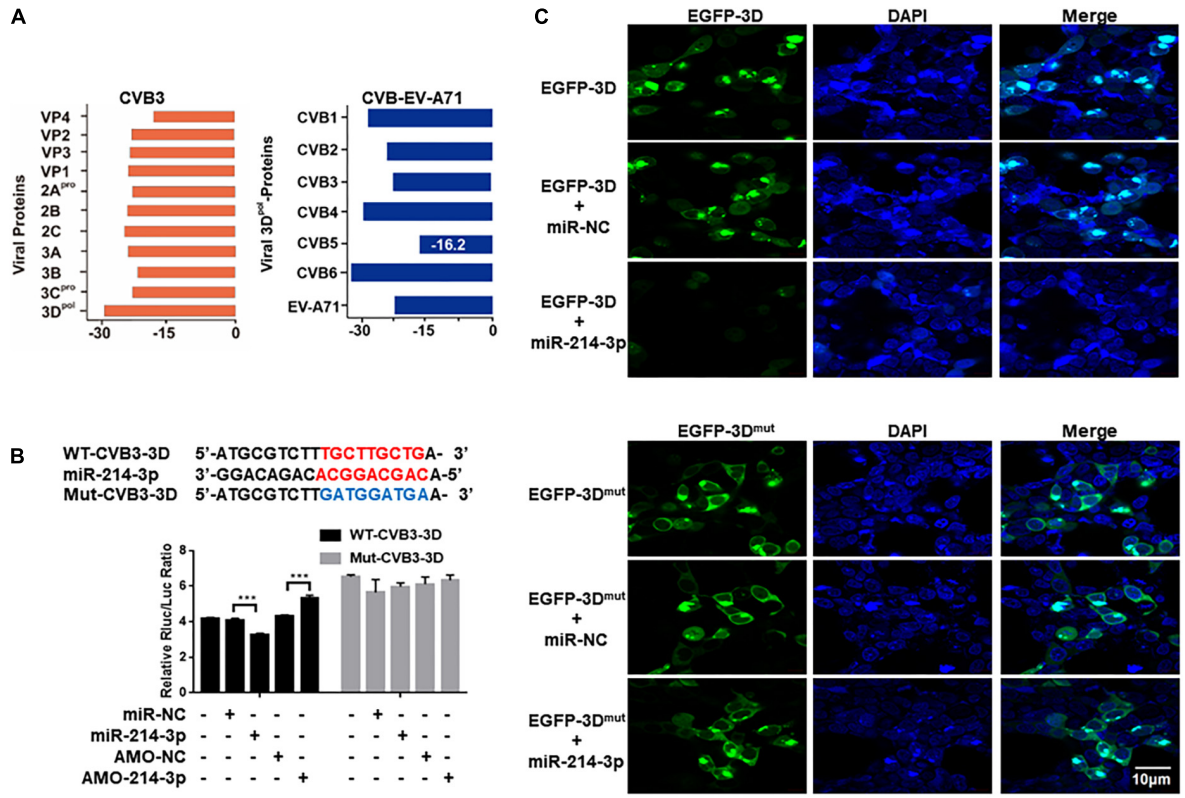

FIGURE 5
Prediction and verification of miR-214-3p tergetig CVB3 genomic RNA. **(A)** Identification of the potential miR-214-3p-binding sites in CVB3 genomic RNA by RNAhybrid. The binding ability of miR-214-3p with CVB1- CVB6 3D and EV-A71 3D sequence. **(B)** The miR-214-3p-binding sequence in the CVB3 3D-coding sequence and the mutated CVB3 3D sequence. Wide-type CVB3 3D sequence (containing miR-214-3p-binding sequence, WT-CVB3-3D) or mutated CVB3 3D sequence (without miR-214-3p-binding sequence, Mut-CVB3-3D) was cloned into a luciferase-expressing plasmid. The plasmid was co-transfected separately with miR-214-3p, miR-NC, AMO-214-3p, or AMO-NC into HEK293T cells, respectively. The luciferase activity was detected with dual luciferase assay. The acitivity of Rluc was normalized with Luc. $n = 3$. ***$P < 0.001$. **(C)** HEK293T cells were co-transfected with pEGFP-CVB3-3D (EGFP-3D) or pEGFP-CVB3-3D^{mut} (EGFP-3D^{mut}) and miR-214-3p for 24 h. Immunofluorescence staining was performed to detect the expression level of the CVB3 3D protein.

miR-214-3p to relieve its suppression on CVB3 biosynthesis by targeting the 3D-coding sequence. To date, little is known about the association between circRNAs and enterovirus infection. CircSIAE is an exception that it can act as a sponge for miR-331-3p and inhibit CVB3 infection indirectly by up-regulating host's TAOK2 expression (Yang et al., 2022). Our finding provides another example of circRNA interfering enterovirus infection in a much more direct way. Furthermore, the target site of miR-214-3p is available in CVB1, CVB2, CVB3, CVB4, CVB6, and EV-A71, the regulation of circ_0076631/miR-214-3p is likely applicable to most serotypes of CVB and other enteroviruses. On the basis of the aforementioned data, a putative mechanism is summarized in **Figure 7**.

There is limitation in this study. The conclusion about the interaction between circ_0076631/miR-214-3p and CVB infection is based solely on *in vitro* data. Considering that CVB is the major pathogen of human viral myocarditis and DCM (Tian et al., 2018), it is a shortage of the study that the role of circ_0076631 in the myocardial pathogenesis of CVB has not been evaluated. *In vivo* investigation is needed to address the question. Unfortunately, mouse model with circ_0076631 knockdown or knockout is not available presently. In addition, only one serotype (CVB3) has been evaluated experimentally, the interaction between circ_0076631 and other serotypes of CVB is yet to be observed.

In summary, circ_0076631 may play a supportive role in CVB3 infection. Circ_0076631 facilitates CVB3 infection by sponging miR-214-3p. Knocking down circ_0076631 or giving miR-214-3p may be a potential approach to treat CVB3 infection.

Materials and methods

Cell culture

Human cell lines including HeLa, HEK-293T were cultured in Dulbecco's modified Eagle medium (DMEM) (HyClone,

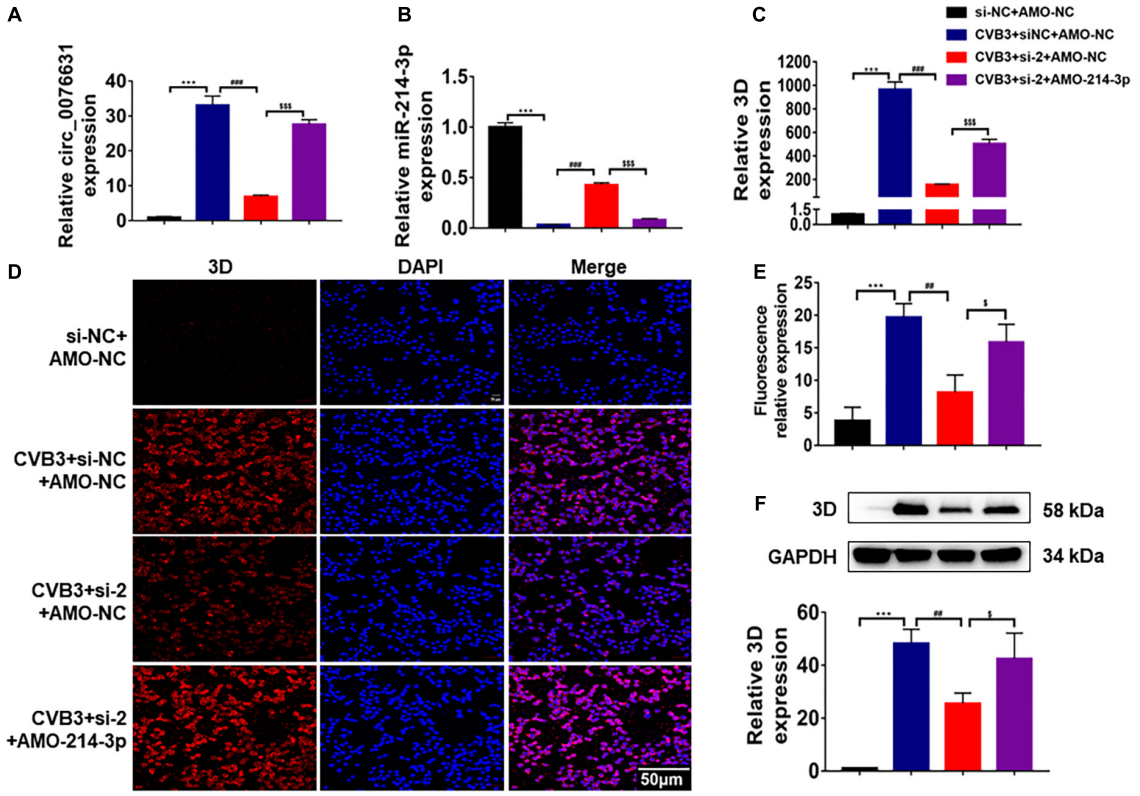

FIGURE 6
Circ_0076631 knockdown suppresses CVB3 replication through miR-214-3p targeting 3D-coding sequence. **(A)** HeLa cells were transfected separately with si-NC + AMO-NC, si-2 + AMO-NC, and si-2 + AMO-214-3p for 24 h, and infected with CVB3 (MOI = 10) for 6 h. **(A–C)** The relative abundance level of circ_0076631, miR-214-3p, and CVB3 3D was detected by RT-qPCR. **(D,E)** Immunofluorescence staining was performed to detect the level of the CVB3 3D protein. **(F)** The relative level of CVB3 3D protein was detected by western blotting. $n = 3$. $^{***}P < 0.001$ compared with the si-NC + AMO-NC group. $^{\#\#}P < 0.01$, $^{\#\#\#}P < 0.001$ compared with the CVB3 + si-NC + AMO-NC group. $\$P < 0.05$, $\$\$\$P < 0.001$ compared with the CVB3 + si-2 + AMO-NC group.

Logan, UT, United States) containing 10% fetal bovine serum (FBS; Gibco, Scoresby VIC, Australia), penicillin (100 U/mL) and streptomycin (0.1 mg/mL). The cells were incubated at 37°C in 5% CO_2 and passaged every 48 h.

Viruses and viral infection

CVB3 Woodruff strain was cultured in HeLa cells. The virus titer was measured by the plaque-forming unit (pfu) as described previously (Tong et al., 2013). The titer of CVB3 was 1×10^8 pfu/mL and a multiplicity of infection (MOI) of 10 was used to infect cells.

Transfection

Nucleotides, including short interfering RNA (siRNA) of circ_0076631, miR-214-3p mimic (miR-214-3p), AMO-214-3p (mAmCmUmGmCmCmUmGmUmCmUmGmUmGmCmCmUmGmCmUmGmU), miR-mock, and AMO-mock were synthesized by RiboBio (Guangzhou, China). HEK293T cells were transiently transfected with the aforementioned nucleotides using X-Treme GENE transfection reagent (Roche, Mannheim, Germany) according to the manufacturer's instructions. In brief, cells were cultured in 12-well plates until they reached 60–75% confluence. The culture medium was then replaced with serum-free medium and transfected with 50 μL of transfection mixture. After incubation for 4 h, the transfection mixture was discarded, and fresh medium with 10% FBS and antibiotics were added to the cells and maintained at 37°C with 5% CO_2.

Construction of mutant 3D-expressing plasmid

A plasmid expressing CVB3 3D with a mutated miR-214-3p-binding site was constructed based on pEGFP-3D, a plasmid expressing CVB3 3D fused with enhanced green fluorescence protein (EGFP) engineered previously in our lab. Briefly, mutant

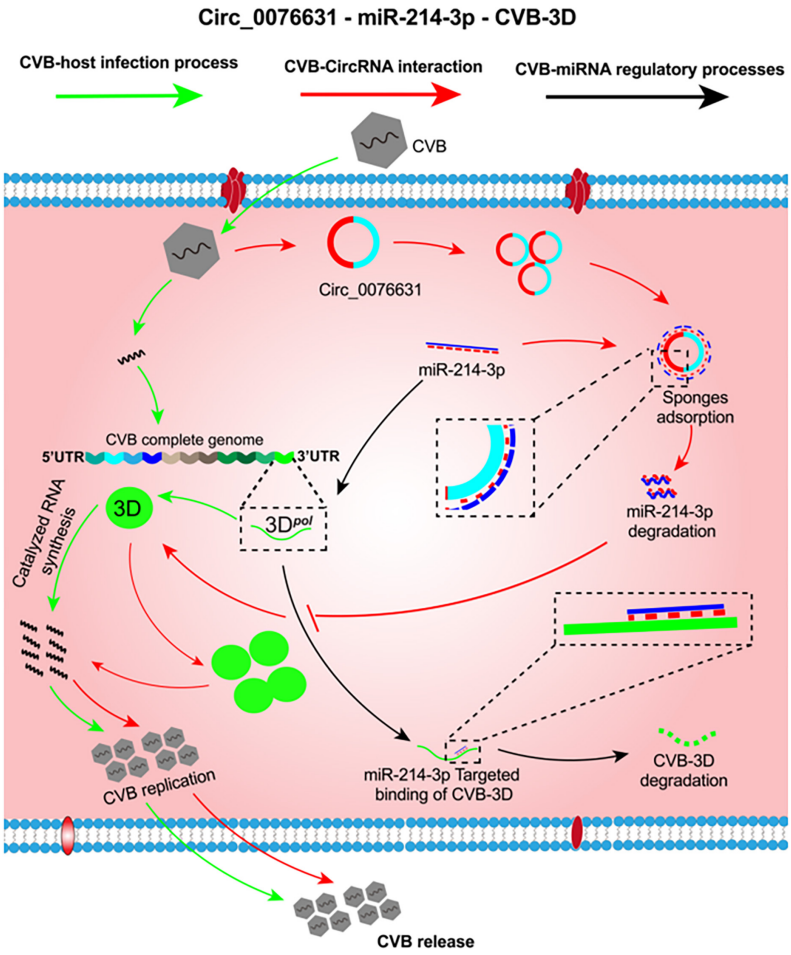

FIGURE 7
The putative mechanism of circ_0076631 regulating CVB3 infection by sponging miR-214-3p. At the early stage of CVB3 infection, miR-214-3p is abundant and can suppress viral biosynthesis by targeting the 3D-coding sequence (black lines). Later, CVB3 infection can somehow trigger circ_0076631 generation. Circ-0076631 facilitates CVB3 replication through sponging miR-214-3p and relieving its suppression on CVB3 biosynthesis (red lines).

pEGFP-3D was prepared with the mutation of nt6977-nt6985 in CVB3 genome by overlapping PCR. The restriction sites of *Hin*d III and *Xba* I were added to both ends of pEGFP-3D with specific primers. After digestion with (TaKaRa, Otsu, Shiga, Japan), the mutant 3D fused with EGFP was inserted to the multiple cloning site of pEGFP-C1 and designated as pEGFP-3D^{mut}.

Reverse transcription and real-time quantitative PCR

Total RNA samples were extracted with TRIzol (Invitrogen, Carlsbad, CA, United States) according to the manufacturer's instructions. After detecting the purity and concentration of the RNA with a NanoDrop2000 spectrophotometer (Thermo Fisher, Waltham, MA, United States), 1 μg of total RNA was used as a template with PrimeScript RT Enzyme Mix I (TaKaRa, Otsu, Shiga, Japan) in a reverse transcription system. RT-qPCR was performed on a LightCycler 96 (Roche, Basel, Switzerland) using SYBR Premix Ex Taq II (TaKaRa, Otsu, Shiga, Japan) mixed with 1 μL of the synthesized cDNA and sense/antisense primers to a final volume of 25 μL. The primer sequences used in this study are listed in **Table 1**. The relative gene expression of the circRNAs, miRNAs and mRNAs level was calculated by the $2^{-\Delta\Delta Ct}$ method (Livak and Schmittgen, 2001). The expression of circ_0076631, miR-214-3p was normalized to that of U6, and the expression of the other sequences was normalized to that of glyceraldehyde-3-phosphate dehydrogenase (GAPDH).

Western blotting

Total protein was extracted with RIPA lysis buffer (Thermo Scientific, Rockford, United States) mixed with

phenylmethane sulfonyl fluoride (PMSF). The protein samples were separated by 10% sodium dodecyl sulfate-polyacrylamide gel electrophoresis (SDS-PAGE), and the proteins were transferred onto the PVDF membrane (Millipore, Billerice, MA, United States). Then, the membrane was blocked with 5% non-fat milk dissolved in TBST for 1 h at room temperature and subsequently incubated with the corresponding primary antibodies overnight at 4°C, followed by HRP-conjugated secondary antibodies for 1 h at room temperature. The membranes were imaged with FluorChem M CCD camera (ProteinSimple, Santa Clara, CA). GAPDH was used as the internal control. The primary antibody against GAPDH was purchased from ZSGB-BIO (Beijing, China). A polyclonal antibody against 3D protein of CVB3 was generated in our laboratory.

Immunofluorescence staining

Cells plated on coverslips were fixed with 4% paraformaldehyde in PBS for 30 min at room temperature. Then, the cells were permeabilized with 0.1% Triton X-100 for 1 h followed by blocking with 500 μL of goat serum for 2 h at 37°C. Then cells were incubated with primary antibodies against 3D (1:200) at 4°C overnight. After three washes, the cells were incubated with FITC-conjugated secondary antibody (1:1,000) for 1 h at 37°C. Then, the nuclei were stained with DAPI (Beyotime, Shanghai, China) for 20 min. Images were collected with a fluorescence microscope (AxioVert 200, Zeiss).

MiRNA target prediction and verification

To predict the targets of miRNAs, we used RNAhybrid 2.2[3] and selected the potential binding sites according to the minimum free energy (mfe) of complementary base sequences. A luciferase reporter was constructed with the putative target sequences of miR-214-3p to verify the target effects (RiboBio, Guangzhou, China).

Luciferase assays

The corresponding linear sequence of circ_0076631 was obtained with circBase software, and dual-luciferase plasmids including circ_0076631 with miR-214-3p-binding sites (WT-circ_0076631) or with a mutated sequence to remove miR-214-3p-binding site (Mut-circ_0076631) were constructed by RiboBio. Similarly, dual-luciferase plasmids including CVB3 3D sequence with with miR-214-3p-binding sites (WT-CVB3-3D) or a mutated sequence to remove miR-214-3p-binding site (Mut-CVB3-3D) were constructed. The wild-type or mutated plasmids with miR-214-3p or AMO-214-3p were transfected into HEK293T cells by Lipofectamine 2000, respectively. Luciferase activity was tested using a Dual-Luciferase Reporter assay (Promega).

Fluorescence *in situ* hybridization

To observe the location of circ_0076631, HeLa cells were cultured in 12-well plates for 24 h until they reached 60–70% confluency. Cells with or without CVB3 infection were fixed in 4% paraformaldehyde and permeabilized in 0.5% Triton X-100. The cell samples were treated with re-hybridization solution and incubation. A hybridization buffer containing a Cy3-labeled FISH probe for detecting circ_0076631 and the internal controls 18 s and U6 were used to replace re-hybridization solution and added into cell samples which were incubated at 37°C overnight in the dark. After washing with sodium citrate (SCC) and PBS, DAPI was added to the samples for nuclear staining. Then, the samples were treated with a mounting medium and observed by fluorescence microscope (AxioVert 200, Zeiss).

Statistical analysis

All data in this study are presented as the means ± standard deviation (SD) and determined via GraphPad Prism 7 software to perform statistical analysis. Student's *t*-test or one-way ANOVA was used to evaluate the significance of difference. All experiments were repeated at least three times.

Data availability statement

The original contributions presented in the study are included in the article/supplementary material, further inquiries can be directed to the corresponding authors.

Ethics statement

The animal study was reviewed and approved by the Ethics Committee of Harbin Medical University.

Author contributions

YQ, LL, and SY conceived and designed the project. YQ, JH, FD, and XY performed the experiments. SY and LR assisted in the collection of data. ZD, CZ, LR, and YF analyzed and interpreted the data. LL wrote the manuscript. YW, ZZ, and WZ

3 https://bibiserv.techfak.uni-bielefeld.de/rnahybrid

reviewed and critically revised the initial draft. All authors contributed to the article and approved the submitted version.

Funding

This work was supported by the National Natural Science Foundation of China grants to ZZ (81871652 and 82072278), YW (81772188), and WZ (81971920 and 82172247), Natural Science Foundation of Heilongjiang Province grant to LL (LH2019H004), Heilongjiang Postdoctoral Scientific Research Developmental Fund to LL (LBH-Q19146), and Innovation Fund of Heilongjiang Provincial Higher Education Institutions to YF (31041220038).

Acknowledgments

We are grateful to the Heilongjiang Provincial Key Laboratory of Pathogens and Immunity and Northern Translational Medicine Research Centre of Harbin Medical University for their technical support.

Conflict of interest

The authors declare that the research was conducted in the absence of any commercial or financial relationships that could be construed as a potential conflict of interest.

Publisher's note

All claims expressed in this article are solely those of the authors and do not necessarily represent those of their affiliated organizations, or those of the publisher, the editors and the reviewers. Any product that may be evaluated in this article, or claim that may be made by its manufacturer, is not guaranteed or endorsed by the publisher.

References

Beermann, J., Piccoli, M. T., Viereck, J., and Thum, T. (2016). Non-coding RNAs in development and disease: Background, mechanisms, and therapeutic approaches. *Physiol. Rev.* 96, 1297–1325. doi: 10.1152/physrev.00041.2015

Ben M'hadheb, M., Souii, A., Harrabi, M., Jrad-Battikh, N., and Gharbi, J. (2015). In vitro-reduced translation efficiency of coxsackievirus B3 Sabin3-like strain is correlated to impaired binding of cellular initiation factors to viral IRES RNA. *Curr. Microbiol.* 70, 756–761. doi: 10.1007/s00284-015-0784-z

Chen, Y. G., Kim, M. V., Chen, X., Batista, P. J., Aoyama, S., Wilusz, J. E., et al. (2017). Sensing self and foreign circular RNAs by intron identity. *Mol. Cell* 67, 228-238.e5. doi: 10.1016/j.molcel.2017.05.022

Corsten, M. F., Papageorgiou, A., Verhesen, W., Carai, P., Lindow, M., Obad, S., et al. (2012). MicroRNA profiling identifies microRNA-155 as an adverse mediator of cardiac injury and dysfunction during acute viral myocarditis. *Circ. Res.* 111, 415–425. doi: 10.1161/CIRCRESAHA.112.267443

Fei, Y., Chaulagain, A., Wang, T., Chen, Y., Liu, J., Yi, M., et al. (2020). MiR-146a down-regulates inflammatory response by targeting TLR3 and TRAF6 in Coxsackievirus B infection. *RNA* 26, 91–100. doi: 10.1261/rna.071985.119

Garmaroudi, F. S., Marchant, D., Hendry, R., Luo, H., Yang, D., Ye, X., et al. (2015). Coxsackievirus B3 replication and pathogenesis. *Future Microbiol.* 10, 629–653. doi: 10.2217/fmb.15.5

He, A. T., Liu, J., Li, F., and Yang, B. B. (2021). Targeting circular RNAs as a therapeutic approach: current strategies and challenges. *Sign. Transduct. Target. Ther.* 6:185. doi: 10.1038/s41392-021-00569-5

Honkimaa, A., Kimura, B., Sioofy-Khojine, A. B., Lin, J., Laiho, J., Oikarinen, S., et al. (2020). Genetic adaptation of coxsackievirus B1 during persistent infection in pancreatic cells. *Microorganisms* 8:1790. doi: 10.3390/microorganisms8111790

Huang, B., Harrower, B., Burtonclay, P., Constantino, T., and Warrilow, D. (2017). Genome sequences of Coxsackievirus B5 isolates from two children with meningitis in Australia. *Genome Announc.* 5:e1125–e1117. doi: 10.1128/genomeA.01125-17

Kelly, E. J., Hadac, E. M., Cullen, B. R., and Russell, S. J. (2010). MicroRNA antagonism of the picornaviral life cycle: alternative mechanisms of interference. *PLoS Pathog.* 6:e1000820. doi: 10.1371/journal.ppat.1000820

Kim, S. H., Shin, H. H., Kim, J. H., Park, J. H., Jeon, E. S., and Lim, B. K. (2022). Protein Kinase B2 (PKB2/AKT2) is essential for host protection in CVB3-induced acute viral myocarditis. *Int. J. Mol. Sci.* 23:1489. doi: 10.3390/ijms23031489

Li, X., Liu, C. X., Xue, W., Zhang, Y., Jiang, S., Yin, Q. F., et al. (2017). Coordinated circRNA Biogenesis and Function with NF90/NF110 in viral infection. *Mol. Cell* 67, 214-227.e7. doi: 10.1016/j.molcel.2017.05.023

Liu, Y. L., Wu, W., Xue, Y., Gao, M., Yan, Y., Kong, Q., et al. (2013). MicroRNA-21 and -146b are involved in the pathogenesis of murine viral myocarditis by regulating TH-17 differentiation. *Arch. Virol.* 158, 1953–1963. doi: 10.1007/s00705-013-1695-6

Livak, K. J., and Schmittgen, T. D. (2001). Analysis of relative gene expression data using real-time quantitative PCR and the 2(-Delta Delta C(T)) Method. *Methods* 25, 402–408. doi: 10.1006/meth.2001.1262

Lu, S., Zhu, N., Guo, W., Wang, X., Li, K., Yan, J., et al. (2020). RNA-seq revealed a circular RNA-microRNA-mRNA regulatory network in hantaan virus infection. *Front. Cell Infect. Microbiol.* 10:97. doi: 10.3389/fcimb.2020.00097

Memczak, S., Jens, M., Elefsinioti, A., Torti, F., Krueger, J., Rybak, A., et al. (2013). Circular RNAs are a large class of animal RNAs with regulatory potency. *Nature* 495, 333–338. doi: 10.1038/nature11928

Pamudurti, N. R., Bartok, O., Jens, M., Ashwal-Fluss, R., Stottmeister, C., Ruhe, L., et al. (2017). Translation of CircRNAs. *Mol. Cell* 66, 9-21.e7. doi: 10.1016/j.molcel.2017.02.021

Sekiba, K., Otsuka, M., Ohno, M., Kishikawa, T., Yamagami, M., Suzuki, T., et al. (2018). DHX9 regulates production of hepatitis B virus-derived circular RNA and viral protein levels. *Oncotarget* 9, 20953–20964. doi: 10.18632/oncotarget.25104

Souii, A., Ben M'hadheb-Gharbi, M., and Gharbi, J. (2013). Role of RNA structure motifs in IRES-dependent translation initiation of the coxsackievirus B3: new insights for developing live-attenuated strains for vaccines and gene therapy. *Mol. Biotechnol.* 55, 179–202. doi: 10.1007/s12033-013-9674-4

Tagawa, T., Gao, S., Koparde, V. N., Gonzalez, M., Spouge, J. L., Serquiña, A. P., et al. (2018). Discovery of Kaposi's sarcoma herpesvirus-encoded circular RNAs and a human antiviral circular RNA. *Proc. Natl. Acad. Sci. U.S.A.* 115, 12805–12810. doi: 10.1073/pnas.1816183115

Tian, L., Yang, Y., Li, C., Chen, J., Li, Z., Li, X., et al. (2018). The cytotoxicity of coxsackievirus B3 is associated with a blockage of autophagic flux mediated by reduced syntaxin 17 expression. *Cell Death Dis.* 9:242. 0271-0 doi: 10.1038/s41419-018-

Tong, L., Lin, L., Wu, S., Guo, Z., Wang, T., Qin, Y., et al. (2013). MiR-10a* up-regulates coxsackievirus B3 biosynthesis by targeting the 3D-coding sequence. *Nucleic Acids Res.* 41, 3760–3771. doi: 10.1093/nar/gkt058

Trobaugh, D. W., and Klimstra, W. B. (2017). MicroRNA regulation of rna virus replication and pathogenesis. *Trends Mol. Med.* 23, 80–93. doi: 10.1016/j.molmed.2016.11.003

Turkki, P., Laajala, M., Flodström-Tullberg, M., and Marjomäki, V. (2020). Human enterovirus group B viruses rely on vimentin dynamics for efficient processing of viral nonstructural proteins. *J. Virol.* 94:e1393-19. doi: 10.1128/JVI.01393-19

Wang, L., Qin, Y., Tong, L., Wu, S., Wang, Q., Jiao, Q., et al. (2012). MiR-342-5p suppresses coxsackievirus B3 biosynthesis by targeting the 2C-coding region. *Antiviral Res.* 93, 270–279. doi: 10.1016/j.antiviral.2011.12.004

Wang, S., Cui, S., Zhao, W., Qian, Z., Liu, H., Chen, Y., et al. (2018). Screening and bioinformatics analysis of circular RNA expression profiles in hepatitis B-related hepatocellular carcinoma. *Cancer Biomark.* 22, 631–640. doi: 10.3233/CBM-170910

Wang, Y., Qin, Y., Wang, T., Chen, Y., Lang, X., Zheng, J., et al. (2018). Pyroptosis induced by enterovirus 71 and coxsackievirus B3 infection affects viral replication and host response. *Sci. Rep.* 8:2887. doi: 10.1038/s41598-018-20958-1

Wen, B. P., Dai, H. J., Yang, Y. H., Zhuang, Y., and Sheng, R. (2013). MicroRNA-23b inhibits enterovirus 71 replication through downregulation of EV71 VPl protein. *Intervirology* 56, 195–200.

Xie, H., Sun, H., Mu, R., Li, S., Li, Y., Yang, C., et al. (2021). The role of circular RNAs in viral infection and related diseases. *Virus Res.* 291:198205. doi: 10.1016/j.virusres.2020.198205

Yang, F., Li, A., Qin, Y., Che, H., Wang, Y., Lv, J., et al. (2019). A novel circular RNA mediates pyroptosis of diabetic cardiomyopathy by functioning as a competing endogenous RNA. *Mol. Ther. Nucleic Acids* 17, 636–643. doi: 10.1016/j.omtn.2019.06.026

Yang, Q., Li, Y., Wang, Y., Qiao, X., Liu, T., Wang, H., et al. (2022). The circRNA circSIAE Inhibits Replication of Coxsackie Virus B3 by Targeting miR-331-3p and Thousand and One Amino-Acid Kinase 2. *Front. Cell Infect. Microbiol.* 11:779919. doi: 10.3389/fcimb.2021.779919

Ye, X., Hemida, M. G., Qiu, Y., Hanson, P. J., Zhang, H. M., and Yang, D. (2013). MiR-126 promotes coxsackievirus replication by mediating cross-talk of ERK1/2 and Wnt/β-catenin signal pathways. *Cel. Mol. Life Sci.* 70, 4631–4644. doi: 10.1007/s00018-013-1411-4

Yu, T., Ding, Y., Zhang, Y., Liu, Y., Li, Y., Lei, J., et al. (2019). Circular RNA GATAD2A promotes H1N1 replication through inhibiting autophagy. *Vet. Microbiol.* 231, 238–245. doi: 10.1016/j.vetmic.2019.03.012

Zhang, H. D., Jiang, L. H., Sun, D. W., Hou, J. C., and Ji, Z. L. (2018). CircRNA: a novel type of biomarker for cancer. *Breast Cancer* 25, 1–7. doi: 10.1007/s12282-017-0793-9

Zhang, L., and Wang, Z. (2020). Circular RNA hsa_circ_0004812 impairs IFN-induced immune response by sponging miR-1287-5p to regulate FSTL1 in chronic hepatitis. *B. Virol. J.* 17:40. doi: 10.1186/s12985-020-01314-0

Zhang, Z., Yang, T., and Xiao, J. (2018). Circular RNAs: promising biomarkers for human diseases. *EBioMedicine* 34, 267–274. doi: 10.1016/j.ebiom.2018.07.036

Zhao, J., Lee, E. E., Kim, J., Yang, R., Chamseddin, B., Ni, C., et al. (2019). Transforming activity of an oncoprotein-encoding circular RNA from human papillomavirus. *Nat. Commun.* 10:2300. doi: 10.1038/s41467-019-10246-5

Zheng, Z., Ke, X., Wang, M., He, S., Li, Q., Zheng, C., et al. (2013). Human microRNA hsamiR-296-5p suppresses enterovirus 71 replication by targeting the viral genome. *J. Virol.* 87, 5645–5656.

frontiers | Frontiers in Microbiology

TYPE Original Research
PUBLISHED 05 October 2022
DOI 10.3389/fmicb.2022.891852

OPEN ACCESS

EDITED BY
Jue Liu,
Yangzhou University, China

REVIEWED BY
Jungnam Cho,
Center for Excellence in Molecular Plant Sciences (CAS), China
Xuming Tang,
Cornell University, United States
Sandra Rose Richardson,
Mater Research Institute, The University of Queensland, Australia

*CORRESPONDENCE
Xiaoyu Li
lixiaoyu@imb.pumc.edu.cn
Shan Cen
shancen@imb.pumc.edu.cn
Jiwei Ding
dingjiwei@imb.pumc.edu.cn

†These authors have contributed equally to this work

SPECIALTY SECTION
This article was submitted to Virology, a section of the journal Frontiers in Microbiology

RECEIVED 08 March 2022
ACCEPTED 08 September 2022
PUBLISHED 05 October 2022

CITATION
Zhang Z, Zhang N, Guo S, Liu Q, Wang S, Zhang A, Yi D, Zhao J, Li Q, Wang J, Zhang Y, Ma L, Ding J, Cen S and Li X (2022) The Zinc-Finger protein ZCCHC3 inhibits LINE-1 retrotransposition.
Front. Microbiol. 13:891852.
doi: 10.3389/fmicb.2022.891852

The Zinc-Finger protein ZCCHC3 inhibits LINE-1 retrotransposition

Zixiong Zhang†, Ning Zhang†, Saisai Guo, Qian Liu, Shujie Wang, Ao Zhang, Dongrong Yi, Jianyuan Zhao, Quanjie Li, Jing Wang, Yongxin Zhang, Ling Ma, Jiwei Ding*, Shan Cen* and Xiaoyu Li*

Institute of Medicinal Biotechnology, Chinese Academy of Medical Sciences and Peking Union Medical School, Beijing, China

Long-interspersed element 1 (LINE-1) is an autonomous non-LTR retrotransposon. Its replication can cause mutation and rearrangement of host genomic DNA, which may result in serious genetic diseases. Host cells therefore developed defense strategies to restrict LINE-1 mobilization. In this study, we reported that CCHC-type zinc-finger protein ZCCHC3 can repress LINE-1 retrotransposition, and this activity is closely related to its zinc-finger domain. Further studies show that ZCCHC3 can post-transcriptionally diminish the LINE-1 RNA level. The association of ZCCHC3 with both LINE-1 RNA and ORF1 suggests that ZCCHC3 interacts with LINE-1 RNP and consequently causes its RNA degradation. These data demonstrate collectively that ZCCHC3 contributes to the cellular control of LINE-1 replication.

KEYWORDS

ZCCHC3, LINE-1, retrotransposon, restricting factor, RNA

Introduction

Long-interspersed element 1 (LINE-1) is a non-LTR (long terminal repeat) retrotransposon that can move its sequences from one site in the genome to the other through an RNA intermediate (Goodier and Kazazian, 2008). The human genome contains more than 500,000 copies of LINE-1 among which ~80–100 copies are capable of retrotransposition (Brouha et al., 2003). Of all transposons in the human genome, including DNA transposons, LTR retrotransposons, and non-LTR retrotransposons, including LINEs and SINEs (short interspersed elements), LINE-1 is the only active autonomous transposon in the human genome. Moreover, LINE-1 also supports the retrotransposition of SINES including Alu and SVA that do not encode their own proteins (Goodier and Kazazian, 2008; Richardson et al., 2015).

The full-length LINE-1 transcript is ~6,000 nucleotides in length, which includes a 5′ untranslated region (5′ UTR) harboring an active promoter, two open reading frames (ORF1p and ORF2p), and a 3′ UTR (Kazazian and Moran, 2017). ORF1p is a 40-kDa RNA-binding protein bearing nucleic acid chaperone activity (Martin, 2006, 2010; Martin et al., 2008), and ORF2p is a 150-kDa protein with endonuclease and reverse transcriptase activities (Feng et al., 1996; Alisch et al., 2006). Both ORF1p and ORF2p

proteins show a strong cis-preference, and they associate with the LINE-1 RNA to form a ribonucleoprotein particle (RNP) in the cytoplasm (Kulpa and Moran, 2006). LINE-1 RNP is then imported into the nucleus, where the LINE-1 RNA is reverse transcribed into cDNA and subsequently incorporated into the host genome through a process termed target-primed reverse transcription (TPRT) (Luan et al., 1993; Cost et al., 2002).

The transposition of LINE-1, Alu, and SVA can cause genetic instability and induce dozens of genetic diseases (Volkman and Stetson, 2014; Hancks and Kazazian, 2016; Burns, 2017; Mita et al., 2020). To avoid the deleterious effects of LINE-1 transposition on the structure and function of the host genome, various strategies have been described to safeguard the host against LINE-1. One mechanism involves DNA methylation and histone modification, which suppresses LINE-1 RNA transcription (Garcia-Perez et al., 2010; Goodier, 2016; Ishak et al., 2016; Fukuda and Shinkai, 2020). Noncoding RNA (ncRNA)-based RNA interference machinery, including siRNA, miRNA, and piRNA, represent another controlling mechanism against these transposable elements (TEs) (Obbard et al., 2009; Newkirk et al., 2017; Teixeira et al., 2017; Fung et al., 2019). Moreover, in recent years, many interferon-inducible host proteins, such as APOBEC3 proteins, MOV10, SAMHD1, and ZAP, also have been found to process inhibitory activities against LINE-1 retrotransposition (Yu et al., 2015; Goodier, 2016).

The CCHC-type zinc-finger protein ZCCHC3 is a CCHC-type zinc-finger protein, which was recently discovered to involve in antiviral innate immune responses. Specifically, ZCCHC3 promotes the interaction between viral nuclear acid and pattern recognition receptors, including cGAS, RIG-I-like receptor, and Toll-like receptor 3, thus positively regulating IFN signaling triggered by RNA and DNA virus (Lian et al., 2018a,b; Zang et al., 2020). Besides, ZCCCH3 was also found to interact with SARS-CoV-2 Nucleocapsid Protein (Zheng et al., 2021), indicating its multifunctional roles in antiviral response. Endogenous retroelement LINE-1 is quite similar to exogenous viruses, which can still replicate itself in our genome and has also been reported to trigger innate immune responses. Therefore, it might be interesting to identify whether ZCCCH3 also involves in LINE-1 retrotransposition.

Materials and methods

Plasmids and antibodies

The LINE-1-firefly-luciferase reporter pWA367 and LINE-1-5′UTR promoter-luciferase reporter L1-FL were described earlier (Esnault et al., 2000; Athanikar et al., 2004; Xie et al., 2011). The Myc-ORF1p, Flag-ZCCHC3, and Flag-ZCCHC3-dc truncation cDNA sequences were cloned into the pcDNA3.0 expression vector (Invitrogen) by standard molecular biology techniques.

Flag-tag (D6W5B) Rabbit mAb (14793), Flag-tag (9A3) Mouse mAb (8146), Myc-Tag (71D10) Rabbit mAb (2278), Myc-Tag (9B11) Mouse mAb (2276), LINE-1 ORF1p (D3W9O) Rabbit mAb (88701), and ZCCHC3 Rabbit antibody (65321) were purchased from the Cell Signaling Technology. Flag-tag Goat antibody (ab95045) was purchased from Abcam. LINE-1-ORF1p Rabbit polyclonal antibody was a kind gift from Fei Guo (Hu et al., 2015). G3BP1 (H-10) Mouse mAb (sc-365338) was purchased from Santa Cruz.

Cell culture and transfection

The human embryonic kidney 293T cells and HeLa cells were purchased from ATCC and were grown in DMEM supplemented with 10% fetal bovine serum (Invitrogen). Cells were transfected with Lipofectamine (Invitrogen) and VigoFect (Vigorous Biotechnology) according to the manufacturer's instructions.

LINE-1 retrotransposition assay

Cells were seeded in six-well plates and transected with pWA367 plasmid and the Relina luciferase control plasmid pGL4.73 with a ratio of 20:1 and ZCCHC3 or empty vector reporter DNA. Twenty-four hours after transfection, puromycin (Sigma) was added in a complete medium at a 2.5 mg/ml final concentration. Cells were harvested 4 days post-transfection and lysed with Cell Culture Lysis Reagent (Promega). Luminescence was measured using the Dual-Luciferase Reporter Assay System (Promega) following the manufacturer's instructions.

LINE-1 promoter-luciferase assay

Cells were seeded in six-well plates 1 day before transfection with 1 ug of the LINE-1 promoter-Luc reporter L1-FL and ZCCHC3 or empty vector reporter DNA. Forty-eight hours after transfection, cells were lysed with 5× Cell Culture Lysis Reagent (Promega), and luciferase activity was quantified using Promega Luciferase Assay Kit (Promega) on a Berthold microplate reader.

Quantitative real-time–PCR

Cells were transected with pWA367 and ZCCHC3 or empty vector reporter DNA. For detecting LINE-1 mRNA, cells were harvested 2 days post-transfection for analysis, and total RNA was extracted with TRIzol reagent (Invitrogen). An equal amount of total cellular RNA was treated with DNase to remove the potential contamination DNA and reverse transcribed with M-MLV Reverse Transcriptase (Promega) using the oligo dT

primer. Q-PCR was performed using the SYBR Green Master Mix (Roche) and the ABI Quant-Studio 1. For detecting the LINE-1 integration, genomic DNA was extracted using QIAamp DNA Blood Mini Kit (Qiagen) 4 days post-transfection. Q-PCR was performed using Premix Ex Taq^{TM} (Takara) and the ABI Quant-Studio 1. The following primer was used in detecting LINE-1, IFNB1, CXCL10, and the housekeeping gene GAPDH (Xie et al., 2011).

GAPDH forward 5-CCCACTCCTCCACCTTTGAC-3,
GAPDH reverse 5-TGTTGCTGTAGCCAAATTCGTT-3,
GAPDH probe 5-AAGCTCATTTCCTGGTATGA-3;
Fluc forward 5-GCAAAAGAAGCTACCGATCATACA-3,
Fluc reverse 5-GAAGCTCTCGGGCACGAA-3,
Fluc exon-exon junction probe 5-CTTCCCACCTG CCACC-3.
IFNB1 forward 5-TTGTTGAGAACCTCCTGGCT-3
IFNB1-reverse 5-TGACTATGGTCCAGGCACAG-3
CXCL10 forward 5-GGTGAGAAGAGATGTCTGAAT CC-3
CXCL10 reverse 5-GTCCATCCTTGGAAGCACTG CA-3

Western blotting

Cells were lysed in RIPA buffer [0.1% SDS, 1% Triton X-100, 1% sodium deoxycholate, 150 mM NaCl, 10 mM Tris (pH 7.5), and 1 mM EDTA]. Equal amounts of cell lysates were separated in SDS-10% PAGE. Proteins were transferred onto PVDF membranes (Whatman), blocked in 5% milk in TBST buffer, and then probed with antibodies as indicated. The same samples were used to detect the bands of different proteins using different gels in one panel because the molecular weights of ZCCHC3 (∼46 kD), ORF1p (∼40 kD), and Tubulin (∼55 kD) are close.

Co-immunoprecipitation

Cells were transfected with plasmids expressing FLAG-tagged ZCCHC3 and pWA367 or Myc-tagged LINE-1 ORF1p. Forty-eight hours after transfection. The transfected cells were lysed with NETN buffer (20 mM Tris–HCl, pH 8.0, 100 mM NaCl, 1 mM EDTA, and 0.5% NonidetP-40) and supplemented with a protease inhibitor cocktail (Roche). Insoluble material was pelleted at 13,000 g for 30 min, followed by RNase (Thermo) or not for 30 min at 37°C. Equal amounts of supernatant were incubated with 5 ul of anti-flag antibody (Abcam, mouse) or anti-Myc antibody (Abcam, mouse) for 16 h at 4°C, followed by the addition of protein A+G Sepharose (Beyotime Biotechnology) for 2 h. Beads were washed three times with NTEN buffer, boiled in 2× SDS loading buffer, followed by Western blot analysis.

RNA immunoprecipitation

Cells were transfected with 1,000 ng pWA367 with 500 ng ZCCHC3 DNA or empty vector. The cells were collected 48 h post-transfection and then lysed in 350 μl of TNT buffer (20 mM Tris. HCl, pH 7.5, 200 mM NaCl, and 1% Triton X-100) with RNase inhibitor (Takara) at a final concentration of 1 U/μl. The expressed ZCCHC3 was immunoprecipitated with an anti-flag antibody as described above. The RNA associated with the precipitated complex was extracted with TRIzol agents (Invitrogen) and subjected to RT–PCR using primers that amplify the luciferase as described above.

Immunofluorescence microscopy

Cells were transfected with plasmids expressing FLAG-tagged ZCCHC3 and pWA367 or Myc-tagged LINE-1 ORF1p. Forty-eight hours after transfection. The cells were fixed with 4% paraformaldehyde (in 1phosphate-buffered saline) for 10 min at room temperature and permeabilized with 4% paraformaldehyde and 0.1% Triton X-100 for 10 min at room temperature. The cells were then stained for 2 h at room temperature with antibodies against FLAG (1:500 dilution, mouse) and Myc (1:500 dilution, rabbit). After being washed with 1 phosphate-buffered saline, the cells were incubated with either Alexa Fluor 488-conjugated secondary anti-mouse antibody or Alexa Fluor 594-conjugated secondary anti-rabbit antibody (1:2,000 dilution; Invitrogen). The images were recorded using the Zeiss Pascal laser scanning confocal microscope.

siRNA knockdown

siRNA against ZCCHC3 (final concentration 50 nM) or non-targeting control (JTS scientific) was transfected to 293T cells using Lipofectamine RNAiMax (Invitrogen) according to the manufacturer's protocol. Forty-eight hours after the transfection, cells were used for experiments.

Statistical analysis

All data are presented as means ± standard deviations (SD). The significance of differences is indicated in the figures. Statistical analyses were performed with a two-tailed, unpaired Student's *t*-test, using the GraphPad Prism software ($^{*}P < 0.05$; $^{**}P < 0.01$; $^{***}P < 0.001$; ns., not significant.).

Results

ZCCHC3 inhibits LINE-1 retrotransposition

As ZCCCH3 was reported to positively regulate virus-triggered IFN production, we first investigated whether ZCCHC3 also plays a role in the LINE-1-induced IFN pathway, which was believed to contribute to the auto-immune response under the circumstance of non-infection of the exogenous virus (Volkman and Stetson, 2014; De Cecco et al., 2019; Saleh et al., 2019; Simon et al., 2019). We transfected LINE-1 DNA with different amounts of ZCCHC3 expression plasmid into the HEK293T cells, and then detected the ability of ZCCHC3 to regulate the LINE-1-induced IFN pathway. Unexpectedly, ectopically expressed ZCCHC3 decreased the production of LINE-1 stimulated Interferon Beta1 (IFNB1) and interferon-γ-inducible protein 10(CXCL10) significantly, and it seems that the expression of 1 ug ZCCHC3 plasmid has reached its saturation concentration for affecting IFNB1 or CXCL10 level in cells, and the effect of more ZCCHC3 DNA(2ug) transfection is not obvious (Figure 1A). Collectively, these data indicated that ZCCHC3 negatively regulates the LINE-1-triggered innate response.

It has been reported that cytoplasmic LINE-1 RNA and cDNA can trigger the IFN-I response (Lagisquet et al., 2021). We therefore speculated that ZCCHC3 may repress LINE-1 elements replication and retrotransposition, which might directly diminish the accumulation of RNA or cDNA derived from LINE-1 elements, thus diminishing LINE-1-triggered innate response. To investigate the effect of ZCCHC3 on LINE-1 retrotransposition, we utilized the established LINE-1 luciferase reporter pWA367 (Xie et al., 2011), which bears an intron-containing firefly luciferase gene in its 3′ UTR. This design ensures that the firefly luciferase will only be produced from the reverse transcribed LINE-1 DNA in the host genome, in which the intron should have been removed during RNA splicing, and therefore, the luciferase activity reflects the events of LINE-1 retrotransposition. Furthermore, a control plasmid encoding Rluc was co-transfected to normalize the expression of the firefly luciferase gene (Figure 1B).

We transfected the pWA367 plasmid with or without ZCCHC3 DNA into the HEK293T cells, followed by a luciferase activity detection assay. Although we did not observe any significant effect of ZCCHC3 ectopic expression on the viability of cells or the Rluc activity, which most likely excludes the possibility that ZCCHC3 might impair luciferase expression or lead to cellular cytotoxicity, the transient expression of ZCCHC3 diminished the luciferase activity by ∼50, 70, and 80% ($p < 0.05$), according to different ZCCHC3 expression levels (Figure 1C), indicating that overexpression of ZCCHC3 can inhibit LINE-1 retrotransposition in a dose-dependent manner. We next depleted the endogenous ZCCHC3 in HEK293T cells using siRNA oligos to investigate how LINE-1 activity was affected. The activity of luciferase which represents LINE-1 retrotransposition increased **∼2**-fold when ZCCHC3 was depleted with siRNA (Figure 1D), suggesting that endogenous ZCCHC3 also has the LINE-1 inhibitory activity. Together, these data indicated that ZCCHC3 can restrict LINE-1 retrotransposition.

ZCCHC3 reduces the LINE-1 insertion

To assess LINE-1 repression by ZCCHC3 independently of reporter gene expression, we imposed TaqMan probe real-time PCR to determine the relative copy number of the novel LINE-1 integrates, which were quantified in triplicate with primers and an exon-exon junction probe specific to the firefly luciferase gene to confirm the intron-removal form of LINE-1 insertions (Figure 2A). The result showed that ectopically expressed ZCCHC3 significantly reduced the copy number of the non-intron luciferase gene (Figure 2B), while knocking down the endogenous ZCCHC3 increased the LINE-1 insertion ∼3-fold (Figure 2C), thus confirming the repression of LINE-1 by ZCCHC3 independently of luciferase reporter gene expression

ZCCHC3 decreases LINE-1 RNA level

We next set up to investigate in which step of the LINE-1 life cycle ZCCHC3 plays a crucial role. For LINE-1 RNA both serve as mRNA for protein expression and templates to produce new cDNA copies. LINE-1 RNA levels affected the copy numbers of LINE-1 DNA. We therefore next examined the effect of ZCCHC3 on LINE-1 RNA. We transfected pWA367 plasmid with or without ZCCHC3 DNA into the HEK293T cells, and then detected the effect of ectopically expressed ZCCHC3 on LINE-1 RNA using RT–qPCR. The result showed that the transient expression of ZCCHC3 can diminish the LINE-1 RNA level at a similar level as it inhibits LINE-1 retrotransposition, suggesting that the inhibitory activity of ZCCHC3 may be derived from diminishing LINE-1 RNA level (Figure 3A).

For LINE-1 RNA serves as mRNA for protein expression, we also detected the LINE-1 ORF1p expression level using immunoblotting and found that ZCCHC3 can reduce the LINE-1 ORF1p expression level as well (Figure 3A). Similarly, when we silenced the expression of endogenous ZCCHC3, LINE-1 RNA, and ORF1p levels increased ∼2-fold (Figure 3B), indicating that both exogenous and endogenous ZCCHC3 can decrease LINE-1 RNA levels.

We speculated that ZCCHC3 decreases the LINE-1 RNA level might through affecting its transcription or influence its stability. We first examined whether ZCCHC3 affected LINE-1 RNA transcription. It has been reported that the 5′-UTR

10.3389/fmicb.2022.891852

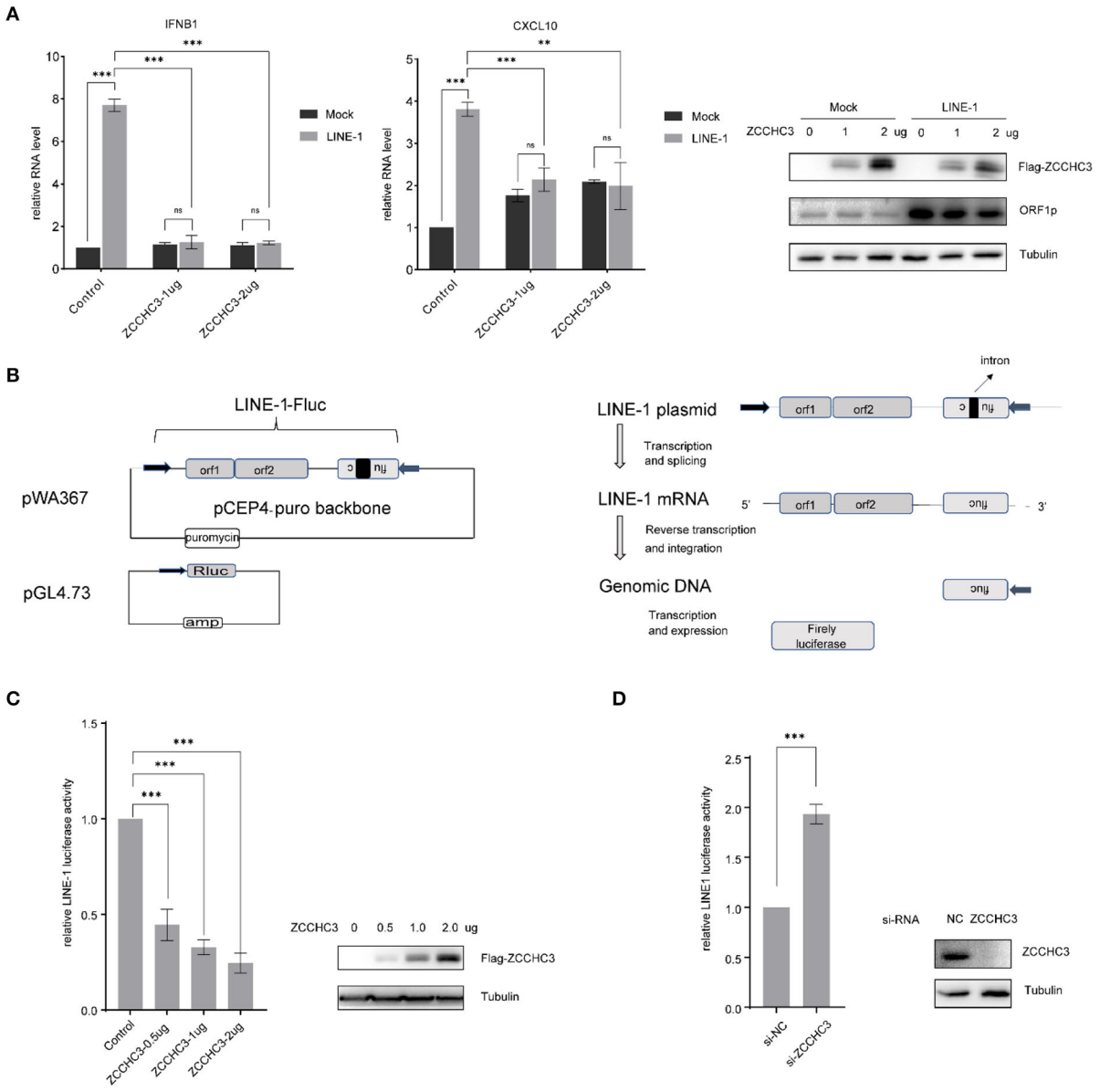

FIGURE 1
ZCCHC3 inhibits LINE-1 retrotransposition. **(A)** ZCCHC3 inhibits LINE-1-induced IFN production. HEK293T cells were transfected with pWA367 and ZCCHC3 DNA. Two days post-transfection, total RNA was extracted for IFNB1 (left panel) and CXCL10 RNA analysis using real-time PCR, and the RNA level was normalized to GAPDH (medial panel). Expression of the LINE-1 ORF1p and Flag-ZCCHC3 were analyzed by immunoblot, and Tubulin was detected as an internal control (right panel). **(B)** Diagrams of the LINE-1 reporter pWA367 plasmid and Rluc plasmid. pWA367 bears an intron-containing firefly luciferase gene in its 3′ UTR. This design ensures that the firefly luciferase will only be produced from the reverse transcribed LINE-1 DNA in the host genome, in which the intron should have been removed during RNA splicing. **(C)** Overexpression of ZCCHC3 inhibits LINE-1 retrotransposition. HEK293T cells were transfected with pWA367, pGL4.73, and either empty vector or increasing amounts of vector encoding ZCCHC3. Four days post-transfection, cell lysates were analyzed for luminescence activity (left panel). Expression of the Flag-ZCCHC3 was analyzed by immunoblot, and Tubulin was detected as an internal control (right panel). **(D)** Knockdown of ZCCHC3 increases LINE-1 retrotransposition. HEK293T cells were transfected with pWA367, pGL4.73, and the siRNA targeting ZCCHC3. Four days post-transfection, cell lysates were analyzed for luminescence (left panel). Expression of the ZCCHC3 was analyzed by immunoblot, and Tubulin was detected as an internal control (right panel). Data are representative of at least three independent experiments, values are expressed as means ± SD, and representative blots and images are shown.

of LINE-1 serves as an internal promoter to drive LINE-1 RNA production (Goodier and Kazazian, 2008). We therefore used another reporter DNA construct, L1-FL, which only bears the LINE-1 5′-UTR sequence upstream of the firefly luciferase reporter gene (Athanikar et al., 2004) to detect the influence of the ZCCHC3 upon the LINE-1 internal

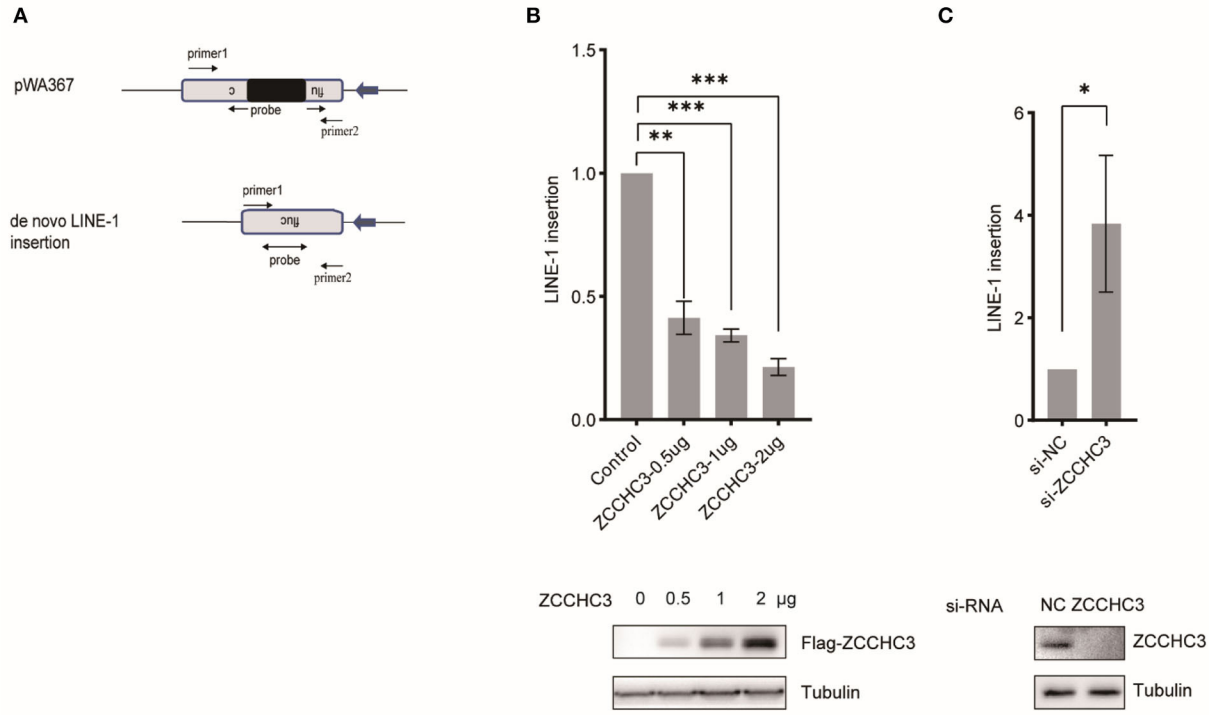

FIGURE 2
ZCCHC3 decreased LINE-1 insertions. **(A)** Diagrams of Taqman real-time PCR to detect novel LINE-1 integrates. The real-time PCR was performed with two primers and one probe across the intron to detect the integrated novel LINE-1. **(B)** Overexpression of ZCCHC3 decreased novel LINE-1 integrates. HEK293T cells were transfected with pWA367 and ZCCHC3 DNA. Four days post-transfection, genomic DNA was extracted and analyzed for Taqman real-time PCR (top panel). Expression of the Flag-ZCCHC3 was analyzed by immunoblot, and Tubulin was detected as an internal control (bottom panel). **(C)** Knockdown of ZCCHC3 increased novel LINE-1 integrates. HEK293T cells were transfected with pWA367 together with the siRNA targeting ZCCHC3. Four days post-transfection, genomic DNA was extracted and analyzed for Taqman real-time PCR (top panel). Expression of the ZCCHC3 was analyzed by immunoblot, and Tubulin was detected as an internal control (bottom panel). Data are representative of at least three independent experiments, values are expressed as means ± SD, and representative blots and images are shown.

promotor. We transfected this reporter DNA into HEK293T cells together with ZCCHC3 DNA, and then detected the luciferase activity. The presence of ZCCHC3 did not negatively affect the luciferase activity according to our results (Figure 3C), suggesting that ZCCHC3 did not influence LINE-1 RNA transcription driven by the 5′-UTR internal promoter, which indicates ZCCHC3 modulates LINE-1 RNA expression at the post-transcriptional stage. To test whether ZCCHC3 influences LINE-1 RNA stability, we used actinomycin D (5 μg/ml) to block the transcription from RNA polymerase II and measure the decay kinetics of LINE-1 RNA with overexpressed ZCCHC3. As shown in Figure 3D, the expression of ZCCHC3 diminished the amount of LINE-1 RNA to ∼50% of that in the control cells at time 0. This phenomenon is similar to that of another host factor MOV10, which was reported to mediate the rapid degradation of LINE-1 RNA (Li et al., 2013; Choi et al., 2018). These results suggested that ZCCHC3 might also promote the rapid degradation of LINE-1 RNA as MOV10 did.

ZCCHC3 interacts with LINE-1

ORF1p and ORF2p proteins associate with the LINE-1 RNA to form LINE-1 RNP in the cytoplasm. Although the role of LINE-1 RNP is still unclear, it protects LINE-1 RNA from degradation by different kinds of host machinery (Taylor et al., 2016). Therefore, it is tempting to speculate that ZCCHC3 might target the components of LINE-1 RNP to destabilize LINE-1 RNA. We therefore performed Immunofluorescence and co-immunoprecipitation (co-IP) to identify whether there is an association between LINE-1 and ZCCHC3. The image showed that ZCCHC3 was mainly presented in the cytoplasm, and co-located with LINE-1 ORF1p (Figure 4A). The co-IP results also indicated that ZCCHC3 is associated with LINE-1 ORF1p (Figure 4B). For LINE-1 ORF1p and ORF2p usually associate with the LINE-1 RNA as an RNP form in the cytoplasm, ZCCHC3 may interact directly with ORF1p or mediated by LINE-1 RNA. Indeed, the interaction between ZCCHC3 and LINE-1 ORF1p seems to be RNA dependent, for the interaction

10.3389/fmicb.2022.891852

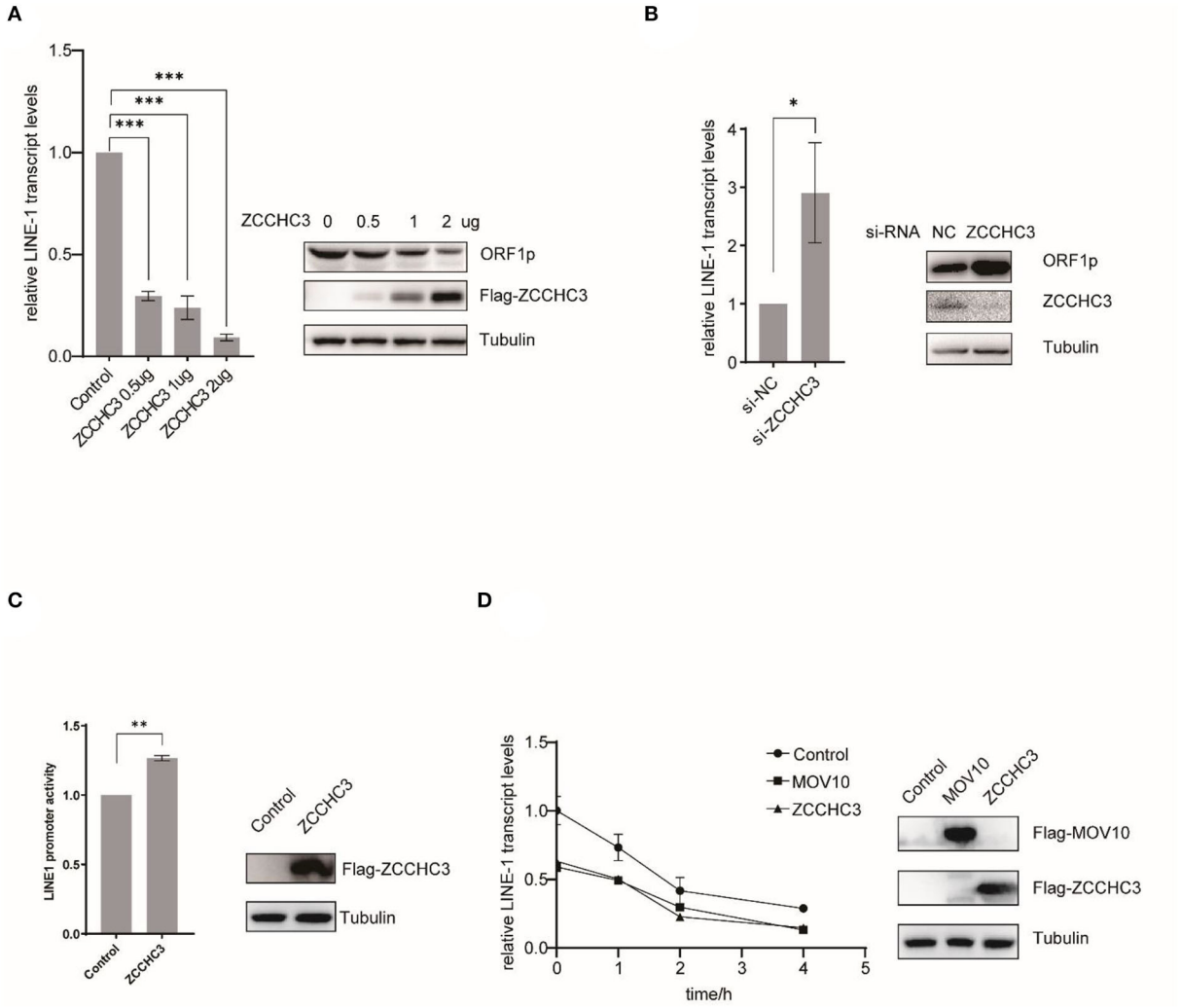

FIGURE 3
ZCCHC3 diminished LINE-1 RNA and ORF1p. **(A)** Overexpression of ZCCHC3 decreases LINE-1 RNA and ORF1p. HEK293T cells were transfected with pWA367 and ZCCHC3 DNA. Total RNA was extracted for Taqman real-time PCR analysis, the RNA level was normalized to GAPDH (left panel). Expression of the LINE-1 ORF1p and Flag-ZCCHC3 were analyzed by immunoblot, and Tubulin was detected as an internal control (right panel). **(B)** Knockdown of ZCCHC3 increases LINE-1 RNA and ORF1p level. HEK 293T cells were transfected with pWA367 together with the siRNA targeting ZCCHC3. Total RNA was extracted for Taqman real-time PCR analysis, the RNA level was normalized to GAPDH (left panel). Expression of the LINE-1 ORF1p and ZCCHC3 were analyzed by immunoblot, and Tubulin was detected as an internal control (right panel). **(C)** ZCCHC3 does not affect the activity of the LINE-1 5′UTR promoter. HEK293T cells were transfected with the L1-FL reporter plasmid and ZCCHC3 DNA. Cell lysates were analyzed for luminescence (left panel). Expression of the ZCCHC3 was analyzed by immunoblot, and Tubulin was detected as an internal control (left panel). **(D)** The detection of RNA stability. HEK293 cells were co-transfected with pWA367 and either ZCCHC3, MOV10 DNA, or pcDNA3.0. Twenty-four hours post-transfection, the cells were treated with actinomycin D, and then detected LINE-1 RNA levels at various times as indicated by Taqman real-time PCR, the RNA level was normalized to GAPDH (left panel). Expression of the ZCCHC3 and MOV10 were analyzed by immunoblot, and Tubulin was detected as an internal control (left panel). Data are representative of at least three independent experiments, values are expressed as means ± SD, and representative blots and images are shown.

was lost after RNase treatment (Figure 4C), suggesting that the interaction between ZCCHC3 and ORF1p might be mediated by LINE-1 RNA. The RNA immunoprecipitation assay result also confirmed that there was an interaction between ZCCHC3 and LINE-1 RNA (Figure 4D). These results indicated that the interaction between ZCCHC3 and ORF1p was mediated by LINE-1 RNA.

The Zinc-Finger domain is necessary to repress LINE-1 retrotransposition

The RNA-dependent interaction between ZCCHC3 and LINE-1 ORF1p suggested the potential role of RNA binding in LINE-1 repression by ZCCHC3. ZCCHC3 bears three tandem zinc finger domains in its c-terminal region

10.3389/fmicb.2022.891852

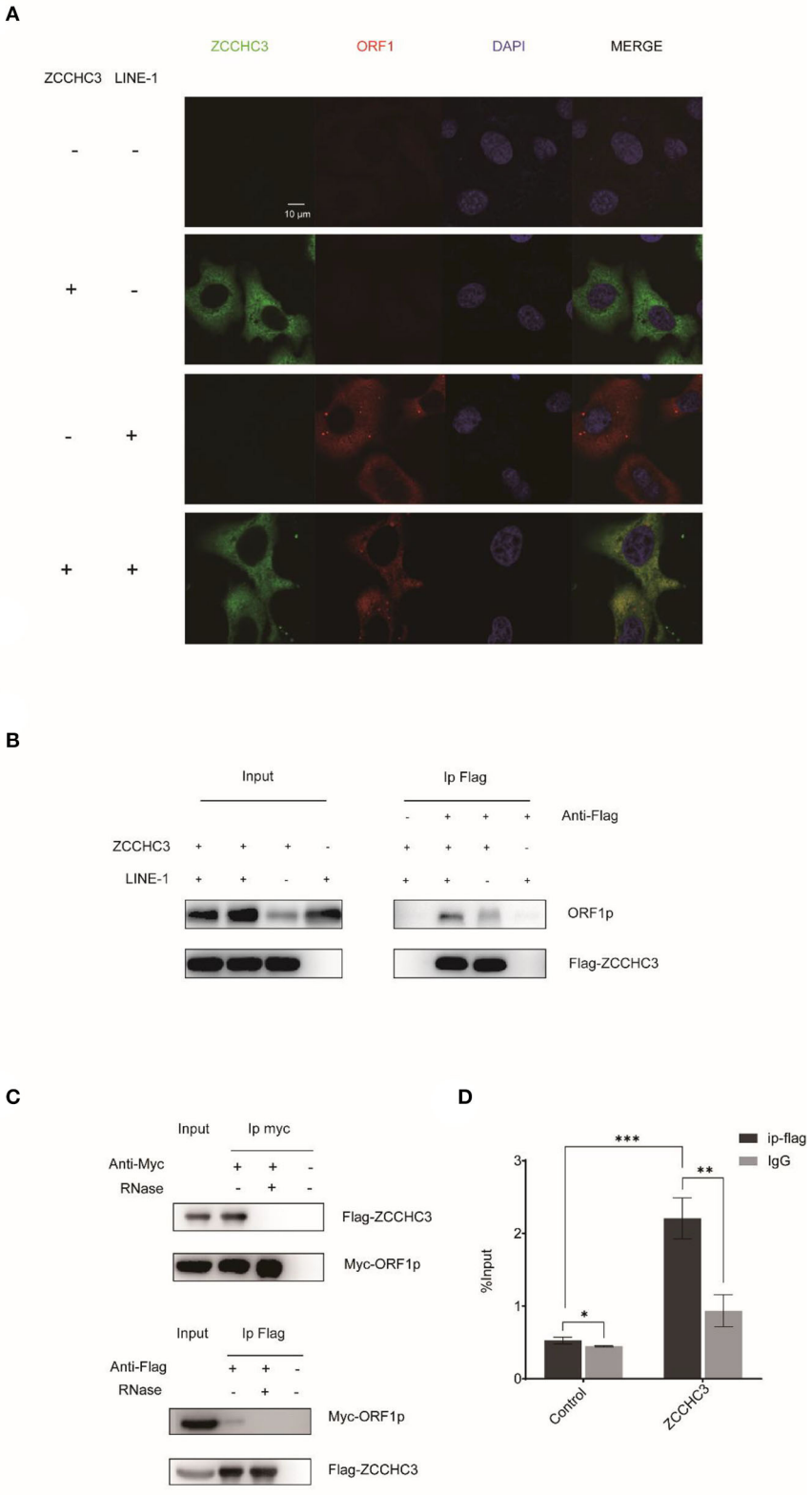

FIGURE 4
ZCCHC3 interacts with LINE-1 in the cytoplasm. **(A)** ZCCHC3 is co-located with LINE-1 ORF1p. Hela cells were transfected with pWA367 plasmid and Flag-ZCCHC3 DNA. Forty-eight hours post-transfection, LINE-1 ORF1p and Flag ZCCHC3 were detected by indirect

(Continued)

FIGURE 4 (Continued)
immunofluorescence staining. **(B)** ZCCHC3 interacts with LINE-1 ORF1p. HEK293T cells were transfected with pWA367 plasmid and Flag-ZCCHC3 DNA. The cells were collected and lysed 48 h post-transfection. Equal amounts of supernatant were incubated with Flag antibody or IgG (mouse), LINE-1 ORF1p, and Flag-ZCCHC3 were analyzed by Western blots using antibodies against ORF1p and Flag (rabbit). **(C)** The interaction between ZCCHC3 and LINE-1 ORF1p is RNA-dependent. HEK293T cells were transfected with Flag-ZCCHC3 and Myc-ORF1p DNA. Forty-eight post-transfection, the cells were collected and lysed, and then treated with RNase at 37°C for 30 min, equal amounts of supernatant were incubated with Flag or Myc antibody (mouse) and then analyzed by Western blots using antibodies against Myc or Flag (rabbit). **(D)** ZCCHC3 binds to LINE-1 RNA. HEK293T cells were co-transfected with pWA367 DNA and ZCCHC3 DNA. Forty-eight hours later, an equal amount of cell lysis was used to detect LINE-1 RNA by RNA-IP. LINE-1 RNA pulled down by ZCCHC3 was quantified by RT–qPCR. These experiments were repeated three times and representative blots and images are shown.

(301-404aa), which was reported to have RNA binding activity (Lian et al., 2018a,b; Zang et al., 2020). We generated a c-terminal truncation mutant of ZCCHC3 and ZCCHC3-dc, which lacks the zinc-finger region, to elucidate whether the zinc-finger domains are necessary for its LINE-1 inhibitory function (Figure 5A). LINE-1 retrotransposition assay showed that ZCCHC3-dc almost completely lost the activity to restrict LINE-1 retrotransposition (Figure 5B). Correspondingly, ZCCHC3-dc also lost the activity to diminish LINE-1 mRNA and ORF1p protein in HEK293T cells (Figure 5C), indicating that the zinc-finger domain is important for ZCCHC3 to restrict LINE-1 elements. Furthermore, the co-IP and RIP results confirmed that ZCCHC3-dc lost the ability to interact with LINE-1 RNP (Figures 5D,E). Immunofluorescence results also showed that, although ZCCHC3-dc is still localized in the cytoplasmic, it lost the association with LINE-1 ORF1p in Hela cells (Figure 5F). To correspond to previous experiments, we also confirmed the same results in 293T cells (Supplementary Figure 1). We speculated the deletion of the zinc-finger made ZCCHC3 lose the ability to bind RNAs and appear in a more diffused distribution in the cytoplasm. These results suggest the important role of the zinc-finger domain for ZCCHC3 to interact with LINE-1.

Discussion

ZCCHC3 possesses three tandem zinc finger domains in its C-terminal region. Zinc finger proteins are primarily considered to be DNA binding transcription factors, However, certain classes of zinc finger proteins can also interact with RNA, and are involved in the regulation of multiple steps of RNA metabolism, such as mRNA splicing, polyadenylation, transportation, translation, and decay (Fu and Blackshear, 2017; Wang et al., 2017). As a CCHC-type zinc finger protein, ZCCHC3 was recently reported to bind viral dsRNA and dsDNA and positively regulate virus-triggered induction of type I IFNs in cGAS, RIG-I, and TLR3-mediated innate immune responses (Lian et al., 2018a,b; Zang et al., 2020). However, in the absence of exogenous microbial infection, endogenous retroelements LINE-1 was believed to be a potential source of immunogenic cytoplasmic nucleic acids in the context of sterile inflammation. Cytoplasmic LINE-1 can trigger IFN-I response through RIG-I- and MDA5-mediated RNA sensing pathways (Zhao et al., 2018; Tunbak et al., 2020) and cGAS-mediated DNA sensing pathways (De Cecco et al., 2019; Simon et al., 2019; Gamdzyk et al., 2020), especially during cellular senescence, when LINE-1 become transcriptionally derepressed.

In this study, we first investigate the role of ZCCHC3 in the IFN-I response of LINE-1. According to our results, ZCCHC3 activated the IFN pathway, especially the expression of CXCL10, which corresponds with the results of Shu's reports (Lian et al., 2018a,b). But unexpectedly, ZCCHC3 negatively regulates LINE-1 triggered IFN production, which is different from the process of the exogenous virus. Our result indicated that ZCCHC3 represses the LINE-1 element retrotransposition by directly diminishing the RNA level of LINE-1. It is plausible that ZCCHC3 negatively regulates LINE-1 triggered IFN production by decreasing the LINE-1 cDNA and RNA levels, which are the source of triggering LINE-1 mediated IFN production.

The association between ZCCHC3 and LINE-1 was confirmed by the observation of the co-localization of ZCCHC3 with ORF1p in the cytoplasm and was further supported by the immunoprecipitation result. However, LINE-1 ORF1p and ORF2p are usually associated with the LINE-1 RNA as an RNP form in the cytoplasm, and the loss of the association between ZCCHC3 and ORF1p upon RNase treatment suggests that ZCCHC3 interact with LINE-1 ORF1p in an RNA-dependent manner, or ZCCHC3 directly bind the LINE-1 RNA but not ORF1p. On the other hand, zinc finger domains in ZCCHC3 were reported to have RNA binding activity. When we deleted the zinc finger domains of the ZCCHC3, it lost the association with LINE-1, further supporting the notion that ZCCHC3 might directly bind to LINE-1 RNA. Indeed, ZCCHC3 was reported to directly bind to viral dsDNA or dsRNA in previous studies, and the double-strand structure is necessary for the binding (Lian et al., 2018a,b). However, LINE-1 RNA is quite similar to cellular single-strand mRNA.

10.3389/fmicb.2022.891852

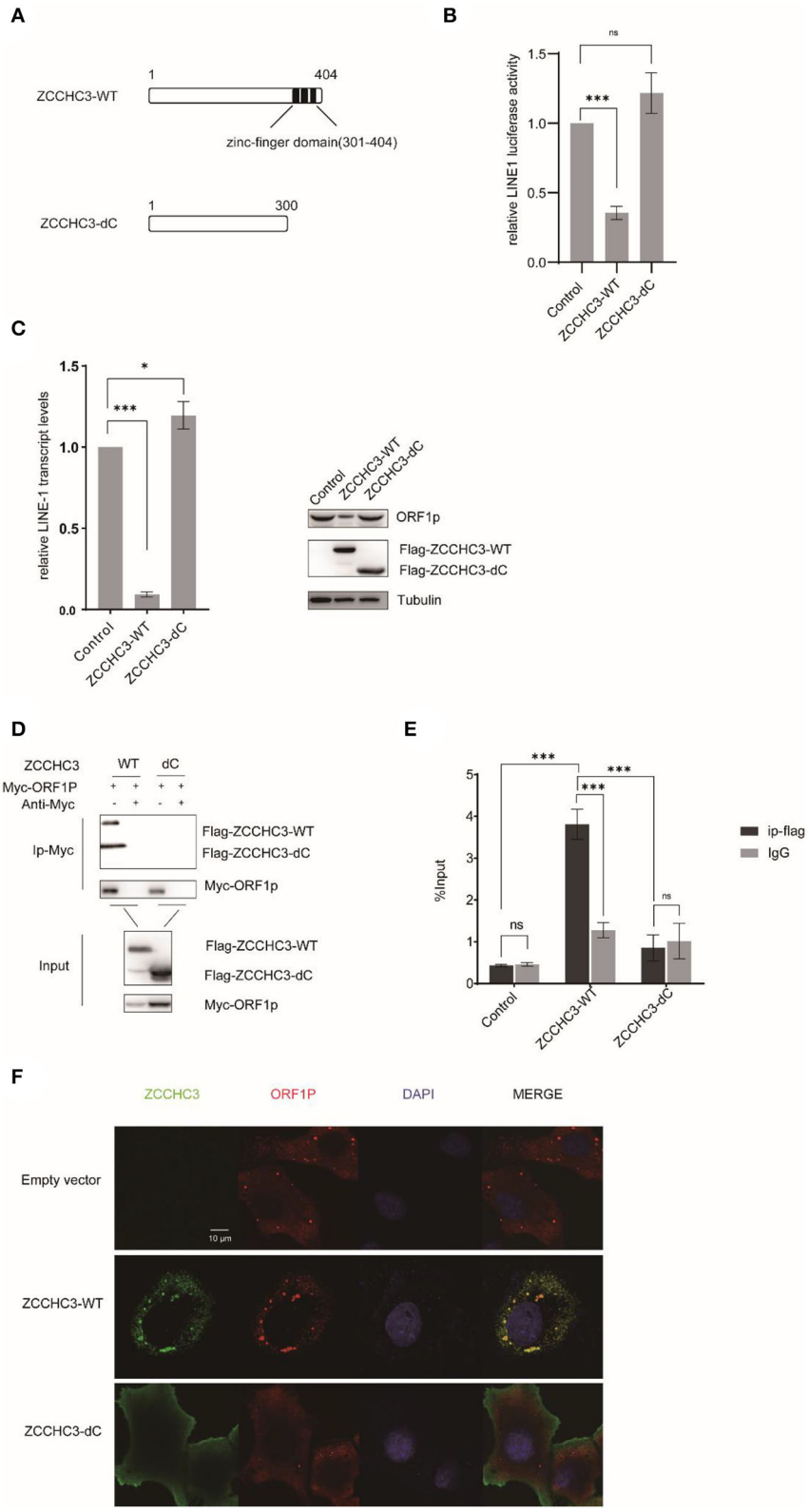

FIGURE 5
The zinc-finger domain is essential for ZCCHC3-mediated LINE-1 restriction. **(A)** The illustration of ZCCHC3 truncation. **(B)** ZCCHC3 dc does not inhibit LINE-1. HEK293T cells were transfected with pWA367 and either empty vector, Flag-ZCCHC3 or Flag-ZCCHC3-dc. 4 days

(Continued)

FIGURE 5 (Continued)
post-transfection, cell lysates were analyzed for luminescence. **(C)** ZCCHC3 dc does not diminish LINE-1 RNA and ORF1p. Two days post-transfection, total RNA was extracted and LINE-1 RNA was normalized by the GAPDH and analyzed for Taqman real-time PCR (left panel). Expression of the LINE-1-ORF1p and Flag-ZCCHC3 were analyzed by immunoblot, and Tubulin was detected as an internal control (right panel). **(D)** ZCCHC3 dc does not interact with LINE-1 ORF1p. HEK293T cells were transfected with Myc-ORF1p and Flag-ZCCHC3 or Flag-ZCCHC3-dc. The cells were collected and lysed 48 h post-transfection. Equal amounts of supernatant were incubated with Myc antibody(mouse), Myc-ORF1p, and Flag-ZCCHC3 or Flag-ZCCHC3-dc and were analyzed by Western blots using antibodies against Myc and Flag(rabbit). **(E)** ZCCHC3 dc does not bind to LINE-1 RNA. HEK293T cells were co-transfected with pWA367 DNA and ZCCHC3-WT or ZCCHC3-dC DNA. Forty-eight hours later, an equal amount of cell lysis was used to detect LINE-1 RNA by RNA-IP. LINE-1 RNA pulled down by ZCCHC3 was quantified by RT–qPCR. **(F)** ZCCHC3 dc is not located with LINE-1 ORF1p. Hela cells were transfected with an empty vector or vector encoding Flag-ZCCHC3 or Flag-ZCCHC3-dc and Myc-ORF1p. Forty-eight hours post-transfection, Myc-ORF1p and Flag ZCCHC3 or Flag-ZCCHC3-dc were detected by indirect immunofluorescence staining. Data are representative of at least three independent experiments, values are expressed as means ± SD, and representative blots and images are shown.

It is worth investigating how ZCCCH3 binds to LINE-1 RNA in the future. A possible explanation would be the stem-loop structure in LINE-1 mRNA, which remains for further exploration.

Our result indicated that the inhibitory activity of ZCCHC3 may be derived from diminishing LINE-1 RNA, although the exact mechanism is still not clear. For immunofluorescence assay showed that ZCCHC3 is a cytoplasmic protein, which is unlikely to affect the transcription of LINE-1 in the nucleus. We also confirmed that ZCCHC3 did not influence LINE-1 RNA transcription driven by the 5′-UTR internal promoter. These results suggested a possibility that ZCCHC3 might induce LINE-1 RNA degradation in the cytoplasm. Indeed, the RNA stability analysis suggests a rapid degradation of LINE-1 RNA caused by ZCCHC3. This phenomenon is also observed in MOV10-induced RNA degradation (Li et al., 2013). We noticed that, upon overexpression of ZCCHC3, ORF1p formed large foci in the cytoplasm, in which ZCCHC3, ORF1p, and stress granule (SG) marker protein, G3bp1, were co-localized (Supplementary Figure 2), which suggests that ZCCHC3 causes sequestration of LINE-1 ORF1p in large stress granules. It is reported previously that endogenous or over-expressed ORF1p can spontaneously aggregate in SGs, in the absence of external stress (Goodier et al., 2007). Several host factors, such as Zinc-Finger Antiviral Protein (ZAP) (Gao et al., 2002), MOV10 (Goodier et al., 2012; Li et al., 2013), and The SAM domain and HD domain-containing protein 1 (SAMHD1) (Hu et al., 2015) were found to co-localize with LINE-1 RNP in SGs and induced the LINE-1 RNA degradation. In another study, Martin Brouha et al. also purified and identified 37 high-confidence host factors, including both MOV10 and ZCCHC3, form LINE-1 RNP complexes using affinity proteomics methods (Taylor et al., 2013). Based on the important role of SG in RNA metabolism, it is not surprising that these proteins co-localize in SGs with LINE-1 RNP and limited LINE-1 mobility. Stress granules might provide a platform to orchestrate the innate immune response to fight the exogenous and endogenous viruses attack, and the exact mechanism needs further investigation.

Data availability statement

The raw data supporting the conclusions of this article will be made available by the authors, without undue reservation.

Author contributions

Conceptualization: XYL, SC, and ZXZ. Performing the main part of the experiment: ZXZ and NZ. Methodology: ZXZ, SSG, and NZ. Software: QL. Validation: SSG, SJW, NZ, and AZ. Investigation: QJL, JW, and LM. Resources: JWD, DRY, JYZ, and YXZ. Writing—original draft preparation: ZXZ. Writing—review and editing: JWD. Supervision: XYL. Project administration: SC. Funding acquisition: XYL and SC. All authors have read and agreed to the published version of the manuscript.

Funding

This research was funded by the CAMS Innovation Fund for Medical Sciences, CIFMS 2021-I2M-1-043 to XL and the National Natural Science Foundation of China Grant, 31870164.

Acknowledgments

We would thank Prof. Wenfeng An for pWA367 construct and Prof. Fei Guo for providing LINE-1 ORF1p primary antibody.

Conflict of interest

The authors declare that the research was conducted in the absence of any commercial or financial relationships that could be construed as a potential conflict of interest.

Publisher's note

All claims expressed in this article are solely those of the authors and do not necessarily represent those

of their affiliated organizations, or those of the publisher, the editors and the reviewers. Any product that may be evaluated in this article, or claim that may be made by its manufacturer, is not guaranteed or endorsed by the publisher.

Supplementary material

The Supplementary Material for this article can be found online at: https://www.frontiersin.org/articles/10.3389/fmicb.2022.891852/full#supplementary-material

References

Alisch, R. S., Garcia-Perez, J. L., Muotri, A. R., Gage, F. H., and Moran, J. V. (2006). Unconventional translation of mammalian LINE-1 retrotransposons. *Genes Dev.* 20, 210–224. doi: 10.1101/gad.1380406

Athanikar, J. N., Badge, R. M., and Moran, J. V. (2004). A YY1-binding site is required for accurate human LINE-1 transcription initiation. *Nucleic Acids Res.* 32, 3846–3855. doi: 10.1093/nar/gkh698

Brouha, B., Schustak, J., Badge, R. M., Lutz-Prigge, S., Farley, A. H., Moran, J. V., et al. (2003). Hot L1s account for the bulk of retrotransposition in the human population. *Proc. Natl. Acad. Sci. U. S. A.* 100, 5280–5285. doi: 10.1073/pnas.0831042100

Burns, K. H. (2017). Transposable elements in cancer. *Nat. Rev. Cancer* 17, 415–424. doi: 10.1038/nrc.2017.35

Choi, J., Hwang, S. Y., and Ahn, K. (2018). Interplay between RNASEH2 and MOV10 controls LINE-1 retrotransposition. *Nucleic Acids Res.* 46, 1912–1926. doi: 10.1093/nar/gkx1312

Cost, G. J., Feng, Q., Jacquier, A., and Boeke, J. D. (2002). Human L1 element target-primed reverse transcription in vitro. *EMBO J.* 21, 5899–5910. doi: 10.1093/emboj/cdf592

De Cecco, M., Ito, T., Petrashen, A. P., Elias, A. E., Skvir, N. J., Criscione, S. W., et al. (2019). L1 drives IFN in senescent cells and promotes age-associated inflammation. *Nature* 566, 73–78. doi: 10.1038/s41586-018-0784-9

Esnault, C., Maestre, J., and Heidmann, T. (2000). Human LINE retrotransposons generate processed pseudogenes. *Nat. Genet.* 24, 363–367. doi: 10.1038/74184

Feng, Q., Moran, J. V., Kazazian, H. H. Jr., and Boeke, J. D. (1996). Human L1 retrotransposon encodes a conserved endonuclease required for retrotransposition. *Cell* 87, 905–916. doi: 10.1016/S0092-8674(00)81997-2

Fu, M., and Blackshear, P. J. (2017). RNA-binding proteins in immune regulation: a focus on CCCH zinc finger proteins. *Nat. Rev. Immunol.* 17, 130–143. doi: 10.1038/nri.2016.129

Fukuda, K., and Shinkai, Y. (2020). SETDB1-mediated silencing of retroelements. *Viruses* 12, 596. doi: 10.3390/v12060596

Fung, L., Guzman, H., Sevrioukov, E., Idica, A., Park, E., Bochnakian, A., et al. (2019). miR-128 restriction of LINE-1 (L1) retrotransposition is dependent on targeting hnRNPA1 mRNA. *Int. J. Mol. Sci.* 20, 1955. doi: 10.3390/ijms20081955

Gamdzyk, M., Doycheva, D. M., Araujo, C., Ocak, U., Luo, Y., Tang, J., et al. (2020). cGAS/STING pathway activation contributes to delayed neurodegeneration in neonatal hypoxia-ischemia rat model: possible involvement of LINE-1. *Mol. Neurobiol.* 57, 2600–2619. doi: 10.1007/s12035-020-01904-7

Gao, G., Guo, X., and Goff, S. P. (2002). Inhibition of retroviral RNA production by ZAP, a CCCH-type zinc finger protein. *Science* 297, 1703–1706. doi: 10.1126/science.1074276

Garcia-Perez, J. L., Morell, M., Scheys, J. O., Kulpa, D. A., Morell, S., Carter, C. C., et al. (2010). Epigenetic silencing of engineered L1 retrotransposition events in human embryonic carcinoma cells. *Nature* 466, 769–773. doi: 10.1038/nature09209

Goodier, J. L. (2016). Restricting retrotransposons: a review. *Mob. DNA* 7, 16. doi: 10.1186/s13100-016-0070-z

Goodier, J. L., Cheung, L. E., and Kazazian, H. H. Jr. (2012). MOV10 RNA helicase is a potent inhibitor of retrotransposition in cells. *PLoS Genet.* 8, e1002941. doi: 10.1371/journal.pgen.1002941

Goodier, J. L., and Kazazian, H. H. Jr. (2008). Retrotransposons revisited: the restraint and rehabilitation of parasites. *Cell* 135, 23–35. doi: 10.1016/j.cell.2008.09.022

Goodier, J. L., Zhang, L., Vetter, M. R., and Kazazian, H. H. Jr. (2007). LINE-1 ORF1 protein localizes in stress granules with other RNA-binding proteins, including components of RNA interference RNA-induced silencing complex. *Mol. Cell. Biol.* 27, 6469–6483. doi: 10.1128/MCB.00332-07

Hancks, D. C., and Kazazian, H. H. Jr. (2016). Roles for retrotransposon insertions in human disease. *Mob. DNA* 7, 9. doi: 10.1186/s13100-016-0065-9

Hu, S., Li, J., Xu, F., Mei, S., Le Duff, Y., Yin, L., et al. (2015). SAMHD1 inhibits LINE-1 retrotransposition by promoting stress granule formation. *PLoS Genet.* 11, e1005367. doi: 10.1371/journal.pgen.1005367

Ishak, C. A., Marshall, A. E., Passos, D. T., White, C. R., Kim, S. J., Cecchini, M. J., et al. (2016). An RB-EZH2 complex mediates silencing of repetitive DNA sequences. *Mol. Cell* 64, 1074–1087. doi: 10.1016/j.molcel.2016.10.021

Kazazian, H. H. Jr., and Moran, J. V. (2017). Mobile DNA in health and disease. *N. Engl. J. Med.* 377, 361–370. doi: 10.1056/NEJMra1510092

Kulpa, D. A., and Moran, J. V. (2006). Cis-preferential LINE-1 reverse transcriptase activity in ribonucleoprotein particles. *Nat. Struct. Mol. Biol.* 13, 655–660. doi: 10.1038/nsmb1107

Lagisquet, J., Zuber, K., and Gramberg, T. (2021). Recognize yourself-innate sensing of non-LTR retrotransposons. *Viruses* 13, 94. doi: 10.3390/v13010094

Li, X., Zhang, J., Jia, R., Cheng, V., Xu, X., Qiao, W., et al. (2013). The MOV10 helicase inhibits LINE-1 mobility. *J. Biol. Chem.* 288, 21148–21160. doi: 10.1074/jbc.M113.465856

Lian, H., Wei, J., Zang, R., Ye, W., Yang, Q., Zhang, X. N., et al. (2018a). ZCCHC3 is a co-sensor of cGAS for dsDNA recognition in innate immune response. *Nat. Commun.* 9, 3349. doi: 10.1038/s41467-018-05559-w

Lian, H., Zang, R., Wei, J., Ye, W., Hu, M. M., Chen, Y. D., et al. (2018b). The zinc-finger protein ZCCHC3 binds RNA and facilitates viral RNA sensing and activation of the RIG-I-like receptors. *Immunity* 49, 438–448.e5. doi: 10.1016/j.immuni.2018.08.014

Luan, D. D., Korman, M. H., Jakubczak, J. L., and Eickbush, T. H. (1993). Reverse transcription of R2Bm RNA is primed by a nick at the chromosomal target site: a mechanism for non-LTR retrotransposition. *Cell* 72, 595–605. doi: 10.1016/0092-8674(93)90078-5

Martin, S. L. (2006). The ORF1 protein encoded by LINE-1: structure and function during L1 retrotransposition. *J. Biomed. Biotechnol.* 2006, 45621. doi: 10.1155/JBB/2006/45621

Martin, S. L. (2010). Nucleic acid chaperone properties of ORF1p from the non-LTR retrotransposon, LINE-1. *RNA Biol.* 7, 706–711. doi: 10.4161/rna.7.6.13766

Martin, S. L., Bushman, D., Wang, F., Li, P. W., Walker, A., Cummiskey, J., et al. (2008). A single amino acid substitution in ORF1 dramatically decreases L1 retrotransposition and provides insight into nucleic acid chaperone activity. *Nucleic Acids Res.* 36, 5845–5854. doi: 10.1093/nar/gkn554

Mita, P., Sun, X., Fenyö, D., Kahler, D. J., Li, D., Agmon, N., et al. (2020). BRCA1 and S phase DNA repair pathways restrict LINE-1 retrotransposition in human cells. *Nat. Struct. Mol. Biol.* 27, 179–191. doi: 10.1038/s41594-020-0374-z

Newkirk, S. J., Lee, S., Grandi, F. C., Gaysinskaya, V., Rosser, J. M., Vanden Berg, N., et al. (2017). Intact piRNA pathway prevents L1 mobilization in male meiosis. *Proc. Natl. Acad. Sci. U. S. A.* 114, E5635–E5644. doi: 10.1073/pnas.1701069114

Obbard, D. J., Gordon, K. H., Buck, A. H., and Jiggins, F. M. (2009). The evolution of RNAi as a defence against viruses and transposable elements. *Philos. Trans. R. Soc. Lond. B. Biol. Sci.* 364, 99–115. doi: 10.1098/rstb.2008.0168

Richardson, S. R., Doucet, A. J., Kopera, H. C., Moldovan, J. B., Garcia-Perez, J. L., and Moran, J. V. (2015). The influence of LINE-1 and SINE retrotransposons on mammalian genomes. *Microbiol. Spectrum* 3, MDNA3–2014. doi: 10.1128/9781555819217.ch51

Saleh, A., Macia, A., and Muotri, A. R. (2019). Transposable elements, inflammation, and neurological disease. *Front. Neurol.* 10, 894. doi: 10.3389/fneur.2019.00894

Simon, M., Van Meter, M., Ablaeva, J., Ke, Z., Gonzalez, R. S., Taguchi, T., et al. (2019). LINE1 derepression in aged wild-type and SIRT6-deficient mice drives inflammation. Cell metabolism, 29, 871–885.e5. doi: 10.1016/j.cmet.2019.02.014

Taylor, M. S., LaCava, J., Dai, L., Mita, P., Burns, K. H., Rout, M. P., et al. (2016). Characterization of L1-Ribonucleoprotein Particles. *Methods Mol. Biol.* 1400, 311–338. doi: 10.1007/978-1-4939-3372-3_20

Taylor, M. S., LaCava, J., Mita, P., Molloy, K. R., Huang, C. R., Li, D., et al. (2013). Affinity proteomics reveals human host factors implicated in discrete stages of LINE-1 retrotransposition. *Cell* 155, 1034–1048. doi: 10.1016/j.cell.2013.10.021

Teixeira, F. K., Okuniewska, M., Malone, C. D., Coux, R. X., Rio, D. C., and Lehmann, R. (2017). piRNA-mediated regulation of transposon alternative splicing in the soma and germ line. *Nature* 552, 268–272. doi: 10.1038/nature25018

Tunbak, H., Enriquez-Gasca, R., Tie, C., Gould, P. A., Mlcochova, P., Gupta, R. K., et al. (2020). The HUSH complex is a gatekeeper of type I interferon through epigenetic regulation of LINE-1s. *Nat. Commun.* 11, 5387. doi: 10.1038/s41467-020-19170-5

Volkman, H. E., and Stetson, D. B. (2014). The enemy within: endogenous retroelements and autoimmune disease. *Nat. Immunol.* 15, 415–422. doi: 10.1038/ni.2872

Wang, T., Li, F., Geng, W., Ruan, Q., and Shi, W. (2017). MicroRNA-122 ameliorates corneal allograft rejection through the downregulation of its target CPEB1. *Cell Death Discov.* 3, 17021. doi: 10.1038/cddiscovery.2017.46

Xie, Y., Rosser, J. M., Thompson, T. L., Boeke, J. D., and An, W. (2011). Characterization of L1 retrotransposition with high-throughput dual-luciferase assays. *Nucleic Acids Res.* 39, e16. doi: 10.1093/nar/gkq1076

Yu, Q., Carbone, C. J., Katlinskaya, Y. V., Zheng, H., Zheng, K., Luo, M., et al. (2015). Type I interferon controls propagation of long interspersed element-1. *J. Biol. Chem.* 290, 10191–10199. doi: 10.1074/jbc.M114.612374

Zang, R., Lian, H., Zhong, X., Yang, Q., and Shu, H. B. (2020). ZCCHC3 modulates TLR3-mediated signaling by promoting recruitment of TRIF to TLR3. *J. Mol. Cell Biol.* 12, 251–262 doi: 10.1093/jmcb/mjaa004

Zhao, K., Du, J., Peng, Y., Li, P., Wang, S., Wang, Y., et al. (2018). LINE1 contributes to autoimmunity through both RIG-I- and MDA5-mediated RNA sensing pathways. *J. Autoimmun.* 90, 105–115. doi: 10.1016/j.jaut.2018.02.007

Zheng, X., Sun, Z., Yu, L., Shi, D., Zhu, M., Yao, H., et al. (2021). Interactome analysis of the nucleocapsid protein of SARS-CoV-2 virus. *Pathogens* 10, 1155. doi: 10.3390/pathogens10091155

Frontiers in Microbiology

Explores the habitable world and the potential of microbial life

The largest and most cited microbiology journal which advances our understanding of the role microbes play in addressing global challenges such as healthcare, food security, and climate change.

Discover the latest Research Topics

See more →

Frontiers

Avenue du Tribunal-Fédéral 34
1005 Lausanne, Switzerland
frontiersin.org

Contact us

+41 (0)21 510 17 00
frontiersin.org/about/contact